

For Reference

NOT TO BE TAKEN FROM THIS ROOM

Ex libris
UNIVERSITATIS
ALBERTAENSIS



T H E U N I V E R S I T Y O F A L B E R T A

RELEASE FORM

NAME OF AUTHOR PETER J. CATANIA
TITLE OF THESIS STABLE AND UNSTABLE
 CONVERGING FLOWS OF
 VISCOELASTIC FLUIDS

DEGREE FOR WHICH THESIS WAS PRESENTED Ph.D.

YEAR THIS DEGREE GRANTED 1977

Permission is hereby granted to THE
UNIVERSITY OF ALBERTA LIBRARY to reproduce single
copies of this thesis and to lend or sell such
copies for private, scholarly or scientific
research purposes only.

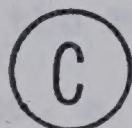
The author reserves other publication
rights, and neither the thesis nor extensive
extracts from it may be printed or otherwise
reproduced without the author's written
permission.

DATED August, 1977

THE UNIVERSITY OF ALBERTA

STABLE AND UNSTABLE CONVERGING FLOWS OF
VISCOELASTIC FLUIDS

by



PETER J. CATANIA

A THESIS

SUBMITTED TO THE FACULTY OF GRADUATE STUDIES AND RESEARCH
IN PARTIAL FULFILMENT OF THE REQUIREMENTS FOR THE DEGREE
OF DOCTOR OF PHILOSOPHY

IN

CHEMICAL ENGINEERING

DEPARTMENT OF CHEMICAL ENGINEERING

EDMONTON, ALBERTA

FALL, 1977

THE UNIVERSITY OF ALBERTA
FACULTY OF GRADUATE STUDIES AND RESEARCH

The undersigned certify that they have read, and
recommend to the Faculty of Graduate Studies and Research,
for acceptance, a thesis entitled STABLE AND UNSTABLE
COVERGING FLOWS OF VISCOELASTIC FLUIDS submitted by
PETER J. CATANIA in partial fulfilment of the requirements
for the degree of

Doctor of Philosophy

ABSTRACT

The objectives of this research were: (a) to measure and correlate axial velocities upstream of an abrupt contraction, (b) to describe the upstream flow field by measuring cone semi-angles and location of eddy centers, (c) to determine the effects of instability on the Bagley plots, the total pressure loss-flow rate curve and contraction losses, and (d) to present a criterion for the onset of fracture based on inlet conditions.

A flow visualization method was used to measure axial and radial velocities. Qualitative observations of the upstream flow field and the jet of fluid issuing from the capillary tube were obtained; pressure traces were measured at a pressure tap upstream of the contraction. The contraction losses and shear stresses for three aqueous sugar solutions, an oil Primol-355 and an 0.20 percent aqueous solution of Separan AP-30 were obtained from Bagley plots. The Newtonian solutions were used to establish the experimental accuracy.

The experimental results and conclusions are: Within region I, (a) a stable wine glass structured flow field was observed, (b) the axial velocities within the central accelerating core are represented by

$$v^* = \exp(-(Z^{**})^{1.4}) [1.0 + 0.4 \ln^2]^{-2.0}$$

(c) the radial velocity component at high flow rates or

small initial cone semi-angles, and for $r < D$ is negligible ($V_r < 0.15V_z$), (d) the initial cone semi-angles are represented by

$$\phi_0 = 19 \left(\frac{D^3}{\theta_0 Q} \right)^{0.60}$$

(e) as flow rate increases the location of the eddy centers progressively moves farther away from the contraction along a well defined path, (f) comparison of eddy centers at the same flow rate reveal that the eddy centers are located farther upstream in larger sized reservoirs, and (g) the pressure traces and the jet of fluid are smooth.

Within region II, the central core of fluid oscillated to and fro (swirling motion); the intensity and frequency of these oscillations increases with flow rate. There are no measurable changes in the pressure traces and on the jet of fluid.

Within region III, (a) the flow field is "chaotic", (b) the onset and magnitude of measurable pressure fluctuations, independent of L/D ratio, coincide reasonably with the visually observed onset of region III, (c) the jet of fluid oscillates with a frequency approximately equal to the frequency of the pressure fluctuations, (d) the oscillation of the flow field between stable and "chaotic" flows results in two Bagley plots, two values of the contraction losses, and a discontinuity in the total pressure loss-flow rate curve. The flow curve is unaffected by the onset of flow instabilities.

The dependence of contraction losses on capillary tube diameter, reservoir size, and Reynolds number can be explained in terms of the upstream flow field, i.e., stable, swirling, or "chaotic". It is incorrect to correlate contraction losses with Reynolds number when, over the same range of Reynolds numbers, the flow field changes from stable to "chaotic".

Hencky's strain measure, based on inlet conditions, suggests that the onset of flow instabilities (region II) commences at a flow rate given by

$$Q_c = 120.52 \left(\frac{n'+1}{3n'+1} \right)^2 \frac{D^3}{\theta_0}$$

At fixed fluid properties, this criterion qualitatively predicts the dependence of tube diameter on the onset of flow instabilities.

ACKNOWLEDGEMENT

This author acknowledges the financial assistance received from the National Research Council of Canada, and comments and suggestions from members of my advisory committee and external examiner, Dr. John Vlachopoulos. Appreciation is extended to Dr. Frederick A. Seyer, the author's advisor. His stimulating discussions and patience will not be forgotten. The cooperation and considerations received from members of the Faculty of Engineering, University of Regina are appreciated. In addition to the above, gratitude is expressed to the following individuals:

- a. Dr. B. Tinker, Vice-President, University of Regina
- b. Dr. E. Bilgen, Department of Mechanical Engineering, Ecole Polytechnique, Montreal, Quebec;
- c. Dr. Cliff Shook, Department of Chemistry and Chemical Engineering, University of Saskatchewan, Saskatoon, Saskatchewan.

The technical competence of Mr. Dave Wier of the Audio Visual Department and the excellent typing provided by Mrs. S. Phillips and Ms. L.C. Lockhart is appreciated.

This dissertation would not have been completed without the patience and moral support received from my family.

TABLE OF CONTENTS

	Page
LIST OF TABLES	xii
LIST OF FIGURES	xix
INTRODUCTION	xxv
I. REVIEW OF LITERATURE	1
1.1 Contraction Losses	1
1.1.1 Newtonian Fluids	1
1.1.2 Purely Viscous non-Newtonian Fluids	7
1.1.3 Viscoelastic Fluids	12
1.2 Instability	23
1.2.1 Capillary Initiation	26
1.2.2 Inlet Initiation	29
1.2.3 Effects of Entry Geometry and Capillary	33
1.2.4 Empirical Correlations - Prediction of Flow Instabilities	36
II. EXPERIMENTAL EQUIPMENT AND PROCEDURE	48
2.1 Experimental Equipment	48
2.1.1 Flow System	48
2.1.2 Entry Region	48
2.1.3 Capillary Tubes	50
2.2 Experimental Fluids and Tracer Particles .	53
2.2.1 Experimental Fluids	53
2.2.2 Tracer Particles	54
2.3 Photographic Methods	55
2.3.1 Optical System	55
2.3.2 Streak Photographs	59
2.3.3 Analysis of Streak Photographs - Digitizer Method	62
2.3.4 Analysis of Streak Photographs - Direct Method	69
2.4 Procedure	72
2.4.1 Preparation of Polymer	72
2.4.2 Data Collection	73
(i) Pressure	73
(ii) Velocity Distributions	78
(iii) Qualitative Observations ...	78

	Page
III. RESULTS AND DISCUSSION	80
3.1 Newtonian Fluids	80
3.1.1 Friction Factor - Reynolds Number	80
3.1.2 Contraction Losses	83
3.2 Viscoelastic Fluid	89
3.2.1 Friction Factor - Reynolds Number	89
3.2.2 Visual Observations	89
(i) Velocity Field Within Reservoir	91
(ii) Pressure Traces	95
(iii) Jet of Fluid	103
3.2.3 Criteria for Onset of Instability .	105
3.3 Effects of Instability	109
3.3.1 Bagley Plot	109
3.3.2 Flow Curve	112
3.3.3 Total Pressure Loss - Flow Rate Curve	113
3.3.4 Contraction Losses	117
3.4 Velocity Field Upstream of Contraction ...	123
3.4.1 Velocity - Digitizer and Direct Methods	123
3.4.2 Cone Angles	135
3.4.3 Eddy Centers	138
3.4.4 Core Velocities	141
(i) Sink Flow Model	146
(ii) K2 Model	151
(iii) Exponential Decay Model	157
(iv) Radial Dependence	181
3.5 Prediction of Instability	199
IV. CONCLUSIONS AND RECOMMENDATIONS	212
4.1 Conclusions	212
4.2 Recommendations	218
REFERENCES	220

APPENDICES

	Page
A. CALIBRATION	234
A.1 Pressure Transducers	235
A.2 Thrust Calibration	236
A.3 Cylinder and Instron Calibration	236
A.4 Normal Force Spring	237
A.5 Aluminum Dust Particles	237
 B. TOTAL PRESSURE LOSS - L/D DATA	 251
 C. CONTRACTION LOSSES	 283
C.1 Newtonian Fluids	284
C.2 Viscoelastic Solution	285
 D. PHYSICAL PROPERTIES	 294
D.1 Newtonian Fluids	295
D.2 Viscoelastic Solution	296
 E. VELOCITY PROFILES	 315
E.1 Axial Velocity Profiles - Direct Method ..	316
E.2 Axial and Radial Velocity Profiles - Digitizer Method	356
E.3 Mathematical Simplifications	419
E.4 Centerline Axial Velocities	427
E.5 Parameter r_0	436
 F. EDDY CENTERS AND CONE SEMI-ANGLES	 441
F.1 Eddy Centers	442
F.2 Cone Semi-Angles	450

	Page
G. ERROR ANALYSIS	456
G.1 Digitizer Method Error	457
G.2 Direct Method Error	466
G.3 Pressure Tranducers and Pressure Tap Error	466
H. NOMENCLATURE	471

LIST OF TABLES

	Page
1.1 Effect of L/D on Onset of Instability	35
1.2 Critical Shear Stress at Onset of Instability .	39
1.3 Recoverable Shear Strain at Onset of Instability	41
2.1 Internal Reservoir Dimensions	49
2.2 Capillary Tube Length to Diameter Ratios	49
2.3 Time Intervals for Streak Analysis	57
3.1 Estimated Standard Error (e.s.e.) for Newtonian Contraction Losses	86
3.2 Observations Within Regions I, II and III	104
3.3 τ_w and S_R at Onset of Instability	106
3.4 Flow Rates and Upstream Axial Locations Where Velocities Were Measured	124
3.5 Critical Extensional Stresses at Onset of Instability	201
3.6 Comparison of P_u with ΔP_c at Onset of Flow Instabilities	203
3.7 Critical Values of S (S_c)	208
A.1 Calibration of Transducer 1	239
A.2 Calibration of Transducer 2	242
A.3 Calibration of Transducer 3	244
A.4 Calibration of Transducer 4	246
A.5 Thrust Calibration	248
A.6 Calibration For Variable Speed Setting	248
B.1 Total Pressure Loss - L/D Data: Sugar Solution #1, 0.20 cm I.D. Capillary Tube, Small Reservoir	254
B.2 Total Pressure Loss - L/D Data: Sugar Solution #3, 0.20 cm I.D. Capillary Tube, Small Reservoir	255

B.3	Total Pressure Loss - L/D Data: Sugar Solution #4, 0.20 cm I.D. Capillary Tube, Small Reservoir ..	257
B.4	Total Pressure Loss - L/D Data: Primol-355 Oil, 0.20 cm I.D. Capillary Tube, Small Reservoir ..	258
B.5	Total Pressure Loss - L/D Data: Sugar Solution #1, 0.20 cm I.D. Capillary Tube, Large Reservoir	259
B.6	Total Pressure Loss - L/D Data: Sugar Solution #3, 0.20 cm I.D. Capillary Tube, Large Reservoir	260
B.7	Total Pressure Loss - L/D Data: Sugar Solution #4, 0.20 cm I.D. Capillary Tube, Large Reservoir	261
B.8	Total Pressure Loss - L/D Data: Primol-355 Oil, 0.20 cm I.D. Capillary Tube, Large Reservoir ...	262
B.9	Total Pressure Loss - L/D Data: 0.20% Separan AP-30, 0.10 cm I.D. Capillary Tube, Small Reservoir	263
B.10	Total Pressure Loss - L/D Data: 0.20% Separan AP-30, 0.20 cm I.D. Capillary Tube, Small Reservoir	266
B.11	Total Pressure Loss - L/D Data: 0.20% Separan AP-30, 0.30 cm I.D. Capillary Tube, Small Reservoir	268
B.12	Total Pressure Loss - L/D Data: 0.20% Separan AP-30, 0.10 cm I.D. Capillary Tube, Large Reservoir	271
B.13	Total Pressure Loss - L/D Data: 0.20% Separan AP-30, 0.20 cm I.D. Capillary Tube, Large Reservoir	274
B.14	Total Pressure Loss - L/D Data: 0.20% Separan AP-30, 0.30 cm I.D. Capillary Tube, Large Reservoir	277
C.1	Contraction Losses and Reynolds Numbers for Newtonian Fluids, Small Reservoir	287
C.2	Contraction Losses and Reynolds Numbers for Newtonian Fluids, Large Reservoir	288
C.3	Contraction Losses and Reynolds Numbers for 0.20% Separan AP-30, Small Reservoir	289

	Page
C.4 Contraction Losses and Reynolds Numbers for 0.20% Separan AP-30, Large Reservoir	291
D.1 Shear Stress - Shear Rate for Newtonian Solutions	300
D.2 Viscosity and Density, Newtonian Solutions	302
D.3 Physical Properties of 0.20% Separan AP-30; Batch 2 - Small Reservoir	303
D.4 Physical Properties of 0.20% Separan AP-30; Batch 1 - Large Reservoir	304
D.5 Normal Force Data	306
E.1 Axial Velocity Data, 0.10 cm I.D. Capillary, $Q = 0.016 \text{ cm}^3/\text{sec}$, Small Reservoir	318
E.2 Axial Velocity Data, 0.10 cm I.D. Capillary, $Q = 0.040 \text{ cm}^3/\text{sec}$, Small Reservoir	320
E.3 Axial Velocity Data, 0.10 cm I.D. Capillary, $Q = 0.119 \text{ cm}^3/\text{sec}$, Small Reservoir	323
E.4 Axial Velocity Data, 0.20 cm I.D. Capillary, $Q = 0.040 \text{ cm}^3/\text{sec}$, Small Reservoir	325
E.5 Axial Velocity Data, 0.20 cm I.D. Capillary, $Q = 0.238 \text{ cm}^3/\text{sec}$, Small Reservoir	327
E.6 Axial Velocity Data, 0.20 cm I.D. Capillary, $Q = 0.318 \text{ cm}^3/\text{sec}$, Small Reservoir	329
E.7 Axial Velocity Data, 0.30 cm I.D. Capillary, $Q = 0.040 \text{ cm}^3/\text{sec}$, Small Reservoir	332
E.8 Axial Velocity Data, 0.30 cm I.D. Capillary, $Q = 0.318 \text{ cm}^3/\text{sec}$, Small Reservoir	333
E.9 Axial Velocity Data, 0.30 cm I.D. Capillary, $Q = 0.635 \text{ cm}^3/\text{sec}$, Small Reservoir	335
E.10 Axial Velocity Data, 0.20 cm I.D. Capillary, $Q = 0.159 \text{ cm}^3/\text{sec}$, Large Reservoir	338

	Page
E.11 Axial Velocity Data, 0.20 cm I.D. Capillary, Q = 0.318 cm ³ /sec, Large Reservoir	340
E.12 Axial Velocity Data, 0.20 cm I.D. Capillary, Q = 0.794 cm ³ /sec, Large Reservoir	342
E.13 Axial Velocity Data, 0.20 cm I.D. Capillary, Q = 1.589 cm ³ /sec, Large Reservoir	345
E.14 Axial Velocity Data, 0.30 cm I.D. Capillary, Q = 0.318 cm ³ /sec, Large Reservoir	348
E.15 Axial Velocity Data, 0.30 cm I.D. Capillary, Q = 0.635 cm ³ /sec, Large Reservoir	350
E.16 Axial Velocity Data, 0.30 cm I.D. Capillary, Q = 1.589 cm ³ /sec, Large Reservoir	353
E.17 Radial Velocities - Digitizer Method, Q = 0.016 cm ³ /sec, 0.10 cm I.D. Capillary Tube, Small Reservoir	358
E.18 Radial Velocities - Digitizer Method, Q = 0.040 cm ³ /sec, 0.10 cm I.D. Capillary Tube, Small Reservoir	360
E.19 Radial Velocities - Digitizer Method, Q = 0.119 cm ³ /sec, 0.10 cm I.D. Capillary Tube, Small Reservoir	362
E.20 Radial Velocities - Digitizer Method, Q = 0.040 cm ³ /sec, 0.20 cm I.D. Capillary Tube, Small Reservoir	364
E.21 Radial and Axial Velocities - Digitizer Method, Q = 0.159 cm ³ /sec, 0.20 cm I.D. Capillary Tube, Small Reservoir	266
E.22 Radial Velocities - Digitizer Method, Q = 0.238 cm ³ /sec, 0.20 cm I.D. Capillary Tube, Small Reservoir	369

	Page
E.23 Radial Velocities - Digitizer Method, Q = 0.318 cm ³ /sec, 0.20 cm I.D. Capillary Tube, Small Reservoir	371
E.24 Radial Velocities - Digitizer Method, Q = 0.040 cm ³ /sec, 0.30 cm I.D. Capillary Tube, Small Reservoir	373
E.25 Radial and Axial Velocities - Digitizer Method, Q = 0.159 cm ³ /sec, 0.30 cm I.D. Capillary Tube, Small Reservoir	373
E.26 Radial Velocities - Digitizer Method, Q = 0.318 cm ³ /sec, 0.30 cm I.D. Capillary Tube, Small Reservoir	378
E.27 Radial Velocities - Digitizer Method, Q = 0.635 cm ³ /sec, 0.30 cm I.D. Capillary Tube, Small Reservoir	381
E.28 Radial and Axial Velocities - Digitizer Method, Q = 1.589 cm ³ /sec, 0.20 cm I.D. Capillary Tube, Large Reservoir	384
E.29 Radial and Axial Velocities - Digitizer Method, Q = 1.906 cm ³ /sec, 0.20 cm I.D. Capillary Tube, Large Reservoir	385
E.30 Radial and Axial Velocities - Digitizer Method, Q = 2.383 cm ³ /sec, 0.20 cm I.D. Capillary Tube, Large Reservoir	387
E.31 Radial and Axial Velocities - Digitizer Method, Q = 2.701 cm ³ /sec, 0.20 cm I.D. Capillary Tube, Large Reservoir	389
E.32 Radial and Axial Velocities - Digitizer Method, Q = 3.177 cm ³ /sec, 0.20 cm I.D. Capillary Tube, Large Reservoir	392
E.33 Radial and Axial Velocities - Digitizer Method, Q = 3.812 cm ³ /sec, 0.20 cm I.D. Capillary Tube, Large Reservoir	395

	Page
E.34 Radial and Axial Velocities - Digitizer Method, Q = 4.866 cm ³ /sec, 0.20 cm I.D. Capillary Tube, Large Reservoir	398
E.35 Radial and Axial Velocities - Digitizer Method, Q = 4.866 cm ³ /sec, 0.30 cm I.D. Capillary Tube, Large Reservoir	401
E.36 Radial and Axial Velocities - Digitizer Method, Q = 6.354 cm ³ /sec, 0.30 cm I.D. Capillary Tube, Large Reservoir	403
E.37 Radial and Axial Velocities - Digitizer Method, Q = 7.148 cm ³ /sec, 0.30 cm I.D. Capillary Tube, Large Reservoir	405
E.38 Radial and Axial Velocities - Digitizer Method, Q = 7.943 cm ³ /sec, 0.30 cm I.D. Capillary Tube, Large Reservoir	406
E.39 Radial and Axial Velocities - Digitizer Method, Q = 8.737 cm ³ /sec, 0.30 cm I.D. Capillary Tube, Large Reservoir	408
E.40 Axial and Radial Velocities - Digitizer Method, Q = 9.531 cm ³ /sec, 0.30 cm I.D. Capillary Tube, Large Reservoir	410
E.41 Axial and Radial Velocities - Digitizer Method, Q = 10.325 cm ³ /sec, 0.30 cm I.D. Capillary Tube, Large Reservoir	413
E.42 Axial and Radial Velocities - Digitizer Method, Q = 11.120 cm ³ /sec, 0.30 cm I.D. Capillary Tube, Large Reservoir	416
E.43 Shear Component of Deformation Rate Tensor	423
E.44 Centerline Axial Velocity at Contraction	428
E.45 Variation of Parameter r_0 with Reservoir Size, Capillary Tube I.D., Flow Rate, and Dimensionless Axial Position Z^{**}	437
F.1 Eddy Center Location, 0.10 cm I.D. Capillary, L/D = 55.08, Small Reservoir	443

	Page
F.2 Eddy Center Location, 0.20 cm I.D. Capillary, L/D = 54.96, Small Reservoir	444
F.3 Eddy Center Location, 0.30 cm I.D. Capillary, L/D = 55.04, Small Reservoir	445
F.4 Eddy Center Location, 0.10 cm I.D. Capillary, L/D = 55.08, Large Reservoir	446
F.5 Eddy Center Location, 0.20 cm I.D. Capillary, L/D = 54.96, Large Reservoir	447
F.6 Eddy Center Location, 0.30 cm I.D. Capillary, L/D = 55.04, Large Reservoir	448
F.7 Cone Semi-Angles, Small Reservoir	451
F.8 Cone Semi-Angles, Large Reservoir	453
G.1 Calibration of Digitizer	459

LIST OF FIGURES

		Page
1.1	Apparatus and Pressure Profile	2
1.2	Hagenbach Correction Factor vs. Flow Behavior Index	11
1.3	Couette Correction Factor vs. Flow Behavior Index	15
1.4	Velocity Flow Field for Viscoelastic Fluid ..	24
1.5	Reservoir Pressure as a Function of Volumetric Flow Rate at Onset of Fracture	28
2.1	Reservoir and Pressure Tap Location	51
2.2	Capillary Holding Device	52
2.3	Schematic of Optical System	56
2.4	Streak Photograph, 0.20 cm I.D., $Q = 0.318 \text{ cm}^3/\text{sec}$	60
2.5	Streak Photograph, 0.20 cm I.D., $Q = 0.040 \text{ cm}^3/\text{sec}$	61
2.6	Eddy Center Location, 0.30 cm I.D., $Q = 9.531 \text{ cm}^3/\text{sec}$	63
2.7	Schematic of Digitizer	64
2.8	Schematic of Streak Analysis	66
2.9	Direct Method; Streak Length Along Several Streamlines	70
2.10	Axial Velocity - Upstream Axial Position Plot	71
2.11	Transient - Steady State Pressure Displacement Trace for Primol-355 Oil	74
2.12	Transient - Steady State Pressure Displacement Trace for Sugar Solution No. 1	75
3.1	Bagley Plot- Newtonian Fluid; Low Reynolds Numbers	81

	Page
3.2 Bagley Plot - Newtonian Fluid	82
3.3 Friction Factor - Reynolds Numbers; Newtonian Solutions	84
3.4 Φ versus Reynolds Number for Newtonian Fluids	88
3.5 Friction Factor - Reynolds Number; 0.20% Separan AP-30	90
3.6 Regions of Flow Instabilities	94
3.7 Pressure Displacement Traces Within Region III	96
3.8 Pressure Fluctuations; 0.10 cm I.D., Small Reservoir	99
3.9 Pressure Fluctuations; 0.20 cm I.D., Small Reservoir	100
3.10 Pressure Fluctuations; 0.30 cm I.D., Small Reservoir	101
3.11 Bagley Plot - 0.20% Separan AP-30	110
3.12 Bagley Plot - 0.20% Separan AP-30; Effect of Flow Instability	111
3.13 Total Pressure Loss - Flow Rate Curve; 0.30 cm I.D. Capillary, Large Reservoir	114
3.14 Total Pressure Loss - Flow Rate Curve; 0.30 cm I.D. Capillary, Small Reservoir	115
3.15 Φ_t versus N'_{Re} - 0.20% Separan AP-30, Large Reservoir	118
3.16 Φ_t versus N'_{Re} - 0.20% Separan AP-30, Small Reservoir	119
3.17 Axial Velocity Profile - Digitizer Method, Large Reservoir, $z/D = 37.59$	127
3.18 Axial Velocity Profile - Digitizer Method, Large Reservoir, $z/D = 25.06$	128
3.19 Axial Velocity Profile - Digitizer Method, Large Reservoir, $z/D = 12.53$	129

	Page
3.20 Axial Velocity Profiles - 0.10 cm I.D., Direct Method, $Q = 0.119 \text{ cm}^3/\text{sec}$	131
3.21 Axial Velocity Profiles - 0.20 cm I.D., Direct Method, $Q = 0.318 \text{ cm}^3/\text{sec}$	132
3.22 Axial Velocity Profiles - 0.30 cm I.D., Direct Method, $Q = 0.318 \text{ cm}^3/\text{sec}$	133
3.23 Initial Cone Semi-Angles	136
3.24 Reservoir Effect on Upstream Cone Angle Development; $Q = 0.318 \text{ cm}^3/\text{sec}$	139
3.25 Reservoir Effect on Upstream Cone Angle Development; $Q = 0.238$ and $0.635 \text{ cm}^3/\text{sec}$	140
3.26 Location of Eddy Centers, 0.30 cm I.D., Small Reservoir	142
3.27 Centerline Velocity; Sink Flow Model	148
3.28 Centerline Stretch Rate; Sink Flow Model	150
3.29 Typical Centerline Axial Velocity; K2 Model; 0.30 cm I.D. Capillary	153
3.30 Typical Centerline Axial Velocity; K2 Model; 0.10 and 0.30 cm I.D. Capillaries	154
3.31 Typical Centerline Stretch Rate; K2 Model; 0.30 cm I.D. Capillary	155
3.32 Typical Centerline Stretch Rate; K2 Model; 0.10 and 0.30 cm I.D. Capillaries	156
3.33 Centerline Axial Velocity; Exponential Decay Model	160
3.34 Axial Centerline Velocity at Contraction versus Flow Rate	162
3.35 Axial Centerline Velocity at Contraction versus Q/A	164
3.36 v^* versus z^* ; 0.10 cm I.D. Capillary, Small Reservoir	169

	Page
3.37 V* versus Z*; 0.20 cm I.D. Capillary, Small Reservoir	170
3.38 V* versus Z*; 0.30 cm I.D. Capillary, Small Reservoir	171
3.39 V* versus Z*; 0.20 cm I.D. Capillary, Large Reservoir	172
3.40 V* versus Z*; 0.30 cm I.D. Capillary, Large Reservoir	173
3.41 b_1 versus $(\theta_0 Q/D^3)$	174
3.42 Axial Velocity (V*) versus Dimensionless Axial Position (Z**)	177
3.43 Typical Centerline Stretch Rates; Exponential Decay Model; 0.30 cm I.D. Capillary	179
3.44 Typical Centerline Stretch Rates; Exponential Decay Model; 0.10 cm I.D. Capillary	180
3.45 Typical Example of Constant Stretch Rate; 0.30 cm I.D., $Q = 0.318 \text{ cm}^3/\text{sec}$	182
3.46 Effect of Reservoir Size and Axial Position on r_0 ; 0.30 cm I.D. Capillary, $Q = 0.318 \text{ cm}^3/\text{sec}$	184
3.47 Effect of Reservoir Size and Axial Position on r_0 ; 0.20 cm I.D. Capillary $Q = 0.318 \text{ cm}^3/\text{sec}$	185
3.48 Radial Dependence of Axial Velocity; 0.10 cm I.D. Capillary ($L/D = 55.08$), Small Reservoir	187
3.49 Radial Dependence of Axial Velocity; 0.20 cm I.D. Capillary ($L/D = 54.96$), Small Reservoir	188
3.50 Radial Dependence of Axial Velocity, 0.30 cm I.D. Capillary ($L/D = 55.04$), Small Reservoir	189
3.51 Radial Dependence of Axial Velocity; 0.20 cm I.D. Capillary ($L/D = 54.96$), Large Reservoir	190
3.52 Radial Dependence of Axial Velocity, 0.30 cm I.D. Capillary ($L/D = 55.04$), Large Reservoir	191

	Page
3.53 Radial Dependence of Axial Velocity	194
3.54 Comparison of Axial Velocities for 0.20 cm I.D. Capillary, $Q = 0.318 \text{ cm}^3/\text{sec}$, Small Reservoir	195
3.55 Comparison of Axial Velocities for 0.30 cm I.D. Capillary, $Q = 1.589 \text{ cm}^3/\text{sec}$, Large Reservoir	197
3.56 Sensitivity of Flow Rate at Onset of Instability, S_c Criterion	210
A-1 Normal Force Spring Calibration	249
A-2 Size Distribution of Aluminum Dust Particles	250
B-1 Pressure Fluctuations; 0.10 cm I.D. Capillary, Large Reservoir	280
B-2 Pressure Fluctuations; 0.20 cm I.D. Capillary, Large Reservoir	281
B-3 Pressure Fluctuations; 0.30 cm I.D. Capillary, Large Reservoir	282
C-1 Pressure Profile and Bagley Plot	293
D-1 Newtonian Viscosities	308
D-2 Flow Curve - 0.20% Separan AP-30; High Apparent Shear Rates	309
D-3 Flow Curve - 0.20% Separan AP-30; Low Apparent Shear Rates	310
D-4 Apparent Viscosity - 0.20% Separan AP-30	311
D-5 Inertial Contribution to Normal Force (Rheogoniometer)	312
D-6 Normal Stress	313
D-7 Relaxation Time	314
E-1 Maximum Ratio $(V_r/V_z)_M$ 0.10 cm I.D. Small Reservoir	424

		Page
E-2	Maximum Ratio $(V_r/V_z)_M$, 0.20 cm I.D. Small Reservoir	425
E-3	Maximum Ratio $(V_r/V_z)_M$, 0.30 cm I.D. Small Reservoir	426
E-4	Axial Centerline Velocity; 0.10 cm I.D. (L/D = 55.08), Small Reservoir	429
E-5	Axial Centerline Velocity; 0.20 cm I.D. (L/D = 54.96), Small Reservoir	430
E-6	Axial Centerline Velocity; 0.30 cm I.D. (L/D = 55.04), Small Reservoir	431
E-7	Axial Centerline Velocity; 0.20 cm I.D. (L/D = 54.96), Large Reservoir (High Flow Rates)	432
E-8	Axial Centerline Velocity; 0.20 cm I.D. (L/D = 54.96), Large Reservoir (Low Flow Rates)	433
E-9	Axial Centerline Velocity; 0.30 cm I.D. (L/D = 55.04), Large Reservoir (High Flow Rates)	434
E-10	Axial Centerline Velocity; 0.30 cm I.D. (L/D = 55.04), Large Reservoir (Low Flow Rates)	435
F-1	Eddy Center Location	449
G-1	Flow Behavior at Pressure Tap	470

INTRODUCTION

The character of velocity fields of polymer melts and solutions is of considerable rheological importance and technological interest. Much time and effort have been spent by rheologists on developing experimental techniques to determine normal stresses of polymer melts and solutions, e.g., the rotational viscometer and capillary rheometer. The rotational viscometer is limited to low shear rates, whereas the latter is suitable for measuring normal stresses at high shear rates. Among the possible geometries for a capillary rheometer, the flow from a reservoir or pipe to a tube of small diameter has received considerable attention during the past decades. The flow at the entrance of a capillary, which is the main focus of this dissertation, is described as a converging accelerative flow. This converging accelerative flow is a particularly important one because of the wealth of data and experience derived from the use of capillary rheometers. Many industrially important processes such as the flow of a polymer melt into a die or spinneret, the drawing-down of a molten polymer fibre, sheet or tube are examples of this kind of flow.

The polymer process industry has long realized that the rate of production is limited by distortions in the extrudate (melt fracture) which is related to flow and stress fields in the entry region. Several onset criteria have been suggested. These criteria, based on correlations of melt fracture with rheologically relevant dimensionless or dimensional para-

meters, seem justified only on empirical grounds since the actual upstream flow field is complex. These correlations, if successful, do not constitute an explanation for the onset of fracture. It has been conjectured that the onset of these flow instabilities may be initiated either in the entry region ahead of the capillary tube or within the tube itself. It is not possible to state unequivocally that the initiation site is either one or the other. There is general agreement (27, 52, 132, 184) that: (a) the initiation site for melts exemplified by low density polyethylene (LDPE) melts and for several polymer solutions occurs within the entry region, and (b) the onset of melt fracture results in the breakdown of the characteristics "wine glass" flow field within the entry region. With high density polyethylene (HDPE) melts, the initiation site is believed to occur within the capillary tube (27, 130, 183). Explanations for melt fracture based on inlet conditions (59) have not been tested severely since details of the upstream velocity field are not well known.

In order that the design of processes involving polymer melts or solutions proceed on a sound engineering basis, a quantitative understanding of entrance flow is urgently needed. Based upon the aforementioned, the objectives of this research are:

1. To measure and correlate the velocity field within the accelerating region of flow upstream of a capillary entrance.

2. To determine the onset of flow instability as observed in the upstream velocity field, the pressure traces, and the jet of fluid.

3. To evaluate onset criteria based on inlet conditions and on steady laminar shear flow (SLSF) in the capillary tube.

4. To determine the effects of reservoir size and capillary tube length to diameter ratio on the onset of flow instabilities.

5. To determine the effects of instability on the contraction losses.

CHAPTER I

REVIEW OF LITERATURE

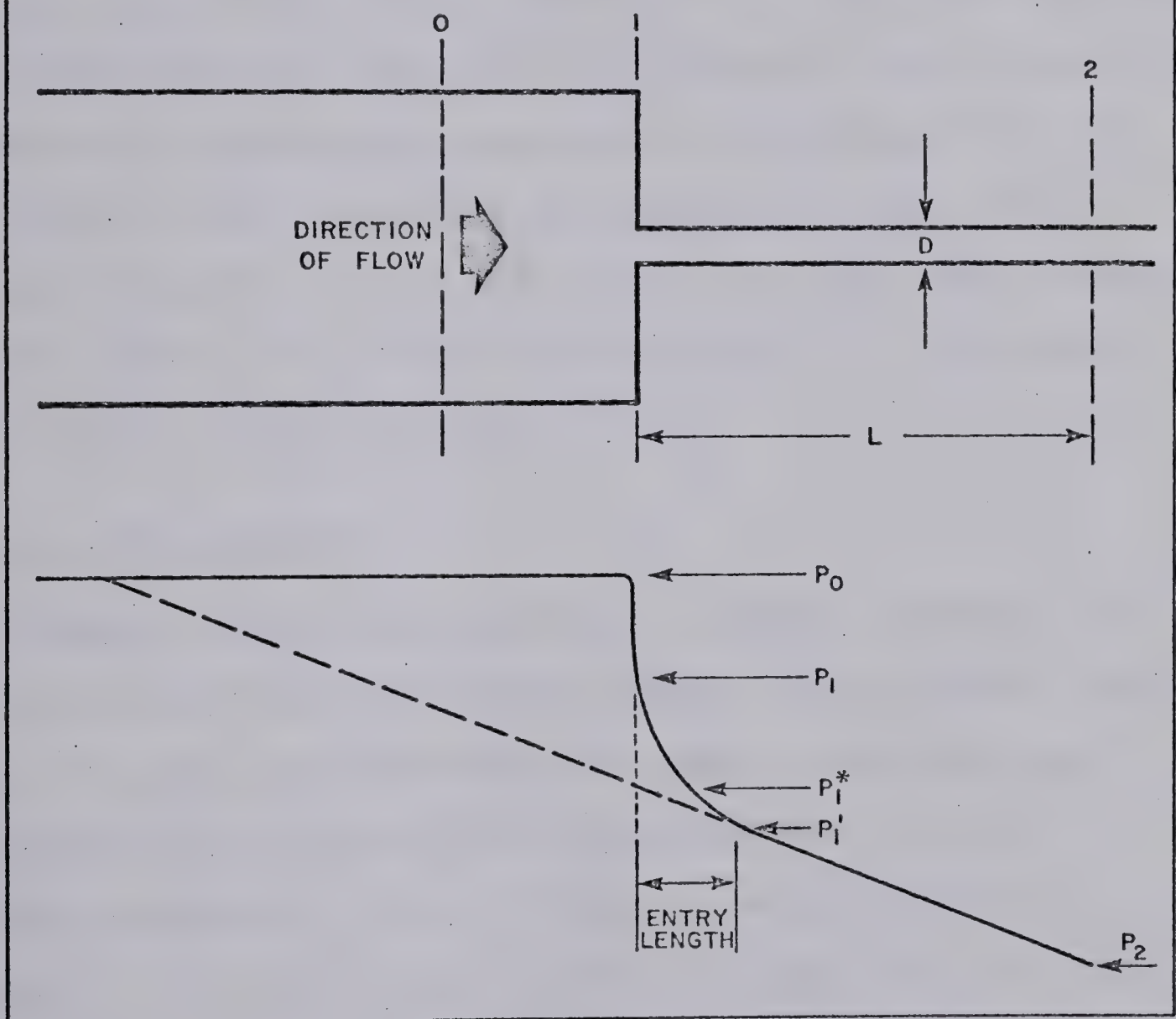
1.1 CONTRACTION LOSSES

The review deals with: (a) the analyses which have been developed to predict contraction losses, and (b) the comparison of contraction losses predicted through these analyses with experimental data for SLSF. The types of fluids considered are Newtonian and non-Newtonian. Non-Newtonian fluids, those whose shear stress is not linearly dependent upon the shear rate, can be classified into purely viscous and viscoelastic. With purely viscous non-Newtonian fluids the shear stress is a function only of the shear rate, whereas with the viscoelastic fluids there is a partial recovery of deformation upon the removal of the deforming stresses (131).

1.1.1 NEWTONIAN FLUIDS

When a fluid flows from a reservoir into a capillary tube the velocity distribution undergoes a change from some initial profile at the inlet of the capillary tube to a fully developed velocity distribution downstream. With reference to Figure 1.1, if fully developed flow existed from Section 2 up to the inlet, referred to as Section 1, the corresponding pressure loss, $P_1^* - P_2$, over the length, L , is given by the Hagen-Poiseuille law (20). This law

FIGURE 1.1
APPARATUS AND PRESSURE PROFILE



states that

$$\frac{P_1^* - P_2}{\rho V^2/2} = \frac{64}{N_{Re}} \frac{L}{D} \quad 1.1$$

where V is the average velocity in the capillary tube, D is the capillary tube internal diameter, N_{Re} is the capillary tube Reynolds number, and ρ is the fluid density.

The contraction losses, defined as $P_0 - P_1^*$, are comprised of: (a) the pressure loss due to frictional dissipation upstream of the contraction (assumed to be negligible), (b) the pressure loss due to the restriction in the cross-sectional area ($P_0 - P_1$), and (c) the pressure loss arising from the development of the velocity profile in the entry length of the capillary tube ($P_1 - P_1'$).

Inertial Contribution

Consider flows with significant inertial effects, i.e., capillary tube Reynolds numbers greater than 1000 but less than 2100 (161). By assuming: (a) negligible frictional dissipation upstream of the contraction (69), (b) an infinite reservoir, and (c) a flat velocity profile at Section 1, the macroscopic mechanical energy (ME) balance when applied between Sections 0 and 1 yields the relationship

$$\frac{P_0 - P_1}{\rho V^2/2} = 1.0 \quad 1.2$$

Hagenbach (69) assumed that the remaining pressure loss, $P_1 - P'_1$, was due to the change in kinetic energy arising from the development of a flat velocity profile at Section 1 to a fully developed parabolic profile downstream of the contraction. This results in

$$\frac{P_1 - P'_1}{\rho V^2/2} = 1.0 \quad 1.3$$

Overall, the contraction loss, Φ_H , is

$$\Phi_H = \frac{P_0 - P^*_1}{\rho V^2/2} = 2.0 \quad 1.4$$

Other theoretical analyses leading to predictions of Φ_H were summarized by Catania (38) and Sylvester (161). Values of Φ_H are reported to vary from 2.08 to 2.41 (26, 33, 35, 36, 45, 100, 148, 150, 167, 181) depending upon the analysis and the assumptions used. Therefore, contraction losses at high Reynolds numbers can be summarized as

$$\Phi_H = K' \quad 2.00 \leq K' \leq 2.41 \quad 1.5$$

where K' is the Hagenbach correction factor. If an infinite contraction is not assumed, then the average velocity at Section 0 is not negligible with respect to the average velocity in the capillary tube (Section 2). Based on kinetic energy considerations alone, the macroscopic ME balance, when applied between Sections 0 and 2, yields

$$\phi_H = 2.0 (1 - \beta^2) \quad 1.6$$

where β is the ratio of the capillary tube area to the reservoir area (93). Equation 1.6 reduces to Equation 1.4 when $\beta = 0$, i.e., an infinite reservoir. The development of Equation 1.6 assumes fully developed flow at Section 0 and negligible frictional dissipation upstream of the contraction (92). The latter assumption was indicated by observing that pressure gradients upstream of the contraction were negligible, as a first approximation, compared to pressure gradients downstream of the contraction (4).

Kaye and Rosen (93), using a 0.409 inch I.D. capillary tube, experimentally measured the contraction losses through a sharp edged contraction for values of β that ranged from 0.026 to 0.636. The data were represented by

$$\phi_H = (2.32 \pm .05) (1 - \beta^2) \quad 1.7$$

Over a wide range of values of β and for geometries other than a sharp edged contraction, experimental results, with one exception (4), can be summarized as Equation 1.8 (6, 59, 96, 97, 161)

$$\phi_H = (2.26 \pm .26) (1 - \beta^2) \quad 1.8$$

Astarita (4) reported a Hagenbach correction factor of 5.48. This large value could be the result of a vena contracta observed in the pressure profiles along the capillary tube which has not been taken into account in Equation 1.7.

This points to a limitation of the preceding analyses - overlooking the existence of a vena contracta and the associated entry losses.

Viscous Contribution

The equations of motion were solved numerically for flow through a sharp edged contraction and for Reynolds numbers less than 200 (180). The predicted contraction losses are represented by

$$\phi_c = \frac{K(N_{Re}, \beta)}{N_{Re}} \quad 1.9$$

where $K(N_{Re}, \beta)$ is the Couette correction factor. With contraction ratios less than 0.25 (36, 180) and under creeping flow conditions, $N_{Re} \ll 1.0$, the Couette correction factor is predicted to be constant. The particular value for this constant depends upon the geometry, the assumptions, and the analysis (40, 86, 127, 145, 146, 164, 185), hence, the value may range from 14.52 to 47.9. Experimentally determined Couette correction factors are reported to vary from 24.0 to 37.3 (28, 30, 40, 102) which agree with the theoretical analyses.

At capillary tube Reynolds numbers between 5 and 100, the experimentally measured contraction losses (4, 93, 162) are greater than those obtained from numerical analyses (36, 180). This difference may be the result of larger circulative flow in the corners of the reservoir. Kaye and Rosen (93) suggested that the Couette correction factor may be

expressed as

$$\phi_c = (159 \pm 30) (1 - \beta^2) \quad 1.10$$

This dependence of the Couette correction factor on the contraction ratio is in agreement with the analysis presented by Vrentas and Duda (180).

Over the complete range of Reynolds numbers, Holmes (84) stated that the results can be cast into the form

$$\phi = \phi_H + \phi_c \quad 1.11$$

or

$$\phi = K'(\beta) + \frac{K(N_{Re}, \beta)}{N_{Re}} \quad 1.12$$

The Hagenbach and Couette factors are given by Equations 1.8 and 1.10 respectively. It must be pointed out that Equation 1.12 was not obtained theoretically, i.e., it is not a solution to the equations of motion for laminar flow of a Newtonian fluid through a sharp edged sudden contraction. The merit of Equation 1.12 is that it can correlate experimental data (93, 154, 161) over a wide range of Reynolds numbers.

1.1.2 PURELY VISCOUS NON-NEWTONIAN FLUID

A simple viscous model that gives good representation of shear behavior for purely viscous non-Newtonian fluids is the power law represented by Equation 1.13 (113)

$$\tau_w = \frac{D\Delta P}{4L} = K_0 \left(\frac{8V}{D} \right)^{n'} \quad 1.13$$

where K_0 and n' are taken as constants. K_0 and n' are obtained from capillary viscometer data as

$$n' = d(\log \tau_w) / d(\log (\frac{8V}{D})) \quad 1.14$$

$$K_0 = \tau_w / (\frac{8V}{D})^{n'} \quad 1.15$$

Here, τ_w is the shear stress evaluated at the capillary tube wall under SLSF and $8V/D$ or $\dot{\gamma}$ is the apparent shear rate. The capillary wall shear rate is obtained from

$$\dot{\gamma}_w \equiv (-\frac{dv_z}{dr})_w = \frac{3n'+1}{4n'} (\frac{8V}{D}) \quad 1.16$$

The power law model predicts that shear stress has a linear relationship with apparent shear rate when plotted on log-log coordinates. Many fluids approximate this behavior over a range of one decade in apparent shear rate but show significant curvature over wider ranges. Hence, compared with Newtonian fluids, the non-Newtonian fluids cannot be characterized simply by one rheological parameter such as viscosity.

Dimensional analysis (13) suggests that the Hagenbach and Couette correction factors depend upon the flow behavior index. Therefore,

$$\phi = K'(\beta, n') + \frac{K(N'_{Re}, \beta, n')}{N'_{Re}} \quad 1.17$$

where the Newtonian Reynolds number has been replaced by the generalized Reynolds number, N'_{Re} . This was defined by

Metzner and Reed (113) as

$$N'_{Re} = \frac{D^{n'} V^{2-n'} \rho}{K_0 8^{n'-1}} \quad 1.18$$

and was developed in the following manner: In SLSF through a circular tube, the friction factor, f , is given by Equation 1.19 (20)

$$f = \tau_w / (\rho V^2 / 2) \quad 1.19$$

The substitution of τ_w from Equation 1.13 into 1.19 gives

$$f = \frac{16K_0 8^{n'-1}}{\rho D^{n'} V^{2-n'}} \quad 1.20$$

For Newtonian fluids in laminar flow the friction factor and Reynolds number are related by

$$f = 16/N_{Re} \quad 1.21$$

The generalized Reynolds number is obtained by equating Equation 1.20 and 1.21. Therefore, all fluids whose shear behavior is represented by a power law model must follow the usual f versus N'_{Re} relationship in the laminar flow region when use is made of the generalized Reynolds number.

The dependence of the Hagenbach and Couette correction factors on the flow behavior index has been predicted by several authors for an infinite reservoir, assuming a flat velocity profile at the contraction (26, 36, 41, 45, 165).

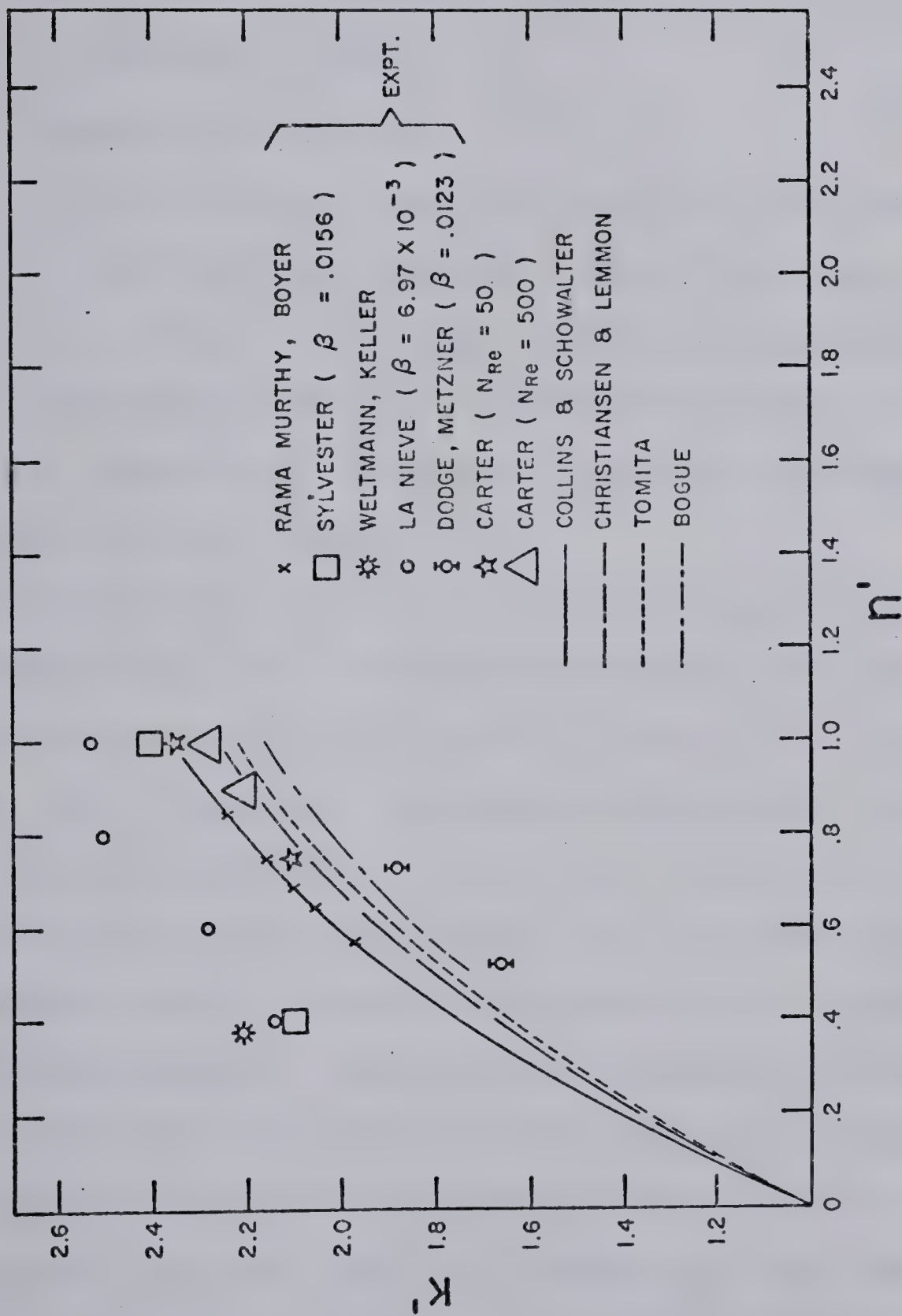
A comparison between these predictions and experimental data is shown in Figure 1.2 for the Hagenbach correction factor with the flow behavior indices being less than unity. Overall, the Hagenbach correction factor, and hence the contraction losses, are predicted to be less than the value for Newtonian fluids ($n' = 1.0$). The relatively large differences between predicted and experimental values of K' is partially attributed to the elastic nature of the experimental fluids. The effect of elasticity, as will be explained in the next section, is an increase in contraction losses at a given Reynolds number. The dependence of K' on the flow behavior index proposed by Collins and Schowalter (45) has been experimentally verified for $0.585 \leq n' \leq 1.00$ and $20 \leq N'_{Re} \leq 1942$ in a 2 to 1 contraction (144) and is in reasonable agreement with experimental results reported by Dodge and Metzner (55). For flow behavior indices less than unity, contraction losses can be represented, therefore, by

$$\Phi_H = K'(\beta, n') = f(n')(1 - \beta^2) \quad 1.22$$

where $f(n')$ is given by Collins and Schowalter (45).

The dependence of the Couette correction factor on the flow behavior index for $N'_{Re} \ll 1.0$, proposed by Tomita (165), was modified by Boles and Bogue (29) and for infinite contraction ratios is given by Equation 1.23 on page 12.

FIGURE 1.2
HAGENBACH CORRECTION FACTOR VS. FLOW BEHAVIOR INDEX



$$\phi_c = \frac{18.88}{(n')^{0.7} N'_{Re}} \quad 1.23$$

To account for finite contraction ratios, Equation 1.23 is modified by the multiplication factor $(1 - \beta^2)$, as is the case for Newtonian fluids.

1.1.3 VISCOELASTIC FLUIDS

For many polymer melts contraction losses were measured at capillary tube Reynolds numbers less than 10^{-3} (22, 30, 73, 102). Contraction losses with polymer solutions, although measured at high Reynolds numbers (5, 144, 154, 161), support the conclusions that can be drawn from data obtained with polymer melts.

A viscoelastic fluid with the same shear stress-shear rate behavior in SLSF but characterized by different elastic properties may result in different values of the contraction losses, ΔP_c . Therefore, the Couette correction may depend upon the elastic nature of the fluid. At a fixed value of β ($\beta = 0.1616$), Astarita, Greco, and Peluso (5) measured contraction losses for several concentrations of Separan ET-597 and Carbopol. For each concentration the flow behavior index, n' , was constant over the range of apparent shear rates where contraction losses were measured. Furthermore, log-log plots of ϕ versus N'_{Re} were linearly related with a slope equal to -1.0. They concluded that the Couette correction factor may be a unique function of the flow behavior index. Unfortunately, the data

for the highly elastic fluids (Separan ET-597) and for the weakly elastic fluids (Carbopol) overlapped only over a limited range of n' (Figure 1.3). This left open the question of whether elastic effects would result in a family of curves relating the Couette correction factor to the flow behavior index. This question was partially resolved by Sylvester (161) who measured contraction losses at a fixed β ($\beta = 0.0156$) and for several concentrations of three different polymers. These polymers were Separan AP-30, Polyox, and CMC and each had a flow behavior index approximately equal to 0.40. The Couette correction factors, plotted in Figure 1.3, ranged from 185 for the weakly elastic Polyox solutions to 490 for the highly elastic Separan AP-30 solutions. The results substantiated the claim that fluids having the same shear stress-shear rate behavior but different elastic properties result in different values of ΔP_c .

Since contraction losses are dependent upon the nature of the flow field in the entry region and since polymer rheology affects the flow field in the entry region, we cannot separate polymer rheology and geometry for viscoelastic fluids as implied by Han (72).

Prediction and Measurement of Contraction Losses

A method widely used to measure contraction losses is the Philippoff-Gaskins analysis (3, 30, 58, 95, 103, 137).

LEGEND FOR FIGURE 1.3









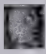
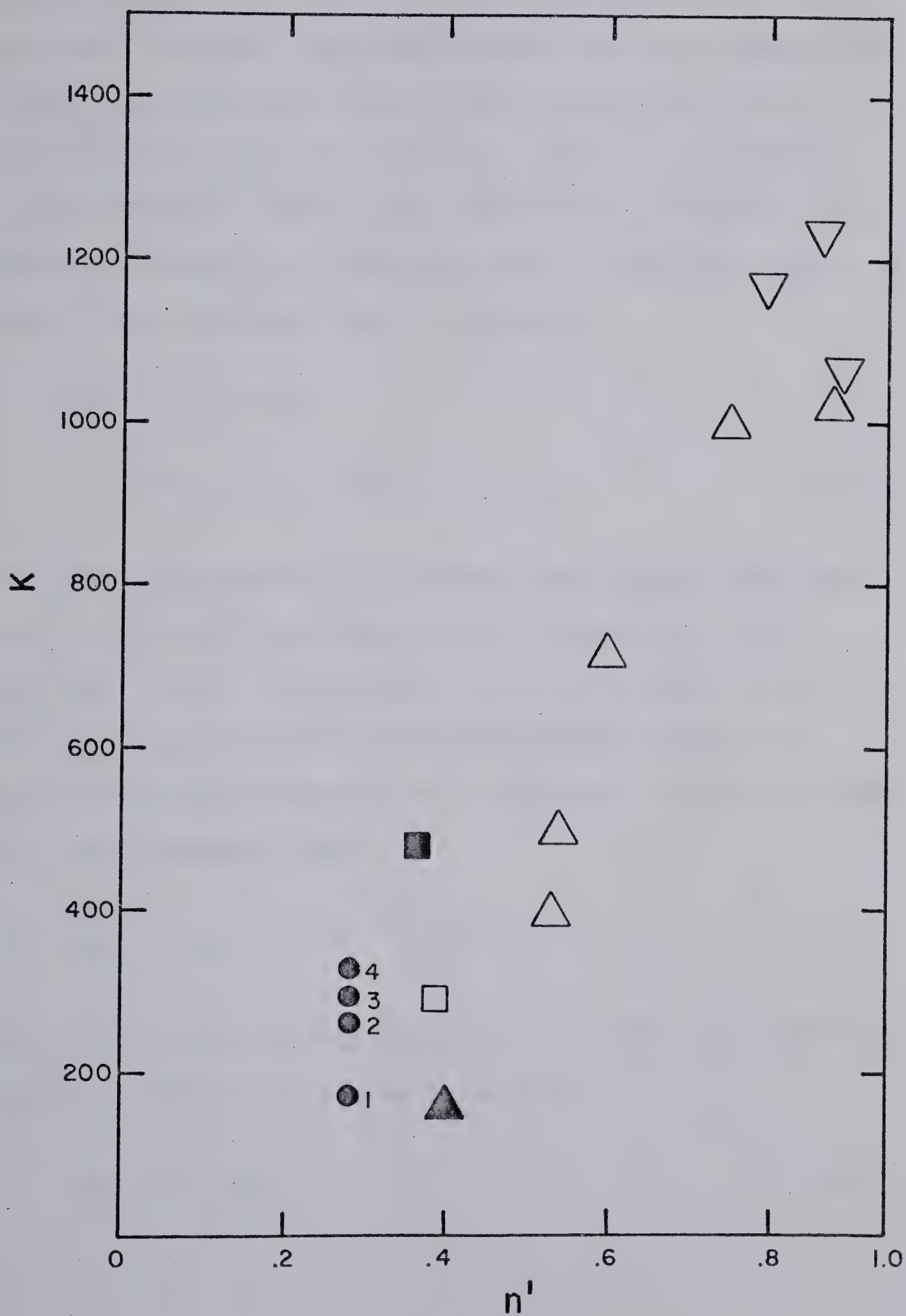
<u>SYMBOL</u>	<u>AUTHOR</u>	<u>POLYMER</u>	<u>β</u>
	Astarita et al.	ET-597	.1616
	Astarita et al.	Carbopol	.1616
	Han	HDPE	.0069
	Han	HDPE	.0123
	Han	HDPE	.0277
	Han	HDPE	.1111
	Sylvester	Polyox	.0156
	Sylvester	CMC	.0156
	Sylvester	Separan	.0156

FIGURE 1.3
COUETTE CORRECTION FACTOR
vs.
FLOW BEHAVIOR INDEX



This analysis was modified by Bagley (8) in order to separate the viscous and elastic contribution of the overall contraction losses and shall be referred henceforth as the PGB analysis. The PGB analysis assumes that the contraction losses can be represented as an additional length of the capillary tube in the developed flow regime, $\epsilon_v D$, where ϵ_v is an end correction factor (8). The total pressure loss, ΔP_t , measured from a position upstream of the contraction to the end of the capillary tube is given as

$$\begin{aligned}\Delta P_t &= \Delta P_d + \Delta P_c \\ &= \Delta P_d + \Delta P_v + \Delta P_e\end{aligned}\tag{1.24}$$

where ΔP_d is the pressure loss under SLSF within the capillary tube, ΔP_v is the fraction of the contraction loss arising from viscous dissipation, and ΔP_e is the remaining fraction arising from the elastic nature of the fluid. Exit pressures are assumed to be negligible. Philippoff and Gaskins (137) assumed that

$$\Delta P_e = \tau_w S_R\tag{1.25}$$

where S_R is the recoverable shear strain. The substitution of Equation 1.25 into Equation 1.24 with

$$\Delta P_d = 4\tau_w L/D\tag{1.26}$$

and

$$\Delta P_v = 4\tau_w \epsilon_v \quad 1.27$$

yields

$$\Delta P_t = 4\tau_w \left(\frac{L}{D} + \epsilon_v + S_R/4 \right) \quad 1.28$$

A plot of ΔP_t versus L/D at a fixed shear rate (Bagley plot) gives a line with slope equal to $4\tau_w$ and an intercept of

$$\Delta P_c = 4\tau_w (\epsilon_v + S_R/4) \quad 1.29$$

Bagley (8) extended this analysis by using Hooke's law (Equation 1.30)

$$\tau_w = G S_R \quad 1.30$$

where G is the elastic modulus. Therefore, for visco-elastic fluids the contraction losses can be represented as

$$\begin{aligned} \Delta P_c &= \Delta P_v + \Delta P_e \\ &= 4\tau_w \epsilon_v + \tau_w^2 / G \end{aligned} \quad 1.31$$

If a power law model (1.13) is assumed, Equation 1.31 becomes

$$\Delta P_c = 4\epsilon_v K_0 \dot{\gamma}^{n'} + \left(\frac{K_0^2}{G} \right) \dot{\gamma}^{2m} \quad 1.32$$

where m is assumed to be equal to n' and $\dot{\gamma}$ is the apparent shear rate in the capillary tube in SLSF. The exponent, $2m$, appearing in Equation 1.32, is the same as that which appears in the relationship of the normal stresses with

apparent shear rate (27)

$$(P_{11} - P_{22})_w = K_1 \dot{\gamma}^{2m} \quad 1.33$$

Variations of either Equation 1.31 or 1.32 have been reported in the literature (72, 102, 161, 169).

The prediction of ΔP_e using the PGB analysis, Equation 1.31 or 1.32, is questionable since Hooke's law is not valid over a wide range of fluids and shear rates. Hooke's law is valid only when the flow behavior index, n' , is equal to the exponent, m , and G is equal to K_0^2/K_1 . This can be shown by writing Equation 1.30 as

$$\tau_w = GS_R = \frac{G(P_{11} - P_{22})_w}{\tau_w} = \frac{GK_1 \dot{\gamma}^{2m-n'}}{K_0} \quad 1.34$$

However, the Bagley plots are useful in determining the total contraction losses and is a preferred method whenever capillary tube diameters are small. It is preferred because of experimental difficulty in ensuring that burrs at each pressure tap are removed when small diameter capillary tubes are used to obtain pressure profiles. Furthermore, even if the burrs were removed the presence of a pressure tap alters the velocity field in the immediate vicinity of the tap (73, 79, 126, 163). This gives rise to pressure tap errors as large as 40% of the primary normal stress difference.

An empirical correlation of ΔP_e with the primary normal

stress difference in SLSF in the capillary tube was presented by LaNieve and Bogue (102). After subtracting the viscous contribution, as estimated by Weissberg's analysis (185), they correlated the experimentally measured contraction losses with the primary normal stress difference by Equation 1.35.

$$\Delta P_e = \alpha_3(m, \beta) (P_{11} - P_{22})_w. \quad 1.35$$

The proportionality constant, α_3 , is empirically related to the exponent, m , and the contraction ratio, β . Therefore, LaNieve and Bogue's results can be rewritten as

$$\Delta P_e = \alpha_3(m, \beta) K_1 \dot{\gamma}^{2m} \quad 1.36$$

Equation 1.36 is equivalent to the second term in Equation 1.32 when $m=n'$ and

$$\alpha_3(m, \beta) K_1 = K_0^2 / G \quad 1.37$$

Metzner et al. (116) presented an analysis whereby ΔP_e was not only predicted independent of Hooke's law but was based on flow conditions within the entry region (prior to the contraction). These authors used a momentum balance to show that the contraction losses, ΔP_e , at high Reynolds numbers are equal to the primary normal stress difference evaluated at the contraction. This primary normal stress difference can be related to measurable physical properties in SLSF in the capillary tube provided

the kinematics upstream of the contraction and a constitutive equation are available.

Uebler's (173) analysis of the velocity field within two diameters of the contraction suggested that, as a first approximation, the flow is radially directed towards the origin of a spherical coordinate system. The origin is located downstream within the capillary tube at a point determined by the extrapolation of the streamlines. This gave rise to kinematics referred to as sink flow kinematics (90). By using sink flow kinematics and a convective Maxwell model (116), the primary normal stresses at the contraction are found to be proportional to the shear stresses evaluated at the capillary tube wall under SLSF. Therefore,

$$\Delta P_e = \alpha_1 (r_\infty) \tau_w \quad 1.38$$

where α_1 is related to a constant r_∞ . This constant enters into the analysis in order to satisfy the boundary condition whereby the primary normal stresses tend to zero at sufficiently large values of r , i.e., $r = r_\infty$. As pointed out by Metzner et al. (116):

Quantitative assessment of the prediction of the analysis, for elongational flow described by the kinematics ... are hindered by the form of the result ... which contains two parameters that are not known precisely in most cases.

The two parameters referred to above are α_1 and r_∞ .

Experimentally, log-log plots of ΔP_e versus τ_w do not re-

sult in a linear relationship as suggested by Equation 1.38 (72). In general, the PGB analysis (8, 137), the empirical correlation of ΔP_e with the primary normal stress difference (102), the analysis of Metzner et al. (116), and experimental results (161, 72) suggest that

$$\Delta P_e = \beta_1 \tau_w + \beta_2 \tau_w^2 + \beta_3 \tau_w^3 + \dots \quad 1.39$$

where parameters β_1 , β_2 , β_3 , etc. are evaluated experimentally.

The sink flow kinematics used by Metzner et al. (116) does not allow for the existence of shear within the converging flow region that was observed in the stress-birefringent patterns (30, 63). The use of this kinematics has been made questionable also by the analyses of the photographs of the flow field in the entry region (24, 130, 140, 142). These photographs show that shear exists within the converging region and the streamlines are not radially directed toward the origin of a spherical coordinate system, except for the immediate vicinity of the contraction. Furthermore, Cogswell (46) and Boger and Rama Murthy (24) measured velocities at the edge of the converging stream of the order 10% of the centerline velocity which is not approximately equal to the centerline velocity as measured by Uebler (173). More recently, Nakamura et al. (123) presented experimental evidence which shows clearly that the axial velocities measured within 1.5 diameters upstream and

for values of $r \leq 0.275D$ are dependent on radial position. For example, at 0.50 tube diameters upstream the axial velocity at $r = 0.275D$ is equal to 0.55 times the centerline axial velocity. The above experimental evidence does not negate Metzner et al.'s method but points out the need for a better description of the upstream velocity field within the accelerating flow region in order to predict contraction losses independent of Hooke's law.

Basically, two flow patterns have been visually observed in the entry region upstream of the contraction for polymer melts and solutions. These flow patterns are exemplified by considering a high density (linear) polyethylene melt (HDPE) and a low density (branched) polyethylene melt (LDPE). For HDPE (27, 132, 188), polybutadiene (176), and polypropylene (10, 47), the flow field is similar to that observed for Newtonian fluids in creeping flow (43). The fluid converges into the capillary through a 180° solid angle with a small recirculation in the corners of the reservoir. For LDPE (10, 12, 188), polymethyl methacrylate (12, 47), polystyrene (27, 188) and for several dilute polymer solutions (12, 67, 119, 142, 168, 116), the flow field is more complex. Under creeping flow conditions the flow field is similar to HDPE. Increasing the flow rate results in a flow field that is described as being "wine glass shaped" (WGS) (116, 173) and hereinafter is referred to as a stable flow field.

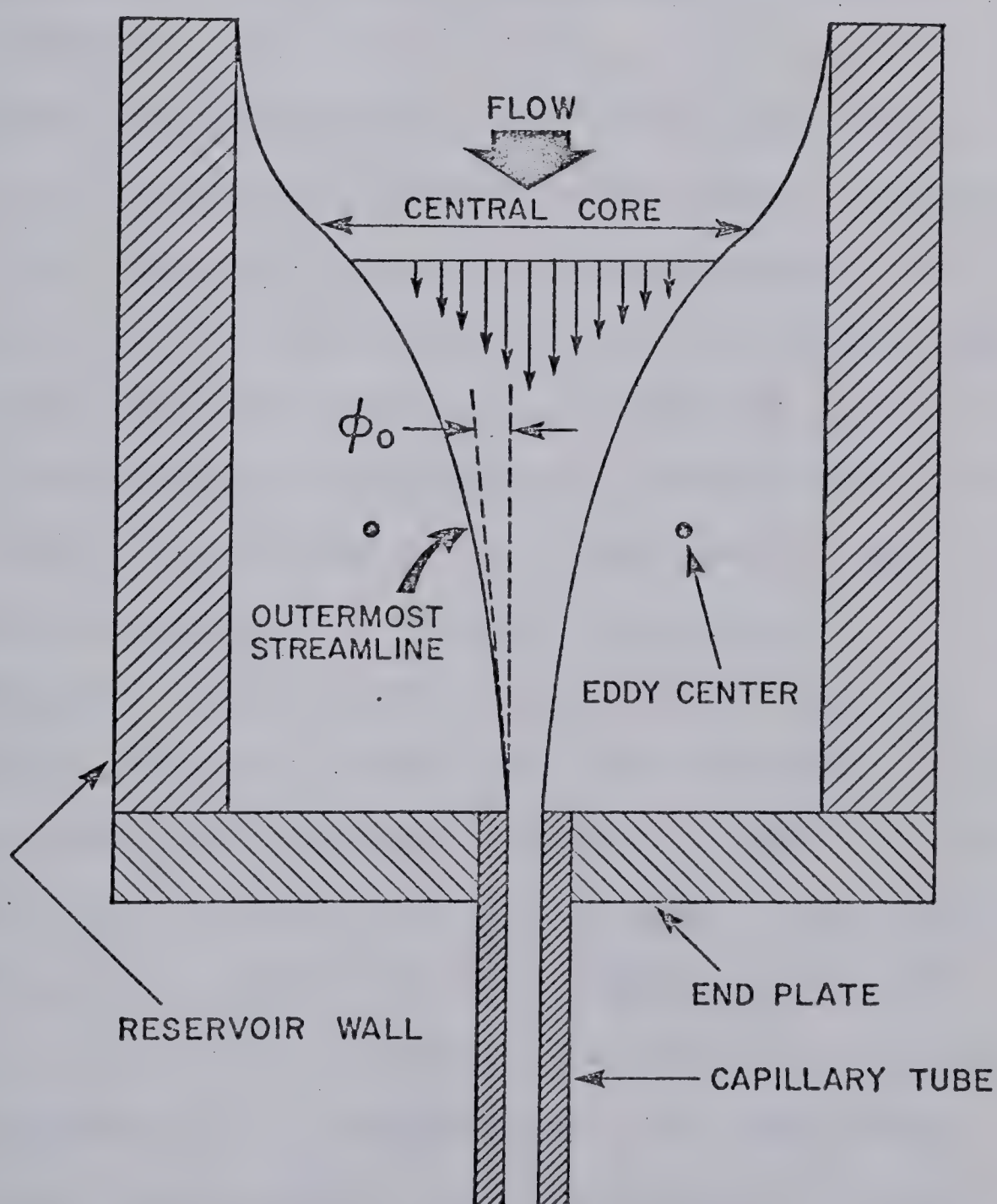
A qualitative description of the stable flow field

is shown in Figure 1.4. The fluid entering into the capillary tube is confined to a central core which extends upstream into the reservoir. This distance is dependent upon the contraction ratio, the flow rate, and the capillary tube diameter. The lengths of the arrows within the central core qualitatively represent the axial distances that a particle would traverse over a short time interval. Surrounding the central core are large eddies that extend up to the walls of the reservoir. The velocities within this region are significantly less than those within the central core. As the flow rate increases the location of the eddy centers move farther away from the contraction with the central core extending farther into the reservoir (50, 188). The tangent to the outermost streamline that enters into the capillary tube at the contraction defines an initial cone semi-angle, ϕ_0 . This initial cone semi-angle decreases with increasing shear rate (46, 47, 116, 129, 130) and elasticity (12, 44, 188). This suggests that the primary correlation quantity for ϕ_0 is $D^3/\theta_0 Q$. White and Kondo (188) have shown that other quantities such as $\frac{1}{2} \frac{(P_{11} - P_{22})_w}{\tau_w}$ and $\frac{\Delta P_c}{\tau_w}$ are derived from this primary correlation quantity.

1.2 INSTABILITY

As polymeric materials are extruded from a capillary tube at high flow rates, irregularities are noted in the extrudate. This phenomenon is known as melt fracture

FIGURE 1.4
VELOCITY FLOW FIELD
FOR VISCOELASTIC FLUID



(27, 177, 188), although it is best described as flow instability (12, 134). Bialas and White (19) extensively reviewed the distorted extrudates of various polymer melts and have categorized them into basically two types:

a. The extrudate has a screw thread-like appearance typical of HDPE.

b. The extrudate has an uneven swell and eventually a very severe distortion at high flow rates. This is typical of LDPE.

The distortions in the extrudate and in the flow field upstream of the contraction observed for polymer solutions (119, 130, 132, 143) are similar to those observed for LDPE melts (12, 188). Therefore, it can be inferred that the initiation site, the mechanisms causing the onset of fracture, and the effects of reservoir geometry and capillary tube length on the onset of melt fracture for LDPE should also be applicable to polymer solutions.

Experimental studies have been directed toward the determination of the initiation site for the onset of flow instabilities and the resulting features of the disturbed flow (12, 24, 53, 63, 130, 142). In general, the initiation site may occur within the inlet region (inlet type fracture) or within the capillary tube (capillary initiation). As pointed out by Rothenberger (149) and others (27, 134, 136) the initiation site itself may be a variable. Visual observations of changes in the velocity field within the reservoir (12, 24, 130, 132, 142) or within the

capillary tube (17, 53, 107) are used in determining the initiation site. Indirect methods such as the total pressure loss-flow rate curve referred to as the apparent shear stress-apparent shear rate curve (52, 53, 105, 120) and the flow curve referred to as true shear stress-apparent shear rate curve (136, 182) have also been used. The flow curve is obtainable from the total pressure loss-flow rate curve once the total pressure losses are corrected for end effects. The end effects are obtainable from Bagley plots or from pressure profiles.

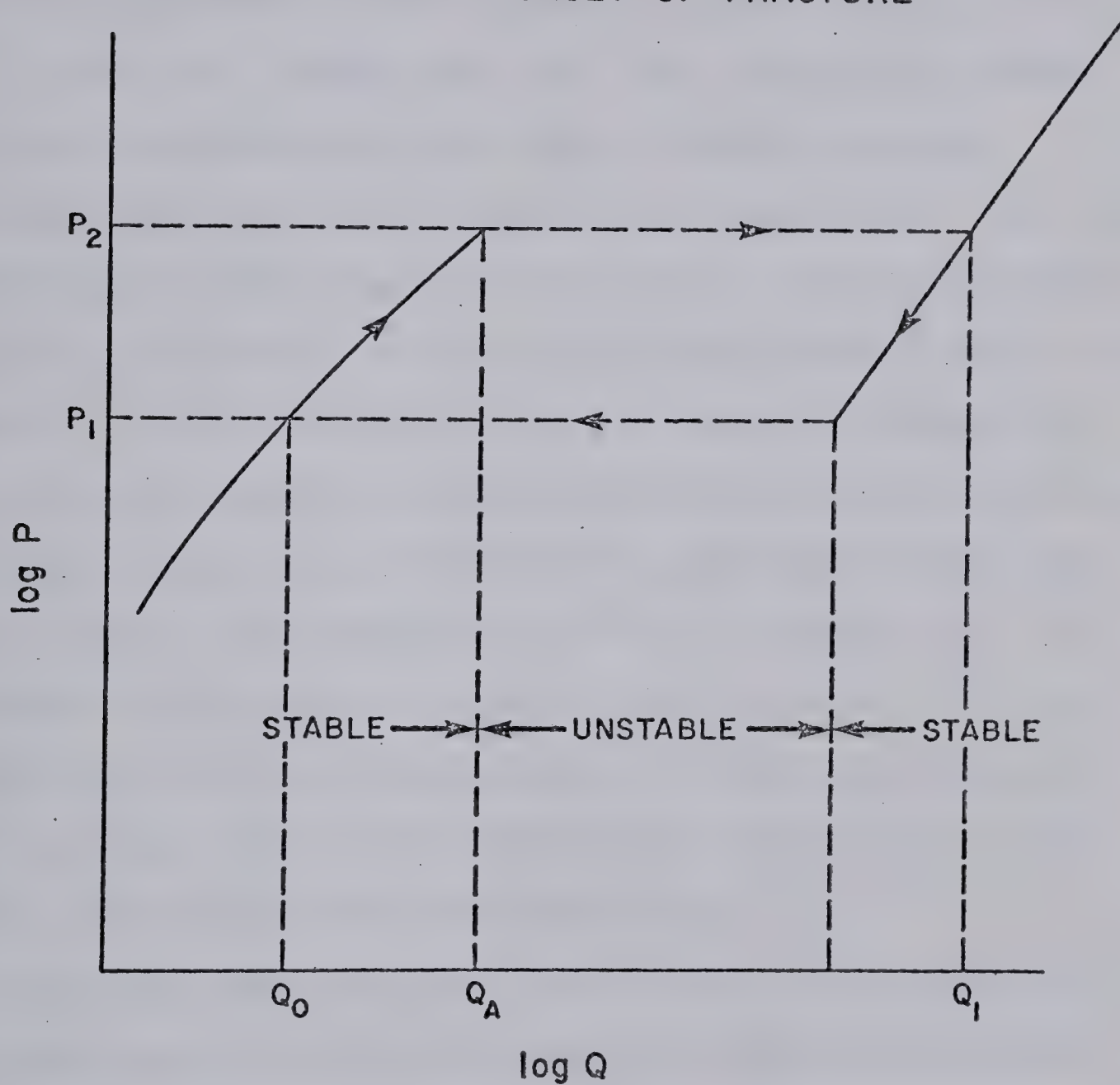
1.2.1 CAPILLARY INITIATION

It has been suggested that the initiation site may exist within the capillary tube rather than in the inlet region (19). In HDPE melts, the flow curve indicates, almost without exception, a double value of the shear stress or apparent shear rate at the onset of flow instabilities (23, 53, 105). However, plots for entrance effects, i.e., log-log plots of the total pressure loss versus flow rate, show that at the onset of instabilities no discontinuity is present.

The existence of a double value of the apparent shear rate is revealed by the use of a constant stress rheometer (1, 3, 179, 183). A constant stress rheometer is achieved by maintaining a constant pressure in the reservoir producing a controlled piston force or by direct application of a gas at a controlled pressure. The volumetric flow rate is measured to obtain the apparent shear rate. On

the other hand, the existence of a fluctuation of the shear rate (53, 120) and a double value of shear stress is revealed by a constant rate rheometer which is a hydraulic cylinder moving at a constant rate. The shear stress can be evaluated either by the Bagley plot or by pressure profiles. It can be deduced that the double value of the shear stress and fluctuating shear rate can be explained best in terms of the relationship between volumetric flow rate and reservoir pressure as given in the flow curve (105, 134). The flow curve given in Figure 1.5 is divided into three regions: a stable region, an unstable region, and a second stable region. At flow rates less than Q_A the velocity field is stable and viscosity decreases with increasing shear stress. The extrudate is smooth. The cyclic path indicated by the arrows represents the periodic pressure flow rate sequence that would be followed for an imposed mean flow rate lying in the unstable region. The horizontal lines represent essentially discontinuous jumps in the flow rate. If the chosen volumetric flow rate lies in the unstable region, the actual volumetric flow rate alternates between the two limits, Q_0 and Q_1 , and the extrudate surface changes accordingly from smooth to rough. This interpretation implies that the nature of the flow field within the capillary tube is important in setting up the instability. The onset of flow instabilities can be shifted to higher apparent shear rates by broadening the molecular weight distribution (120), by reducing the mole-

FIGURE 1.5
RESERVOIR PRESSURE AS A FUNCTION OF VOLUMETRIC
FLOW RATE AT ONSET OF FRACTURE



cular weight (179), or by increasing the temperature of the polymer melt (103, 117, 177).

Most authors attribute the cause of melt fracture in HDPE melts to slip at the wall (18, 135, 182) although other mechanisms or explanations have been discussed by Casey (37), Hagler (70), Bogue and White (27), Petrie and Denn (136) and Myerholtz (120). Direct evidence of slip at the wall is limited. Benbow and Lamb (18) presented evidence that this occurred above the onset of melt fracture. Recently, den Otter (54) found slip at the wall in low temperature flows of ethylene-propylene melts. Indirect evidence has been presented by Lupton and Regester (105) and Blyler and Hart (23) by the inclusion of a non-zero velocity at the wall as a boundary condition for flow through a circular tube; the shear rate or the velocity gradient at the tube wall is linear with respect to D^{-1} at a constant τ_w . In the event of slip at the tube wall the slope of this line is positive while for zero slip at the wall the slope is equal to zero. Results for HDPE melts substantiated the mechanism of slip at the wall (23, 105).

Although photographs of the unstable flow field in the entry region are few and not very detailed, Bagley and Birks (10) concluded that the frequency of observed recoiling in the flow field (description given on page 30) are greater than those observed for the flow of LDPE melts.

1.2.2 INLET INITIATION

The discontinuity noted in the flow curve of HDPE

melts is absent for LDPE melts (16, 23, 105, 179), polystyrene (179), and polymethyl methacrylate (16). The plots of the entrance effects, i.e., log-log plots of the total pressure loss versus flow rate, exhibit a discontinuity at the onset of melt fracture. Hence, for the flow of LDPE melts, polystyrene, and polymethyl methacrylate, the onset of flow instabilities is believed to occur within the inlet region (136, 187, 188). The plotting of the experimental data for LDPE according to the analysis presented by Blyler and Hart (23) confirmed that slip at the wall was nonexistent. In addition, the experimental measurements of velocity within the vicinity of the capillary tube wall (17, 53) showed that the velocity at the capillary tube wall was equal to zero for polybutadiene and LDPE melts. Maxwell and Galt (107) measured velocity profiles but their results are doubtful due to errors in measuring the distance from the wall.

The stable flow field within the inlet region for LDPE melts was described in pages 22-23 wherein the melt enters into the capillary tube through a central accelerating core as it passes from the reservoir into the capillary tube. At the onset of flow instabilities the stable flow field breaks down (12, 188). The fluid normally entering the capillary tube through the WGS core recoils and as the material recoils the fluid enters into the capillary tube from the eddies surrounding the core. This phenomenon is periodic and its frequency increases with

flow rate. Correspondingly, the extrudate is distorted. Prior to the recoiling of the fluid, observations of a slight swirling or spiraling motion have been observed (12, 132, 188). The intensity increased with increasing flow rate with a corresponding helical distortion of the extrudate. Fluctuations in the pressure were measured when the spiraling motion became more accentuated (12).

An unstable flow field similar to that reported for LDPE melts has been observed for polymer solutions (30, 119, 130, 142). Recently, Rama Murthy (142) reported visual observations based on the flow field for a 1.49% solution of Separan AP-30 in a 50% by weight glycerol-water mixture. He observed that at low flow rates the flow field was WGS but at a certain flow rate this flow field developed a "spiraling flow" (description given by Rama Murthy) whose intensity increased with flow rate. The flow field failed to exhibit any regularity with further increases in flow rate and was described as being "chaotic" (description given by Rama Murthy). At even higher flow rates this "chaotic" flow field abruptly changed to the stable flow field that is associated with the stable flow of HDPE melts. In all of the above observations no attempt was made to obtain photographs from which the details of the velocity components can be measured. These observations do suggest, however, that failure of the material, as an explanation of melt fracture, need not be involved.

In an attempt to predict the onset of flow instabili-

ties certain theoretical considerations such as linear stability theory (135), the accelerating wave mechanism (37), and the growth and magnitude of the normal forces within the entry region (116, 119, 173) have been considered. The application of such theories requires a tractable constitutive equation and a detailed knowledge of the upstream velocity field. Since the stable flow field is complex and has not been fully described either mathematically or empirically, existing analyses have dealt only with the stability of shearing flows in the capillary tube (147). This was simplified even further to the analysis of the stability of shearing flows between infinite parallel plates (109, 138). Ultman and Denn (174) suggested that when the velocity of propagation of the shear wave is of the same order of magnitude as the frictional velocity, a discontinuity occurs in the slope of the streamline. Although the streamlines were not obtained directly, Boger and Rama Murthy (24) observed that for several aqueous polymer solutions the velocity distribution at the entrance of the capillary tube underwent an abrupt change. This occurred when the ratio of the shear wave velocity to the frictional velocity, evaluated under SLSF in the capillary tube, was equal to unity.

Since there is no detailed empirical description of the stable flow field in the entry region, mechanisms previously mentioned cannot be tested rigorously as to their ability to predict the onset of instabilities in

polymers where initiation occurs in the inlet.

1.2.3 EFFECTS OF ENTRY GEOMETRY AND CAPILLARY

The effects of entry geometry (48, 70, 114, 152, 170, 188) and capillary length to diameter ratio (12, 13, 70, 85, 134) on the onset of flow instabilities are not firmly established. When the initiation site is inlet initiation, Tordella (170) reported that shear rates at the onset of flow instabilities increased by an order of magnitude as the die entry half-angle was altered from 90 degrees to 20 degrees. Metzner, Carley and Park (114) reported a slight increase in shear rates which was significantly less than the two orders of magnitude increase observed by Cogswell and Lamb (48). On the other hand, Schreiber, Bagley and Birks (152) stated that the entry half-angle had no effect on the delay of flow instabilities. They concluded that for flows in conical shaped entrances the frequency of recoiling of the center flow is higher and the magnitude lower. This reduced the distortion in the extrudate and could cause misjudgement in estimating the flow rate at which instability commences. Finally, Hagler (70) reported critical shear rates (or shear stresses) 30 to 50 percent lower in a 45° entrance than in a 90° entrance. When the initiation site is in the capillary, the effect of the die entry geometry on the onset of flow instabilities was found to be independent of die entry geometry (53). However, Hagler (70) observed that the shear rates at the onset of flow instabilities for HDPE

melts decreased two to three times as the die entry half-angle increased from 45 degrees to 90 degrees. This is consistent with results reported by Cogswell and Lamb (48) and Ferrari (62) for polypropylene melts. Cogswell and Lamb (48) used slightly tapered die entry half-angles, half-angles less than 4.5 degrees, whereas Ferrari (62) varied the tapered angle from 90 to 3 degrees. A more detailed investigation of the flow field within the entry region would assist in understanding the effects of entry geometry on the onset of flow instabilities.

The effect of the length to diameter ratio on the onset of flow instabilities for several polymer melts is summarized in Table 1.1. With the exception of the results reported by Hagler (70) and Ballenger et al. (13) for HDPE melt and Ferrari (62) for polypropylene, all the cited authors reported that the length to diameter ratio of the capillary tube had an effect on the onset of flow instabilities. The majority of these results indicated that as the length to diameter ratio increased the critical shear stress increased, i.e., higher throughputs could be achieved prior to the extrudate being distorted. It was postulated that fluctuations should decay down the capillary tube so that increasing the length of the capillary tube should tend to stabilize the extrudate (85, 134, 152). Han and Lamonte (80) measured the pressure fluctuations for a LDPE melt along the capillary tube length. They found that the pressure fluctuations decreased along the

TABLE 1.1

EFFECT OF L/D ON ONSET OF INSTABILITY

<u>AUTHOR</u>	<u>POLYMER</u>	<u>CASE 1</u>	<u>CASE 2</u>	<u>CASE 3</u>
Ballenger et al.	polystyrene		x	
	LDPE		x	
	HDPE	x		
Bartos, Holomek	polybutadiene			x
Cogswell, Lamb	polypropylene		x	
Dennison	HDPE		x	
den Otter	LDPE		x	
	HDPE			x
Ferrari	polypropylene	x		
Hagler	LDPE		x	
	HDPE	x		
Han, Lamonte	LDPE		x	
Klein, Fusser	polyisobutylene		x	
Myerholtz	HDPE			x
Rama Murthy	Separan AP-30 Solution		x	
Tomita, Shimbo	polyethylene oxide solution		x	
Westover	HDPE		x	

Case 1 - No effect of L/D

Case 2 - As L/D increases the shear stress evaluated at the onset of fracture, $(\tau_w)_c$, increases

Case 3 - As L/D increases the shear stress evaluated at the onset of fracture, $(\tau_w)_c$, decreases

capillary tube length and distortions in the extrudate occurred only when the pressure fluctuations existed up to the tube exit. Contrary evidence was presented by den Otter (53). He showed that when LDPE melts were extruded between flat, parallel plates there were no pressure fluctuations downstream of the entry region, even at very high shear stresses when the extrudate was severely distorted. The reason for this contradiction is not resolved, therefore, the results must be considered with caution.

To summarize, in LDPE melt flow, the pressure fluctuations in the entry region arise from velocity fluctuations or from a vortex-induced alternating flow. This points out the need for details on the upstream velocity field and theories which "determine the ability of the system to propagate a disturbance" (136).

1.2.4 EMPIRICAL CORRELATIONS - PREDICTION OF FLOW INSTABILITIES

The correlations of melt fracture with rheologically relevant dimensionless parameters seem justified only on empirical grounds since actual flow patterns are complex (134). These correlations, if successful, do not constitute an explanation for the onset of flow instabilities.

It was suggested (134, 136) that the Reynolds number (inertial phenomenon) which successfully correlates the transition from laminar to turbulent flow (20) was relevant

because there appeared to be a slight correlation between the Reynolds number and the onset of flow instability. Experimental values of the Reynolds number at the onset of melt fracture varied from 10^{-4} (114) to values of the order 100 (142). Consequently, a suitable criterion was not found. The inertial phenomenon would predict: (a) at fixed fluid properties, the critical flow rate would be directly proportional to D , and (b) at a fixed die diameter, the critical flow rate would be directly proportional to the apparent viscosity. However, experimental evidence, as indicated by Tordella's results (171), showed that for fixed fluid properties the critical flow rate is directly proportional to D^3 , whereas at a fixed die diameter the critical flow rate is inversely proportional to the apparent viscosity.

The experiment of Spencer and Dillon (158) indicated that the onset of melt fracture for several polymer melts and several die diameters occurred at a constant value of V/D or, equivalently, a constant apparent shear rate, $8V/D$. With the aid of a flow curve, this implied a constant shear stress. The introduction of a dimensional quantity, having the dimensions of time, allows for the formation of a dimensionless group, $V\theta/D$, which has been used also as a criterion (24). Spencer and Dillon (158) further proposed that melt fracture for polymer melts occurs when the shear stress is of the order 10^6 dyn/cm². The dependence of instability on entry geometry and L/D ratios need not imply a simple straightforward critical shear

stress or shear rate criterion. The critical shear stress for polymer melts and solutions tabulated in Table 1.2 show a sevenfold variation for polymer melts, a 250-fold variation for polymer solutions and over four orders of magnitude variation between polymer melts and solutions. Therefore, the shear stress criterion proposed for polymer melts, i.e., melt fracture occurs whenever the shear stress is 10^6 dyn/cm^2 , is not applicable to polymer solutions.

Bagley (8) attempted to correlate the onset of fracture with a critical value of the recoverable shear strain (equation given below)

$$S_R = (\tau_w)_M / G \quad 1.40$$

where $(\tau_w)_M$ is the shear stress evaluated at the onset of fracture for polymer melts. By using a Maxwell model, the elastic modulus, G , can be related to the viscosity and the relaxation time of the fluid (147, 190) by

$$G = \mu / \theta \quad 1.41$$

The substitution of Equation 1.41 into Equation 1.40 with $(\tau_w)_M$ evaluated under SLSF in the capillary tube yields

$$S_R = 8 \frac{V\theta}{D} \quad 1.42$$

The Weissenberg number, defined as the ratio of the primary normal stress to the shear stress in SLSF in the capillary

TABLE 1.2

CRITICAL SHEAR STRESS AT ONSET OF INSTABILITY

<u>AUTHOR</u>	<u>POLYMER MELTS</u>	<u>$(\tau_w)_c \times 10^{-6}$ (dyn/cm²)</u>
Bagley	Polyethylene	1.28 - 2.26
Bartos	numerous polymers	0.695 - 4.0
Blyler, Hart	LDPE	2.0
Hagler	LDPE	0.586 - 0.863
	HDPE	2.04 - 3.21
Lupton, Regester	HDPE	3.0
Metzner, et al.	Polyethylene	3.17
Myerholtz	HDPE	2.9 - 3.3
Oyanagi	HDPE	1.96 - 3.49
Vlachopoulos, Alam	LDPE	1.02 - 1.433
	HDPE	1.464 - 2.592
	Polypropylene	1.062 - 1.41
Vlachopoulos, Lidorikis	Polystyrene	0.68 - 2.15
Westover	HDPE	1.65 - 3.78
<u>SOLUTIONS</u>		
Murch	0.5% Separan AP-30; 30% glycerine-water mixture	0.0003
Oliver, Bragg	0.10% ET-597	0.0006
Paul, Southern	Polystyrene- benzene	0.015 - 0.932
Rama Murthy	1.49% Separan AP-30; 50% glycerine-water mixture	0.00006 - 0.00024
Vinogradov, Martin	Aluminum naphthenate	0.00075 - 0.006

tube, has been suggested also as a criterion (134). This is equal to twice the recoverable shear strain as shown by the equation below

$$N_{ws} = \frac{(P_{11} - P_{22})_w}{\tau_w} = 2\gamma\theta = 16 \frac{V\theta}{D} = 2S_R \quad 1.43$$

Reported values of the recoverable shear strain at the onset of fracture are given in Table 1.3. S_R varies from 2.2 to 66.81 for both polymer melts and solutions. This variation is due in part to the variation in methods of estimating the elastic modulus, i.e., the pressure loss measurements (Equation 1.31), or the normal stress measurements.

Southern and Paul (157) extended the criterion of a recoverable shear strain by noting that

$$(S_R)_M \approx (S_R)_S \quad 1.44$$

The proposed criterion for polymer solutions takes the form of

$$\left(\frac{C}{\rho}\right)^2 (\tau_w)_M \leq (\tau_w)_S \leq \left(\frac{C}{\rho}\right) (\tau_w)_M \quad 1.45$$

where ρ is the density of the polymer melt, C is the concentration of the polymer solution, (C/ρ) is the polymer volume fraction, and $(\tau_w)_S$ is the shear stress evaluated at the onset of fracture for polymer solutions. The shear stresses at melt fracture predicted by Equation 1.45 for several polymer solutions are in agreement with experimental

TABLE 1.3

RECOVERABLE SHEAR STRAIN AT ONSET OF INSTABILITY

<u>AUTHOR</u>	<u>POLYMER MELTS</u>	<u>S_R</u>
Bagley	LDPE	15.0
	HDPE	6.4
Barnett	Polypropylene	12.2 - 35.5
Gruver, Kraus	Polybutadiene	11.0 - 19.6
Han, Lamonte	Polystyrene	2.2
Howells, Benbow	Polymethyl- methacrylate	7.2
Huseby	theory	25.1
Rothenberger	theory	2.6
McCoy, Denn, Schott	HDPE	7.42 - 8.08
Spencer, Dillon	Polystyrene	7.08 - 7.67
Tordella	Polyethylene	5.0
Vlachopoulos, Alam	Polystyrene	3.0 - 66.81
	Polypropylene	13.59 - 28.74
	LDPE	5.46 - 13.65
	HDPE	31.08 - 53.87

SOLUTIONS

Kroesser	Vistanex L100	17.0 - 27.0
	B100	12.7 - 42.8
Williams	Polyethylene	11.0 - 28.0
Boger, Rama Murthy	Separan AP-30	6.0

results (119, 133, 142).

In general, the preceding criteria correlate fracture with measurements in SLSF in the capillary tube. This is not consistent with experimental observations. Experimental observations show that for many polymer melts and solutions, fracture occurs within the inlet region (inlet initiation) and within this region the fluid is subjected to both shear and elongation deformations (12, 24, 47, 63, 77). For these fluids, the mechanisms put forward as the cause of fracture, based on inlet conditions, have not been severely tested since details of the converging velocity field are not well known. If one assumes, as a first approximation, that the converging velocity field is effectively an extensional flow then a criterion for the onset of fracture should be related to fluid properties in extensional flow (48, 60). den Otter (53) stated that "when the pressure has reached a sufficiently high value, a breakdown of melt fracture takes place." Thus, melt fracture as a consequence of tensile failure in extensional flow may be correlated with the pressure losses in the entry region (70, 88). The concept of a critical pressure loss is also reflected in the apparent shear rate-apparent shear stress curve wherein, at fracture, a discontinuity is observed in the curve (page 27).

Cogswell (46) assumed that the converging flow through an orifice can be analyzed in terms of the extensional and shear components separately. This allowed for derivation

of the relationships between volumetric flow rate, pressure drop, and the maximum extensional stress at the die entry. In summary, melt fracture is predicted to occur whenever the extensional stress, τ , exceeds some critical value given by

$$(\tau)_{cr} = \frac{3}{8} (3n'+1)P_u \quad 1.46$$

and P_u is the pressure loss in the upstream entry region given by

$$P_u = \frac{8}{3(n'+1)} \frac{\gamma\mu_A}{\tan\phi_0} \quad 1.47$$

where μ_A is the apparent viscosity evaluated at $\dot{\gamma}$. As ϕ_0 tends to 90 degrees, the entry pressure losses and the extensional stresses tend to zero. However, as ϕ_0 tends to zero degrees both P_u and $(\tau)_{cr}$ tend to infinity. This is believed to be highly unlikely. At intermediate values of ϕ_0 , P_u and $(\tau)_{cr}$ are directly proportional to the shear stresses evaluated under SLSF in the capillary. Hürlimann and Knappe (88) also postulated a critical contraction loss. From the PGB analysis, the contraction losses are given by

$$\Delta P_c = 4\tau_w \epsilon_t \quad 1.48$$

At melt fracture

$$(\tau_w)_M^{MW} = \text{critical value} \quad 1.49$$

hence, Equations 1.48 and 1.49 imply that whenever ΔP_c exceeds a critical value, $(\Delta P_c)_{cr}$, fracture will occur. Hagler (70) measured the contraction losses for a LDPE and a HDPE melt for flows in an abrupt contraction and found that at the onset of fracture $(\Delta P_c)_{cr} \approx .29$ to $.30 \times 10^8$ dyn/cm² for LDPE and $(\Delta P_c)_{cr} \approx .72$ to $.76 \times 10^8$ dyn/cm² for HDPE. These data lend support to a critical value of ΔP_c at the onset of fracture. The significance of Hürlimann and Knappe's analysis is the correlation of $(\Delta P_c)_{cr}$ with a critical extensional stress level at fracture. They concluded that "melt fracture starts when the extensional stress in the die inlet exceeds a critical value."

Everage and Ballman (60) proposed a critical extensional stress level directly by postulating that fracture is a consequence of tensile failure in extensional deformation. Whenever the material attains a critical value of the stretch rate, Γ_c , given by the limiting condition

$$2\theta\Gamma_c = 1.0 \quad 1.50$$

the material is unable to reach steady-state or as stated by Everage and Ballman (60) "... the material is unable to deform with sufficient rapidity to reach a steady-state stress level and fracture may result." From a Maxwell model, the relaxation time of a fluid is

$$\theta = \mu_E / G_E \quad 1.51$$

where the subscript E refers to extensional deformation and the elastic modulus is given by

$$G_E = \frac{\tau}{\epsilon_R} = \frac{\mu_E \Gamma}{\epsilon_R} \quad 1.52$$

where ϵ_R is the recoverable extensional strain. Combining Equation 1.51 and 1.52 yields

$$\theta \Gamma = \epsilon_R \quad 1.53$$

Everage and Ballman's (60) hypothesis implies, therefore, a critical value of the recoverable extensional strain. This hypothesis can be tested quantitatively by determining if the maximum stretch rate is effectively constant at the onset of melt fracture. An approximate calculation of the maximum stretch rate, utilizing the velocity field for the flow of an incompressible Newtonian fluid through a cone (60), yields

$$\Gamma_{\max} = \frac{12Q}{\pi D^3 \cot \phi_0^3} \left[\frac{(1 - \cos 2\phi_0)}{(1 - \cos \phi_0)^2 (1 + 2\cos \phi_0)} \right] \quad 1.54$$

In terms of the capillary wall shear rate, the maximum stretch rate is

$$\Gamma_{\max} = \frac{3\dot{\gamma}_w}{8 \cot \phi_0^3} \left[\frac{(1 - \cos 2\phi_0)}{(1 - \cos \phi_0)^2 (1 + 2\cos \phi_0)} \right] \quad 1.55$$

Therefore, for a constant initial cone semi-angle, ϕ_0 , a critical volumetric flow rate or a critical capillary tube

apparent shear rate criterion is implied from the recoverable extensional strain criterion. By using Equation 1.54 and the data reported by Ferrari (62), Everage and Ballman (60) calculated that $\dot{\Gamma}_{\max}$ at the onset of fracture was reasonably constant ($760 \text{ sec}^{-1} \leq \dot{\Gamma}_{\max} \leq 1195 \text{ sec}^{-1}$). These results quantitatively support the proposal which states "... that melt fracture is a consequence of tensile failure of the material in elongation deformation" (60). It has been shown in the previous section (Section 1.2.3) that the onset of instabilities within the inlet region varies with the entry geometry, the capillary tube length and the type of polymer. Hence $\dot{\Gamma}_{\max}$ is expected to vary accordingly.

The hypothesis presented by Everage and Ballman (60), which is an extension of the work of Denn and Marrucci (51), is based upon a time dependent stress growth resulting from the converging flow field. Since this converging flow field is affected by the magnitude of the flow rate (see pages 22-23) for a description of the flow field with flow rate), the fluid is subjected to different strain histories. It seems sensible, therefore, to compare all fluids at a constant strain level, S , which takes into account not only the magnitude of the stretch rate but also time, i.e., Hencky's strain measure (70), which is also referred to as the total strain (98). The total strain is defined as

$$S = \int_{t_i}^{t_f} \dot{\Gamma} \, dt \quad 1.56$$

Parameter S has been used successfully to correlate velocity data (90) and transient elongational viscosity data (1). Acierno et al. (1) found that the transient elongational viscosity-total strain curves obtained from spinning (where the melt is extruded, solidified, and then drawn up as a filament) and inverse siphon experiments (fluid is drawn vertically into a capillary tube creating a vertical liquid filament) resulted in a single curve. The data obtained from the inverse siphon experiment covered the initial part of the transient curve while the data from the spinning experiment yielded the upper part of the same transient curve. By using the total strain rather than the strain rate in a fibre spinning experiment, the axial stresses, measured at different rates of extrusion, and take-up rates were correlated by a single curve (87). Therefore, an extension of Everage and Ballman's proposal integrated with the work of Acierno et al. (1) suggests the total strain as a criterion for the onset of melt fracture.

CHAPTER II

EXPERIMENTAL EQUIPMENT AND PROCEDURE

2.1 EXPERIMENTAL EQUIPMENT

The experimental equipment consisted of the flow system (Instron and a stainless steel hydraulic cylinder), the entry region, and the capillary tubes.

2.1.1 FLOW SYSTEM

A constant flow rate was maintained by an Instron, Model TM, and two stainless steel hydraulic cylinders which were 15.24 cm I.D. (cylinder 1) and 15.60 cm I.D. (cylinder 2). Cylinder 1 was used in obtaining the data for the Newtonian solutions while cylinder 2 was used for the viscoelastic solution. The calibration of each cylinder, given in Appendix A, revealed that the calculated and measured flow rates were within one half of one percent of each other. Hence, it was concluded that there was no seepage of fluid between the inner cylinder wall and the piston. The cross head speed of the Instron was calibrated as outlined in the Instron manual.

2.1.2 ENTRY REGION

The physical dimensions of the two square reservoirs are given in Table 2.1. The internal length of each reservoir assured that the velocity distributions for the Newtonian and viscoelastic solutions were developed at

TABLE 2.1

INTERNAL RESERVOIR DIMENSIONS

<u>RESERVOIR</u>	<u>WIDTH (cm)</u>	<u>LENGTH (cm)</u>
Small (S)	2.62	25.40
Large (L)	25.49	71.70

TABLE 2.2

CAPILLARY TUBE LENGTH TO DIAMETER RATIOS

<u>CAPILLARY NO.</u>	<u>L/D RATIOS</u>		
	<u>CAPILLARY</u> <u>TUBE 1</u>	<u>CAPILLARY</u> <u>TUBE 2</u>	<u>CAPILLARY</u> <u>TUBE 3</u>
	<u>0.10 cm</u>	<u>0.20 cm</u>	<u>0.30 cm</u>
A	---	31.60	---
B	35.03	34.99	34.97
C	55.08	54.96	55.04
D	71.32	71.23	71.13
E	96.45	96.38	96.36
F	---	---	145.00
G	148.48	148.45	148.53
H	---	151.00	---
I	---	160.16	---
J	222.08	222.36	213.38
K	305.08	304.95	304.83
L	450.00	457.43	---

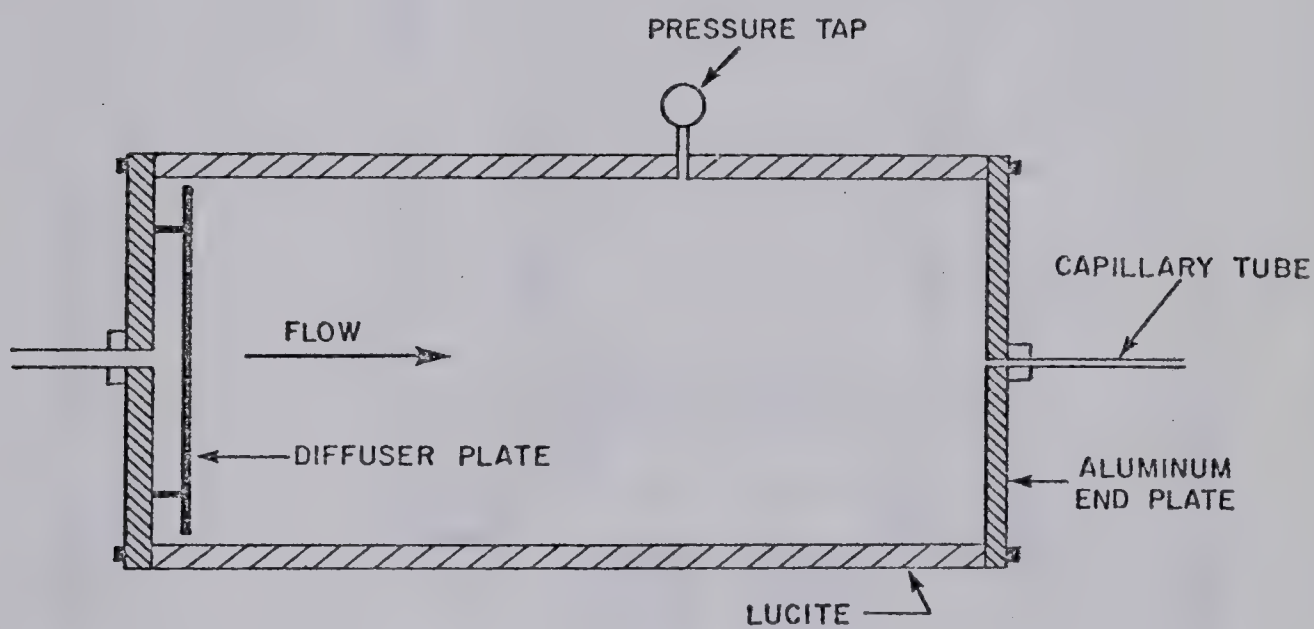
the location of the pressure taps even under the worst possible condition, i.e., the highest Reynolds number. The pressure taps, schematically shown in Figure 2.1, were located 10.2 cm and 27.9 cm from the entrance in reservoirs S and L respectively where pressures and pressure traces were measured. In reservoir S the fluid entered through a diverging cone having a maximum diameter of 2.54 cm while in reservoir L a diffuser plate was located approximately 5 cm from the inlet end. The sides of each reservoir were constructed of 2.54 cm thick transparent lucite plate to allow for flow visualization. The end plates were of anodized aluminum.

2.1.3 CAPILLARY TUBES

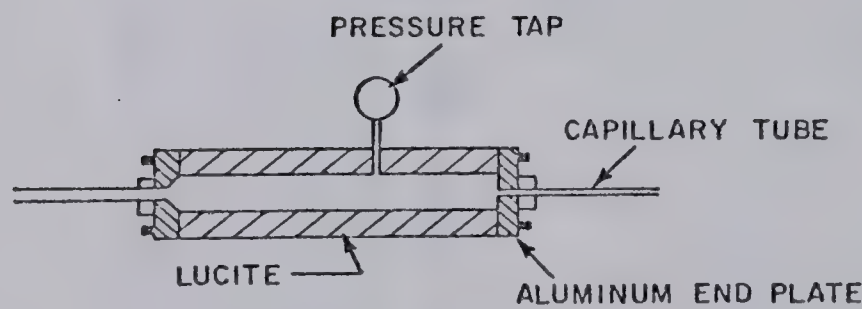
The precision bore 0.10, 0.20, and 0.30 cm I.D. borosilicate glass capillary tubes, hereinafter referred to as capillary tubes 1, 2, and 3 respectively, were manufactured by Fischer & Porter Co. The internal diameters of the capillaries had a tolerance of ± 0.00076 cm. For each diameter, several tube lengths were cut into length to diameter ratios that varied from 31.60 to a maximum of 457.43. The various length to diameter ratios for the three capillary tubes are given in Table 2.2; capillary no. C was used in the measurement of velocities. The capillary tube lengths used in the measurement of pressure losses are given in Appendix B.

Schematically shown in Figure 2.2 is the device for

FIGURE 2.1
RESERVOIR AND PRESSURE TAP LOCATION

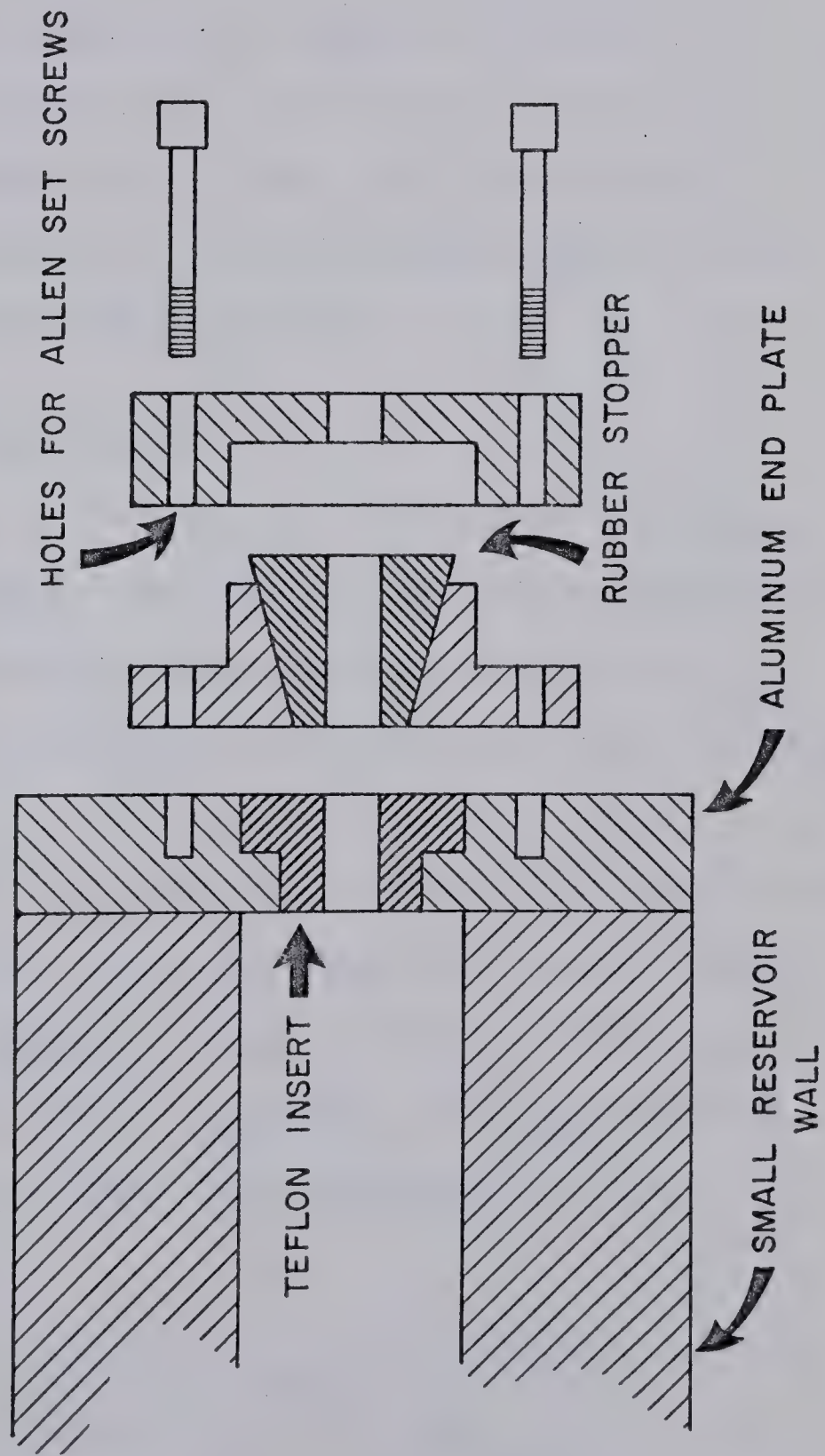


RESERVOIR L



RESERVOIR S

FIGURE 2.2
CAPILLARY HOLDING DEVICE



holding the capillary tubes firmly in place flush with the inside surface of the aluminum end plate. This holding device was capable of withstanding maximum pressures of 7×10^6 and 4×10^6 dyn/cm² in reservoirs S and L respectively.

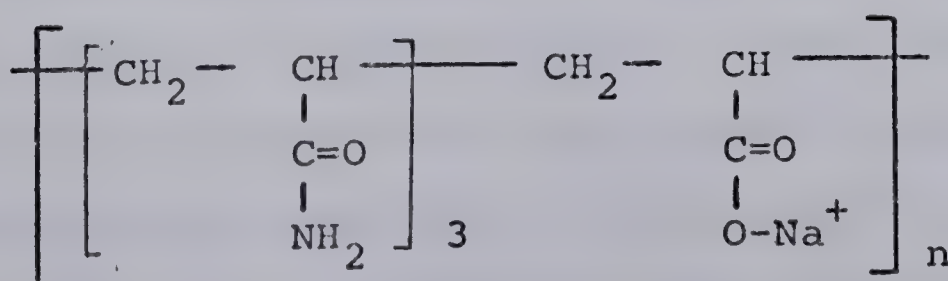
2.2 EXPERIMENTAL FLUIDS AND TRACER PARTICLES

Several aqueous sugar solutions, an oil, and one concentration of Separan AP-30 were the experimental fluids while aluminum dust particles were used as tracer particles in the photographic method.

2.2.1 EXPERIMENTAL FLUIDS

The Newtonian fluids used were three aqueous sugar solutions of 46%, 53%, and 61% by weight and an oil, Primol-355. The physical properties of these sugar solutions and the oil are tabulated in Appendix D, Section D.1.

The polymer solution was a 0.20% aqueous solution of Separan AP-30 which is a high molecular weight synthetic polymer (molecular weight between 2 and 3×10^6) manufactured by the Dow Chemical Company. The approximate composition of this polymer is represented by the formula given below:



The physical properties are given in Appendix D, Section D.2. The solution showed no significant changes in physical properties over a two month interval. Degradation due to bacterial presence was eliminated by the addition of a small amount of sodium benzoate. Furthermore, the solution was used only once to ensure that the physical properties did not change from run to run owing to mechanical degradation.

2.2.2 TRACER PARTICLES

The flow visualization method of injecting hydrogen bubbles (approximately .01 cm diameter) into the fluid proved to be impractical. This impracticality resulted from the extremely small velocities in the recirculation region surrounding the central core of fluid that entered into the capillary tube. The hydrogen bubbles accumulated and adhered to the viewing surface of the reservoir distorting the image when viewed through the camera lens. To circumvent this problem aluminum dust particles (manufactured by Baker, lot number 2347) at approximately 0.00075 volume percent were used as the tracer. The measured maximum width of each of these thin, irregularly shaped particles, given in Appendix A, Section A.4, varied from 3 to 34 microns with a mean maximum length of 13 microns. The maximum width was 0.7 times the maximum length with the thickness estimated to be 1 micron. To prevent the particles from adhering to each other in the solution they were dispersed in a small quantity of water (approximately 1 cm^3) prior to being mixed with the polymer solution.

2.3 PHOTOGRAPHIC METHODS

An optical method of measurement was used to obtain streak photographs of aluminum dust particles in the polymeric solution in order to measure the local axial and radial velocities within the converging flow field.

2.3.1 OPTICAL SYSTEM

The optical system, schematically shown in Figure 2.3, consisted of an arc lamp, a converging lens, a chopping disc, a reservoir, and a camera assembly. A Christie transformer with a maximum output of 3300 watts D.C. operated the Christie Xenon arc-lamp. The set of converging mirrors in the lamp-housing, No. BSF 50, were located so that they directed the light beam through the narrow slit located on the reservoir. An adjustable slit placed immediately prior to the converging lens produced a light beam smaller than the slits on the chopping disc.

The 38.1 cm diameter, 0.32 cm thick, chopping disc was divided into an equal number of radial slits and spokes. The variable speed motor driving the chopping disc and the interchangeable pulley sizes allowed the time interval (the time for the slit to cut the beam of light) to vary over the desired range. A stroboscope was used to determine the revolutions per minute (R.P.M.) of the motor. Table 2.3 lists the various combinations of motor R.P.M. and pulley turndown ratios that allowed the time interval to vary from 8.98×10^{-3} seconds to 137.92

FIGURE 2.3
SCHEMATIC OF OPTICAL SYSTEM

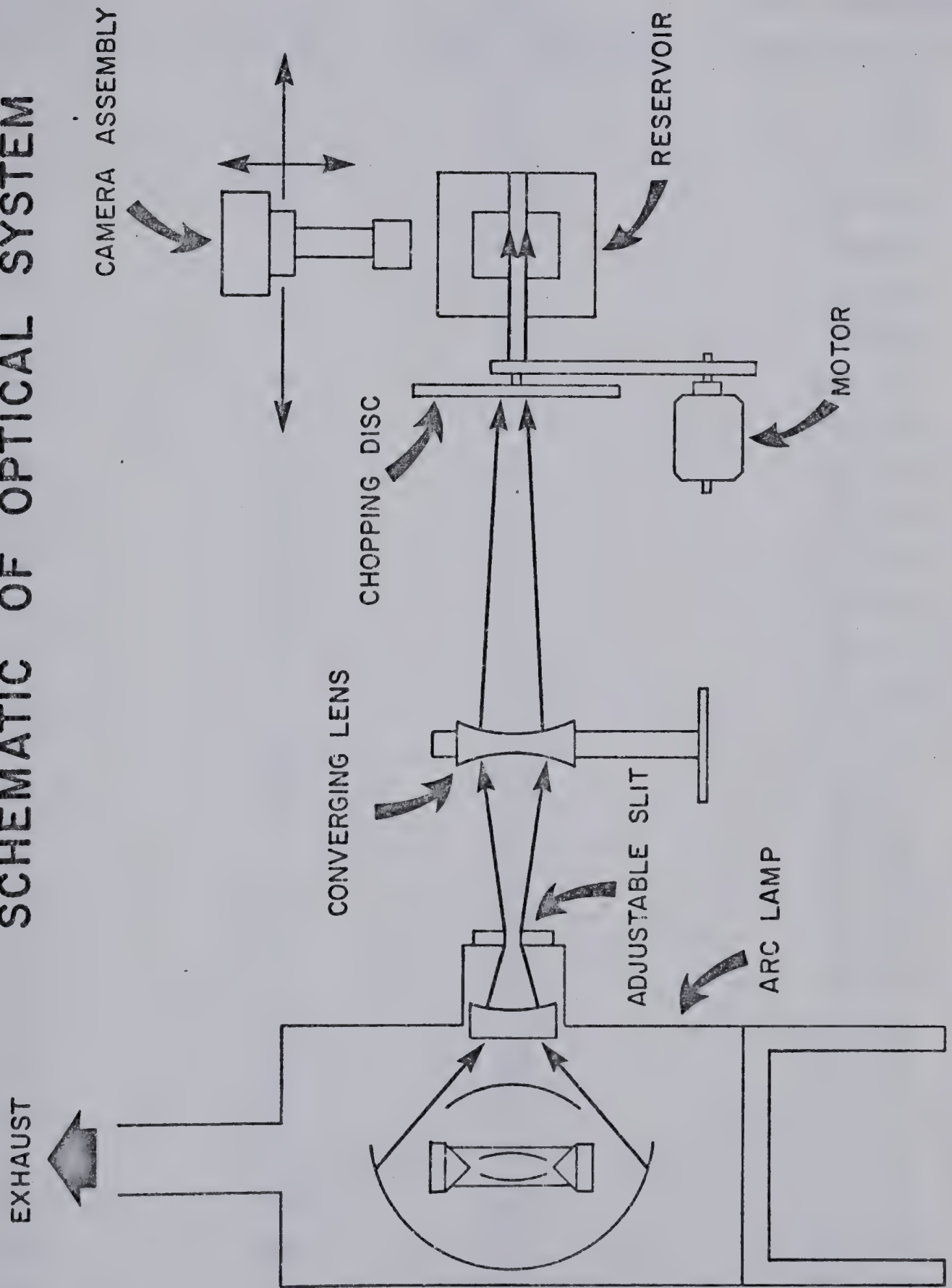


TABLE 2.3

TIME INTERVALS FOR STREAK ANALYSIS

<u>PULLEY TURNDOWN RATIO (P.T.R.)</u>	<u>MOTOR R.P.M.</u>	<u>NUMBER SLITS-SPOKES</u>	<u>TIME INTERVAL (sec x 10⁻³)</u>
1.0	334	20	8.98
1.0	259	20	11.61
1.0	218	20	13.76
1.0	79	20	38.10
1.0	75	20	39.87
1.0	71	20	42.10
.375	141	20	113.41
.375	306	30	52.28
.375	302	20	26.49
.375	97	20	82.47
.375	462	20	6.50
.375	158	20	17.32
.375	82	20	50.79
.375	87	20	91.95
.375	60.5	20	132.23
.375	175	20	45.72
.375	87	20	91.95
.375	137	20	64.78
.375	291	20	27.49
.375	145	20	55.14
.375	330	20	24.24
.375	90	20	88.85
.375	58	20	137.92
.375	73	20	54.61
.375	172.5	20	46.38
.375	63.5	20	125.98
.375	63	20	126.98
.375	177	20	45.19
.375	325	20	24.61

$\times 10^{-3}$ seconds. The pulley turndown ratio is the ratio of the diameter of the pulley on the chopping disc to the diameter of the pulley attached to the motor. The chopping disc was located perpendicular to the light beam with its center in the plane of the light beam. To minimize reflections, the interior surfaces, with the exception of the light slit on the side of each reservoir and the camera viewing area, were painted black. In addition, the room was in total darkness during the experimental run.

A rod having a diameter equal to the internal diameter of the Teflon insert (shown in Figure 2.2) was tapered to a point at one end so that the camera could focus on the center of the capillary tube. This rod was painted black to minimize reflections. It was pushed through the teflon insert such that only the tapered portion protruded into the reservoir. A Miranda 35 mm camera was located perpendicular to the light beam and was secured to Setco Building Blocks which were equipped with micrometers graduated in 0.001 inch increments in the vertical and horizontal planes. The camera was focused on the tip of the tapered rod. Since the depth of the field of the camera was greater than the thickness of the beam of light, aluminum particles within the beam's thickness were illuminated and recorded on the film. The error in measured velocities associated with the depth of the field of the camera and the thickness of the light beam is discussed in Appendix G.

The projection of a frame onto the digitizer screen using the digitizer method (a detailed description of the method is given in Section 2.3.3 and a schematic representation of the digitizer is shown in Figure 2.7) was used to magnify the photos obtained. The data obtained from reservoir S were magnified using a 1:2.8/105 mm lens and extension tubes. The depth of field of the camera was 0.20 cm and the resulting magnifications were 8.225, 9.063, 18.00, and 24.50. For reservoir L data, a 1:1.9/50 mm lens and an unextended helicoid tube adaptor resulted in the magnification of 2.175; the depth of field of the camera was 0.40 cm. Tri-X film with ASA rating of 400 was used throughout the experiment.

2.3.2 STREAK PHOTOGRAPHS

Typical streak photographs are shown in Figures 2.4 and 2.5. The flow field shown in Figure 2.4 was obtained with capillary tube 2 in reservoir S at the maximum flow rate of $0.318 \text{ cm}^3/\text{sec}$ (flow moving from left to right) with the velocities being tabulated in Appendix E, Section E.1. The film exposure time was one second and the time interval for a streak was 55.14×10^{-3} seconds. Figure 2.4 shows the typical WGS core surrounded by large eddies and the acceleration along several streamlines with the maximum at the center of the core. Velocities were determined by either the digitizer or direct method using several photographs similar to Figure 2.4. Figure 2.5 shows

FIGURE 2.4
STREAK PHOTOGRAPH, 0.20 cm I.D.
 $Q = 0.318 \text{ cm}^3/\text{sec}$



FIGURE 2.5
STREAK PHOTOGRAPH, 0.20 cm I.D.
 $Q = 0.040 \text{ cm}^3/\text{sec}$



that even at the lowest flow rate of $0.040 \text{ cm}^3/\text{sec}$ the flow field is still of a central core surrounded by large eddies. However, the eddy centers are significantly nearer to the plane of the capillary entrance than at higher flow rates.

In addition to measuring the velocity development upstream, the location of the eddy centers and cone semi-angles were measured to complete the description of the flow field. Figure 2.6 is a representative photograph used in determining the location of the eddy centers. Photographs similar to this figure were obtained with the film exposure time of 5 seconds and a f stop of f:5.6. Cone semi-angles were measured from photographs similar to those shown in Figures 2.4 and 2.5. The results (cone semi-angles and location of eddy centers) are reported in Appendix F and discussed in Chapter III (pages 135-141).

2.3.3 ANALYSIS OF STREAK PHOTOGRAPHS - DIGITIZER METHOD

The digitizer is comprised of a projector and a stand, a mirror, and a frosted glass screen as shown schematically in Figure 2.7. The X-Y frame of the digitizer screen was 58.10 cm by 55.10 cm. The mirror was positioned such that the reflected light was normal to the glass screen. To determine the magnification, a Keuffel and Esser ruler graduated in 0.01 inches as well as a cross hair device graduated in 0.10 mm intervals were photographed, projected onto the digitizer screen, and measured. The

FIGURE 2.6
EDDY CENTER LOCATION, 0.30 cm I.D.
 $Q = 9.531 \text{ cm}^3/\text{sec}$

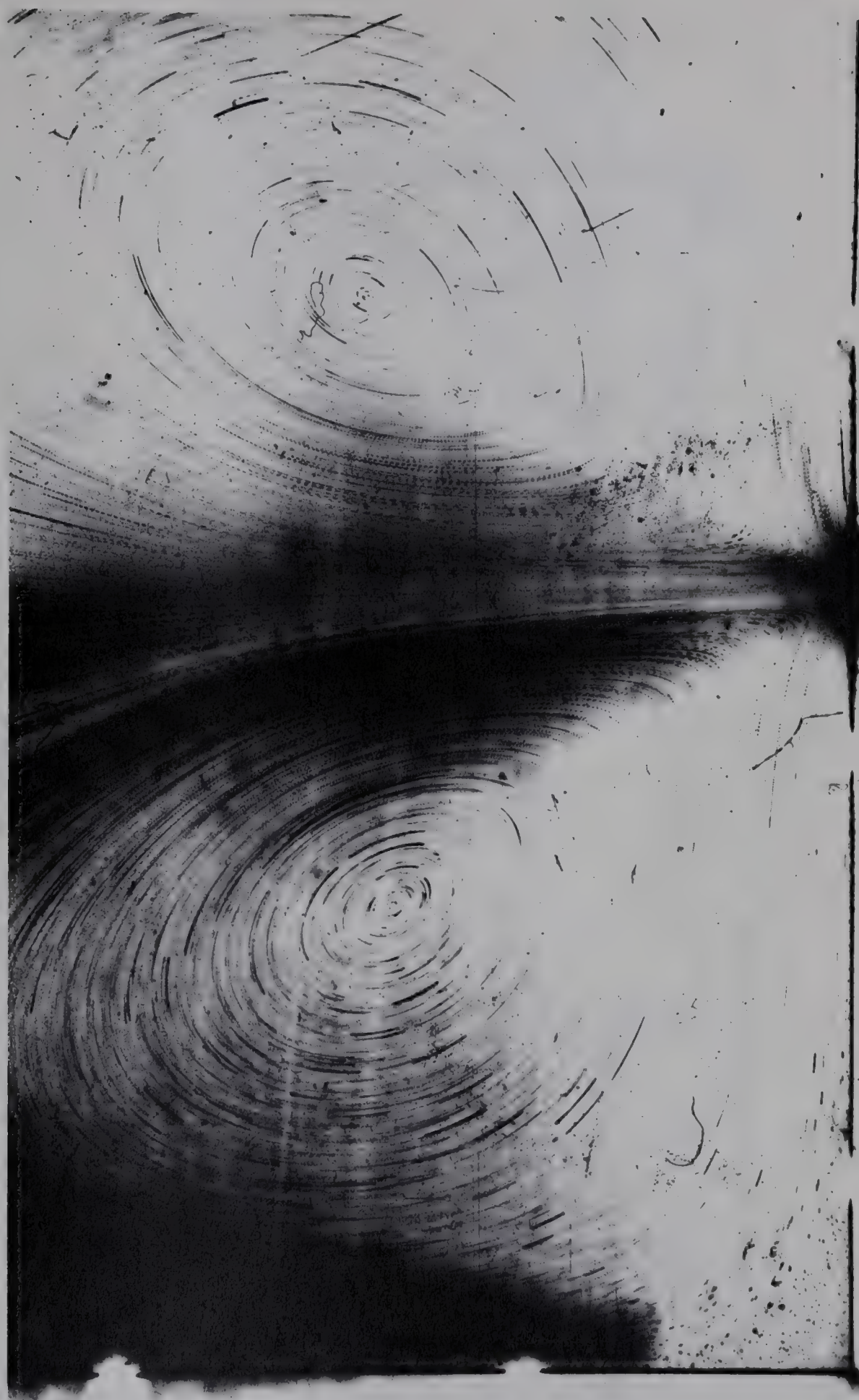
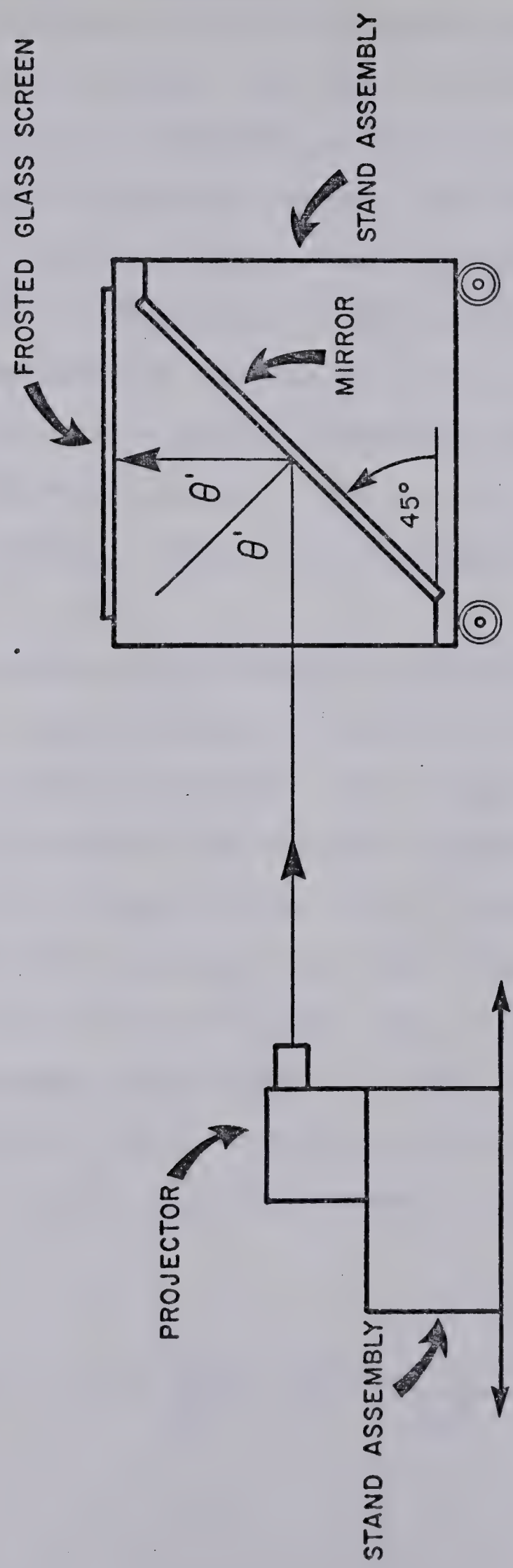


FIGURE 2.7
SCHEMATIC OF DIGITIZER



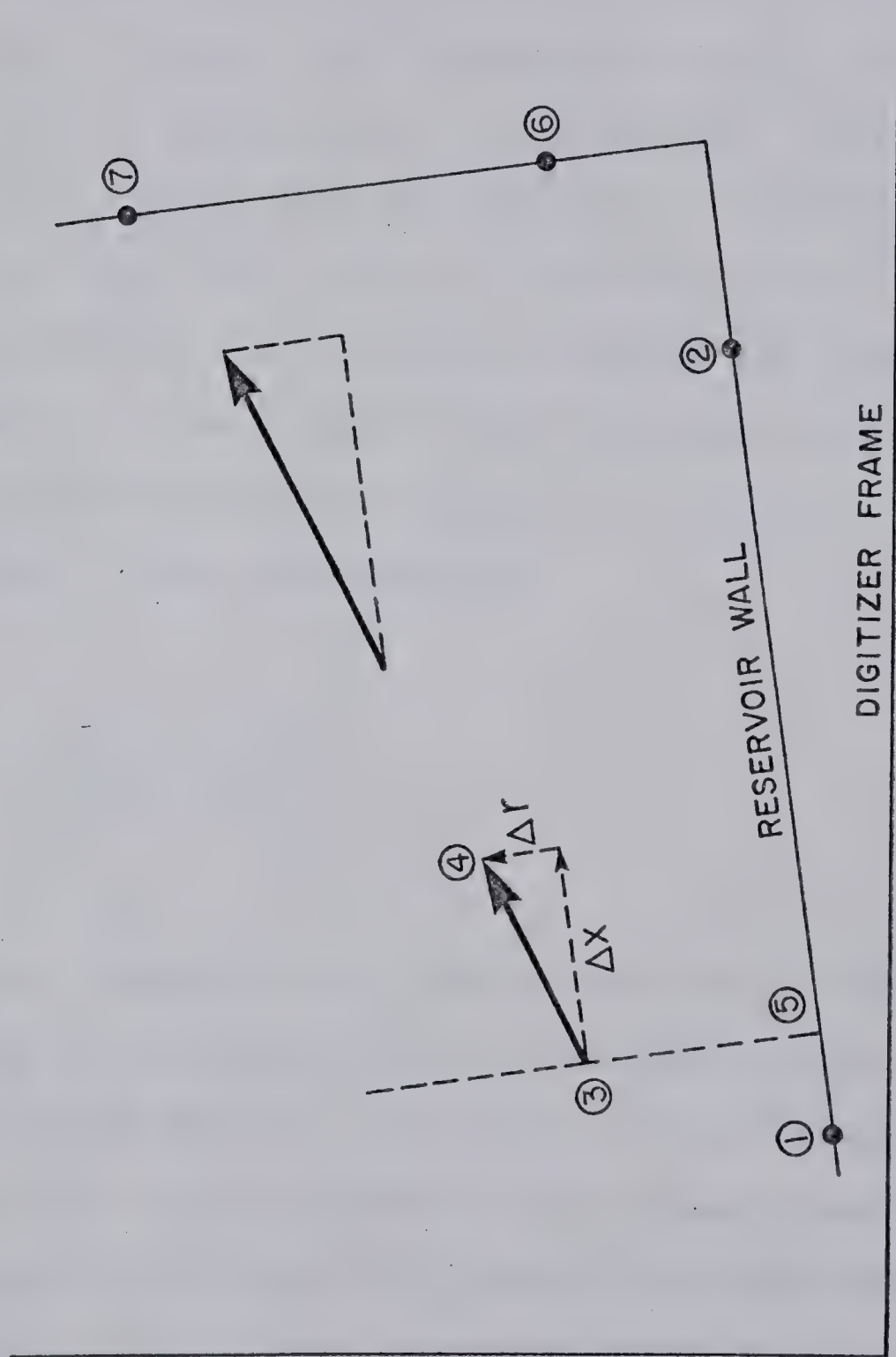
magnification was altered by moving the projector and the stand either closer to or farther away from the mirror.

The digitizer method consists of projecting a series of frames onto the digitizer screen. The coordinates of the reservoir wall and the streaks coordinates were recorded and stored in an IBM computer. The location of each coordinate was obtained by the use of a cross hair device that was connected to a variable resistor for the X and Y axes of the digitizer screen. The errors associated with the digitizer method are discussed in Appendix G.

Figure 2.8 schematically depicts a projected series of streaks viewed in a plane normal to the camera assembly in an accelerating region of the flow. The arrows represent the streaks and their direction for the time interval required by a slit in the chopping disc to cut the beam of light. The dotted lines represent the axial and radial distances measured relative to the wall of the reservoir. These distances (for a given streak), obtained from the transformation of coordinates from one Cartesian coordinate system to another, are represented by Equations 2.1 and 2.2.

$$\text{axial distance} = \Delta x = \frac{(Y_4 - Y_3)m_1}{(m_1^2 + 1)^{\frac{1}{2}}} + \frac{(X_4 - X_3)}{(m_1^2 + 1)^{\frac{1}{2}}} \quad 2.1$$

FIGURE 2.8
SCHEMATIC OF STREAK ANALYSIS



$$\text{radial distance} = \Delta r = \frac{(Y_4 - Y_3)}{(m_1^2 + 1)^{\frac{1}{2}}} + \frac{(X_3 - X_4)m_1}{(m_1^2 + 1)^{\frac{1}{2}}} \quad 2.2$$

where m_1 is the slope of the wall of the reservoir relative to the digitizer's X axis. The coordinates (X_1, Y_1) and (X_2, Y_2) were used to determine m_1 for reservoir L while (X_6, Y_6) and (X_7, Y_7) were used for reservoir S. Different coordinates were used for reservoir S because at the magnification of 24.50 and with the center of the reservoir coincident with the center of the digitizer frame the reservoir wall was projected beyond the screen. Hence, the slope m_1 was calculated by

$$m_1 = - \left[\frac{(Y_7 - Y_6)}{(X_7 - X_6)} \right]^{-1} \quad 2.3$$

It was necessary, therefore, to record four coordinates relative to the digitizer's X axis in determining the location of a streak and the velocities. In most cases a single streak was used to determine the local velocity. In regions where the flow was slow several streaks were used since single streaks were too short to be measured accurately. The distance from coordinate 3 to the wall of the reservoir (coordinate 5) was determined by

$$r' = [(x_5 - x_3)^2 + (y_3 - y_5)^2]^{\frac{1}{2}} \quad 2.4$$

The location of coordinate 5 was determined by the intersection of a line passing through coordinate 3 and having a slope equal to $-1/m_1$, i.e., perpendicular to the reservoir wall.

With the axial and radial distances, the number of streaks, and the time interval per streak known, the local axial and radial velocities were determined by

$$V_z = \Delta x / tM \quad 2.5$$

$$V_r = \Delta r / tM \quad 2.6$$

where

$$t = \frac{60}{WN} \times \frac{1}{\text{P.T.R.}} \quad 2.7$$

M = number of streaks

N = number of slits and spokes on the chopping disc

W = number of revolutions per minute

P.T.R. = pulley turndown ratio.

These velocities, which were measured only at three upstream axial positions, are tabulated in Appendix E,

Section E.2. The three axial positions corresponding to 1.5, 1.0, and 0.5 times the axial location of the eddy center are given in Table 3.4 (page 124).

2.3.4 ANALYSIS OF STREAK PHOTOGRAPHS - DIRECT METHOD

In the later stages of this work it was found more convenient to project the photographs directly onto graph paper which was graduated in 0.10 inch divisions. The streak lengths were traced directly onto the paper for all frames on the film corresponding to an experimental run. The axial velocities were determined as a continuous function of axial location. Thus, in contrast to the digitizer method, axial velocities were measured for all axial locations upstream of the contraction. A discussion of the error associated with this method is given in Appendix G, Section G.2. Figure 2.9 shows streaks along several streamlines as traced onto the graph paper with capillary tube 3 in reservoir S and at a flow rate of $0.40 \text{ cm}^3/\text{sec}$. The streak lengths were converted into axial velocities by using Equations 2.1, 2.5, and 2.7. The resulting axial velocities are plotted in Figure 2.10 for streamlines corresponding to those in Figure 2.9. Radial velocities were measured with the digitizer method and are tabulated in Appendix E, Section E.2.

The direct method was used also to measure cone semi-angles within the entry region. These angles are defined as the tangent to the outermost streamline that

FIGURE 2.9
DIRECT METHOD, STREAK LENGTH ALONG SEVERAL STREAMLINES

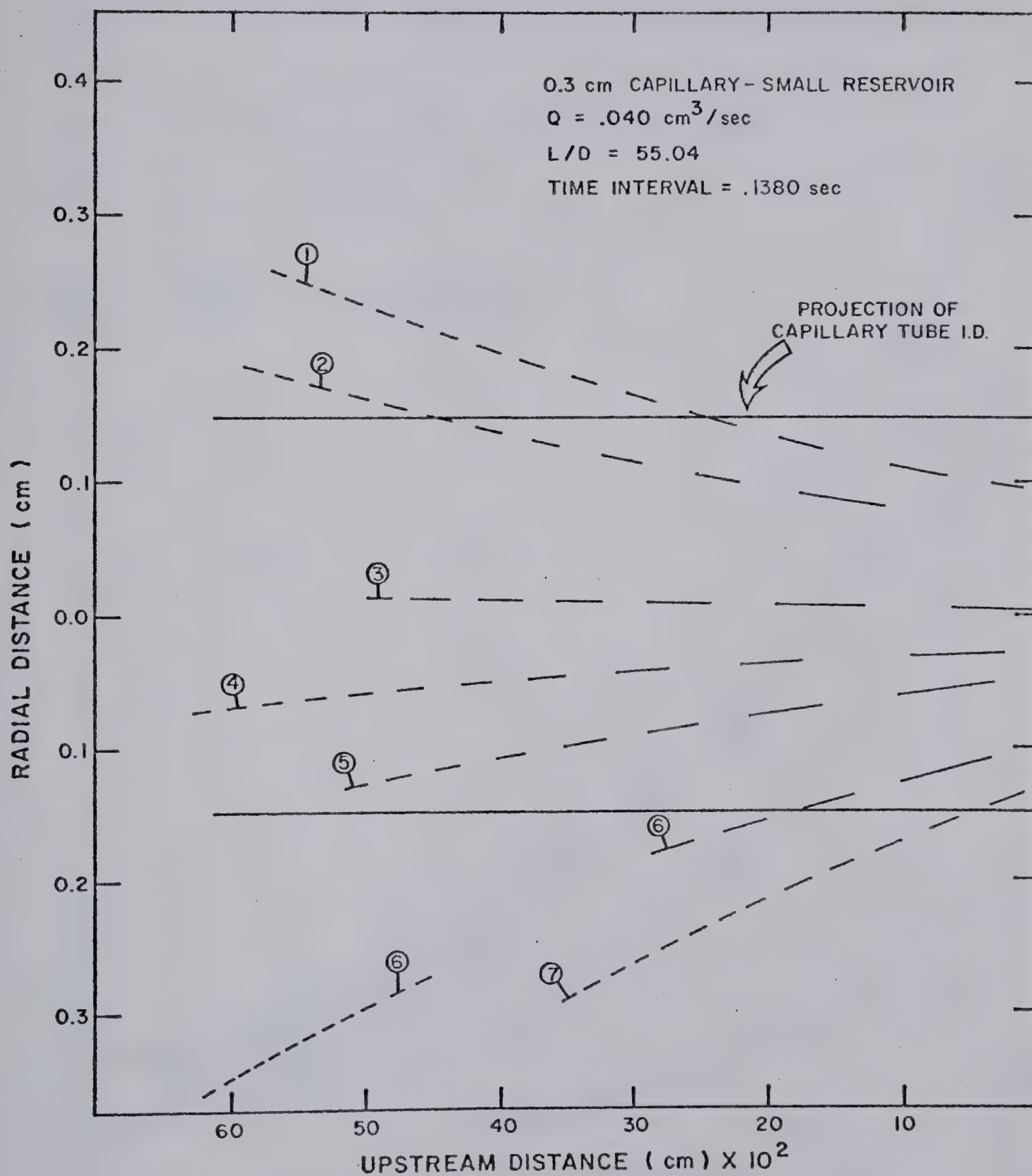
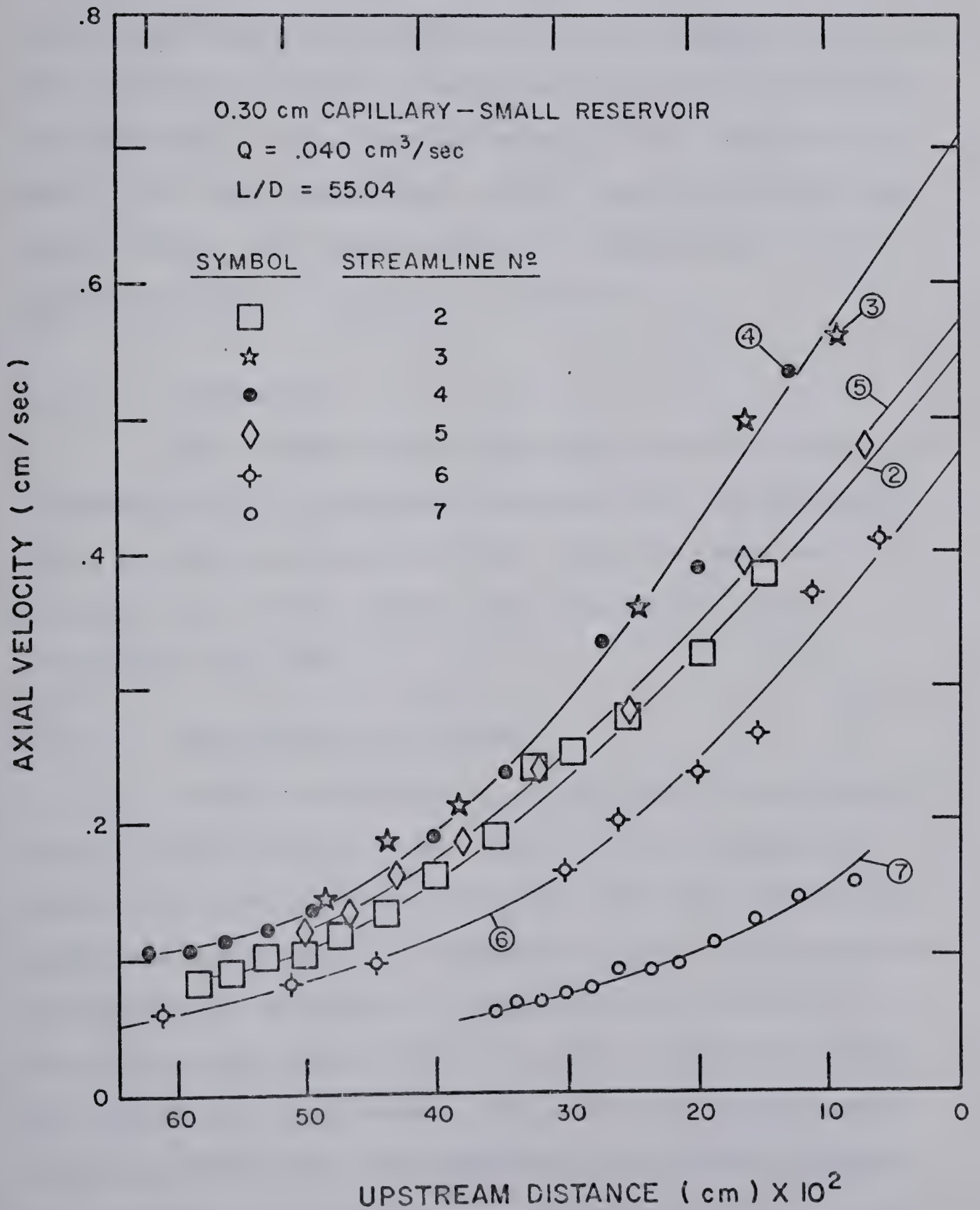


FIGURE 2.10

AXIAL VELOCITY - UPSTREAM AXIAL POSITION PLOT



entered into the capillary tube. This streamline, however, was not known precisely for all of the experimental runs. For example, in Figure 2.9 the initial cone semi-angle, i.e., the cone angle at the contraction, and the cone angles upstream of the contraction were estimated by streamline labeled as number 7, which as shown, was not exactly the outermost streamline that entered into the capillary tube. For this example the initial cone semi-angle was equal to 20° . The maximum error in estimating the cone semi-angles was as large as 15 percent.

2.4 PROCEDURE

This section describes the procedure used in the preparation of the polymeric solution and the procedures used in obtaining pressure data, velocity data, and observations of the jet of fluid issuing from the capillary tube exit.

2.4.1 PREPARATION OF POLYMER

Since two batches of a 0.20% weight solution of Separan AP-30 were used and since it was necessary to ensure that the physical properties were the same, each batch was prepared in an identical manner. The following procedure was adhered to in dissolving the solute: A stainless steel tank, 79 cm I.D., was filled to a height of 91.5 cm with tap water. The solute was added slowly so as to ensure that all particles were wetted without the formation of large lumps. At the same time, a mixer

agitated the solution at a moderate speed and continued to do so for a period of 10 hours after the final amount of solute was added to the solution. The solution was left unsheared for a period of 24 hours.

The fluid properties were measured and results are reported in Appendix D, Section D.2. The data indicated no significant differences in the physical properties for the two batches. The first batch was used in obtaining the total pressure losses which in turn were used to construct the Bagley plots. The second batch was used in the measurement of velocity distributions upstream of the contraction. In all experimental runs the temperature of the polymer solution was maintained at $68 \pm 0.5^{\circ}\text{F}$.

2.4.2 DATA COLLECTION

(i) PRESSURE

The transducers were balanced and then checked against the calibration curves given in Appendix A, Section A.1 prior to the commencement of every experimental run. The pressure transmission line and transducer were filled with the solution used in the experimental run with one side of the transducer open to the atmosphere. After ensuring that no air pockets were trapped in either the pressure line or in the transducer, pressures were measured with typical transient-steady state pressure displacement traces given in Figures 2.11 and 2.12. The time required to attain steady state at a Reynolds number equal to 10.49

FIGURE 2.11
TRANSIENT-STEADY STATE PRESSURE DISPLACEMENT
TRACE FOR PRIMOL - 355 OIL

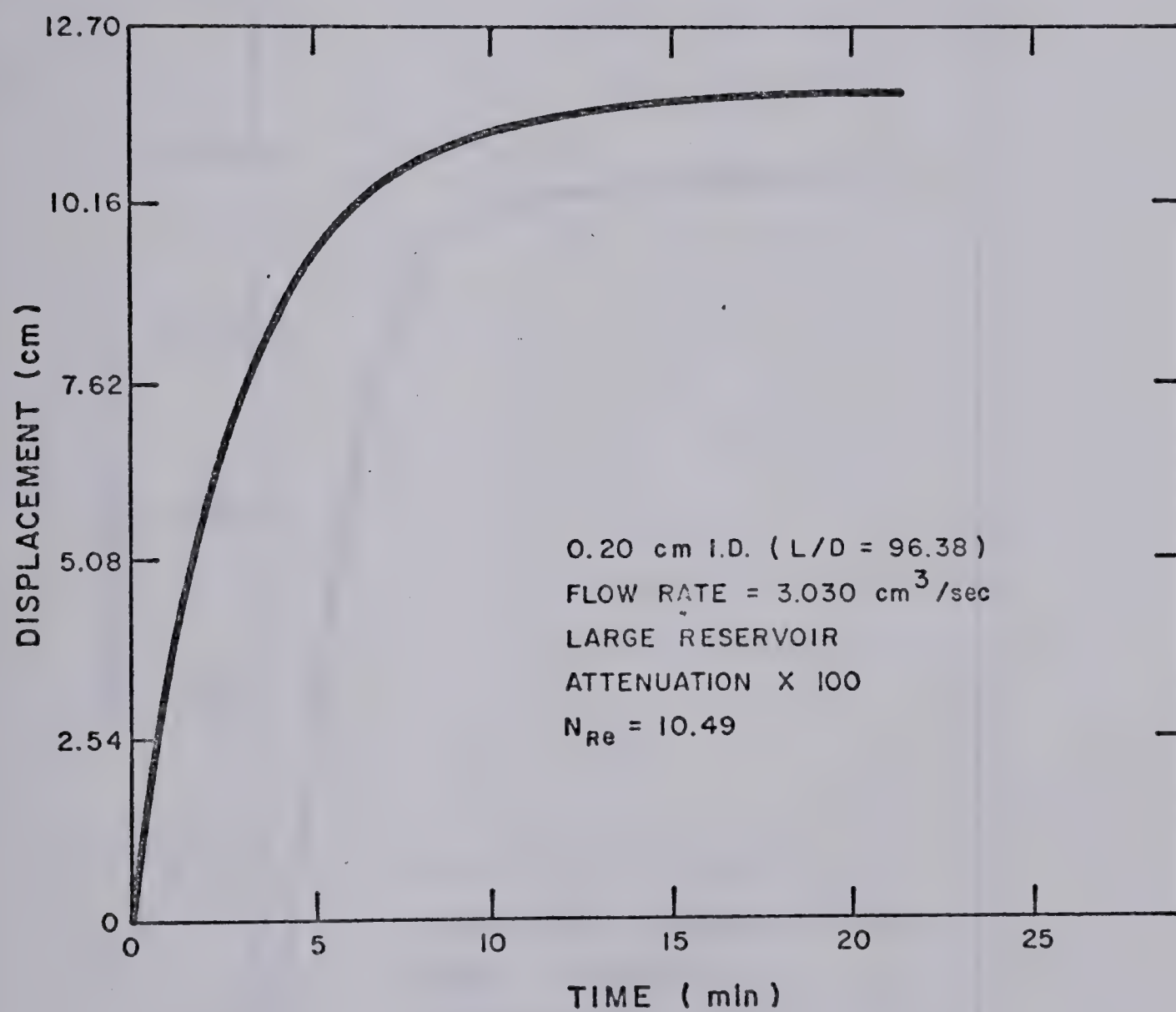
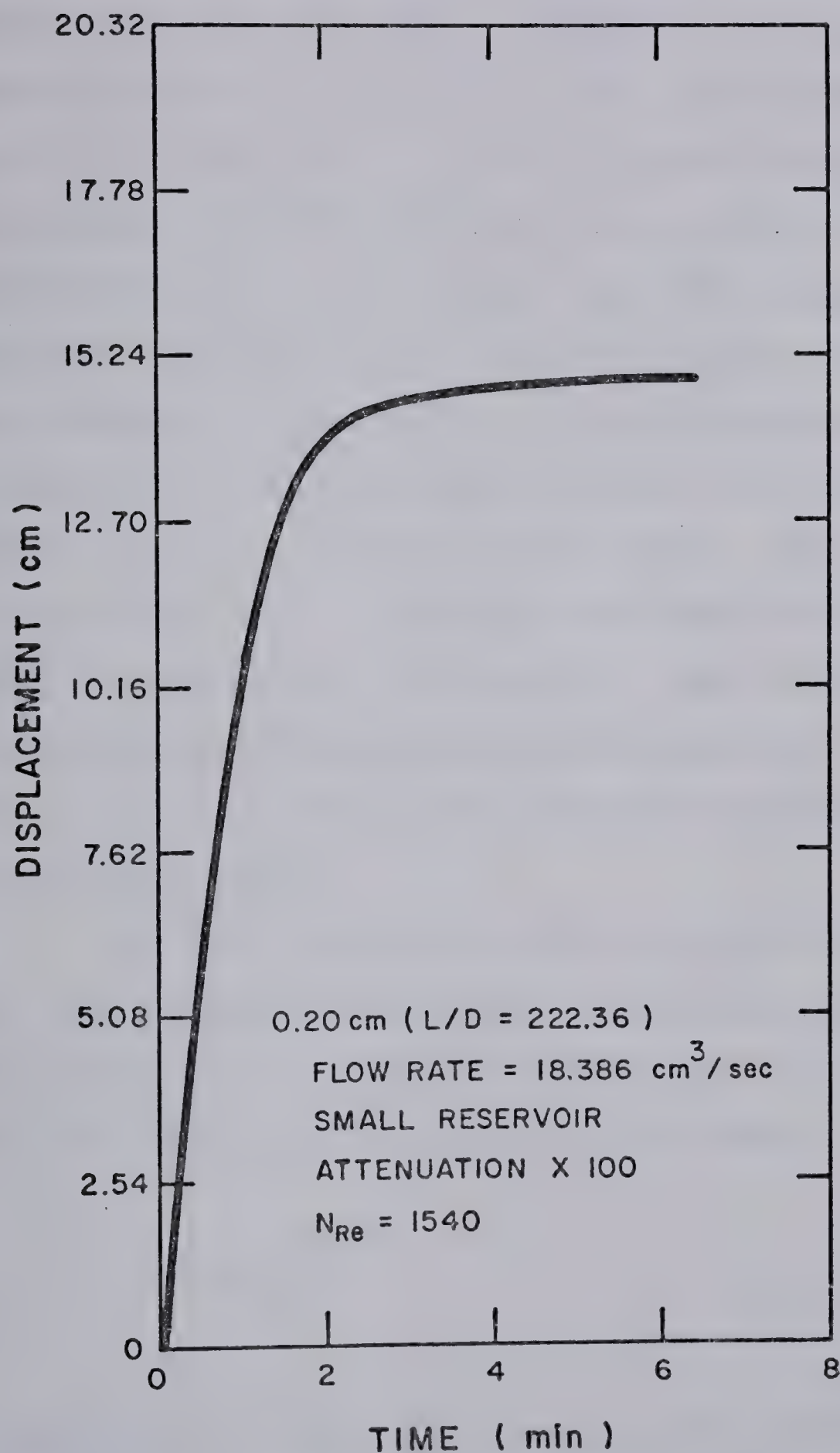


FIGURE 2.12

TRANSIENT-STEADY STATE PRESSURE DISPLACEMENT
TRACE FOR SUGAR SOLUTION N° 1

(shown in Figure 2.11) was approximately 18 minutes in comparison to 4 minutes at a Reynolds number of 1540 (shown in Figure 2.12). The steady state values of pressure obtained with several length to diameter ratios are tabulated in Appendix B. These data, as discussed in Appendix C, were used in constructing the Bagley plots. The pressure correction factors given in the tables in Appendix B account for the fact that the centers of the capillary tube and pressure transducer were not in the same horizontal plane. These pressure corrections must be added to the intercept of the Bagley plot to obtain the correct values of the contraction losses. The shear stresses under SLSF in the capillary tube were obtained from the slope of the Bagley plots. These data (contraction losses and shear stresses) are tabulated in Appendices C and D respectively for both Newtonian solutions and the polymer solution.

The time required for the centerline velocity to reach 99% of the fully developed centerline velocity, t_{∞} , was approximated by considering the reservoir to be an infinitely long, horizontal tube (20): thus,

$$t_{\infty} \approx \frac{0.8\rho R^2}{\mu} \quad 2.8$$

The experimental values of t_{∞} , $(t_{\infty})_e$, for the data in Figure 2.11 and 2.12 were 18 minutes and 4 minutes

respectively. These are significantly longer than the 1.2 and 0.3 minutes calculated by the use of Equation 2.8 and are representative of the maximum difference between experimental and calculated values of t_{∞} . Initially the difference was attributed to the trapped air within the hydraulic cylinder. This was examined by comparing the experimental and calculated values of t_{∞} for the remaining runs in both reservoirs (this was possible since the same procedure was used to fill the hydraulic cylinder in all experimental runs). In reservoir S results can be summarized as

$$2t_{\infty} \lesssim (t_{\infty})_e \lesssim 20t_{\infty} \quad 2.9$$

whereas in reservoir L summary of results is

$$.01t_{\infty} \lesssim (t_{\infty})_e \lesssim 20t_{\infty} \quad 2.10$$

In view of the large discrepancies between experimental and calculated values of t_{∞} we cannot conclusively state that trapped air within the hydraulic cylinder resulted in the large values of $(t_{\infty})_e$ obtained from the data in Figures 2.11 and 2.12. With polymer solutions in a parallel flat plate viscometer the time to attain steady state increased with elasticity number (128) defined as

$$EL = \frac{4\theta\mu_0}{\rho D^2} \quad 2.11$$

The elasticity numbers for the polymer solution were equal to 3.2 and 0.03 in reservoirs S and L respectively. This suggests that as a first approximation $(t_\infty)_e$ should be at least equal to or greater than the Newtonian values. However, experimental values of t_∞ were, in a significant number of experimental runs, less than the Newtonian values. It can be concluded that the time to reach steady state seemed to be a result of experimental design.

(ii) VELOCITY DISTRIBUTIONS

No velocity profiles were measured for the Newtonian solutions. The two methods used to measure velocity profiles for the polymer solution are discussed in Sections 2.3.3 and 2.3.4 of this chapter. The digitizer method was used to measure the axial velocity profiles at high flow rates in the reservoir L; the results are tabulated in Appendix E, Section E.2. The direct method was used with reservoir L at low flow rates and for all flow rates in reservoir S; the results are tabulated in Appendix E, Section E.1. All radial velocities were measured using the digitizer method and the data are tabulated in Appendix E, Section E.2.

(iii) QUALITATIVE OBSERVATIONS

The qualitative observations are: (a) visual observations of changes in the flow pattern upstream of

the contraction, (b) recording pressure traces at the pressure tap located upstream of the contraction, and (c) visual observations of the jet of fluid issuing from the capillary tube. The instabilities affected the observations, the discussion of which can be found in Chapter III.

CHAPTER III

RESULTS AND DISCUSSION

3.1 NEWTONIAN FLUIDS

The discussion deals with friction factors and contraction losses obtained from Bagley plots for all Newtonian fluids used in this research - three aqueous sugar solutions and an oil, Primol-355.

3.1.1 FRICTION FACTOR - REYNOLDS NUMBER

A comparison between the experimental and theoretical values of the friction factor determined under SLSF in the capillary tube was used to establish the accuracy of the experimental technique. Bagley plots were constructed for the four Newtonian fluids by plotting the total pressure losses, measured in both reservoirs and for several lengths of capillary tube 2, against the capillary tube length to diameter ratio. The total pressure loss - L/D data are tabulated in Appendix B. By curve fitting these data to Equation 1.28 using the least squares method, the shear stresses at the capillary tube wall and the contraction losses were obtained from the slope and intercept respectively. The recoverable shear strain, S_R , in Equation 1.28 is equal to zero for Newtonian fluids. Typical Bagley plots for the Primol-355 oil and for the sugar solution #1 are shown in Figures 3.1 and 3.2 respectively. Figure 3.1 represents Bagley plots for low

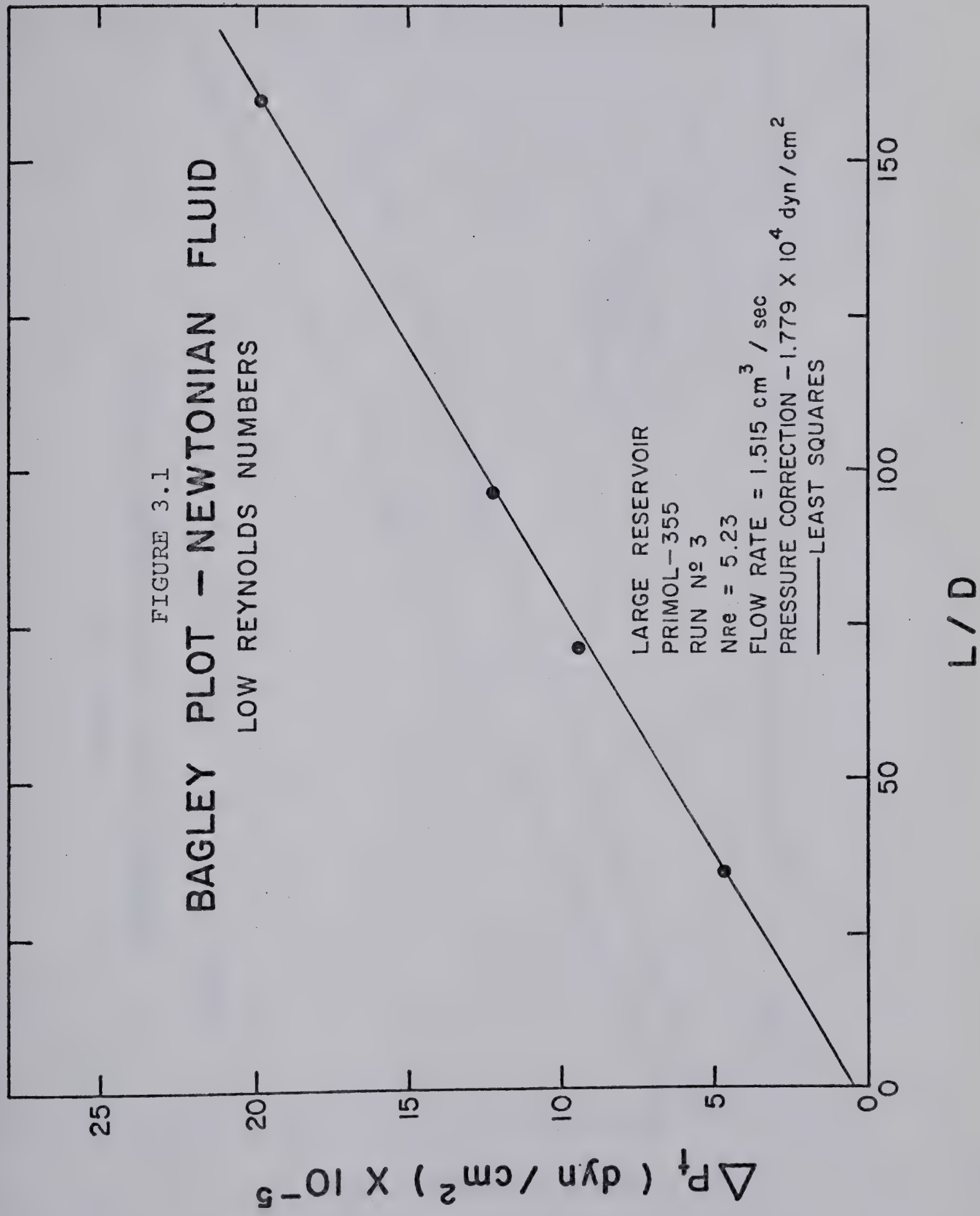
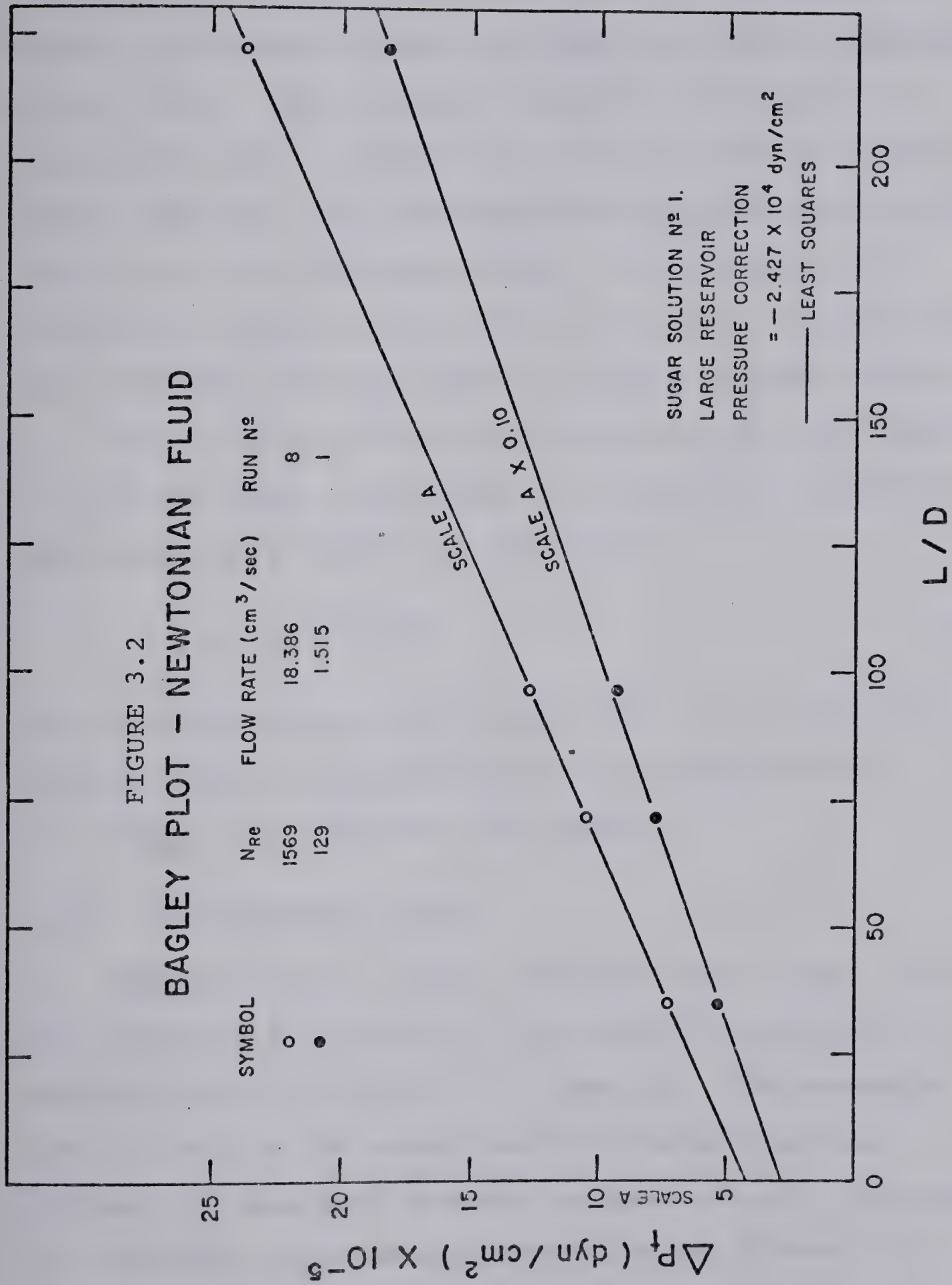


FIGURE 3.2
BAGLEY PLOT - NEWTONIAN FLUID



Reynolds numbers while Figure 3.2 presents those for intermediate and high Reynolds numbers. These and the Bagley plots obtained with the remaining data in Appendix B are linear. The pressure correction referred to in Figures 3.1 and 3.2 arose from the fact that the centers of the capillary tube and the pressure transducers were not in the same horizontal plane. Consequently, the correction factor must be added to the value of the intercept to obtain the true value of the contraction losses.

The friction factors were calculated by using Equation 3.1 and the shear stress data are tabulated in Appendix D. The results are plotted in Figure 3.3.

$$f = \tau_w / (\rho V^2 / 2) \quad 3.1$$

For Reynolds numbers that varied from 2.60 to 1569, the average deviation from the theoretical relationship, $f = 16/N_{Re}$, was less than four percent.

3.1.2 CONTRACTION LOSSES

The contraction losses, obtained from Bagley plots and tabulated in Appendix C, are plotted against the Reynolds number in Figure 3.4 (page 88). To determine the accuracy in the measurement of the contraction losses, the estimated standard errors (e.s.e.), Equation 3.2 (page 85), were obtained at a low, an intermediate, and at a high Reynolds number for each Newtonian fluid.

$$\text{e.s.e.} = \frac{s^2 \sum_{i=1}^n x_i^2}{n \sum_{i=1}^n (x_i - \bar{x})^2} \quad 3.2$$

where

$$s^2 = \sum_{i=1}^n \epsilon_i^2 / n-2 \quad 3.3$$

The minimum values of the e.s.e. are given in Table 3.1. For a given fluid, the contraction losses became an increasingly larger fraction of the total pressure losses as the Reynolds number increased. Hence, the percent error, as shown in Table 3.1, decreased with increasing Reynolds number. Consider as an example the data for sugar solution No. 3. Although the e.s.e. increased from $0.09 \times 10^4 \text{ dyn/cm}^2$ to $1.55 \times 10^4 \text{ dyn/cm}^2$ as the Reynolds number increased from 46.73 to 870.7, the percent error (as determined by Equation 3.4 below) decreased from 16 percent to 3 percent.

$$\% \text{ error} = \frac{\text{e.s.e.}}{\Delta P_c} \times 100 \quad 3.4$$

The largest percent error occurred with the Primol-355 oil where the contraction losses were small, hence, difficult to measure accurately. In addition there was substantial scatter in the total pressure loss-L/D data. This scatter was a result of experimental location wherein temperature fluctuations of $\pm 1^\circ\text{F}$ resulted in the viscosity varying by 3.9 percent. (The experimental location was changed when data were taken with the sugar solutions. In

TABLE 3.1
ESTIMATED STANDARD ERROR (e.s.e.) FOR NEWTONIAN CONTRACTION LOSSES

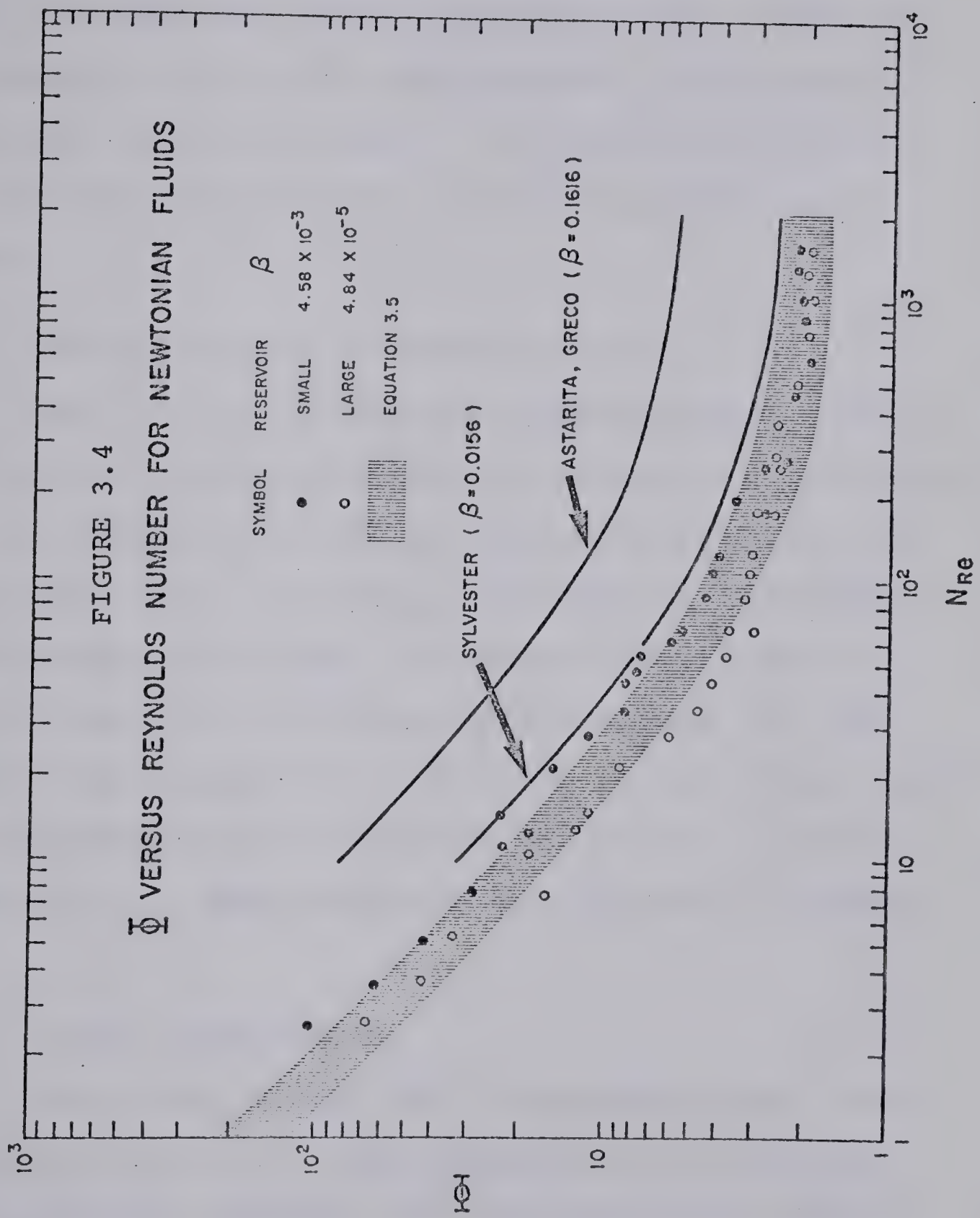
<u>Solution</u>	<u>Run Number</u>	<u>N_{Re}</u>	<u>$\Delta P_c \times 10^{-4}$ (dyn/cm²)</u>	<u>e.s.e. $\times 10^{-4}$ (dyn/cm²)</u>	<u>Percent Error</u>
Primol - 355	1	2.60	2.77	1.12	40
	3	5.16	4.43	2.05	46
	7	14.58	18.63	1.31	7
Sugar #4	1	20.63	2.32	0.54	23
	3	33.22	3.39	0.09	3
	6	62.15	7.21	1.12	16
Sugar #3	8	46.73	0.57	0.09	16
	3	268.1	5.76	0.94	16
	7	870.7	51.75	1.55	3
Sugar #1	1	126.9	0.57	0.12	21
	4	509.2	4.98	0.08	2
	8	1539.8	44.90	1.85	4

the new location the temperature of the fluids was maintained within $\pm 0.5^\circ\text{F.}$) This temperature fluctuation resulted in a 1.7 percent change in the viscosity of the sugar solutions, hence, there were smaller percent errors. As a result of the large percent errors in measuring the contraction losses it was not possible to claim significant differences between the contraction losses obtained with either reservoir.

The contraction losses plotted in Figure 3.4 and the data reported by Sylvester (161) as well as those reported by Astarita and Greco (4) can be represented by Equation 1.12. More specifically, for contraction ratios approaching zero, the contraction losses, according to Kaye and Rosen (93), can be represented by Equation 3.5

$$\phi = (2.26 \pm .26) + \frac{159 \pm 30}{N_{\text{Re}}} \quad 3.5$$

Equation 3.5 is plotted in Figure 3.4 and is indeed representative of the contraction losses measured in this research for contraction ratios approaching zero. At finite contraction ratios, ϕ is predicted to decrease as β increases (Equations 1.8 and 1.10). Sylvester (161) and Astarita and Greco (4) reported an increase in ϕ as β increased. This contradiction can be explained in terms of the presence of a vena contracta and inaccurate measurements of pressure both of which gave rise to larger values of ϕ .



3.2 VISCOELASTIC FLUID

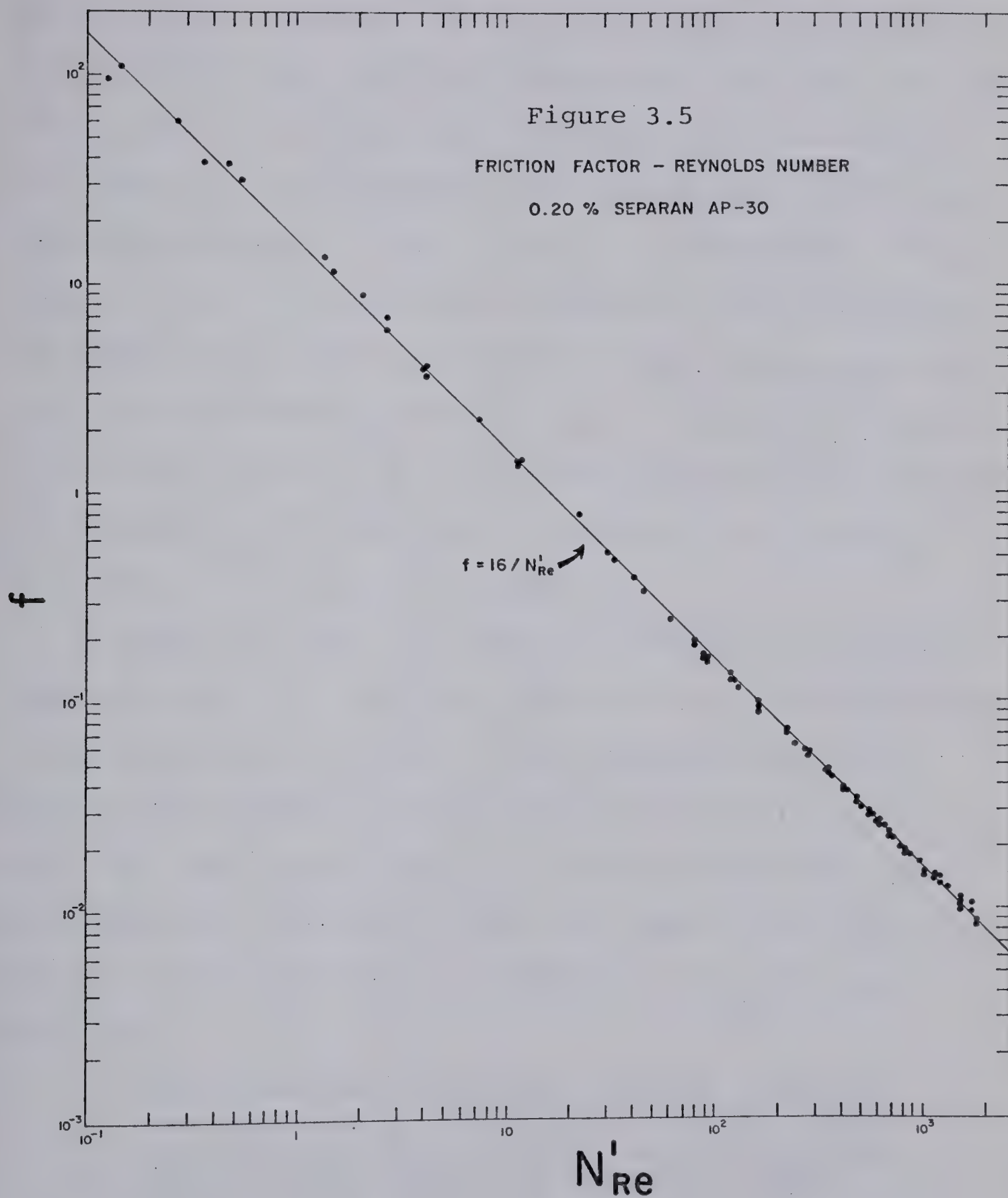
The friction factors and Reynolds numbers obtained from the aqueous 0.20% solution of Separan AP-30 are discussed. In addition, visual observations are given on: (a) velocity field within the reservoir, (b) pressure traces, and (c) jet of fluid. A discussion on criteria for the onset of instability is also included in this section.

3.2.1 FRICTION FACTOR - REYNOLDS NUMBERS

The friction factors and Reynolds numbers obtained with the viscoelastic fluid are shown graphically in Figure 3.5. Individual points deviate less than 8 percent from the straight line, $f = 16/N'_{Re}$, for generalized Reynolds numbers from 0.13 to 1866. The shear stresses used in computing the friction factors were estimated from the slopes of the Bagley plots. Measured pressure losses used in constructing the Bagley plots can be found in Appendix B; the resulting shear stresses are tabulated in Appendix D.

3.2.2 VISUAL OBSERVATIONS

Three observations used in determining the limits of stability were: (a) visual observations of the flow field within the reservoir, (b) observations of fluctuations in the pressure traces, and (c) visual observations of the jet of fluid issuing from the capillary tube.



(i) Velocity Field Within Reservoir

At low flow rates, hereinafter referred to as region I, stable flow fields existed within the reservoir. The qualitative features of the stable flow field discussed in Chapter I, i.e., the cone semi-angles, the center of the eddies, and the velocity distribution within the converging flow field, were measured and will be discussed in the following sections of this chapter. At intermediate flow rates, in what will be termed region II, a departure from the stable flow field was observed; within this region the flow field developed a swirling motion. A further increase in flow rate resulted in a flow field that failed to exhibit any regularity and could best be described as "chaotic." This will be referred to as region III.

A departure from the stable flow field occurred at the onset of region II. In this region the flow field developed a very slow swirling motion. The following description given by Rama Murthy (142) and observed by Ballanger and White (12) and Oyanagi (132) is also representative of the features of the flow field that were observed in this study when the word "reservoir" is substituted for the word "barrel":

The stream entering into the tube appeared to oscillate to and fro in the barrel like a snake tail when viewed in a single plane. This swirling motion in the barrel swept the fluid in the secondary flow region, continuously dragging it into the tube ... At increased shear rates, the swirling flow became more vigorous ... The overall nature of the flow appeared to remain similar

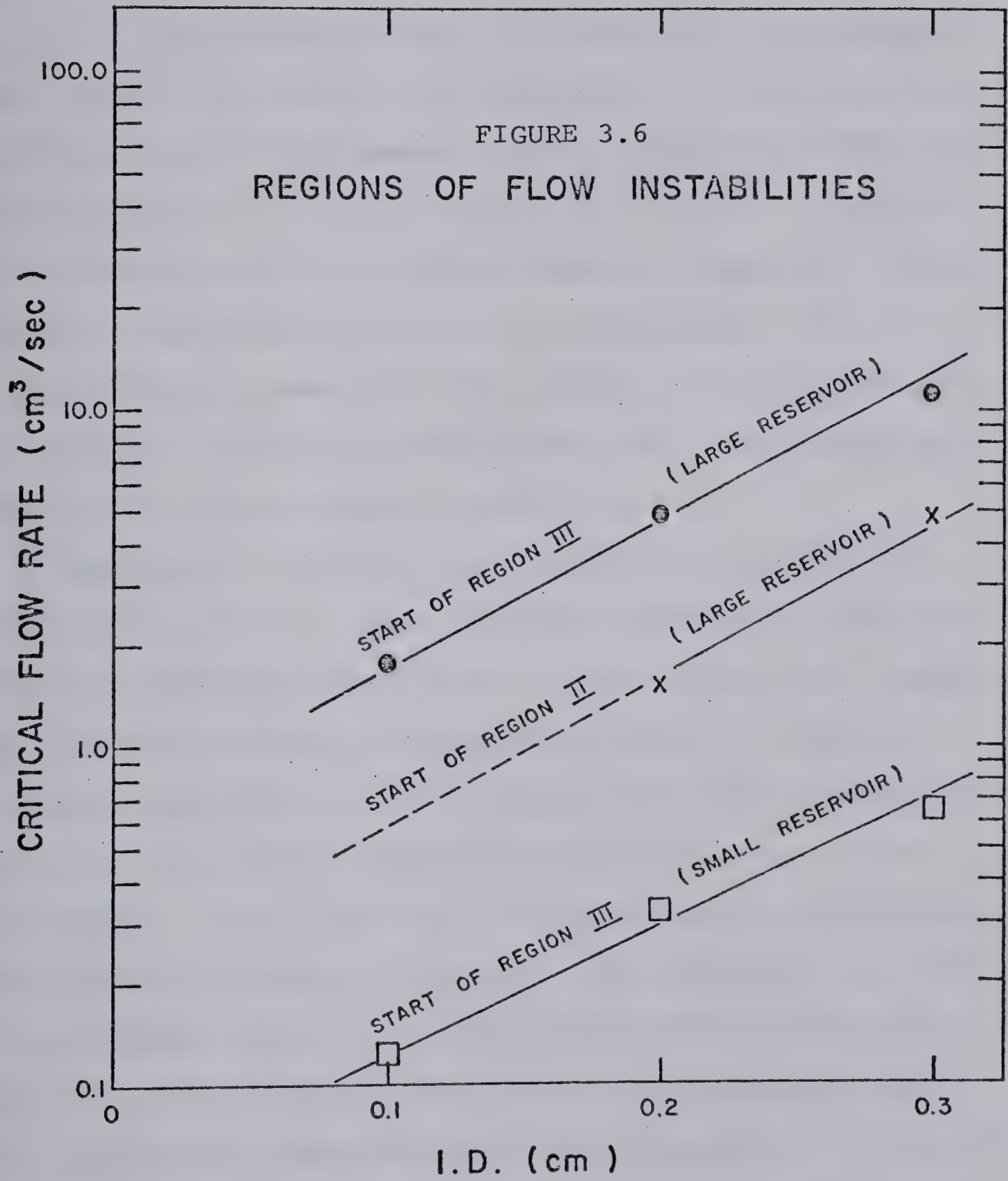
except for the intensity of swirling.

It was found in this research that if the crosshead speed of the Instron was gradually increased to the desired setting, which amounts to a gradual increase in flow rate, a stable flow field could exist within region II. This procedure did not always guarantee success. The procedure had to be repeated several times before obtaining a sufficient number of photographs from which the velocity profiles could be constructed.

Within region III the flow field failed to exhibit any regularity and it is described as "chaotic." In a few experimental runs the flow field within the reservoir was observed to oscillate between stable and "chaotic" flow fields. This seemed to occur at random and the duration of time that the flow field remained stable or "chaotic" was long enough so that the oscillation could be observed by eye. In a preliminary experimental run a stable flow field was observed over a four minute duration before the flow field abruptly became "chaotic." The seven experimental runs where the oscillating flow field was observed in reservoir L were run number 11 for capillary tube 1, run numbers 8, 9, and 10 for capillary tube 2, and run numbers 10, 12, and 16 for capillary tube 3. In reservoir S, this was observed for run number 9 with capillary tube 1. To the best of the author's knowledge, this is the first time that observations of the flow field oscillating between a stable and a "chaotic" flow regime within the reservoir

have been reported. This observation offers an explanation for the behavior in the pressure traces reported by Kizior (94) and in the jet of fluid issuing from the capillary tube reported by Kroesser (98). In both experiments the flow rate was constant.

The flow rates at the visually observed onset of regions II and III are plotted in Figure 3.6 against the capillary tube diameter. Since the velocity profiles were not measured for capillary tube 1 in reservoir L, the flow rate defining the commencement of region II was estimated by extrapolation. Region II, as shown in Figure 3.6, extended over flow rates that ranged from approximately $1.6 \text{ cm}^3/\text{sec}$ to $4.9 \text{ cm}^3/\text{sec}$ for capillary tube 2 and $4.9 \text{ cm}^3/\text{sec}$ to $11.1 \text{ cm}^3/\text{sec}$ for capillary tube 3 in reservoir L. The flow rates covered by region II in reservoir S, although not documented, were observed to be less than 0.01, 0.06 and $0.10 \text{ cm}^3/\text{sec}$ for capillary tubes 1, 2, and 3 respectively. These were smaller than the increments of flow rate used in obtaining the velocity profiles and were within the accuracy of measuring flow rates used to define the onset of region III. Therefore, the onset of region III was considered to be coincident with the onset of region II in reservoir S. A broad classification of the flow field into three regions has been reported for other dilute polymer solutions (142) and melts (12, 188). However, the observations of Rama Murthy (142) indicated that beyond region III the flow field abruptly changed to a



stable flow field that is similar to that observed with the flow of HDPE melts. This was not observed in this research.

(ii) Pressure Traces

All pressure traces were taken at the pressure taps located 10.2 and 27.9 cm upstream of the contraction. Smooth pressure displacement traces, similar to those shown in Figures 2.11 and 2.12 in Chapter II (pages 74 and 75), were obtained with stable flow fields in region I. Within region II the pressure traces remained smooth, i.e., pressure fluctuations, if they existed, were too small to be measured. Pressure fluctuations were measurable only for the flow rates within region III.

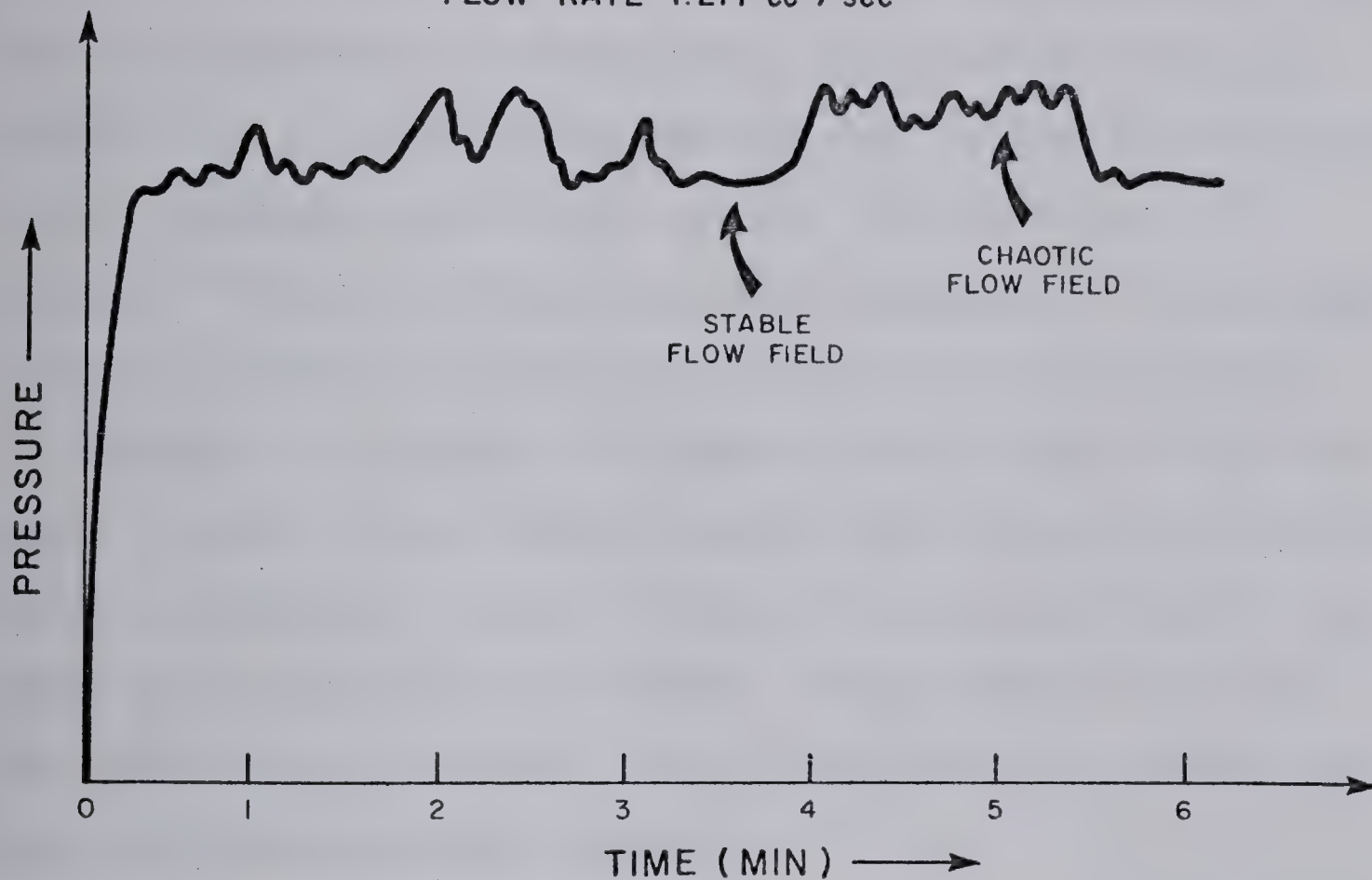
Two typical pressure traces within region III are shown in Figure 3.7. When the flow field within the reservoir was observed to oscillate between stable and "chaotic," the resulting pressure traces were similar to trace A. In trace A the difference in pressure between stable and "chaotic" flow fields was most discernible. At higher flow rates, it was difficult to differentiate between the two levels of pressure directly. With reference to trace A, the lowest level of pressure corresponds to the existence of a stable flow field within the reservoir while the upper level corresponds to the existence of a "chaotic" flow field within the reservoir. Pressure traces similar to trace A were reported by Kizior (94); the results of Kizior's research indicated that both the upper and lower

FIGURE 3.7

PRESSURE DISPLACEMENT TRACES WITHIN REGION III

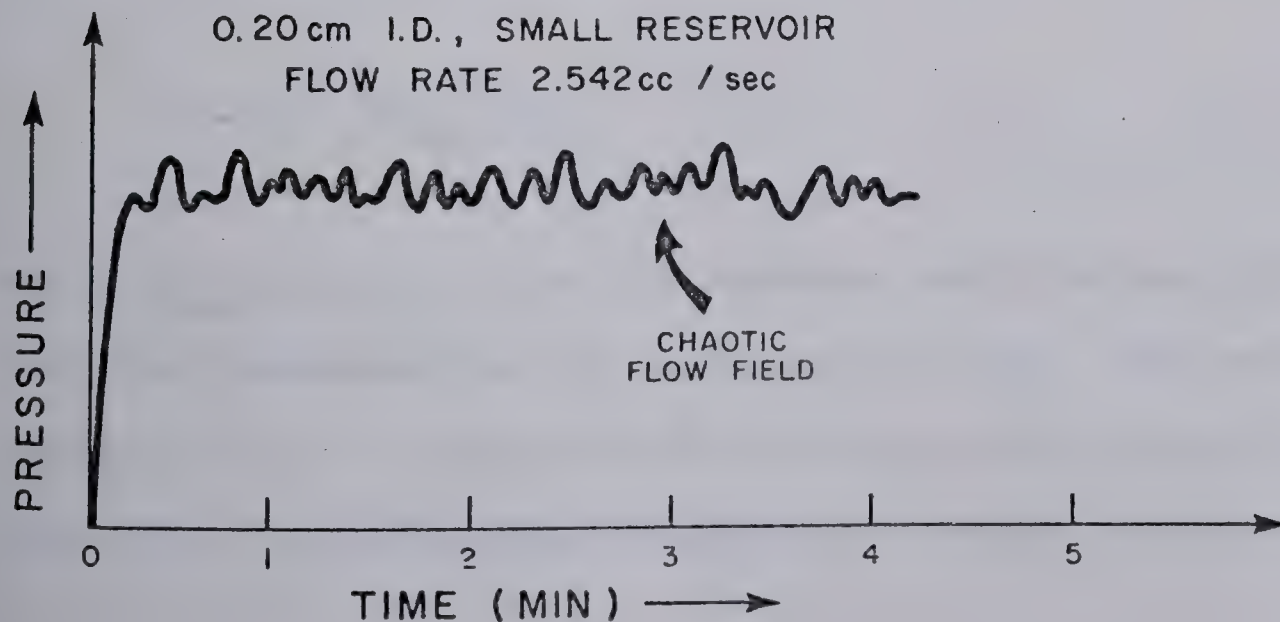
TRACE A

0.10 cm I.D., SMALL RESERVOIR
FLOW RATE 1.271 cc / sec



TRACE B

0.20 cm I.D., SMALL RESERVOIR
FLOW RATE 2.542 cc / sec



values of pressure remained constant with respect to time. This means that if pressure fluctuations existed they were too small to be measured. Therefore, the upper level of pressure in trace A measured by Kizior (94) corresponded to a flow field which was neither funnel-shaped nor "chaotic." As mentioned previously, the oscillation of the flow field between a stable and a "chaotic" flow was observed only for eight experimental runs in the present work. In the remaining runs within region III where only a "chaotic" flow field was observed, the pressure traces were similar to trace B. With the exception of a time scale, the changes in pressure in traces A and B appear to be the same. However, upon closer examination one may discern that these two pressure traces resulted from differences in the state of the upstream flow field. These results indicate the significance of having both visual observations of the flow field and pressure traces.

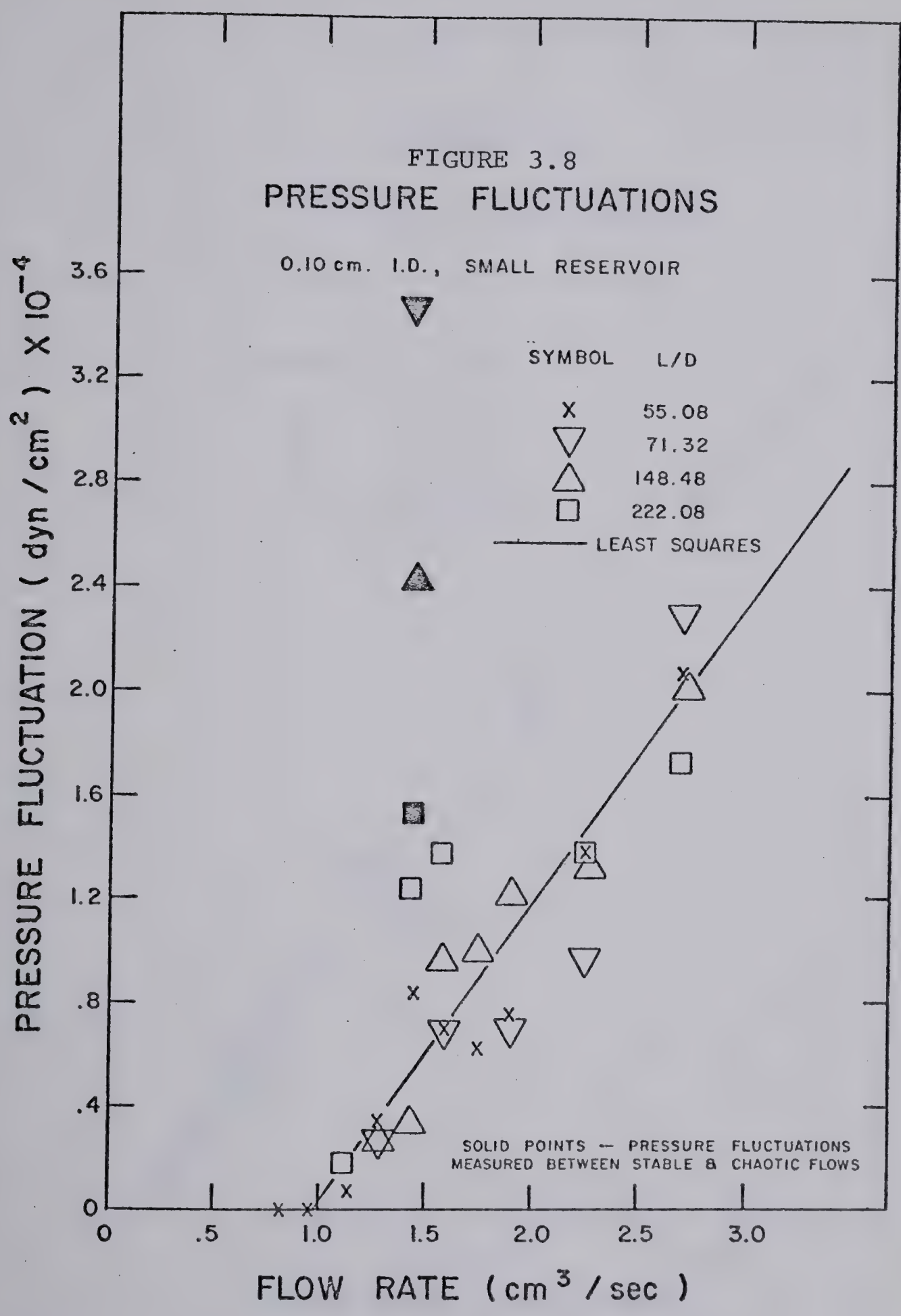
With respect to the pressure traces in Figure 3.7, an average value of pressure, calculated after the transient period, was defined as

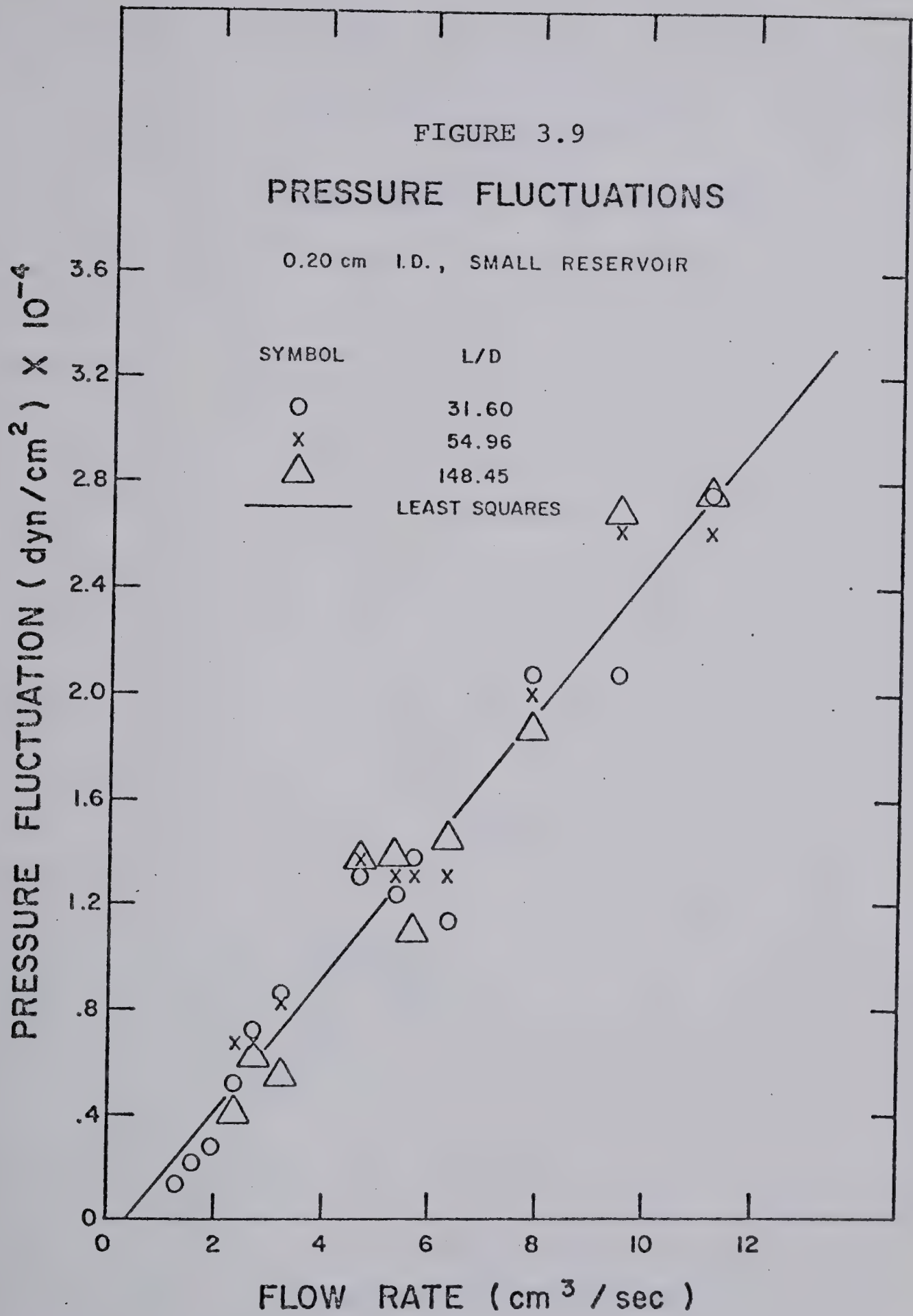
$$\bar{P} = \frac{P_{\max} + P_{\min}}{2} \quad 3.6$$

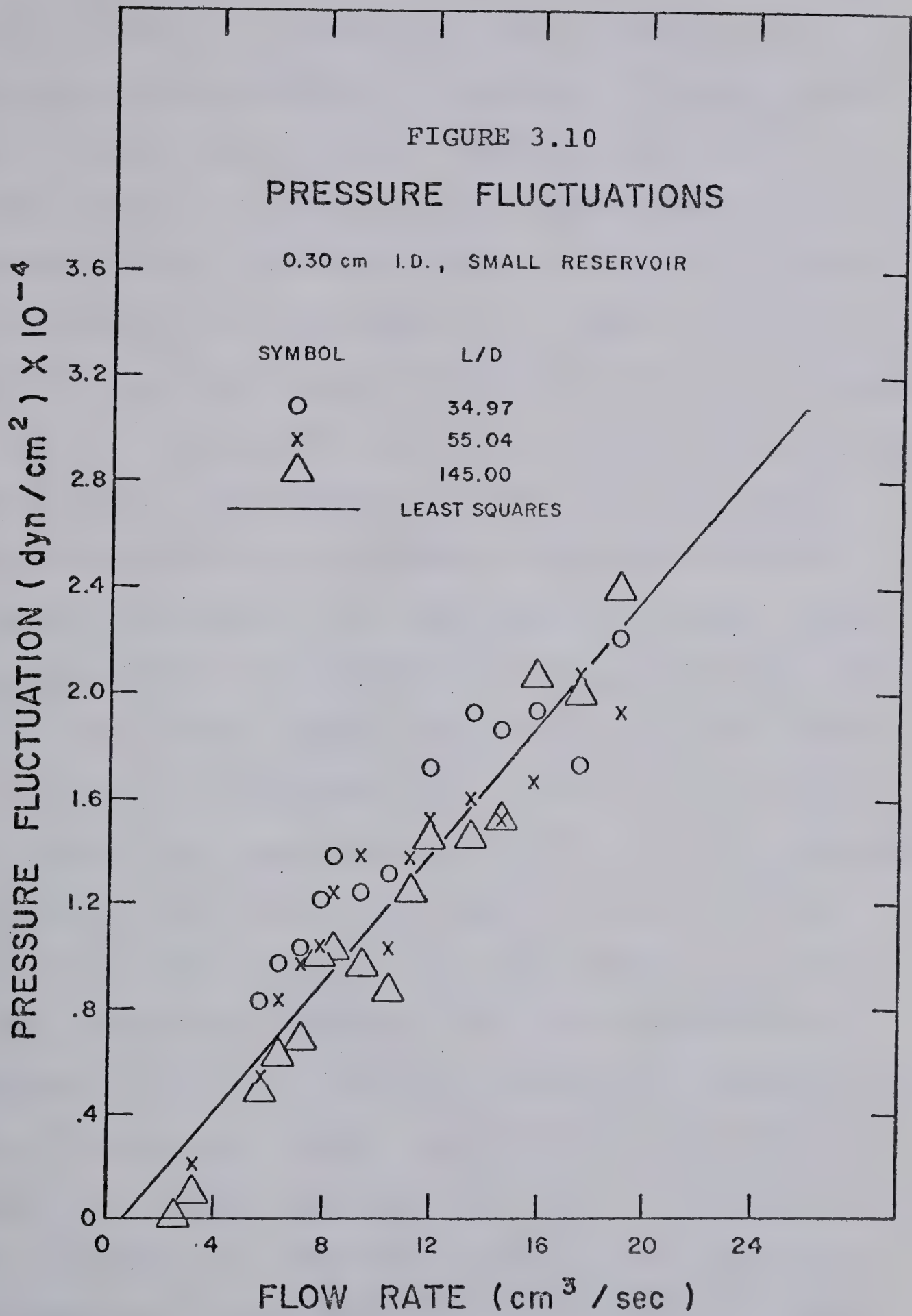
where P_{\max} and P_{\min} are the maximum and minimum values of pressure recorded for an experimental run. The pressure fluctuation, P , reported in this work was defined to be equal to the difference between the average value of

pressure and the maximum deviation or fluctuation from the average. The resulting pressure fluctuations for the experimental runs in reservoir S are shown graphically in Figures 3.8, 3.9 and 3.10 for capillary tubes 1, 2, and 3 respectively for several length to diameter ratios. Although there is considerable scatter about a single line, the data show that pressure fluctuations are largely independent of the capillary tube length to diameter ratio. This suggests that the onset of flow instability is also independent of the capillary tube length to diameter ratio. The line drawn through the data points in Figures 3.9 and 3.10 intersects the abscissa at flow rates that coincide reasonably with the onset flow rates that were obtained by visual observations of the flow field. The latter flow rates were used to define the onset of region III (Figure 3.6, page 94). Plots similar to those shown in Figures 3.8 to 3.10 were also obtained with reservoir L and can be found in Appendix B. In spite of the subjectivity of visual observations and the limited resolution in measuring pressure fluctuations, the agreement between the two kinds of data is considered good.

The onset of pressure fluctuations did not coincide with the onset of visually observed "chaotic" flow field for capillary tube 1. In this case, the flow rate defining the onset of region III was $0.119 \text{ cm}^3/\text{sec}$ when determined visually and $1.0 \text{ cm}^3/\text{sec}$ from the pressure measurements (Figure 3.8). It is not possible to explain







this discrepancy directly but it may have been caused by air in the system. Experimentally, it was observed that when an air pocket of substantial size was deliberately trapped within the reservoirs it acted as a damping mechanism which delays the onset of a "chaotic" flow field to higher flow rates. These flow rates were at least an order of magnitude larger than the critical flow rates in which no air was trapped in the reservoirs. Hence, the limits of stability can be significantly increased if a gas is trapped in the system. All visible trapped air was removed from the reservoirs in the experimental runs but some air always remained in the hydraulic cylinder. Although care was exercised in reproducing the experimental procedure, there was no guarantee that the quantity of trapped air was constant. In view of the sensitivity of the stability limit to air pockets, an unaccounted for variation in the quantity of trapped air could have caused the noted discrepancy. Another factor which could have caused the discrepancy was the use of two batches of the 0.20% Separan solution. Since the solution was prepared in a limited quantity, it was necessary to have two batches. The first was used in obtaining the pressure traces and the second was used in measuring the velocity profiles and recording visual observations. However, the physical properties of these two batches tabulated in Appendix D are essentially the same over a wide range of apparent shear rates. Therefore, it is unlikely that the discrepancy was a result of the

differences between the physical properties of the two batches.

At a flow rate equal to $1.43 \text{ cm}^3/\text{sec}$, several of the data points in Figure 3.8, given as solid points, are considerably above the straight line. Similar results are shown in Figures B.1 to B.3 in Appendix B (pages 280-282). These large pressure fluctuations are representative of the fluctuations which occurred when the flow field was observed to oscillate between stable and "chaotic" flows. If pressure fluctuations were measured only over the interval of time when the flow field was observed to be "chaotic" the pressure fluctuations are consistent with the remaining data.

In summary, the following generalizations can be made:

(a) The onset of measurable pressure fluctuations coincide reasonably with the visually observed onset of region III.

(b) The onset of region III is independent of the capillary tube length to diameter ratio.

(c) Pressure fluctuations that lie significantly above the remaining data can be explained in terms of the state of the flow field within the reservoir.

(iii) Jet of Fluid

The third set of observations involved the qualitative features of the jet of fluid issuing from the capillary tube. For flow rates within regions I and II the jet of fluid was observed to be smooth. With the

"chaotic" flow field that was observed in region III, the jet of fluid fluctuated with a frequency that was approximately equal to the frequency of the pressure fluctuations. When the flow field within the reservoir was observed to oscillate between stable and "chaotic" the jet of fluid oscillated between two different trajectories. In one trajectory, corresponding to the stable flow field, the jet of fluid was smooth; in the other, corresponding to the "chaotic" flow field, the jet was distorted. This offers an explanation for the "curious phenomenon" reported by Kroesser (98) wherein the jet of fluid, at a constant flow rate, oscillated between the above mentioned two trajectories.

A summary of observations of the flow field within the reservoir, the pressure fluctuations, and the jet of fluid issuing from the capillary tube is given in Table 3.2.

TABLE 3.2

OBSERVATIONS WITHIN REGIONS I, II, AND III

<u>OBSERVATION</u>	<u>REGION I</u>	<u>REGION II</u>	<u>REGION III</u>
Flow field in reservoir	Stable	Swirling or Stable	Chaotic or Chaotic- Stable
Pressure fluctuations	Zero	Not Measurable	Measurable
Jet of fluid	Smooth	Smooth	Oscillating

These observations together with: (a) the visual observations reported by Rama Murthy (142), and others (12, 130, 132), (b) the pressure profiles measured by Han and Lamonte (80), and (c) the fact that the flow curve for this polymer solution is smooth, suggest that for polymer solutions or melts characterized by a WGS upstream flow field, the initiation site may occur within the inlet region rather than within the capillary tube.

3.2.3 CRITERIA FOR ONSET OF INSTABILITY

The flow rates defining the onset of regions II and III, Figure 3.6 (page 94), lead to the evaluation of dimensional and dimensionless parameters as a means of correlating the limits of stability. The two most commonly used parameters referred to in the literature, the critical shear stress and the recoverable shear strain, were calculated and are tabulated in Table 3.3. Parameters with no asterisk were evaluated at the onset of region II while those with an asterisk were evaluated at the onset of region III. The flow rate used in evaluating the shear stress and the recoverable shear strain for capillary tube 1 in reservoir L was determined by extrapolating the data in Figure 3.6. The data in Table 3.3 indicate that the shear stress and the recoverable shear strain (which is directly proportional to the shear stress): (a) vary somewhat with capillary tube diameter, (b) vary strongly with reservoir size, and (c) depend upon the type of instability

TABLE 3.3

 τ_w and S_R AT ONSET OF INSTABILITY

RESERVOIR S	I.D. (cm)		
	0.10	0.20	0.30
Q^* (cm ³ /sec)	0.119	0.318	0.635
τ_w^* (dyn/cm ²)	125.0	72.6	56.0
$S_R^* = \left(\frac{\tau_w^{MW}}{CR_0 T}\right)$	7.7	4.5	3.5
τ_w^{***} (dyn/cm ²)	167-1667	167-1667	167-1667
RESERVOIR L			
Q^* (cm ³ /sec)	1.750	4.866	11.120
Q (cm ³ /sec)	0.580**	1.589	4.866
τ_w^* (dyn/cm ²)	630.1	305.0	240.0
τ_w (dyn/cm ²)	296.0	162.0	154.0
$S_R^* = \left(\frac{\tau_w^{MW}}{CR_0 T}\right)$	38.8	18.8	14.8
$S_R = \left(\frac{\tau_w^{MW}}{CR_0 T}\right)$	18.2	10.0	9.5
τ_w^{***} (dyn/cm ²)	167-1667	167-1667	167-1667

* Onset of region III

** By extrapolation of data in Figure 3.6

*** Southern and Paul (157) assuming the shear stress at the onset of instability for polymer melts varies from 10^5 to 10^6 dyn/cm² and the density of the melt is 1.20 gm/cm³

(regions II or III).

Variations in τ_w or S_R with the type of instability and capillary is exemplified by the data in reservoir L. At the onset of region II, S_R increased from 9.5 to 18.2 as the capillary tube diameter decreased from 0.30 to 0.10 cm. On the other hand, at the onset of region III, S_R was almost twice as large, $14.8 \leq S_R \leq 38.8$. These values are within the range reported for other polymer solutions (98, 190) wherein S_R ranged from 6.0 to 42.8 and 2.2 to 66.81 (see Table 1.3, page 41) for polymer melts. With a fixed tube diameter, stable flow fields within the inlet region were observed to exist up to higher flow rates or equivalently higher shear stresses in reservoir L. For example, with capillary tube 3 the shear stress evaluated at the onset of region II was 56 dyn/cm^2 in reservoir S, whereas in reservoir L it was 154 dyn/cm^2 . Although reasons for this behavior are not clear it is postulated that the difference may be due to differences in the upstream velocity field (Section 3.4.4, page 141) with reservoir size.

The range of shear stresses at the onset of flow instabilities (region II or III), although four orders of magnitude less than 10^6 dyn/cm^2 for polymer melts, are in reasonable agreement with shear stresses calculated from the analysis presented by Southern and Paul (157), $167 \leq \tau_w \leq 1667 \text{ dyn/cm}^2$. Furthermore, shear stresses evaluated at the onset of region II or III compare favourably with critical shear stresses obtained by other re-

searchers (98, 119, 130, 142). Murch (119), using a 0.5% solution of Separan AP-30 in a 30 percent by weight glycerine-water mixture and with $\beta = 1.86 \times 10^{-6}$, observed that the stable flow field broke down at shear stresses approximately equal to 500 dyn/cm^2 . It is not clear, however, whether this breakdown corresponded with the onset of region II or III. In a more concentrated solution, 1.49% Separan AP-30 in a 50 percent by weight glycerol-water mixture and with $\beta = 18.5 \times 10^{-3}$, the estimated shear stress at the onset of regions II and III were 500 and 3000 dyn/cm^2 respectively (142). Oliver and Bragg (130) reported inlet flow instabilities for orifice flows and with a 0.10% aqueous solution of ET-597, β varying from 92.2×10^{-4} to 4.0×10^{-2} , the estimated shear stress at the onset of region III varied from 225 to 20 dyn/cm^2 .

In summary, variations in S_R may arise from: (a) the type of instability (region II or III), (b) variations with the reservoir size, and (c) variations with the capillary tube diameter. The recoverable shear strain or shear stress criterion, although simple to evaluate and requiring little, if any, additional experimentation, does not account for the observed dependence on capillary tube diameter and reservoir size. More critically, these criteria, which are based on conditions in SLSF in the capillary tube, are not consistent with experimental observation wherein initiation occurs within the inlet region. Criteria based on inlet conditions have been proposed by Cogswell (46),

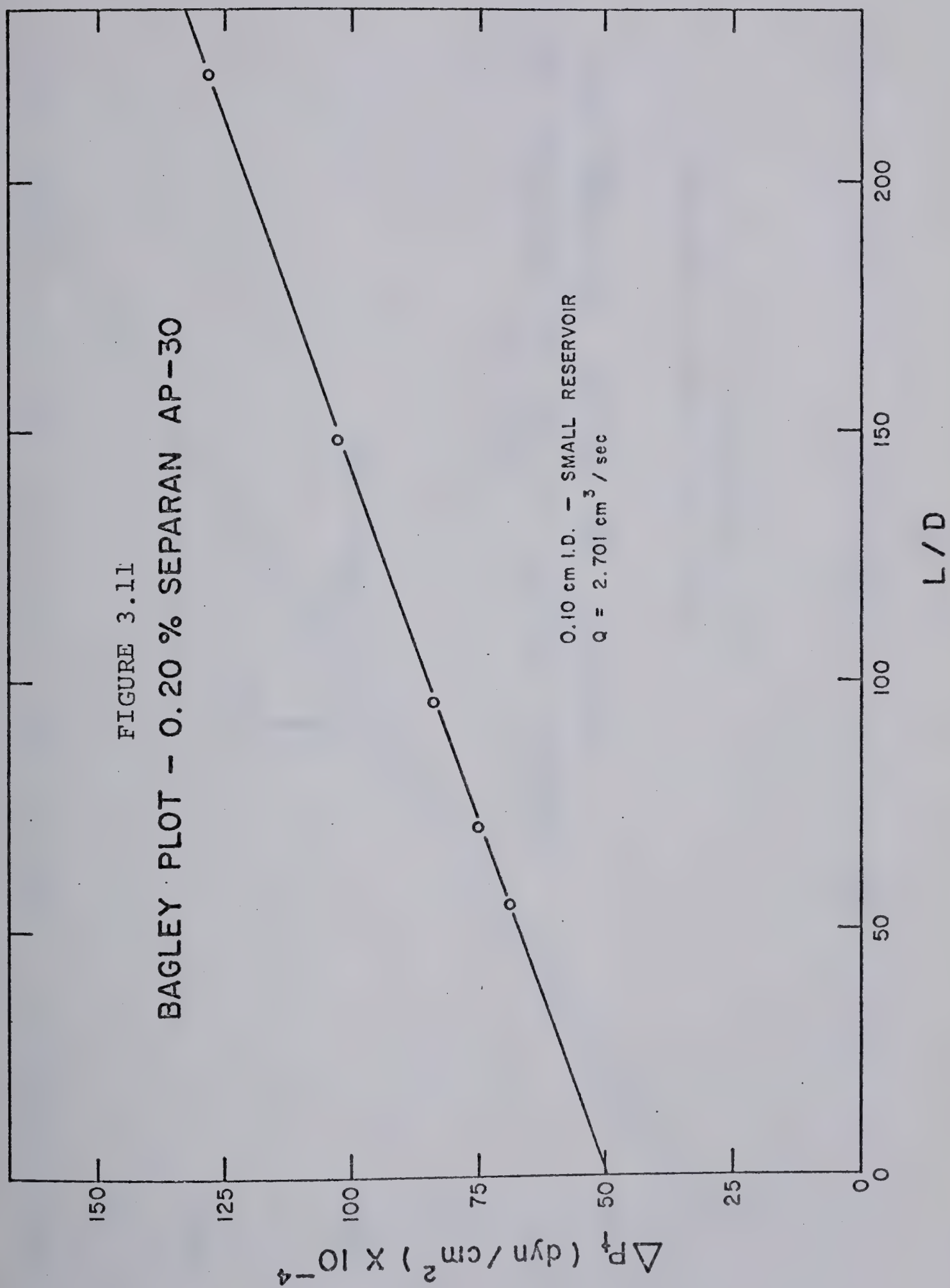
Everage and Ballman (60), and Hürlimann and Knappe (88). Since these criteria depend upon inlet conditions, i.e., initial cone semi-angle and the velocity field, the discussion of these criteria is delayed to Section 3.5. The features of the flow field, the cone semi-angles, and the velocity field are discussed in Section 3.4.

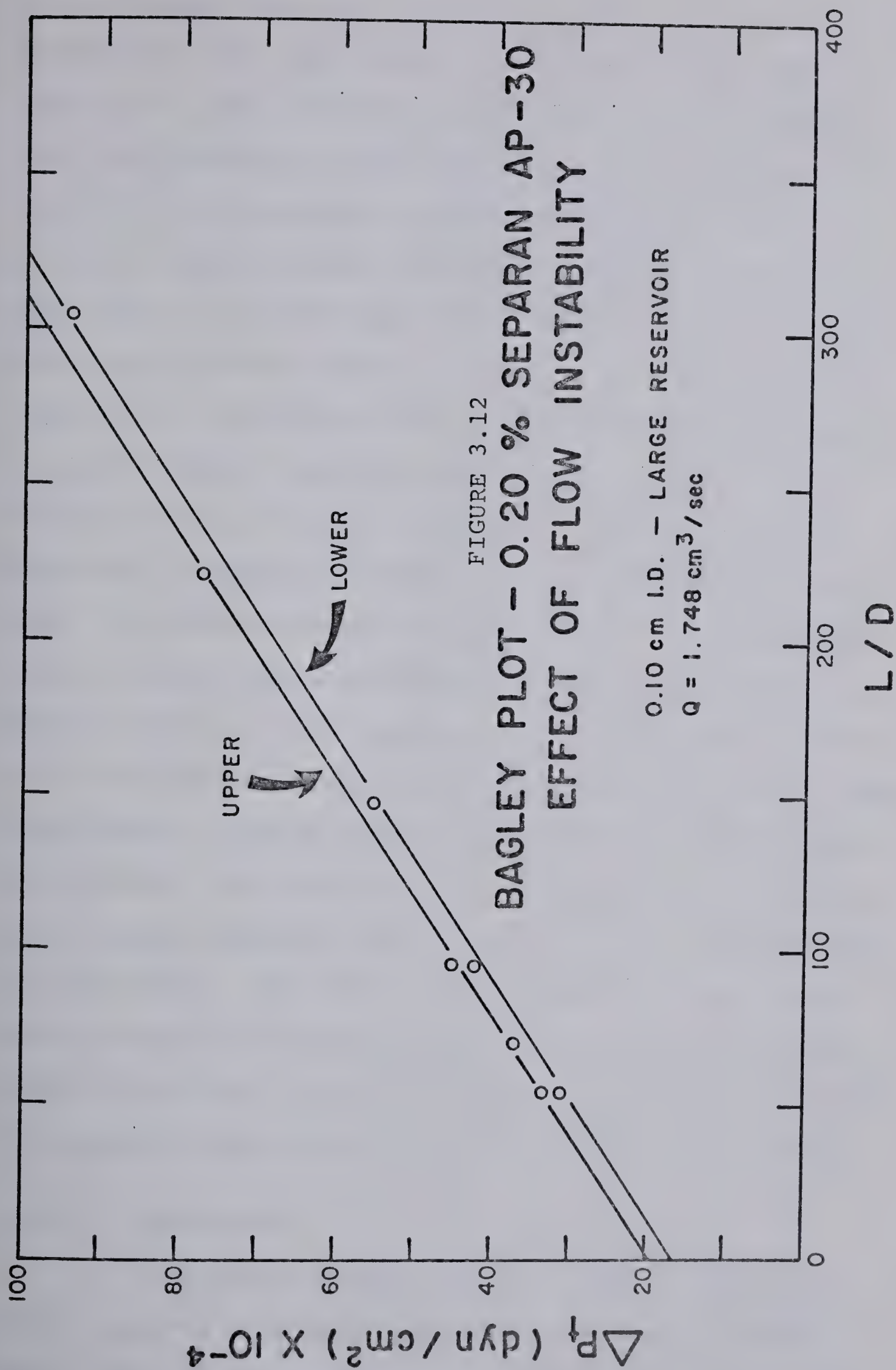
3.3 EFFECTS OF INSTABILITY

The effects of instability are discussed in conjunction with the Bagley plots, the flow curve, the total pressure loss-flow rate curve, and the contraction losses.

3.3.1 BAGLEY PLOT

The average values of pressure (Equation 3.6, page 97), measured at the reservoir wall at a location upstream of the contraction, were used in constructing the Bagley plots. A typical Bagley plot is given in Figure 3.11 for a flow rate within region III. The plot is linear and the shear stress, equal to four times the slope, is in good agreement with the extrapolation of the shear stress data obtained with a Weissenberg rheogoniometer (Appendix D). Figure 3.12 shows two Bagley plots for an experimental run where oscillations between a stable and a "chaotic" flow field were observed within the reservoir. In this case the two Bagley plots resulted from pressures measured with a stable flow field (lower plot) and for pressures measured with a "chaotic" flow field (upper plot).





In both cases, the plots are linear and the resulting shear stresses are the same whether evaluated from the upper or lower plot. The intercept of the upper plot is greater than the intercept of the lower plot, hence, instability resulted in an increase in the contraction losses.

At a constant flow rate within region III and for a given capillary tube length to diameter ratio the pressure trace may be either smooth or similar to trace A or B in Figure 3.7. In terms of the flow field within the reservoir it may be stable, may oscillate between a stable and a "chaotic" flow or may be "chaotic". The total pressure losses are related to the state of the flow field. Therefore, in constructing true Bagley plots, i.e., measuring total pressure losses for several capillary tube length to diameter ratios, it is necessary to know the state of the flow field with each capillary tube length to diameter ratio. Furthermore, although stable flow fields are implied from zero pressure fluctuations it is not possible to differentiate between pressure trace A or B without a knowledge of the flow field. The construction of Bagley plots using average values of pressure (Equation 3.6) without a knowledge of the state of the flow field will result in errors in evaluating shear stresses and the contraction losses.

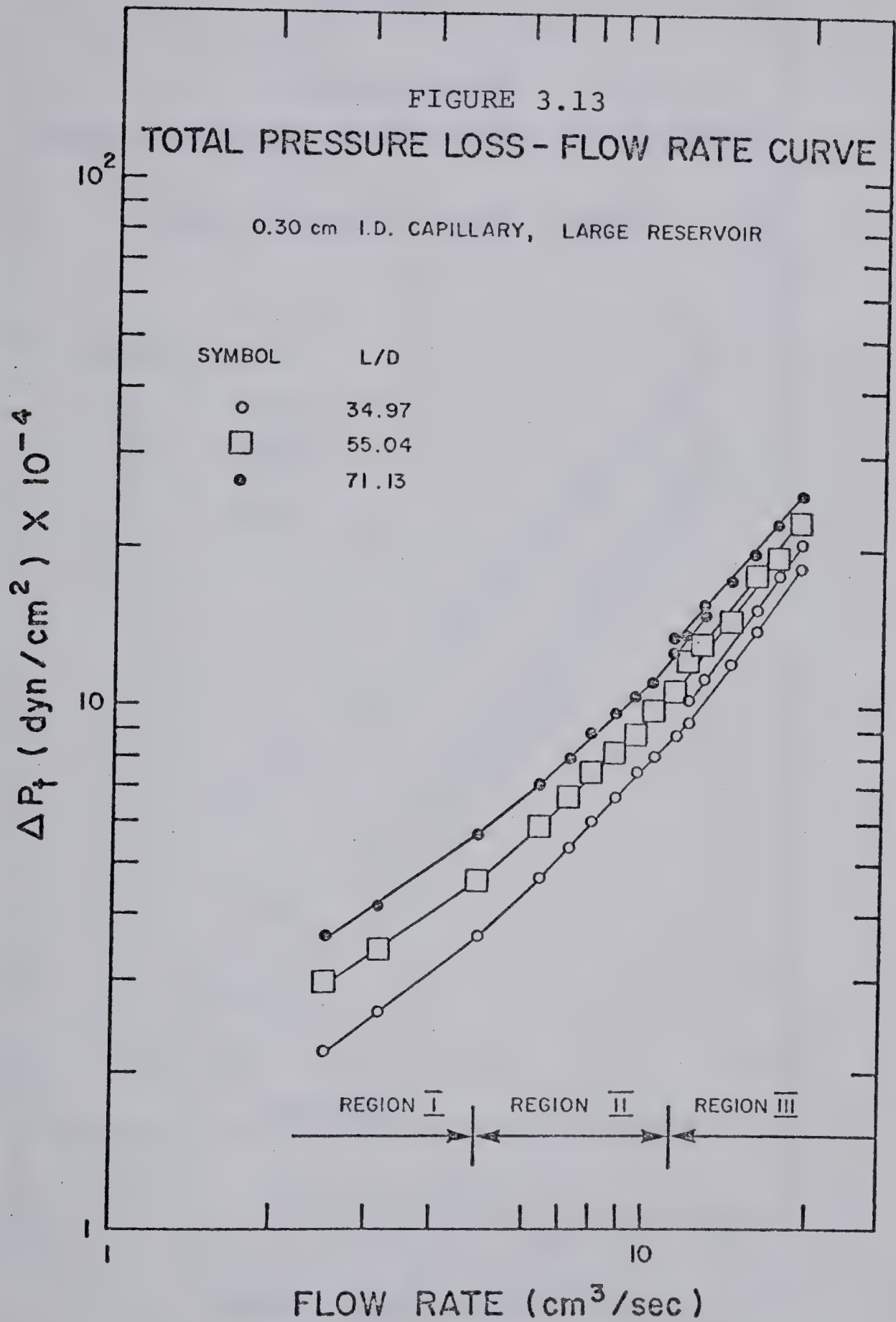
3.3.2 FLOW CURVE

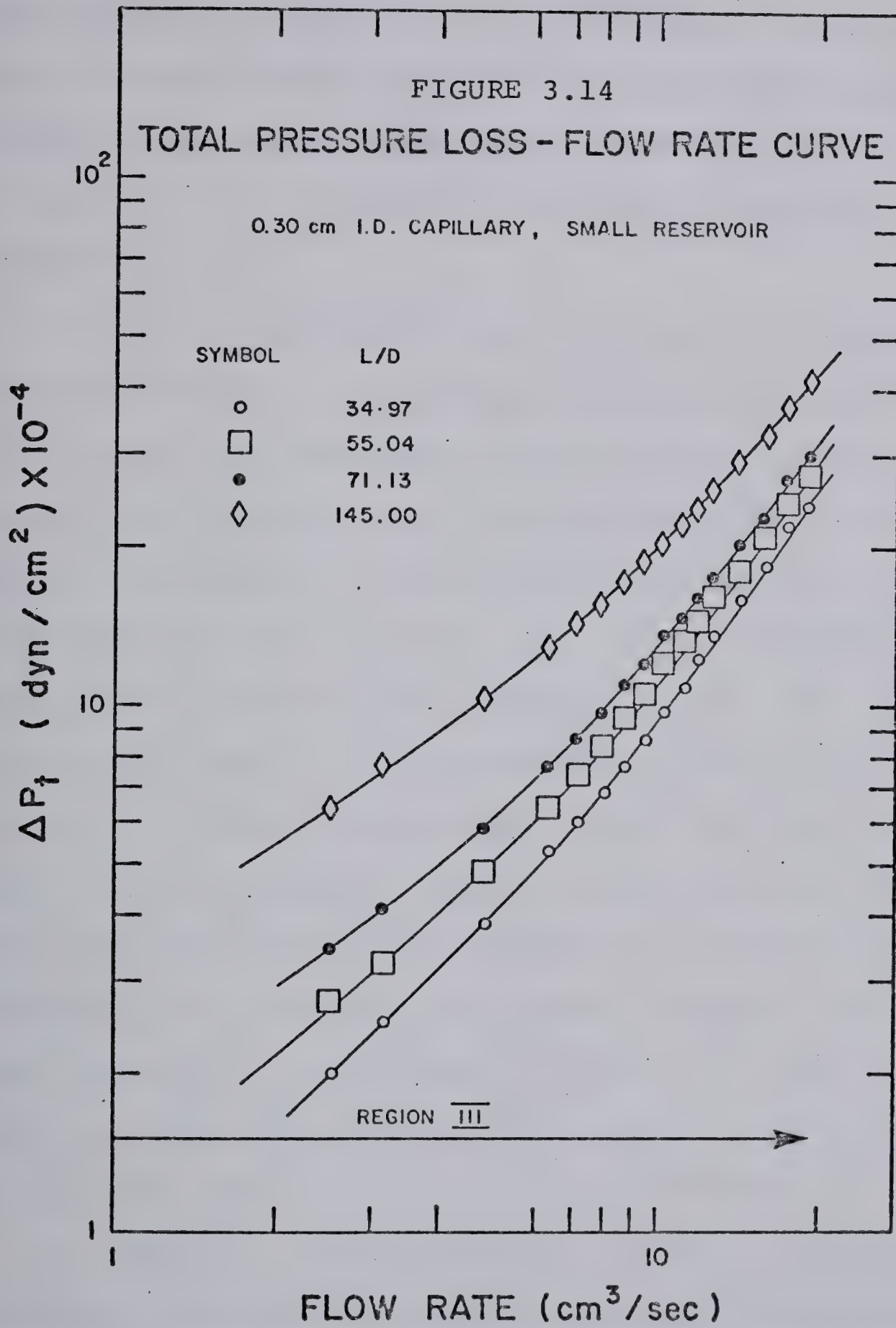
The shear stresses used to construct the flow curve, Figure D.2 in Appendix D, were obtained from the Bagley plots for reservoir L. No significant differences

in shear stresses were found when reservoir S was used. The flow curve was smooth and continuous over a wide range of apparent shear rates. The onset of flow instability had no effect on the flow curve. This is consistent with results reported for other polymer solutions and melts where instability occurs within the inlet region (inlet initiation).

3.3.3 TOTAL PRESSURE LOSS - FLOW RATE CURVE

Typical ΔP_t -Q plots, Figures 3.13 and 3.14, were constructed with the data tabulated in Appendix B. Values of ΔP_t , were averaged over the time interval that the flow field was either "chaotic" or stable. Figure 3.13 shows that the total pressure losses within regions I and II increased with increasing flow rate although the flow field in region I was stable and within region II a swirling motion was observed. No abrupt increase in pressure was measurable. At several flow rates within region III two values of pressures were measured. For the remaining flow rates within region III and for all flow rates within regions I and II only one value of pressure was measured. The sudden increase in ΔP_t (pressure jump) at the onset of region III can be explained in terms of a change from a stable to "chaotic" flow field within the reservoir. With reference to Figure 3.7 (page 96), at a given flow rate the upper level of pressure corresponds to a "chaotic" flow field and the lower level of pressure corresponds to the existence of a stable flow field. If Equation 3.6





were used to determine an average value of ΔP_t , a pressure jump would still exist. The magnitude of the pressure jump would be reduced since the new value of ΔP_t would now lie midway between the two measured levels of pressure. Therefore, the sudden increase in the ΔP_t -Q curve is not a result of interpretation of the pressure displacement traces.

The data graphically shown in Figure 3.13 indicate that the difference in pressure arising from changes in the state of the flow field within region III was independent of the L/D ratio. As the capillary tube length increased, the ratio of this difference in pressure to the total measured pressure loss, ΔP_t , tended to zero. Therefore, in the limit of very large L/D ratios, the ΔP_t -Q curve would appear to be smooth even at the onset of region III. The curves passing through the data in Figure 3.14 are smooth, although these data were obtained with flow rates well within region III. Visual observations indicated that the flow field became "chaotic" for flow rates exceeding $0.635 \text{ cm}^3/\text{sec}$ (Figure 3.6). The lowest flow rate where the total pressure losses were measured for the data shown in Figure 3.14 was $2.5 \text{ cm}^3/\text{sec}$.

In summary, sudden increase in pressure observed in the total pressure loss-flow rate curves occurred at the onset of region III and this pressure jump can be explained in terms of the transition between a stable motion to one described as "chaotic." Furthermore, this sudden increase

in pressure occurred at a flow rate that was independent of L/D ratios, i.e., the onset of fracture was independent of L/D ratios. It is important to emphasize that these plots, ΔP_t vs Q , are useful in determining the onset of fracture (region III) only when the pressure jump is of such magnitude that it can be measured.

3.3.4 CONTRACTION LOSSES

Contraction losses are shown graphically in Figure 3.15 and 3.16 as a function of the capillary tube generalized Reynolds numbers. Included for comparison purposes are the data for Newtonian fluids that were reported in Section 3.1.2, page 83. The flow rates defining the onset of region III as obtained from the onset of measurable pressure fluctuations and the visually observed onset of a "chaotic" flow field were coincident. The only exception was for capillary tube 1 in reservoir S; hence, contraction losses obtained with the 0.10 cm I.D. capillary are not plotted in Figure 3.16.

Day (50) measured contraction losses and observed the qualitative features of the flow field for the flow of poly (ethylene oxide) solutions through an orifice. The results can be summarized as follows:

(a) Under creeping flow conditions the fluid behaved like a Newtonian fluid, i.e., it entered into the orifice through a 180 degree solid angle and the contraction losses were equal to the Newtonian contraction losses.

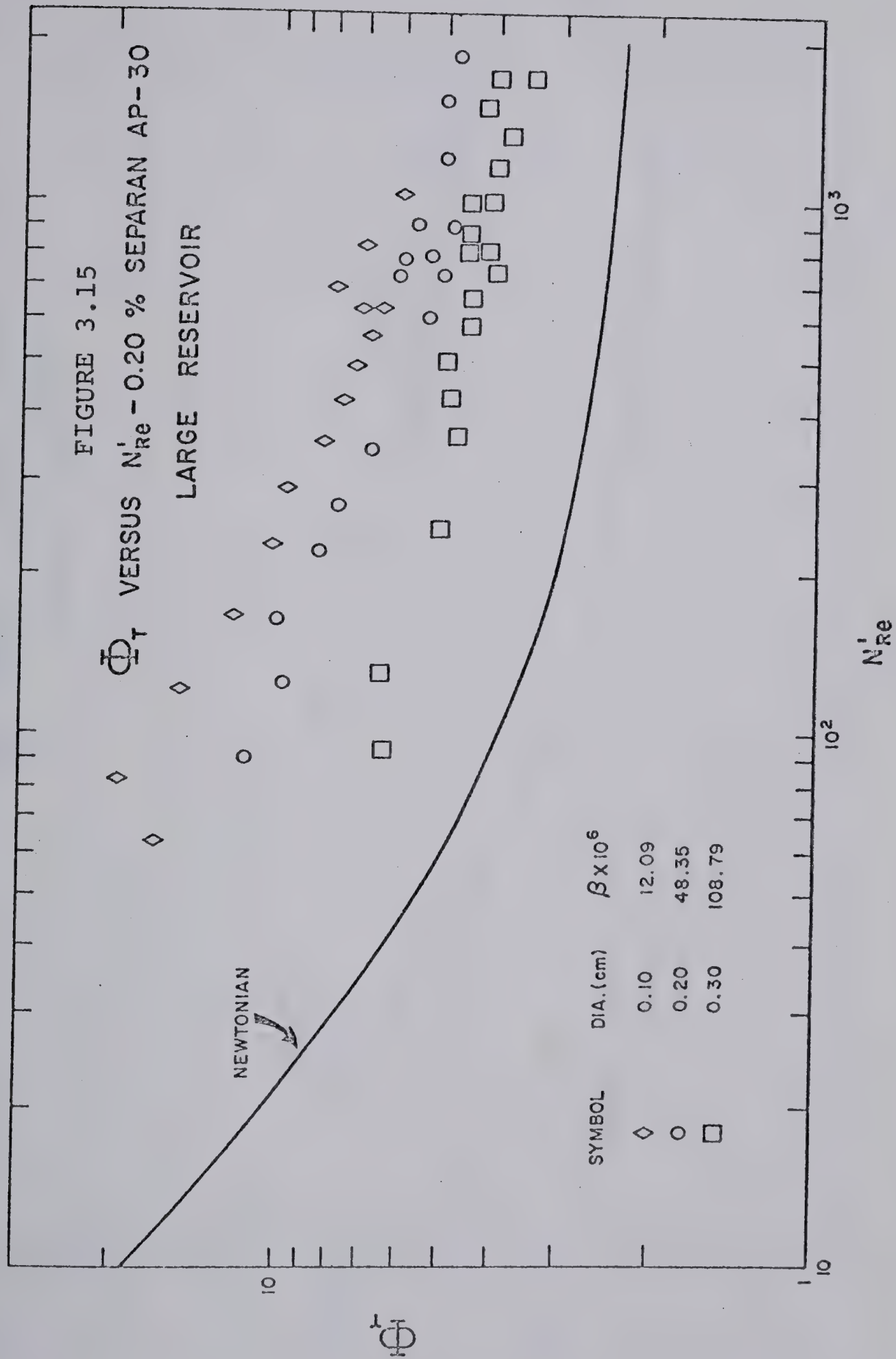
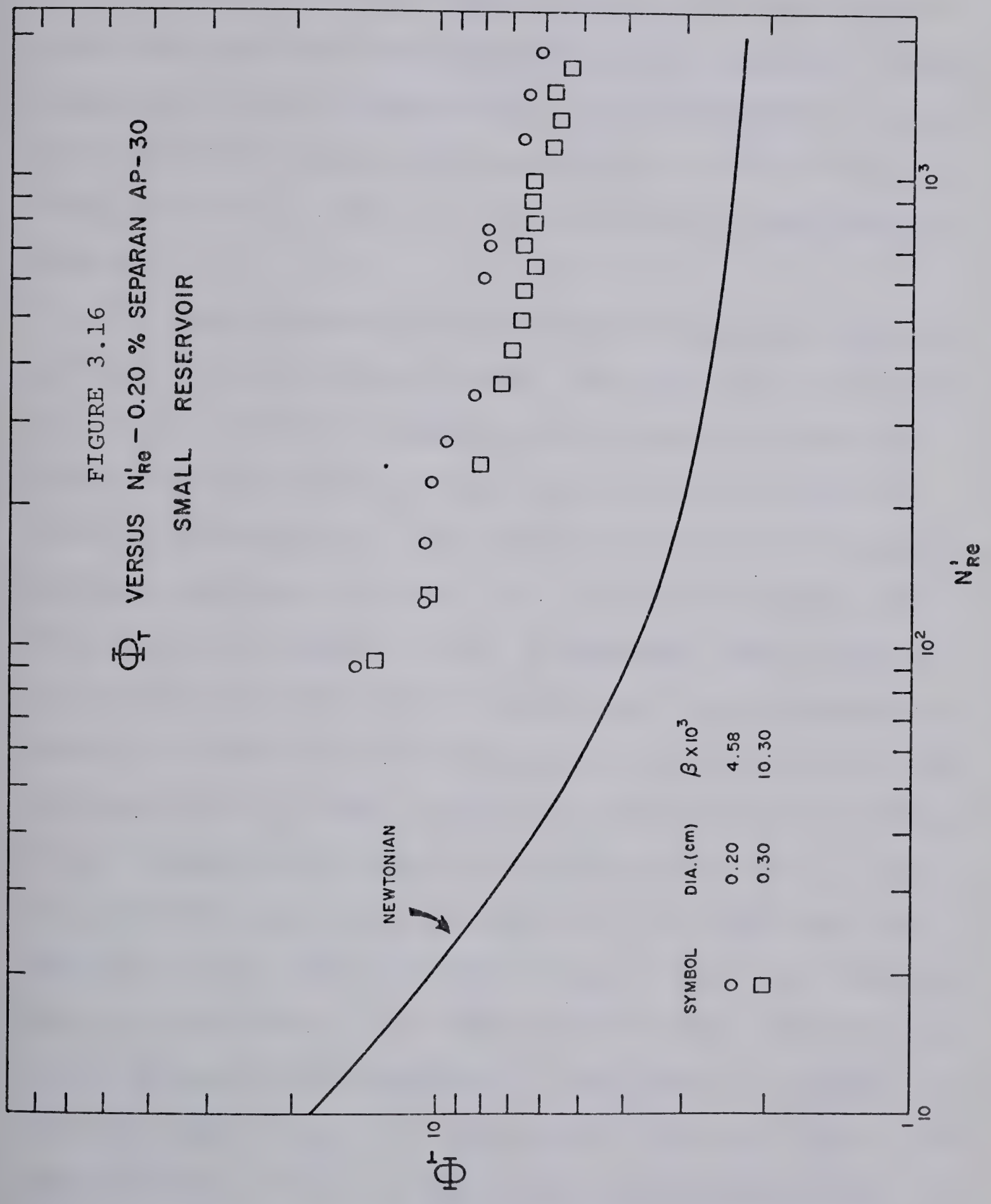


FIGURE 3.16
 Φ_T VERSUS N'_{Re} - 0.20 % SEPARAN AP-30
SMALL RESERVOIR



(b) When a certain Reynolds number was reached the fluid behavior changed abruptly. An extremely small vortex appeared exactly at the edge of the orifice which grew in both width and depth as Reynolds number increased. Correspondingly, the contraction losses increased to the extent that they were greater than Newtonian results at the same Reynolds number. This will be classified as the onset of region I.

In this dissertation contraction losses were measured at Reynolds numbers approaching the upper limit of region I as well as Reynolds numbers within regions II and III where a swirling motion and a "chaotic" flow field were observed respectively. The effects of these flow fields (stable, swirling, chaotic) on ϕ_t is exemplified by the data plotted in Figure 3.15. At Reynolds numbers evaluated at the onset of region II, 121, 126 and 246 for capillary tubes 1, 2, and 3 respectively, there is insufficient data in Figure 3.15 to show conclusively an effect of the change from a stable to an observed swirling motion on ϕ_t . At the onset of region III, however, the data indicated an increase in ϕ_t . This occurred at $N'_{Re} = 620, 721, \text{ and } 816$, for capillary tubes 1, 2, and 3 respectively. Contraction losses measured with reservoir S and plotted in Figure 3.16, were obtained at $N'_{Re} \geq 91$, whereas the onset of region III was observed to occur at $N'_{Re} \approx 10$. Hence, contraction losses in reservoir S were measured only within region III. At several N'_{Re} within region III two values of ϕ_t

are shown in Figure 3.15. For example, with capillary tube 1 and at $N'_{Re} = 620$, the two values of ϕ_t are 6.46 and 7.08. As the flow field oscillated between stable and "chaotic" the pressure displacement traces were similar to trace A in Figure 3.7. This gave rise to two Bagley plots (Section 3.3.1, page 111), hence, two values of ϕ_t .

The effect of tube diameter on contraction losses can be rationalized in terms of the condition of the flow field within the inlet region. With reference to the data plotted in Figure 3.15, flow fields were observed to be stable for all capillary tube I.D.'s at $N'_{Re} < 125$ but, at $N'_{Re} < 125$, ϕ_t increased as capillary tube I.D. decreased. At $N'_{Re} \approx 90$ the initial cone semi-angles for capillary tubes 1, 2, and 3 were 0.5, 0.90, and 1.2 degrees (Figure 3.23, page 136) respectively. Hence, the area occupied by the recirculation region was greatest for capillary tube 1. The effect of the larger recirculation region was a measured increase in contraction losses. At $N'_{Re} > 125$ the difference in ϕ_t with I.D. arose from differences in the state of the flow field. This is exemplified by comparing contraction losses measured with capillary tubes 1 and 3. At $N'_{Re} \approx 246$ a stable flow field was observed with capillary tube 3, whereas a swirling motion was observed with capillary tube 1. At a higher Reynolds number, e.g., $N'_{Re} \approx 730$, a "chaotic" flow field and a swirling motion were observed with capillary tube 1 and 3 respectively. The flow fields were observed to be "chaotic" in both capillary tubes only

at $N'_{Re} > 816$.

Comparison of data obtained with both reservoirs revealed that ϕ_t was consistently larger when obtained with reservoir S. This is not surprising since contraction losses measured with reservoir S were obtained only within region III, whereas in reservoir L contraction losses were measured in regions I, II, and III. At Reynolds numbers approaching 2000 the flow field was "chaotic" in both reservoirs. Equation 1.12 in Chapter I suggests that when the flow fields are the same in both reservoirs contraction losses may be correlated with N'_{Re} . We have shown that the Hagenbach correction factors are evaluated when a "chaotic" flow field exists and the Couette correction factor, although not measured, would have been obtained when the flow field was stable. Therefore, we conclude that it is not correct to correlate contraction losses over a wide range of Reynolds numbers when over the same range of Reynolds numbers the flow field changes from stable to "chaotic."

In summary, contraction losses depend upon capillary tube diameter and reservoir size. This dependence can be rationalized in terms of the conditions of the flow field within the inlet region. Furthermore, correlation of ϕ_t with N'_{Re} should be based on the same inlet flow field, as with Newtonian fluids. For the polymer solution used in this research and over the range of N'_{Re} where contraction losses were measured, three distinct flow fields were observed in the inlet region. Hence, a correlation of ϕ_t

with N'_{Re} is not presented.

3.4 VELOCITY FIELD UPSTREAM OF CONTRACTION

Three features of the flow field upstream of the contraction were measured:

(a) the axial and radial velocity components within the central accelerating core measured by the digitizer and direct methods,

(b) the cone semi-angles at and upstream of the contraction, and

(c) the location of the center of the eddies.

The cone semi-angles and the location of the eddy centers are given in order to present a complete description of the flow field within the reservoir.

3.4.1 VELOCITY - DIGITIZER AND DIRECT METHODS

Table 3.4 summarizes flow rates and dimensionless upstream axial locations where axial velocity profiles were measured. As indicated in the table, the velocity profiles obtained by the digitizer method were measured only at three upstream axial locations hereinafter referred to as axial locations 1, 2, and 3 respectively. The resulting total of approximately 10,000 individual data points obtained by the digitizer method are tabulated in Appendix E, Section E.2. The digitizer method was used also in measuring radial velocity components with the results tabulated in Appendix E, Section E.2.

As a typical example of the digitizer data, consider

TABLE 3.4

FLOW RATES AND UPSTREAM AXIAL LOCATIONS

WHERE VELOCITIES WERE MEASURED

RESERVOIR	CAPILLARY I.D.	$Q(\text{cm}^3/\text{sec})$	z/D
S	0.10 ($L/D = 55.08$)	0.016	*
		0.040	*
		0.119	*
	0.20 ($L/D = 54.96$)	0.040	*
		0.159	3.29
		0.159	6.57
		0.159	9.86
		0.238	*
		0.318	*
	0.30	0.040	*
		0.159	1.46
		0.159	2.92
		0.159	4.38
		0.318	*
		0.635	*
L	0.20 ($L/D = 54.96$)	0.159	*
		0.318	*
		0.794	*
		1.589**	15.34
		1.589**	30.67
		1.589**	46.00
		1.906	15.60
		1.906	31.20
		1.906	46.80
		2.383	17.33
		2.383	34.65
		2.383	51.98
		2.701	17.71
		2.701	35.42
		2.701	53.13

* velocities measured by the direct method

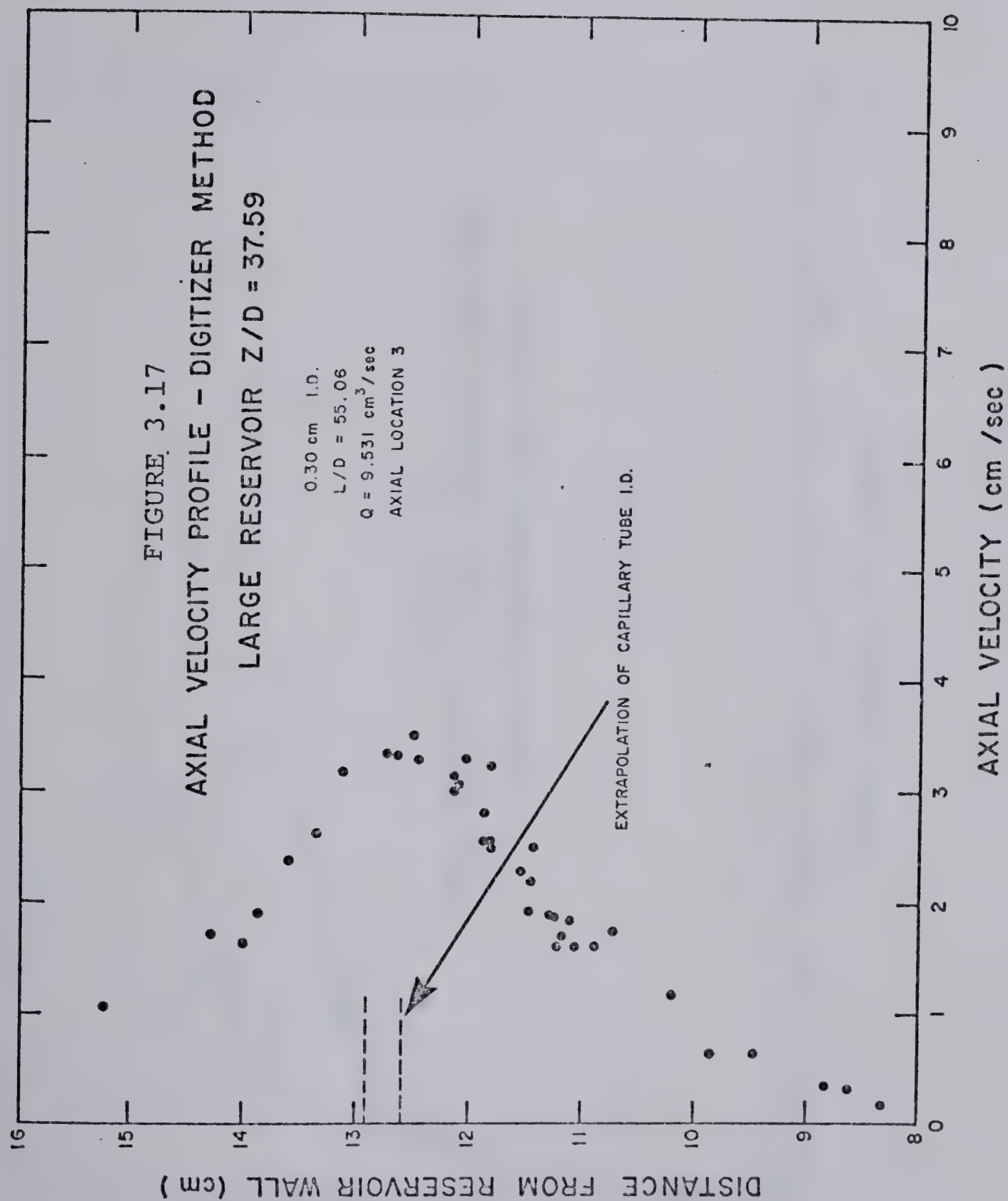
TABLE 3.4 (continued)

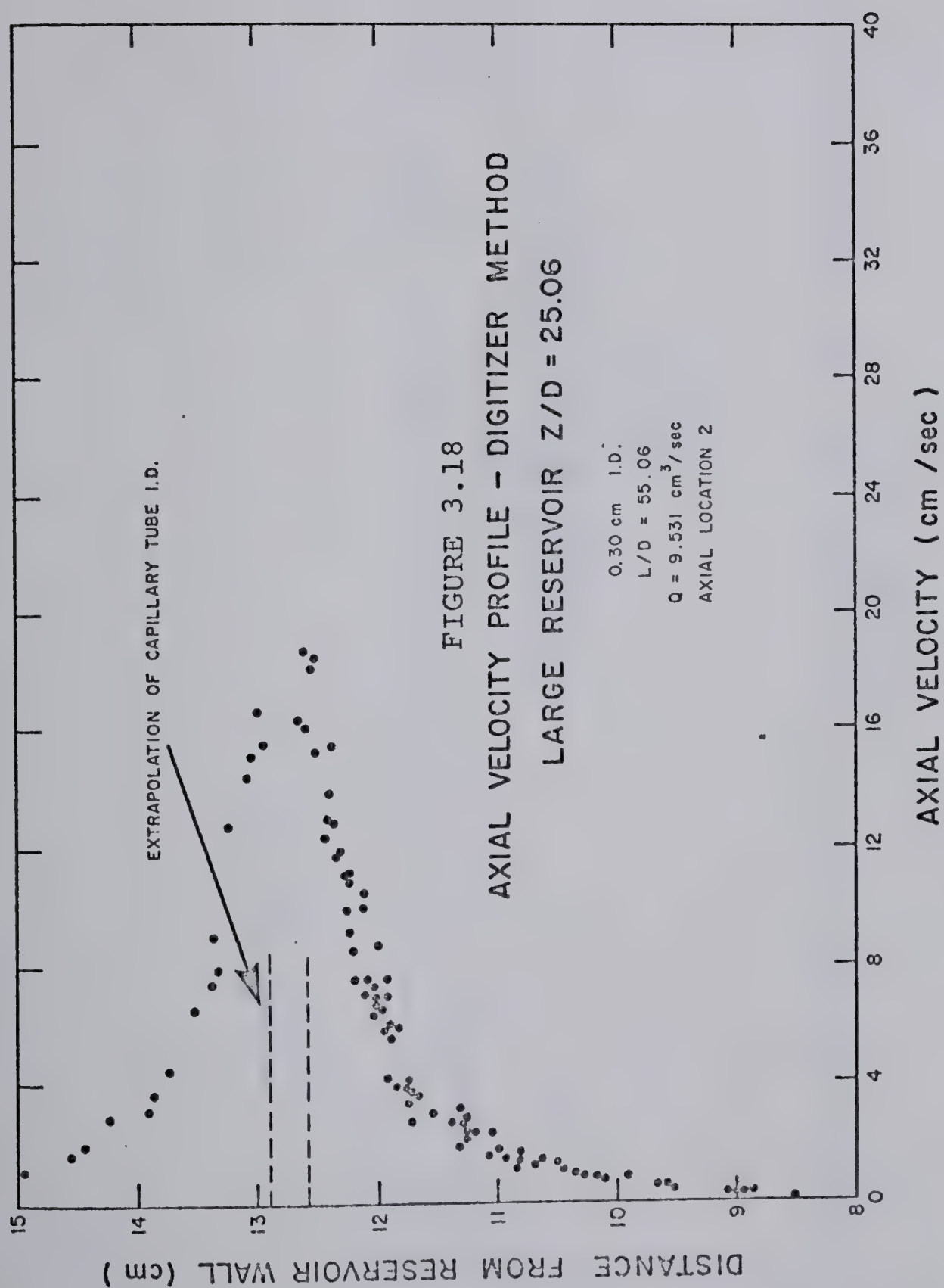
RESERVOIR	CAPILLARY I.D.	Q (cm ³ /sec)	z/D
		3.177	18.26
		3.177	36.52
		3.177	54.78
		3.812	19.39
		3.812	38.78
		3.812	58.17
		4.866	19.73
		4.866	39.45
		4.866	59.18
	0.30	0.318	*
	(L/D = 55.04)	0.635	*
		1.589	*
		4.866	10.95
		4.866	21.90
		6.354	11.56
		6.354	23.12
		7.148	11.92
		7.148	23.12
		7.943	12.04
		7.943	24.08
		8.737	12.45
		8.737	24.90
		9.531	12.53
		9.531	25.06
		9.531	37.59
		10.325	12.72
		10.325	25.44
		10.325	38.16
		11.120	12.72
		11.120	25.44
		11.120	38.16

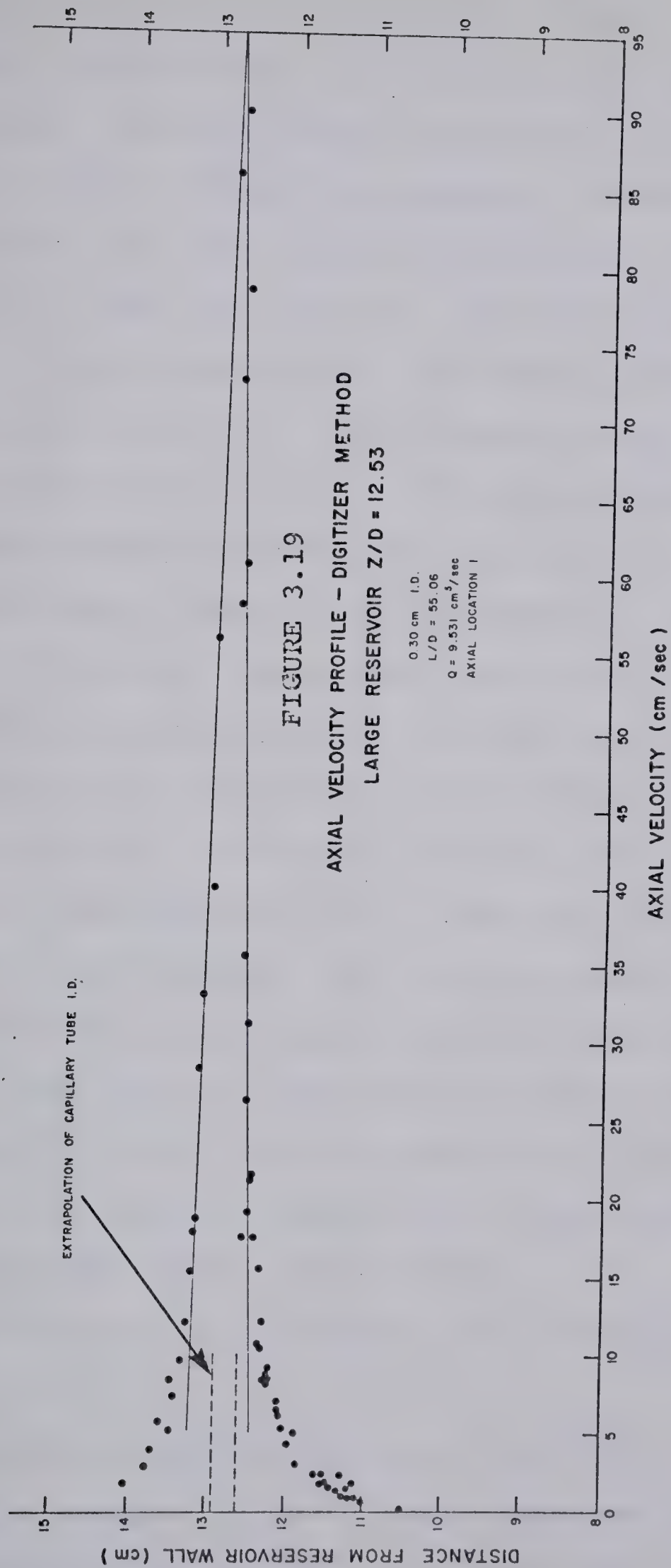
* velocities measured by the direct method

the axial velocities measured with capillary tube 3 at a flow rate of $9.531 \text{ cm}^3/\text{sec}$ in reservoir L. One may recall from Figure 3.6 (page 94) that flow rates between $4.866 \text{ cm}^3/\text{sec}$ and $11.120 \text{ cm}^3/\text{sec}$ were within region II. Stable flow fields within this region were obtainable only when the crosshead speed of the Instron was gradually increased to the desired setting; this amounted to a gradual increase in flow rate. The velocity profiles shown in Figures 3.17 to 3.19 are for the stable flow field. Forty to 300 individual data points were measured to determine velocity profiles. The velocity profiles shown in Figures 3.17 to 3.19 are axially symmetric with the axial velocity along the centerline being well defined at axial locations 2 and 3. The centerline velocities obtained from Figures 3.17 and 3.18 were 3.4 and 22.0 cm/sec respectively. At axial position 1 the velocity along the centerline was not well defined and was estimated in the following manner: With the data in Figure 3.19, lines were drawn through the individual data points that were close to the centerline. These lines were extrapolated until they intersected. The velocity corresponding to this intersection was used as an estimate of the centerline axial velocity which, for this example, was 93.0 cm/sec .

The flow rates where the velocity profiles were measured by the direct method, as tabulated in Table 3.4, have been denoted by an asterisk. Raw data are tabulated in Appendix E, Section E.1. With these data velocity







profiles were constructed and are given in Figures 3.20 to 3.22 at several upstream axial locations for the three capillary tubes. The data plotted in Figure 3.22 were obtained with capillary tube 3 in reservoir S and at a flow rate of $0.318 \text{ cm}^3/\text{sec}$. This flow rate was within region I, i.e., it is less than $0.635 \text{ cm}^3/\text{sec}$. The axial velocity profiles at the contraction, $z/D = 0.0$, were not measured directly but were obtained in the following manner: From the projected photographs, consecutive streaks along a streamline were measured and the axial velocity was determined as a function of position in the reservoir. This allowed plots of velocity versus axial position to be made which included measured velocities to within one or two streak lengths of the capillary entrance. Between this axial location and the contraction, the axial velocity was estimated by a linear extrapolation of the axial velocity-position plot to the entrance. The location nearest to the contraction where the axial velocity could be measured moved farther away from the contraction as the streak length increased. In all cases the length of extrapolation was less than one tube diameter and in some cases was as small as one sixth of the tube diameter.

Several conclusions can be drawn from the data plotted in Figures 3.17 to 3.22:

(a) The axial velocity profiles are not flat. In Figure 3.22, for example, at one diameter upstream of the contraction the axial velocities at the centerline and at a

FIGURE 3.20
AXIAL VELOCITY PROFILES
0.10 cm I.D. DIRECT METHOD
 $Q = 0.119 \text{ cm}^3/\text{sec}$

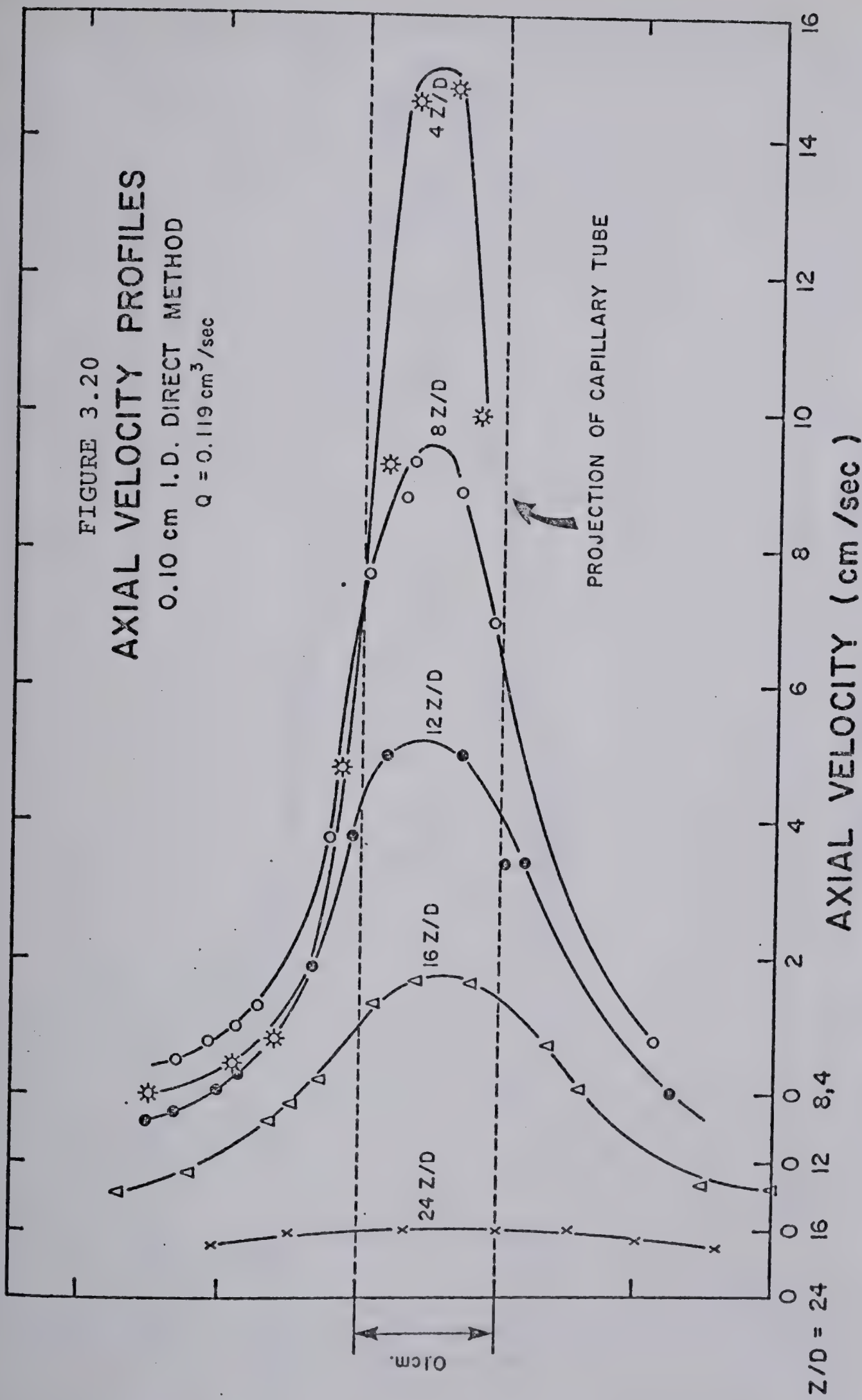
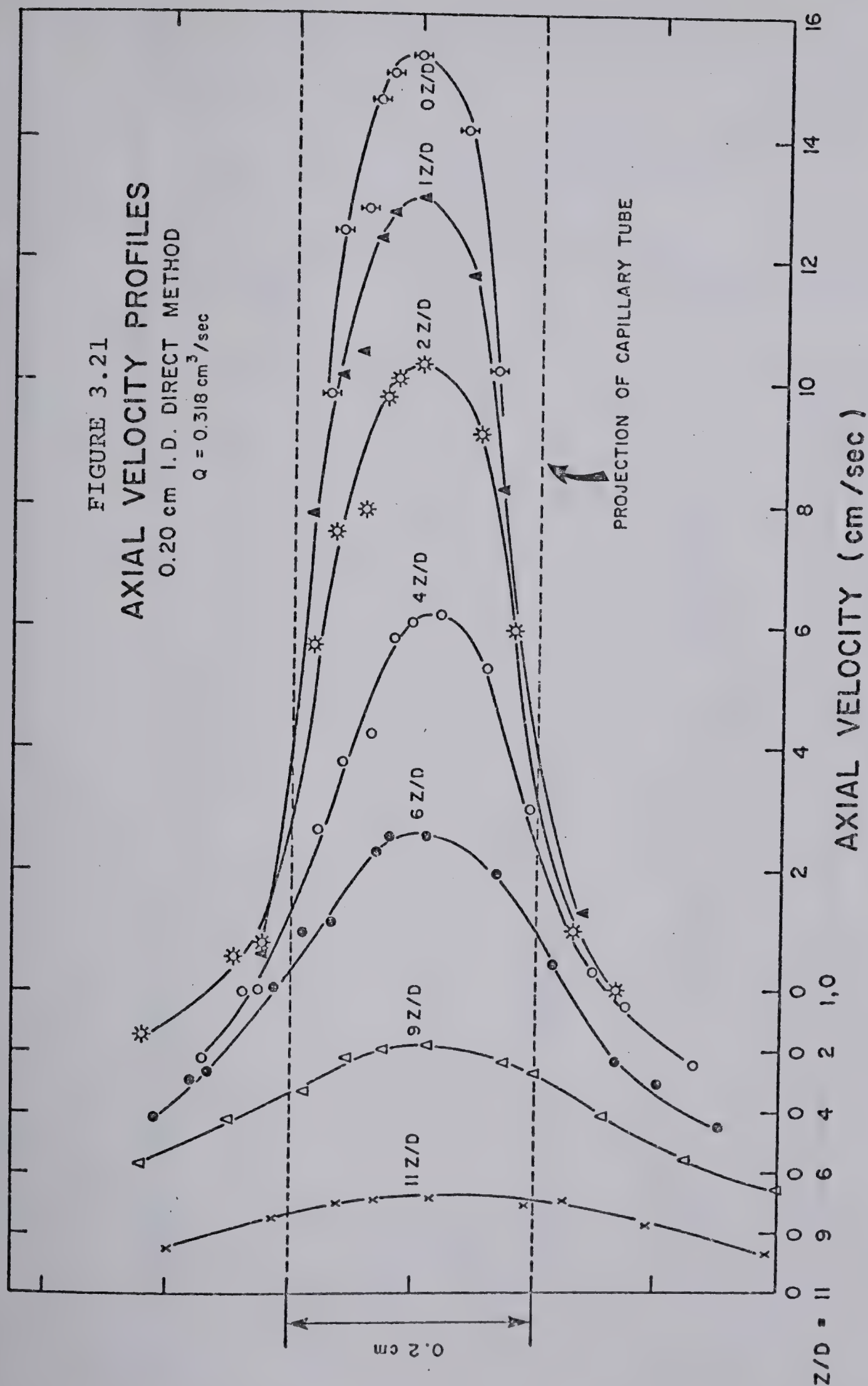
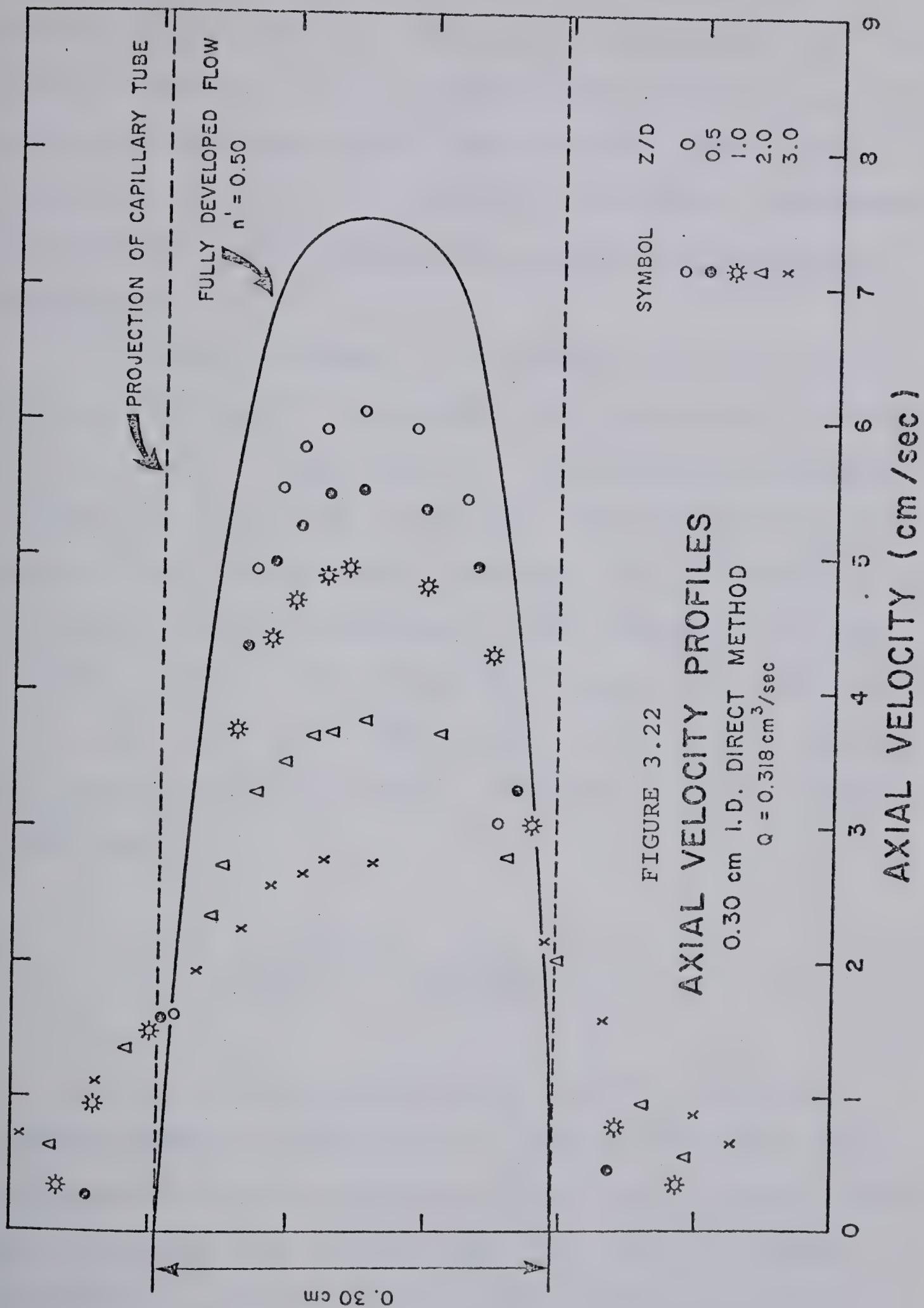


FIGURE 3.21
 AXIAL VELOCITY PROFILES
 0.20 cm I.D. DIRECT METHOD
 $Q = 0.318 \text{ cm}^3/\text{sec}$





radial position equal to $D/2.0$ were 4.9 cm/sec and 1.5 cm/sec respectively. At these same coordinates $z/D = 1.0$, $r = 0.0$, and $z/D = 1.0$, $r = D/2.0$, the respective velocities with capillary tube 2 at a flow rate of $0.318 \text{ cm}^3/\text{sec}$ (Figure 3.21) were 13.0 cm/sec and 4.0 cm/sec. Therefore, any empirical relationship must include axial and radial dependence.

(b) The development of the axial velocity profiles was such that as z/D approached zero the velocity profiles in the reservoir approached the fully developed velocity profile for flow in the capillary. The degree of development at the contraction was estimated from the ratio of the velocity along the centerline at the contraction to the velocity along the centerline for a power law fluid in SLSF in the capillary tube. This ratio, given by Equation 3.7, was approximately 0.75 and it remained constant for all of the data.

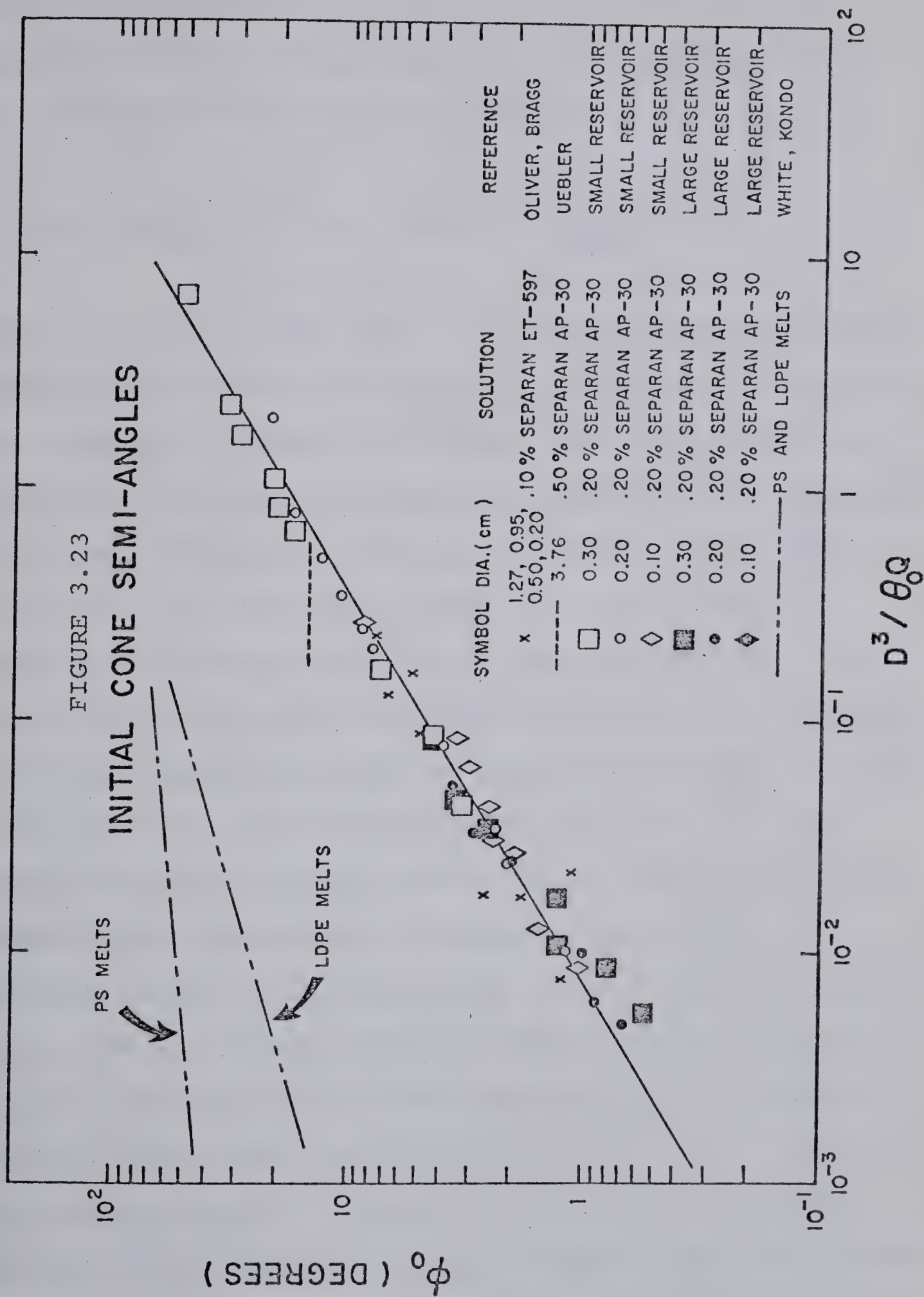
$$\frac{V_z|_c \text{ @ } z/D = 0}{V_z|_c \text{ @ SLSF}} = \frac{V_0}{V(\frac{3n'+1}{n'+1})} = 0.75 \quad 3.7$$

(c) At large upstream axial locations the axial velocity profiles over a radial distance less than $D/2.0$ approached a flat distribution. This axial location varied with capillary tube diameter and flow rate. In Figure 3.20, the velocity profiles were considered to be reasonably flat at distances approaching 24 diameters upstream. At

upstream axial locations beyond the development of the WGS structured flow field, the velocity profiles, although not measured directly, were assumed to be those associated with fully developed flow in the reservoirs.

3.4.2 CONE ANGLES

In many experimental runs the visualization of the outermost streamline did not extend up to the contraction. It was necessary in these cases to extrapolate the outermost streamline to the contraction in order to estimate the initial cone semi-angle, ϕ_0 . This resulted in errors as large as 15 percent in ϕ_0 . Initial cone semi-angles less than one half of a degree were too small to be measured with confidence. The measured initial cone semi-angles tabulated in Appendix F are plotted in Figure 3.23 against the parameter, $D^3/\theta_0 Q$. This parameter was suggested indirectly by independent experimental observations of Metzner et al. (116), Cogswell and Lamb (48), and Clegg (44). Metzner et al. (116) suggested that for a given fluid the initial cone semi-angles were proportional to D^3/Q ; this was also suggested independently by Cogswell and Lamb (48). Clegg (44) observed that at a constant D^3/Q the initial cone semi-angles were inversely proportional to the relaxation time of the fluid. The integration of these experimental observations leads to the formation of the dimensional group, $D^3/\theta_0 Q$ (188).



By using the zero shear relaxation time, θ_0 , as a characteristic relaxation time, the data in Figure 3.23 can be reasonably represented by Equation 3.8. Equation 3.8 is shown as the solid line in Figure 3.23.

$$\phi_0 = 19 \left(\frac{D^3}{\theta_0 Q} \right)^{0.6} \text{ for } 6 \times 10^{-3} < \left(\frac{D^3}{\theta_0 Q} \right) < 10 \quad 3.8$$

Values of $(D^3/\theta_0 Q)$ less than 6×10^{-3} corresponded approximately with the onset of region III, whereas for exceedingly small flow rates, values of $D^3/\theta_0 Q > 10$, the initial cone semi-angles, although not measured, asymptotically approach 90 degrees. The data in Figure 3.23 also indicate that the initial cone semi-angles were the same in both reservoirs for values of $(D^3/\theta_0 Q)$ that overlapped. The initial cone semi-angles measured by Oliver and Bragg (130) for a 0.10% aqueous solution of Separan ET-597 ($\theta_0 = 1$ sec) as well as those reported by Uebler (173) for a 0.50% aqueous solution of Separan AP-30 ($\theta_0 = 5$ sec) are in good agreement with these data as shown in Figure 3.23.

Ballenger and White (12) presented a correlation of ϕ with $\Delta P_c/\tau_w$. We have found, with the limited data where both ΔP_c and ϕ were measured, a similar correlation, however, there is significant scatter in the data. The initial cone semi-angles measured in this research as well as those measured by others (12, 130, 188) suggest that the exponent and the proportionality constant in Equation 3.8 are dependent upon concentration and type of polymer.

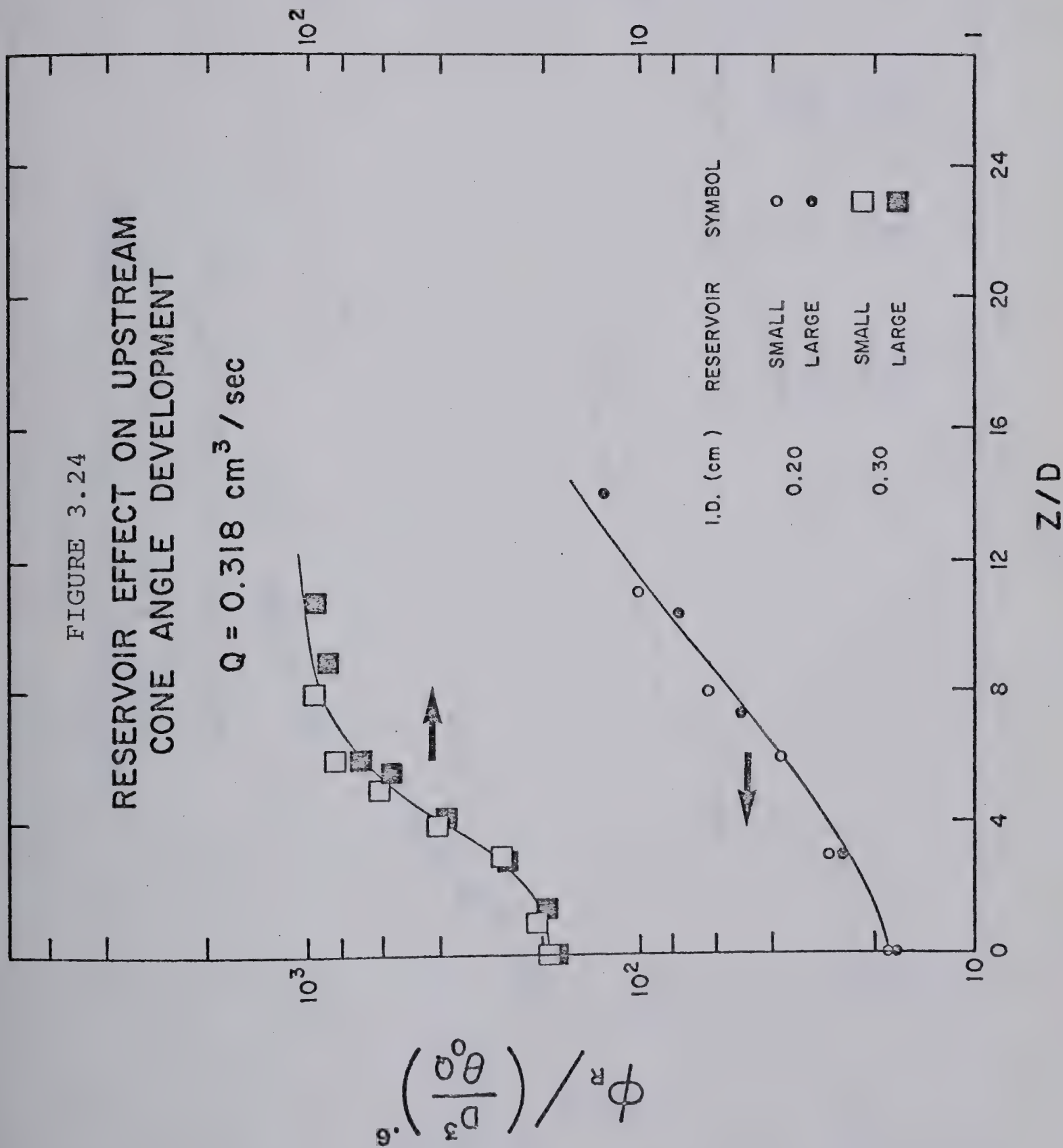
The cone semi-angles were measured at axial locations other than at the contraction. Like the initial cone semi-angles, these were measured tangent to the outermost streamline. A typical example of the growth of the cone semi-angles at several flow rates for both capillary tubes 2 and 3 is given in Figures 3.24 and 3.25. The remaining data can be found in Appendix F, Section F.2. The cone semi-angles were independent of reservoir size within the accuracy of measurement and over the range of z/D where they were measured. Although ϕ_R was not measured directly at axial locations greater than those tabulated in the Appendix, the dependence of the growth of ϕ_R with reservoir size was implied from observations of the flow field in both reservoirs. At the maximum values of z/D , where cone semi-angles were measured in reservoir S, the cross-sectional area of the central core of fluid was approximately equal to the reservoir's cross-sectional area. At the same flow rate and within reservoir L, the core area occupied a small fraction of the total cross-sectional area due to the order of magnitude increase in the physical dimensions of reservoir L. Hence, in reservoir L the core extended farther upstream and the cone semi-angles could be measured to larger values of z/D .

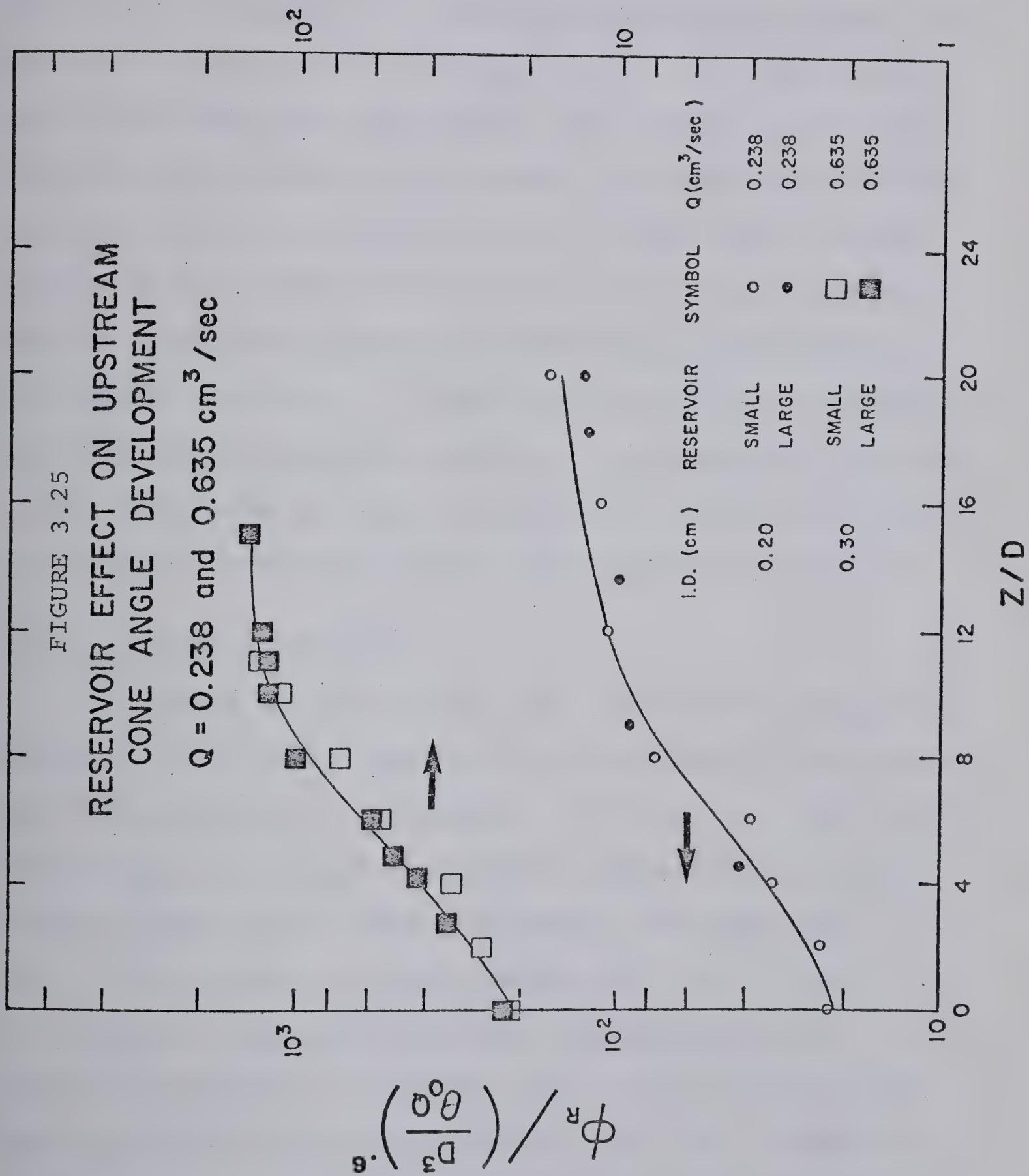
3.4.3 EDDY CENTERS

A third characteristic of the flow field within the reservoir is the location of the eddies that surround

FIGURE 3.24
RESERVOIR EFFECT ON UPSTREAM
CONE ANGLE DEVELOPMENT

$Q = 0.318 \text{ cm}^3 / \text{sec}$





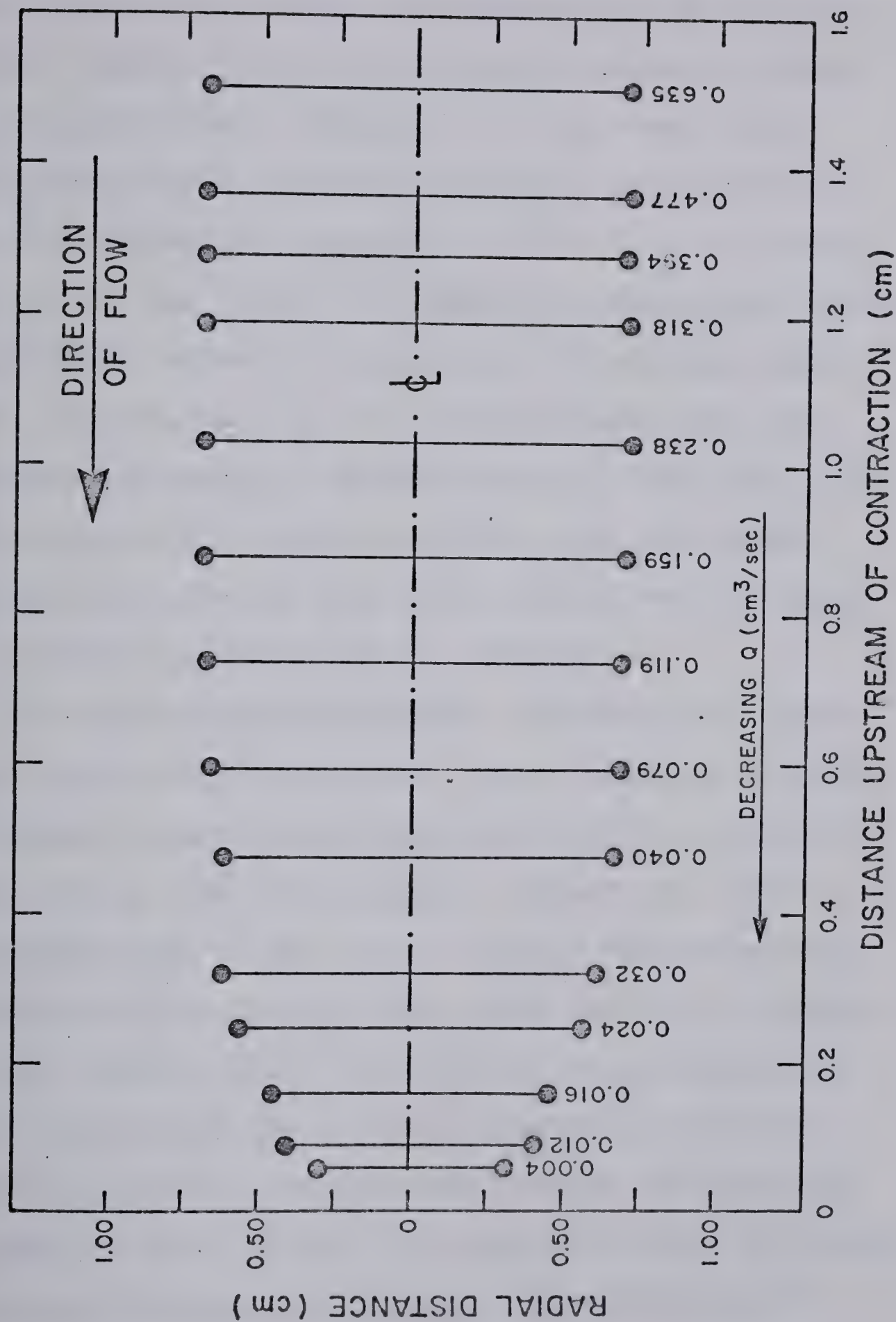
the central core of the fluid. The relative size and the location of these eddies are reported in terms of the location of the center of the eddies and the data are tabulated in Appendix F. The data for capillary tube 3 in reservoir S are plotted in Figure 3.26. The figure shows that as the flow rate increased, the location of the eddy centers progressively moved farther away from the contraction and along a well defined path. Comparison of eddy centers in both reservoirs at the same flow rate revealed that the location of the eddy center was located farther upstream in reservoir L. This was not surprising since as mentioned in the previous section it was observed that for a given flow rate and capillary tube the accelerating core was observed to extend farther upstream in reservoir L.

3.4.4 CORE VELOCITIES

Based on the typical axial velocities plotted in Figures 3.17 to 3.22, empirical correlations must include both axial and radial dependence. To obtain an empirical relationship that would describe the dependence on axial location three models were considered: the sink flow model, the K2 model, and the exponential decay model.

The sink flow model has been used previously to describe the velocity field for the flow of polymer solutions through a sudden contraction (116, 173). Velocity profiles within two diameters upstream of the contraction were measured for a 2 inch I.D. tube protruding 4.05

FIGURE 3.26
LOCATION OF EDDY CENTERS
0.30 cm I.D., SMALL RESERVOIR



diameters into a 18 inch square reservoir (173). Within the experimental scatter and over the range of available data, the velocity field was adequately represented by the sink flow model. Since the flow field was described as being WGS the streamlines were curved, i.e., the cone semi-angles increased with increasing upstream axial location. The sink flow kinematics assumes that the flow is radially directed toward the origin of a spherical coordinate system, i.e., cone semi-angles are independent of upstream axial location. This results in smaller cross-sectional flow areas farther upstream of the contraction. Therefore, the centerline velocities predicted by the sink flow model are expected to be larger than experimental data at axial locations farther upstream of the contraction.

In an inverse siphon experiment, the fluid is drawn vertically into a capillary tube. This creates a vertical liquid filament which is qualitatively similar to the flow field observed in the inlet region. Hence, the velocity flow field measured in the inverse siphon experiment may approximate the flow field in the inlet region. A description of the velocity field was obtained by photographing the cross sections of the vertical filament, assuming a flat velocity profile at each cross section and equating the integral of velocity over the cross-sectional flow area with the known volumetric flow rate. With this method, Kanel (90) presented an empirical relationship between velocity and axial location that is referred to as the

"K 2 kinematics." However, 83% of his experimental runs and 30% of Weinberger's experimental runs (184), which were reported in Kanel's dissertation, are not represented by the K 2 model. In general, velocity was correlated with axial position by

$$V_z = \frac{4Q}{\pi} (C_1 z + C_2)^{2/p} \quad 3.9$$

where z is the distance up into the liquid column and V_z is the velocity in the z direction. Parameter p varied from 0.50 to 3.0 (1, 90, 184) and the constants C_1 and C_2 were evaluated experimentally for each run. With p equal to unity, Equation 3.9 is referred to as the K 2 model. As pointed out by Kanel (90) reasons for the variations in the values of p are not known. More recently, Halmos and Boger (71) measured centerline axial velocities downstream of a sudden expansion for aqueous solutions of Methocel 90HG and Separan AP-30. Centerline velocities were measured by Boger and Rama Murthy (25) in the 2 to 1 contraction using the same experimental apparatus and polymer solutions. Velocities predicted using Equation 3.9, with p equal to a constant, resulted in consistent deviations from the experimentally measured velocities in the sudden expansion or sudden contraction experiment. To be consistent, p must vary with axial position, z/D . This variation in p is brought into focus by comparing predicted and experimental stretch rates. Downstream of the sudden

expansion, the experimentally determined stretch rates decreased from values that ranged from 32.3 to 43.3 sec^{-1} at the expansion to values approaching zero (6 to 20 tube diameters downstream). Between these two limits the stretch rate passed through a maximum value which was 2 to 4 times as large as stretch rates evaluated at the expansion (71). The axial location of the maximum stretch rates varied from 2 to 6 diameters downstream. Similar results were obtained for flow through a sudden contraction (25), i.e., the stretch rates passed through a maximum value as the contraction was approached. Stretch rates derived with Equation 3.9, with p equal to a constant, are not consistent with these experimental data. To be so, p must vary with axial position. In summary, since there have been significant variations from a K_2 model, i.e., p varies from experiment to experiment, and the fact that parameter p varies with axial position, it is purely by chance if the K_2 model is representative of velocity-position data obtained in this research.

The first part of Section 3.4.4 attempted to fit the velocities along the centerline to the sink flow and the K_2 models over a range of upstream axial locations. As a rule of thumb, the maximum axial location was chosen to be approximately equal to an axial distance one and one half times the axial location of the eddy center.

This axial location defined the major portion of the converging flow field. Beyond this, velocities were too small to be measured accurately. This maximum axial location corresponded with an axial position where the product of the derivative of the centerline velocity, Γ , times the zero shear relaxation time of the fluid, θ_0 , was equal to unity. This dimensionless parameter, $\Gamma\theta_0$, employed by Acierno et al. (1) in analyzing the transient elongational behavior of dilute polymer solutions, is also used in the determination of an empirical criterion to predict the onset of flow instabilities (Section 3.5, page 199). The derivative of the centerline velocity (where stretch rates are a maximum) is an integral part of the stability analysis, as will be shown in this section. Therefore, the chosen model should predict derivatives of velocities that are in quantitative agreement with experimental data in addition to being representative of velocity data. The final part of Section 3.4.4 discusses the exponential decay model and the development of an empirical relationship with radial location.

(i) Sink Flow Model

If it is assumed that the flow upstream of the capillary is radially directed toward the origin of a spherical coordinate system, with the origin determined by the extrapolation of streamlines, the continuity equation for a symmetric flow field (116) reduces to

$$V_1 = \frac{f(\phi_0)}{r^2} \quad 3.10$$

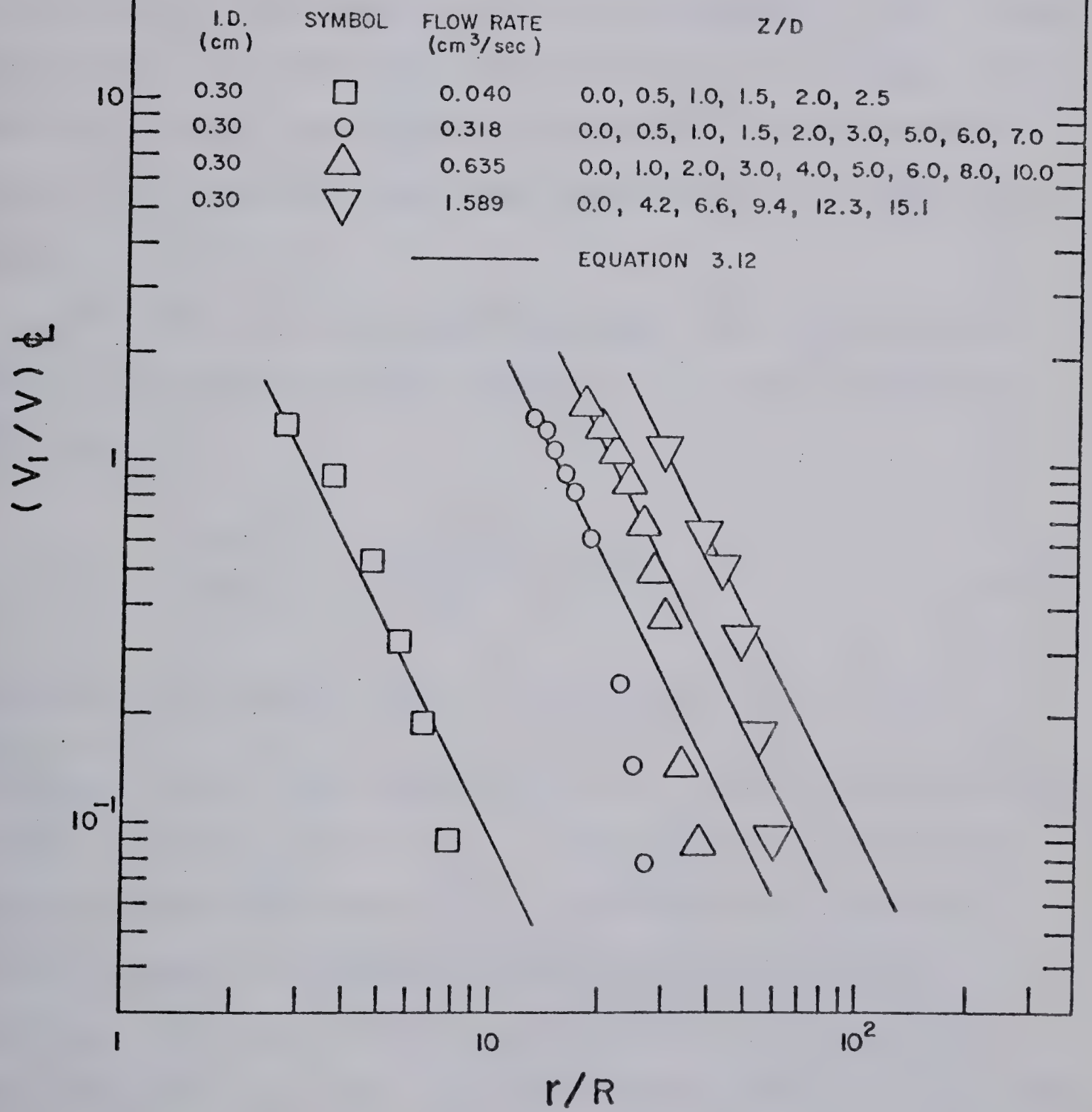
$$V_2 = V_3 = 0 \quad 3.11$$

where r is the radial coordinate and V_1 , V_2 , and V_3 are velocity components in the r , θ and ϕ directions. By normalizing the radial velocity with respect to the average velocity in the capillary, V , and radial position with respect to the capillary tube radius, R , Equation 3.10 can be rewritten as

$$\left(\frac{V_1}{V}\right)_\phi = \frac{f(\phi_0)}{VR^2} \left(\frac{r}{R}\right)^{-2.0} \quad 3.12$$

Therefore, in logarithmic coordinates the slope of a plot of dimensionless velocity along the centerline, $\left(\frac{V_1}{V}\right)_\phi$, versus $\left(\frac{r}{R}\right)$ should be equal to -2.0 if Equation 3.12 is valid. Consider as a typical example velocity data measured with capillary tube 3. Measured centerline velocities for flow rates that range from 0.040 cm³/sec to 1.589 cm³/sec are plotted in Figure 3.27. The respective upstream axial locations, z/D , are also given for each data point. Plots similar to those in Figure 3.27, although not reported, were obtained with capillary tubes 1 and 2. The solid lines representing Equation 3.12 are in good agreement with experimental data only in the vicinity of the contraction. This was originally suggested by Murch (119) and Kanel (90).

FIGURE 3.27
CENTERLINE VELOCITY
SINK FLOW MODEL



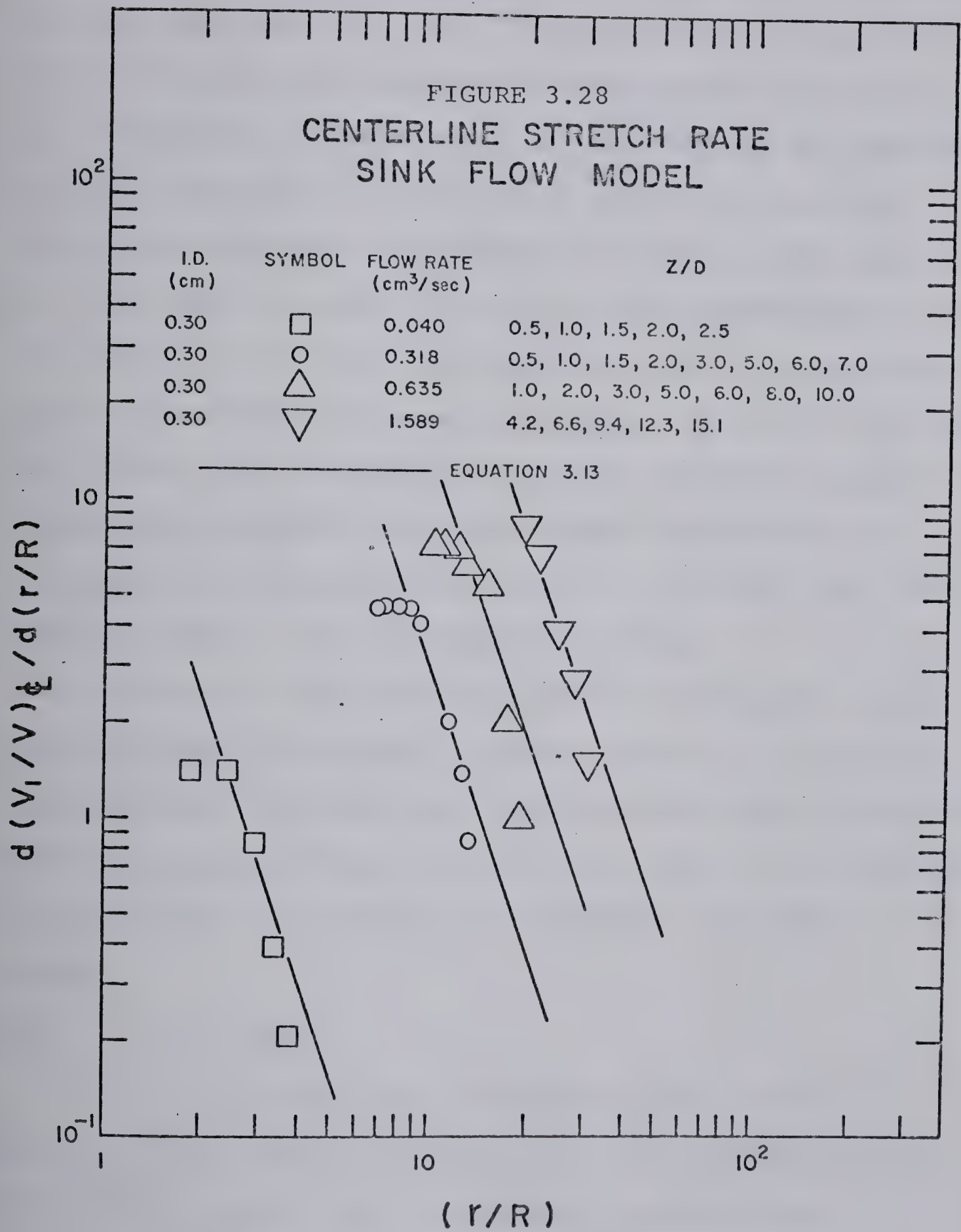
At a flow rate of $0.040 \text{ cm}^3/\text{sec}$ agreement was obtained for upstream axial locations as large as 2.0 diameters upstream, whereas at a flow rate of $1.589 \text{ cm}^3/\text{sec}$ good agreement was obtained at upstream axial locations as large as 6.6 diameters. At axial locations greater than 2.0 or 6.6 diameters the sink flow model predicts velocities that are significantly higher than the experimental data. This discrepancy, as mentioned earlier (page 143), arises from the WGS central core wherein the actual cross-sectional flow area is greater than that predicted by the sink flow model.

The derivative of velocity along the centerline obtained by differentiating Equation 3.12 with respect to r/R yields

$$\frac{d(V_1/V)}{d(r/R)} = \frac{-2f(\phi_0)}{VR^3} \left(\frac{r}{R}\right)^{-3.0} \quad 3.13$$

Equation 3.13 states that on logarithmic coordinates

$\frac{d(V_1/V)}{d(r/R)}$ versus $\left(\frac{r}{R}\right)$ should result in a linear relationship having a slope equal to -3.0. The solid lines in Figure 3.28 represent Equation 3.13. Significant differences exist between the predicted and measured derivatives of velocity. The derivative of experimental velocity along the centerline, as shown in Figure 3.28, remained relatively constant over a wide range of upstream axial locations. The range of upstream axial locations was observed to vary



with capillary tube and flow rate. For example, the data in Figure 3.28 indicate that at a flow rate of $0.040 \text{ cm}^3/\text{sec}$ the range was from 0.50 to 1.00 diameters upstream, whereas at a flow rate of $0.635 \text{ cm}^3/\text{sec}$ the range was from 1.0 to 3.0 diameters. Derivatives of velocity are not reported for axial locations less than 0.50 diameters upstream since velocities were not measured at these axial locations. At a flow rate of $1.589 \text{ cm}^3/\text{sec}$, velocity measurements were not available for axial locations less than 4.2 diameters, hence, experimental data are not shown. At axial locations far removed from the contraction poor agreement existed between the predicted and experimental derivatives of velocity; the predicted derivatives of velocity were consistently higher than experimental values.

In summary, the sink flow model is inadequate in representing the relationship between velocity and its derivative along the centerline with upstream axial location. The flow upstream of the capillary entrance is not radially directed toward the origin of a spherical coordinate system.

(ii) K 2 Model

In a cylindrical coordinate system with its origin at the center of the capillary tube at the contraction, the K 2 model can be rewritten in general as

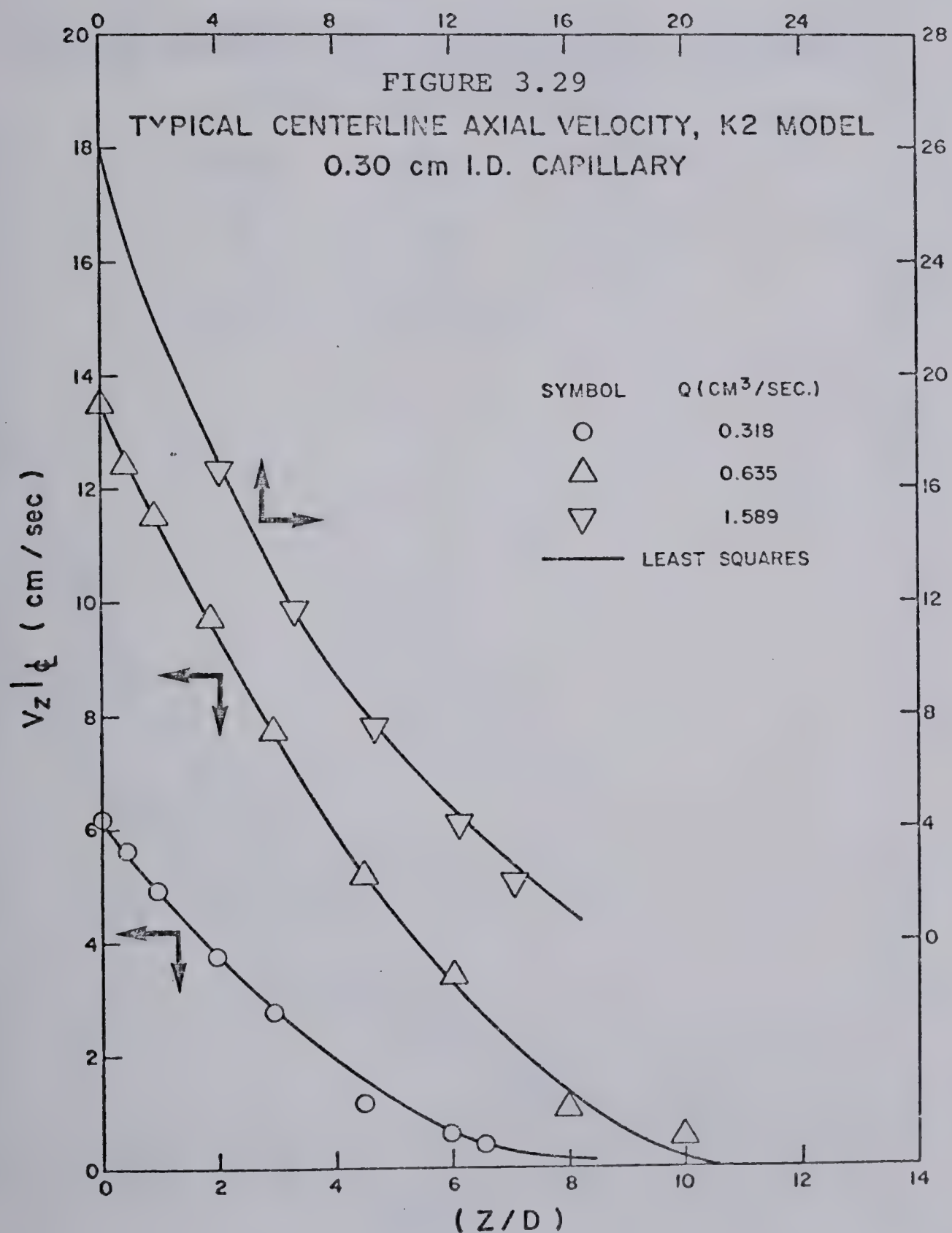
$$V_z|_d = a + a_1(z/D) + a_2(z/D)^2 \quad 3.14$$

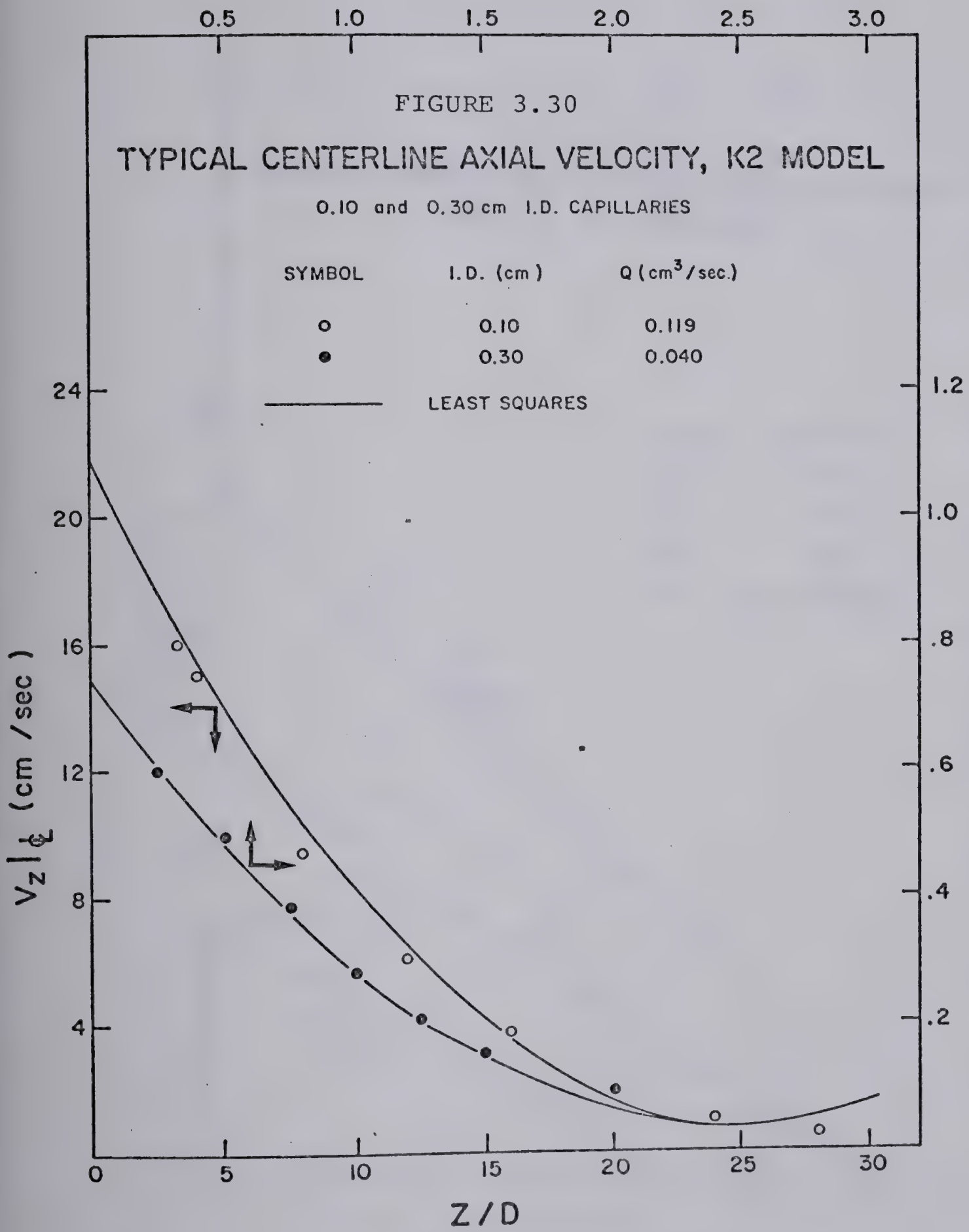
The values of the three parameters a , a_1 , and a_2 in Equation 3.14 and their dependence on capillary tube diameter and flow rate must be evaluated experimentally. Although deviations from the K 2 model are known to exist (25, 71, 90), it was expected to be a better approximation of the velocity data compared to the sink flow model. Differentiation of Equation 3.14 with respect to z yields

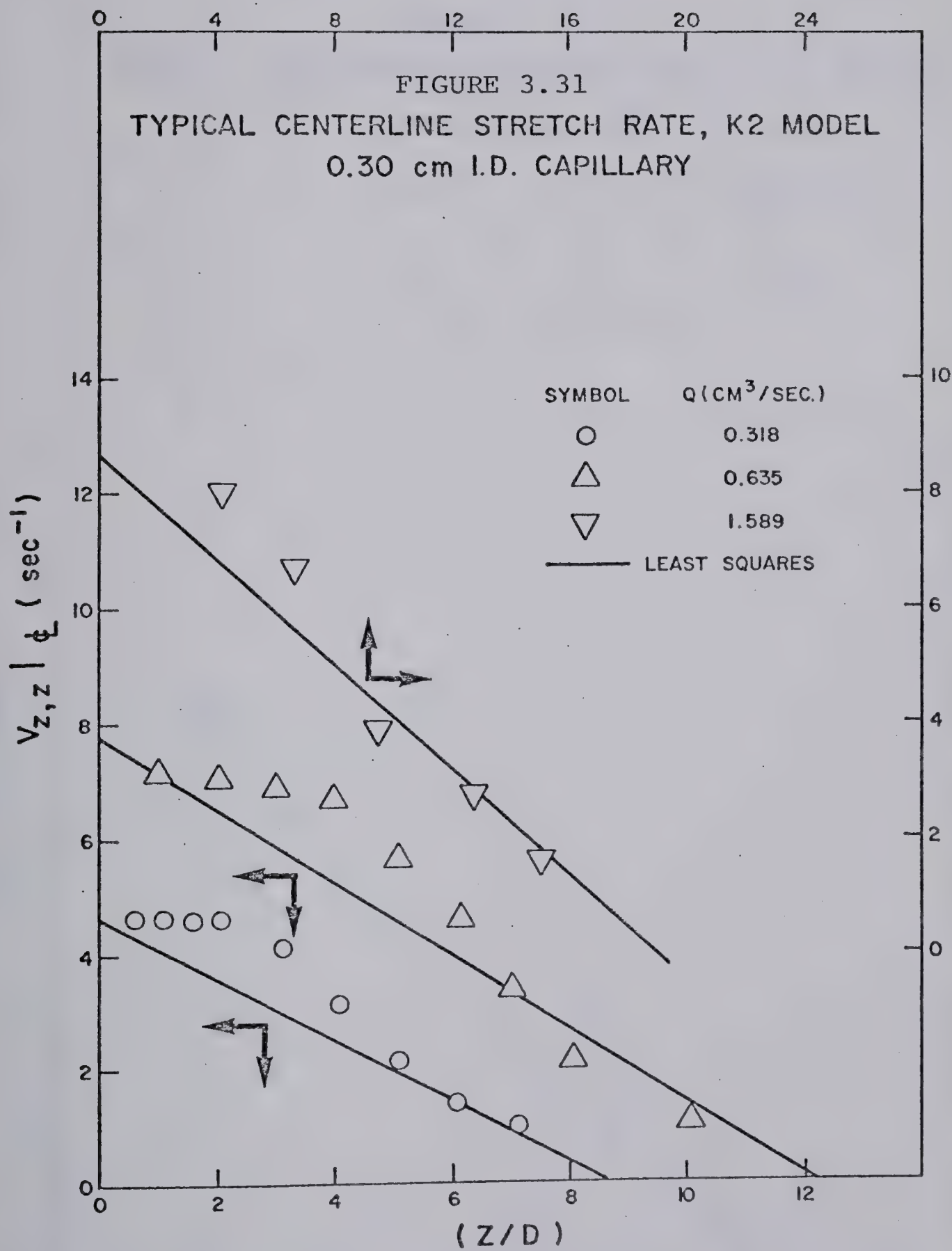
$$v_{z,z}|_{\xi} = \left(\frac{a_1}{D}\right) + 2\left(\frac{a_2}{D}\right)\left(\frac{z}{D}\right) \quad 3.15$$

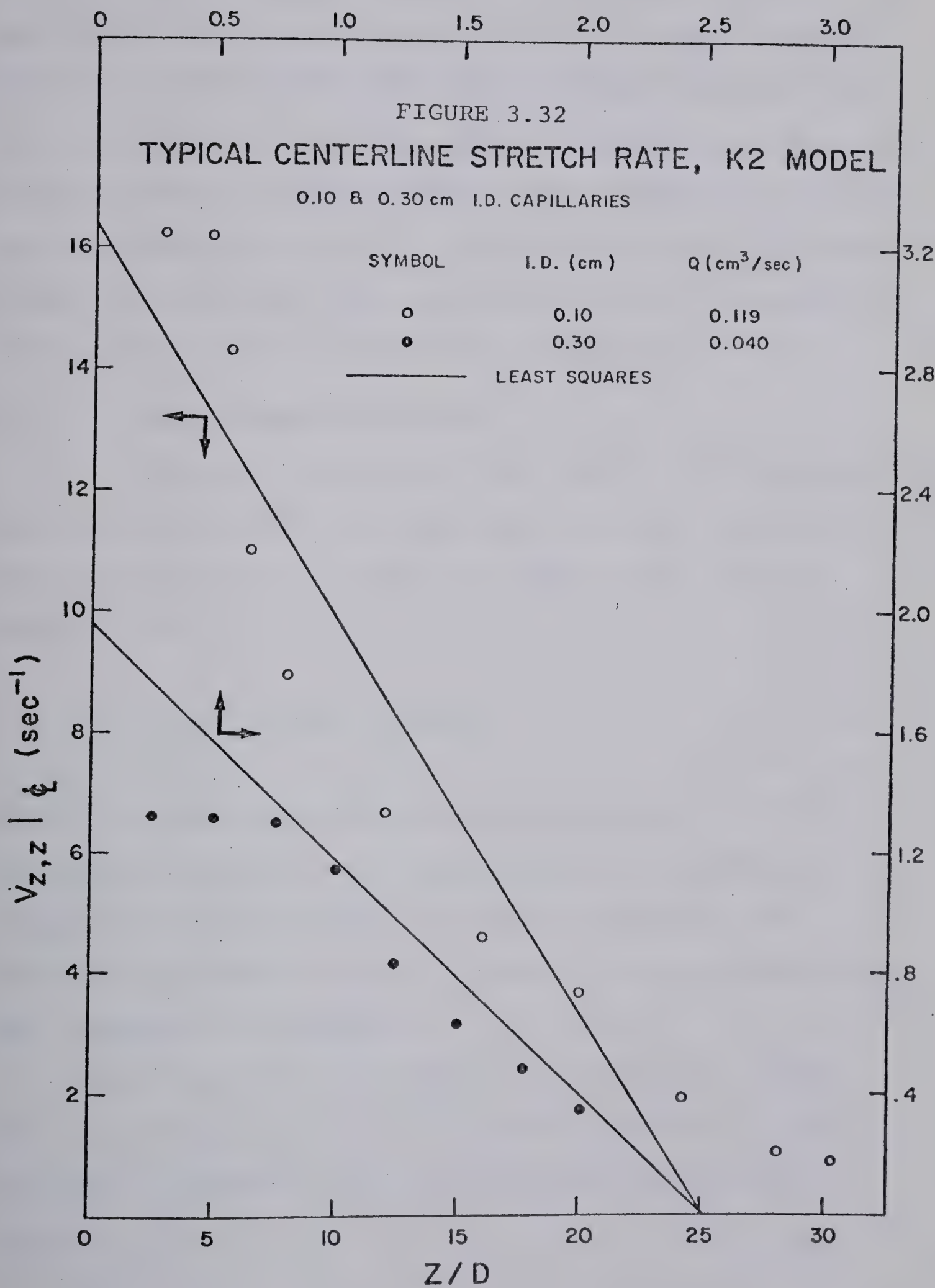
Equation 3.15 predicts that the derivative of velocity is linear with respect to axial location. As pointed out in page 144 this is inconsistent with data obtained by Halmos and Boger (71) and Boger and Rama Murthy (25); the data obtained in the present study are consistent with those reported by these authors.

Typical experimental velocities and derivatives along the centerline are given in Figures 3.29 to 3.32 for capillary tube 3. In addition, results are also shown for capillary tube 1 at a flow rate of $0.119 \text{ cm}^3/\text{sec}$ (Figures 3.30 and 3.32) where the accelerating core extended farthest into reservoir S. The parameters a , a_1 , and a_2 in Equation 3.14 were obtained by the least squares method. The K 2 model is in good agreement with the velocity data but consistent large deviations in the derivatives of velocity were observed for all of the data with typical results shown in Figures 3.31 and 3.32. The derivatives of









experimental velocity are not linear with respect to axial location as given by Equation 3.15. As the contraction was approached, the derivatives of velocity increased exponentially to a value which remained reasonably constant over a range of upstream axial locations. For the data shown, the range over which the derivatives were considered to be constant is given on page 151. As a result of poor agreement between predicted and experimental derivatives of velocity, the K 2 model was considered to be inadequate.

(iii) Exponential Decay Model

Plots of velocity and derivatives of velocity along the centerline versus upstream axial location obtained in this study suggest an exponential decay model given by Equation 3.16

$$V_z|_c = V_0 \exp(-b(z/D)) \quad 3.16$$

where V_0 is the velocity along the centerline at the contraction and z/D is the axial position measured upstream of the contraction. This model predicts the dependence of velocity upon z/D which is in agreement with other experimental evidence (25, 71, 123).

The K 2 model is included in the exponential decay model since Equation 3.14 is a truncated Taylor series expansion of Equation 3.16. A Taylor series expansion of Equation 3.16 is

$$v_z|_c = v_0 \left(1 - b\left(\frac{z}{D}\right) + \frac{b^2}{2!}\left(\frac{z}{D}\right)^2 - \frac{b^3}{3!}\left(\frac{z}{D}\right)^3 + \dots \right) \quad 3.17$$

Truncating Equation 3.17 after the third term yields

$$v_z|_c = v_0 \left(1 - b\left(\frac{z}{D}\right) + \frac{b^2}{2!}\left(\frac{z}{D}\right)^2 \right) \quad 3.18$$

Equation 3.18 is equivalent to Equation 3.14 when

$$a = v_0$$

$$a_1 = -v_0 b$$

$$a_2 = v_0 b^2 / 2! \quad 3.19$$

Equation 3.16 implies that the slope of a plot of v_z versus z/D on semi-log coordinates is a constant equal to $-b$ with the intercept at $z/D = 0$ being equal to v_0 . The velocity - z/D data measured in this study showed consistent deviations when plotted on semi-log coordinates in accordance with Equation 3.16. A better, although a more complicated relationship, was

$$v_z|_c = v_0 \exp(-b(z/D)^c) \quad 3.20$$

where c is constant. The evaluation of c was obtained in the following manner: For a given reservoir, capillary tube, and flow rate, v_z was plotted against $(z/D)^c$ on semi-log coordinates for various values of c until it was

judged by eye that errors between experimental and predicted values over the characteristic flow pattern length were a minimum. This procedure was repeated for the remaining flow rates, capillary tubes and both reservoirs. In the final analysis, c was determined to be equal to 1.4. Typical plots of velocity versus $(z/D)^{1.4}$ are shown in Figure 3.33 for the data obtained with capillary tube 3. The solid lines representing Equation 3.20 are in excellent agreement with experimental data. Plots similar to those in Figure 3.33 can be found in Appendix E and are in excellent agreement with the data. Further support of Equation 3.20 as representative of centerline velocities is evidenced by data reported by Boger and Rama Murthy (25) in a 2 to 1 contraction (5.08 cm I.D. to 2.54 cm I.D.), by Halmos and Boger (71) in a 2 to 1 expansion and by Nakamura et al. (123) in a sudden contraction (7.0 cm I.D. to 2.0 cm I.D.) In all experiments centerline velocities were represented by Equation 3.20 with $c = 1.4$.

Since the velocities were measured only to within one streak length from the contraction, the velocities at the contraction, V_0 , were not measured directly. These velocities were estimated by curve fitting the data to Equation 3.21 by the least squares method.

$$\log(V_z|_{\phi}) = \log V_0 - b \left(\frac{z}{D}\right)^{1.4} \quad 3.21$$

The resulting values of V_0 are plotted against flow rate in

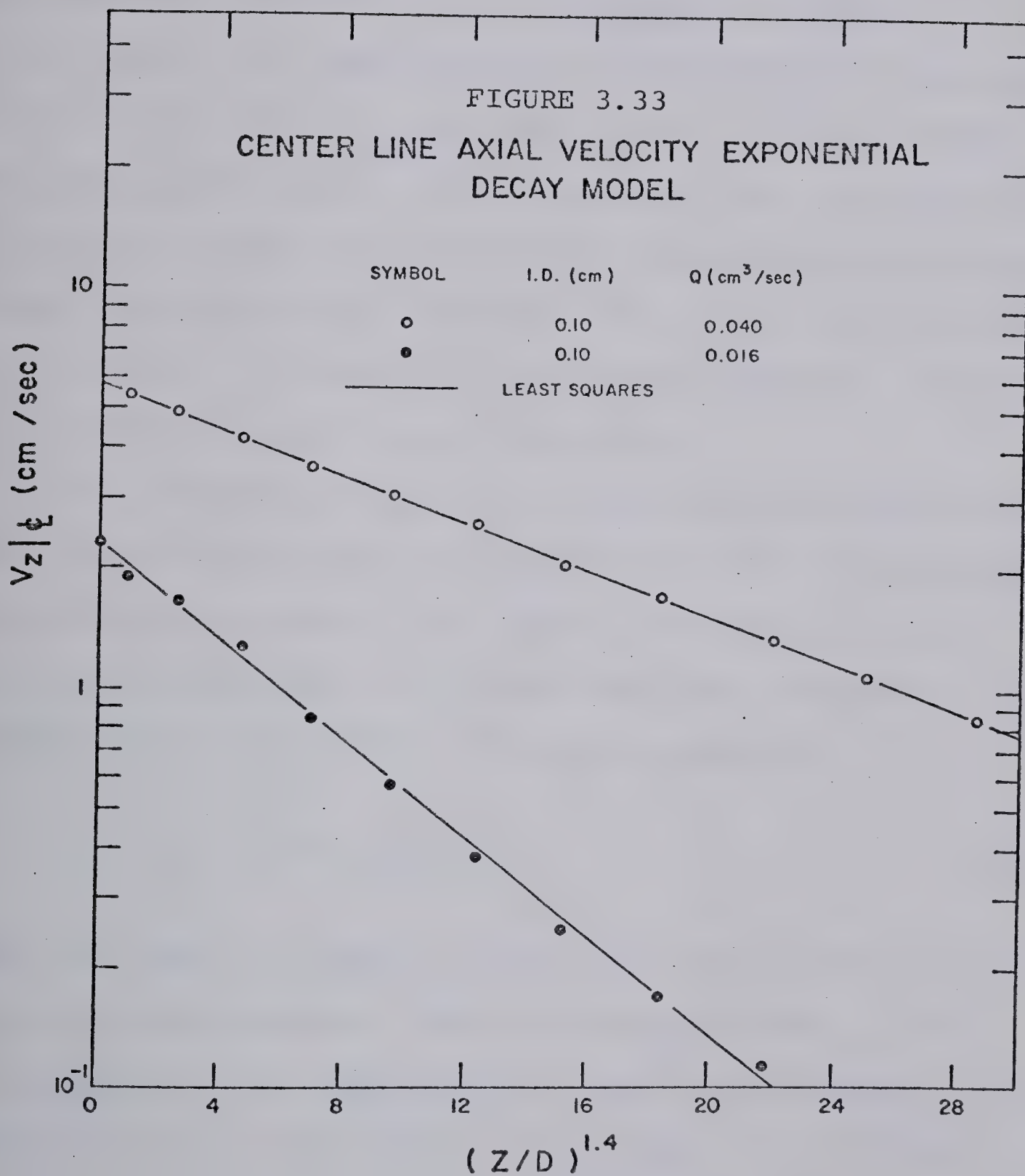


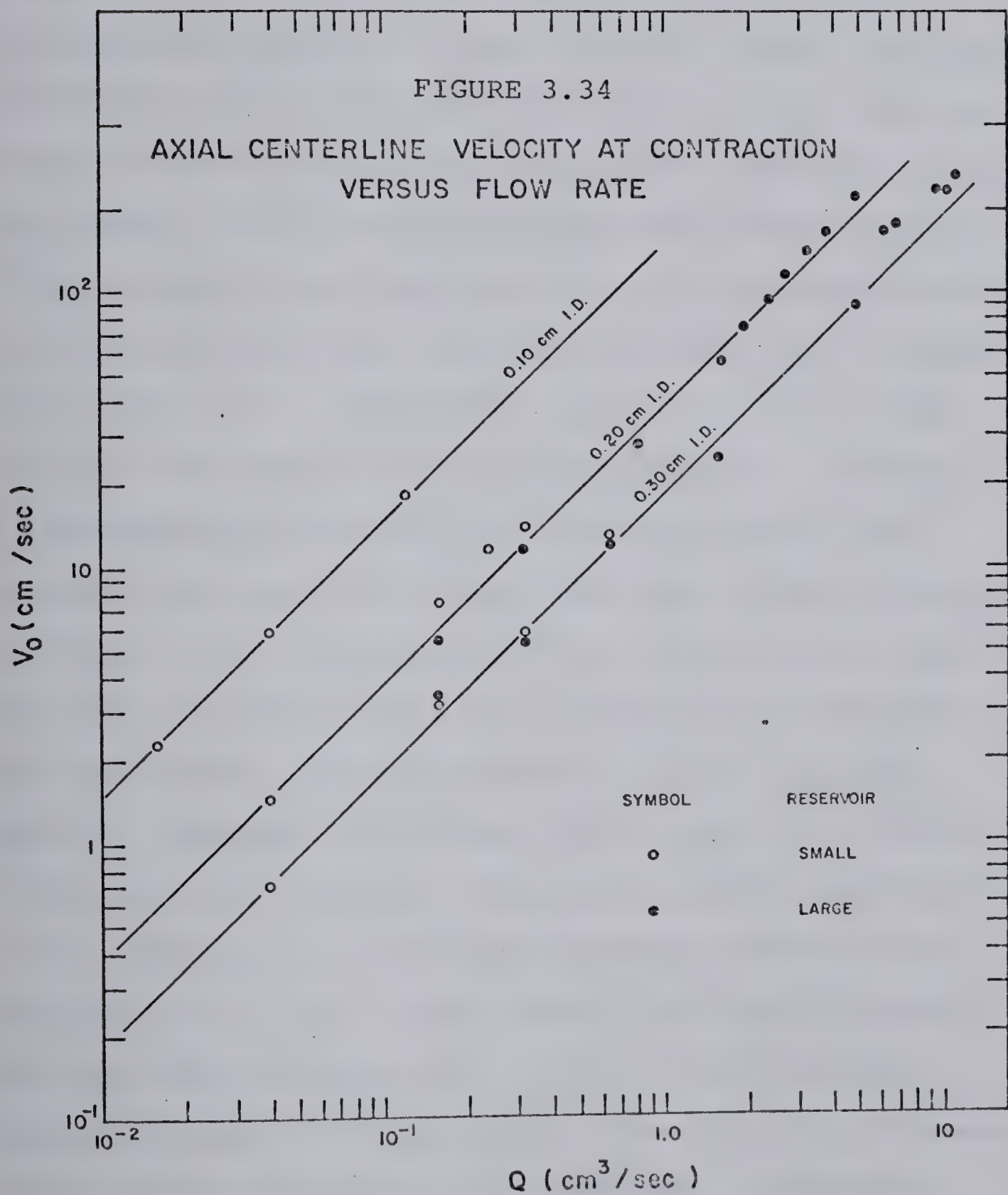
Figure 3.34. No significant differences in the values of V_0 were noted over the range of flow rates in region I where data from both reservoirs overlapped. It was conjectured, therefore, that the values of V_0 were independent of reservoir size for all flow rates within region I. From Figure 3.6, the flow rates in question for capillary tubes 1, 2, and 3 are less than 0.119, 0.318, and 0.635 cm^3/sec respectively. The data between the two sizes of reservoirs cannot be compared for flow rates greater than these since the flow fields were different; the flow field was "chaotic" in reservoir S while in reservoir L it was stable even to much higher flow rates.

The degree to which the velocity profiles were developed at the contraction was estimated by the ratio of V_0 to the centerline velocity for SLSF in the capillary tube. This ratio was equal to 0.75 and remained constant for all experimental runs. Hence, V_0 can be expressed as

$$V_0 = 0.75 \left(\frac{3n'+1}{n'+1} \right) \left(\frac{Q}{A} \right) \quad 3.22$$

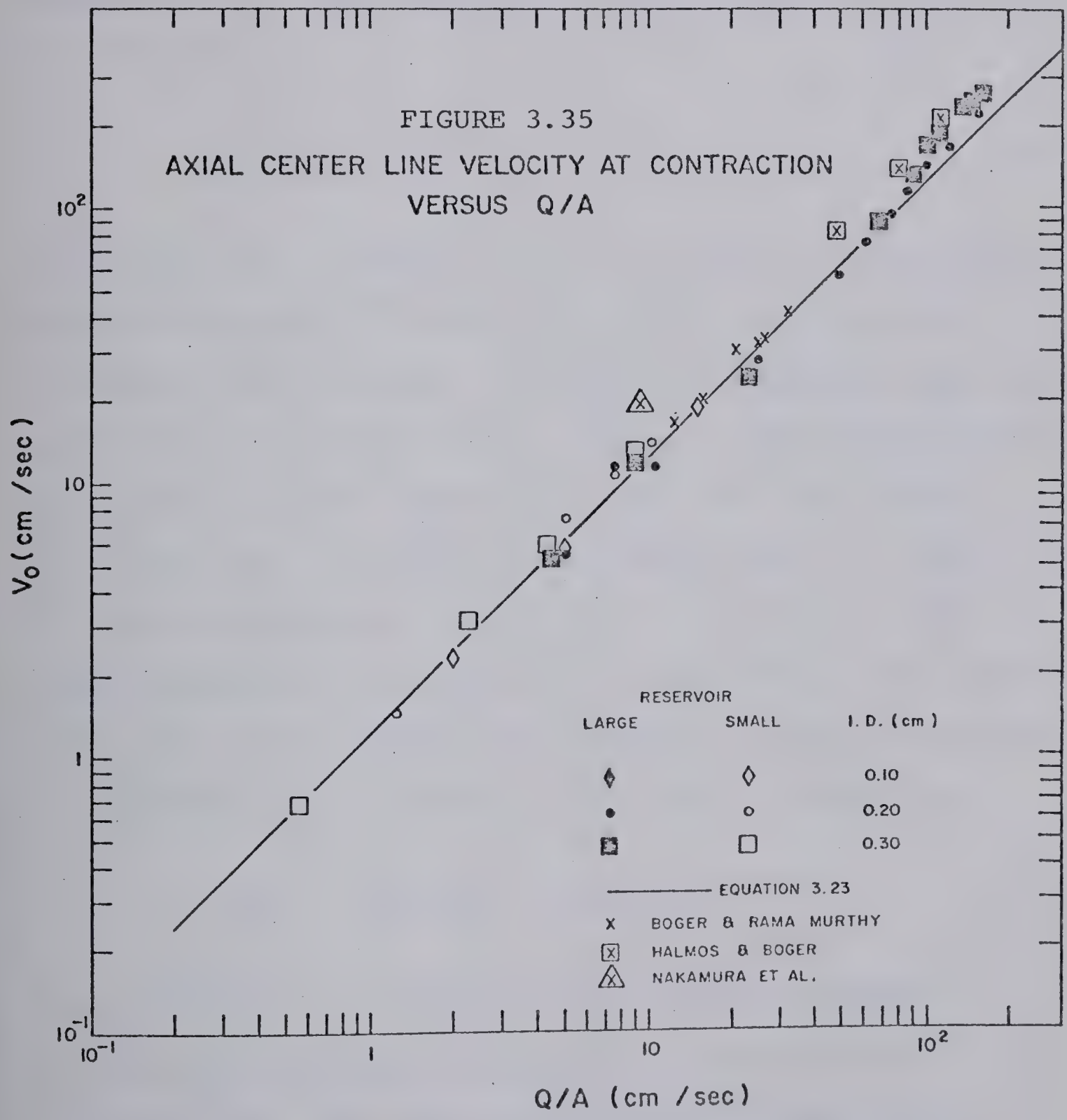
Over the range of apparent shear rates where the velocity profiles were measured, the flow behavior index, given in Appendix D, was approximately equal to a constant, 0.50. Substitution of this value n' into Equation 3.22 yields

$$V_0 = 1.25 (Q/A) \quad 3.23$$



Equation 3.23 is plotted as the solid line in Figure 3.35 and shows that the preceding approximations are in reasonable agreement with the experimental data for capillary tube velocities that ranged from 0.60 to 160 cm/sec. Experimental values of V_0 were slightly higher than the predicted values (Equation 3.23) for capillary tube average velocities greater than 70 cm/sec. At first this may not appear to be a major discrepancy but closer examination revealed that these capillary tube average velocities corresponded with flow rates defining the onset of region II in reservoir L. Therefore, Equation 3.23 is valid only for flow rates that are within region I. Values of V_0 obtained by replotting the centerline velocities measured and reported by Boger and Rama Murthy (25), Halmos and Boger (71), and Nakamura et al. (123) against $(z/D)^{1.4}$ are given in Figure 3.35. The solutions used by Boger and Rama Murthy (75) and Halmos and Boger (71) were aqueous solutions of Methocel 90HG having $(n' = 0.521, 0.550 \text{ and } 0.580)$ whereas, the solution used by Nakamura et al. (123) was a 0.40% weight aqueous solution polyacrylite ($n' = 0.46$). Only the data obtained by Halmos and Boger (25) and Nakamura et al. (71) are somewhat higher; Equation 3.22 represents their data when the constant 0.75 is replaced by 0.89 and 1.26 respectively.

Velocity measurements as far as 60 diameters upstream were necessary to define the major portion of the velocity field at high flow rates. At low flow rates, measurements



within two diameters were sufficient to define the major portion of the velocity field. In order to scale the velocity fields with respect to axial location and achieve axial similarity, the velocities were normalized with respect to V_0 . The normalized axial location variable, Z^* , was defined as

$$Z^* = (z/D)/(X/D) \quad 3.24$$

where (X/D) is a characteristic flow pattern length which defines the major portion of the flow field over which velocities were measured. Normalized velocities range from zero to unity and by a proper choice of the characteristic flow pattern length normalized axial locations should range from zero to values approximately equal to unity. The following outlines the method used to obtain Z^* : The velocity along the centerline is a function of the physical properties of the fluid, the geometry, the flow rate, and the upstream axial location. This can be written as

$$V_z|_{\phi} = f(\rho, K_0, \theta, n', D, D_R, Q, z) \quad 3.25$$

Since dimensional consistency must exist rearrangement of the variables in Equation 3.25 by Rayleigh's method so that each term is dimensionless must give

$$V_z|_{\phi} = f(\beta, N'_{Re}, \frac{D^3}{\theta Q}, \frac{z}{D}, n') \quad 3.26$$

By substituting the relationship given by Equation 3.20 into Equation 3.26 we have

$$V^* = \frac{V_z|_c}{V_0} = f_1(\beta, N'_{Re}, \frac{D^3}{\theta Q}, \frac{z}{D}, n') \quad 3.27$$

It was mentioned on page 145 that velocities were measured over the major portion of the flow field which corresponded to one and one half times the center of the eddies. This axial location was approximately equal to the axial location where the product $\Gamma\theta_0$ was equal to unity. It is this axial position that is referred to as the characteristic flow pattern length. Qualitatively, as the initial cone semi-angle decreased, the axial location, where $\Gamma\theta_0$ was equal to unity, increased (the central core protruded farther upstream). The sink flow kinematics, although not representative of velocities and derivatives along the centerline, may qualitatively indicate the dependence of the characteristic flow pattern length with D , θ_0 and Q . By equating the integral of the radial velocity component, Equation 3.10, over the flow cross-sectional area to flow rate, yields

$$V_1 = \frac{Q}{2\pi r^2 (1 - \cos\phi_0)} \quad 3.28$$

The derivative of Equation 3.28 with respect to radial location r , is

$$V_{1,1} = \frac{-Q}{\pi r^3 (1 - \cos\phi_0)} \quad 3.29$$

As an approximation for small cone initial semi-angles we have

$$1 - \cos\phi_0 \approx x^2/2 \quad 3.30$$

where x is expressed in radians. The product of the stretch rate times the zero shear relaxation time is therefore given by

$$V_{1,1}^{\theta_0} = \frac{2\theta_0 Q}{\pi r^3 x^2} \quad 3.31$$

Hence, the radial location where $V_{1,1}^{\theta_0}$ is equal to unity, r_1 , is

$$r_1 = \left(\frac{2\theta_0 Q}{\pi x^2} \right)^{1/3} \quad 3.32$$

From Equation 3.8 we have

$$x = \left(\frac{19}{180} \right) \left(\frac{D^3}{\theta_0 Q} \right)^{0.60} \quad 3.33$$

and substitution of Equation 3.33 into Equation 3.32 yields

$$r_1 \approx 3.9 \left(\frac{\theta_0^2 Q^2}{D^3} \right)^{1/3} \quad 3.34$$

This suggests that the dimensionless axial position, Z^* , can be derived from dimensionless groups in Equation 3.27 as

$$Z^* = \frac{(z/D)}{\left(\frac{\theta_0 Q}{D^3} \right)^{2/3}} = \frac{z}{\left(\frac{\theta_0^2 Q^2}{D^3} \right)^{1/3}} \quad 3.35$$

where $(\theta_0^2 Q^2 / D^3)$ has the dimension of length cubed. The combination of Equations 3.20, 3.27, and 3.35 yields

$$V^* = \exp[-b_1(\beta, N'_{Re}, \frac{D^3}{\theta_0 Q}, n')(Z^*)^{1.4}] \quad 3.36$$

Equation 3.36 is equivalent to Equation 3.20 and suggests that on semi-log coordinates V^* is linear with respect to $(Z^*)^{1.4}$. The functional form for parameter b_1 with β , N'_{Re} , $D^3/\theta_0 Q$ and n' must be evaluated empirically.

Semi-log plots of V^* versus $(Z^*)^{1.4}$ are given in Figures 3.36 to 3.40 with Equation 3.36 being represented as the solid lines. Experimental values of V^* are related linearly to $(Z^*)^{1.4}$ on semi-log coordinates with a slope equal to $-b_1/2.303$. The dimensionless axial locations were condensed to values of $(Z^*)^{1.4}$ less than 2.2. Parameter b_1 , estimated by the method of least squares, is plotted in Figure 3.41 against $(\theta_0 Q / D^3)$. The data in this figure show clearly that the extrapolation of the relationship between b_1 and $(\theta_0 Q / D^3)$ obtained with flow rates within region I is not applicable within region II where the first signs of flow instabilities were observed. Therefore, for flow rates within region I Equation 3.37 is applicable.

$$b_1 = 1.0(\theta_0 Q / D_3)^{0.216} \quad 3.37$$

FIGURE 3.36
 V^* VERSUS Z^*
0.10 cm I.D. CAPILLARY, SMALL RESERVOIR

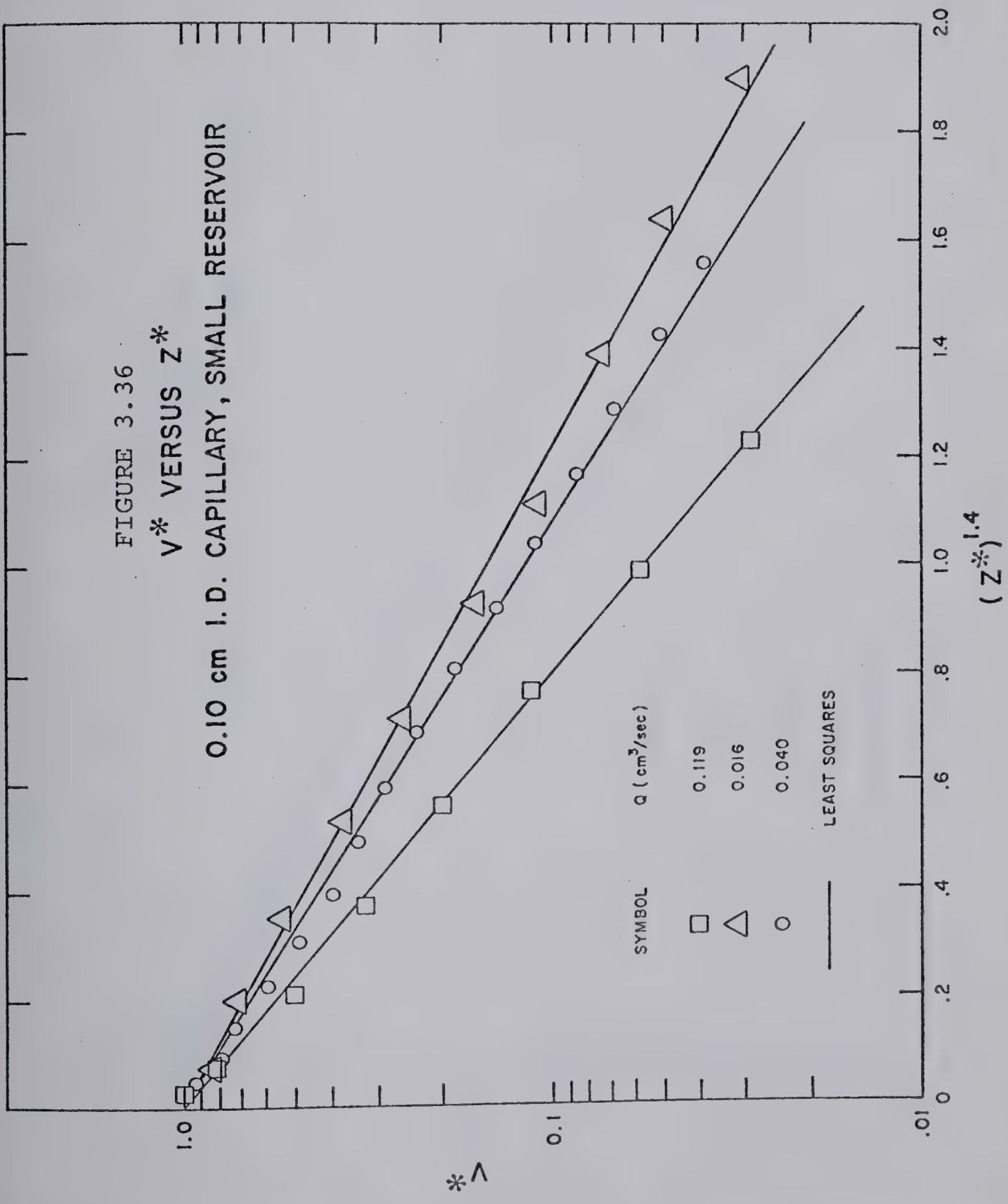


FIGURE 3.37

 V^* VERSUS Z^*

0.20 cm I.D. CAPILLARY, SMALL RESERVOIR

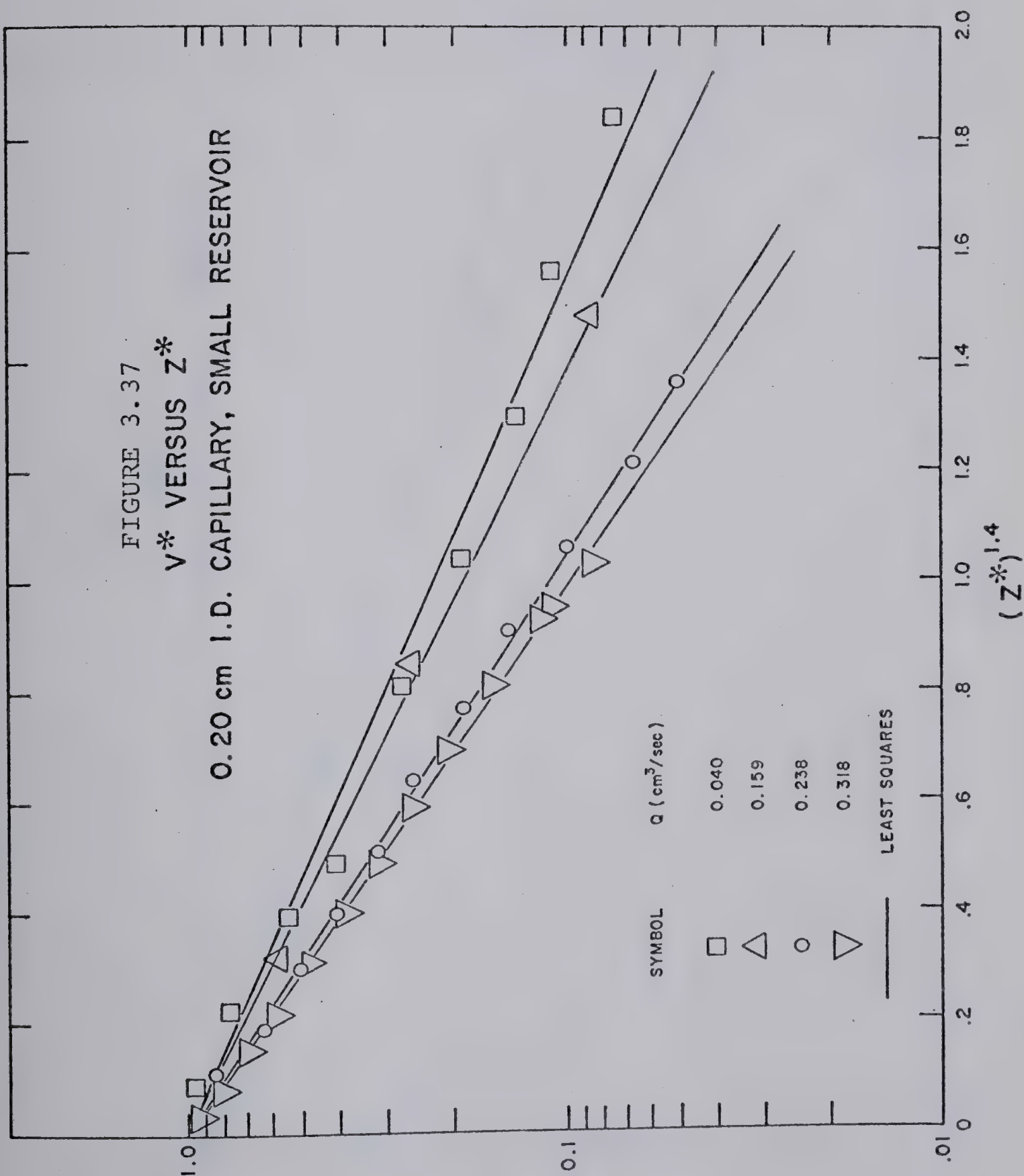
 V^* $(Z^*)^{1.4}$ 

FIGURE 3.38

 V^* VERSUS Z^*

0.30 cm I.D. CAPILLARY, SMALL RESERVOIR

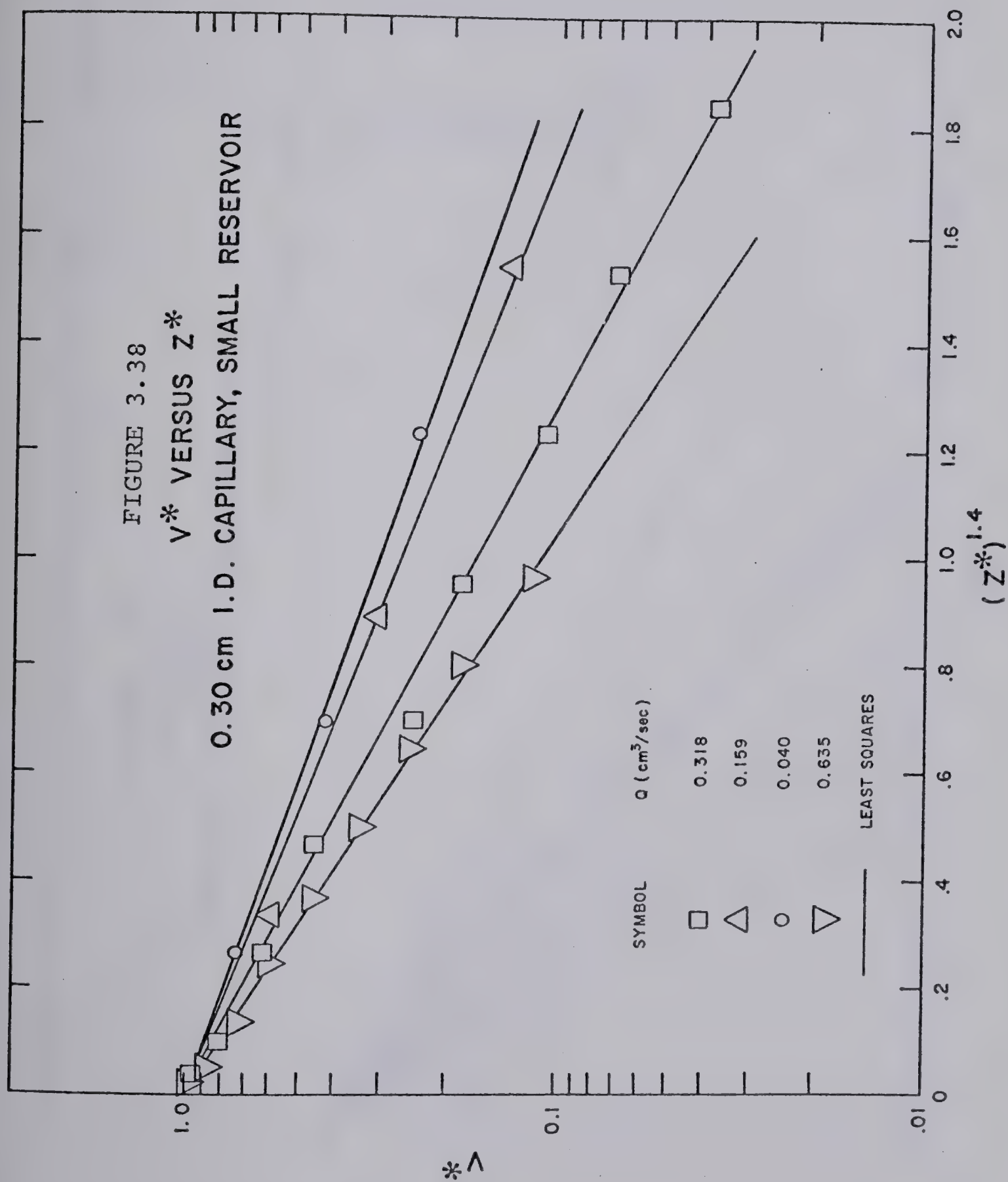


FIGURE 3.39
 V^* VERSUS Z^*
0.20 cm I.D. CAPILLARY, LARGE RESERVOIR

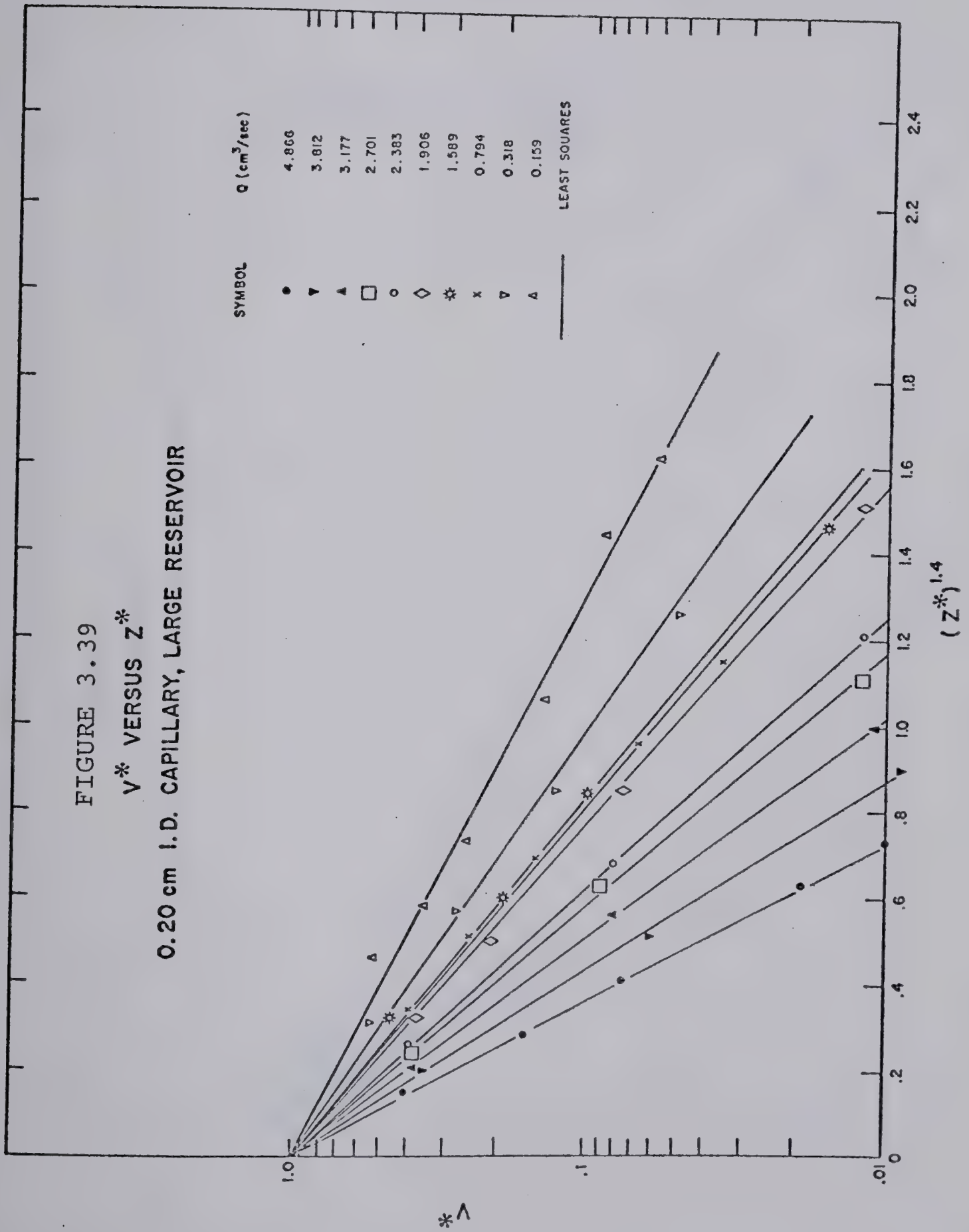
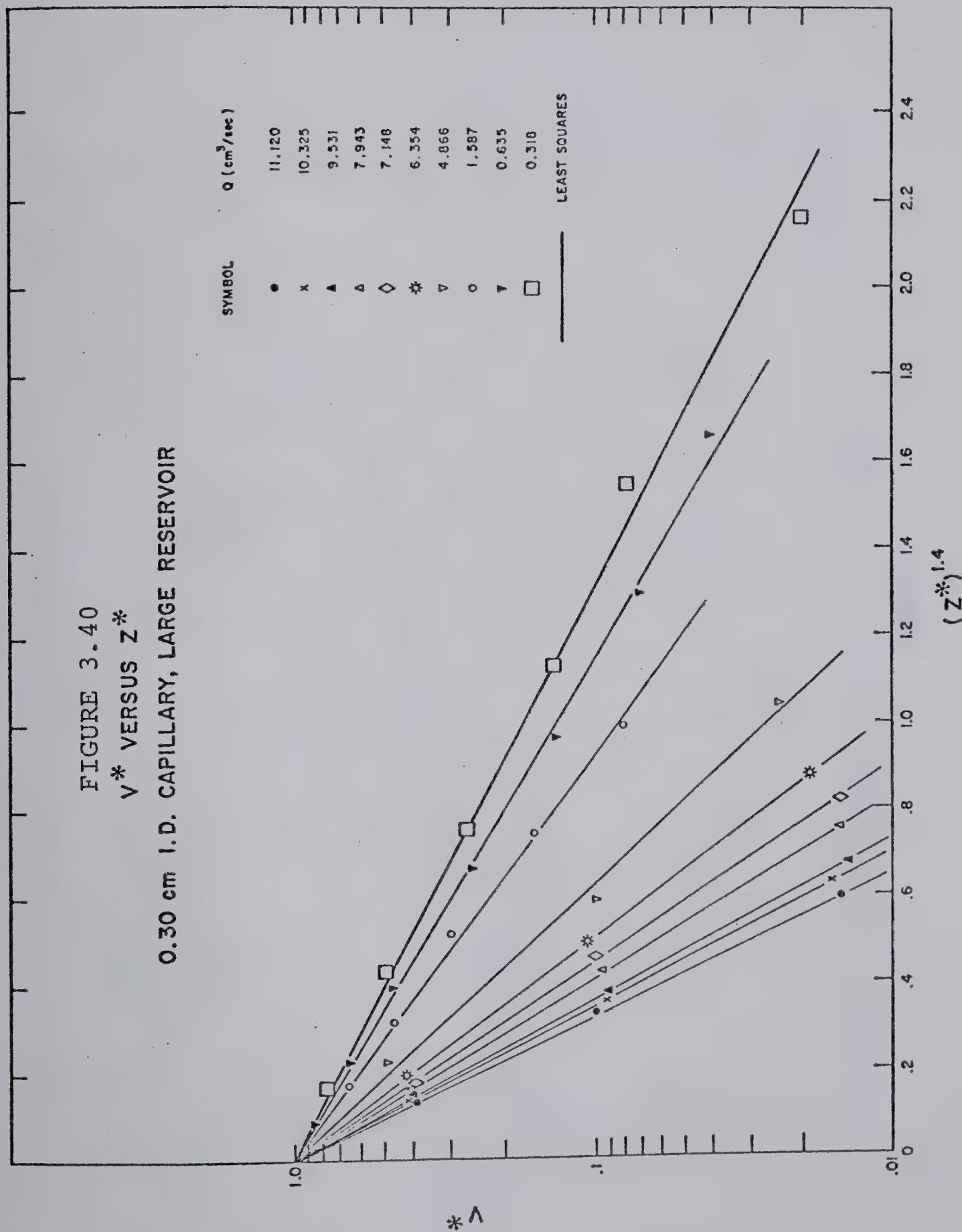
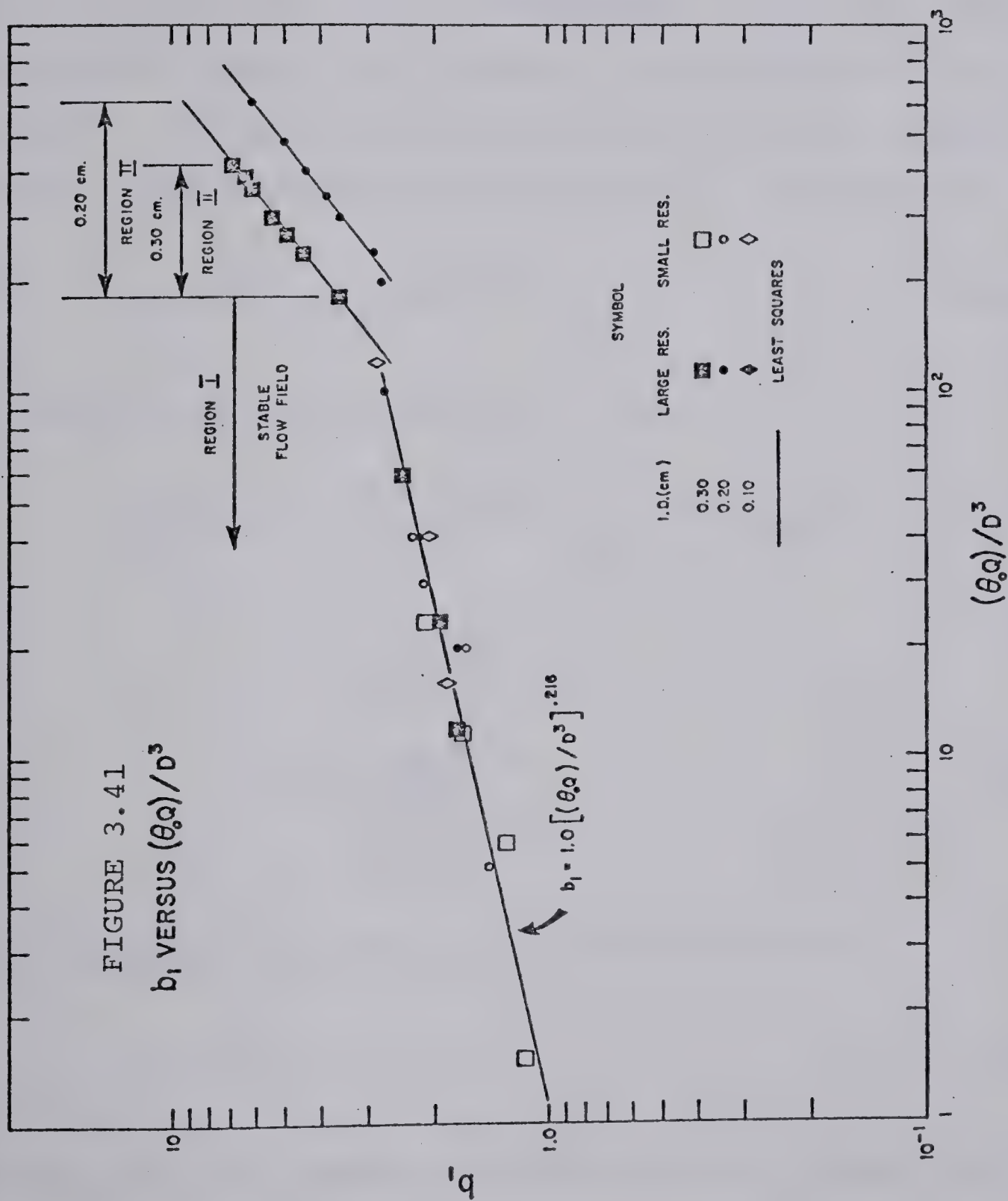


FIGURE 3.40
 V^* VERSUS Z^*
 0.30 cm I.D. CAPILLARY, LARGE RESERVOIR





Over the range $10 < \theta_0 Q/D^3 < 40$, no significant differences in the values of b_1 were noted with reservoir size. This conclusion was also reported for V_0 (page 161). It was conjectured, therefore, that the effect of reservoir size on b_1 was negligible for all experimental runs. The limited data further suggest that parameter b_1 is independent of N'_{Re} and n' . Hence, it was assumed that as a first approximation b_1 was dependent only on $(\theta_0 Q/D^3)$. By defining

$$(Z^{**})^{1.4} = b_1 (Z^*)^{1.4} \quad 3.38$$

and using Equation 3.37 and 3.38 we have

$$\begin{aligned} (Z^{**})^{1.4} &= \left(\frac{\theta_0 Q}{D^3}\right)^{0.216} \left[\frac{z}{(\theta_0^2 Q^2/D^3)^{1/3}}\right]^{1.4} \\ &= \frac{(z/D)^{1.4}}{(\theta_0 Q/D^3)^{.717}} \\ &\approx \left[\frac{z/D}{\sqrt{\frac{\theta_0 Q}{D^3}}}\right]^{1.4} \end{aligned} \quad 3.39$$

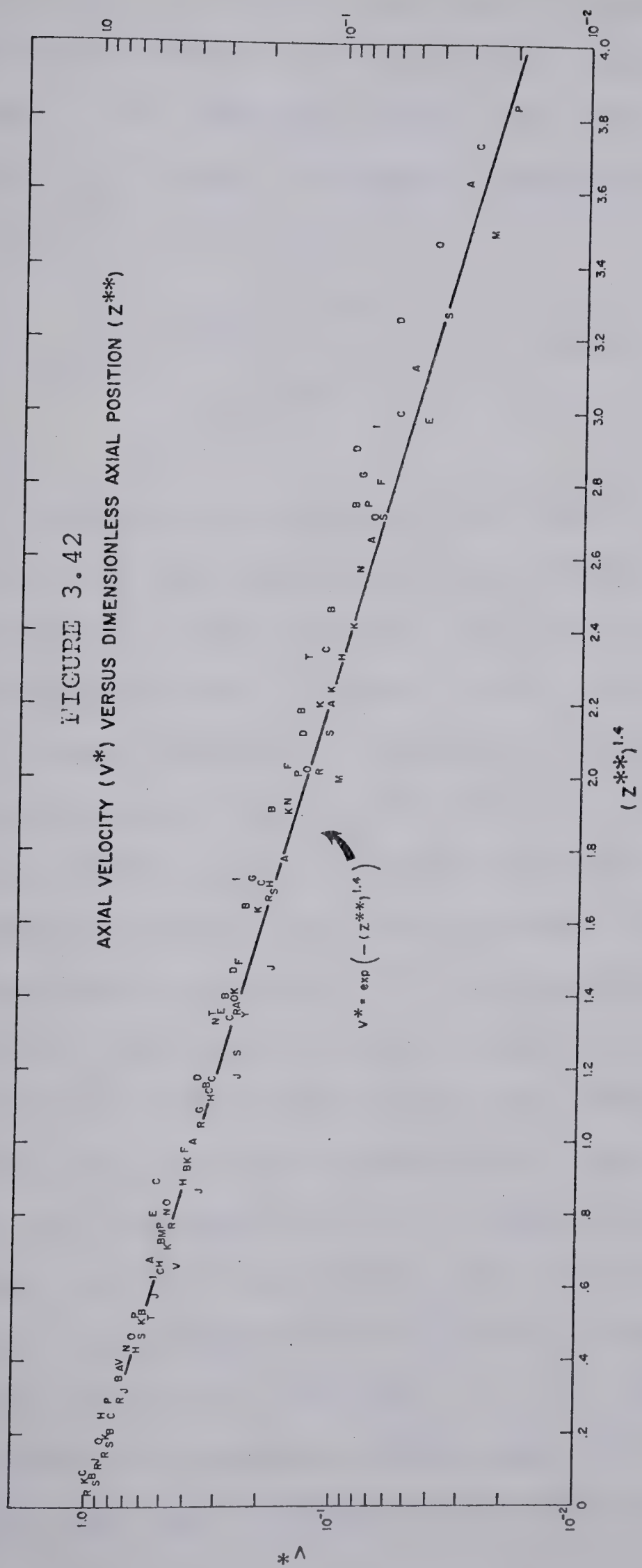
which eliminates b_1 . Equivalent plots would be

$$V^* = \exp(-(Z^{**})^{1.4}) \quad 3.40$$

If valid, all data should be represented by a single line given by Equation 3.40. The velocity data replotted in Figure 3.42 (semi-log coordinates) show that Equation 3.40 is indeed representative of data within region I.

LENGEND FOR FIGURE 3.42

<u>Symbol</u>	<u>I.D. (cm)</u>	<u>Q (cm³/sec)</u>	<u>Reservoir</u>
A	0.10	0.016	S
B	0.10	0.040	S
C	0.10	0.119	S
D	0.20	0.160	L
E	0.20	0.318	L
F	0.20	0.794	L
G	0.20	1.589	L
H	0.20	0.239	S
I	0.20	0.159	S
J	0.20	0.040	S
K	0.20	0.318	S
M	0.30	4.866	L
N	0.30	1.589	L
O	0.30	0.635	L
P	0.30	0.318	L
R	0.30	0.635	S
S	0.30	0.318	S
T	0.30	0.159	S
V	0.30	0.040	S



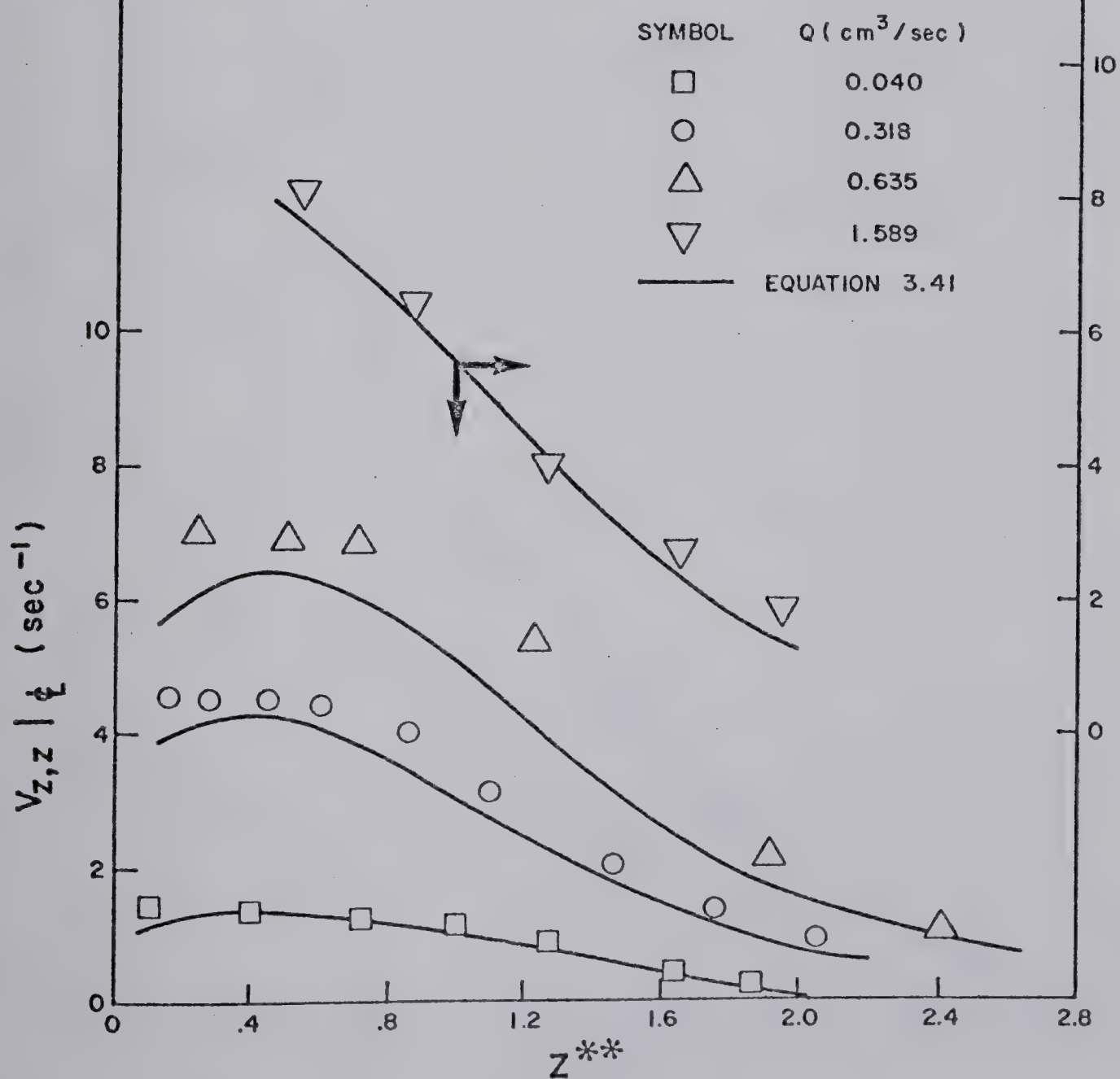
* ^

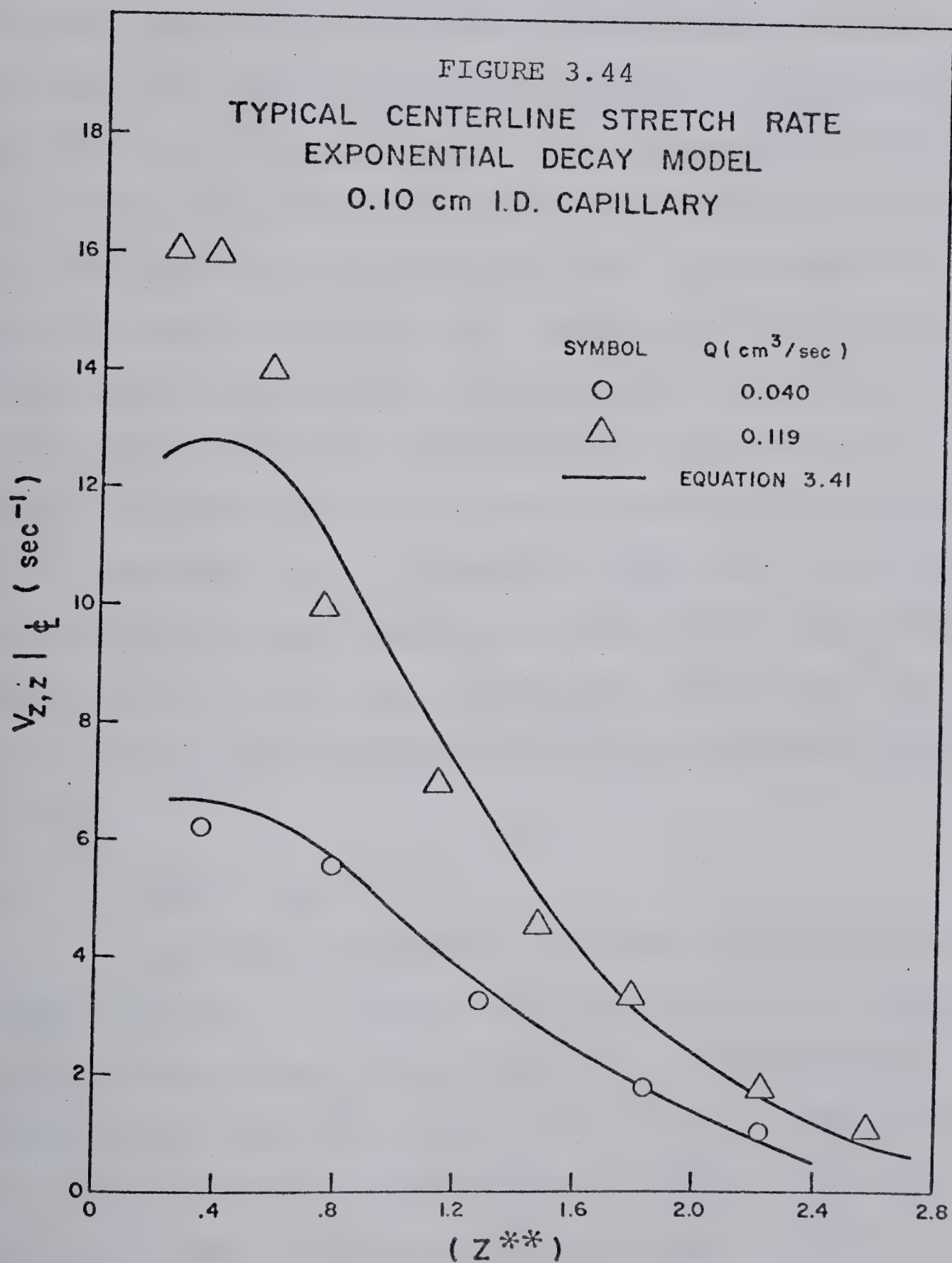
As a further test of the "goodness" of Equation 3.40 comparison is made between the experimental and predicted stretch rates. The predicted stretch rates along the centerline, $V_{z,z}|_{\xi}$, were obtained by differentiation of Equation 3.40. The result is

$$V_{z,z}|_{\xi} = \frac{1.4V_0(Z^{**})^{0.4}}{D\left(\frac{\theta_0 Q}{3}\right)^{0.5}} \exp(-(Z^{**})^{1.4}) \quad 3.41$$

The stretch rates given by Equation 3.41 show excellent agreement with the experimental values at several flow rates with capillary tube 3 (Figure 3.43) and at two flow rates with capillary tube 1 (Figure 3.44). In these experimental runs, the smallest value of Z^{**} where axial velocities were measured was 0.10, hence the experimental stretch rates are not shown in Figures 3.43 and 3.44 for Z^{**} less than 0.10. With the remaining data, velocities were also measured as close as $Z^{**} \approx 0.10$ and up to these axial locations, the predicted stretch rates are in good agreement with the data. Furthermore, the predicted stretch rates over a range of values of Z^{**} near to the contraction are predicted to be reasonably constant which is consistent with the experimental data. At larger values of Z^{**} , the stretch rates are again in good agreement with the data and in the limit, $Z^{**} \geq 2$, the stretch rates are predicted to asymptotically approach zero. At values of Z^{**} less than 0.10 the stretch rates are predict-

FIGURE 3.43
TYPICAL CENTERLINE STRETCH RATES
EXPONENTIAL DECAY MODEL
0.30 cm I.D. CAPILLARY



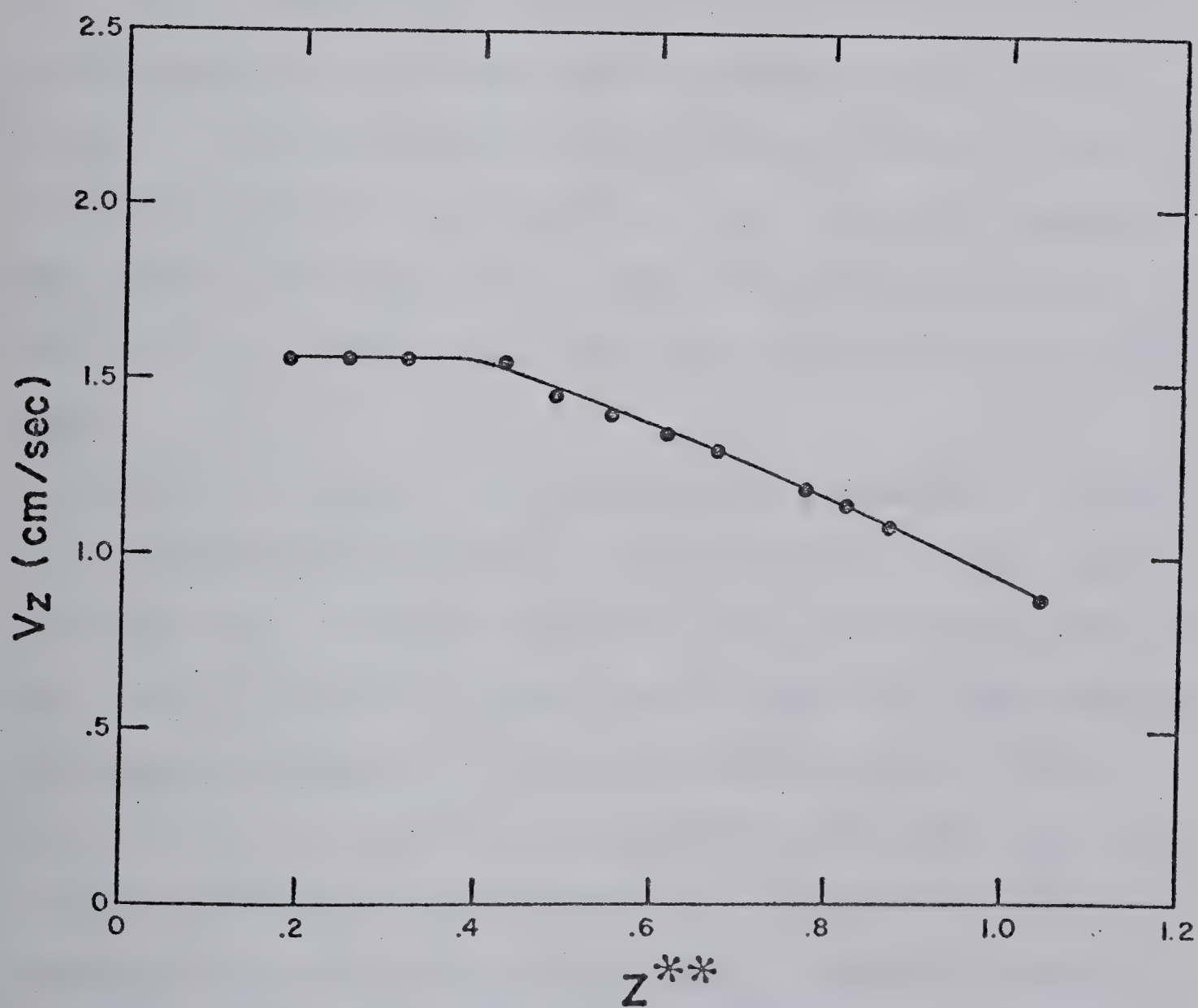


ed to decrease to a value equal to zero at the contraction. Since velocities were not measured within this range it was not possible to confirm this experimentally. However, for a few streamlines other than along the centerline, velocities were measured to within one streak length from the contraction. For these streamlines a plot of velocity versus axial location revealed that as the contraction was approached the velocity was independent of axial location, i.e., the stretch rate approached zero. An example of such a plot is given in Figure 3.45. Boger and Rama Murthy (24) did not measure centerline velocities at the contraction but the measured velocities upstream of the capillary entrance reported by them support the observations noted in this research, i.e., the stretch rates tend to a value equal to zero in the immediate vicinity of the contraction. Nakamura et al. (123) show clearly that only along the centerline was the stretch rate at the contraction equal to zero.

(iv) Radial Dependence

The data in Appendix E and the data plotted in Figures 3.17 to 3.22 clearly indicate a strong dependence of axial velocity upon radial location. Qualitatively, these velocity profiles resemble the velocity profiles for a jet of fluid issuing into a stagnant body of the same fluid (free jet). Therefore, in an attempt to obtain similarity, a dimensionless axial velocity defined as

FIGURE 3.45

TYPICAL EXAMPLE
OF CONSTANT STRETCH RATE $0.30 \text{ cm I.D.}, Q = 0.318 \text{ cm}^3/\text{sec}$ 

$$f(\eta) = \frac{V_z}{V_z|_{\eta=0}} \quad 3.42$$

was plotted against a dimensionless radial coordinate, $\eta = r/r_0$. The parameter r_0 is defined as the radial location where the axial velocity is equal to one half of the centerline velocity. The values of r_0 determined from the plots of velocity profiles similar to those shown in Figures 3.19 to 3.22 are tabulated in Appendix E, Section E.4. Other definitions of r_0 such as the distance from the centerline to the outermost streamline were used to define η . This definition of r_0 did not result in the velocity profiles being similar, i.e., when the dimensionless axial velocities, $f(\eta)$, were plotted against the variable η all of the data did not superimpose on a single curve.

From the values of r_0 tabulated in Appendix E it can be concluded that: (a) for a given capillary tube I.D., r_0 approached a constant value at $z^{**} = 0.0$ independent of flow rate or reservoir size, and (b) over the characteristic flow pattern length, r_0 was consistently larger within reservoir L. The effect of decreasing the capillary tube I.D. was a decrease in values of r_0 . The author was unsuccessful in correlating these data. Typical examples of the variation of r_0 with reservoir size and axial location upstream of the contraction are given in Figures 3.46 and 3.47. The data plotted in these figures indicate

FIGURE 3.46

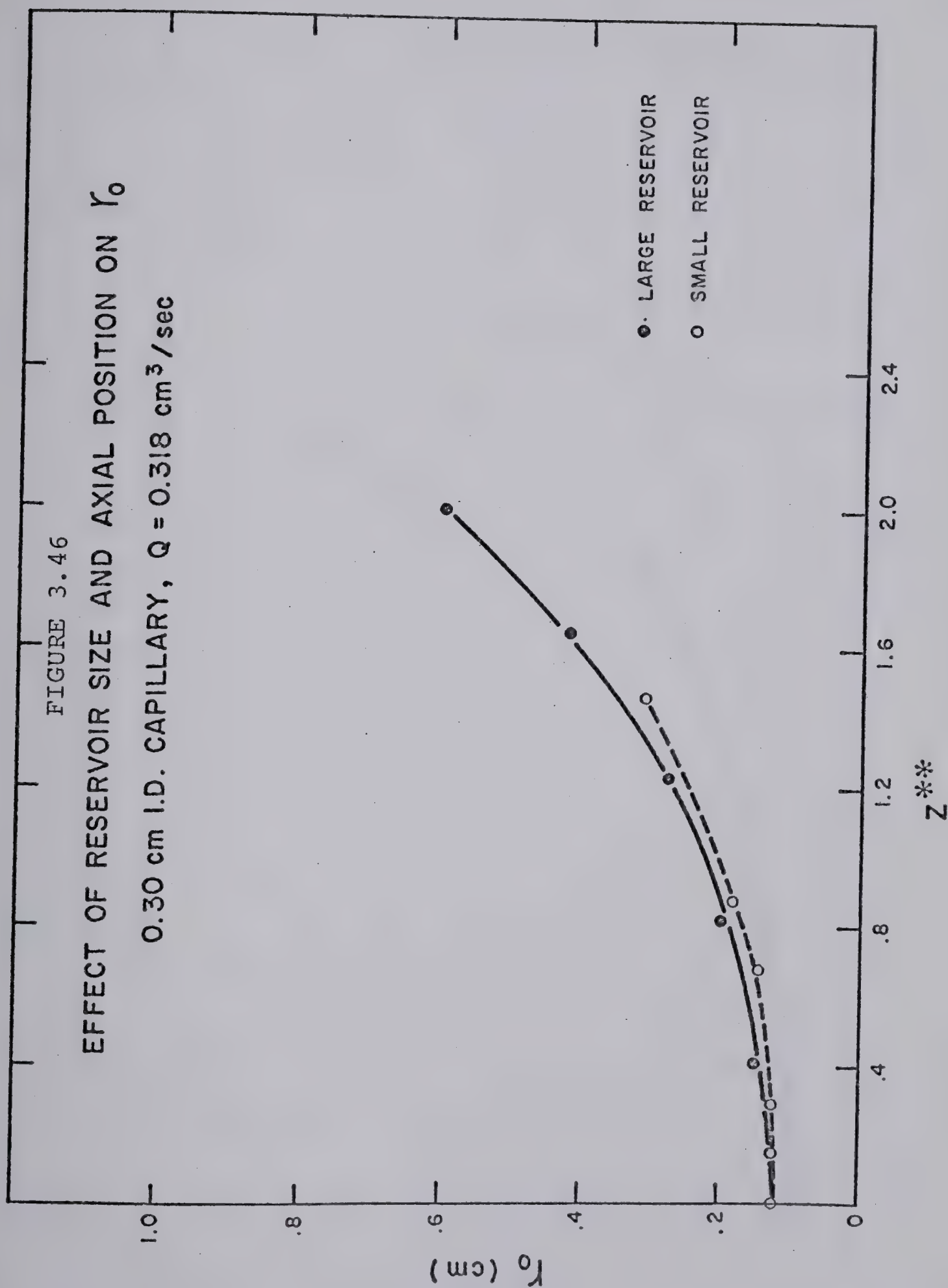
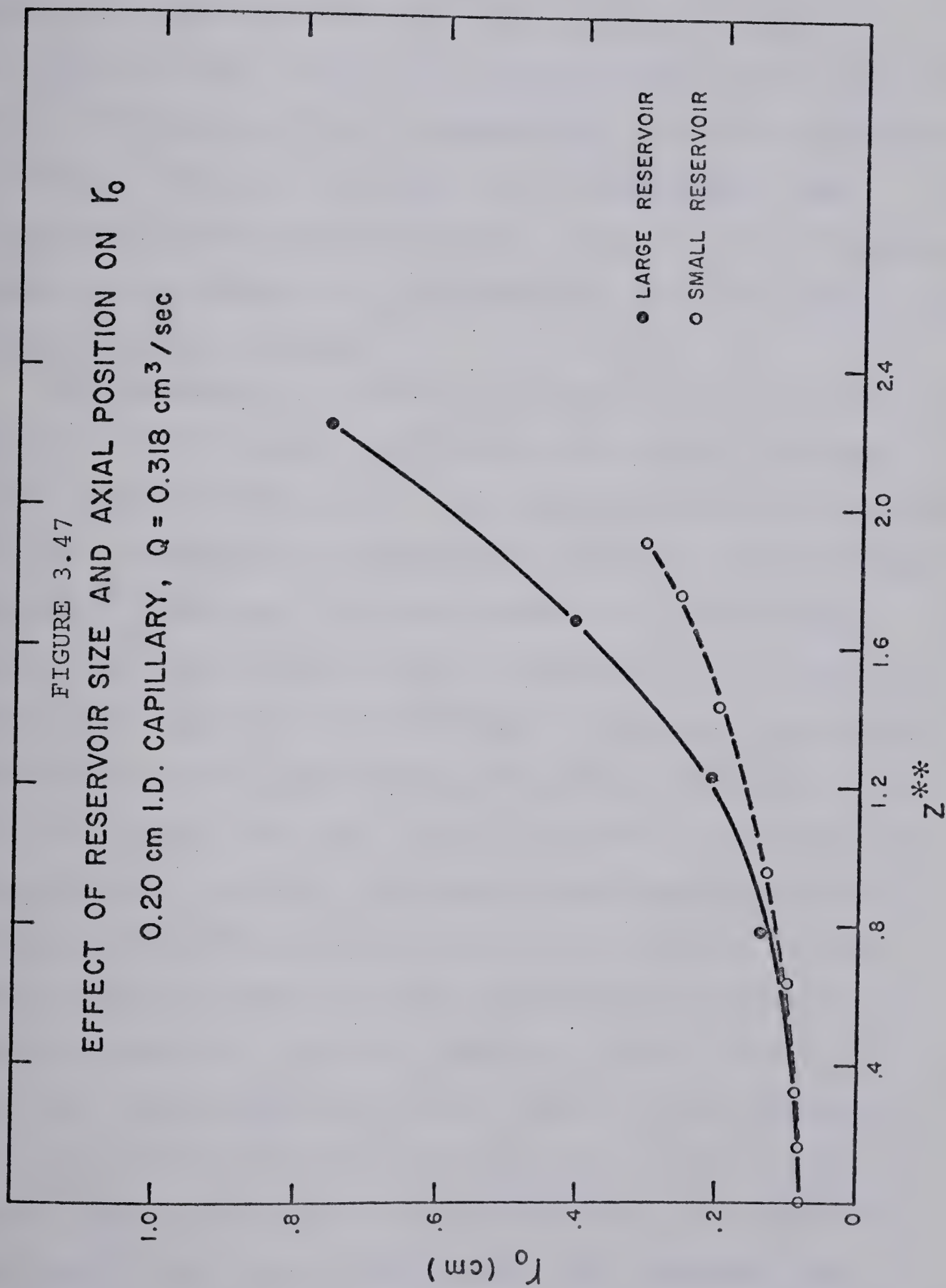
EFFECT OF RESERVOIR SIZE AND AXIAL POSITION ON r_0 0.30 cm I.D. CAPILLARY, $Q = 0.318 \text{ cm}^3/\text{sec}$ 

FIGURE 3.47

EFFECT OF RESERVOIR SIZE AND AXIAL POSITION ON r_0 0.20 cm I.D. CAPILLARY, $Q = 0.318 \text{ cm}^3/\text{sec}$ 

that r_0 is independent of reservoir size for values of $z^{**} \leq 0.40$. At values of $z^{**} > 0.40$ a strong dependence on reservoir size was observed. At a fixed flow rate, $Q = 0.318 \text{ cm}^3/\text{sec}$ and at $z^{**} = 1.4$, r_0 was equal to 0.29 and 0.33 in reservoirs S and L respectively with capillary tube 3 (Figure 3.46) and 0.19 and 0.28 in reservoirs S and L respectively with capillary tube 2 (Figure 3.47). The above shows the dependence of r_0 on reservoir size at a fixed flow rate and axial position.

The dimensionless axial velocities, $f(\eta)$, are graphically plotted against the dimensionless radial location, η , in Figures 3.48 to 3.52. Log-log coordinates were chosen in order to discern differences in the values of $f(\eta)$ less than 10^{-1} . The data in these figures were arbitrarily chosen from the tabulated data in Appendix E. If all the data in the appendix were plotted, it would not be possible to distinguish the individual data points for a given flow rate at various axial and radial locations. At values of η less than 1.5 a single curve may be representative of the data with deviations being less than 16 percent. Larger deviations were noted at dimensionless radial locations greater than 1.5. Consider values of η equal to 1.5, 2.0, and 2.75. The respective average values of the dimensionless axial velocities for capillary tube 2 were 0.275, 0.175, and 0.100 for the data obtained with reservoir L and 0.250, 0.125, and 0.055 for the data obtained with reservoir S. Similar variations were noted for the other data. However, it must be emphasized that at these values

FIGURE 3.48

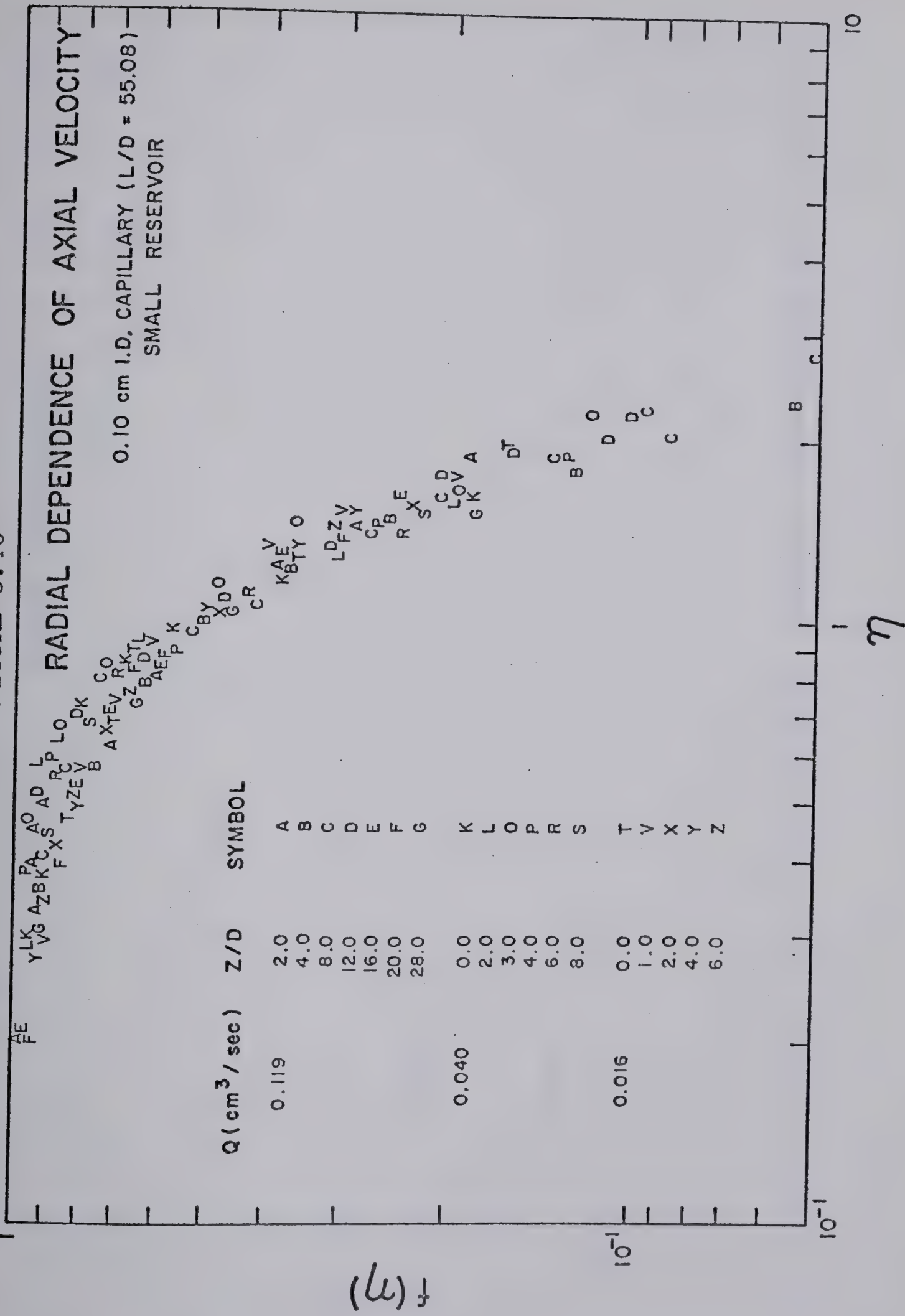


FIGURE 3.49

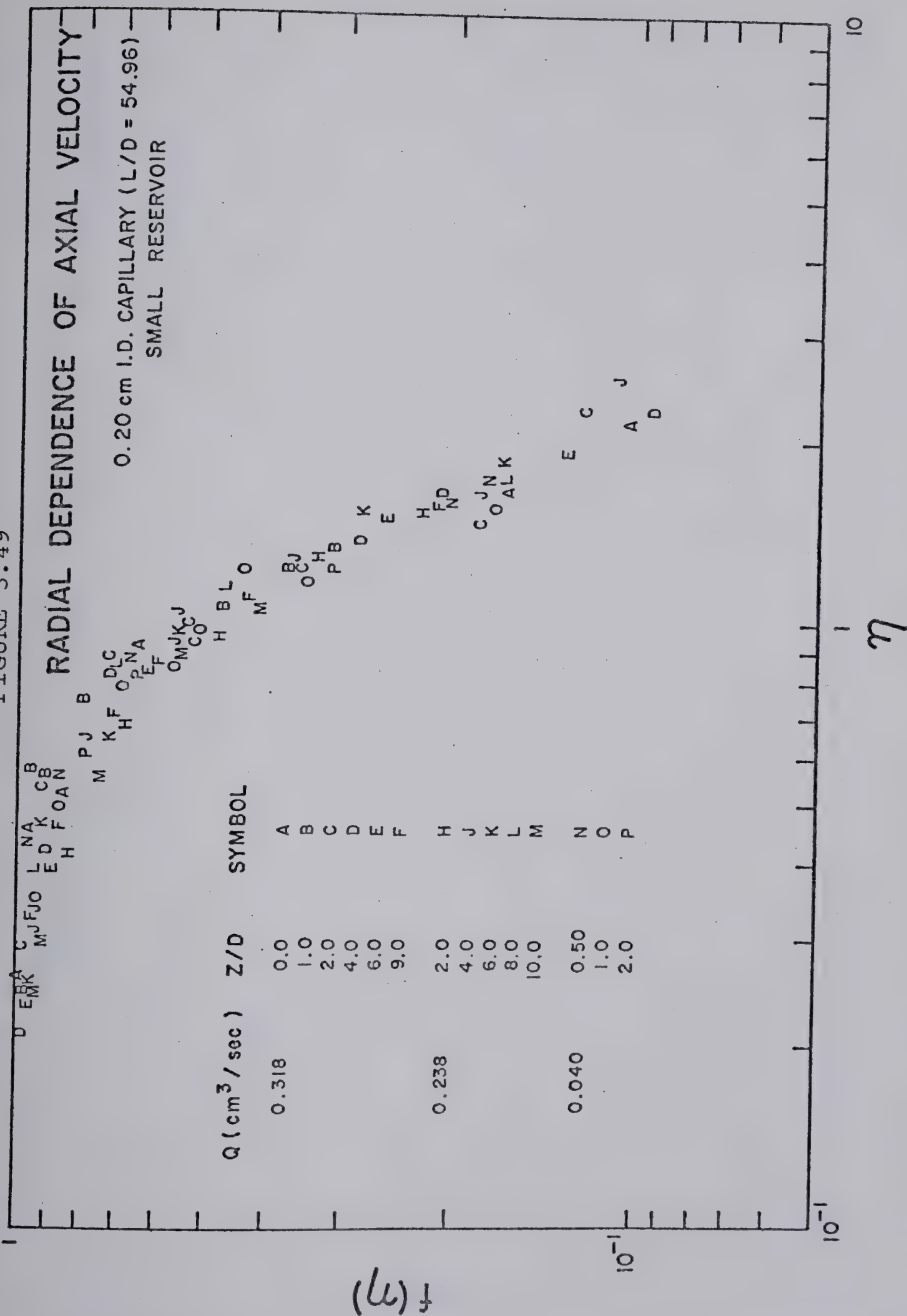


FIGURE 3.50

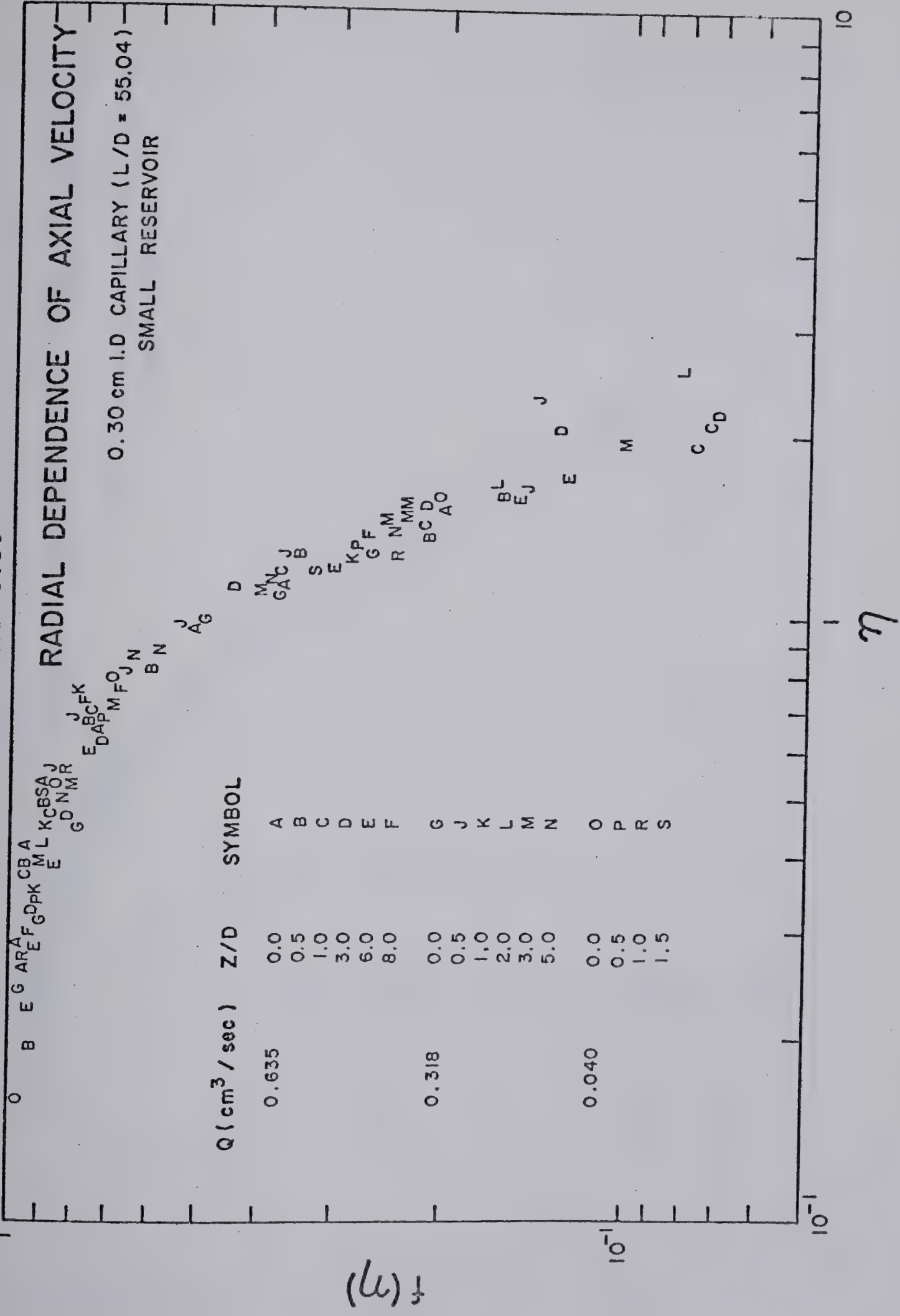


FIGURE 3.51

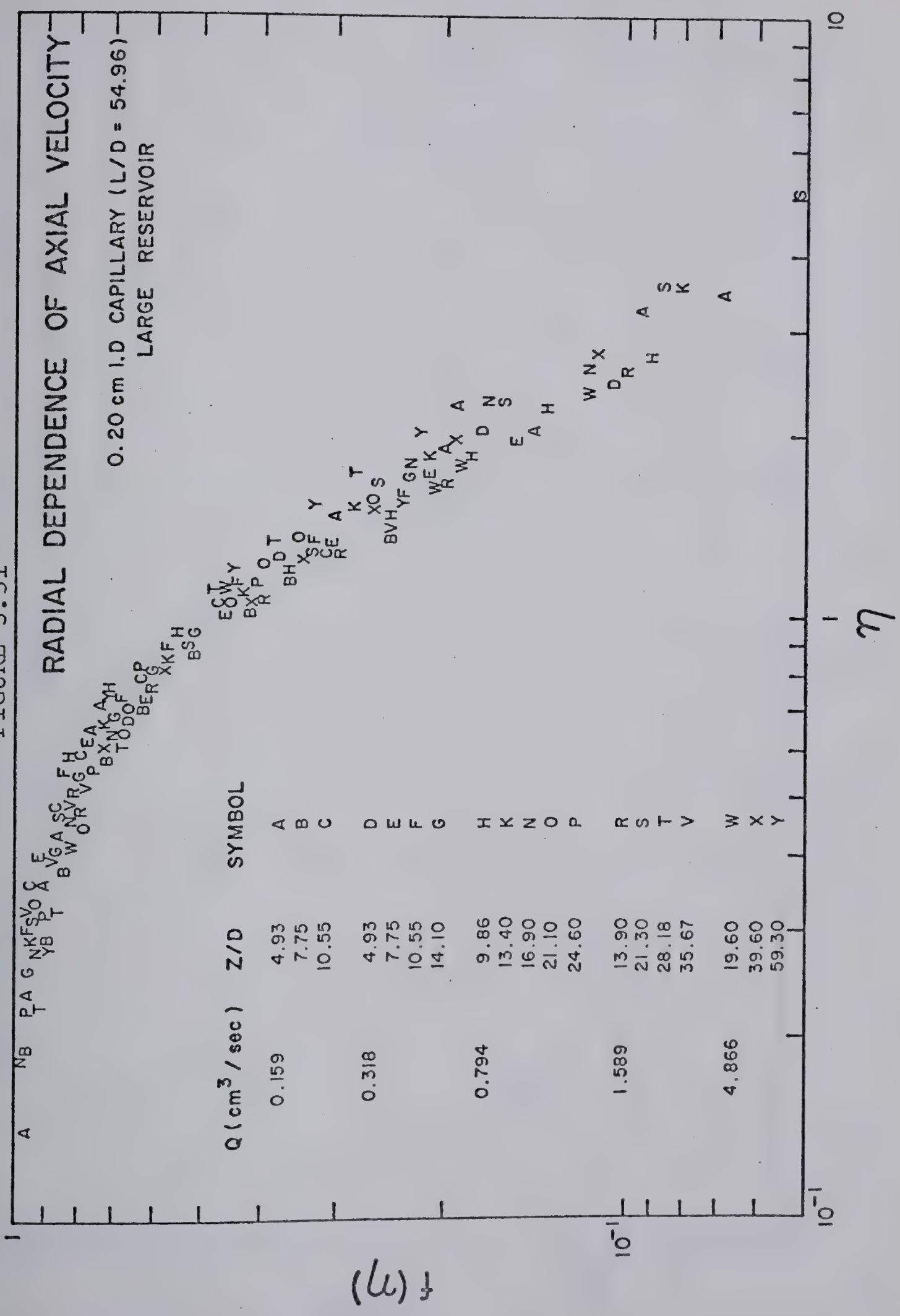
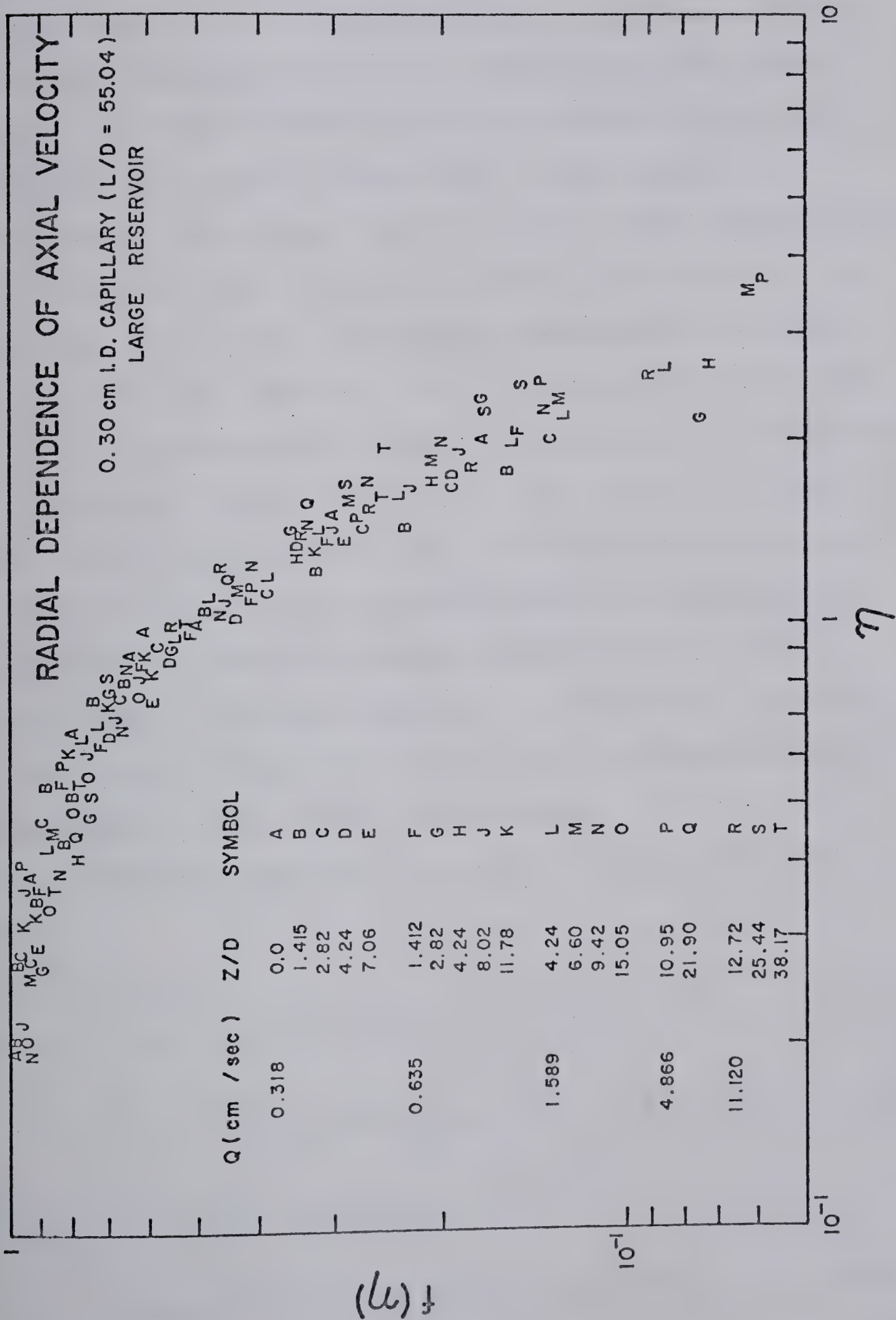


FIGURE 3.52



of η , the axial velocities were measured outside of the central core region. As a result, velocities were small in comparison to the centerline axial velocities and were difficult to measure accurately. Even though the velocities in this region were difficult to measure accurately, the discrepancy was not solely due to the accuracy in measurement. If a single curve is made to pass through the mean of all the data in Figures 3.48 to 3.52 inclusive up to values of $\eta = 2.75$, the maximum discrepancies between the data and this curve at $\eta = 1.5$, 2.0 , and 2.75 are 16%, 17% and 42% respectively. The large discrepancies measured for values of η greater than 2.0 , e.g., 42% at $\eta = 2.75$, are a result of reservoir size. At large radial positions, $r = 2r_0$, the predicted velocities would be approximately 40% larger than measured values in reservoir S or 40% smaller than velocities measured in reservoir L. However, at these large values of η , axial velocities were measured well outside of the central core region.

A universal curve that is made to pass through data points

$$v_z = v_z|_{\zeta} \quad @ \quad r=0 \quad \text{or} \quad f(\eta) = 1.0 \quad @ \quad \eta=0 \quad 3.43$$

$$v_z = \frac{1}{2} v_z|_{\zeta} \quad @ \quad r=r_0 \quad \text{or} \quad f(\eta) = 0.5 \quad @ \quad \eta=1.0 \quad 3.44$$

and subject to the condition

$$v_{z,r} = 0 \quad @ \quad r=0 \quad \text{or} \quad f'(\eta) = 0 \quad @ \quad \eta=0 \quad 3.45$$

is given by Equation 3.46.

$$f(\eta) = (1 + 0.41 \eta^2)^{-2.0} \quad 3.46$$

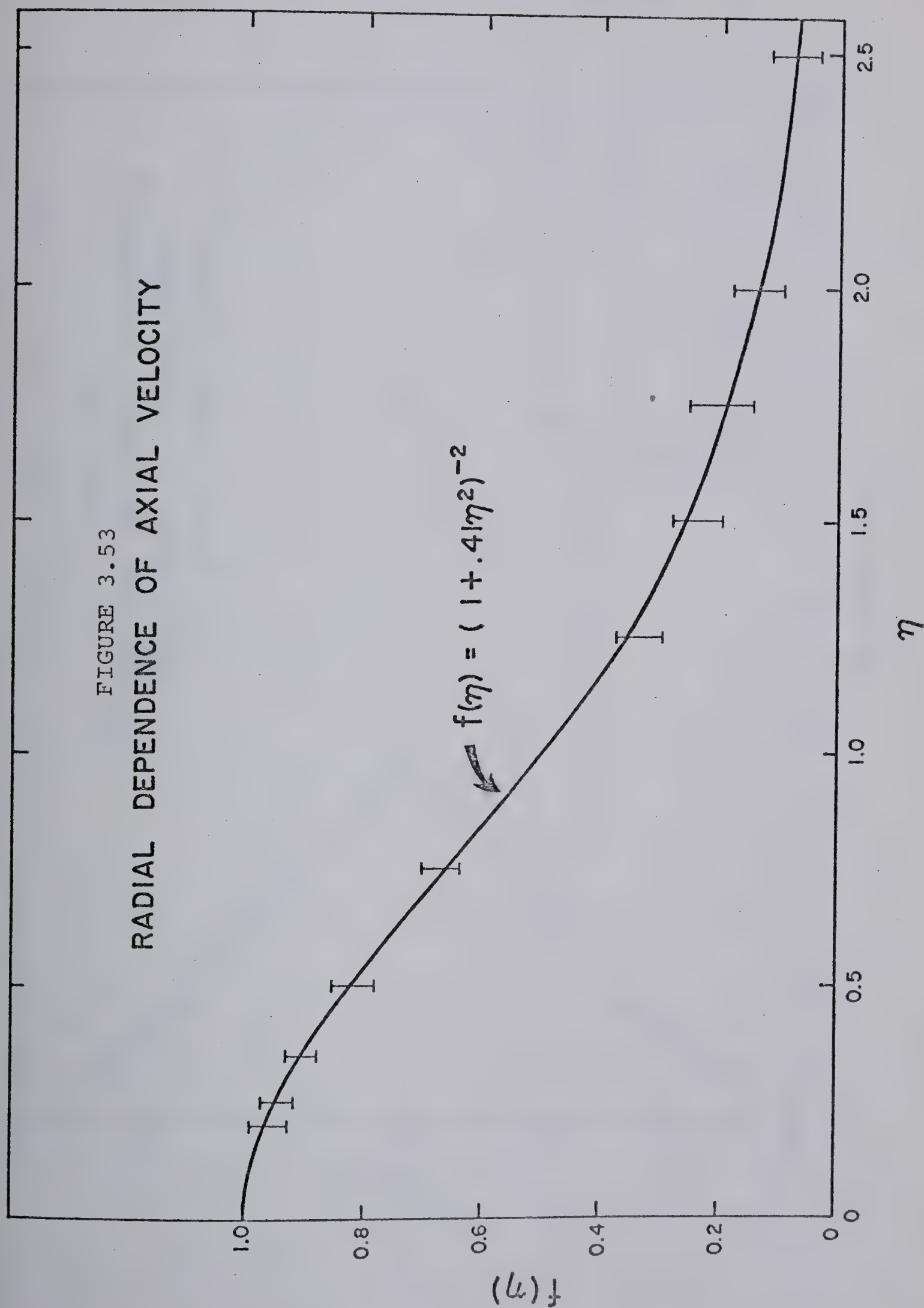
Equation 3.46 is plotted as the solid line in Figure 3.53 with the vertical bands representing the maximum scatter in the data obtained from Figures 3.48 to 3.52 inclusive. Equation 3.46 passes through the vertical bands up to values of η equal to 2.5. A replot of experimental axial velocities ($f(\eta)$ vs η) measured upstream of an abrupt contraction (123) for $\beta = 8.16 \times 10^{-2}$, $z/D \leq 3.0$ and $r/R \leq 0.550$ are within 10 percent of predicted values, Equation 3.46. Thus, Equation 3.46 predicts velocities which are in reasonable agreement with experimental velocities over a wider range of parameters than studied in this research.

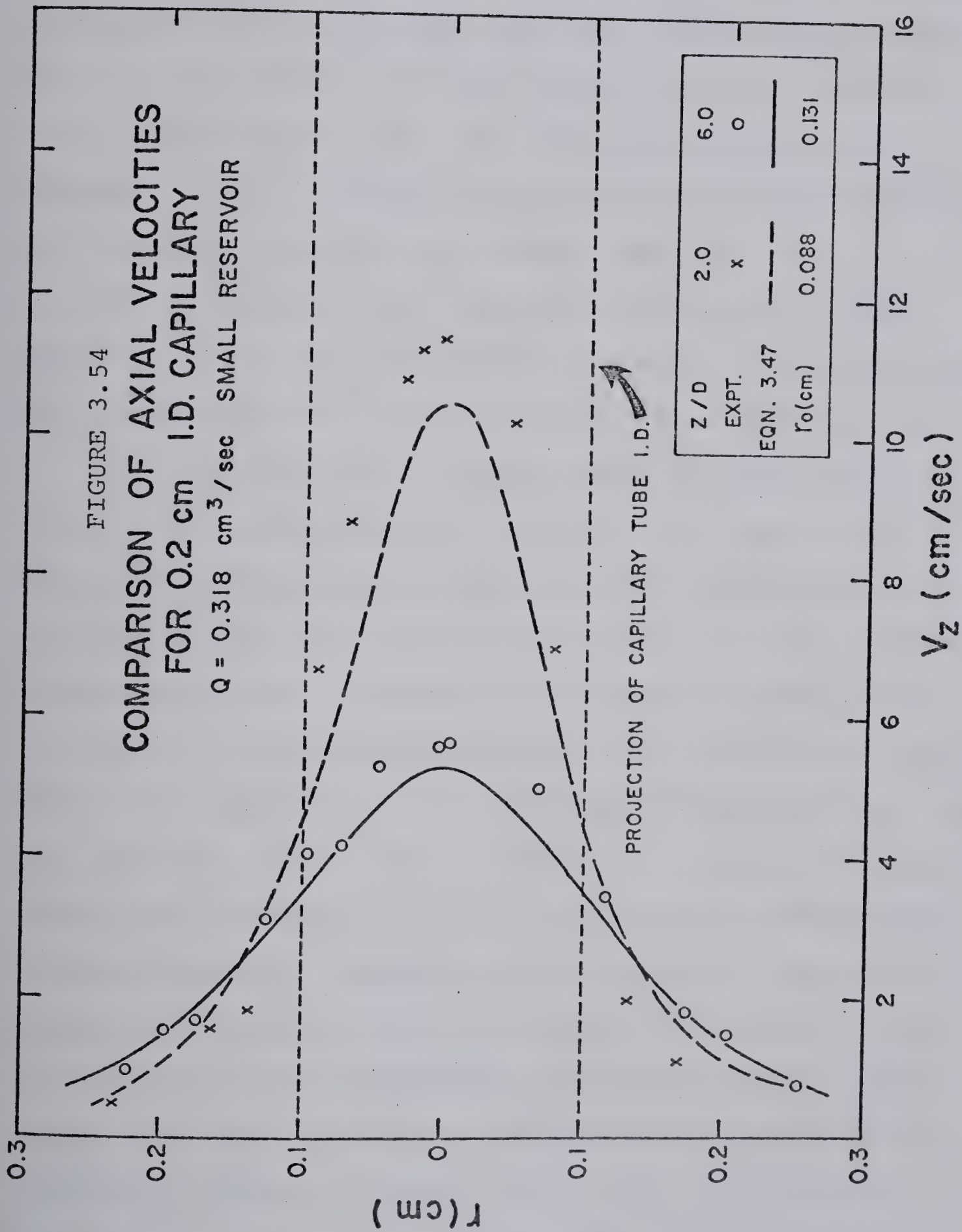
Axial velocities, predicted by combining Equations 3.40 and 3.46, that is

$$v^* = \exp(-(Z^{**})^{1.4}) (1 + 0.41 \eta^2)^{-2.0} \quad 3.47$$

are compared to experimental data for two typical runs. The data in Figure 3.54 typify the maximum discrepancy of 17% between experimental and predicted velocities for values of η less than 2.0. In this example, η less than 2.0 corresponds to values of r less than 0.196 cm at 2.0 diameters upstream of the contraction, whereas at 6.0 diameters upstream of the contraction, η less than 2.0

FIGURE 3.53
RADIAL DEPENDENCE OF AXIAL VELOCITY



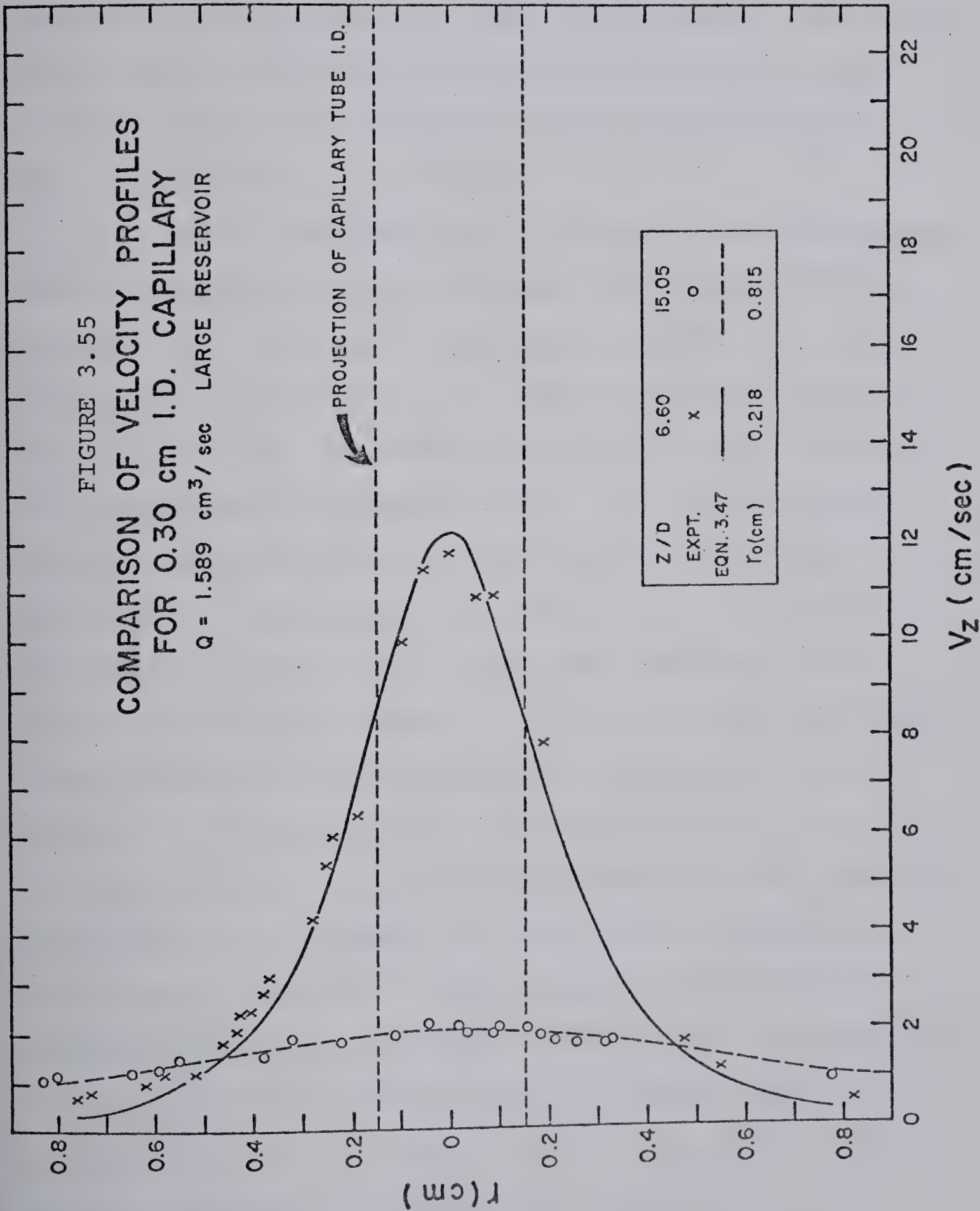


corresponds to values of r less than 0.262 cm. An example of good agreement with experimental data is shown in Figure 3.55. This figure also shows that at 6.60 diameters upstream of the contraction the axial velocities at values of $r = 0.80$ cm or $\eta = 4.0$ are in good agreement with the data. This suggests that for some experimental runs Equation 3.47 is capable of predicting reasonably velocities at values of η considerably larger than 2.0.

The features of the flow field (discussed in this section), i.e., cone semi-angles, location of eddy centers, and axial velocities, can be summarized as follows:

(a) The initial cone semi-angles measured within region I are independent of reservoir size and are represented by Equation 3.8, and cone semi-angles measured upstream of the contraction and for $Z^{**} < Z_{\infty}^{**}$ are, within experimental error, independent of reservoir size. The value of Z_{∞}^{**} varies with capillary tube diameter and flow rate. For example, at $0.318 \text{ cm}^3/\text{sec}$, Z_{∞}^{**} was 2.2 and 3.2 for capillary tubes 2 and 3 (Figure 3.24, page 162). Beyond these axial locations, the cone semi-angles, although not measured directly, depend on reservoir size. This can be explained in terms of the qualitative differences in the flow fields in both reservoirs. Since the central core within reservoir S occupied a significant fraction of the reservoir's cross-sectional area at $Z^{**} = Z_{\infty}^{**}$ further cone angle development was restricted. On the other hand, the cross-sectional area in reservoir L was two orders of

FIGURE 3.55
COMPARISON OF VELOCITY PROFILES
FOR 0.30 cm I.D. CAPILLARY
 $Q = 1.589 \text{ cm}^3/\text{sec}$ LARGE RESERVOIR



magnitude larger which allowed cone angle development farther upstream at a given flow rate. The development continued until the central core area approached the reservoir's cross-sectional area. As a result, the center of the eddies were located farther upstream of the contraction and the area occupied by the recirculation region was larger in size in reservoir L.

(b) Within the WGS core the dimensionless centerline axial velocity-axial position plots (V^* vs $(Z^{**})^{1.4}$) are similar, i.e., all of the data superimposed on a single curve given by Equation 3.40. The velocities measured up to values of Z_0^{**} , where the product $\Gamma\theta_0$ is equal to unity, are independent of reservoir size. This axial location defined the major portion of the flow field and was approximately equivalent to a distance upstream of the contraction equal to one and one half times the location of the center of the eddies. Axial velocities other than along the centerline, represented by Equation 3.46, are within 17% of experimentally measured velocities for $\eta \leq 2.0$. Parameter r_0 used in the definition of η was not independent of reservoir size over the full range of upstream axial locations. This parameter was independent of reservoir size only for values of $Z^{**} \leq 0.40$. Farther away from the contraction, $Z^{**} > 0.40$, r_0 becomes dependent on reservoir size to the extent that at a fixed Z^{**} and flow rate it increased as reservoir size increased.

(c) The radial velocity component is derived from the

use of Equation 3.47, the continuity equation and the boundary condition $V_r = 0$, and $r = 0$. Experimental values are tabulated in Appendix E, Section E.2.

3.5 PREDICTION OF INSTABILITY

Empirical criteria presented to date, such as the critical shear stress or recoverable shear strain, attempt to correlate the onset of instabilities with physical properties of the fluid measured under SLSF in the capillary tube. These criteria, although simple to evaluate and require little, if any additional experimentation, do not take into account such variables as reservoir size and the type of instability. More critically, these criteria are inconsistent with experimental observations wherein for many polymer melts and solutions fracture has been observed to occur within the inlet region. Criteria based on inlet conditions have not been tested severely since a detailed quantitative description of the flow field was not known. This led Everage and Ballman (60) to resort to approximating the flow field using the velocity distribution of a Newtonian fluid. Although the onset criteria based on inlet conditions differ significantly, there is a consensus of opinion that instability is a consequence of tensile failure in extensional deformation (46, 60, 88).

Cogswell's (46) expression for a critical extensional stress at the die entry is given by

$$(\tau)_{cr} = \frac{3n'+1}{n'+1} \frac{\tau_w}{\tan \phi_0} \quad 3.48$$

The practical difficulty in utilizing Equation 3.48 for flows through a sudden contraction is that the initial cone semi-angle, ϕ_0 , must be known or measured in order to predict $(\tau)_{cr}$. In reservoir L and at the onset of region III, ϕ_0 was too small to be measured accurately ($\phi_0 < 0.5$ degrees) which immediately points to a limitation of Equation 3.48, i.e, not only must ϕ_0 be known but it must be known accurately. Furthermore, as ϕ_0 tends to zero, Equation 3.48 predicts infinite extensional stresses. Since ϕ_0 was too small to be measured accurately at the onset of region III in reservoir L, a conservative estimate of $(\tau)_{cr}$ was obtained by assuming that ϕ_0 was equal to 0.5 degrees. Critical extensional stresses calculated with Equation 3.48 are given in Table 3.5. These data show that $(\tau)_{cr}$ was not reasonably constant but varied from 1669 dyn/cm² to values exceeding 100,000 dyn/cm² (two orders of magnitude variation). If, on the other hand, $(\tau)_{cr}$ was reasonably constant then Equation 3.48 would predict a critical value of the shear stress which is related to inlet conditions by $\tan \phi_0$. The initial cone semi-angle for polymer melts exemplified by HDPE is 90 degrees, hence Equation 3.48 would predict, for a constant $(\tau)_{cr}$, a shear stress criterion. Cogswell (46) also showed that the critical extensional stress is related to the pressure losses in the entry region, P_u , by

TABLE 3.5

CRITICAL EXTENSIONAL STRESSES AT ONSET OF INSTABILITY

	I.D. (cm)		
	Capillary tube 1	Capillary tube 2	Capillary tube 3
Reservoir S			
$(\tau)_{cr}$ (dyn/cm ²)	11,935	3,465	1,669
Reservoir L			
$(\tau)_{cr}$ (dyn/cm ²)	67,299**	23,798	26,737
$(\tau)_{cr}^*$ (dyn/cm ²)	> 120,318	> 58,249	> 45,835

* Evaluated at the onset of region III

** Flow rate obtained by extrapolation of data plotted in Figure 3.6.

$$(\tau)_{cr} = \frac{3}{8} (n'+1) P_u \quad 3.49$$

Predicted values of P_u (obtained by equating Equations 3.48 and 3.49) are compared to the experimentally measured contraction losses, ΔP_c , in Table 3.6. P_u should always be less than ΔP_c since ΔP_c includes the pressure losses in the capillary tube entry length as well as within the entry region. With the exception of capillary tubes 2 and 3 in reservoir S, P_u was significantly greater than ΔP_c . Cogswell's own data indicated that for a LDPE melt the predicted value of P_u at the onset of fracture was 0.00 N/m^2 , and by Equation 3.49 $(\tau)_{cr}$ is equal to 0.00 N/m^2 . This contradicts the hypothesis that melt fracture is a consequence of tensile failure. We conclude, therefore, that due to: (a) the above contradiction, (b) the predicted values of P_u in the majority of cases being greater than ΔP_c , and (c) the prediction of infinite extensional stresses as ϕ_0 tends to zero, the generality of Equation 3.48 or 3.49 is seriously limited in predicting parameters at the onset of fracture.

The recoverable extensional strain criterion presented by Everage and Ballman (60) may be quantitatively tested by evaluating the maximum stretch rate at the onset of fracture. If applicable, this stretch rate should be reasonably constant. Experimental maximum stretch rates (along the centerline) varied from 7 to 16 sec^{-1} in reservoir S and in reservoir L they varied from 16.5 to

TABLE 3.6

COMPARISON OF P_u WITH ΔP_c AT ONSET
OF FLOW INSTABILITIES

RESERVOIR	PRESSURE (dyn/cm^2)	I.D. (cm)		
		0.10	0.20	0.30
S				
Region II	P_u	21238	6160	2967
	ΔP_c	9500 **	6947 **	4826 **
L				
Region II	P_u	119643	42308	47532
	ΔP_c	36500 *	12510	12010
Region III	P_u	> 213899	> 103554	> 81484
	ΔP_c	141700	61430	53440

* interpolation of data in Appendix C

** extrapolation of data in Appendix C

to 23.5 sec^{-1} (region II) or from 32 to 49 sec^{-1} (region III). These data would appear to support the recoverable extensional strain as a criterion for the onset of fracture. However, examination of experimentally measured centerline velocities revealed that over the major portion of the flow field the centerline velocities were independent of reservoir size. Therefore, maximum stretch rates evaluated in reservoir S, which resulted in an unstable flow field, (region II), should have resulted in an unstable flow field in reservoir L. Contrary to this, Figure 3.6 clearly shows that flow fields were stable at significantly higher flow rates in reservoir L. Consequently, although the maximum stretch rates are reasonably constant (7 to 28.5 sec^{-1} at the first signs of an unstable flow field), this is not sufficient evidence to support the recoverable extensional strain criterion.

The hypothesis presented by Everage and Ballman (60), which is an extension of the work of Denn and Marrucci (51), is based upon a time dependent stress growth resulting from the converging flow field. Since this flow field has been shown to be dependent on flow rate and reservoir size, the fluid is subjected to different strain histories. This lends itself to the Hencky's strain measure or total strain as a means of correlating the onset of instability. This measure, which has been used successfully in correlating velocity data (90), i.e., parameter p in Equation 3.9 with the total strain and transient elongational vis-

cosities with the total strain (1), is given as

$$S = \int_{t_i}^{t_f} \Gamma \, dt \quad 3.50$$

where t_i is the initial time when elongation commences. Acierno et al. (1), using this definition, found that elongation viscosity-total strain curves obtained from spinning and inverse siphon experiments, resulted in a single curve. The data obtained from the inverse siphon experiment covered the initial part of the transient curve while the data from the spinning experiment yielded the upper part of the same transient curve. The basis to their analysis assumes that beyond an axial location, Z_0^{**} , the polymer molecules, represented by elastic dumbbells, are aligned in the direction of stretching without appreciable change in their length, whereas for axial locations less than Z_0^{**} they elongate. Therefore, time, t_i , in Equation 3.50 is considered to be equal to zero at $Z^{**} = Z_0^{**}$. The evaluation of Z_0^{**} was determined by a dimensionless stretch rate where the product of the stretch rate times the zero shear relaxation time of the fluid was equal to unity.

Acierno et al. (1) showed that the transient elongational viscosity curve deviates from linear Hookean behavior beyond a value of S . In an attempt to rationalize the effect of reservoir size and capillary tube diameter on the onset of flow instabilities, it is postulated in this dissertation that instabilities may occur whenever the polymer mole-

cules exceed the linear Hookean range. Equivalently, instabilities may occur at a critical value of S , S_c . An analytical expression for S_c derived from the empirical equation for the centerline velocity, Equation 3.40, is

$$\begin{aligned}
 S_c &= \int_0^t \Gamma \, dt = \int_0^t \frac{-1.4 V_z (Z^{**})^{0.4}}{D(\theta_0 Q/D^3)^{0.5}} \, dt \\
 &= \frac{-1.4}{D(\theta_0 Q/D^3)^{0.5}} \int_{Z_0^{**}}^0 (Z^{**})^{0.4} \, dZ \\
 &= -1.4 \int_{Z_0^{**}}^0 (Z^{**})^{0.4} \, dZ^{**} \\
 &= (Z_0^{**})^{1.4}
 \end{aligned} \tag{3.51}$$

Therefore, the stretch history is determined uniquely by a dimensionless parameter, Z_0^{**} . This dimensionless parameter is not independent of flow rate and other variables since it was obtained from the condition

$$\Gamma \theta_0 = 1.0 \tag{3.52}$$

The substitution of Equation 3.40 into Equation 3.52 yields

$$1.0 = \frac{1.4 V_0 (Z_0^{**})^{0.4}}{D(\theta_0 Q/D^3)^{0.5}} \exp(-(Z^{**})^{1.4}) \theta_0 \tag{3.53}$$

From Equation 3.51 we have

$$1.0 = \frac{1.4V_0 S_c^{.286} \theta_0}{D(\theta_0 Q/D^3)^{0.5}} \exp(-S_c) \quad 3.54$$

For the system considered here, the zero shear relaxation time is equal to 1 sec and with n' equal to 0.50 Equation 3.22 reduces to

$$V_0 = 5.0 \left(\frac{Q}{\pi D^2} \right) \quad 3.55$$

Therefore, Equation 3.54 can be rewritten as

$$1 = 2.228 \left(\frac{Q_c}{D^3} \right)^{0.5} (S_c)^{.286} \exp(-S_c) \quad 3.56$$

where Q_c is the volumetric flow rate evaluated at the onset of region II. Equation 3.56 cannot be used to calculate S_c at the onset of region III (reservoir L) since Equation 3.40 is valid only for flow rates within region I. Given the critical flow rate, Q_c , at the onset of region II (Figure 3.6, page 94) and diameter, D , Equation 3.56 yields S_c . Following this procedure values of S_c were determined at the onset of region II with the results tabulated in Table 3.7 (next page). The values of S_c are not grossly different, $2.8 \leq S_c \leq 4.2$, and it appears that the difference is largely the result of the insensitivity of S_c to flow rate. On the other hand, if one back calculates a critical flow rate, a small change in S_c results in a large change in

critical flow rate. If we accept that S_c is dependent on reservoir size, the question arises whether S_c is a useful ordering parameter for a given system.

TABLE 3.7
CRITICAL VALUES OF S (S_c)

	<u>I.D. (cm)</u>		
	<u>0.10</u>	<u>0.20</u>	<u>0.30</u>
Reservoir L	4.2	3.8	3.8
Reservoir S	3.6	3.0	2.8

From Table 3.7 it is observed that S_c depends moderately on capillary tube diameter. Suppose the criterion for the onset of flow instabilities was $S_c = 3.0$, then by Equation 3.51

$$S_c = 3.0 = (Z_0^{**})^{1.4} \quad 3.57$$

or

$$Z_0^{**} = 2.19 \quad 3.58$$

Substitution of Equation 3.57 into 3.56 yields

$$1.0 = 2.228 \left(\frac{Q_c}{D^3} \right)^{0.5} (3.0)^{.286} \exp(-3.0) \quad 3.59$$

which after simplification reduces to

$$Q_c = 43.41 D^3 \quad 3.60$$

In general, Equation 3.60 is written as

$$Q_c = 120.54 \left(\frac{n'+1}{3n'+1} \right)^2 \left(\frac{D^3}{\theta_0} \right) \quad 3.61$$

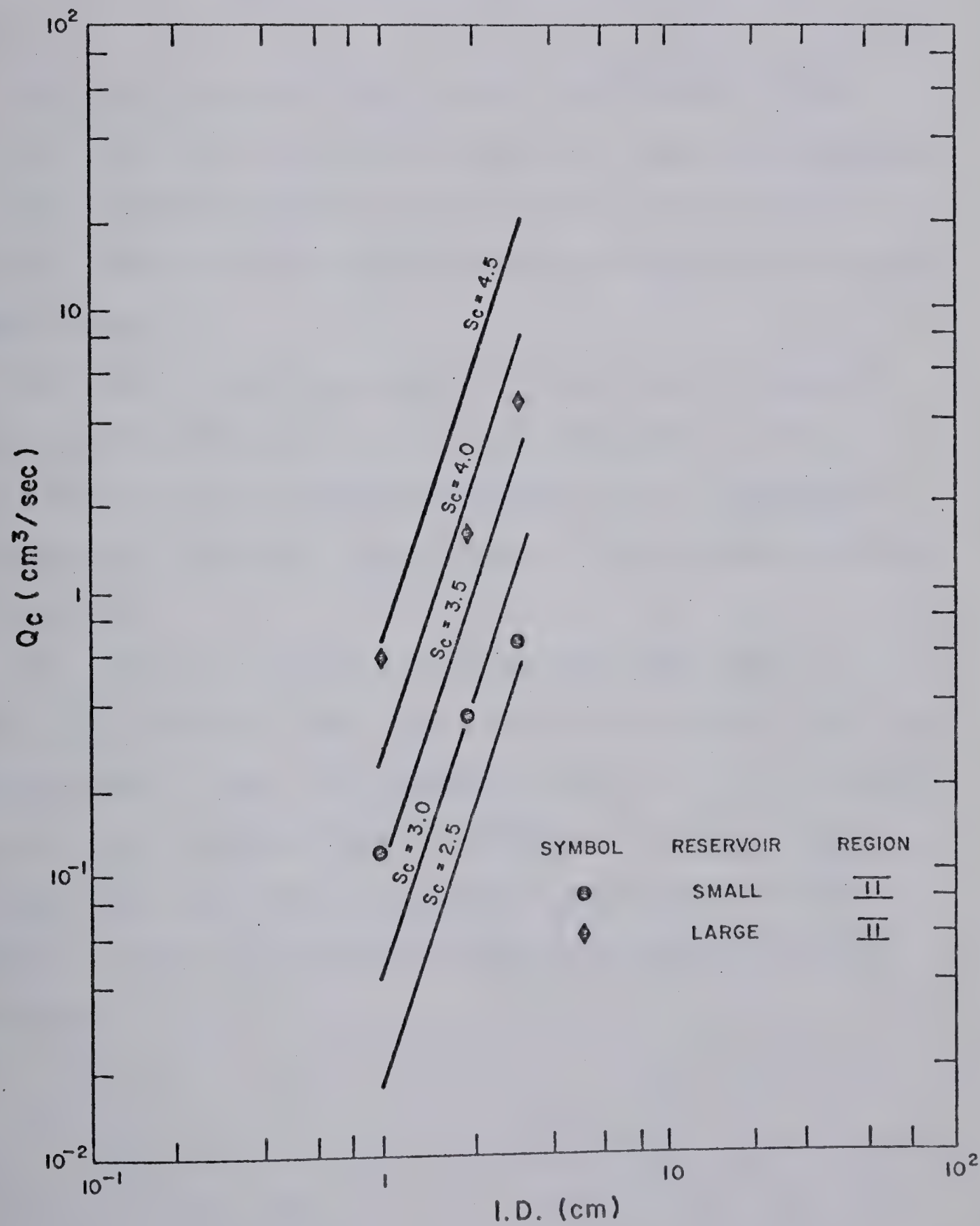
The relationships between the critical flow rate and capillary tube diameter were obtained for other values of S_c , namely 2.5, 3.5, 4.0, and 4.5 and are plotted in Figure 3.56. Before evaluating the results, the critical flow rate-diameter dependence predicted from the recoverable shear strain criterion is examined. The recoverable shear strain evaluated at the onset of region II was found to vary with reservoir size and capillary tube diameter (Table 3.3, page 106). By Equation 1.42 (page 38) and for an assumed constant value of S_R we have

$$Q_c = \frac{S_R \pi}{32} \left(\frac{D^3}{\theta} \right) \quad 3.62$$

The data plotted in Figure 3.56 and Equation 3.61 and 3.62 show the following points:

- (a) The predicted flow rates at the onset of flow instabilities (region II) are sensitive to the assumed value of S_c or S_R .
- (b) At constant fluid properties the predicted diameter dependence from both the S_R and S_c criteria ($Q_c \propto D^3$)

FIGURE 3.56
SENSITIVITY OF FLOW RATE AT ONSET
OF INSTABILITY, S_c CRITERION



is only qualitatively correct.

(c) The flow rates defining the onset of flow instabilities at region II are inversely proportional to a characteristic relaxation time of the fluid.

(d) Both the S_c and S_R criteria depend upon reservoir size.

Based on the above four points, we conclude that:

(a) The first sign of instability, which is manifested by an observed swirling motion in the inlet region, may occur whenever the polymer molecules exceed the linear Hookean range.

(b) The S_c and S_R criteria do not directly account for the effect of reservoir size on the onset of flow instabilities but they agree qualitatively in predicting the effect of capillary tube diameter on the onset of flow instabilities.

(c) The S_c criterion predicts that the onset of instability depends upon the inelastic nature of the fluid characterized by the flow behavior index, n' . The critical flow rate decreases as the flow behavior index, n' , increases. The flow rate at the onset of region II for fixed D , θ_0 and S_c decreases as the flow behavior index increases.

CHAPTER IV

CONCLUSIONS AND RECOMMENDATIONS

4.1 CONCLUSIONS

1. For capillary tube Reynolds numbers less than 2100, the Newtonian contraction losses for values of β approaching zero are represented by

$$\Phi = K + \frac{K'}{N_{Re}} \quad 4.1$$

$$\text{where,} \quad K = 2.26 \pm 0.26 \quad 4.2$$

$$\text{and} \quad K' = 159 \pm 30 \quad 4.3$$

2. Qualitative observations of the upstream velocity field, the pressure traces, and the jet of fluid in the three regions are as follows: Within region I, the velocity field is stable, the pressure traces, (measured at a pressure tap located upstream of the contraction) are smooth, and the jet of fluid issuing from the capillary tube is also smooth. The stable flow field is characterized by a WGS central accelerating core surrounded by large eddies. Within region II the central core of fluid oscillates to and fro; the intensity and frequency of these oscillations increase with flow rate. There are no measurable changes in the pressure traces and in the jet of fluid. At the onset of region III (melt fracture) the flow field is described as "chaotic". Measured pressure fluctuations

coincide reasonably with the visually observed onset of region III. The jet of fluid oscillates with a frequency approximately equal to the frequency of the pressure fluctuations. Since the onset and magnitude of measurable pressure fluctuations are independent of the capillary tube length, the onset of region III (melt fracture) is also independent of the capillary tube L/D ratio. When the velocity field oscillates between stable and "chaotic" flows, the pressure fluctuations are significantly higher than the remaining data and the jet of fluid oscillates between two different trajectories. In one trajectory, corresponding to the stable flow field, the jet of fluid is smooth; in the other, corresponding to the "chaotic" flow field, the jet is distorted. Pressure fluctuations measured only over the interval of time that the flow field was observed to be "chaotic" are consistent with the remaining data.

3. The shear stresses evaluated in the capillary tube under SLSF and at the onset of regions II and III, although four orders of magnitude less than 10^6 dyn/cm² for polymer melts, are in reasonable agreement with shear stresses calculated from the analysis presented by Southern and Paul (157). The recoverable shear strain, S_R , evaluated at the onset of regions II and III, are within the range reported for polymer melts ($2.2 \leq S_R \leq 67$). However, these criteria are not consistent with experimental observations wherein initiation occurs within the inlet region. A criterion based on inlet conditions, the Hencky's strain measure,

S_c , predicts that instability may occur whenever the volumetric flow rate exceeds a critical value given by

$$Q_c = 120.54 \left(\frac{n'+1}{3n'+1} \right)^2 \left(\frac{D}{\theta_0} \right)^3 \quad 4.4$$

The S_c criterion agrees qualitatively in predicting the effect of capillary tube diameter and degree of elasticity on the onset of instabilities.

4. The onset of flow instabilities does not affect the flow curve. Effects are noted in the total pressure loss - flow rate plots, Bagley plots, and the contraction losses.

4.1 The onset and magnitude of an abrupt increase in the total pressure losses at the onset of region III are independent of the capillary tube L/D ratio. The discontinuity, resulting from the commencement of a "chaotic" flow field within the reservoir, is obtainable only for short capillary tube lengths. As capillary tube length increases, the abrupt increase in pressure cannot be detected and under these conditions the ΔP_t -Q plots are not useful in determining the onset of region III.

4.2 Only when the velocity field oscillates between stable and "chaotic" flows do two Bagley plots exist: one for the stable and one for the "chaotic" velocity field with the only change being with the contraction losses (intercept). The contraction losses are greater whenever a "chaotic" velocity field exists. It is necessary to know

the state of the velocity field with each capillary tube L/D ratio; otherwise, erroneous results in the contraction losses and shear stresses are likely to occur.

4.3 The effects of capillary tube diameter and reservoir size on contraction losses can be rationalized in terms of the state of the flow field within the reservoir, i.e., stable, swirling or "chaotic". Furthermore, we conclude that it is not correct to correlate contraction losses with Reynolds number over a wide range of Reynolds numbers when, over the same range of Reynolds numbers, the flow field changes from stable to "chaotic".

5. Within region I the cone semi-angles, eddy center locations and axial velocity profiles are summarized as follows:

5.1 The initial cone semi-angles are represented by

$$\phi_0 = 19 \left(\frac{D^3}{\theta_0 Q} \right)^{0.6} \text{ for } 6 \times 10^{-3} \leq \left(\frac{D^3}{\theta_0 Q} \right) \leq 10 \quad 4.5$$

and are independent of reservoir size for values of $(D^3/\theta_0 Q)$ that overlap. At values of $(D^3/\theta_0 Q) > 10$ the initial cone semi-angles approach 90° and $(D^3/\theta_0 Q)$ less than 6×10^{-3} corresponds with the onset of region II. The cone semi-angles, measured at axial locations upstream of the contraction, within the accuracy of measurement and over the range of z/D where they were measured, are independent of reservoir size.

5.2 The location of the eddy centers move farther

away from the contraction along a well defined path as flow rates increase. At a given flow rate the center of the eddies are located farther upstream of the contraction in larger size reservoirs.

5.3 The dimensionless axial velocity profiles for values of $\eta \leq 2.0$ can be expressed as

$$f(\eta) = \frac{V_z}{V_z|_d} = (1.0 + 0.41 \eta^2)^{-2.0} \quad 4.6$$

where $\eta = r/r_0$. The maximum error is 17%. For values of η greater than 2.0 errors as large as 40% are not uncommon but these large radial locations are well outside of the WGS central core of fluid. The variable r_0 is the radial position where the axial velocity is equal to one half of the centerline velocity given by

$$V^* = \frac{V_z|_d}{V_0} = \exp(-(Z^{**})^{1.4}) \quad 4.7$$

where

$$Z^{**} = z/D \sqrt{\frac{\theta_0 Q}{D^3}} \quad 4.8$$

and V_0 is the axial velocity along the centerline at the contraction given by

$$V_0 = 0.75 \frac{3n'+1}{n'+1} \left(\frac{Q}{A}\right) \quad 4.9$$

The derivatives of axial velocity with respect to axial location are in good agreement with experimental data.

The axial velocity profiles within the WGS core, defined by combining Equations 4.6, 4.7 and 4.9 are independent of reservoir size. Parameter r_0 , however, depends on reservoir size. At a fixed flow rate, and at values of $Z^{**} > 0.40$, r_0 increases as reservoir size increases. Therefore, plots of V_z versus r are not independent of reservoir size.

5.4 Mathematical simplifications (discussed in Appendix E. Section E.3), can be employed when predicting the magnitude and growth of normal stresses within the WGS core. These simplifications are:

(a) At flow rates approaching the upper limit of region I

$$V_r < V_z$$

and

$$V_{r,z} + V_{z,r} \approx V_{z,r}$$

where $<$ implies an order of magnitude.

(b) At the lower limit of region I

$$V_r \approx V_z$$

and

$$V_{z,r} + V_{r,z} \approx V_{z,r}$$

Only within the immediate vicinity of the centerline ($r < 0.2D$) can we assume $V_r < V_z$.

4.2 RECOMMENDATIONS

This author recommends the following:

1. Contraction losses and visual observations of the flow field be measured over a range of Reynolds numbers which overlap regions I, II, and III.
2. The Hencky strain measure be used as criterion for predicting parameters at the onset of flow instabilities.
3. Velocity profiles for flow rates within region I be measured for other polymer solutions that exhibit a characteristic WGS flow field and be compared with the predictions given by Equation 4.6, 4.7, 4.8, and 4.9.
4. The empirical relationship for axial velocity and the approximations for radial velocity be used to determine the magnitude and rate of growth of normal stresses within the entry region. Furthermore, the empirical relationship for axial velocity should be used with other initiation mechanisms.
5. The axial velocity component, V_z , be measured for axial locations less than Z^{**} equal to 0.10 to supplement the limited data that the derivative of velocity with respect to axial position decreases to zero at the contraction.

6. That additional experimental data supplement the limited data in this research which lead to the assumption that parameter b_1 is independent of N'_{Re} and n' .

7. That an empirical relationship between r_0 and independent parameters be found.

8. That a hydraulic cylinder (rigid plunger system) be used in place of inert gases in future experimental research.

9. That the direct method be used in future research when measuring velocity components.

REFERENCES

REFERENCES

1. Acierno, D., Titomanlio, G., and Nicodemo, L., paper presented at the 6th Congress International de Rheologie, Lyon, France, September (1972)
2. Arai, T., Rheol. Acta., 13, 359 (1974)
3. Arai, T., and Aoyama, H., Trans. Soc. Rheol., 7, 333 (1963)
4. Astarita, G., and Greco, G., Jr., Ind. Eng. Chem. Fundam., 7, 27 (1968)
5. Astarita, G., Greco, G., and Peluso, L., Ind. Eng. Chem. Fundam., 7, 595 (1968)
6. Atkinson, B., Brocklebank, M.P., Card, C.C.H., and Smith, J.M., A.I.Ch.E.J., 15, 548 (1969)
7. Atkinson, B., Kemblowski, Z., and Smith, J.M., A.I.Ch.E.J., 13, 17 (1967)
8. Bagley, E.B., Trans. Soc. Rheol., 5, 355 (1961)
9. Bagley, E.B., J. Appl. Phys., 28, 624 (1957)
10. Bagley, E.B., and Birks, A.M., J. Appl. Phys., 31, 556 (1960)
11. Balakrishnan, C., and Gordon, R.J., A.I.Ch.E.J., 21, 1225 (1975)
12. Ballenger, T.F., and White, J.L., J. Appl. Polym. Sci., 15, 1949 (1971)
13. Ballenger, T.F., et al., Trans. Soc. Rheol., 15, 195 (1971)

14. Ballman, R.L., Rademacher, L.E., and Farnham, W.H., Appl. Polym. Symp., 20 63 (1973)
15. Barnett, S.M., Polym. Eng. Sci., 7, 168 (1967)
16. Bartos, O., J. Appl. Phys., 35, 2767 (1964)
17. Bartos, O., and Holomek, J., Polym. Eng. Sci., 11, 324 (1971)
18. Benbow, J.J., and Lamb, P., S.P.E. Trans., 3, 7 (1963)
19. Bialas, G.A., and White, J.L., Rubber Chem. Technol., 42, 683 (1969), 42, 675 (1969); 42, 683 (1969)
20. Bird, R.B., Stewart, W.E., and Lightfoot, E.N., Transport Phenomena, John Wiley and Sons Inc., New York, (1965)
21. Black, J.R., Denn, M.M., and Hsiao, G.C., see Section 1 of Theoretical Rheology, edited by Hutton, J.F., et al., Applied Science Publishers Ltd., London (1975)
22. Blum, D., Private Communication
23. Blyler, L.L., Jr., and Hart, A.C., Jr., Polym. Eng. Sci., 10, 193 (1970)
24. Boger, D.V., and Rama Murthy, A.V., paper presented at the Cancam Conference, Calgary, Alberta, May (1971)
25. Boger, D.V., and Rama Murthy, A.V., Rheol. Acta., 11, 61 (1972)
26. Bogue, D.C., Ind. Eng. Chem., 51, 874 (1959)
27. Bogue, D.C., and White, J.L., AGARD-AG-144-70, July (1970)

28. Boles, R.L., Ph.D. Dissertation, The University of Tennessee, December (1967)
29. Boles, R.L., and Bogue, D.C., paper presented at 27th Annual Technical Conference, Society Plastics Engineers, May (1968)
30. Boles, R.L., Davis, H.L., and Bogue, D.C., Polym. Eng. Sci., 10, 24 (1970)
31. Bond, W.N., Proc. Phys. Soc., 33, 225 (1921)
32. Bond, W.N., *ibid*, 34, 139 (1922)
33. Boussinesq, J., Compt. Rend., 110, 1160, 1238, (1890)
34. Brenschede, E., and Klein, J., Rheol. Acta., 9, 130 (1970)
35. Campbell, W.D., and Slattery, J.C., Trans. A.S.M.E., J. Basic Eng., 85, Series D, 41 (1963)
36. Carter, T.R., Ph.D. Dissertation, University of Utah (1969)
37. Casey, J.O., Ph.D. Dissertation, University of Tennessee (1969)
38. Catania, P.J., M.Sc. Thesis, The University of Alberta, May (1969)
39. Chen, F.C., J. Appl. Polym. Sci., 16, 2175 (1972)
40. Chong, J.S., Christiansen, E.B., and Baer, A.D., J. Appl. Polym. Sci., 15, 369 (1971)
41. Christiansen, E.B., and Lemmon, H.E., A.I.Ch.E.J., 11, 995 (1965)
42. Christiansen, E.B., and Kelsey, S.J., A.I.Ch.E.J., 18, 713 (1972)

43. Christiansen, E.B., Kelsey, S.J., and Carter, T.R.,
A.I.Ch.E.J., 18, 372 (1972)
44. Clegg, P.L., The Rheology of Elastomers, edited by
Mason P., and Wookey N., p. 174, Pergamon Press,
New York, N.Y. (1958)
45. Collins, M., and Schowalter, W.R., A.I.Ch.E.J.,
9, 804 (1963)
46. Cogswell, F.N., Polym. Eng. Sci., 12, 64 (1972)
47. Cogswell, F.N., Trans. Soc. Rheol., 16, 383 (1972)
48. Cogswell, F.N., and Lamb, P., Plast. Inst. Trans. J.,
35, 809 (1967)
49. Datta, A.B., and Strauss, K., Rheol. Acta., 15,
283 (1976)
50. Day, D.R., M.Sc. Thesis, University of Toronto (1971)
51. Denn, M.M., and Marrucci, G., A.I.Ch.E.J., 14, 329
(1975)
52. Dennison, M.T., Plast. Inst. Trans. J., 35, 803
(1967)
53. den Otter, J.L., Rheol. Acta., 10, 200 (1971)
54. den Otter, J.L., Rheol. Acta., 14, 329 (1975)
55. Dodge, D.W., and Metzner, A.B., A.I.Ch.E.J., 5,
189 (1959)
56. Dorsey, N.E., Phys. Rev., 28, 833 (1926)
57. Duda, J.L., and Vrentas, J.S., Trans. Soc. Rheol.,
17, 89 (1973)
58. Duvdenavi, I.J., and Klein, I., S.P.E.J., 23,
41 (1967)

59. Emery, A.F., and Chen, C.S., Trans. A.S.M.E., 35, 134 (1968)
60. Everage, A.E., Jr., and Ballman, R.L., J. Appl. Polym. Sci., 18, 933 (1974)
61. Fehn, G.M., Rheol. Acta., 13, 767 (1974)
62. Ferrari, G.A., Wire and Wire Prod., 39, 1036 (1964)
63. Fields, T.R., Jr., and Bogue, D.C., Trans. Soc. Rheol., 12, 39 (1968)
64. Forsyth, T.H., Polym. Plast. Technol. Eng., 6, 101 (1976)
65. Franklin, R.E., and Wallace, J.M., J. Fluid, Mech., 42, 33 (1970)
66. Giesekus, H., Rheol. Acta., 7, 127 (1968)
67. Giesekus, H., Rheol. Acta., 8, 411 (1969)
68. Haddow, J.B., Personal Communication
69. Hagenbach, see Goldstein, S., Modern Developments in Fluid Dynamics, Vol. 1, p. 300, Dover Publications Inc. (1965)
70. Hagler, G.E., Ph.D. Dissertation, University of Tennessee (1972)
71. Halmos, A.L., and Boger, D.V., Trans. Soc. Rheol., 20, 253 (1976)
72. Han, C.D., A.I.Ch.E.J., 17, 1480 (1971)
73. Han, C.D., A.I.Ch.E.J., 18, 116 (1972)
74. Han, C.D., J. Appl. Polym. Sci., 17, 1403 (1973)
75. Han, C.D., A.I.Ch.E.J., 19, 649 (1973)

76. Han, C.D., Trans. Soc. Rheol., 17, 375 (1973)
77. Han, C.D., Rheol. Acta., 14, 173 (1975)
78. Han, C.D., and Charles, M., A.I.Ch.E.J., 16, 499 (1970)
79. Han, C.D., and Kim, K.U., Trans. Soc. Rheol., 17, 151 (1973)
80. Han, C.D., and Lamonte, R.R., Polym. Eng. Sci., 11, 385 (1971)
81. Han, C.D., and Lamonte, R.R., J. Appl. Polym. Sci., 16, 3307 (1972)
82. Higashitani, K., and Lodge, A.S., Trans. Soc. Rheol., 19, 307 (1975)
83. Hlavacek, B., Personal Communication
84. Holmes, D.B., Ph.D. Dissertation, Delft (1967)
85. Howells, E.R., and Benbow, J.J., Plast. Inst. Trans. J., 30, 240 (1962)
86. Hosking, R., Philos. Mag., 18, 260 (1909)
87. Hudson, N.E., and Ferguson, J., Trans. Soc. Rheol., 20, 265 (1976)
88. Hürlimann, H.P., and Knappe, W., Rheol. Acta., 11, 292 (1972)
89. Huseby, T.W., Trans. Soc. Rheol., 10, 181 (1966)
90. Kanel, F.A., Ph.D. Dissertation, University of Delaware (1972)
91. Kawata, M., Kurase, K., and Yoshida, K., Rheol. Acta., 13, 757 (1974).

92. Kaye, S.E., Ph.D. Dissertation, Carnegie-Mellon University (1973)
93. Kaye, S.E., and Rosen, S.L., A.I.Ch.E.J., 17, 1269 (1971)
94. Kizior, T.E., M.Sc. Thesis, University of Alberta (1973)
95. Klein, J., and Fusser, H., Rheol. Acta., 7, 118 (1968)
96. Knibbs, G.H., Proc. R. Soc. N.S. Wales, 29, 77 (1895)
97. Kreith, F., and Eisenstadt, R., Trans. A.S.M.E., 79, 1070 (1957)
98. Kroesser, F.W., Ph.D. Dissertation, University of Rochester (1968)
99. Kraus, G., and Gruver, J.T., J. Polym. Sci., 2A, 797 (1964)
100. Langhaar, J., Appl. Mech., 9, No. 2A55-9 (1942)
101. La Nieve, H.L., III, M.Sc. Thesis, The University of Tennessee (1963)
102. La Nieve, H.L., III, and Bogue, D.C., J. Appl. Polym. Sci., 12, 353 (1968)
103. Lidorikis, S., and Vlachopoulos, J., paper presented at the 63rd A.I.Ch.E. meeting, Chicago (1970)
104. Lundgren, T.S., Sparrow, E.M., and Starr, J.B., J. Basic Eng., 86, 620 (1964)
105. Lupton, J.M., and Regester, J.W., Polym. Eng. Sci., 5, 235 (1965)

106. Lynch, M.D., and Huntsberger, D.V., Elements of Statistical Inference for Education and Psychology, Allyn and Bacon Inc., Boston (1976)
107. Maxwell, B., and Galt, J.C., J. Polym. Sci., 62, 550 (1962)
108. McHugh, T.W., Harrell, E.R., Powell, J.W., and Chartoff, R.P., Trans. Soc. Rheol., 16, 331 (1972)
109. McIntire, L.V., J. Appl. Poly. Sci., 16, 2901 (1972)
110. Meissner, J., Trans. Soc. Rheol., 16, 405 (1972)
111. Metzger, A.P., and Brodkey, R.S., J. Appl. Polym. Sci., 7, 399 (1963)
112. Metzger, A.P., and Knox, J.R., Trans. Soc. Rheol., 9, 13 (1965)
113. Metzner, A.B., and Reed, J.C., A.I.Ch.E.J., 1, 434 (1955)
114. Metzner, A.B., Carley, E.L., and Park, I.K., Mod. Plast., 38, 133 (1960)
115. Metzner, A.B., and Metzner, A.P., Rheol. Acta., 9, 174 (1970)
116. Metzner, A.B., Uebler, E.A., and Chan Man Fong, C.F., A.I.Ch.E.J., 15, 750 (1969)
117. Michiyoshi, L., Mizuno, K., and Hoshinai, Y., Int. Chem. Eng., 6, 373 (1966)
118. Middleman, S., The Flow of High Polymers; Continuum and Molecular Rheology, Interscience Pub., New York (1968)

119. Murch, R.E., Ph.D. Dissertation, University of Delaware (1970)
120. Myerholtz, R.W., J. Appl. Polym. Sci., 11, 687 (1967)
121. Nason, H.K., J. Appl. Phys., 16, 338 (1945)
122. Nicodemo, L., and Marrucci, G., J. Polym. Sci., 10, 1351 (1972)
123. Nakamura, R., et al., J. Chem. Eng. Japan, 9, 291 (1976)
124. Nikuradse, J., See Goldstein, S., Modern Developments in Fluid Dynamics, Vol. 1, p. 304, Dover Publications Inc. (1965)
125. Nishimura, J., and Oka, S., J. Phys. Soc. Japan, 20, 449 (1965)
126. Novotny, E.J., Jr., and Eckert, R.E., Trans. Soc. Rheol., 17, 227 (1973)
127. Oka, S., J. Phys. Soc. Japan, 19, 1481 (1964)
128. Okeson, J.K., and Emery, A.H., Jr., Trans. Soc. Rheol., 19, 81 (1975)
129. O'Casey, J.O., Jr., Ph.D. Dissertation, University of Tennessee (1969)
130. Oliver, D.R., and Bragg, R., Can. J. Chem. Eng., 51, 287 (1973)
131. Owczarek, J.A., Introduction to Fluid Mechanics, International Textbook Company, Scranton, Pa. (1968)
132. Oyanagi, Y., Appl. Polym. Symp., 20, 123 (1973)
133. Paul, D.R., and Southern, J.H., J. Appl. Polym. Sci., 19, 3375 (1975)
134. Pearson, J.R.A., Plast. Polym., 37, 285 (1969)

135. Pearson, J.R.A., and Petrie, C.J.S., Proc. Fourth Intern. Cong. Rheol., 3, 265 (1965)
136. Petrie, C.J.S., and Denn, M.M., A.I.Ch.E.J., 22, 209 (1976)
137. Philippoff, W., and Gaskins, F.H., Trans. Soc. Rheol., 2, 263 (1958)
138. Porteous, K.C., and Denn, M.M., Trans. Soc. Rheol., 16, 295 (1972)
139. Powell, R.J., Ph.D. Dissertation, University of Rochester (1968)
140. Prados, J.W., and Peebles, F.N., A.I.Ch.E.J., 5, 225 (1959)
141. Ram, A., and Narkis, M., J. Appl. Polym. Sci., 10, 361 (1966)
142. Rama Murthy, A.V., Trans. Soc. Rheol., 18, 431 (1974)
143. Rama Murthy, A.V., Trans. Soc. Rheol., 20, 503 (1976)
144. Rama Murthy, A.V., and Boger, D.V., Trans. Soc. Rheol., 15, 709 (1971)
145. Rivas, M.A., Jr., and Shapiro, A.H., Trans. A.S.M.E., 78, 489 (1956)
146. Roscoe, R., Philos. Mag., 40, 338 (1949)
147. Rothenberger, R., McCoy, D.H., and Denn, M.M., Trans. Soc. Rheol., 17, 259 (1973)
148. Schiller, L., see Goldstein, S., Modern Developments Fluid Dynamics, Vol. 1, p. 303, Dover Publications Inc. (1965)

149. Schmidt, F.W., and Wimmer, K., A.I.Ch.E.J., 17, 1248 (1971)
150. Schmidt, F.W., and Zeldin, B., A.I.Ch.E.J., 15, 612 (1969)
151. Schott, H., J. Polym. Sci., A2, 3791 (1964)
152. Schreiber, H.P., Bagley, E.B., and Birks, A.M., J. Appl. Polym. Sci., 4, 362 (1960)
153. Schulken, R.M., and Boy, R.E., S.P.E.J., 16, 423 (1960)
154. Seyer, F.A., and Catania, P.J., Paper presented at the 21st Canadian Chemical Engineering Conference, Montreal, October (1971)
155. Shaw, R., J. Fluid Mech., 7, 550 (1960)
156. Siegel, R., Sc. D. Thesis, M.I.T. (1953)
157. Southern, J.H., and Paul, D.R., Polym. Eng. Sci., 14, 560 (1974)
158. Spencer, R.S., and Dillon, R.E., J. Colloid Sci., 4, 241 (1949)
159. Sutterby, J.L., Trans. Soc. Rheol., 9, 227 (1965)
160. Swindles, J.F., Coe, J.R., and Godfrey, T.B., J. Res. Nat. Bur. Stand., 48, 1 (1952)
161. Sylvester, N.D., Ph.D. Dissertation, Carnegie-Mellon University, September (1968)
162. Sylvester, N.D., and Rosen, S.L., A.I.Ch.E.J., 16, 964 (1970)
163. Tanner, R.I., and Pipkin, A.C., Trans. Soc. Rheol., 13, 471 (1969)

164. Tomita, Y., Trans. Japan Soc. Mech. Eng., 25, 938 (1959)
165. Tomita, Y., Bull. Japan Soc. Mech. Eng., 4, 77 (1961)
166. Tomita, Y., Bull. Japan Soc. Mech. Eng., 5, 443 (1962)
167. Tomita, Y., J. Chem. Eng. Japan, 23, 525 (1969)
168. Tomita, Y., and Shimbo, T., Appl. Polym. Symp., 20, 137 (1973)
169. Tomita, Y., and Tsuchiya, K., Bull. Japan Soc. Mech. Eng., 6, 709 (1963)
170. Tordella, J.P., J. Appl. Phys., 27, 754 (1956)
171. Tordella, J.P., Rheol. Acta., 1, 216 (1958)
172. Tordella, J.P., J. Appl. Poly. Sci., 7, 215 (1963)
173. Uebler, E.A., Ph.D. Dissertation, University of Delaware (1966)
174. Ultman, J., and Denn, M.M., Paper presented at 40th Meeting, Society of Rheology, St. Paul, Minnesota, October (1969)
175. Vinogradov, G.V., Rheol. Acta., 12, 357 (1973)
176. Vinogradov, G.V., et al., Eur. Polym. J., 9, 1231 (1973)
177. Vlachopoulos, J., and Lidorikis, S., Polym. Eng. Sci., 11, 1 (1971)
178. Vlachopoulos, J., Horie, M., and Lidorikis, S., Trans. Soc. Rheol., 16, 669 (1972)
179. Vlachopoulos, J., and Alam, M., Polym. Eng. Sci., 12, 184 (1972)

180. Vrentas, J.S., and Duda, J.L., Appl. Sci. Res., 28, 241 (1973)
181. Wang, Y.L., and Longwell, P.A., A.I.Ch.E.J., 10, 323 (1964)
182. Westover, R.F., Polym. Eng. Sci., 6, 83 (1966)
183. Westover, R.F., and Maxwell, B., S.P.E.J., 13, 27 (1957)
184. Weinberger, C.B., Ph.D. Dissertation, University of Michigan (1970)
185. Weissberg, H.L., Phys. Fluids, 5, 1033 (1962)
186. Weltmann, R., and Keller, T., Natl. Advis. Comm. Aeronaut., TN 3889 (1957)
187. White, J.A., Appl. Polym. Symp., 20, 155 (1973)
188. White, J.A., and Kondo, A., Polym. Sci. Eng., Report No. 70 (1976)
189. White, J.L., and Metzner, A.B., A.I.Ch.E.J., 11, 324 (1965)
190. Williams, M.C., Ph.D. Dissertation, University of Wisconsin (1964)

APPENDIX A
CALIBRATION

A.1 PRESSURE TRANSDUCERS

Three Pace pressure transducers with diaphragms of 1 p.s.i.g. (transducer 1), 10 p.s.i.g. (transducer 2), and 100 p.s.i.g. (transducer 3) were used in order to obtain more reliable data (pressures varied from 3×10^4 dyn/cm² to 6×10^6 dyn/cm²). Each transducer was connected to a separate Sanborn preamplifier with the output voltage being recorded on a 10 inch Mosely strip chart recorder, Model 7100B. The range selector on the recorder was set at 5 volts full scale, i.e., 2 inch displacement per volt. The recorder's mechanical zero was set at 1 inch displacement. The gain on the preamplifier was adjusted so that a 2 volt signal would displace 4 inches on the recorder chart. With zero load on the transducers each electrical circuit was balanced. This procedure minimized the output voltage when the preamplifier attenuation setting decreased from X200 to X1. At X5 the output voltage for both transducers 1 and 2 was such that the displacement was greater than 9 inches, hence off scale. This resulted in the output voltage varying with preamplifier attenuation settings.

A water manometer was used to calibrate transducer 1, a mercury manometer for transducer 2, and a Ruska Dead Weight Tester, Model 2400 HL for transducer 3. A period of 10 minutes was allowed to elapse between consecutive readings to ensure that the upper and lower meniscuses in both manometers were stationary even after an incremental change in pressure. The calibration data are given in Tables A.1 to A.4.

Transducer 3 (calibration data in Table A.3) was used to obtain pressure data only for the sugar solution #1 and the Primol-355 oil. Due to damage to this transducer another was calibrated (data for transducer 4 given in Table A.4) to obtain pressure data for the remaining Newtonian solutions and the polymer solution.

To assess the presence of a hysteresis loop, the applied pressure was allowed to vary in small incremental steps from a maximum value determined by the transducer being calibrated to a minimum value (10% of the maximum) and then back to the maximum value again. The results showed, however, that the transducers exhibited little or no hysteresis.

A.2 THRUST CALIBRATION

The thrust apparatus used in this research was described by Kizior (94). The output voltage corresponding to a given thrust, measured in grams, was recorded on a Hewlett Packard recorder (Model number 770213). The Sanborn pre-amplifier (Model number 8805A) had the gain set to a minimum and the calibration factor set at 200. The data tabulated in Table A.5 resulted in a sensitivity of 293.020 dyn/cm^2 per volt.

A.3 CYLINDER AND INSTRON CALIBRATION

Two stainless steel cylinders, approximately 15.24 cm I.D. (cylinder 1) and 15.60 cm I.D. (cylinder 2) were used in this research. Cylinder 1 was used for all of the Newtonian runs while cylinder 2 was used for the remaining

runs. At a synchronous setting of 1 cm/min, cylinders 1 and 2 resulted in measured flow rates of 3.030 and 3.177 cm³/sec respectively. At crosshead speeds greater or less than 1 cm/sec the resultant flow rate was a multiple of the flow rate determined at the crosshead speed of 1 cm/sec. Measured flow rates agreed to within one half of one percent of these values.

The variable speed settings were calibrated by collecting and weighing an amount of water over a period of 15 minutes with the synchronous setting at 1 cm/min. The calibrated variable speed settings tabulated in Table A.6 were used in the calculation of flow rate with cylinder 1. After replacing the faulty tachometer no detectable errors were measured between the crosshead speed of the Instron tester and the variable speed settings.

A.4 NORMAL FORCE SPRING

The calibration of the normal force spring used in the rheogoniometer to determine the first normal stress difference is given in Figure A.1. The resultant sensitivity is 194.040 dyn/cm² per volt at a temperature of 68 ± 1°F.

A.5 ALUMINUM DUST PARTICLES

The thin, irregularly shaped dust particles used as the tracer was a commercial grade Baker aluminum, lot number 2347. The particle size distribution, plotted and shown in Figure A.2, was determined from a sample size of 200 particles using a microscope and a graduated screen.

Thirty-nine divisions of the graduated screen was equivalent to 30 microns at a magnification of 1000. An approximated relationship that seems to hold for a positively skewed distribution (106) is

$$\bar{Y} = \frac{3m-M}{2} \quad A.1$$

where m is the median, M is the mode, and \bar{Y} is the mean.

Using this equation and the data in Figure A.2

$$\bar{Y} = \frac{3(11)-7.5}{2} \quad A.2$$

gives the mean length of 13 microns. The maximum width of the particles was equal to 0.70 times the maximum length with the thickness estimated to be 1 micron. Therefore, the average volume of the aluminum dust particles was $118 \times 10^{-12} \text{ cm}^3$.

In summary, Appendix A contains the following tables and figures:

<u>TABLE NO.</u>	<u>DESCRIPTION</u>
A.1	Calibration of Transducer 1
A.2	Calibration of Transducer 2
A.3	Calibration of Transducer 3
A.4	Calibration of Transducer 4
A.5	Thrust Calibration
A.6	Calibration For Variable Speed Setting

<u>FIGURE NO.</u>	
A-1	Normal Force Spring Calibration
A-2	Size Distribution of Aluminum Dust Particles

TABLE A.1
CALIBRATION OF TRANSDUCER 1

$$\rho = 0.9896 \text{ gm/cm}^3$$

<u>Pressure (in. water)</u>	<u>Preamp. attenuation</u>	<u>Preamp. Reading Volts @ X 1</u>
29.57	200	94.00
	100	94.50
	50	92.75
28.72	200	88.50
	100	88.75
	50	87.125
26.64	200	80.00
	100	81.50
	50	80.50
24.64	200	74.50
	100	75.75
	50	74.75
22.48	200	68.00
	100	69.00
	50	68.00
20.64	200	61.00
	100	63.00
	50	61.375
18.48	200	55.00
	100	56.25
	50	55.625
16.28	200	48.00
	100	49.50
	50	49.125
14.44	200	42.00
	100	44.00
	50	43.50
12.74	100	38.50
	50	38.00
10.95	100	32.50
	50	32.75

TABLE A.1 (continued)

$$\rho = 0.9896 \text{ gm/cm}^3$$

<u>Pressure (in. water)</u>	<u>Preamp. attenuation</u>	<u>Preamp. Reading Volts @ x 1</u>
8.66	100	25.50
	50	26.00
6.67	100	19.50
	50	19.75
4.66	50	13.75
	20	12.75
2.89	20	7.90
3.66	20	10.00
4.91	20	13.50
5.55	20	15.20
6.69	50	20.25
	20	18.25
7.88	50	23.625
	20	21.30
9.64	100	29.25
	50	29.00
12.55	100	38.50
	50	37.625
14.84	200	44.00
	100	45.00
	50	44.75
17.20	200	51.50
	100	53.00
	50	52.00
18.55	200	56.00
	100	56.25
	50	56.00

TABLE A.1 (continued)

$$\rho = 0.9896 \text{ gm/cm}^3$$

<u>Pressure (in. water)</u>	<u>Preamp. attenuation</u>	<u>Preamp. Reading Volts @ x 1</u>
22.63	200	69.00
	100	69.75
	50	68.00
26.51	200	80.00
	100	81.00
	50	80.125
30.66	200	93.00
	100	95.00
	50	93.00
20.76	200	61.50
	100	62.50
	50	63.25

TABLE A.2
CALIBRATION OF TRANSDUCER 2

$$\rho = 13.5201 \text{ gm/cm}^3$$

<u>Pressure (in. mercury)</u>	<u>Preamp. Attenuation</u>	<u>Preamp. Reading Volts @ X1</u>
1.86	100	23.25
	50	22.375
2.95	100	37.50
	50	36.875
4.04	100	50.75
	50	50.00
5.06	100	62.50
	50	61.25
6.21	100	77.50
	50	75.50
7.36	100	92.00
	50	90.00
8.89	100	110.50
	50	108.00
10.31	100	129.00
	50	125.75
11.92	100	149.50
14.13	100	177.00
16.36	100	205.50
18.12	100	229.00
19.80	100	250.50
20.30	100	257.25
18.14	100	230.00
16.71	100	211.00
15.55	100	196.00

TABLE A.2 (continued)

$$\rho = 13.5201 \text{ gm/cm}^3$$

<u>Pressure (in. mercury)</u>	<u>Preamp. Attenuation</u>	<u>Preamp. Reading Volts @ X1</u>
13.66	100	172.25
12.18	100	153.75
10.96	100	137.50
	50	134.75
9.89	100	124.50
	50	121.75
8.18	100	103.75
	50	101.50
6.43	100	80.75
	50	79.50
4.99	100	62.75
	50	61.625
4.24	100	53.50
	50	52.00
3.46	100	42.50
	50	41.75
3.00	100	37.50
	50	35.125
2.26	100	28.00
	50	27.50

TABLE A.3
CALIBRATION OF TRANSDUCER 3

Preamplifier Gain Setting: at X200 and 100 p.s.i.g. displaced 8.49 inches

<u>Pressure (p.s.i.g.)</u>	<u>Preamp. Attenuation</u>	<u>Preamp. Reading Volts @ X1</u>
6.0	200	55.00
	100	55.00
	50	55.00
8.0	200	68.50
	100	68.00
	50	67.75
10.0	200	84.50
	100	85.00
	50	84.75
12.0	200	101.00
	100	101.00
	50	101.25
15.0	200	128.00
	100	127.25
	50	126.50
18.0	200	152.00
	100	153.00
	50	151.50
20.0	200	170.00
	100	169.75
	50	168.00
25.0	200	211.00
	100	211.50
	50	209.75
30.0	200	254.50
	100	254.00
35.0	200	297.50
	100	296.00
40.0	200	340.00
	100	338.00

TABLE A.3 (continued)

Preamplifier Gain Setting: at X200 and 100 p.s.i.g. displaced 8.49 inches

<u>Pressure (p.s.i.g.)</u>	<u>Preamp. Attenuation</u>	<u>Preamp. Reading Volts @ X1</u>
45.0	200	381.50
	100	380.00
50.0	200	423.00
	100	421.25
60.0	200	509.50
70.0	200	594.00
80.0	200	679.00
100.0	200	849.00
90.0	200	766.00
80.0	200	680.00
70.0	200	595.50
60.0	200	510.50
50.0	200	426.00
40.0	200	340.00
	100	339.75
30.0	200	256.00
	100	255.25
20.0	200	170.00
	100	170.50
	50	169.50
10.0	200	85.00
	100	85.50
	50	85.25

TABLE A.4
CALIBRATION OF TRANSDUCER 4

<u>Pressure (p.s.i.g.)</u>	<u>Preamp. Attenuation</u>	<u>Preamp. Reading Volts @ X1</u>
6.0	50	33.25
10.0	100	55.00
	50	53.75
12.0	100	65.00
	50	63.75
14.0	100	75.00
	50	73.75
16.0	100	86.00
	50	84.00
18.0	100	96.50
	50	94.75
20.0	100	107.00
	50	104.50
30.0	100	159.00
	50	156.00
40.0	200	214.00
	100	212.00
50.0	200	267.00
	100	265.00
60.0	200	322.00
70.0	200	375.00
80.0	200	432.00
90.0	200	488.00
100.00	200	545.00
90.00	200	488.00
80.00	200	433.00
70.00	200	377.00

TABLE A.4 (continued)

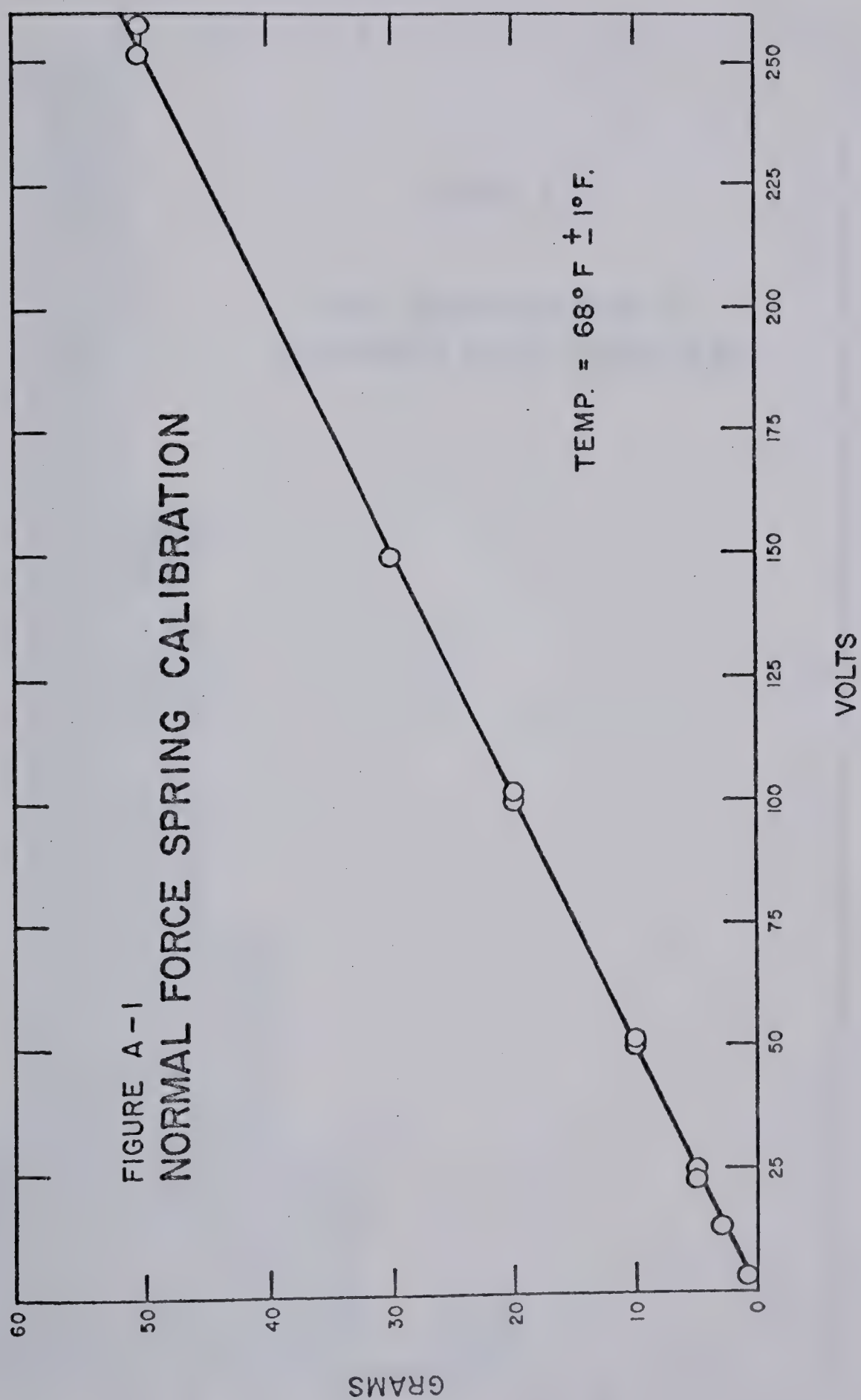
<u>Pressure (p.s.i.g.)</u>	<u>Preamp. Attenuation</u>	<u>Preamp. Reading Volts @ X1</u>
60.0	200	323.00
50.0	200	269.00
40.0	200	214.00
	100	213.50
30.0	200	160.00
	100	160.50
	50	157.50
20.0	200	107.00
	100	107.00
	50	106.00
10.0	100	55.00
	50	54.00
6.0	100	33.50
	50	33.25

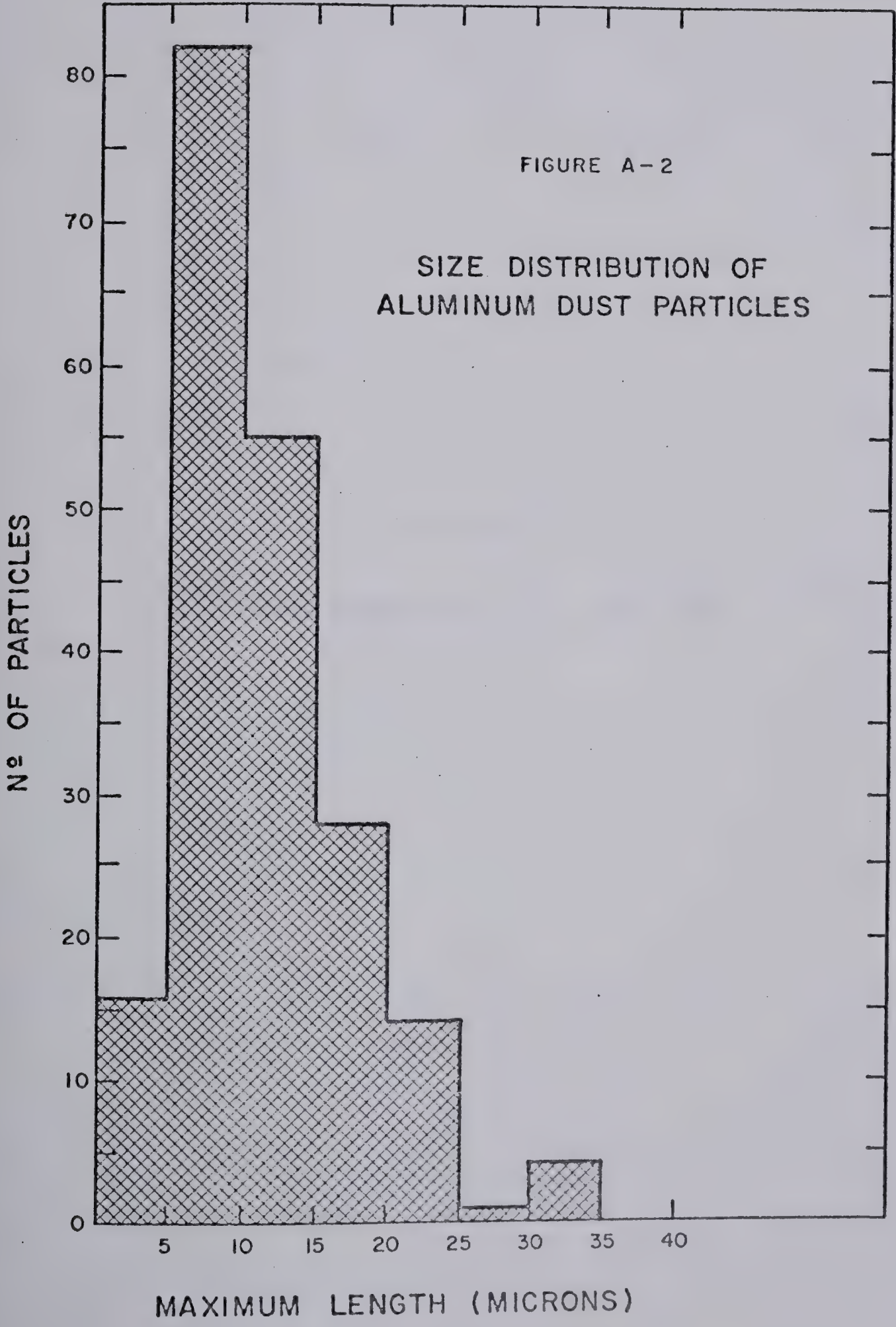
TABLE A.5
THRUST CALIBRATION

<u>Thrust (grams)</u>	<u>Volts</u>
2.14	7.40
4.19	14.10
6.23	21.00
8.27	28.10
10.29	34.80
12.33	41.20
14.37	48.00
2.15	7.50
2.15	7.20
10.33	35.50
12.38	42.50

TABLE A.6
CALIBRATION FOR VARIABLE SPEED SETTING

<u>Setting</u>	<u>Corrected Setting</u>
0.4	0.4020
0.5	0.5022
0.6	0.6086
0.7	0.7029
0.8	0.8068
0.9	0.9091





APPENDIX B

TOTAL PRESSURE LOSS - L/D DATA

This appendix contains the total pressure loss- L/D data for the Newtonian solutions and the 0.20% solution of Separan AP-30. The pressure was measured at pressure taps located 10.2 cm and 27.9 cm upstream of the entrance of the capillary tube in reservoirs S and L respectively. The data were used in the construction of the Bagley plots (discussed in Chapter I, Section 1.1.3 and in Appendix C, Sections C.1 and C.2). The pressure correction value given in each table accounts for the fact that the centers of the capillary tube and the transducer were not in the same plane. Since these correction factors do not affect the slope of the Bagley plots they have to be added only to the intercept in order to obtain the true value for the contraction losses.

The contraction losses and shear stresses obtained from the Bagley plots are given in Appendices C and D respectively. The shear stresses obtained from the Bagley plots and the rheogoniometer were compared at low apparent shear rates. At these shear rates the contraction losses were too small to be measured accurately and were negligible when compared to the total pressure losses measured at large L/D ratios. Therefore, for run numbers 15 to 22 (inclusive) in Table B.9, 14 to 17 (inclusive) in Table B.10, and 17 to 29 (inclusive) in Table B.11 the total pressure losses were measured only at ratios $L/D=305.08$ in Table B.9, $L/D=304.95$ in Table B.10, and $L/D=304.83$ in Table B.11.

Pressure fluctuations were measurable beyond certain flow rates. The pressure fluctuations measured in reservoir

S for several tube lengths of each of the three capillary tubes are reported and discussed in Chapter III, Section 3.2.2. The pressure fluctuations in reservoir L for the same capillary tubes are plotted in Figures B.1 to B.3.

The following lists the order in which the data appear in this appendix:

<u>TABLE NO.</u>	<u>SOLUTION</u>	<u>CAPILLARY I.D.</u> (cm)	<u>RESERVOIR</u>
B-1	SUGAR #1	0.20	SMALL
B-2	SUGAR #3	0.20	SMALL
B-3	SUGAR #4	0.20	SMALL
B-4	PRIMOL-355	0.20	SMALL
B-5	SUGAR #1	0.20	LARGE
B-6	SUGAR #3	0.20	LARGE
B-7	SUGAR #4	0.20	LARGE
B-8	PRIMOL-355	0.20	LARGE
B-9	0.20% SEPARAN AP-30	0.10	SMALL
B-10		0.20	SMALL
B-11		0.30	SMALL
B-12	0.20% SEPARAN AP-30	0.10	LARGE
B-13		0.20	LARGE
B-14		0.30	LARGE

TABLE B-1

TOTAL PRESSURE LOSS - L/D DATA: SUGAR SOLUTION #1,
0.20 cm I.D. CAPILLARY TUBE, SMALL RESERVOIR

Temp.: 72.5°F

Pressure Correction:
 $-.448 \times 10^4 \text{ dyn/cm}^2$

Run	Trans- ducer	Attenua- tion	Pressure ₂ x 10^4 (dyn/cm ²)	Flow (cc/sec)	L/D
1	1	50	3.089	1.515	31.60
2	1	50	4.688	2.285	31.60
3	2	20	6.378	3.030	31.60
4	2	50	14.203	6.080	31.60
5	2	100	24.924	9.193	31.60
6	2	100	37.748	12.187	31.60
7	2	100	52.227	15.090	31.60
8	3	50	70.671	18.386	31.60
1	2	100	6.074	1.515	71.23
2	2	20	8.791	2.285	71.23
3	2	20	11.790	3.030	71.23
4	2	50	25.338	6.080	71.23
5	2	100	42.265	9.193	71.23
6	2	100	61.535	12.187	71.23
7	3	50	81.357	15.090	71.23
8	3	50	108.592	18.386	71.23
1	2	20	7.722	1.515	96.38
2	2	50	11.549	2.285	96.38
3	2	50	15.272	3.030	96.38
4	2	100	32.474	6.080	96.38
5	2	100	53.060	9.193	96.38
6	3	50	76.531	12.187	96.38
7	3	50	100.663	15.090	96.38
8	3	50	130.310	18.386	96.38
1	2	50	16.375	1.515	222.36
2	2	100	24.476	2.285	222.36
3	2	100	32.577	3.030	222.36
4	3	50	67.568	6.080	222.36
5	3	50	108.247	9.193	222.36
6	3	50	148.581	12.187	222.36
7	3	100	189.604	15.090	222.36
8	3	100	237.867	18.386	222.36

TABLE B-2

TOTAL PRESSURE LOSS - L/D DATA: SUGAR SOLUTION #3,
0.20 cm I.D. CAPILLARY TUBE, SMALL RESERVOIR

Temp.: 72.10°F

Pressure Correction:

$$-.462 \times 10^4 \text{ dyn/cm}^2$$

<u>Run</u>	<u>Trans- ducer</u>	<u>Attenua- tion</u>	<u>Pressure₂ x 10⁻⁴ (dyn/cm²)</u>	<u>Flow (cc/sec)</u>	<u>L/D</u>
1	1	100	3.999	1.060	31.60
2	1	100	5.516	1.515	31.60
3	2	20	7.136	1.975	31.60
4	2	50	8.963	2.440	31.60
5	2	50	14.824	3.970	31.60
6	2	50	23.994	6.080	31.60
7	2	100	35.680	8.425	31.60
8	2	100	48.711	10.650	31.60
9	4	50	64.465	13.800	31.60
10	4	50	109.488	19.750	31.60
1	2	20	7.860	1.060	71.23
2	2	20	11.032	1.515	71.23
3	2	50	14.286	1.975	71.23
4	2	50	18.064	2.440	71.23
5	2	50	29.475	3.970	71.23
6	2	100	47.056	6.080	71.23
7	4	100	66.706	8.425	71.23
8	4	50	84.460	10.650	71.23
9	4	50	115.486	13.800	71.23
10	4	100	185.467	19.750	71.23
1	2	50	10.342	1.060	96.38
2	2	50	14.617	1.515	96.38
3	2	50	18.788	1.975	96.38
4	2	100	23.545	2.440	96.38
5	2	100	38.266	3.970	96.38
6	2	100	60.294	6.080	96.38
7	4	50	82.736	8.425	96.38
8	4	50	108.592	10.650	96.38
9	4	50	146.857	13.800	96.38
10	4	100	229.594	19.750	96.38

TABLE B.2 (continued)

<u>Run</u>	<u>Trans- ducer</u>	<u>Attenua- tion</u>	<u>Pressure $\times 10^{-4}$ (dyn/cm²)</u>	<u>Flow (cc/sec)</u>	<u>L/D</u>
1	2	50	15.168	1.060	148.45
2	2	50	21.511	1.515	148.45
3	2	100	27.958	1.975	148.45
4	2	100	34.991	2.440	148.45
5	2	100	57.571	3.970	148.45
6	4	50	86.873	6.080	148.45
7	4	50	122.726	8.425	148.45
8	4	50	160.647	10.650	148.45
9	4	100	213.736	13.800	148.45
10	4	200	325.430	19.750	148.45

TABLE B-3

TOTAL PRESSURE LOSS - L/D DATA: SUGAR SOLUTION #4,
0.20 cm I.D. CAPILLARY TUBE, SMALL RESERVOIR

Temp.: 71.50°F

Pressure Correction:
 $-.490 \times 10^4 \text{ dyn/cm}^2$

Run	Trans- ducer	Attenua- tion	Pressure ₂ x 10 ⁻⁴ (dyn/cm ²)	Flow (cc/sec)	L/D
1	2	100	17.409	1.515	31.60
2	2	100	22.753	1.975	31.60
3	2	100	27.820	2.440	31.60
4	2	100	34.645	3.030	31.60
5	2	100	43.954	3.800	31.60
6	2	100	46.677	4.565	31.60
1	2	100	37.231	1.515	71.23
2	2	100	47.367	1.975	71.23
3	2	100	59.984	2.440	71.23
4	4	50	71.705	3.030	71.23
5	4	50	90.665	3.800	71.23
6	4	50	109.281	4.565	71.23
1	2	100	48.952	1.515	96.38
2	2	100	63.638	1.975	96.38
3	4	50	75.152	2.440	96.38
4	4	50	94.802	3.030	96.38
5	4	50	118.934	3.800	96.38
6	4	100	144.099	4.565	96.38
1	4	50	73.773	1.515	148.45
2	4	50	94.802	1.975	148.45
3	4	50	118.934	2.440	148.45
4	4	100	148.581	3.030	148.45
5	4	100	179.262	3.800	148.45
6	4	100	219.251	4.565	148.45

TABLE B-4

TOTAL PRESSURE LOSS - L/D DATA: PRIMOL-355 OIL,
0.20 cm I.D. CAPILLARY TUBE, SMALL RESERVOIR

Temp.: 73.0°F

Pressure Correction:
-.331 x 10⁴ dyn/cm²

Run	Trans- ducer	Attenua- tion	Pressure ₂ x 10 ⁻⁴ (dyn/cm ²)	Flow (cc/sec)	L/D
1	2	50	24.407	0.758	34.99
2	2	50	33.991	1.060	34.99
2	2	100	34.060	1.060	34.99
3	2	100	48.125	1.515	34.99
3	3	50	47.573	1.515	34.99
4	3	50	73.773	2.285	34.99
5	3	100	96.526	3.030	34.99
6	3	50	116.176	3.636	34.99
7	3	50	136.170	4.242	34.99
1	3	50	48.952	0.758	71.23
2	3	50	67.568	1.060	71.23
3	3	50	98.043	1.515	71.23
4	3	50	146.857	2.285	71.23
5	3	100	195.120	3.030	71.23
6	3	100	236.143	3.636	71.23
7	3	100	274.064	4.242	71.23
1	3	50	65.844	0.758	96.38
2	3	50	92.044	1.060	96.38
3	3	50	126.518	1.515	96.38
4	3	100	191.328	2.285	96.38
5	3	100	251.657	3.030	96.38
6	3	100	303.367	3.636	96.38
7	3	200	351.630	4.242	96.38
1	3	50	101.352	0.758	151.00
2	3	50	139.962	1.060	151.00
3	3	100	198.567	1.515	151.00
4	3	100	295.783	2.285	151.00
5	3	200	392.998	3.030	151.00
6	3	200	467.116	3.636	151.00
7	3	200	544.681	4.242	151.00
1	3	50	143.410	0.758	222.36
2	3	100	203.394	1.060	222.36
3	3	100	287.854	1.515	222.36
4	3	200	436.090	2.285	222.36

TABLE B-5

TOTAL PRESSURE LOSS - L/D DATA: SUGAR SOLUTION #1,
0.20 cm I.D. CAPILLARY TUBE, LARGE RESERVOIR

Temp.: 73.0°F

Pressure Correction:
 $-2.427 \times 10^4 \text{ dyn/cm}^2$

Run	Trans- ducer	Attenua- tion	Pressure ₂ x 10 ⁻⁴ (dyn/cm ²)	Flow (cc/sec)	L/D
1	1	50	5.364	1.515	34.99
2	1	100	6.998	2.285	34.99
3	2	20	8.480	3.030	34.99
4	2	50	16.892	6.080	34.99
5	2	50	27.579	9.193	34.99
6	2	100	40.506	12.187	34.99
7	2	100	55.709	15.090	34.99
8	3	50	73.084	18.386	34.99
1	2	20	7.791	1.515	71.23
2	2	20	10.025	2.285	71.23
3	2	20	13.514	3.030	71.23
4	2	50	26.751	6.080	71.23
5	2	100	42.920	9.193	71.23
6	2	100	61.225	12.187	71.23
7	3	50	81.357	15.090	71.23
8	3	100	105.144	18.386	71.23
1	2	20	9.308	1.515	96.38
2	2	20	12.928	2.285	96.38
3	2	50	16.685	3.030	96.38
4	2	100	33.267	6.080	96.38
5	2	100	52.744	9.193	96.38
6	3	50	74.807	12.187	96.38
7	3	50	99.973	15.090	96.38
8	3	50	126.862	18.386	96.38
1	2	50	18.271	1.515	222.36
2	2	50	26.338	2.285	222.36
3	2	100	34.336	3.030	222.36
4	2	100	69.292	6.080	222.36
5	3	50	108.592	9.193	222.36
6	3	50	148.926	12.187	222.36
7	3	100	191.190	15.090	222.36
8	3	100	237.178	18.386	222.36

TABLE B-6

TOTAL PRESSURE LOSS - L/D DATA: SUGAR SOLUTION #3,
0.20 cm I.D. CAPILLARY TUBE, LARGE RESERVOIR

Temp.: 72.0°F

Pressure Correction:

$$-2.517 \times 10^4 \text{ dyn/cm}^2$$

<u>Run</u>	<u>Trans- ducer</u>	<u>Attenua- tion</u>	<u>Pressure₂ x 10⁻⁴ (dyn/cm²)</u>	<u>Flow (cc/sec)</u>	<u>L/D</u>
2	2	50	7.584	1.515	31.60
3	2	50	9.135	1.975	31.60
4	2	50	10.825	2.440	31.60
5	2	50	15.927	3.970	31.60
6	2	50	26.131	6.080	31.60
7	2	100	37.576	8.425	31.60
2	2	50	13.169	1.515	71.23
3	2	50	16.409	1.975	71.23
4	2	50	19.788	2.440	71.23
5	2	100	29.647	3.970	71.23
6	2	100	48.504	6.080	71.23
7	2	100	68.395	8.425	71.23
2	2	50	16.720	1.515	96.38
3	2	50	21.029	1.975	96.38
4	2	100	25.304	2.440	96.38
5	2	100	38.403	3.970	96.38
6	2	100	62.363	6.080	96.38
7	4	50	84.115	8.425	96.48
2	2	100	23.994	1.515	148.45
3	2	100	30.337	1.975	148.45
4	2	100	36.714	2.440	148.45
5	2	100	56.261	3.970	148.45
6	4	50	88.252	6.080	148.45
7	4	50	124.105	8.425	148.45

TABLE B-7

TOTAL PRESSURE LOSS - L/D DATA: SUGAR SOLUTION #4,
0.20 cm I.D. CAPILLARY TUBE, LARGE RESERVOIR

Temp.: 72.0°F

Pressure Correction:
 $-2.517 \times 10^4 \text{ dyn/cm}^2$

Run	Trans- ducer	Attenua- tion	Pressure $\times 10^{-4}$ (dyn/cm ²)	Flow (cc/sec)	L/D
1	2	100	18.409	1.515	31.60
2	2	100	23.270	1.975	31.60
3	2	100	28.165	2.440	31.60
4	2	100	34.577	3.030	31.60
5	2	100	43.264	3.800	31.60
6	2	100	52.917	4.565	31.60
1	2	100	33.887	1.515	71.23
2	2	100	45.643	1.975	71.23
3	2	100	55.847	2.440	71.23
4	2	100	68.947	3.030	71.23
5	4	50	86.184	3.800	71.23
6	4	50	105.489	4.565	71.23
1	2	100	46.126	1.515	96.38
2	2	100	59.639	1.975	96.38
3	4	50	70.671	2.440	96.38
4	4	50	88.252	3.030	96.38
5	4	50	111.349	3.800	96.38
6	4	50	134.447	4.565	96.38
1	4	50	68.947	1.515	148.45
2	4	50	89.631	1.975	148.45
3	4	50	110.315	2.440	148.45
4	4	50	138.583	3.030	148.45
5	4	100	173.746	3.800	148.45
6	4	100	208.909	4.565	148.45

TABLE B-8

TOTAL PRESSURE LOSS - L/D DATA: PRIMOL-355-OIL,
0.20 cm I.D. CAPILLARY TUBE, LARGE RESERVOIR

Temp.: 73.5°F

Pressure Correction:

$-1.779 \times 10^4 \text{ dyn/cm}^2$

Run	Trans- ducer	Attenua- tion	Pressure ₂ $\times 10^{-4}$ (dyn/cm ²)	Flow (cc/sec)	L/D
1	2	50	24.683	0.762	34.99
2	2	50	33.819	1.066	34.99
3	2	100	47.436	1.515	34.99
4	3	50	71.420	2.285	34.99
5	3	50	94.457	3.030	34.99
6	3	50	113.073	3.704	34.99
7	3	50	132.516	4.277	34.99
1	3	50	47.229	0.762	71.23
2	3	50	66.534	1.066	71.23
3	3	50	94.457	1.515	71.23
4	3	50	142.376	2.285	71.23
5	3	100	186.157	3.030	71.23
1	2	100	47.987	0.762	71.23
6	3	100	222.699	3.704	71.23
7	3	100	258.551	4.242	71.23
1	3	50	63.914	0.762	96.38
2	3	50	86.873	1.066	96.38
3	3	50	122.381	1.515	96.38
4	3	100	187.708	2.285	96.38
5	3	100	244.762	3.030	96.38
1	3	50	102.042	0.762	160.16
2	3	50	142.720	1.066	160.16
3	3	100	198.223	1.515	160.16

TABLE B-9

TOTAL PRESSURE LOSS - L/D DATA: 0.20% SEPARAN AP-30,
0.10 cm I.D. CAPILLARY TUBE, SMALL RESERVOIR

Temp.: 68°F

Pressure Correction
 $-1.669 \times 10^4 \text{ dyn/cm}^2$

Run	Trans- ducer	Attenua- tion	Pressure ₂ $\times 10^{-4}$ (dyn/cm ²)	Flow (cc/sec)	L/D
1	2	50	21.822	0.318	222.08
2	2	50	24.338	0.381	222.08
3	2	50	29.372	0.508	222.08
4	2	100	34.129	0.635	222.08
5	2	100	40.196	0.794	222.08
6	2	100	46.022	0.953	222.08
7	2	100	51.883	1.112	222.08
8	2	100	56.778	1.271	222.08
9	2	100	64.569	1.430	222.08
9	4	50	70.326	1.430	222.08
10	4	50	77.221	1.589	222.08
11	4	50	85.839	1.747	222.08
12	4	50	93.078	1.908	222.08
13	4	50	105.489	2.224	222.08
14	4	50	128.241	2.701	222.08
1	2	50	15.685	0.318	148.48
2	2	50	17.513	0.381	148.48
3	2	50	21.029	0.508	148.48
4	2	50	24.338	0.635	148.48
5	2	100	28.613	0.794	148.48
6	2	100	33.267	0.953	148.48
7	2	100	37.404	1.112	148.48
8	2	100	41.885	1.271	148.48
9	2	100	48.814	1.430	148.48
9	2	100	53.606	1.430	148.48
10	2	100	59.708	1.589	148.48
11	2	100	66.534	1.747	148.48
12	4	50	72.050	1.908	148.48
13	4	50	84.115	2.224	148.48
14	4	50	102.731	2.701	148.48
1	2	50	11.376	0.318	96.45
2	2	50	12.755	0.381	96.45
3	2	50	15.306	0.508	96.45
4	2	50	17.995	0.635	96.45
5	2	50	21.236	0.794	96.45
6	2	50	24.752	0.953	96.45

TABLE B-9 (continued)

Run	Trans- ducer	Attenua- tion	Pressure ₂ x10 ⁻⁴ (dyn/cm ²)	Flow (cc/sec)	L/D
7	2	50	28.096	1.112	96.45
8	2	100	31.543	1.271	96.45
9	2	100	35.163	1.430	96.45
9	2	100	41.575	1.430	96.45
10	2	100	46.815	1.589	96.45
11	2	100	53.779	1.747	96.45
12	2	100	58.088	1.908	96.45
13	4	50	67.223	2.224	96.45
14	4	50	84.115	2.701	96.45
1	2	50	9.515	0.318	71.32
2	2	50	10.480	0.381	71.32
3	2	50	12.410	0.508	71.32
4	2	50	14.755	0.635	71.32
5	2	50	17.740	0.794	71.32
6	2	50	20.546	0.953	71.32
7	2	50	23.408	1.112	71.32
8	2	50	27.372	1.271	71.32
9	2	100	36.749	1.430	71.32
9	2	100	29.854	1.430	71.32
10	2	100	41.092	1.589	71.32
11	2	100	46.126	1.747	71.32
12	2	100	51.538	1.908	71.32
13	2	100	59.984	2.224	71.32
14	4	50	75.497	2.701	71.32
1	2	50	8.101	0.318	55.08
2	2	50	9.032	0.381	55.08
3	2	50	10.549	0.508	55.08
4	2	50	12.617	0.635	55.08
5	2	50	15.237	0.794	55.08
6	2	50	17.857	0.953	55.08
7	2	50	20.581	1.112	55.08
8	2	50	23.235	1.271	55.08
9	2	100	32.198	1.430	55.08
10	2	100	36.887	1.589	55.08
11	2	100	42.127	1.747	55.08
12	2	100	46.194	1.908	55.08
13	2	100	54.882	2.224	55.08
14	2	100	69.292	2.701	55.08
15*	1	100	6.837	0.238	55.08
16*	1	100	6.155	0.159	55.08
17*	1	50	4.609	0.079	55.08
18*	1	20	3.608	0.032	55.08
19*	1	20	3.298	0.023	55.08

TABLE B-9 (continued)

<u>Run</u>	<u>Trans- ducer</u>	<u>Attenua- tion</u>	<u>Pressure₂ x 10⁻⁴ (dyn/cm²)</u>	<u>Flow (cc/sec)</u>	<u>L/D</u>
15*	2	50	23.881	0.238	305.08
16*	2	50	21.978	0.159	305.08
17*	2	50	15.712	0.079	305.08
18*	2	50	10.958	0.032	305.08
19*	2	50	9.600	0.023	305.08
20*	1	50	5.357	0.012	305.08
21*	1	50	3.722	0.008	305.08
22*	1	50	2.343	0.004	305.08

* Data obtained with batch number two

TABLE B-10

TOTAL PRESSURE LOSS - L/D DATA; 0.20% SEPARAN AP-30,
0.20 cm I.D. CAPILLARY TUBE, SMALL RESERVOIR

Temp.: 68°F

Pressure Correction:
 $-1.669 \times 10^4 \text{ dyn/cm}^2$

Run	Trans- ducer	Attenua- tion	Pressure ₂ x 10 ⁻⁴ (dyn/cm ²)	Flow (cc/sec)	L/D
1	2	20	4.688	1.271	31.60
2	2	20	5.171	1.589	31.60
3	2	50	6.033	1.906	31.60
4	2	50	7.239	2.383	31.60
5	2	50	7.984	2.701	31.60
6	2	50	8.998	3.177	31.60
7	2	50	14.479	4.866	31.60
8	2	50	17.237	5.401	31.60
9	2	50	18.891	5.719	31.60
10	2	100	21.098	6.354	31.60
11	2	100	28.337	7.943	31.60
12	2	100	37.645	9.531	31.60
13	2	100	46.746	11.120	31.60
1	2	50	5.792	1.271	54.96
2	2	50	6.515	1.589	54.96
3	2	50	7.343	1.906	54.96
4	2	50	9.032	2.383	54.96
5	2	50	9.790	2.701	54.96
6	2	50	11.032	3.177	54.96
7	2	100	17.513	4.866	54.96
8	2	100	20.270	5.401	54.96
9	2	100	21.615	5.719	54.96
10	2	100	24.200	6.354	54.96
11	2	100	32.922	7.943	54.96
12	2	100	42.954	9.531	54.96
13	2	100	52.262	11.120	54.96
1	2	50	6.826	1.271	71.23
2	2	20	7.446	1.589	71.23
3	2	50	8.515	1.906	71.23
4	2	50	10.121	2.383	71.23
5	2	50	11.169	2.701	71.23
6	2	50	12.617	3.177	71.23
7	2	100	19.133	4.866	71.23
8	2	100	22.063	5.401	71.23
9	2	100	24.545	5.719	71.23

TABLE B-10 (continued)

Run	Trans- ducer	Attenua- tion	Pressure ₂ x10 ⁻⁴ (dyn/cm ²)	Flow (cc/sec)	L/D
10	2	100	26.614	6.354	71.23
11	2	100	35.577	7.943	71.23
12	2	100	45.298	9.531	71.23
13	2	100	55.158	11.120	71.23
1	2	50	8.067	1.271	96.38
2	2	50	9.135	1.589	96.38
3	2	50	10.514	1.906	96.38
4	2	50	11.583	2.383	96.38
5	2	50	13.720	2.701	96.38
6	2	50	14.996	3.177	96.38
7	2	100	22.856	4.866	96.38
8	2	100	26.027	5.401	96.38
9	2	100	27.510	5.719	96.38
10	2	100	31.819	6.354	96.38
11	2	100	41.575	7.943	96.38
12	2	100	51.572	9.531	96.38
13	2	100	61.914	11.120	96.38
1	2	50	11.032	1.271	148.45
2	2	50	12.583	1.589	148.45
3	2	50	14.134	1.906	148.45
4	2	100	16.444	2.383	148.45
5	2	100	17.892	2.701	148.45
6	2	100	19.960	3.177	148.45
7	2	100	28.268	4.866	148.45
8	2	100	32.198	5.401	148.45
9	2	100	34.129	5.719	148.45
10	2	100	38.817	6.354	148.45
11	2	100	49.469	7.943	148.45
12	2	100	61.087	9.531	148.45
13	4	50	72.394	11.120	148.45
14*	2	50	15.731	0.636	304.95
15*	2	50	11.222	0.318	304.95
16*	2	50	10.073	0.239	304.95
17*	2	50	8.007	0.159	304.95

* Data obtained with batch number 2

TABLE B-11

TOTAL PRESSURE LOSS - L/D DATA: 0.20% SEPARAN AP-30,
0.30 cm I.D. CAPILLARY TUBE, SMALL RESERVOIR

Temp.: 68°F

Pressure Correction:
 $-1.669 \times 10^4 \text{ dyn/cm}^2$

Run	Trans- ducer	Attenua- tion	Pressure ₂ x 10 ⁻⁴ (dyn/cm ²)	Flow (cc/sec)	L/D
1	2	20	3.930	2.542	34.97
2	2	20	4.447	3.177	34.97
3	2	50	5.757	4.866	34.96
4	2	50	7.239	6.354	34.97
5	2	50	7.929	7.148	34.97
6	2	50	8.791	7.943	34.97
7	2	50	9.653	8.737	34.97
8	2	100	10.549	9.531	34.97
9	2	100	11.790	10.325	34.97
10	2	100	12.824	11.120	34.97
11	2	100	14.272	11.914	34.97
12	2	100	15.616	12.708	34.97
13	2	100	17.926	14.297	34.97
14	2	100	20.270	15.885	34.97
15	2	100	24.131	17.474	34.97
16	2	100	26.338	19.062	34.97
1	2	50	4.688	2.542	55.04
2	2	50	5.205	3.177	55.04
3	2	50	6.757	4.866	55.04
4	2	50	8.412	6.354	55.04
5	2	50	9.377	7.148	55.04
6	2	50	10.342	7.943	55.04
7	2	50	11.445	8.737	55.04
8	2	100	12.583	9.531	55.04
9	2	100	14.031	10.325	55.04
10	2	100	15.134	11.120	55.04
11	2	100	16.478	11.914	55.04
12	2	100	18.133	12.708	55.04
13	2	100	19.995	14.297	55.04
14	2	100	22.890	15.885	55.04
15	2	100	26.269	17.474	55.04
16	2	100	29.475	19.062	55.04
1	2	20	5.378	2.542	71.13
2	2	20	6.067	3.177	71.13
3	2	50	7.757	4.866	71.13
4	2	50	9.584	6.354	71.13

TABLE B-11 (continued)

Run	Trans- ducer	Attenua- tion	Pressure ₂ x10 ⁻⁴ (dyn/cm ²)	Flow (cc/sec)	L/D
5	2	50	10.514	7.148	71.13
6	2	50	11.583	7.943	71.13
7	2	100	12.928	8.737	71.13
8	2	100	13.962	9.531	71.13
9	2	100	15.548	10.325	71.13
10	2	100	16.754	11.120	71.13
11	2	100	18.064	11.914	71.13
12	2	100	19.374	12.708	71.13
13	2	100	22.235	14.297	71.13
14	2	100	24.683	15.885	71.13
15	2	100	29.096	17.474	71.13
16	2	100	32.198	19.062	71.13
1	2	50	6.398	2.542	96.36
2	2	50	7.170	3.177	96.36
3	2	50	9.239	4.866	96.36
4	2	50	11.169	6.354	96.36
5	2	50	12.548	7.148	96.36
6	2	100	13.789	7.943	96.36
7	2	100	14.941	8.737	96.36
8	2	100	16.306	9.531	96.36
9	2	100	17.685	10.325	96.36
10	2	100	18.960	11.120	96.36
11	2	100	20.891	11.914	96.36
12	2	100	22.235	12.708	96.36
13	2	100	25.200	14.297	96.36
14	2	100	28.510	15.885	96.36
15	2	100	32.405	17.474	96.36
16	2	100	36.266	19.062	96.36
1	2	50	8.274	2.542	145.00
2	2	50	9.549	3.177	145.00
3	2	50	12.204	4.866	145.00
4	2	100	14.893	6.354	145.00
5	2	100	16.203	7.148	145.00
6	2	100	17.685	7.943	145.00
7	2	100	19.167	8.737	145.00
8	2	100	20.753	9.531	145.00
9	2	100	22.235	10.325	145.00
10	2	100	24.131	11.120	145.00
11	2	100	25.683	11.914	145.00
12	2	100	27.682	12.708	145.00
13	2	100	31.164	14.297	145.00
14	2	100	34.336	15.885	145.00
15	2	100	39.058	17.474	145.00
16	2	100	43.609	19.062	145.00

TABLE B-11 (continued)

<u>Run</u>	<u>Trans- ducer</u>	<u>Attenua- tion</u>	<u>Pressure₂x10⁻⁴ (dyn/cm²)</u>	<u>Flow (cc/sec)</u>	<u>L/D</u>
17*	2	50	13.423	1.589	304.83
18*	2	50	12.272	1.271	304.83
19*	2	50	9.214	0.636	304.83
20*	1	50	6.764	0.318	304.83
21*	1	50	6.461	0.238	304.83
22*	1	50	5.267	0.159	304.83
23*	1	10	2.399	0.012	304.83
24*	1	10	2.199	0.008	304.83
25*	1	20	2.787	0.024	304.83
26*	1	20	3.014	0.032	304.83
27*	1	20	4.099	0.080	304.83
28*	1	50	5.872	0.238	304.83
29*	1	50	6.293	0.318	304.83

* Data obtained with batch number two.

TABLE B-12

TOTAL PRESSURE LOSS - L/D DATA: 0.20% SEPARAN AP-30,
0.10 cm I.D. CAPILLARY TUBE, LARGE RESERVOIR

Temp.: 68°F

Pressure Correction:
 $-1.937 \times 10^4 \text{ dyn/cm}^2$

Run	Trans- ducer	Attenua- tion	Pressure $\times 10^{-4}$ (dyn/cm ²)	Flow (cc/sec)	L/D
1	2	50	7.756	0.318	55.08
2	2	50	9.135	0.381	55.08
3	2	50	10.859	0.508	55.08
4	2	100	12.721	0.635	55.08
5	2	100	15.341	0.794	55.08
6	2	100	18.340	0.953	55.08
7	2	100	20.684	1.112	55.08
8	2	100	22.753	1.271	55.08
9	2	100	25.683	1.430	55.08
10	2	100	28.061	1.589	55.08
11	2	100	31.200	1.748	55.08
11	2	100	33.200	1.748	55.08
12	2	100	39.403	1.908	55.08
13	2	100	46.746	2.224	55.08
14	2	100	57.571	2.701	55.08
1	2	100	9.446	0.318	71.32
2	2	100	10.514	0.381	71.32
3	2	100	12.548	0.508	71.32
4	2	100	14.582	0.635	71.32
5	2	100	17.340	0.794	71.32
6	2	100	20.133	0.953	71.32
7	2	100	22.753	1.112	71.32
8	2	100	25.683	1.271	71.32
9	2	100	29.820	1.430	71.32
10	2	100	32.853	1.589	71.32
11	2	100	39.782	1.748	71.32
12	2	100	44.953	1.908	71.32
13	2	100	52.641	2.240	71.32
14	2	100	63.604	2.701	71.32
1	2	100	10.549	0.318	96.45
2	2	100	12.617	0.381	96.45
3	2	100	15.237	0.508	96.45
4	2	100	17.513	0.635	96.45
5	2	100	20.960	0.794	96.45
6	2	100	24.304	0.953	96.45
7	2	100	27.337	1.112	96.45
8	2	100	31.164	1.271	96.45
9	2	100	33.991	1.430	96.45

TABLE B-12 (continuous)

Run	Trans- ducer	Attenua- tion	Pressure ₂ x10 ⁻⁴ (dyn/cm ²)	Flow (cc/sec)	L/D
10	2	100	37.231	1.589	96.45
11	2	100	42.230	1.748	96.45
11	2	100	44.540	1.748	96.45
12	2	100	50.400	1.908	96.45
13	2	100	58.950	2.224	96.45
14	4	50	71.705	2.701	96.45
1	2	100	15.548	0.318	148.48
2	2	100	17.444	0.381	148.48
3	2	100	21.029	0.508	148.48
4	2	100	23.959	0.635	148.48
5	2	100	28.130	0.794	148.48
6	2	100	32.750	0.953	148.48
7	2	100	37.300	1.112	148.48
8	2	100	41.230	1.271	148.48
9	2	100	45.919	1.430	148.48
10	2	100	50.400	1.589	148.48
11	2	100	55.227	1.748	148.48
12	2	100	63.948	1.908	148.48
13	4	50	73.084	2.224	148.48
14	4	50	88.942	2.701	148.48
1	2	100	21.511	0.318	222.08
2	2	100	23.890	0.381	222.08
3	2	100	27.924	0.508	222.08
4	2	100	33.095	0.635	222.08
5	2	100	39.024	0.794	222.08
6	2	100	44.609	0.953	222.08
7	2	100	50.331	1.112	222.08
8	2	100	55.847	1.271	222.08
9	2	100	61.535	1.430	222.08
10	2	100	68.258	1.589	222.08
11	4	50	76.186	1.748	222.08
12	4	50	84.115	1.908	222.08
13	4	50	97.215	2.224	222.08
14	4	50	117.899	2.701	222.08
1	2	100	27.924	0.318	305.08
2	2	100	31.026	0.381	305.08
3	2	100	37.231	0.508	305.08
4	2	100	43.092	0.635	305.08
5	2	100	50.848	0.794	305.08
6	2	100	57.743	0.953	305.08
7	2	100	65.086	1.112	305.08
8	4	50	71.705	1.271	305.08
9	4	50	84.460	1.430	305.08

TABLE B-12 (continued)

<u>Run</u>	<u>Trans- ducer</u>	<u>Attenua- tion</u>	<u>Pressure $\times 10^{-4}$ (dyn/cm²)</u>	<u>Flow (cc/sec)</u>	<u>L/D</u>
10	4	100	93.768	1.589	305.08
11	4	50	104.799	1.748	305.08
11	4	50	84.460	1.748	305.08
12	4	50	93.906	1.908	305.08
13	4	50	122.036	2.224	305.08
14	4	50	144.789	2.701	305.08

TABLE B-13

TOTAL PRESSURE LOSS - L/D DATA: 0.20% SEPARAN AP-30,
0.20 cm I.D. CAPILLARY TUBE, LARGE RESERVOIR

Temp.: 68°F

Pressure Correction:
 $-1.937 \times 10^4 \text{ dyn/cm}^2$

Run	Trans- ducer	Attenua- tion	Pressure ₂ x 10 ⁻⁴ (dyn/cm ²)	Flow (cc/sec)	L/D
1	2	50	11.859	1.271	148.45
2	2	50	10.549	1.589	148.45
3	2	50	13.203	1.906	148.45
4	2	50	15.203	2.383	148.45
5	2	50	16.547	2.701	148.45
6	2	50	18.443	3.177	148.45
7	2	50	25.304	4.866	148.45
9	2	100	29.406	5.719	148.45
9	2	100	31.026	5.719	148.45
10	2	100	32.267	6.354	148.45
10	2	100	33.164	6.354	148.45
11	2	100	42.644	7.943	148.45
12	2	100	51.745	9.531	148.45
13	2	100	62.742	11.120	148.45
1	2	50	8.067	1.271	96.38
2	2	50	9.101	1.589	96.38
3	2	50	10.170	1.906	96.38
4	2	50	11.721	2.383	96.38
5	2	50	12.686	2.701	96.38
6	2	50	14.134	3.177	96.38
7	2	50	19.719	4.866	96.38
9	2	50	22.925	5.719	96.38
9	2	50	24.132	5.719	96.38
10	2	100	26.889	6.354	96.38
11	2	100	34.922	7.943	96.38
12	2	100	43.747	9.531	96.38
13	2	100	53.365	11.120	96.38
1	1	50	6.881	1.271	71.23
2	1	100	7.708	1.589	71.23
3	2	50	8.515	1.906	71.23
4	2	50	9.722	2.383	71.23
5	2	50	10.455	2.701	71.23
6	2	50	11.790	3.177	71.23
7	2	50	16.616	4.866	71.23
8	2	50	18.719	5.401	71.23
8	2	50	19.857	5.401	71.23
9	2	50	19.995	5.719	71.23

TABLE B-13 (continued)

Run	Trans- ducer	Attenua- tion	Pressure $\times 10^{-4}$ (dyn/cm ²)	Flow (cc/sec)	L/D
9	2	50	21.236	5.719	71.23
10	2	50	21.564	6.354	71.23
10	2	50	23.270	6.354	71.23
11	2	100	30.337	7.943	71.23
12	2	100	38.507	9.531	71.23
13	2	100	47.367	11.120	71.23
1	1	100	5.750	1.271	54.96
2	1	100	6.426	1.589	54.96
3	2	50	7.343	1.906	54.96
4	2	50	8.343	2.383	54.96
5	2	50	9.135	2.701	54.96
6	2	50	10.204	3.177	54.96
7	2	50	14.582	4.866	54.96
8	2	50	15.449	5.401	54.96
9	2	50	17.581	5.719	54.96
9	2	50	18.754	5.719	54.96
10	2	50	19.374	6.354	54.96
10	2	50	20.891	6.354	54.96
11	2	50	27.062	7.943	54.96
12	2	50	35.439	9.531	54.96
13	2	50	42.920	11.120	54.96
1	1	100	4.671	1.271	31.60
2	1	100	5.188	1.589	31.60
3	1	100	5.826	1.906	31.60
4	1	100	6.688	2.384	31.60
5	2	50	7.446	2.701	31.60
6	2	50	8.308	3.177	31.60
7	2	50	12.066	4.866	31.60
8	2	50	14.893	5.401	31.60
9	2	50	14.798	5.719	31.60
9	2	50	15.823	5.719	31.60
10	2	50	17.788	6.354	31.60
11	2	100	23.442	7.943	31.60
12	2	100	29.820	9.531	31.60
13	2	100	38.266	11.120	31.60
1	2	50	14.755	1.271	222.36
2	2	50	16.616	1.589	222.36
3	2	50	18.443	1.906	222.36
4	2	50	21.098	2.383	222.36
5	2	100	22.753	2.701	222.36
6	2	100	25.338	3.177	222.36
7	2	100	33.956	4.866	222.36
8	2	100	37.576	5.401	222.36
9	2	100	39.231	5.719	222.36
9	2	100	40.472	5.719	222.36

TABLE B-13 (continued)

<u>Run</u>	<u>Trans- ducer</u>	<u>Attenua- tion</u>	<u>Pressure₂ × 10⁻⁴ (dyn/cm²)</u>	<u>Flow (cc/sec)</u>	<u>L/D</u>
10	2	100	44.471	6.354	222.36
11	2	100	54.744	7.943	222.36
12	2	100	65.844	9.531	222.36
13	4	50	76.876	11.120	222.36
1	2	50	18.960	1.271	304.95
2	2	100	21.236	1.589	304.95
3	2	100	23.649	1.906	304.95
4	2	100	27.027	2.383	304.95
5	2	100	29.302	2.701	304.95
6	2	100	32.681	3.177	304.95
7	2	100	43.816	4.866	304.95
8	2	100	48.435	5.401	304.95
9	2	100	50.848	5.719	304.95
10	2	100	55.227	6.354	304.95
11	2	100	69.395	7.943	304.95
12	4	50	81.013	9.531	304.95
13	4	50	95.147	11.120	304.95
1	2	100	27.510	1.271	457.43
2	2	100	31.026	1.589	457.43
7	2	100	63.673	4.866	457.43
8	4	50	68.258	5.401	457.43
9	4	50	70.671	5.719	457.43
10	4	50	76.531	6.354	457.43
11	4	50	95.492	7.943	457.43
12	4	50	108.247	9.531	457.43
13	4	50	129.620	11.120	457.43

TABLE B-14

TOTAL PRESSURE LOSS - L/D DATA: 0.20% SEPARAN AP-30,
0.30 cm I.D. CAPILLARY TUBE, LARGE RESERVOIR

Temp.: 68°F

Pressure Correction:
 $-1.937 \times 10^4 \text{ dyn/cm}^2$

Run	Trans- ducer	Attenua- tion	Pressure ₂ x 10 ⁻⁴ (dyn/cm ²)	Flow (cc/sec)	L/D
1	2	50	3.861	2.542	34.97
2	2	50	4.275	3.177	34.97
3	2	50	5.309	4.866	34.97
4	2	50	6.378	6.354	34.97
5	2	50	6.998	7.148	34.97
6	2	50	7.722	7.943	34.97
7	2	50	8.343	8.764	34.97
8	2	50	9.135	9.531	34.97
9	2	50	9.722	10.325	34.97
10	2	50	10.514	11.120	34.97
11	2	100	11.962	11.914	34.97
12	2	100	12.893	12.708	34.97
13	2	100	13.720	14.297	34.97
14	2	100	17.064	15.885	34.97
15	2	100	19.478	17.474	34.97
16	2	100	19.995	19.062	34.97
16	2	100	21.925	19.062	34.97
1	2	50	4.654	2.542	55.04
2	2	50	5.102	3.177	55.04
3	2	50	6.343	4.866	55.04
4	2	50	7.584	6.354	55.04
5	2	50	8.412	7.148	55.04
6	2	50	9.135	7.943	55.04
7	2	50	9.894	8.764	55.04
8	2	50	10.583	9.531	55.04
9	2	50	11.514	10.325	55.04
10	2	50	12.410	11.120	55.04
11	2	50	13.927	11.914	55.04
12	2	50	14.686	12.708	55.04
13	2	100	16.306	14.297	55.04
14	2	100	19.478	15.885	55.04
15	2	100	21.718	17.474	55.04
16	2	100	24.476	19.062	55.04
1	2	50	5.309	2.542	71.13
2	2	50	5.895	3.177	71.13
3	2	50	7.343	4.866	71.13
4	2	50	8.777	6.354	71.13

TABLE B-14 (continued)

Run	Trans- ducer	Attenua- tion	Pressure ₂ × 10 ⁻⁴ (dyn/cm ²)	Flow (cc/sec)	L/D
5	2	50	9.653	7.148	71.13
6	2	50	10.514	7.943	71.13
7	2	50	11.307	8.764	71.13
8	2	50	12.204	9.531	71.13
9	2	100	12.514	10.325	71.13
10	2	100	14.307	11.120	71.13
10	2	100	14.617	11.120	71.13
11	2	100	15.341	11.914	71.13
12	2	100	16.168	12.708	71.13
12	2	100	16.823	12.708	71.13
13	2	100	19.098	14.297	71.13
14	2	100	21.374	15.885	71.13
15	2	100	23.959	17.474	71.13
16	2	100	26.820	19.062	71.13
1	2	100	6.412	2.542	96.36
2	2	100	7.136	3.177	96.36
3	2	100	8.791	4.866	96.36
4	2	100	10.584	6.354	96.36
5	2	100	11.480	7.148	96.36
6	2	100	13.203	7.943	96.36
7	2	100	13.514	8.764	96.36
8	2	100	14.479	9.531	96.36
9	2	100	15.582	10.325	96.36
10	2	100	16.547	11.120	96.36
11	2	100	18.202	11.914	96.36
12	2	100	18.788	12.708	96.36
12	2	100	19.374	12.708	96.36
13	2	100	21.856	14.297	96.36
14	2	100	24.338	15.885	96.36
15	2	100	27.131	17.474	96.36
16	2	100	30.681	19.062	96.36
1	2	50	8.515	2.542	148.52
2	2	50	9.515	3.177	148.52
3	2	50	11.790	4.866	148.52
4	2	50	13.996	6.354	148.52
5	2	50	15.237	7.148	148.52
6	2	50	16.409	7.943	148.52
7	2	50	17.650	8.764	148.52
8	2	50	18.754	9.531	148.52
9	2	50	20.064	10.325	148.52
10	2	50	21.856	11.120	148.52
11	2	50	23.304	11.914	148.52
12	2	50	24.683	12.708	148.52
13	2	50	27.406	14.297	148.52
14	2	100	30.681	15.885	148.52

Table B-14 (continued)

<u>Run</u>	<u>Trans- ducer</u>	<u>Attenua- tion</u>	<u>Pressure $\times 10^{-4}$ (dyn/cm²)</u>	<u>Flow (cc/sec)</u>	<u>L/D</u>
15	2	100	33.887	17.474	148.52
16	2	100	37.576	19.062	148.52
1	2	50	11.169	2.542	213.38
2	2	50	12.583	3.177	213.38
3	2	50	15.685	4.866	213.38
4	2	50	18.616	6.354	213.38
5	2	50	20.133	7.148	213.38
6	2	50	21.718	7.943	213.38
7	2	50	23.235	8.764	213.38
8	2	50	24.717	9.531	213.38
9	2	50	26.234	10.325	213.38
10	2	100	27.717	11.120	213.38
10	2	100	28.958	11.120	213.38
11	2	100	29.820	11.932	213.38
12	2	100	31.130	12.708	213.38
13	2	100	34.474	14.297	213.38
14	2	100	38.438	15.885	213.38
15	2	100	42.265	17.474	213.38
16	2	100	46.953	19.062	213.38
1	2	50	15.168	2.542	304.83
2	2	50	16.823	3.177	304.83
3	2	50	21.167	4.866	304.83
4	2	50	24.993	6.354	304.83
6	2	100	28.613	7.943	304.83
8	2	100	32.543	9.531	304.83
10	2	100	36.542	11.120	304.83
12	2	100	41.368	12.708	304.83
12	2	100	40.610	12.708	304.83
13	2	100	45.643	14.297	304.83
14	2	100	49.849	15.885	304.83
15	2	100	54.330	17.474	304.83
16	2	100	58.777	19.062	304.83

FIGURE B.1
PRESSURE FLUCTUATIONS
0.10 cm I.D. CAPILLARY, LARGE RESERVOIR

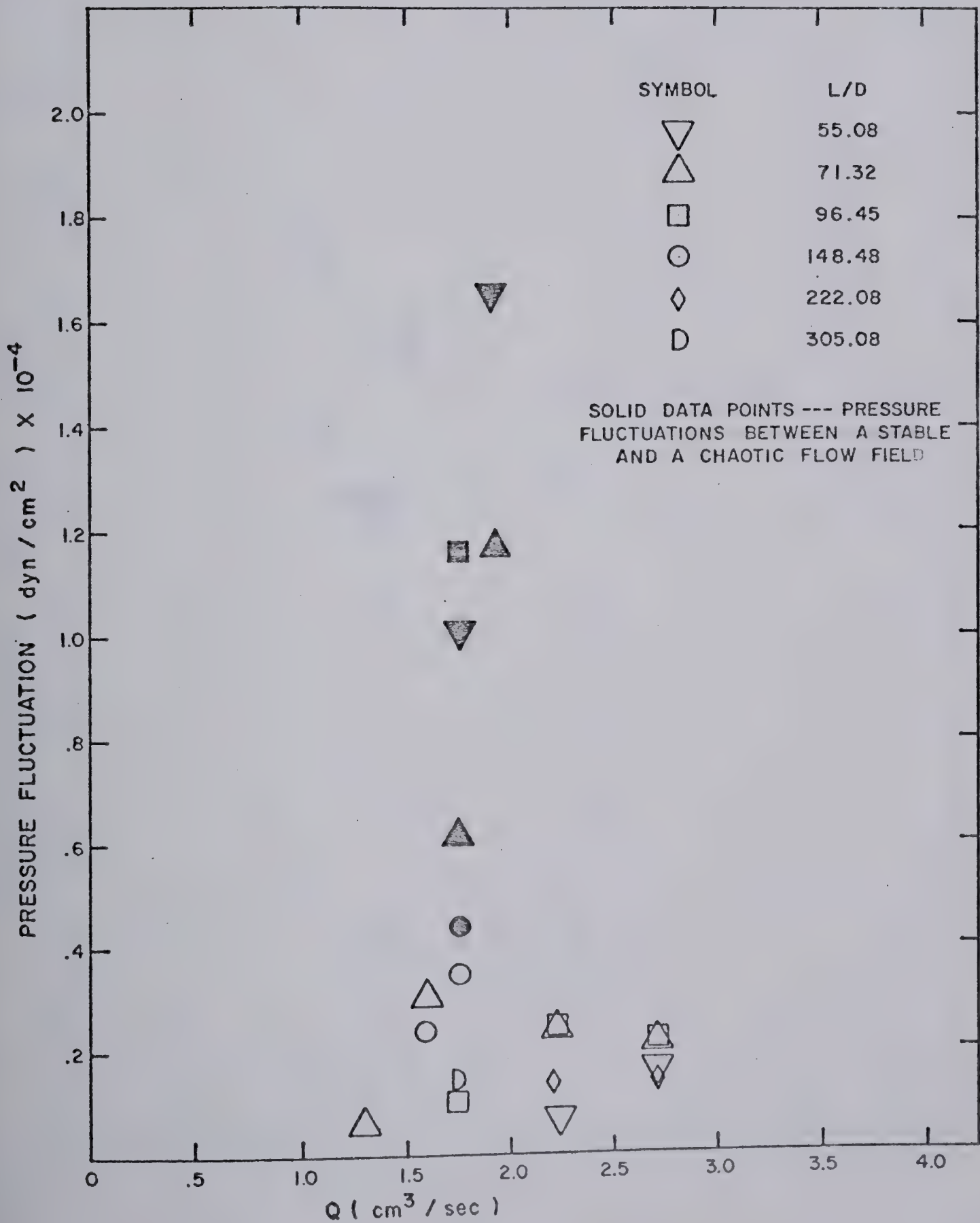


FIGURE B.2
PRESSURE FLUCTUATIONS
0.20 cm I.D. CAPILLARY, LARGE RESERVOIR

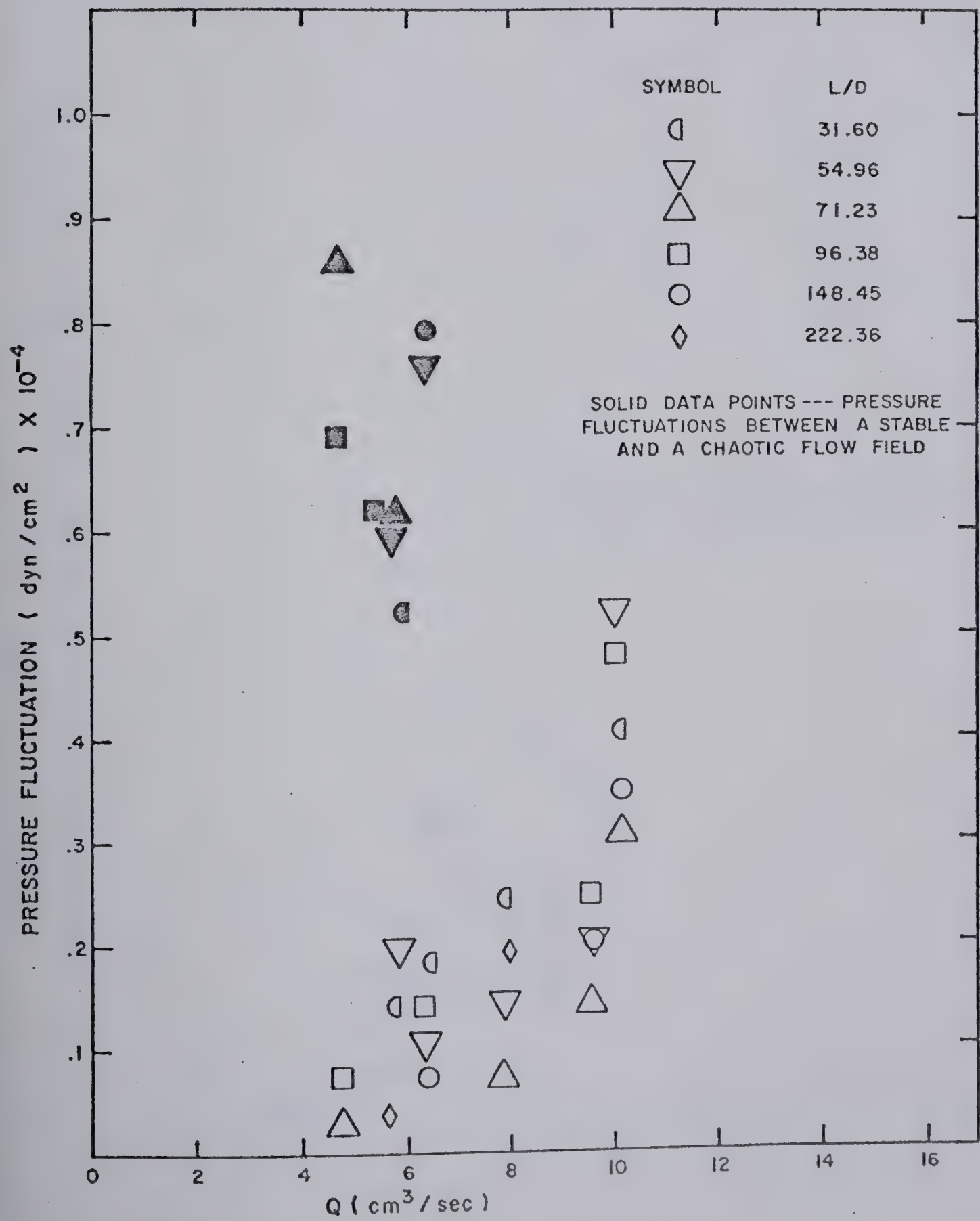
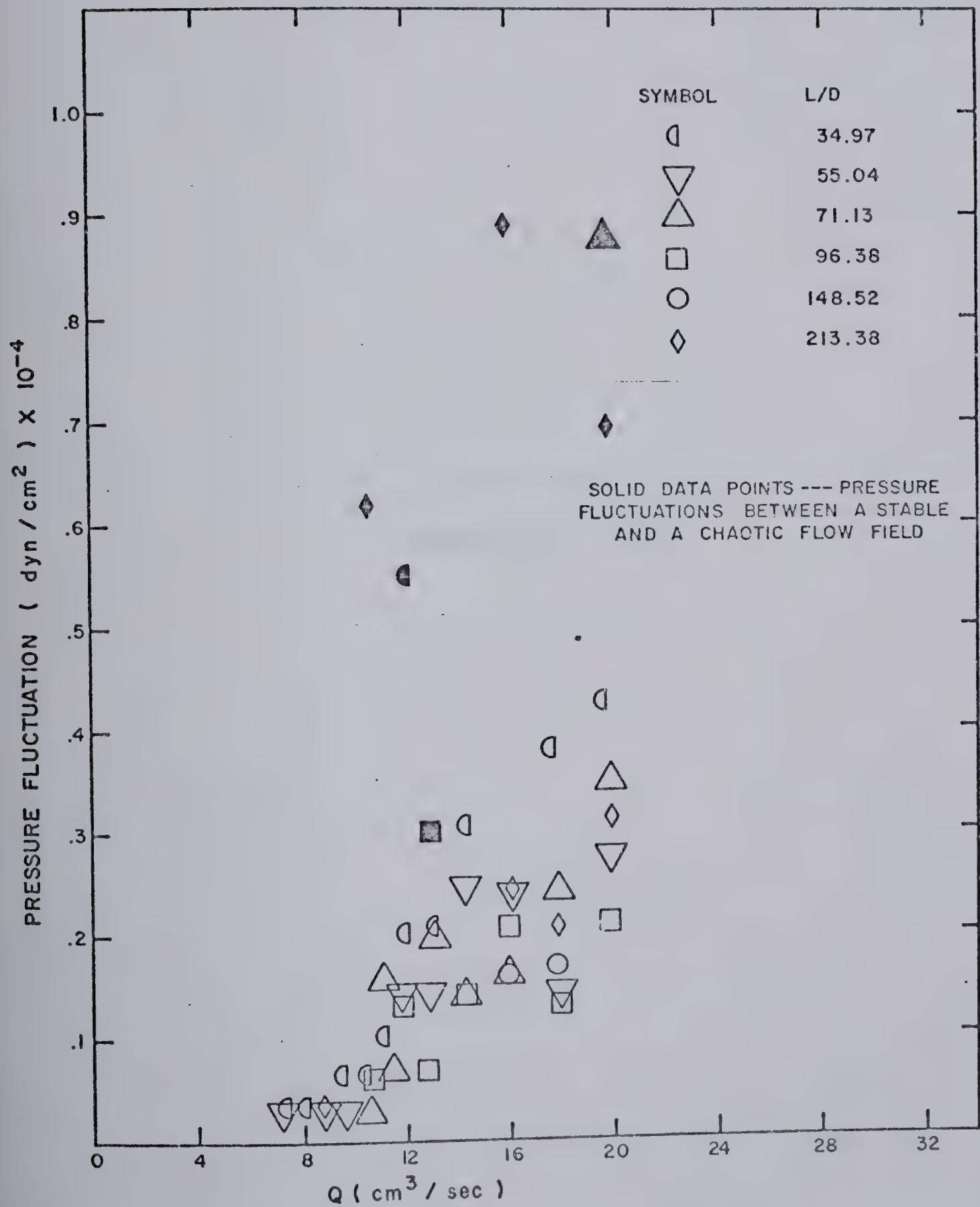


FIGURE B.3
PRESSURE FLUCTUATIONS
0.30 cm I.D. CAPILLARY, LARGE RESERVOIR



APPENDIX C
CONTRACTION LOSSES

C.1 NEWTONIAN FLUIDS

The Bagley plot was constructed using the total pressure loss-L/D data tabulated in Appendix B. In this analysis the velocity field is assumed to be fully developed prior to the end of the capillary tube. The total pressure loss is comprised, therefore, of the developed pressure losses, ΔP_d , and the contraction losses, ΔP_c , given by

$$\Delta P_t = \Delta P_d + \Delta P_c \quad \text{C.1}$$

where

$$\Delta P_d = 4\tau_w L/D \quad \text{C.2}$$

Equating the contraction loss to the developed pressure loss measured over an equivalent length of capillary tube, $\epsilon_v D$, yields

$$\Delta P_t = 4\tau_w (L/D + \epsilon_v) \quad \text{C.3}$$

where ϵ_v is the Bagley entrance correction (76). The contraction losses and the shear stresses are evaluated from the intercept and slope of Equation C.3. The data in Appendix B was curve fitted to Equation C.3 in the sense of least squares. The resulting values for the contraction losses and the Bagley entrance correction factors are tabulated in Tables C.1 and C.2 for reservoirs S and L respectively. The shear stresses can be found in Appendix D, Table D.1.

Values of the dimensionless contraction loss, ϕ ,

defined by

$$\Phi = \Delta P_c / (\rho \frac{V^2}{2}) \quad C.4$$

are also tabulated in Tables C.1 and C.2.

C.2 VISCOELASTIC FLUID

Bagley plots were used also in the evaluation of the contraction losses and shear stresses for the 0.20% aqueous solution of Separan AP-30. The contraction loss - Reynolds number data are tabulated in Tables C.3 and C.4 for reservoirs S and L respectively. To distinguish the difference in the contraction losses, ϵ_t was used in place of ϵ_v in Equation C.3 where ϵ_t includes both the viscous and elastic contributions. The only assumption in estimating the contraction losses with the Bagley plot for the viscoelastic fluid was the assumption of a zero exit pressure.

For capillary tube lengths longer than the entry length, the exit pressures are constant (161). Figure C.1 qualitatively depicts the effect of this exit pressure on the pressure profile and on the Bagley plot. If the exit pressure is not equal to zero then Equation C.3 must be modified to

$$\Delta P_t - \Delta P_{\text{exit}} = 4\tau_w (L/D + \epsilon_t) \quad C.5$$

where the equivalent length for the viscoelastic fluid is ϵ_t . Failure to subtract the exit pressure from the total pressure loss would result in an overestimation of the contraction

losses. Although the exit pressure was not measured directly, an estimate of its magnitude can be obtained from the results reported by Sylvester (161). He estimated that the exit pressure was $\pm 6.89 \times 10^2 \text{ dyn/cm}^2$ by using a pressure profile and by extrapolation of the developed pressure gradient, dP/dx , to the end of the capillary tube. Since the solutions used by Sylvester were approximately an order of magnitude greater in concentration than that used in this research and since the exit pressure decreased with increase in concentration, it can be reasonably assumed that the exit pressure for the 0.20% aqueous solutions of Separan AP-30 was less than 70 dyn/cm^2 . Under the worst condition this exit pressure resulted in a 1.5% error in the contraction losses and was assumed to be negligible for all experimental runs.

The list of tables and a figure contained in this appendix is given below:

<u>TABLE NO.</u>	<u>DESCRIPTION</u>
C.1	Contraction Losses and Reynolds Numbers for Newtonian Fluids, Small Reservoir
C.2	Contraction Losses and Reynolds Numbers for Newtonian Fluids, Large Reservoir
C.3	Contraction Losses and Reynolds Numbers for 0.20% Separan AP-30 - Small Reservoir
C.4	Contraction Losses and Reynolds Numbers for 0.20% Separan AP-30 - Large Reservoir

FIGURE NO.

C.1	Pressure Profile and Bagley Plot
-----	----------------------------------

TABLE C.1

CONTRACTION LOSSES AND REYNOLDS NUMBERS
FOR NEWTONIAN FLUIDS, SMALL RESERVOIR

<u>Solution</u>	<u>Run No.</u>	$\Delta P_C \times 10^{-4}$ <u>(dyn/cm²)</u>	<u>Φ</u>	<u>ϵ_v</u>	<u>N_{Re}</u>
Sugar #1	1	0.572	4.08	8.26	126.88
	2	0.999	3.13	9.65	191.36
	3	1.575	2.81	11.47	253.75
	4	4.980	2.21	17.81	509.18
	5	10.298	2.00	23.62	769.89
	6	19.605	2.16	33.85	1020.63
	7	29.644	2.13	41.19	1263.75
	8	44.940	2.18	51.68	1539.78
Sugar #3	1	0.569	8.05	5.95	46.73
	2	0.800	5.54	5.84	66.79
	3	1.096	4.47	6.15	87.07
	4	1.606	4.29	7.23	107.57
	5	2.834	2.86	7.76	175.03
	6	5.757	2.48	10.02	268.05
	7	11.824	2.65	15.85	371.44
	8	16.713	2.34	17.54	469.53
	9	23.759	1.98	18.62	608.41
	10	51.752	2.11	28.09	870.72
Sugar #4	1	2.324	15.42	4.88	20.63
	2	2.930	11.44	4.80	26.89
	3	3.385	8.66	4.42	33.22
	4	5.171	8.58	5.58	41.25
	5	7.233	7.63	6.26	51.74
	6	7.205	5.96	5.04	62.15
Primol-355	1	2.772	108.71	4.36	2.60
	2	3.241	64.87	3.59	3.63
	3	4.426	43.45	3.47	5.16
	4	6.722	29.01	3.49	7.79
	5	9.280	22.78	3.65	10.33
	6	11.411	19.50	3.76	12.62
	7	18.629	23.33	5.36	14.58

TABLE C.2

CONTRACTION LOSSES AND REYNOLDS NUMBERS
FOR NEWTONIAN FLUIDS, LARGE RESERVOIR

<u>Solution</u>	<u>Run No.</u>	$\Delta P_C \times 10^{-4}$ <u>(dyn/cm²)</u>	<u>Φ</u>	<u>ϵ_v</u>	<u>N_{Re}</u>
Sugar #1	1	0.439	3.13	6.39	129.28
	2	0.843	2.65	8.18	194.98
	3	1.390	2.48	10.34	258.55
	4	4.985	2.21	18.40	517.11
	5	10.445	2.02	24.92	784.45
	6	17.843	1.97	31.17	1039.93
	7	28.792	2.07	40.58	1287.65
	8	40.686	1.97	46.76	1568.90
Sugar #3	2	0.448	3.10	3.19	66.98
	3	0.793	3.23	4.37	87.32
	4	1.172	3.13	5.30	107.87
	5	2.379	2.40	6.70	175.52
	6	5.964	2.57	10.42	268.80
	7	11.687	2.62	15.89	372.48
Sugar #4	1	1.343	8.91	3.08	21.81
	2	1.517	5.95	2.66	28.44
	3	1.862	4.77	2.62	35.13
	4	2.572	4.26	2.89	43.63
	5	3.654	3.85	3.23	54.72
	6	4.454	3.69	3.25	65.73
Primol-355	1	1.731	67.18	2.80	2.66
	2	2.213	43.88	2.56	3.72
	3	3.434	33.71	2.79	5.29
	4	3.709	16.01	1.95	7.98
	5	7.405	18.17	3.02	10.49
	6	7.474	12.28	2.50	12.93
	7	9.053	11.15	2.60	14.93

TABLE C.3

CONTRACTION LOSSES AND REYNOLDS NUMBERS FOR
0.20% SEPARAN AP-30, SMALL RESERVOIR

Capillary I.D. (cm)	Run No.	$\Delta P_c \times 10^{-4}$ (dyn/cm ²)	ϕ_t	ϵ_t	N'_{Re}
0.10	1	1.904	23.28	23.23	62.59
	2	2.271	19.28	24.76	81.21
	3	2.720	13.03	24.19	121.56
	4	3.891	12.00	30.37	164.92
	5	5.307	10.38	35.73	224.72
	6	6.843	9.29	40.66	286.49
	7	8.391	8.37	44.83	350.53
	8	10.945	8.36	55.16	416.26
	9	12.589	7.60	55.61	483.36
	9	18.358	11.08	81.10	483.36
	10	22.039	10.77	91.36	551.32
	11	26.196	10.58	100.24	619.97
	12	29.553	10.01	106.39	689.96
	13	36.553	9.12	120.12	828.20
	14	48.499	8.20	137.68	1036.98
	15*	1.158	33.00	21.00	41.37
	16*	1.000	49.00	17.00	22.72
	17*	0.525	65.00	13.50	11.34
	18*	0.320	385.00	10.60	2.04
	19*	0.241	525.00	9.40	1.32
0.20	1	1.221	14.92	22.35	90.95
	2	1.359	10.63	21.29	126.36
	3	1.954	10.61	27.67	164.99
	4	2.959	10.29	38.08	228.04
	5	3.515	9.51	40.86	273.00
	6	4.260	8.33	45.19	344.21
	7	9.231	8.02	77.83	607.31
	8	11.489	7.77	88.94	721.05
	9	13.104	7.91	99.88	779.53
	10	13.789	6.74	83.65	908.31
	11	21.201	6.63	116.09	1209.25
	12	29.872	6.49	148.75	1532.84
	13	38.273	6.11	173.60	1865.85
0.30	1	0.872	13.49	21.98	93.84
	2	1.054	10.43	22.52	131.00
	3	1.916	8.09	32.41	246.44
	4	2.970	7.35	42.54	364.53
	5	3.561	6.96	47.10	432.63
	6	4.222	6.69	51.91	504.02
	7	5.032	6.59	58.49	578.11

* obtained with batch number two

TABLE C.3 (continued)

Capillary I.D. (cm)	Run No.	$\Delta P_c \times 10^{-4}$ (dyn/cm ²)	ϕ_t	ϵ_t	N'_{Re}
0.30	8	5.740	6.31	62.26	655.00
	9	7.064	6.62	75.57	734.14
	10	7.743	6.26	76.48	815.51
	11	9.056	6.38	87.27	899.03
	12	10.200	6.31	93.95	984.53
	13	11.868	6.80	97.81	1160.78
	14	14.103	5.59	109.52	1343.36
	15	17.452	5.71	126.90	1531.31
	16	19.237	5.29	122.20	1724.41

TABLE C.4

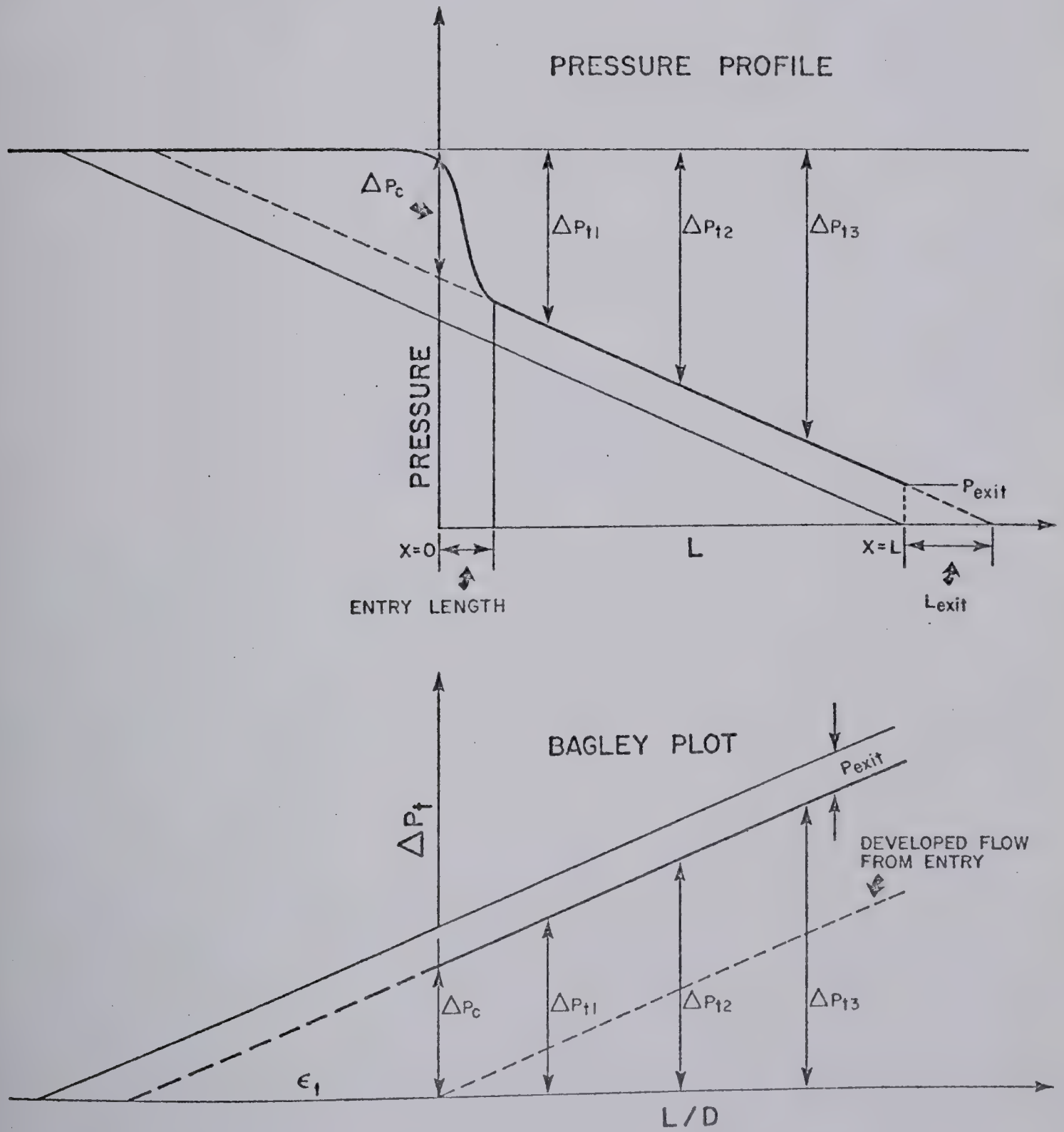
CONTRACTION LOSSES AND REYNOLDS NUMBERS FOR
0.20% SEPARAN AP-30, LARGE RESERVOIR

Capillary I.D. (cm)	Run No.	$\Delta P_c \times 10^{-4}$ (dyn/cm ²)	ϕ_t	ε_t	N'_{Re}
0.10	1	1.377	16.83	16.98	62.59
	2	2.324	19.73	26.41	81.20
	3	3.195	15.30	30.52	121.56
	4	3.943	12.05	32.31	165.92
	5	5.288	10.34	37.03	224.72
	6	7.166	9.73	44.95	286.49
	7	8.398	8.39	46.73	350.53
	8	10.038	7.67	51.09	416.26
	9	12.054	7.28	56.32	483.36
	10	14.171	6.93	62.23	551.32
	11	15.995	6.46	64.21	619.97
	11	17.535	7.08	68.55	619.97
	12	23.612	8.00	90.54	689.96
	13	28.235	7.04	94.09	828.20
	14	36.134	6.11	102.71	1036.99
0.20	1	0.938	11.46	17.55	90.95
	2	1.251	9.79	20.75	126.36
	3	1.846	10.03	28.30	164.99
	4	2.413	8.39	32.35	228.04
	5	2.862	7.75	35.62	273.00
	6	3.459	6.76	38.69	344.21
	7	6.143	5.34	51.26	607.31
	8	7.558	5.11	59.04	721.05
	8	8.997	6.09	71.82	721.05
	9	8.741	5.28	68.41	779.53
	9	9.896	5.97	77.00	779.53
	10	9.807	4.79	70.96	898.75
	10	11.523	5.63	83.59	898.75
	11	16.081	5.03	95.38	1209.25
	12	23.269	5.06	127.74	1532.84
	13	29.651	4.73	140.12	1865.85
0.30	1	0.416	6.43	9.95	93.84
	2	0.657	6.50	14.06	131.00
	3	1.201	5.07	20.38	246.44
	4	1.918	4.75	27.72	364.53
	5	2.457	4.80	33.41	432.63
	6	3.176	5.03	41.03	504.02
	7	3.437	4.50	41.19	578.11
	8	4.036	4.44	46.26	655.00
	9	4.390	4.11	47.15	734.14

TABLE C.4 (continued)

Capillary I.D. (cm)	Run No.	$\Delta P_c \times 10^{-4}$ (dyn/cm ²)	ϕ_t	ϵ_t	N'_{Re}
0.30	10	5.344	4.32	55.55	815.51
	10	5.508	4.45	54.64	815.51
	11	6.451	4.54	64.22	873.00
	12	6.933	4.29	66.57	984.53
	12	7.201	4.46	68.62	984.53
	13	8.266	4.04	71.34	1160.78
	14	9.649	3.82	71.57	1343.36
	15	12.780	4.18	98.64	1531.31
	16	14.499	3.99	102.90	1724.41
	16	12.569	3.46	89.20	1724.41

FIGURE C.1
PRESSURE PROFILE & BAGLEY PLOT



APPENDIX D
PHYSICAL PROPERTIES

D.1 NEWTONIAN SOLUTIONS

The shear stresses and the corresponding shear rates for each experimental run are tabulated in Table D.1. The shear stresses were obtained from the slope of the Bagley plots as discussed in Appendix C. For the duration of a complete experimental run, i.e., obtaining the total pressure losses for several tube lengths used to construct a Bagley plot, the temperature of each solution fluctuated by as much as $\pm 1^\circ\text{F}$. This temperature fluctuation is typical of that which occurred between experimental runs. Therefore, for each solution an average viscosity was determined by summing up the viscosities from each experimental run and dividing by the number of experimental runs. The viscosities for each experimental run are plotted in Figure D.1. The average viscosity and mean temperature for each Newtonian solution is given in Table D.2. These average values of viscosity were used in evaluating the Reynolds number. The viscosity of each Newtonian solution was measured with an Ostwald viscometer at the mean temperature and at $\pm 1^\circ\text{F}$ of the mean temperature. The results are also reported in Table D.2. Acceptable agreement was obtained between the measured and experimental values.

The density of each Newtonian fluid was determined to be insensitive to temperature fluctuations of $\pm 1^\circ\text{F}$ of the mean temperature, hence was assumed constant. The densities are reported in Table D.2.

D.2 VISCOELASTIC SOLUTION

The flow curve for the aqueous 0.20% solution of Separan AP-30 at high apparent shear rates is given in Figure D.2 while that at apparent shear rates less than 2 sec^{-1} is shown in Figure D.3. The solid line through the data in Figure D.2 was determined by the least squares criterion to be

$$\begin{aligned} \ln \tau_w = & 0.99765 + 0.52691 \left[\ln \left(\frac{8V}{D} \right) \right] + 0.03464 \left[\ln \left(\frac{8V}{D} \right)^2 \right] \\ & - 0.00844 \left[\ln \left(\frac{8V}{D} \right)^3 \right] + 0.00053 \left[\ln \left(\frac{8V}{D} \right)^4 \right] \end{aligned} \quad \text{D.1}$$

where $(8V/D)$ is the apparent shear rate. Equation D.1 adequately represents the data for apparent shear rates greater than unity. Data plotted in Figure D.2 were obtained from both reservoirs (S and L) and the shear stresses were, as expected, independent of reservoir size. The Weissenberg rheogoniometer was used to measure shear stresses at apparent shear rates less than 426 sec^{-1} . These data superimpose upon the data obtained from the Bagley plots. Two batches of 0.20% aqueous polymeric solution of Separan AP-30 were used in this research and as shown in Figure D.2 there were no significant differences in the shear stresses for overlapping apparent shear rates, i.e., apparent shear rates greater than 3 sec^{-1} .

Since the shear stresses were independent of reservoir size, physical properties summarized in Tables D.3 and D.4 were arbitrarily chosen from the data obtained with

batch 2 in reservoir S and batch 1 in reservoir L. The flow behaviour index tabulated in Tables D.3 and D.4 is equal to the derivative of Equation D.1 and is given by

$$n' = \frac{d(\ln \tau_w)}{d \ln \left(\frac{8V}{D}\right)} = 0.52691 + 0.06928 \left[\ln \left(\frac{8V}{D}\right) \right] - 0.02532 \left[\ln \left(\frac{8V}{D}\right)^2 \right] + 0.00212 \left[\ln \left(\frac{8V}{D}\right)^3 \right] \quad D.2$$

The apparent viscosities determined by Equation D.3

$$\mu_A = \tau_w / \left(\frac{8V}{D}\right) \quad D.3$$

and plotted in Figure D.4, resulted in the zero shear apparent viscosity being equal to 5.2 poise.

The thrust apparatus and the Weissenberg rheogoniometer were used to measure the first normal stress difference. The calibration curve for the normal force spring used with the Weissenberg rheogoniometer, 5 cm diameter 2° cone, discussed in Appendix A, resulted in a sensitivity of 194.040 dyn/cm² per volt at 68±1°F. For a given apparent shear rate the inertial contribution to the normal force measurements was subtracted from the total force exerted by the polymer solution. This inertial correction was determined by a Newtonian fluid having a viscosity of 5 poise. The inertial correction factor plotted in Figure D.5 was essentially zero for apparent shear rates less than 10² sec⁻¹. For apparent shear rates greater than this, the inertial correction increased to a maximum of 7.840 dyn/cm² at an apparent shear

rate of 850 sec^{-1} . The resulting first normal stress differences, given in Table D.5, are plotted in Figure D.6. The solid lines in Figure D.6 were determined by the least squares criterion, and for batches 1 and 2 were

$$\ln(P_{11}-P_{22})_w = 0.6178 + 1.013[\ln(\frac{8V}{D})] \quad \text{D.4}$$

and

$$\ln(P_{11}-P_{22})_w = 0.7204 + 1.024[\ln(\frac{8V}{D})] \quad \text{D.5}$$

These data indicate no significant differences in the first normal stress difference between batches 1 and 2 and are in agreement with the extrapolation of the data obtained from the rheogoniometer.

In SLSF the relaxation time of the fluid using a Maxwell model (116) is defined as

$$\theta = \frac{(P_{11}-P_{22})_w}{2(\frac{8V}{D})\tau_w} \quad \text{D.6}$$

The relaxation times determined by Equation D.6 and the data in Table D.5 are plotted in Figure D.7. The zero shear relaxation time, θ_0 , was somewhat greater than 0.4 sec which was measured at an apparent shear rate approximately equal to 10 sec^{-1} . Hlavacek (83) estimated the zero shear relaxation time to be 1 sec and it was this value that was used in the analysis presented in Chapter III. The zero shear relaxation time calculated by Bueche's analysis (118) was equal to 0.40 sec.

The tables and figures contained in Appendix D are listed below:

<u>TABLE NO.</u>	<u>DESCRIPTION</u>
D.1	Shear Stress - Shear Rate for Newtonian Solutions
D.2	Viscosity and Density, Newtonian Solutions
D.3	Physical Properties of 0.20% Separan AP-30; Batch 2, Small Reservoir
D.4	Physical Properties of 0.20% Separan AP-30; Batch 1, Large Reservoir
D.5	Normal Force Data

<u>FIGURE NO.</u>	<u>DESCRIPTION</u>
D-1	Newtonian Viscosities
D-2	Flow Curve 0.20% Separan AP-30, High Apparent Shear Rates
D-3	Flow Curve 0.20% Separan AP-30, Low Apparent Shear Rates
D-4	Apparent Viscosity, 0.20% Separan AP-30
D-5	Internal Contribution to Normal Force (Rheogonimeter)
D-6	Normal Stress
D-7	Relaxation Time

TABLE D.1

SHEAR STRESS - SHEAR RATE FOR
NEWTONIAN SOLUTIONS

SHEAR RATE (sec^{-1})

<u>Run No.</u>	<u>Sugar #1</u>	<u>Sugar #3</u>	<u>Sugar #4</u>	<u>Primol-355</u>
1	1929	1350	1929	971
2	2909	1929	2515	1357
3	3858	2515	3107	1929
4	7741	3107	3858	2909
5	11705	5055	4838	3858
6	15517	7741	5812	4716
7	19213	10727	-	5446
8	23410	13560	-	-
9	-	17571	-	-
10	-	25416	-	-

LARGE RESERVOIR - SHEAR STRESS (dyn/cm^2)

<u>Run No.</u>	<u>Sugar #1</u> <u>(73.0°F)</u>	<u>Sugar #3</u> <u>(72.0°F)</u>	<u>Sugar #4</u> <u>(72.0°F)</u>	<u>Primol-355</u> <u>(73.5°F)</u>
1	172	-	1089	1544
2	258	351	1427	2165
3	336	454	1776	3075
4	677	553	2225	4753
5	1048	888	2830	6129
6	1431	1431	3423	7467
7	1774	1839	-	8694
8	2175	-	-	-
9	-	-	-	-
10	-	-	-	-

TABLE D.1 (continued)

SMALL RESERVOIR - SHEAR STRESS (dyn/cm²)

<u>Run No.</u>	<u>Sugar #1 (72.5°F)</u>	<u>Sugar #3 (72.0°F)</u>	<u>Sugar #4 (73.5°F)</u>	<u>Primol-355 (73.0°F)</u>
1	173	239	1190	1588
2	259	343	1527	2254
3	343	445	1914	3189
4	716	556	2318	4812
5	1090	913	2890	6348
6	1448	1437	3573	7581
7	1799	1862	-	8687
8	2174	2400	-	-
9	-	3190	-	-
10	-	4606	-	-

TABLE D.2

VISCOCITY AND DENSITY
NEWTONIAN SOLUTIONS

SOLUTIONS

<u>Sugar #1</u>	<u>Sugar #3</u>	<u>Sugar #4</u>	<u>Primol-355</u>
-----------------	-----------------	-----------------	-------------------

SMALL RESERVOIR

Mean Temperature (°F)	72.5	72.0	71.5	73.0
Average Viscosity (cp)	9.16	17.92	60.60	163.62
*Ostwald Viscometer (cp)	9.4±.25	17.60±.5	59.0±2	171.75±6.5
Density (gm/cm ³)	1.205	1.241	1.296	0.876

LARGE RESERVOIR

Mean Temperature (°F)	73.0	72.0	72.0	73.5
Average Viscosity (cp)	8.99	17.87	57.30	159.76
*Ostwald Viscometer (cp)	9.3±.25	17.60±.5	58±2	168.5±6.5
Density (gm/cm ³)	1.205	1.241	1.296	0.876

*Viscosity determined at the mean temperature and at ±1°F of the mean temperature

TABLE D.3

PHYSICAL PROPERTIES OF 0.20% SEPARAN AP-30

BATCH 2 - SMALL RESERVOIR

Capillary I.D. (cm)	Run No.	τ_w (dyn/cm ²)	$\frac{8V}{D}$ (sec ⁻¹)	n'
0.10	15	182	2427	.542
	16	158	1618	.520
	17	110	809	.498
	18	73.5	324	.494
	19	63.0	243	.497
	20	43.9	121	.511
	21	30.5	80.9	.522
	22	19.2	40.5	.542
0.20	14	104	810	.498
	15	72.7	405	.493
	16	65.2	304	.495
	17	50.3	202	.500
0.30	17	84.8	600	.494
	18	77.9	480	.493
	19	57.9	240	.497
	20	41.8	120	.511
	21	39.3	90	.519
	22	29.5	60	.530
	23	5.98	4.5	.583
	24	4.35	3	.579
	25	9.17	9	.579
	26	11.0	12	.574
	27	19.9	30	.551
	28	34.4	90	.519
	29	37.9	120	.511

TABLE D.4

PHYSICAL PROPERTIES OF 0.20% SEPARAN AP-30

BATCH 1 - LARGE RESERVOIR

Capillary I.D. (cm)	Run No.	τ_w (dyn/cm ²)	$\frac{8V}{D}$ (sec ⁻¹)	n'
0.10	1	203	3236	.562
	2	220	3883	.577
	3	262	5169	.604
	4	305	6472	.628
	5	357	8091	.655
	6	399	9708	.680
	7	449	11327	.702
	8	491	12944	.723
	9	535	14563	.742
	10	569	16180	.760
	11	623	17799	.777
	12	652	19437	.793
	13	750	22653	.822
	14	879	27507	.862
0.20	1	134	1618	.520
	2	151	2023	.531
	3	163	2427	.542
	4	186	3034	.557
	5	201	3438	.567
	6	223	4045	.580
	7	300	6068	.621
	8	320	6877	.635
	9	319	7281	.642
	10	345	8090	.655
	11	421	10113	.686
	12	455	12135	.713
	13	529	14158	.737
0.30	1	104	959	.502
	2	117	1199	.508
	3	147	1836	.523
	4	173	2397	.541
	5	184	2697	.549
	6	193	2996	.556

TABLE D.4 (continued)

Capillary I.D. (cm)	Run No.	τ_w (dyn/cm ²)	$\frac{8V}{D}$ (sec ⁻¹)	n'
0.30	7	209	3296	.563
	8	218	3596	.570
	9	233	3895	.577
	10	241	4195	.584
	11	251	4495	.585
	12	260	4794	.586
	13	290	5394	.608
	14	337	5993	.620
	15	324	6592	.630
	16	352	7191	.641

TABLE D.5

NORMAL FORCE DATA

Capillary I.D. (cm)	L/D	$\frac{8V}{D}(\text{sec}^{-1})$	$(P_{11}-P_{22})_w$ (dyn/cm ²)
0.4452*	196	3667	11232
		3300	9901
		2933	10513
		2567	6272
		2200	3952
		1833	3590
		1466	3483
		1100	2566
		733	2804
		2933	7120
		3300	6527
		1466	2601
0.2076*	294	10850	27354
		9042	22552
		7233	18710
		6510	15009
		6148	10361
		5425	6745
		5063	10089
		4701	4712
		3616	4687
		7233	14971
		4340	8888
		3978	11972
		3616	6231
0.0861*	268	50664	131906
		45598	103658
		40531	77835
		35465	60554
		30398	43687
		25332	56133
		20265	50614
		45598	103658
		50664	131906

* Data obtained with batch number one

TABLE D.5 (continued)

Capillary I.D. (cm)	L/D	$\frac{8V}{D}(\text{sec}^{-1})$	$(P_{11}-P_{22})_w$ (dyn/cm ²)
Rheogonimeter*		8.48	60
		13.5	40
		26.5	128
		42.6	115
		84.8	204
		135	240
		265	368
		426	460
0.4452**	196	3667	7962
		3300	9981
		2933	10581
		2567	8037
		2200	5719
		1833	4490
		1466	3499
		1100	3277
		1466	2799
0.2076**	294	10850	20009
		9042	29360
		8138	17231
		7233	22564
		6510	18859
		5787	8396
		5063	8610
		4701	12389
		4340	11996
		9946	26032
		2531	10000
0.0861**	268	50664	142534
		45598	108029
		40531	98636
		35465	114611
		30398	72953
		25332	39796
		35465	81428
		50664	142534

* Data obtained with batch number one

** Data obtained with batch number two

FIGURE D - 1
NEWTONIAN VISCOSITIES

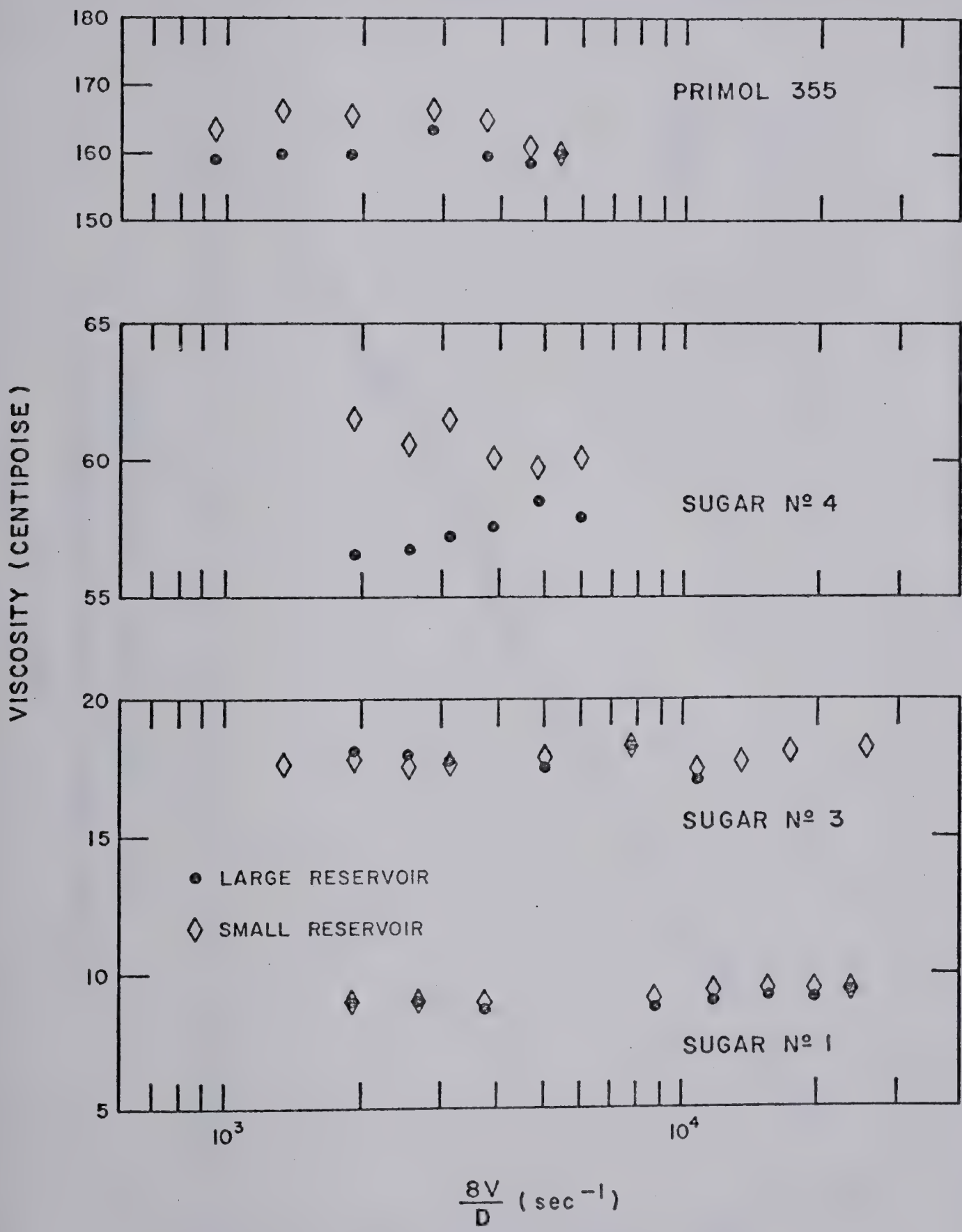


FIGURE D-2
FLOW CURVE, 0.20% SEPARAN AP-30
HIGH APPARENT SHEAR RATES

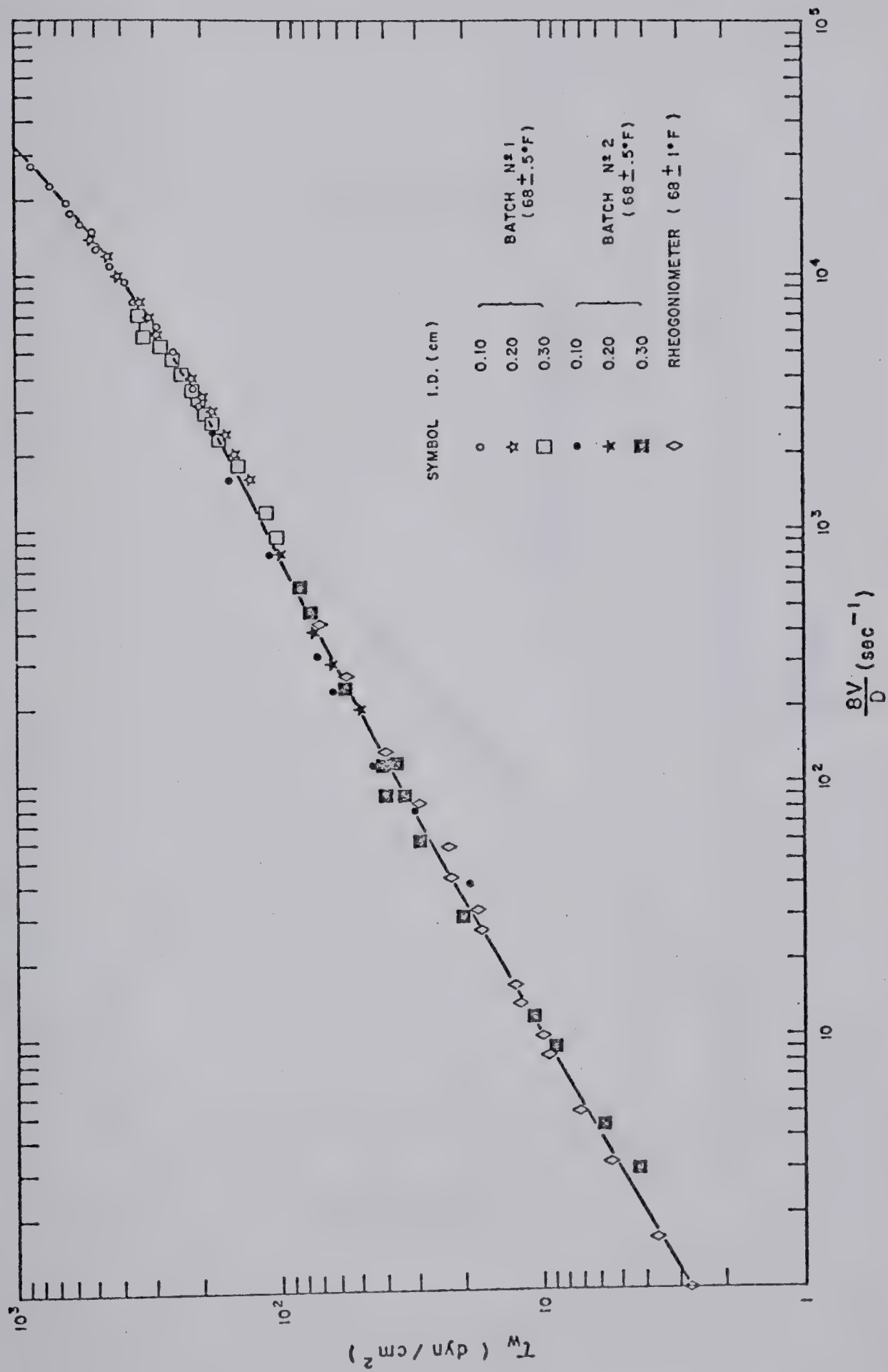


FIGURE D - 3
 FLOW CURVE, 0.20% SEPARAN AP-30
 LOW APPARENT SHEAR RATES

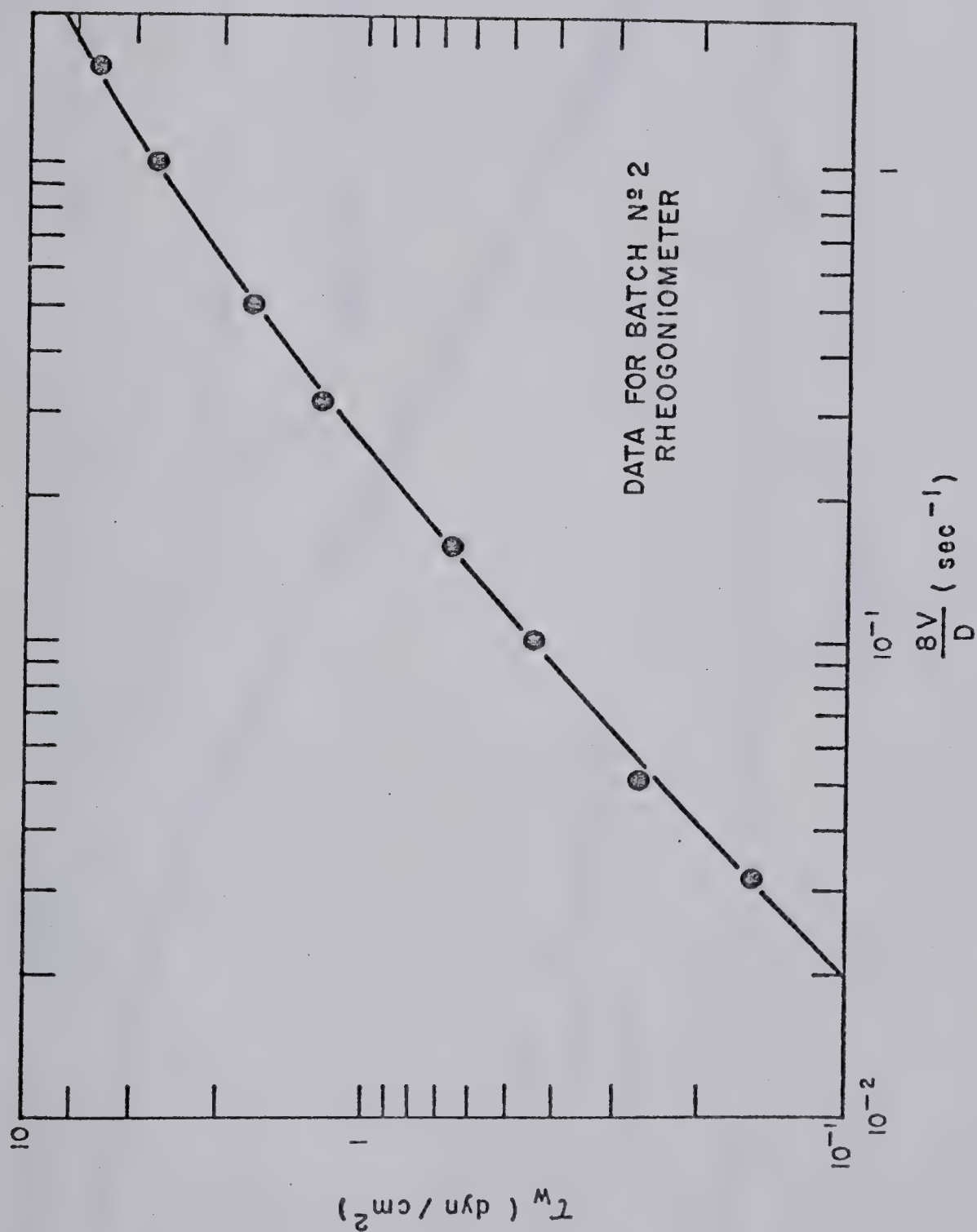
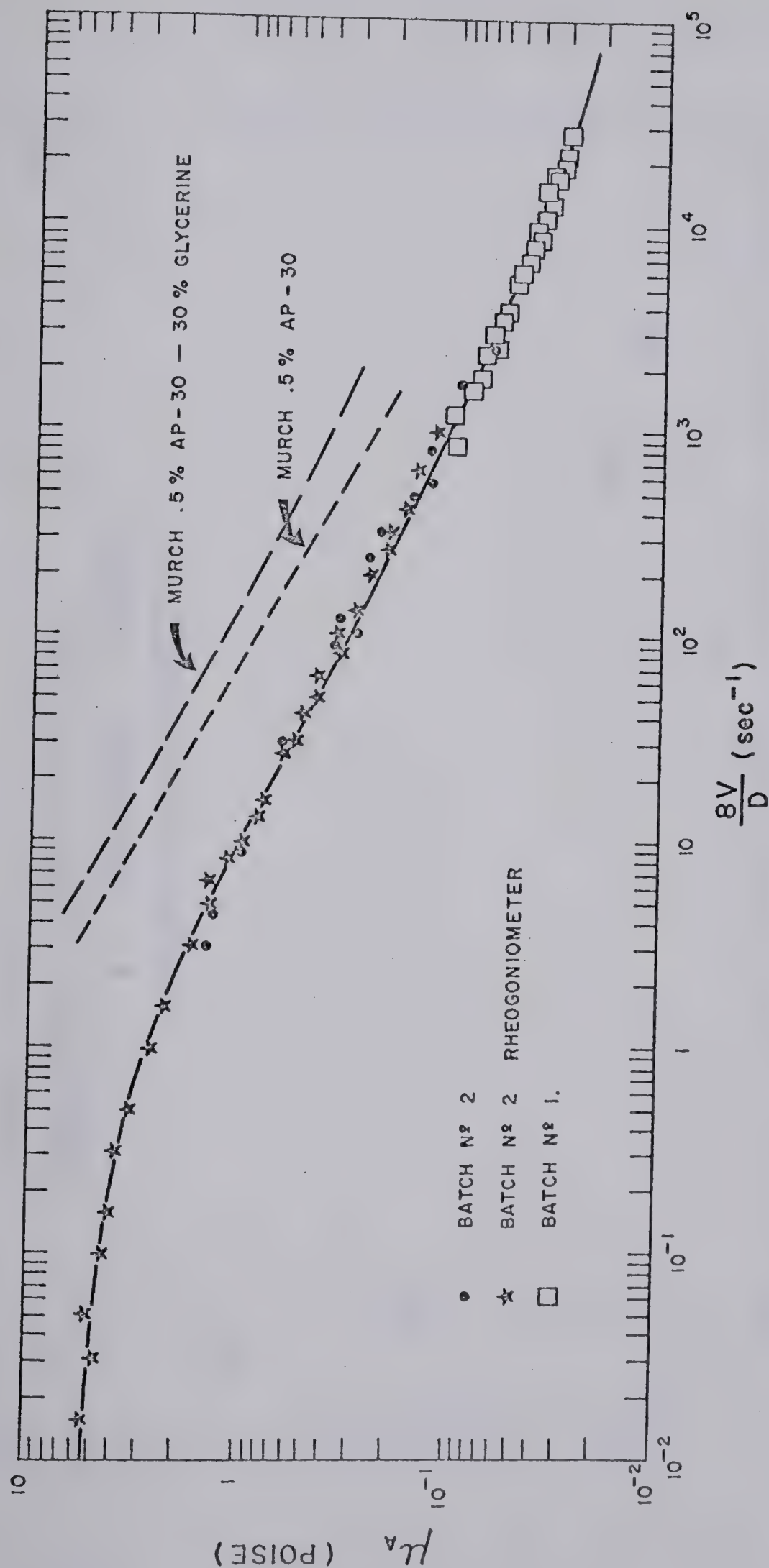
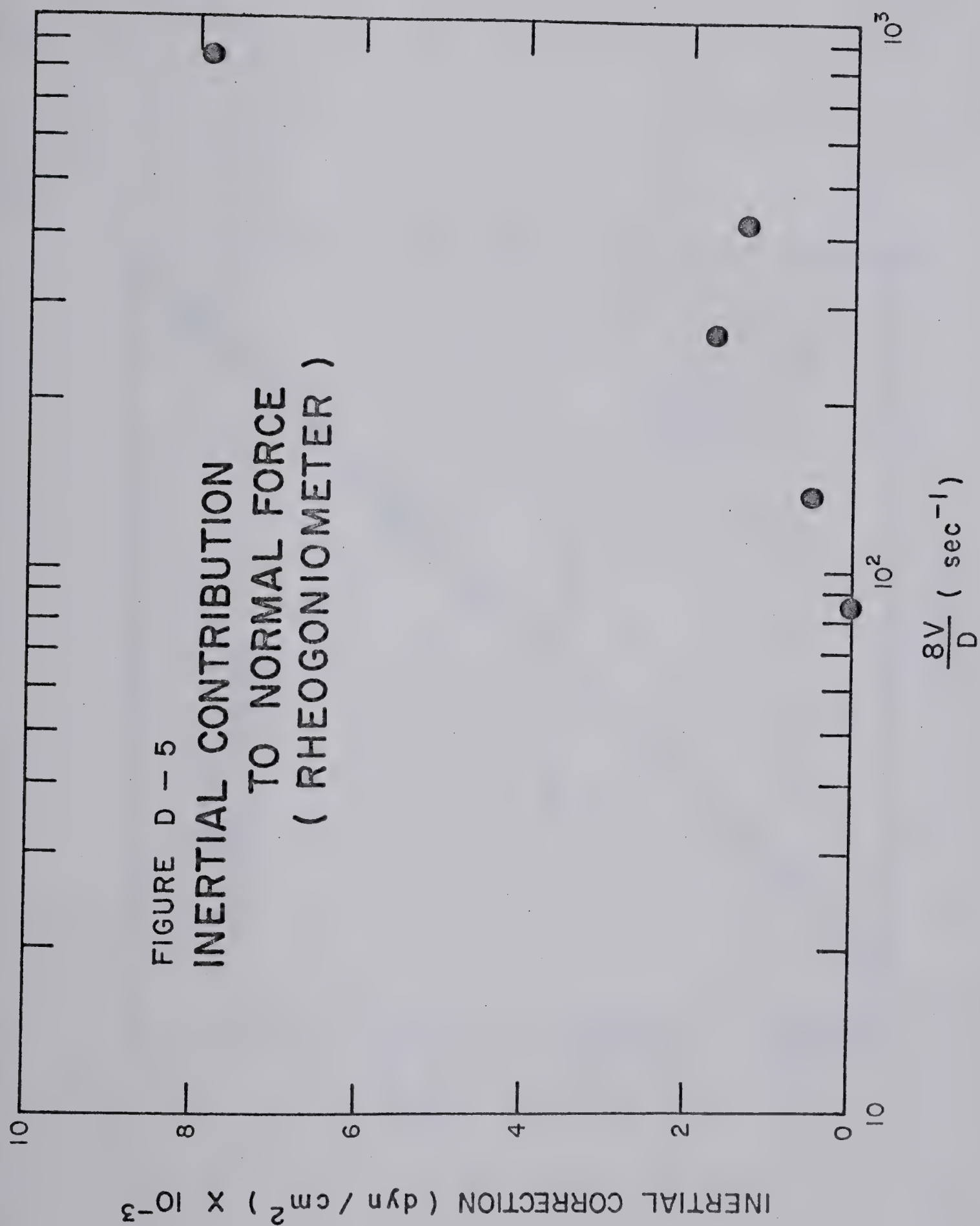


FIGURE D-4
 APPARENT VISCOSITY, 0.20% SEPARAN AP-30





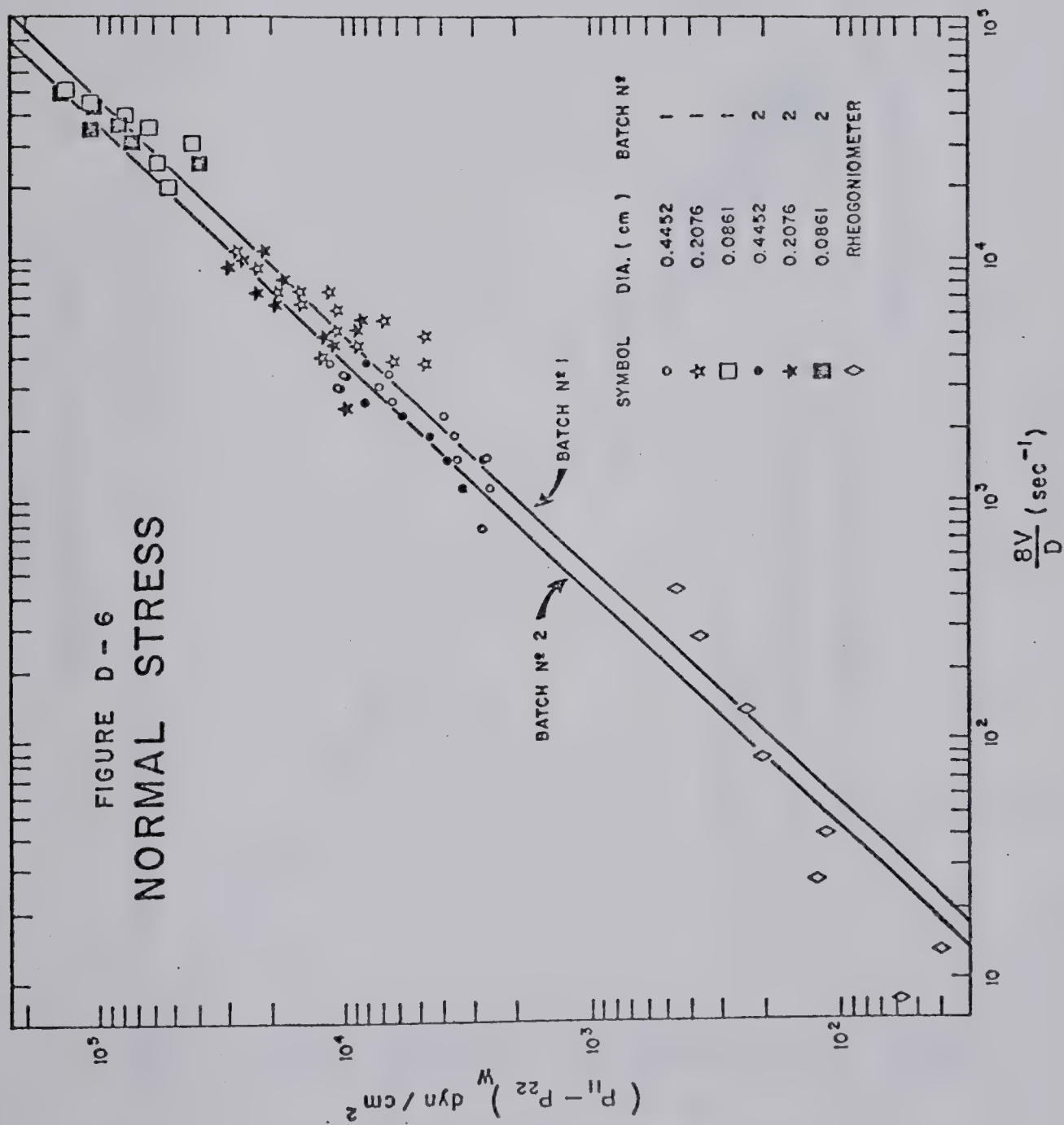
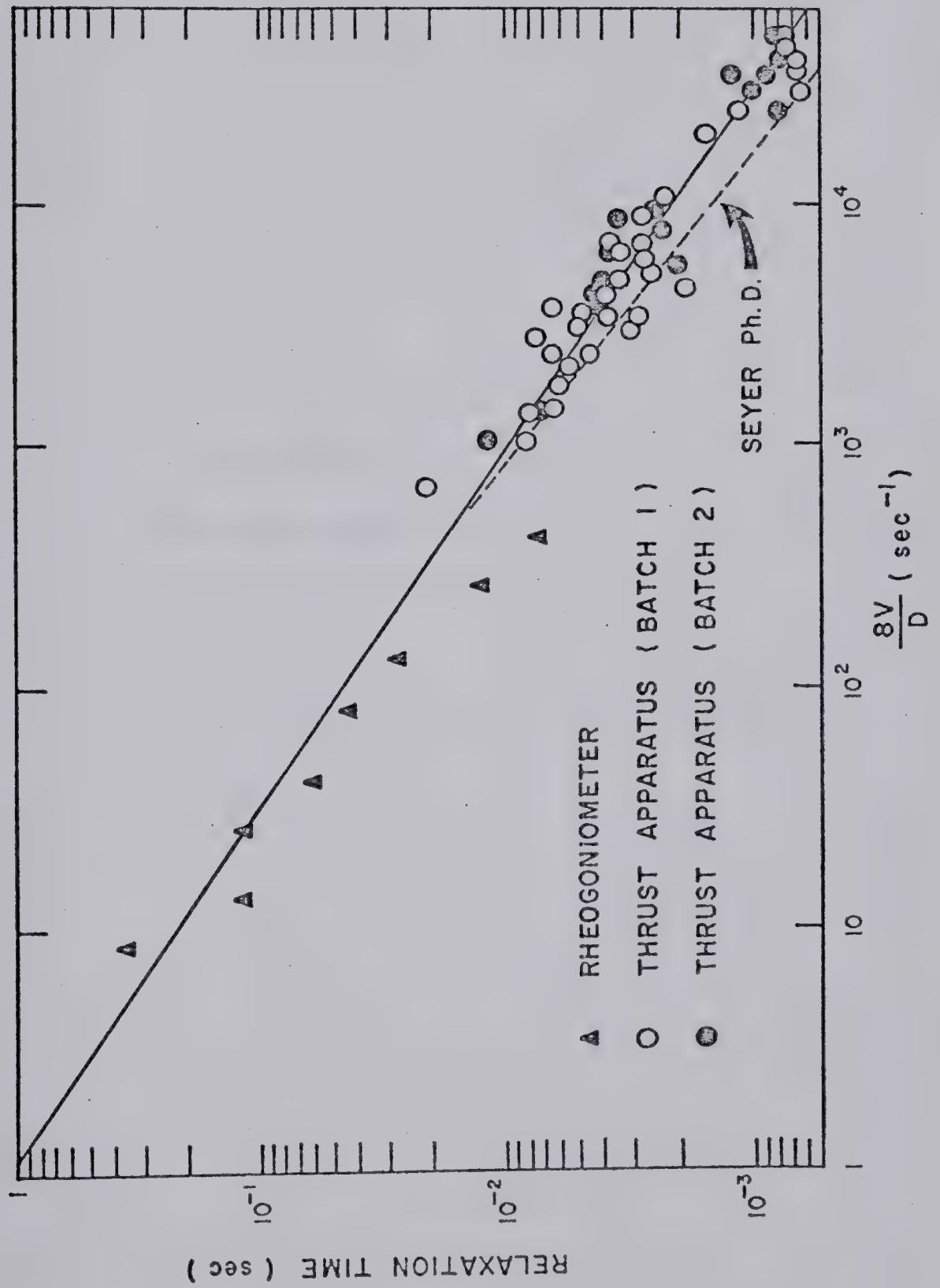


FIGURE D-7
RELAXATION TIME



APPENDIX E
VELOCITY PROFILES

E.1 AXIAL VELOCITY PROFILES - DIRECT METHOD

Contained in this section are axial velocities measured at several upstream axial locations for various flow rates and with the three capillary tubes in reservoirs S and L. The method used, the projection of the film directly on to graph paper graduated in 0.10 inches, was discussed in Chapter II. The errors associated with this technique are given in Appendix G.

Since the velocity profiles were axially symmetric, radial locations can be measured relative to an arbitrary reference. The following was used to determine the radial location of a velocity observation: Consider the first two entries in Table E.1 where the centerline corresponds to 12.45 inches. The radial distance between the first two entries under the column labeled "Axial velocity" is

$$\frac{(12.35-12.20)}{24.50} \text{ inches} \times 2.54 \text{ cm/inch} = 0.0155 \text{ cm}$$

where 24.50 is the magnification.

The following lists the tables as they are presented in this section as well as listing the appropriate magnification for each table:

TABLE NO.	RESERVOIR	MAGNIFICATION	I.D. (cm)	L/D	Q (cm ³ /sec)
E.1	Small	24.50	0.10	55.08	0.016
E.2	Small	24.50	0.10	55.08	0.040
E.3	Small	24.50	0.10	55.08	0.119
E.4	Small	24.50	0.20	54.96	0.040
E.5	Small	24.50	0.20	54.96	0.238
E.6	Small	24.50	0.20	54.96	0.318
E.7	Small	24.50	0.30	55.04	0.040
E.8	Small	24.50	0.30	55.04	0.318
E.9	Small	24.50	0.30	55.04	0.635
E.10	Large	18.00	0.20	54.96	0.159
E.11	Large	18.00	0.20	54.96	0.318
E.12	Large	18.00	0.20	54.96	0.794
E.13	Large	8.22	0.20	54.96	1.589
E.14	Large	18.00	0.30	55.04	0.318
E.15	Large	18.00	0.30	55.04	0.635
E.16	Large	18.00	0.30	55.04	1.589

TABLE E.1

AXIAL VELOCITY DATA, 0.10 cm I.D. CAPILLARY
 $Q=0.016 \text{ cm}^3/\text{sec}$, SMALL RESERVOIR

Axial Location (No. of Dia.)	Radial Location (in)	Axial Velocity (cm/sec)
0.0 ($\phi=12.45$ in)	12.20	1.62
	12.35	1.90
	12.45	2.30
	12.60	1.90
	12.70	1.62
	12.75	1.48
1.0 ($\phi=12.45$ in)	11.70	0.39
	12.15	1.40
	12.30	1.65
	12.40	2.00
	12.65	1.65
	12.70	1.40
	12.80	1.23
	13.10	0.55
2.0 ($\phi=12.45$ in)	13.20	0.45
	11.70	0.43
	11.85	0.86
	12.10	1.18
	12.25	1.33
	12.40	1.70
	12.60	1.33
	12.75	1.18
	12.85	0.96
	13.00	0.68
	13.15	0.56
3.0 ($\phi=12.45$ in)	13.25	0.43
	11.75	0.39
	12.05	0.90
	12.25	1.05
	12.35	1.25
	12.60	1.05
	12.65	1.05
	12.80	0.90
	12.90	0.73
	13.05	0.58
	13.25	0.47
	13.30	0.38

TABLE E.1 (continued)

Axial Location (No. of Dia.)	Radial Location (in)	Axial Velocity (cm/sec)
4.0 (ϕ = 12.45 in)	11.30	0.27
	11.65	0.47
	12.00	0.68
	12.20	0.77
	12.35	0.83
	12.55	0.77
	12.65	0.77
	12.80	0.68
	13.15	0.47
	13.35	0.37
	13.45	0.32
	13.65	0.24
6.0 (ϕ = 12.45 in)	10.90	0.15
	11.40	0.25
	11.85	0.32
	12.10	0.37
	12.30	0.37
	12.75	0.37
	13.00	0.32
	13.25	0.26
	13.40	0.25
	13.75	0.20
	13.85	0.18
7.0 (ϕ = 12.45 in)	10.60	0.12
	11.15	0.16
	11.65	0.20
	12.05	0.23
	12.25	0.22
	12.75	0.22
	12.85	0.24
	13.10	0.21
	13.40	0.20
	13.65	0.16
	14.00	0.16
8.0 (ϕ = 12.45 in)	10.25	0.08
	10.90	0.12
	11.45	0.16
	12.00	0.18
	12.25	0.17
	12.80	0.16
	13.05	0.16
	13.85	0.11
	14.30	0.10

TABLE E.2

AXIAL VELOCITY DATA, 0.10 cm I.D. CAPILLARY
 $Q=0.040 \text{ cm}^3/\text{sec}$, SMALL RESERVOIR

Axial Location (No. of Dia.)	Radial Location (in)	Axial Velocity (cm/sec)
1.0 ($\phi = 12.55 \text{ in}$)	11.60	0.10
	12.35	4.80
	12.60	5.25
	12.80	4.25
	12.90	2.60
	13.15	0.45
2.0 ($\phi = 12.55 \text{ in}$)	11.75	0.55
	12.30	4.25
	12.45	4.60
	12.65	4.60
	12.80	4.10
	13.05	2.35
	13.30	0.95
	13.65	0.20
3.0 ($\phi = 12.55 \text{ in}$)	11.70	0.80
	12.30	3.70
	12.65	4.00
	12.75	4.00
	12.80	3.60
	12.95	2.10
	13.35	1.15
	13.60	0.50
4.0 ($\phi = 12.55 \text{ in}$)	11.65	0.90
	12.25	3.25
	12.30	3.40
	12.35	3.40
	12.65	3.40
	12.75	3.25
	12.85	2.65
	13.00	1.90
	13.40	1.15
	13.60	0.45
6.0 ($\phi = 12.55 \text{ in}$)	10.75	0.30
	11.60	1.80
	12.20	2.20
	12.35	2.30
	12.50	2.30
	12.70	2.30

TABLE E.2 (continued)

Axial Location (No. of Dia.)	Radial Location (in)	Axial Velocity (cm/sec)
	12.80	2.30
	12.85	1.85
	13.15	1.55
	13.55	1.05
	13.70	0.50
8.0 (ϕ =12.55 in)	10.10	0.18
	10.55	0.22
	11.40	0.65
	11.90	1.30
	12.30	1.65
	12.45	1.60
	12.75	1.60
	12.85	1.60
	13.00	1.25
	13.20	1.15
	13.70	0.75
	13.90	0.55
	14.05	0.40
10.0 (ϕ =12.55 in)	9.85	.16
	10.35	.25
	11.10	.47
	11.75	.79
	12.05	.94
	12.25	.94
	12.35	1.09
	12.40	1.08
	12.45	1.04
	13.35	.76
	13.95	.50
	14.15	.42
	14.30	.32
12.0 (ϕ =12.55 in)	10.85	.33
	11.55	.45
	11.90	.53
	12.15	.56
	12.25	.59
	12.40	.61
	12.50	.62
	12.65	.62
	12.95	.56
	13.20	.52
	13.55	.47

TABLE E.2 (continued)

Axial Location (No. of Dia.)	Radial Location (in)	Axial Velocity (cm/sec)
14.0 (ϕ = 12.55 in)	10.40	.20
	11.25	.28
	11.70	.31
	12.00	.33
	12.20	.34
	12.35	.35
	12.45	.36
	12.55	.36
	12.95	.35
	13.40	.34
	13.90	.33
16.0 (ϕ = 12.55 in)	10.85	.17
	11.45	.20
	11.85	.19
	12.05	.20
	12.50	.19
	12.60	.21
	15.00	.14

TABLE E.3

AXIAL VELOCITY DATA, 0.10 cm I.D. CAPILLARY
 $Q=0.119 \text{ cm}^3/\text{sec}$, SMALL RESERVOIR

Axial Location (No. of Dia.)	Radial Location (in)	Axial Velocity (cm/sec)
2.0 ($\phi=12.55$ in)	12.30	12.00
	12.45	18.40
	12.70	18.30
	12.95	10.80
	13.20	5.60
4.0 ($\phi=12.55$ in)	12.25	10.00
	12.45	14.80
	12.70	14.60
	12.95	9.30
	13.20	4.90
	13.65	0.90
	13.95	0.50
8.0 ($\phi=12.55$ in)	13.55	0.10
	10.90	0.80
	12.10	6.90
	12.35	8.80
	12.65	9.20
	12.75	8.70
	13.05	7.70
	13.00	5.90
	13.25	3.80
	13.75	1.30
12.0 ($\phi=12.55$ in)	13.95	1.00
	14.10	0.80
	14.35	0.50
	10.80	1.00
	11.85	4.40
	12.00	4.40
	12.35	6.00
	12.85	6.00
	13.10	4.80
	13.40	2.90
16.0 ($\phi=12.55$ in)	13.90	1.30
	14.05	1.10
	14.35	0.80
	14.55	0.60
	10.00	0.60
	10.55	0.70
	11.45	2.10
	11.70	2.80

TABLE E.3 (continued)

Axial Location (No. of Dia.)	Radial Location (in)	Axial Velocity (cm/sec)
	12.25	3.70
	12.65	3.70
	12.95	3.40
	13.35	2.35
	13.55	1.90
	13.65	1.60
	14.25	0.90
	14.75	0.60
20.0	9.60	0.40
(ϕ =12.55 in)	10.65	1.02
	11.15	1.28
	11.40	1.68
	11.80	1.96
	12.15	2.08
	12.65	2.20
	13.25	1.65
	13.70	1.36
	14.00	1.06
24.0	8.45	0.21
(ϕ =12.55 in)	9.90	0.65
	10.45	0.75
	10.60	0.80
	11.50	1.04
	11.75	1.17
	12.00	1.04
	12.75	1.08
	13.55	0.96
	14.05	0.80
28.0	9.00	0.28
(ϕ =12.55 in)	9.60	0.34
	10.50	0.44
	11.10	0.46
	11.45	0.50
	11.75	0.53
	12.80	0.58
	14.00	0.43
	14.85	0.36
	15.00	0.33

TABLE E.4

AXIAL VELOCITY DATA, 0.20 cm I.D. CAPILLARY
 $Q=0.040 \text{ cm}^3/\text{sec}$, SMALL RESERVOIR

Axial Location (No. of Dia.)	Radial Location (in)	Axial Velocity (cm/sec)
0.5 ($\phi = 12.3 \text{ in}$)	11.15	0.24
	11.55	0.93
	11.72	1.40
	11.90	1.34
	12.10	1.42
	12.35	1.36
	12.50	1.40
	12.70	1.20
	13.10	0.64
	13.25	0.72
	13.55	0.30
1.0 ($\phi = 12.3 \text{ in}$)	10.85	0.16
	11.05	0.24
	11.45	0.63
	11.65	0.91
	11.85	1.02
	12.05	1.02
	12.10	1.09
	12.35	1.16
	12.37	1.21
	12.65	1.10
	12.75	0.90
	12.85	0.87
	13.05	0.76
	13.40	0.52
	13.45	0.49
	13.65	0.31
	13.75	0.18
2.0 ($\phi = 12.3 \text{ in}$)	10.65	0.18
	11.15	0.34
	11.45	0.47
	11.75	0.58
	11.95	0.58
	12.35	0.58
	12.55	0.62
	12.70	0.56
	12.95	0.49
	13.10	0.55
	13.40	0.51
	13.60	0.28
	13.75	0.24
	14.10	0.20

TABLE E.4 (continued)

Axial Location (No. of Dia.)	Radial Location (in)	Axial Velocity (cm/sec)
3.0 (ϕ =12.3 in)	11.20	0.10
	11.80	0.28
	12.50	0.32
	12.65	0.30
	13.25	0.24
	14.20	0.16
	14.75	0.13
4.0 (ϕ =12.3 in)	10.05	0.10
	10.80	0.13
	11.45	0.13
	11.60	0.16
	12.55	0.18
	12.60	0.18
	13.15	0.13
	13.70	0.13
	14.95	0.08
	15.70	0.06

TABLE E.5

AXIAL VELOCITY DATA, 0.20 cm I.D. CAPILLARY
 $Q=0.238 \text{ cm}^3/\text{sec}$, SMALL RESERVOIR

Axial Location (No. of Dia.)	Radial Location (in)	Axial Velocity (cm/sec)
2.0 ($\phi=12.80$ in)	11.05	0.75
	11.55	3.10
	11.85	4.40
	12.20	6.20
	12.45	7.80
	12.70	8.90
	13.05	7.80
	13.65	4.40
	13.80	2.35
	14.00	0.70
	14.80	0.25
4.0 ($\phi=12.80$ in)	10.20	0.40
	10.70	0.80
	11.40	2.45
	11.70	3.05
	12.10	4.25
	12.40	5.45
	12.65	5.60
	12.75	5.60
	12.85	5.60
	13.15	5.10
	13.90	3.03
	14.20	1.60
	14.65	0.75
	14.85	0.60
6.0 ($\phi=12.80$ in)	9.95	0.55
	11.05	1.65
	11.35	1.95
	11.85	2.60
	12.30	3.50
	12.65	3.55
	12.75	3.55
	12.85	3.55
	13.25	3.20
	14.45	1.15
	14.95	0.70
8.0 ($\phi=12.80$ in)	9.40	0.36
	10.15	0.74
	10.65	1.05
	11.65	1.60

TABLE E.5 (continued)

Axial Location (No. of Dia.)	Radial Location (in)	Axial Velocity (cm/sec)
10.0 (ϕ = 12.80 in)	12.20	2.15
	12.60	2.15
	12.70	2.15
	12.95	2.15
	13.40	1.95
	14.80	0.89
	15.05	0.89
	15.55	0.55
	9.30	0.44
	9.95	0.60
	11.05	0.80
	12.05	1.10
	12.50	1.10
	12.60	1.10
	13.00	1.10
	13.70	1.00
	15.86	0.46
	16.55	0.25

TABLE E.6

AXIAL VELOCITY DATA, 0.20 cm I.D. CAPILLARY
 $Q=0.318 \text{ cm}^3/\text{sec}$, SMALL RESERVOIR

Axial Location (No. of Dia.)	Radial Location (in)	Axial Velocity (cm/sec)
0.0 ($\phi = 12.70$ in)	12.10	9.30
	12.35	13.20
	12.70	14.40
	12.95	14.20
	13.05	13.80
	13.15	11.90
	13.30	11.60
	13.45	8.90
1.0 ($\phi = 12.70$ in)	11.35	1.30
	12.05	8.25
	12.15	11.80
	12.70	13.10
	12.90	12.80
	13.05	12.40
	13.20	10.60
	13.35	10.20
	13.50	7.90
	14.00	0.70
2.0 ($\phi = 12.70$ in)	11.10	1.10
	11.95	7.00
	12.25	10.20
	12.75	11.40
	12.90	11.20
	13.00	10.80
	13.15	8.90
	13.40	8.60
	13.60	6.70
	14.00	1.80
	14.25	1.60
	14.95	0.50
4.0 ($\phi = 12.70$ in)	10.45	0.80
	11.00	1.80
	11.25	1.35
	11.80	5.00
	12.15	7.35
	12.55	8.25
	12.75	8.15
	12.90	7.80
	13.10	6.20

TABLE E.6 (continued)

Axial Location (No. of Dia.)	Radial Location (in)	Axial Velocity (cm/sec)
	13.35	5.80
	13.50	4.70
	13.95	2.00
	14.15	1.90
	14.45	1.00
6.0 (ϕ =12.70 in)	10.25	0.80
	10.75	1.50
	11.05	1.77
	11.60	3.45
	12.05	4.95
	12.65	5.60
	12.95	5.60
	13.15	5.30
	13.40	4.15
	13.65	4.05
	13.90	3.10
	14.40	1.67
	14.60	1.57
	14.85	0.95
8.0 (ϕ =12.70 in)	9.85	0.74
	10.40	1.12
	10.70	1.35
	11.35	2.40
	11.85	3.35
	12.60	3.90
	12.95	3.80
	13.25	3.70
	13.55	2.90
	14.10	2.20
	14.75	1.30
	15.15	0.85
9.0 (ϕ =12.70 in)	9.55	0.63
	10.50	1.14
	11.20	1.85
	11.75	2.50
	12.00	2.70
	12.60	2.85
	13.00	2.90
	13.30	2.80
	13.65	2.20
	14.25	1.75
	14.95	1.05

TABLE E.6 (continued)

Axial Location (No. of Dia.)	Radial Location (in)	Axial Velocity (cm/sec)
11.0 (ϕ = 12.70 in)	9.45	0.57
	9.85	0.70
	10.70	1.16
	11.50	1.60
	11.80	1.52
	12.55	1.65
	13.05	1.65
	13.45	1.58
	13.90	1.27
	14.75	0.96
	15.45	0.58
12.0 (ϕ = 12.70 in)	8.95	0.42
	10.35	0.82
	11.25	1.02
	12.55	1.16
	12.65	1.13
	13.55	1.15
	14.10	0.95
	15.00	0.80

TABLE E.7

AXIAL VELOCITY DATA, 0.30 cm I.D. CAPILLARY
 $Q=0.040 \text{ cm}^3/\text{sec}$, SMALL RESERVOIR

Axial Location (No. of Dia.)	Radial Location (in)	Axial Velocity (cm/sec)
0.0 ($\phi = 12.50$ in)	11.65	0.48
	11.85	0.51
	12.10	0.60
	12.35	0.71
	12.65	0.71
	13.45	0.48
0.5 ($\phi = 12.50$ in)	10.85	0.127
	11.25	0.255
	11.50	0.332
	11.95	0.410
	12.25	0.50
	12.70	0.50
	13.45	0.385
	13.80	0.385
1.0 ($\phi = 12.50$ in)	10.10	0.072
	10.85	0.207
	11.70	0.255
	12.15	0.295
	12.70	0.295
	13.70	0.245
	14.15	0.163
1.5 ($\phi = 12.50$ in)	10.00	0.059
	11.45	0.160
	12.05	0.178
	12.75	0.178
	14.00	0.136
	14.65	0.106
2.0 ($\phi = 12.50$ in)	9.20	0.035
	11.15	0.092
	11.95	0.105
	12.80	0.105
	14.45	0.080
	15.30	0.060

TABLE E.8

AXIAL VELOCITY DATA, 0.30 cm I.D. CAPILLARY
 $Q=0.318 \text{ cm}^3/\text{sec}$, SMALL RESERVOIR

Axial Location (No. of Dia.)	Radial Location (in)	Axial Velocity (cm/sec)
0.0 ($\phi = 12.60$ in)	11.85	5.40
	12.20	5.90
	12.60	6.05
	12.85	5.90
	13.05	5.75
	13.20	5.50
	13.40	4.90
	13.90	1.60
0.5 ($\phi = 12.60$ in)	10.75	0.45
	11.45	3.27
	11.75	4.90
	12.15	5.32
	12.60	5.45
	12.85	5.40
	13.05	5.20
	13.20	4.90
	13.40	4.30
	14.00	1.56
	14.55	0.25
1.0 ($\phi = 12.60$ in)	10.25	0.31
	10.70	0.75
	11.35	3.00
	11.65	4.25
	12.15	4.75
	12.70	4.90
	12.85	4.85
	13.10	4.65
	13.25	4.35
	13.50	3.70
	14.05	1.50
	14.50	0.95
	14.75	0.35
2.0 ($\phi = 12.60$ in)	10.15	0.54
	10.50	0.96
	11.15	2.00
	11.50	2.75
	12.00	3.65
	12.55	3.75
	12.85	3.70
	12.95	3.67

TABLE E.8 (continued)

Axial Location (No. of Dia.)	Radial Location (in)	Axial Velocity (cm/sec)
	13.15	3.45
	13.35	3.20
	13.60	2.70
	13.65	2.35
	14.25	1.36
	14.55	0.92
	14.80	0.62
3.0	9.05	0.29
(ϕ = 12.60 in)	9.85	0.65
	10.10	0.84
	10.80	1.55
	11.25	2.13
	11.95	2.55
	12.50	2.70
	12.85	2.75
	13.00	2.62
	13.20	2.56
	13.45	2.23
	13.75	1.93
	14.50	1.08
	15.05	0.69
5.0	8.50	0.30
(ϕ = 12.60 in)	8.90	0.39
	9.85	0.65
	10.55	0.81
	11.60	1.03
	12.55	1.11
	13.05	1.01
	13.25	1.07
	13.60	1.00
	13.95	0.95
	14.45	0.86
	15.35	0.57
	15.90	0.43
6.0	9.05	0.30
(ϕ = 12.60 in)	11.30	0.57
	12.55	0.65
	13.50	0.63
	15.05	0.45
	16.30	0.32

TABLE E.9

AXIAL VELOCITY DATA, 0.30 cm I.D. CAPILLARY
 $Q=0.635 \text{ cm}^3/\text{sec}$, SMALL RESERVOIR

Axial Location (No. of Dia.)	Radial Location (in)	Axial Velocity (cm/sec)
0.0 ($\phi=12.60$ in)	11.50	6.90
	12.20	12.40
	12.80	13.50
	12.90	13.35
	13.05	12.90
	13.15	12.05
	13.30	10.00
	13.80	5.10
0.5 ($\phi=12.60$ in)	11.15	2.60
	11.45	6.90
	12.15	11.55
	12.80	12.40
	12.90	12.30
	13.05	11.80
	13.15	11.10
	13.35	11.35
	13.85	4.85
	13.95	4.65
	14.20	2.00
1.0 ($\phi=12.60$ in)	11.05	2.60
	11.35	6.65
	12.15	10.60
	12.75	11.45
	12.90	11.30
	13.05	10.90
	13.15	10.15
	13.35	8.55
	13.90	4.40
	14.05	4.30
	14.25	2.45
	14.60	0.85
	14.80	0.75
2.0 ($\phi=12.60$ in)	10.05	0.85
	10.85	2.50
	11.20	4.45
	12.00	8.70
	12.75	9.50
	12.85	9.40

TABLE E.9 (continued)

Axial Location (No. of Dia.)	Radial Location (in)	Axial Velocity (cm/sec)
	13.05	9.00
	13.25	8.20
	13.45	7.10
	14.05	4.00
	14.15	3.60
	14.40	2.55
	14.65	1.90
	15.10	1.00
	15.30	0.70
	15.90	0.30
3.0	9.90	1.05
(ϕ = 12.60 in)	10.65	1.23
	11.00	3.50
	11.90	6.85
	12.75	7.65
	12.90	7.55
	13.05	7.20
	13.25	6.50
	13.60	5.70
	14.15	3.50
	14.55	2.40
	14.75	1.70
	15.70	0.55
6.0	8.85	0.72
(ϕ = 12.60 in)	9.65	1.15
	10.15	1.60
	11.50	2.95
	12.35	3.20
	12.75	3.35
	12.95	3.15
	13.15	3.15
	13.50	2.75
	13.85	2.50
	14.90	1.65
	15.20	1.40
	15.60	0.95
	15.95	0.70
	16.50	0.50
	16.75	0.40

TABLE E.9 (continued)

Axial Location (No. of Dia.)	Radial Location (in)	Axial Velocity (cm/sec)
8.0	7.00	0.27
(4 =12.60 in)	8.25	0.525
	8.95	0.76
	10.95	1.29
	11.20	1.27
	12.85	1.19
	13.95	1.16
	13.55	1.16
	15.25	0.495

TABLE E.10

AXIAL VELOCITY DATA, 0.20 cm I.D. CAPILLARY
 $Q=0.159 \text{ cm}^3/\text{sec}$, LARGE RESERVOIR

Axial Location (No. of Dia.)	Radial Location (in)	Axial Velocity (cm/sec)
4.93 ($\phi = 14.50$ in)	10.65	1.38
	11.35	2.06
	11.85	3.06
	13.30	10.60
	13.53	12.50
	14.05	18.10
	14.45	19.30
	14.65	20.00
	14.80	19.30
	15.25	15.00
	15.85	8.96
	16.20	6.44
	16.75	4.84
	16.85	3.80
	17.10	3.54
	17.35	3.06
	17.80	1.75
7.75 ($\phi = 14.50$ in)	10.30	1.89
	10.95	2.83
	11.50	3.74
	12.10	4.00
	12.55	5.42
	13.05	5.63
	13.30	5.90
	13.60	6.22
	14.75	7.75
	15.00	7.08
	15.35	6.78
	15.80	6.35
	16.45	4.60
	17.30	3.30
	17.75	3.06
	18.40	1.89
10.55 ($\phi = 14.50$ in)	10.85	2.00
	11.25	2.21
	11.85	2.72
	12.20	3.05
	12.70	3.07
	13.45	3.20
	14.20	3.38

TABLE E.10 (continued)

Axial Location (No. of Dia.)	Radial Location (in)	Axial Velocity (cm/sec)
14.10 (ϕ = 14.50 in)	14.50	3.14
	14.85	3.07
	15.55	2.90
	15.80	3.02
	17.00	2.48
	17.75	1.95
	19.02	1.50
	10.15	1.02
	11.15	1.10
	13.70	1.26
	13.95	1.37
	15.15	1.18
	15.60	1.26
	16.35	1.26
	16.70	1.14
	17.00	1.18
	18.20	1.06
	19.80	1.00

TABLE E.11

AXIAL VELOCITY DATA, 0.20 cm I.D. CAPILLARY
 $Q=0.318 \text{ cm}^3/\text{sec}$, LARGE RESERVOIR

Axial Location (No. of Dia.)	Radial Location (in)	Axial Velocity (cm/sec)
4.93 ($\phi = 17.30 \text{ in}$)	15.10	0.77
	15.55	1.10
	15.85	1.54
	16.15	2.36
	16.45	3.28
	16.85	6.20
	17.05	6.40
	17.70	4.25
	18.65	2.48
	18.95	1.32
	19.45	1.09
	19.90	0.58
	20.60	0.36
7.75 ($\phi = 17.30 \text{ in}$)	13.15	0.37
	14.25	0.92
	14.85	0.95
	15.20	0.97
	15.50	1.37
	15.75	1.37
	16.15	2.36
	16.50	2.46
	17.00	2.96
	17.30	2.92
	17.85	3.15
	17.95	3.28
	18.75	1.99
	19.00	1.16
	19.70	0.90
	20.10	0.65
	20.55	0.55
	21.90	0.30
	22.50	0.18
10.55 ($\phi = 17.30 \text{ in}$)	12.35	0.35
	14.10	0.64
	14.85	0.71
	15.40	1.07
	15.60	1.10
	16.05	1.51
	16.70	1.36
	17.35	1.56

TABLE E.11 (continued)

Axial Location (No. of Dia.)	Radial Location (in)	Axial Velocity (cm/sec)
14.10 (ϕ = 17.30 in)	18.15	1.44
	18.50	1.23
	18.80	1.09
	19.00	1.23
	19.60	0.86
	19.75	0.91
	20.20	0.74
	20.95	0.51
	21.95	0.34
	10.40	0.19
	11.85	0.46
	12.45	0.43
	14.65	0.49
	15.60	0.58
	16.05	0.58
	16.25	0.61
	16.55	0.57
	17.20	0.56
	17.55	0.55
	18.50	0.61
	19.45	0.48
	21.05	0.39
	22.00	0.32
	22.75	0.28
	23.50	0.30

TABLE E.12

AXIAL VELOCITY DATA, 0.20 cm I.D. CAPILLARY
 $Q=0.794 \text{ cm}^3/\text{sec}$, LARGE RESERVOIR

Axial Location (No. of Dia.)	Radial Location (in)	Axial Velocity (cm/sec)
9.86 ($\phi = 12.50$ in)	10.50	0.96
	11.10	2.24
	11.50	4.40
	11.60	4.86
	12.30	9.90
	12.45	10.90
	12.65	10.30
	13.00	7.55
	13.30	2.71
	13.75	1.88
	14.20	1.45
	14.40	1.02
	14.65	0.72
	15.15	0.40
13.40 ($\phi = 12.50$ in)	9.35	0.62
	9.65	0.75
	10.50	1.32
	11.45	3.60
	11.65	4.46
	12.30	6.63
	12.45	7.30
	12.75	6.13
	12.90	5.92
	13.15	5.15
	13.40	2.88
	14.20	1.49
	14.30	1.50
	14.50	1.24
	14.60	1.20
	15.15	0.76
16.90 ($\phi = 12.50$ in)	15.50	0.60
	15.80	0.44
	15.85	0.48
	9.10	0.56
	9.40	0.80
	9.70	0.85
	10.65	1.56
	11.25	2.25
	11.35	2.62
	11.60	2.80

TABLE E.12 (continued)

Axial Location (No. of Dia.)	Radial Location (in)	Axial Velocity (cm/sec)
	11.80	3.16
	12.05	3.90
	12.25	4.22
	12.50	4.32
	12.60	4.30
	12.85	4.00
	12.90	3.82
	13.35	3.00
	13.45	2.71
	14.35	1.51
	14.60	1.07
	14.95	0.96
	15.25	0.96
	15.35	0.83
	15.50	0.72
	16.00	0.50
21.10 (ϕ =12.50 in)	9.60	0.56
	10.75	1.12
	11.05	1.39
	11.25	1.44
	11.60	1.65
	11.80	1.70
	12.05	1.88
	12.20	1.90
	12.80	1.90
	13.05	1.68
	13.25	1.88
	13.65	1.55
	13.75	1.52
	14.85	1.03
	15.35	0.73
	16.00	0.62
24.60 (ϕ =12.50 in)	16.35	0.53
	8.60	0.48
	9.35	0.55
	10.15	0.74
	11.00	0.80
	11.20	0.88
	11.60	0.92
	11.85	0.92
	12.10	0.96
	12.35	0.98
	12.90	0.96
	13.15	0.89

TABLE E.12 (continued)

<u>Axial Location</u> <u>(No. of Dia.)</u>	<u>Radial Location</u> <u>(in)</u>	<u>Axial Velocity</u> <u>(cm/sec)</u>
	13.45	0.95
	14.25	0.79
	15.15	0.72
	15.60	0.61
	16.00	0.59
	17.05	0.40

TABLE E.13

AXIAL VELOCITY DATA, 0.20 cm I.D. CAPILLARY
 $Q=1.589 \text{ cm}^3/\text{sec}$, LARGE RESERVOIR

Axial Location (No. of Dia.)	Radial Location (in)	Axial Velocity (cm/sec)
13.90 ($\phi=16.60$ in)	13.95	1.35
	14.75	2.35
	15.15	3.32
	15.40	4.35
	15.60	6.68
	15.95	11.30
	16.20	15.60
	16.50	23.10
	16.90	20.20
	17.75	3.47
	18.00	2.95
	18.25	2.17
	18.40	2.30
	18.85	1.45
21.30 ($\phi=16.60$ in)	11.50	0.51
	13.25	1.10
	13.35	1.15
	14.25	1.45
	14.45	2.32
	15.00	3.04
	15.25	3.76
	15.55	5.50
	15.80	6.06
	15.95	6.80
	16.10	8.40
	16.15	9.70
	16.25	10.10
	16.40	10.80
	16.60	11.55
	17.00	9.20
	17.10	9.70
	17.50	6.36
	18.35	2.60
	18.55	2.31
	19.00	1.58
	19.40	1.44
	20.25	0.87
	20.55	0.89
	21.25	0.53
	22.05	0.36

TABLE E.13 (continued)

Axial Location (No. of Dia.)	Radial Location (in)	Axial Velocity (cm/sec)
28.18 (ϕ = 16.60 in)	10.15	0.36
	11.35	0.61
	12.75	0.94
	12.90	1.15
	13.40	1.25
	13.55	1.37
	14.35	2.04
	14.65	2.54
	15.15	2.90
	15.30	3.20
	15.45	3.67
	15.65	3.76
	16.20	5.65
	16.40	5.50
	16.85	4.90
	17.20	4.30
	17.35	4.34
	18.40	2.68
	18.70	2.30
	19.25	1.74
	19.55	1.56
	19.95	1.23
	20.45	1.04
	20.75	1.04
	21.15	0.55
35.67 (ϕ = 16.60 in)	12.25	0.75
	12.90	0.78
	13.80	1.15
	14.10	1.20
	14.25	1.20
	14.75	1.30
	15.15	1.44
	15.85	1.66
	16.15	1.63
	16.60	1.64
	16.80	1.62
	16.95	1.62
	17.20	1.59
	17.40	1.54
	18.05	1.49
	18.45	1.45
	18.75	1.30
	20.35	0.98
	21.25	0.81
	21.95	0.61

TABLE E.13 (continued)

<u>Axial Location</u> <u>(No. of Dia.)</u>	<u>Radial Location</u> <u>(in)</u>	<u>Axial Velocity</u> <u>(cm/sec)</u>
42.00 (d_c = 16.60 in)	22.45	0.54
	22.85	0.50
	23.45	0.39
	10.65	0.42
	11.90	0.53
	13.15	0.58
	14.35	0.68
	14.85	0.75
	15.55	0.79
	16.70	0.90
	17.45	0.87
	18.35	0.81
	18.80	0.77
	19.10	0.70
	19.90	0.56
	20.20	0.53
	21.05	0.49

TABLE E.14

AXIAL VELOCITY DATA, 0.30 cm I.D. CAPILLARY
 $Q=0.318 \text{ cm}^3/\text{sec}$, LARGE RESERVOIR

Axial Location (No. of Dia.)	Radial Location (in)	Axial Velocity (cm/sec)
1.42 ($\phi = 14.50$ in)	13.20	0.87
	13.45	2.08
	14.35	4.10
	14.45	4.41
	14.65	4.09
	14.85	3.84
	15.00	3.55
	15.20	3.78
	15.35	2.84
	15.55	2.36
	15.80	1.32
	15.95	0.96
	16.40	0.66
2.82 ($\phi = 14.50$ in)	12.95	0.95
	13.25	1.48
	14.35	2.64
	14.43	2.68
	14.70	2.52
	14.90	2.58
	15.15	2.39
	15.40	2.02
	15.65	1.98
	15.85	1.64
	16.15	1.10
	16.25	0.95
	16.55	0.69
	16.65	0.79
	16.85	0.53
	17.45	0.35
4.24 ($\phi = 14.50$ in)	12.50	0.63
	13.25	1.15
	14.35	1.45
	14.55	1.45
	14.80	1.39
	15.00	1.42
	15.35	1.26
	15.70	1.10
	16.00	0.85
	16.20	0.85
	16.75	0.67

TABLE E.14 (continued)

Axial Location (No. of Dia.)	Radial Location (in)	Axial Velocity (cm/sec)
5.65 (ϕ =14.50 in)	17.20	0.60
	18.00	0.33
	18.40	0.28
	12.25	0.57
	13.35	0.63
	14.60	0.76
	15.00	0.76
	15.15	0.76
	15.40	0.73
	15.55	0.70
	15.70	0.76
	16.55	0.55
	17.05	0.50
	17.40	0.45
	18.05	0.38
7.06 (ϕ =14.50 in)	13.10	0.39
	13.60	0.38
	14.70	0.40
	15.35	0.44
	15.80	0.41
	17.20	0.31
	17.90	0.29
8.95 (ϕ =14.50 in)	19.10	0.21
	10.30	0.16
	13.30	0.20
	13.50	0.18
	15.05	0.23
	15.60	0.20
	16.80	0.20

TABLE E.15

AXIAL VELOCITY DATA, 0.30 cm I.D. CAPILLARY
 $Q=0.635 \text{ cm}^3/\text{sec}$, LARGE RESERVOIR

Axial Location (No. of Dia.)	Radial Location (in)	Axial Velocity (cm/sec)
1.41	14.55	2.65
(ϕ =16.00 in)	15.65	9.77
	16.15	7.87
	16.25	8.27
	16.30	8.07
	16.55	7.70
	17.30	2.37
2.83	13.65	1.49
(ϕ =16.00 in)	14.50	3.05
	15.65	7.60
	16.15	6.20
	16.25	6.45
	16.35	6.37
	16.65	5.79
	17.70	1.21
	19.00	0.37
4.24	13.55	1.37
(ϕ =16.00 in)	15.60	5.55
	15.95	5.75
	16.20	4.47
	17.20	2.24
	17.40	2.18
	17.95	1.57
	18.05	1.24
6.13	13.00	1.20
(ϕ =16.00 in)	13.45	1.22
	13.85	1.68
	15.55	3.14
	16.35	2.76
	16.45	2.40
	16.50	2.46
	16.95	2.56
	17.55	1.65
	17.80	1.57
	17.95	1.57
	18.35	1.24
	18.45	1.01

TABLE E.15 (continued)

Axial Location (No. of Dia.)	Radial Location (in)	Axial Velocity (cm/sec)
8.02 (ϕ =16.00 in)	12.05	0.63
	12.20	0.80
	12.25	0.76
	13.10	1.04
	13.20	1.08
	14.85	1.57
	15.50	1.61
	16.55	1.66
	16.70	1.49
	16.80	1.53
	16.95	1.53
	17.20	1.36
	18.05	1.11
	18.15	1.02
	18.40	1.00
	19.20	0.73
	20.95	0.39
	21.75	0.31
9.89 (ϕ =16.00 in)	10.75	0.44
	11.00	0.46
	12.20	0.60
	12.30	0.61
	12.95	0.70
	14.00	0.77
	14.50	0.83
	15.45	0.87
	15.75	0.87
	17.15	0.80
	17.40	0.77
	17.70	0.76
	17.95	0.72
	18.45	0.66
	18.80	0.64
	19.05	0.62
	19.70	0.53
	20.35	0.44
	20.60	0.46
11.78 (ϕ =16.00 in)	11.10	0.36
	11.25	0.38
	11.85	0.41
	14.40	0.50
	15.75	0.50
	16.35	0.50
	17.25	0.50

TABLE E.15 (continued)

Axial Location (No. of Dia.)	Radial Location (in)	Axial Velocity (cm/sec)
	17.60	0.46
	18.50	0.43
	19.25	0.38
	19.45	0.39
	19.70	0.39
	20.85	0.33
	21.50	0.25
	21.95	0.25

TABLE E.16

AXIAL VELOCITY DATA, 0.30 cm I.D. CAPILLARY
 $Q=1.589 \text{ cm}^3/\text{sec}$, LARGE RESERVOIR

Axial Location (No. of Dia.)	Radial Location (in)	Axial Velocity (cm/sec)
4.24 ($\phi = 15.60$ in)	14.70	23.10
	15.00	26.80
	15.20	29.00
	15.30	32.80
	15.60	31.80
	16.00	32.80
	16.20	24.80
	16.75	17.10
	17.10	13.50
	17.85	5.64
	18.30	4.05
	18.80	2.42
6.60 ($\phi = 15.60$ in)	11.65	2.51
	12.25	3.49
	14.60	15.25
	14.95	21.80
	15.25	21.80
	15.50	23.60
	16.00	22.90
	16.30	20.00
	16.90	13.00
	17.25	12.10
	17.40	10.93
	17.60	8.67
	18.20	6.38
	18.35	5.78
	18.45	4.90
	18.60	4.88
	18.75	4.14
	18.95	3.63
	19.50	2.52
9.42 ($\phi = 15.60$ in)	19.75	2.48
	20.05	2.12
	20.75	1.75
	21.05	1.48
	11.90	3.72
	12.70	5.60
	13.40	6.54
	14.65	11.90
	14.90	12.80

TABLE E.16 (continued)

Axial Location (No. of Dia.)	Radial Location (in)	Axial Velocity (cm/sec)
	15.25	13.65
	15.55	14.00
	15.70	15.10
	16.10	14.30
	16.45	12.20
	17.05	10.00
	17.70	8.50
	18.05	6.48
	18.70	5.61
	18.80	4.55
	18.95	4.23
	19.35	4.25
	19.65	3.66
	19.85	3.42
	20.25	2.80
	20.75	2.22
	21.20	1.90
	22.05	1.42
	22.20	1.55
12.25	14.70	7.30
(ϕ =15.60 in)	15.10	8.01
	15.20	7.30
	15.60	7.60
	15.70	8.30
	15.90	7.80
	16.35	8.29
	16.40	7.42
	17.45	6.48
	18.05	4.93
	18.35	5.16
	18.70	4.74
	18.85	4.25
	18.95	3.88
	19.75	3.68
	20.50	2.80
	21.95	2.08
	22.40	1.84
	23.30	1.34
15.05	13.25	3.62
(ϕ =15.60 in)	13.40	3.48
	13.80	3.52
	14.10	3.60
	14.20	3.67
	14.30	3.81

TABLE E.16 (continued)

Axial Location (No. of Dia.)	Radial Location (in)	Axial Velocity (cm/sec)
	14.50	4.14
	14.90	4.15
	15.00	3.96
	15.60	3.96
	15.70	4.25
	16.05	4.30
	16.60	3.90
	17.15	3.62
	17.90	3.84
	18.25	3.12
	19.45	3.04
	19.80	2.46
	20.20	2.38
	20.35	2.75
	21.25	2.22
	21.55	2.13
	22.05	1.83
	22.65	2.13
	23.80	1.42

E.2 AXIAL AND RADIAL VELOCITY PROFILES - DIGITIZER METHOD

The digitizer method was used in measuring both axial and radial velocities at three axial locations upstream of the contraction. These axial locations were at distances equal to one and one half times the location of the eddy center, at the eddy center and at a distance equal to one half times the eddy center location. The locations of the eddy centers are tabulated in Appendix F, Section F.1 (page 444). Since the direct method was used to measure the axial velocities for the data in Tables E.17 to E.20, E.22 to E.24, and E.26 to E.27, only radial velocities were measured with the digitizer method.

The radial distance Δr (Equation 2.2, page 67), measured by the digitizer method was of the opposite sign for values of r' greater than 1.327 cm in reservoir S and greater than 12.745 in reservoir L. Data given in this manner allows for a clear graphical presentation of V_r versus r' .

The following table lists the order in which the data are presented in this section. In each of the tables the distance measured from the reservoir wall r' was determined by Equation 2.4 (page 68).

<u>Table No.</u>	<u>Reservoir</u>	<u>I.D. (cm)</u>	<u>Q (cm³/sec)</u>
17	S	0.10	0.016
18	S	0.10	0.040
19	S	0.10	0.119
20	S	0.20	0.040
21	S	0.20	0.159
22	S	0.20	0.238
23	S	0.20	0.318
24	S	0.30	0.040
25	S	0.30	0.159
26	S	0.30	0.318
27	S	0.30	0.654
28	L	0.20	1.589
29	L	0.20	1.906
30	L	0.20	2.383
31	L	0.20	2.701
32	L	0.20	3.177
33	L	0.20	3.813
34	L	0.20	4.766
35	L	0.30	4.766
36	L	0.30	6.354
37	L	0.30	7.148
38	L	0.30	7.943
39	L	0.30	8.737
40	L	0.30	9.531
41	L	0.30	10.325
42	L	0.30	11.120

TABLE E.18

RADIAL VELOCITIES - DIGITIZER METHOD, Q=0.040 cm³/sec
0.10 cm I.D. CAPILLARY TUBE, SMALL RESERVOIR

(Z/D) = 16.82 (ζ = 1.327 cm)

r' (cm)	V _r (cm/sec)	r' (cm)	V _r (cm/sec)	r' (cm)	V _r (cm/sec)	r' (cm)	V _r (cm/sec)	r' (cm)	V _r (cm/sec)	r' (cm)	V _r (cm/sec)
1.155	0.062	1.213	0.023	0.876	0.057	1.137	0.036	1.240	0.029	1.379	-0.006
1.417	-0.024	1.541	-0.044	1.589	-0.059	1.219	0.036	1.242	0.051	1.256	0.056
1.294	0.027	1.319	-0.013	1.339	-0.007	1.035	0.043	1.174	0.056	1.241	0.033
1.269	0.022	1.280	0.009	1.353	-0.023	1.359	-0.006	1.379	-0.012	1.419	-0.030
1.467	-0.041	1.524	-0.060	1.583	-0.056	0.980	0.052	1.155	0.046	1.261	0.056
1.316	0.011	1.383	-0.009	1.419	-0.042	1.563	-0.055				

(Z/D) = 11.21 (ζ = 1.327 cm)

r' (cm)	V _r (cm/sec)	r' (cm)	V _r (cm/sec)	r' (cm)	V _r (cm/sec)	r' (cm)	V _r (cm/sec)	r' (cm)	V _r (cm/sec)	r' (cm)	V _r (cm/sec)
1.222	0.131	1.238	0.087	1.266	0.079	1.454	-0.030	1.105	0.082	1.123	0.042
1.261	0.082	1.318	-0.058	1.376	-0.060	1.400	-0.075	1.528	-0.074	1.218	0.120
1.255	0.037	1.316	-0.030	1.375	-0.078	1.379	-0.018	1.462	-0.127	1.474	-0.073
1.269	0.037	1.359	0.033	1.396	-0.058	1.515	-0.119	1.530	-0.089	1.541	-0.088
1.593	-0.005	1.343	-0.046	1.382	-0.064	1.421	-0.066	1.444	-0.090	1.289	0.119
1.323	0.065	1.334	-0.059	1.343	0.059	1.386	-0.039	1.272	0.085	1.503	-0.143
1.530	-0.024	1.151	-0.033	1.306	0.106	1.337	-0.044	1.366	-0.051	1.238	0.058
1.263	0.047	1.358	0.060	1.385	-0.045	1.492	-0.024	1.514	-0.110	1.554	-0.077
1.590	-0.029	1.355	0.020	1.384	-0.016	1.461	-0.102	1.243	0.045	1.250	0.034
1.387	-0.007	1.509	-0.117	1.569	-0.084	1.176	0.080	1.266	0.072	1.303	0.035
1.388	-0.047	1.396	-0.063	1.457	-0.094	1.489	-0.040	1.334	0.001	1.413	-0.043
1.598	0.017	1.248	0.042	1.261	0.084	1.360	-0.058	1.419	-0.055	1.616	-0.065
1.239	0.069	1.275	0.074	1.292	0.027	1.310	0.044	1.226	0.052	1.408	-0.085
1.520	-0.101	1.555	-0.074	1.569	-0.008	1.117	0.049				

TABLE E.18 (continued)

(Z/D) = 11.21				(ξ = 1.327 cm)			
r' (cm)	V _r (cm/sec)	r' (cm)	V _r (cm/sec)	r' (cm)	V _r (cm/sec)	r' (cm)	V _r (cm/sec)
1.326	-0.027	1.336	0.029	1.348	0.006	1.452	-0.068
1.252	0.070	1.359	-0.016	1.440	-0.123	1.478	-0.038
1.184	0.090	1.223	0.053	1.244	0.098	1.297	0.016
1.098	0.053	1.174	0.109	1.227	0.083	1.366	-0.013
1.534	-0.054						
(Z/D) = 5.61				(ξ = 1.327 cm)			
r' (cm)	V _r (cm/sec)	r' (cm)	V _r (cm/sec)	r' (cm)	V _r (cm/sec)	r' (cm)	V _r (cm/sec)
1.267	0.139	1.489	-0.017	1.616	-0.011	1.231	0.053
1.349	0.001	1.428	0.030	1.470	0.016	1.280	0.048
1.404	-0.028	1.496	-0.012	1.237	0.024	1.450	0.002
1.305	0.156	1.410	0.038	1.429	-0.035	1.464	-0.014
1.386	-0.077	1.410	-0.065	1.484	-0.013	1.358	0.134
1.411	-0.081	1.458	-0.047	1.476	-0.063	1.299	0.075
1.396	-0.075	1.413	-0.057	1.429	-0.008	1.474	-0.006
1.496	-0.012	1.348	0.115	1.508	-0.030	1.131	-0.056
1.464	-0.018	1.496	-0.030	1.485	-0.021	1.525	-0.027
1.560	0.037	1.598	0.023	1.477	0.025	1.551	0.015
1.120	-0.054	1.259	0.109	1.424	-0.027	1.338	-0.055
(Z/D) = 11.21				(ξ = 1.327 cm)			
r' (cm)	V _r (cm/sec)	r' (cm)	V _r (cm/sec)	r' (cm)	V _r (cm/sec)	r' (cm)	V _r (cm/sec)
1.326	-0.027	1.336	0.029	1.348	0.006	1.452	-0.068
1.252	0.070	1.359	-0.016	1.440	-0.123	1.478	-0.038
1.184	0.090	1.223	0.053	1.244	0.098	1.297	0.016
1.098	0.053	1.174	0.109	1.227	0.083	1.366	-0.013
1.534	-0.054						
(Z/D) = 5.61				(ξ = 1.327 cm)			
r' (cm)	V _r (cm/sec)	r' (cm)	V _r (cm/sec)	r' (cm)	V _r (cm/sec)	r' (cm)	V _r (cm/sec)
1.267	0.139	1.489	-0.017	1.616	-0.011	1.231	0.053
1.349	0.001	1.428	0.030	1.470	0.016	1.280	0.048
1.404	-0.028	1.496	-0.012	1.237	0.024	1.450	0.002
1.305	0.156	1.410	0.038	1.429	-0.035	1.464	-0.014
1.386	-0.077	1.410	-0.065	1.484	-0.013	1.358	0.134
1.411	-0.081	1.458	-0.047	1.476	-0.063	1.299	0.075
1.396	-0.075	1.413	-0.057	1.429	-0.008	1.474	-0.006
1.496	-0.012	1.348	0.115	1.508	-0.030	1.131	-0.056
1.464	-0.018	1.496	-0.030	1.485	-0.021	1.525	-0.027
1.560	0.037	1.598	0.023	1.477	0.025	1.551	0.015
1.120	-0.054	1.259	0.109	1.424	-0.027	1.338	-0.055

TABLE E.19

RADIAL VELOCITIES - DIGITIZER METHOD, $Q=0.119 \text{ cm}^3/\text{sec}$
 0.10 cm I.D. CAPILLARY TUBE, SMALL RESERVOIR

(Z/D) = 18.22		(ϕ = 1.327 cm)							
r' (cm)	V _r (cm/sec)	r' (cm)	V _r (cm/sec)	r' (cm)	V _r (cm/sec)	r' (cm)	V _r (cm/sec)	r' (cm)	V _r (cm/sec)
1.237	0.346	1.248	0.159	1.320	-0.021	1.172	0.122	1.325	0.022
1.277	0.205	1.239	0.076	1.275	0.031	1.287	-0.124	1.242	0.180
1.231	-0.095	1.272	0.081	1.288	0.298	1.326	-0.270	1.286	0.198
1.257	0.205	1.334	0.137	1.365	-0.096	1.388	-0.025	1.481	-0.102
1.412	-0.290	1.470	-0.168	1.367	0.020	1.413	-0.094	1.461	-0.253
1.538	-0.031	1.572	-0.003	1.298	-0.011	1.322	-0.023	1.383	-0.150
1.585	-0.130	1.227	0.262	1.253	0.250	1.301	-0.194	1.383	-0.094
1.455	-0.227	1.468	-0.247	1.500	-0.060	1.508	-0.028	1.540	-0.051
1.211	0.102	1.527	-0.130	1.537	-0.187	1.561	-0.025	1.291	0.135
1.363	0.018	1.391	-0.171	1.525	-0.100	1.566	-0.038	1.582	-0.006
1.268	0.014	1.287	-0.167	1.377	0.046	1.491	-0.184	1.566	-0.124
1.231	-0.113	1.452	-0.204	1.490	-0.167	1.511	-0.114	1.531	-0.009
1.293	0.130	1.421	-0.201	1.438	-0.232	1.490	-0.162	1.550	-0.136
1.290	0.127	1.460	0.114	1.536	-0.136	1.554	-0.152	1.570	-0.153
1.261	0.196	1.391	-0.120	1.462	-0.105	1.506	-0.209	1.525	-0.148
1.654	-0.030	1.300	0.250	1.395	-0.296	1.438	-0.213	1.500	-0.034
1.277	-0.122	1.362	-0.143	1.510	-0.229	1.557	-0.154	1.605	-0.106
1.284	0.034	1.500	-0.156	1.533	-0.157	1.543	-0.142	1.636	-0.083
1.283	0.191	1.309	0.055	1.454	-0.146	1.436	-0.098	1.546	-0.087
1.624	-0.083	1.799	-0.026	1.031	0.061	1.240	0.106	1.345	0.017
1.553	-0.169	1.569	-0.100	1.586	-0.058	1.755	-0.020	0.951	0.021
1.394	-0.185	1.426	-0.191	1.558	-0.150	1.597	-0.160	1.663	-0.054
1.220	0.077	1.291	0.126	1.603	-0.079	1.640	-0.032	1.669	-0.075
1.055	0.025	1.132	0.045	1.259	0.107	1.493	-0.204	1.593	-0.026
1.825	-0.031	0.901	0.004	0.962	0.023	1.004	0.015	1.081	0.057
1.213	0.116	1.246	0.126	1.536	-0.096	1.595	-0.034	1.707	-0.016
1.867	0.000								

TABLE E.20

RADIAL VELOCITY - DIGITIZER METHOD, $Q=0.040\text{ cm}^3/\text{sec}$
0.20 cm I.D. CAPILLARY TUBE, SMALL RESERVOIR

(Z/D) = 5.00 (\dot{Q} = 1.327 cm)

r' (cm)	V_r (cm/sec)	r' (cm)	V_r (cm/sec)	r' (cm)	V_r (cm/sec)	r' (cm)	V_r (cm/sec)	r' (cm)	V_r (cm/sec)	r' (cm)	V_r (cm/sec)
1.107	0.042	1.433	0.003	0.997	0.034	1.590	-0.031	1.410	-0.014	1.573	-0.038
1.598	-0.063	1.057	0.030	1.358	-0.019	1.471	-0.026	1.523	-0.031	1.297	-0.006
1.342	-0.017	1.395	-0.040	1.153	0.024	1.306	0.011	1.346	-0.012	1.404	-0.014
1.479	-0.023	1.618	-0.036	1.113	0.034	1.256	0.015	1.350	0.018	1.365	-0.017
1.380	-0.023	1.394	-0.008	1.655	-0.056	1.096	0.045	1.294	-0.013	1.395	-0.024
1.294	0.032	1.350	0.000	1.441	-0.034	1.045	0.022	1.253	-0.008	1.546	-0.053
1.278	0.014	1.480	-0.025	1.519	-0.037	1.583	-0.058	1.091	0.030	1.244	0.007
1.310	0.001	1.323	-0.006	1.362	-0.016	1.429	-0.026	1.452	-0.055	1.211	0.020
1.261	0.005	1.226	0.030	1.735	-0.036	1.411	0.003	1.531	-0.021	1.662	-0.027
1.174	0.025	1.398	-0.016	1.640	-0.043	1.372	0.005	1.396	-0.013	1.426	-0.004
1.552	-0.053	1.563	-0.083	1.261	0.024	1.326	0.026	1.444	-0.003		

(Z/D) = 3.33 (\dot{Q} = 1.327 cm)

r' (cm)	V_r (cm/sec)	r' (cm)	V_r (cm/sec)	r' (cm)	V_r (cm/sec)	r' (cm)	V_r (cm/sec)	r' (cm)	V_r (cm/sec)	r' (cm)	V_r (cm/sec)
1.420	-0.008	1.436	-0.027	1.531	-0.063	1.231	0.081	1.286	0.008	1.357	-0.025
1.390	-0.016	1.496	-0.053	1.510	-0.049	1.131	0.054	1.386	-0.028	1.533	-0.037
1.549	-0.014	1.182	0.030	1.437	-0.075	1.453	-0.085	1.094	0.063	1.412	-0.057
1.379	-0.030	1.420	-0.047	1.192	0.046	1.288	0.046	1.380	-0.043	1.484	-0.035
1.640	-0.047	1.164	0.027	1.289	-0.005	1.495	-0.083	1.514	-0.072	1.625	-0.046
1.137	0.084	1.277	0.054	1.376	-0.111	1.582	-0.064	1.602	-0.050	1.208	0.012
1.286	0.019	1.305	0.016	1.431	-0.024	1.534	-0.083	1.320	-0.011	1.332	-0.019
1.405	-0.045	1.542	-0.056	1.240	0.043	1.259	0.047	1.272	0.058	1.288	0.018
1.491	-0.065	1.538	-0.057	1.195	0.063	1.357	0.000	1.476	-0.020	1.561	-0.038
1.389	-0.009	1.400	-0.024	1.416	-0.020	1.563	-0.060	1.125	0.022	1.336	-0.010

TABLE E.20 (continued)

(Z/D) = 3.33			(ϕ = 1.327 cm)		
r' (cm)	V _r (cm/sec)	r' (cm)	V _r (cm/sec)	r' (cm)	V _r (cm/sec)
1.411	-0.065	1.526	-0.070	1.194	0.066
1.498	-0.104	1.591	-0.049	1.114	0.064
1.448	-0.037	1.316	-0.004	1.376	-0.031
(Z/D) = 1.67			(ϕ = 1.327 cm)		
r' (cm)	V _r (cm/sec)	r' (cm)	V _r (cm/sec)	r' (cm)	V _r (cm/sec)
1.206	0.024	1.431	-0.086	1.448	-0.069
1.301	0.004	1.440	-0.140	1.461	-0.105
1.443	-0.116	1.474	-0.045	1.543	-0.024
1.387	-0.038	1.401	-0.095	1.416	-0.065
1.250	0.033	1.266	0.090	1.369	-0.060
1.370	-0.005	1.384	-0.059	1.399	-0.056
1.443	-0.042	1.485	-0.154	1.205	0.017
1.223	0.062	1.162	0.001	1.177	0.002
1.422	0.000	1.190	-0.005	1.346	-0.014
1.297	0.071	1.440	-0.065	1.477	-0.113
1.454	-0.069	1.134	0.002	1.255	0.033
1.447	-0.097	1.147	0.028	1.222	0.060
r' (cm)	V _r (cm/sec)	r' (cm)	V _r (cm/sec)	r' (cm)	V _r (cm/sec)
1.264	-0.136	1.483	-0.069	1.448	-0.069
1.198	-0.021	1.351	-0.105	1.461	-0.105
1.273	0.091	1.229	-0.024	1.543	-0.024
1.415	0.022	1.282	-0.065	1.416	-0.065
1.267	-0.080	1.405	-0.060	1.369	-0.060
1.559	-0.105	1.447	-0.056	1.399	-0.056
1.507	-0.029	1.357	0.017	1.205	0.017
1.300	0.051	1.255	0.002	1.177	0.002
1.470	-0.060	1.354	-0.014	1.346	-0.014
1.249	0.032	1.143	-0.113	1.477	-0.113
1.381	0.019	1.340	0.033	1.255	0.033
1.351	0.057	1.319	0.060	1.222	0.060
r' (cm)	V _r (cm/sec)	r' (cm)	V _r (cm/sec)	r' (cm)	V _r (cm/sec)
1.264	0.070	1.483	-0.069	1.448	-0.069
1.198	0.057	1.351	-0.105	1.461	-0.105
1.273	0.065	1.229	-0.024	1.543	-0.024
1.415	-0.108	1.282	-0.065	1.416	-0.065
1.267	0.058	1.405	-0.060	1.369	-0.060
1.312	0.030	1.447	-0.056	1.399	-0.056
1.324	-0.034	1.357	0.017	1.205	0.017
1.522	-0.034	1.255	0.002	1.177	0.002
1.318	0.087	1.354	-0.014	1.346	-0.014
1.274	-0.088	1.143	-0.113	1.477	-0.113
1.379	0.053	1.340	0.033	1.255	0.033
1.398	-0.025	1.319	0.060	1.222	0.060
1.507	0.022				
r' (cm)	V _r (cm/sec)	r' (cm)	V _r (cm/sec)	r' (cm)	V _r (cm/sec)
1.411	-0.019	1.384	0.019	1.194	0.066
1.421	0.009	1.343	0.031	1.114	0.064
	-0.045	1.561	-0.038	1.376	-0.031
r' (cm)	V _r (cm/sec)	r' (cm)	V _r (cm/sec)	r' (cm)	V _r (cm/sec)
1.411	-0.011	1.384	0.019	1.194	0.066
	-0.047	1.343	0.031	1.114	0.064
		1.561	-0.038	1.376	-0.031

TABLE E.21 (continued)

(Z/D) = 6.57				(ξ = 1.327 cm)			
r' (cm)	V _r (cm/sec)	V _z (cm/sec)	r' (cm)	V _r (cm/sec)	V _z (cm/sec)	r' (cm)	V _r (cm/sec)
0.997	0.018	0.177	1.274	0.022	1.937	1.320	0.082
1.539	-0.113	1.212	1.389	-0.161	1.795	1.812	-0.062
1.626	-0.189	0.642	1.576	-0.064	0.584	1.644	-0.133
1.662	-0.100	0.471	1.800	-0.031	0.103	1.169	0.027
1.186	0.119	1.102	1.380	-0.026	1.705	1.262	0.090
1.340	-0.036	2.058	1.455	-0.229	1.502	1.365	-0.034
1.384	-0.073	1.720	1.559	-0.130	0.647	1.413	-0.089
1.439	-0.197	1.621	1.183	0.041	0.878	1.554	-0.231
1.722	-0.018	0.203	1.289	0.097	1.671	0.995	0.021
1.426	-0.023	1.591	1.659	-0.078	0.502	1.668	-0.106
1.701	-0.061	0.399	1.152	0.110	0.911	1.062	0.054
1.208	0.048	1.154	1.264	0.057	1.499	1.361	0.085
1.387	0.000	1.551	1.414	-0.058	1.652	1.400	-0.137
1.478	-0.148	1.235	1.643	-0.112	0.475	1.048	0.023
1.092	0.051	0.616	1.327	0.076	1.841	1.107	0.082
1.237	0.109	1.355	1.446	-0.038	1.664	1.379	-0.105
1.488	-0.090	0.944	1.577	-0.107	0.928	1.611	-0.094
1.075	0.066	0.427	0.885	0.008	0.138	1.247	0.026
1.261	0.032	1.936	1.648	-0.103	0.456	1.476	-0.211
1.532	-0.099	0.676	1.502	-0.186	1.241	1.561	-0.110
1.882	0.010	0.100	1.509	-0.137	1.017	1.199	0.072
1.228	0.108	1.602	1.549	-0.103	0.830	1.299	0.056
1.426	-0.150	1.768	1.741	-0.024	0.172	1.518	-0.147
1.169	0.097	1.023	0.955	0.008	0.214	1.207	0.058
1.236	0.134	1.593	1.124	0.075	0.702	1.365	-0.075
1.420	-0.070	1.852	1.286	0.091	1.990	1.549	-0.161
1.674	-0.051	0.300	1.380	-0.067	2.042	1.698	-0.071
1.067	0.059	0.324	1.635	-0.093	0.537	1.175	0.102
1.195	0.082	0.839	1.529	-0.170	1.281	1.384	-0.029
0.930	0.021	0.126	1.619	-0.106	0.612	1.110	0.054
1.337	0.096	2.142	1.093	0.087	0.507	1.659	-0.066

r' (cm)	V _r (cm/sec)	V _z (cm/sec)	r' (cm)	V _r (cm/sec)	V _z (cm/sec)	r' (cm)	V _r (cm/sec)	V _z (cm/sec)
1.297	0.025	1.873	1.320	0.082	1.937	1.320	0.082	1.873
1.515	-0.180	0.184	1.812	-0.062	1.795	1.812	-0.062	0.184
1.590	-0.065	0.627	1.644	-0.133	0.584	1.644	-0.133	0.627
1.342	-0.046	0.703	1.169	0.027	0.103	1.169	0.027	0.703
1.426	-0.084	1.739	1.262	0.090	1.705	1.262	0.090	1.739
1.499	-0.099	1.924	1.365	-0.034	1.502	1.365	-0.034	1.924
1.742	-0.053	1.594	1.413	-0.089	0.647	1.413	-0.089	1.594
1.261	0.145	0.849	1.554	-0.231	0.878	1.554	-0.231	0.849
1.604	-0.026	0.182	0.995	0.021	1.671	0.995	0.021	0.182
0.484	0.065	0.477	1.668	-0.106	0.502	1.668	-0.106	0.477
1.251	0.247	0.413	1.062	0.054	0.911	1.062	0.054	0.413
1.541	-0.108	2.040	1.361	0.085	1.499	1.361	0.085	2.040
0.640	-0.084	1.897	1.400	-0.137	1.652	1.400	-0.137	1.897
0.603	0.087	0.433	1.048	0.023	0.475	1.048	0.023	0.433
1.737	-0.069	0.599	1.107	0.082	1.841	1.107	0.082	0.599
1.063	-0.278	1.801	1.379	-0.105	1.664	1.379	-0.105	1.801
0.179	-0.037	0.548	1.611	-0.094	0.928	1.611	-0.094	0.548
0.862	-0.175	1.588	1.247	0.026	0.138	1.247	0.026	1.588
0.435	-0.044	0.889	1.476	-0.211	0.456	1.476	-0.211	0.889
0.965	0.126	0.589	1.561	-0.110	1.241	1.561	-0.110	0.589
0.772	-0.165	1.370	1.199	0.072	1.017	1.199	0.072	1.370
0.503	-0.091	1.832	1.299	0.056	0.830	1.299	0.056	1.832
0.114	-0.001	1.069	1.518	-0.147	0.172	1.518	-0.147	1.069
0.476	0.067	1.307	1.207	0.058	0.214	1.207	0.058	1.307
1.829	-0.079	1.880	1.365	-0.075	0.702	1.365	-0.075	1.880
2.006	-0.046	0.934	1.549	-0.161	1.990	1.549	-0.161	0.934
1.522	-0.114	0.273	1.698	-0.071	2.042	1.698	-0.071	0.273
0.097	0.015	0.680	1.175	0.102	0.537	1.175	0.102	0.680
0.939	-0.116	1.784	1.384	-0.029	1.281	1.384	-0.029	1.784
0.221	-0.071	0.342	1.110	0.054	0.612	1.110	0.054	0.342
1.331	0.109	0.511	1.659	-0.066	0.507	1.659	-0.066	0.511

TABLE E.22
RADIAL VELOCITIES - DIGITIZER METHOD, $Q=0.238\text{ cm}^3/\text{sec}$
0.20 cm I.D. CAPILLARY TUBE, SMALL RESERVOIR

$(z/D) = 7.27$		$(\xi = 1.327\text{ cm})$	
r' (cm)	V_r (cm/sec)	r' (cm)	V_r (cm/sec)
0.910	0.038	1.476	-0.273
1.846	0.004	0.955	0.037
1.228	0.132	1.706	-0.058
1.388	-0.038	1.488	-0.199
1.268	0.110	1.459	-0.063
1.258	0.048	1.382	-0.102
1.163	0.050	1.184	0.123
1.423	-0.014	1.517	-0.242
1.128	0.042	1.194	0.105
1.623	-0.112	1.702	-0.056
1.655	-0.089	1.669	-0.132
1.235	0.086	1.246	0.243
1.383	-0.024	1.626	-0.104
1.041	0.012	1.134	0.124
1.634	-0.212	1.251	0.118
1.357	0.004	1.607	-0.224
1.155	0.127	1.253	0.129
1.362	-0.074	1.380	-0.097
1.720	-0.073	1.630	-0.078
1.660	-0.126	1.719	-0.029
1.141	0.069	1.505	-0.140
1.517	-0.192	1.532	-0.128
0.938	0.020	1.166	0.102
1.085	0.067	1.199	0.117
		r' (cm)	V_r (cm/sec)
		1.566	-0.179
		1.089	0.105
		1.857	0.036
		1.499	-0.213
		1.592	-0.251
		1.577	-0.259
		1.266	0.146
		1.625	-0.115
		1.335	-0.056
		1.751	-0.061
		1.054	0.021
		1.308	0.056
		1.166	0.099
		1.356	0.002
		1.348	-0.023
		1.799	-0.108
		1.382	-0.068
		1.396	-0.046
		1.669	-0.090
		1.749	-0.043
		1.776	-0.078
		1.566	-0.111
		1.436	-0.134
		1.307	0.022
		r' (cm)	V_r (cm/sec)
		1.631	-0.077
		1.125	0.097
		1.225	0.105
		1.577	-0.191
		1.697	-0.120
		1.588	-0.147
		1.308	0.156
		1.650	-0.136
		1.377	-0.094
		1.115	0.105
		1.023	0.044
		1.323	0.075
		1.213	0.102
		1.467	-0.100
		1.516	-0.218
		1.084	0.060
		1.568	-0.187
		1.478	-0.251
		1.714	-0.071
		1.811	-0.037
		1.050	0.065
		1.602	-0.107
		1.594	-0.161
		1.397	-0.094
		r' (cm)	V_r (cm/sec)
		1.659	-0.175
		1.168	0.140
		1.260	0.140
		0.941	0.030
		1.713	-0.125
		1.652	-0.112
		1.361	-0.085
		1.687	-0.081
		1.597	-0.176
		1.204	0.118
		1.085	0.107
		1.350	-0.082
		1.400	-0.146
		1.571	-0.089
		1.172	0.062
		1.102	0.052
		1.681	-0.099
		1.578	-0.131
		1.438	-0.149
		0.797	0.009
		1.080	0.067
		1.712	-0.072
		1.672	-0.127
		1.640	-0.110
		r' (cm)	V_r (cm/sec)
		1.828	-0.059
		1.205	0.141
		1.355	-0.078
		1.127	0.123
		1.230	0.199
		1.119	0.112
		1.410	-0.080
		1.793	-0.070
		1.606	-0.229
		1.527	-0.176
		1.150	0.143
		1.356	-0.026
		1.567	-0.135
		1.620	-0.248
		1.270	0.174
		1.138	0.065
		1.139	0.088
		1.661	-0.125
		1.505	-0.140
		1.044	0.051
		1.139	0.098
		1.784	-0.050
		1.783	-0.076
		1.779	-0.051

TABLE E.22 (continued)

(Z/D) = 3.62		(t = 1.327 cm)	
r' (cm)	V _r (cm/sec)	r' (cm)	V _r (cm/sec)
1.430	-0.195	1.489	-0.191
1.211	0.083	1.222	0.098
1.144	0.110	1.329	-0.037
1.282	0.064	1.345	-0.071
1.513	-0.133	1.622	0.025
1.266	0.230	1.396	-0.113
1.207	0.092	1.339	-0.084
1.219	0.133	1.456	-0.234
1.592	-0.018	1.079	-0.038
1.341	-0.065	1.378	-0.116
1.379	-0.150	1.388	-0.149
1.435	-0.191	1.457	-0.210
1.269	0.132	1.384	-0.280
1.186	0.036	1.431	-0.179
1.206	0.104	0.925	-0.095
1.189	0.132	1.506	-0.126
1.527	-0.073	1.566	0.012
1.136	-0.017	1.240	0.179
		r' (cm)	V _r (cm/sec)
		1.549	-0.136
		1.563	-0.175
		1.404	-0.282
		1.391	-0.114
		1.514	-0.039
		1.573	-0.080
		1.408	-0.234
		1.495	-0.255
		1.136	0.041
		1.470	-0.229
		1.435	-0.309
		1.544	-0.141
		1.435	-0.281
		1.095	0.045
		0.989	-0.060
		1.545	-0.051
		1.660	0.039
		1.560	-0.105
		r' (cm)	V _r (cm/sec)
		1.576	-0.090
		1.577	-0.030
		1.414	-0.167
		1.434	-0.283
		1.584	-0.009
		1.606	-0.003
		1.521	-0.118
		1.500	-0.209
		1.190	0.043
		1.546	-0.067
		1.558	-0.017
		1.567	-0.124
		1.448	-0.230
		1.436	-0.272
		1.053	-0.007
		1.131	-0.044
		1.596	-0.012
		1.544	-0.087
		r' (cm)	V _r (cm/sec)
		1.083	-0.041
		0.864	0.017
		1.689	0.111
		1.503	-0.171
		1.595	-0.036
		1.076	-0.005
		1.546	-0.070
		1.562	-0.074
		1.222	0.041
		1.180	0.060
		1.306	0.122
		1.625	0.015
		1.132	-0.012
		1.567	-0.044
		1.078	0.002
		1.219	0.159
		1.645	-0.002
		r' (cm)	V _r (cm/sec)
		1.194	-0.041
		1.119	0.017
		1.776	0.111
		1.285	-0.171
		1.125	-0.036
		1.180	-0.005
		1.627	-0.070
		1.577	-0.074
		1.261	0.041
		1.245	0.060
		1.356	0.122
		1.212	0.015
		1.149	-0.012
		1.581	-0.044
		1.163	0.002
		1.491	0.159
		1.746	-0.002
		r' (cm)	V _r (cm/sec)
		1.194	-0.041
		1.119	0.017
		1.776	0.111
		1.285	-0.171
		1.125	-0.036
		1.180	-0.005
		1.627	-0.070
		1.577	-0.074
		1.261	0.041
		1.245	0.060
		1.356	0.122
		1.212	0.015
		1.149	-0.012
		1.581	-0.044
		1.163	0.002
		1.491	0.159
		1.746	-0.002
		r' (cm)	V _r (cm/sec)
		1.194	-0.041
		1.119	0.017
		1.776	0.111
		1.285	-0.171
		1.125	-0.036
		1.180	-0.005
		1.627	-0.070
		1.577	-0.074
		1.261	0.041
		1.245	0.060
		1.356	0.122
		1.212	0.015
		1.149	-0.012
		1.581	-0.044
		1.163	0.002
		1.491	0.159
		1.746	-0.002
		r' (cm)	V _r (cm/sec)
		1.194	-0.041
		1.119	0.017
		1.776	0.111
		1.285	-0.171
		1.125	-0.036
		1.180	-0.005
		1.627	-0.070
		1.577	-0.074
		1.261	0.041
		1.245	0.060
		1.356	0.122
		1.212	0.015
		1.149	-0.012
		1.581	-0.044
		1.163	0.002
		1.491	0.159
		1.746	-0.002
		r' (cm)	V _r (cm/sec)
		1.194	-0.041
		1.119	0.017
		1.776	0.111
		1.285	-0.171
		1.125	-0.036
		1.180	-0.005
		1.627	-0.070
		1.577	-0.074
		1.261	0.041
		1.245	0.060
		1.356	0.122
		1.212	0.015
		1.149	-0.012
		1.581	-0.044
		1.163	0.002
		1.491	0.159
		1.746	-0.002
		r' (cm)	V _r (cm/sec)
		1.194	-0.041
		1.119	0.017
		1.776	0.111
		1.285	-0.171
		1.125	-0.036
		1.180	-0.005
		1.627	-0.070
		1.577	-0.074
		1.261	0.041
		1.245	0.060
		1.356	0.122
		1.212	0.015
		1.149	-0.012
		1.581	-0.044
		1.163	0.002
		1.491	0.159
		1.746	-0.002
		r' (cm)	V _r (cm/sec)
		1.194	-0.041
		1.119	0.017
		1.776	0.111
		1.285	-0.171
		1.125	-0.036
		1.180	-0.005
		1.627	-0.070
		1.577	-0.074
		1.261	0.041
		1.245	0.060
		1.356	0.122
		1.212	0.015
		1.149	-0.012
		1.581	-0.044
		1.163	0.002
		1.491	0.159
		1.746	-0.002
		r' (cm)	V _r (cm/sec)
		1.194	-0.041
		1.119	0.017
		1.776	0.111
		1.285	-0.171
		1.125	-0.036
		1.180	-0.005
		1.627	-0.070
		1.577	-0.074
		1.261	0.041
		1.245	0.060
		1.356	0.122
		1.212	0.015
		1.149	-0.012
		1.581	-0.044
		1.163	0.002
		1.491	0.159
		1.746	-0.002
		r' (cm)	V _r (cm/sec)
		1.194	-0.041
		1.119	0.017
		1.776	0.111
		1.285	-0.171
		1.125	-0.036
		1.180	-0.005
		1.627	-0.070
		1.577	-0.074
		1.261	0.041
		1.245	0.060
		1.356	0.122
		1.212	0.015
		1.149	-0.012
		1.581	-0.044
		1.163	0.002
		1.491	0.159
		1.746	-0.002
		r' (cm)	V _r (cm/sec)
		1.194	-0.041
		1.119	0.017
		1.776	0.111
		1.285	-0.171
		1.125	-0.036
		1.180	-0.005
		1.627	-0.070
		1.577	-0.074
		1.261	0.041
		1.245	0.060
		1.356	0.122
		1.212	0.015
		1.149	-0.012
		1.581	-0.044
		1.163	0.002
		1.491	0.159
		1.746	-0.002
		r' (cm)	V _r (cm/sec)
		1.194	-0.041
		1.119	0.017
		1.776	0.111
		1.285	-0.171
		1.125	-0.036
		1.180	-0.005
		1.627	-0.070
		1.577	-0.074
		1.261	0.041
		1.245	0.060
		1.356	0.122
		1.212	0.015
		1.149	-0.012
		1.581	-0.044
		1.163	0.002
		1.491	0.159
		1.746	-0.002
		r' (cm)	V _r (cm/sec)
		1.194	-0.041
		1.119	0.017
		1.776	0.111
		1.285	-0.171
		1.125	-0.036
		1.180	-0.005
		1.627	-0.070
		1.577	-0.074
		1.261	0.041
		1.245	0.060
		1.356	0.122
		1.212	0.015
		1.149	-0.012
		1.581	-0.044
		1.163	0.002
		1.491	0.159
		1.746	-0.002
		r' (cm)	V _r (cm/sec)
		1.194	-0.041
		1.119	0.017
		1.776	0.111
		1.285	-0.171
		1.125	-0.036
		1.180	-0.005
		1.627	-0.070
		1.577	-0.074
		1.261	0.041
		1.245	0.060
		1.356	0.122
		1.212	0.015
		1.149	-0.012
		1.581	-0.044
		1.163	0.002
		1.491	0.159
		1.746	-0.002
		r' (cm)	V _r (cm/sec)
		1.194	-0.041
		1.119	0.017
		1.776	0.111
		1.285	-0.171
		1.125	-0.036
		1.180	-0.005
		1.627	-0.070
		1.577	-0.074
		1.261	0.041
		1.245	0.060
		1.356	0.122
		1.212	0.015
		1.149	-0.012
		1.581	-0.044
		1.163	0.002
		1.491	0.159
		1.746	-0.002
		r' (cm)	V _r (cm/sec)
		1.194	-0.041
		1.119	0.017
		1.776	0.111
		1.285	-0.171
		1.125	-0.036
		1.180	-0.005
		1.627	-0.070
		1.577	-0.074
		1.261	0.041
		1.245	0.060
		1.356	0.122
		1.212	0.015
		1.149	-0.012
		1.581	-0.044
		1.163	0.002
		1.491	0.159
		1.746	-0.002
		r' (cm)	V _r (cm/sec)
		1.194	-0.041
		1.119	0.017
		1.776	0.111
		1.285	-0.171
		1.125	-0.036
		1.180	-0.005
		1.627	-0.070
		1.577	-0.074
		1.261	0.041
		1.245	0.060
		1.356	0.122
		1.212	0.015
		1.149	-0.012
		1.581	-0.044
		1.163	0.002

TABLE E.23 (continued)

(Z/D) = 3.99		(t = 1.327 cm)											
r' (cm)	V _r (cm/sec)	r' (cm)	V _r (cm/sec)	r' (cm)	V _r (cm/sec)	r' (cm)	V _r (cm/sec)	r' (cm)	V _r (cm/sec)	r' (cm)	V _r (cm/sec)	r' (cm)	V _r (cm/sec)
1.305	0.416	1.013	-0.051	1.632	-0.007	1.337	0.053	1.165	0.087	1.180	0.114		
1.155	-0.214	1.499	-0.166	1.237	0.171	1.301	0.097	1.502	-0.124	1.620	-0.028		
1.312	0.046	1.533	-0.098	1.196	0.221	1.300	0.277	1.591	-0.013	1.333	-0.274		
1.374	-0.305	1.517	-0.297	1.475	0.003	1.398	-0.103	1.585	-0.58	1.286	-0.136		
1.159	0.331	1.629	-0.030	1.561	-0.124	1.309	-0.263	1.651	-0.061	1.170	-0.038		
1.359	-0.208	1.039	-0.029	1.519	-0.161	1.274	-0.347	1.177	0.200	1.585	0.017		
1.294	0.035	1.462	-0.138	1.099	-0.022	1.319	-0.151	1.077	0.039	1.160	0.091		
1.340	-0.208	1.179	0.099	1.247	0.292	1.359	0.190	1.481	-0.115	1.265	-0.037		
1.366	-0.268	1.583	0.018	1.537	-0.122	1.430	0.083	1.476	-0.152	1.349	-0.142		
1.111	0.019	1.568	-0.012	1.475	-0.175	1.492	-0.176	1.375	-0.150	1.478	0.016		
1.562	-0.022	1.019	-0.026	1.366	-0.256	1.596	-0.009	1.136	0.138	1.440	-0.114		
1.646	-0.006	1.180	0.080	1.454	-0.039	1.524	-0.202	1.195	0.089	1.600	-0.030		
1.585	-0.032	1.316	0.229	1.312	-0.152	1.633	-0.045	1.433	-0.159	1.336	-0.379		
1.353	-0.331	1.506	-0.070	1.577	-0.104	1.404	-0.300	1.532	-0.022	1.588	-0.070		
1.485	-0.147	1.233	0.101	1.060	-0.103								

TABLE E.24

RADIAL VELOCITIES - DIGITIZER METHOD, $Q=0.040 \text{ cm}^3/\text{sec}$
 0.30 cm I.D. CAPILLARY TUBE, SMALL RESERVOIR

(Z/D) = 2.19 ($\xi = 1.327 \text{ cm}$)

r' (cm)	V_r (cm/sec)	r' (cm)	V_r (cm/sec)	r' (cm)	V_r (cm/sec)	r' (cm)	V_r (cm/sec)	r' (cm)	V_r (cm/sec)	r' (cm)	V_r (cm/sec)	r' (cm)	V_r (cm/sec)
1.489	-0.040	1.567	-0.025	1.346	-0.005	1.577	-0.045	1.034	0.022	1.445	-0.013		
1.661	-0.031	1.145	0.032	1.282	0.020	1.386	0.002	1.535	-0.029	1.228	0.029		
1.479	-0.011	1.613	-0.032	1.163	0.027	1.241	0.000	1.638	-0.034	1.680	-0.025		
1.365	-0.040	1.047	0.033	1.431	-0.020	1.229	-0.019	1.254	0.003	1.349	0.001		
1.394	-0.018	1.278	0.008	1.705	-0.030	1.472	-0.035	1.346	-0.013	1.407	-0.009		
1.209	0.000	1.280	0.011	1.217	0.012	1.346	-0.008	1.294	-0.006	1.489	-0.026		
1.445	-0.021	1.556	-0.030	1.661	-0.020	1.246	0.006	0.908	0.018	1.241	0.000		
1.250	0.020	1.270	0.013	1.365	-0.026	1.304	0.015	1.302	0.005	1.229	-0.013		
1.496	-0.037	1.365	-0.006	1.472	-0.023	1.575	-0.036	1.407	-0.011	1.209	0.000		
1.241	0.032	1.632	-0.025										

(Z/D) = 1.46 ($\xi = 1.327 \text{ cm}$)

r' (cm)	V_r (cm/sec)	r' (cm)	V_r (cm/sec)	r' (cm)	V_r (cm/sec)	r' (cm)	V_r (cm/sec)	r' (cm)	V_r (cm/sec)	r' (cm)	V_r (cm/sec)	r' (cm)	V_r (cm/sec)
1.364	0.028	0.954	0.017	1.225	-0.031	1.405	-0.017	1.224	0.030	1.293	0.000		
1.420	-0.015	1.546	-0.046	1.420	-0.047	1.520	-0.037	1.255	0.051	1.608	-0.016		
1.193	0.036	1.405	-0.033	1.405	-0.011	1.533	-0.052	1.481	-0.078	1.420	-0.010		
1.251	-0.007	1.275	0.077	1.520	-0.024	1.333	-0.027	1.535	-0.060	1.193	0.023		
1.427	-0.054	1.261	0.031	1.533	-0.034	0.957	0.023	1.274	0.015	1.251	-0.005		
1.017	0.059	1.484	-0.058	0.957	0.015	1.232	-0.005	1.549	-0.058	1.017	0.038		
1.344	-0.050	1.561	-0.052	1.126	0.035	1.140	0.049	1.136	0.011	1.232	-0.003		
1.319	-0.004	1.269	0.027	1.140	0.031	1.435	-0.047	1.285	0.028	1.319	-0.003		
1.512	-0.055	1.352	-0.051	1.435	-0.030	1.216	0.003	1.402	-0.048	1.216	0.002		
1.342	-0.032	1.307	0.000	1.342	-0.021	1.348	0.006	1.365	-0.004	1.348	0.004		

TABLE E.24 (continued)

(Z/D) = 1.46 (t = 1.327 cm)											
r' (cm)	V _r (cm/sec)	r' (cm)	V _r (cm/sec)	r' (cm)	V _r (cm/sec)	r' (cm)	V _r (cm/sec)	r' (cm)	V _r (cm/sec)	r' (cm)	V _r (cm/sec)
1.412	-0.069	1.380	-0.008	1.412	-0.044	1.481	-0.060	1.352	-0.001	1.481	-0.039
1.282	0.020	1.359	0.010	1.519	-0.032	1.319	0.021	1.544	-0.035	1.590	-0.013
1.398	-0.011	1.567	-0.044	1.402	0.025	1.377	-0.013	1.109	0.017	1.537	-0.047
(Z/D) = 0.73 (t = 1.327 cm)											
r' (cm)	V _r (cm/sec)	r' (cm)	V _r (cm/sec)	r' (cm)	V _r (cm/sec)	r' (cm)	V _r (cm/sec)	r' (cm)	V _r (cm/sec)	r' (cm)	V _r (cm/sec)
1.437	-0.080	1.560	-0.057	1.495	-0.036	1.366	-0.003	1.102	0.035	1.513	-0.075
1.395	-0.030	1.120	0.038	1.288	-0.014	1.437	-0.066	1.275	0.071	1.366	-0.002
1.235	0.104	1.350	-0.015	1.395	-0.019	1.322	0.051	1.530	-0.051	1.437	-0.042
1.477	-0.060	1.688	-0.006	1.478	-0.042	1.499	-0.063	1.281	0.041	1.374	-0.006
1.595	-0.032	1.408	-0.049	1.477	-0.039	1.247	0.018	1.445	-0.058	1.499	-0.041
1.331	-0.092	1.487	-0.071	1.595	-0.020	1.372	-0.061	1.349	0.010	1.247	0.011
1.040	-0.012	1.369	0.004	1.227	0.028	1.148	0.084	1.086	0.018	1.441	-0.048
1.225	-0.009	1.334	-0.011	1.598	-0.032	1.243	0.001	1.343	-0.028	1.621	-0.030
1.306	-0.076	1.370	-0.064	1.224	0.084	1.227	0.044	1.495	-0.074	1.447	-0.054
1.350	-0.017	1.313	0.032	1.358	-0.006	1.441	-0.075	1.368	-0.016	1.471	-0.072
1.336	0.032	1.449	-0.045	1.495	-0.063	1.384	0.006	1.488	-0.050	1.280	0.081
1.431	-0.036	1.303	0.016	1.483	-0.109	1.400	-0.058				

TABLE E.25 (continued)

(Z/D) = 2.92		$(\psi = 1.327 \text{ cm})$															
$r' \text{ (cm)}$	$V_r \text{ (cm/sec)}$	$V_z \text{ (cm/sec)}$	$r' \text{ (cm)}$	$V_r \text{ (cm/sec)}$	$V_z \text{ (cm/sec)}$	$r' \text{ (cm)}$	$V_r \text{ (cm/sec)}$	$V_z \text{ (cm/sec)}$	$r' \text{ (cm)}$	$V_r \text{ (cm/sec)}$	$V_z \text{ (cm/sec)}$	$r' \text{ (cm)}$	$V_r \text{ (cm/sec)}$	$V_z \text{ (cm/sec)}$	$r' \text{ (cm)}$	$V_r \text{ (cm/sec)}$	$V_z \text{ (cm/sec)}$
1.123	0.136	0.421	1.752	-0.055	0.100	1.324	0.088	0.944	1.140	0.171	0.813	1.569	-0.081	0.413	1.676	-0.064	0.349
1.393	-0.031	0.958	1.530	-0.141	0.677	1.447	-0.122	0.973	1.569	-0.081	0.413	1.569	-0.081	0.413	1.676	-0.064	0.349
1.671	-0.084	0.297	1.685	-0.058	0.183	1.695	-0.059	0.238	0.918	0.030	0.164	1.301	0.014	0.999	1.523	-0.138	0.663
1.069	0.100	0.385	1.081	0.042	0.405	1.283	0.073	1.025	1.579	-0.014	0.999	1.301	0.014	0.999	1.523	-0.138	0.663
1.347	-0.002	0.969	1.545	-0.176	0.542	1.379	-0.039	0.992	1.672	-0.100	0.322	1.569	-0.018	0.833	1.676	-0.064	0.349
1.466	-0.072	0.862	1.600	-0.090	0.416	1.628	-0.104	0.399	1.339	0.069	0.987	1.526	-0.140	0.692	1.676	-0.064	0.349
1.717	-0.060	0.193	1.142	0.117	0.589	1.771	-0.056	0.125	1.708	-0.090	0.263	1.531	-0.122	0.519	1.676	-0.064	0.349
1.068	0.103	0.366	1.397	-0.059	0.888	1.390	-0.075	0.872	1.270	0.064	0.949	1.343	-0.016	0.966	1.676	-0.064	0.349
1.397	-0.055	0.951	1.580	-0.111	0.439	1.405	-0.011	0.905	1.531	-0.122	0.519	1.676	-0.064	0.349	1.676	-0.064	0.349
1.423	-0.039	1.021	1.743	-0.034	0.158	1.453	-0.036	0.886	1.526	-0.140	0.692	1.676	-0.064	0.349	1.676	-0.064	0.349
1.509	-0.097	0.825	1.426	-0.054	0.971	1.539	-0.157	0.819	1.526	-0.140	0.692	1.676	-0.064	0.349	1.676	-0.064	0.349
1.587	-0.100	0.577	1.639	-0.155	0.452	0.961	0.034	0.172	1.676	-0.064	0.349	1.676	-0.064	0.349	1.676	-0.064	0.349
1.172	0.190	0.708	1.382	0.007	0.932	1.352	-0.035	1.029	1.423	-0.018	0.833	1.569	-0.018	0.833	1.676	-0.064	0.349
1.368	-0.064	1.035	1.446	-0.050	0.772	1.570	-0.104	0.569	1.565	-0.106	0.652	1.565	-0.106	0.652	1.676	-0.064	0.349
1.748	-0.057	0.174	1.578	-0.138	0.558	1.107	0.114	0.567	1.708	-0.090	0.263	1.531	-0.122	0.519	1.676	-0.064	0.349
1.314	0.052	0.883	1.313	-0.023	1.016	1.436	-0.089	0.853	1.531	-0.122	0.519	1.676	-0.064	0.349	1.676	-0.064	0.349
0.871	0.029	0.116	1.170	0.150	0.715	1.466	-0.086	0.821	1.270	0.064	0.949	1.343	-0.016	0.966	1.676	-0.064	0.349
1.624	-0.101	0.311	1.288	0.026	0.944	1.399	-0.053	0.840	1.507	-0.073	0.385	1.576	-0.073	0.385	1.676	-0.064	0.349
1.030	0.096	0.250	1.437	-0.100	0.789	1.047	0.078	0.298	1.576	-0.073	0.385	1.576	-0.073	0.385	1.676	-0.064	0.349
1.133	0.110	0.577	1.549	-0.091	0.515	1.342	0.004	0.931	1.576	-0.073	0.385	1.576	-0.073	0.385	1.676	-0.064	0.349
1.367	-0.070	1.074	1.804	-0.026	0.075	1.388	-0.034	0.951	1.688	0.019	0.925	1.288	0.034	0.925	1.676	-0.064	0.349
1.557	-0.134	0.605	1.261	0.103	0.856	1.600	-0.102	0.338	1.288	0.019	0.925	1.288	0.034	0.925	1.676	-0.064	0.349
1.111	0.093	0.592	1.044	0.103	0.347	1.184	0.123	0.848	1.259	0.058	0.875	1.259	0.058	0.875	1.676	-0.064	0.349
1.319	0.020	0.965	1.338	-0.056	1.039	1.353	-0.052	1.072	1.348	-0.023	0.990	1.348	-0.023	0.990	1.676	-0.064	0.349
1.702	-0.033	0.167	1.573	-0.095	0.466	1.364	0.010	0.942	1.284	0.029	0.979	1.284	0.029	0.979	1.676	-0.064	0.349
1.385	-0.013	1.028	1.421	-0.082	0.771	1.436	-0.077	0.854	1.523	-0.081	0.502	1.523	-0.081	0.502	1.676	-0.064	0.349
1.629	-0.095	0.403	1.109	0.127	0.666	1.656	-0.097	0.298	1.301	0.024	0.963	1.301	0.024	0.963	1.676	-0.064	0.349
1.678	-0.061	0.234	1.431	-0.069	0.900	0.852	0.041	0.103	1.731	-0.078	0.257	1.731	-0.078	0.257	1.676	-0.064	0.349

TABLE E.25 (continued)

(Z/D) = 1.46						(ϕ = 1.327 cm)					
r' (cm)	V_r (cm/sec)	V_z (cm/sec)	r' (cm)	V_r (cm/sec)	V_z (cm/sec)	r' (cm)	V_r (cm/sec)	V_z (cm/sec)	r' (cm)	V_r (cm/sec)	V_z (cm/sec)
1.383	-0.061	2.321	1.499	-0.108	0.657	1.402	-0.054	1.688	1.589	0.001	0.192
1.415	-0.071	1.960	1.024	-0.007	0.231	1.335	-0.015	2.036	1.309	0.003	2.050
1.593	-0.098	0.346	1.383	-0.083	1.655	1.136	0.042	0.429	1.425	-0.098	1.580
1.298	-0.011	1.553	1.453	-0.078	1.096	1.344	0.040	1.690	1.490	-0.044	0.557
1.369	-0.088	1.783	1.143	0.115	1.072	1.385	-0.065	2.038	1.353	-0.073	2.004
1.395	-0.010	1.696	1.403	-0.023	1.556	1.408	-0.136	1.802	1.501	-0.065	0.825
1.415	-0.038	1.811	1.201	0.110	1.060	1.455	-0.072	1.529	1.243	0.040	1.293
1.504	-0.121	1.042	1.366	-0.065	1.926	1.554	-0.092	0.610	1.398	-0.040	1.791
1.642	0.020	0.172	1.435	-0.027	1.390	1.426	-0.030	1.859	1.509	-0.122	0.905
1.462	-0.070	1.489	1.351	0.051	1.963	1.524	-0.066	1.086	1.404	-0.111	2.064
1.280	0.105	1.722	1.523	-0.066	1.195	1.026	-0.006	0.123	1.088	-0.013	0.163
1.182	0.017	0.996	1.384	0.004	1.785	1.361	-0.056	1.777	1.413	-0.049	1.719
1.390	-0.066	1.882	1.440	-0.129	1.078	1.427	-0.108	1.701	1.456	-0.090	0.915
1.093	0.066	0.426	1.528	-0.074	0.318	1.305	0.042	2.020	1.551	-0.037	0.271
1.342	-0.083	1.627	1.209	0.051	1.877	1.334	-0.075	1.836	1.342	-0.054	1.527
1.390	-0.113	1.680	1.521	-0.040	0.265	1.491	-0.108	0.776	1.543	-0.034	0.244
1.565	-0.036	0.302	1.601	0.018	0.080	1.464	-0.122	0.980	1.116	0.074	0.516
1.480	-0.087	0.831	1.210	0.110	1.295	1.482	-0.116	1.174	1.607	-0.023	0.336
1.530	-0.124	0.751	1.742	0.032	0.055	1.551	-0.081	0.594	1.183	0.119	1.428
1.090	0.047	0.312	1.456	-0.136	1.024	1.178	0.084	1.388	0.895	0.005	0.113
1.212	0.113	1.547	1.267	0.044	1.617	1.562	-0.023	0.296	1.117	0.080	0.668
1.066	0.058	0.471	1.271	0.042	1.546	1.138	0.116	1.271	1.502	-0.121	0.666
1.285	0.023	1.794	1.123	0.126	1.152	1.429	-0.115	1.011	1.459	-0.098	0.796
1.491	-0.052	0.466	1.552	-0.050	0.194	1.501	-0.062	0.425	1.642	-0.045	0.302
1.541	-0.038	0.400	1.691	-0.006	0.164	1.564	-0.057	0.510			

TABLE E.26
RADIAL VELOCITIES - DIGITIZER METHOD, Q=0.318 cm³/sec
0.030 cm I.D. CAPILLARY TUBE, SMALL RESERVOIR

(Z/D) = 5.96				(ϕ = 1.327 cm)			
r' (cm)	V _r (cm/sec)	r' (cm)	V _r (cm/sec)	r' (cm)	V _r (cm/sec)	r' (cm)	V _r (cm/sec)
0.873	0.163	1.916	-0.112	1.894	-0.105	1.315	-0.051
1.389	-0.081	1.068	0.160	1.345	-0.060	1.403	-0.092
1.433	-0.025	1.587	-0.165	1.433	-0.064	1.488	-0.177
1.562	-0.129	1.138	0.161	1.563	-0.178	1.587	-0.179
1.707	-0.152	1.338	-0.052	1.728	-0.184	1.753	-0.152
1.812	-0.117	1.597	-0.152	1.939	-0.069	1.332	0.004
1.366	-0.067	0.802	0.096	0.951	0.140	1.390	-0.055
1.381	-0.024	1.402	-0.056	1.384	-0.068	1.491	-0.071
1.670	-0.116	1.495	-0.085	1.590	-0.120	1.756	-0.150
1.814	-0.115	1.993	-0.090	1.984	-0.088	1.180	0.123
1.388	-0.019	1.405	-0.032	1.521	-0.106	1.399	-0.103
1.441	-0.043	1.655	-0.179	1.608	-0.106	1.518	-0.151
1.655	-0.204	1.785	-0.152	2.041	-0.063	1.689	-0.138
1.739	-0.133	1.824	-0.115	0.994	0.141	1.042	0.135
1.325	-0.057	1.030	0.143	1.521	-0.157	1.345	-0.039
1.508	-0.140	1.391	-0.007	1.661	-0.135	1.711	-0.165
1.812	-0.151	1.657	-0.163	1.933	-0.089	0.743	0.067
1.042	0.139	1.785	-0.175	1.727	-0.150	1.304	0.042
1.426	-0.033	1.284	0.052	1.155	0.133	1.455	-0.073
1.547	-0.101	1.588	-0.099	1.362	-0.052	1.961	-0.085
0.960	0.172	1.868	-0.111	1.407	-0.035	0.981	0.142
1.084	0.106	0.875	0.076	1.531	-0.125	1.167	0.122
1.390	-0.018	1.340	-0.006	1.446	-0.097	1.398	0.003
1.427	-0.036	1.387	-0.027	1.777	-0.152	1.460	-0.078
1.616	-0.120	1.494	-0.153	1.414	-0.071	1.880	-0.095
1.965	-0.106	1.381	-0.024	1.532	-0.104	0.713	0.074
0.893	0.144	1.403	-0.005	1.350	-0.017	1.364	-0.023

r' (cm)	V _r (cm/sec)	r' (cm)	V _r (cm/sec)	r' (cm)	V _r (cm/sec)	r' (cm)	V _r (cm/sec)
1.326	0.132	0.956	-0.051	1.315	-0.051	0.956	0.132
1.414	-0.060	1.432	-0.092	1.403	-0.092	1.432	-0.060
1.512	-0.133	1.622	-0.177	1.488	-0.177	1.622	-0.133
1.628	-0.034	1.318	-0.179	1.587	-0.179	1.318	-0.034
1.812	-0.086	1.501	-0.152	1.753	-0.152	1.501	-0.086
0.919	-0.165	1.791	0.004	1.332	0.004	1.791	-0.165
1.172	0.124	0.833	-0.055	1.390	-0.055	0.833	0.124
1.419	-0.024	1.381	-0.071	1.491	-0.071	1.381	-0.024
1.625	-0.103	1.788	-0.150	1.756	-0.150	1.788	-0.103
1.448	-0.034	1.397	0.123	1.180	0.123	1.397	-0.034
1.581	-0.071	1.501	-0.103	1.399	-0.103	1.501	-0.071
1.829	-0.160	1.678	-0.151	1.518	-0.151	1.678	-0.160
0.954	-0.112	1.798	-0.138	1.689	-0.138	1.798	-0.112
1.473	-0.130	1.806	0.135	1.042	0.135	1.806	-0.130
1.612	0.003	1.272	-0.039	1.345	-0.039	1.272	0.003
1.867	-0.067	1.448	-0.165	1.711	-0.165	1.448	-0.067
1.427	-0.181	1.709	0.067	0.743	0.067	1.709	-0.181
1.985	-0.089	1.936	0.042	1.304	0.042	1.936	-0.089
1.349	-0.011	1.409	-0.073	1.455	-0.073	1.409	-0.011
1.378	-0.171	1.811	-0.085	1.961	-0.085	1.811	-0.171
1.473	-0.109	1.944	0.142	0.981	0.142	1.944	-0.109
1.547	0.058	1.327	0.122	1.167	0.122	1.327	0.058
-0.153	-0.055	1.346	0.003	1.398	0.003	1.346	-0.055
0.184	-0.023	1.395	-0.078	1.460	-0.078	1.395	-0.023
0.091	-0.112	1.567	-0.095	1.880	-0.095	1.567	-0.112
-0.102	-0.031	1.367	0.074	0.713	0.074	1.367	-0.031
-0.003	-0.129	1.424	-0.023	1.364	-0.023	1.424	-0.129

TABLE E.26 (continued)

(Z/D) = 3.97 ($\zeta = 1.327$ cm)

r' (cm)	V_r (cm/sec)	r' (cm)	V_r (cm/sec)	r' (cm)	V_r (cm/sec)	r' (cm)	V_r (cm/sec)	r' (cm)	V_r (cm/sec)	r' (cm)	V_r (cm/sec)
1.026	0.124	1.594	-0.140	1.383	-0.071	1.313	-0.052	1.639	-0.115	1.475	-0.171
1.364	-0.053	1.670	-0.124	1.549	-0.178	1.373	-0.113	0.987	0.063	1.611	-0.170
1.383	-0.013	1.244	0.117	1.671	-0.116	1.483	-0.137	1.433	-0.027	1.760	-0.076
1.567	-0.197	1.470	-0.112	1.825	-0.031	1.575	-0.138	1.527	-0.154	0.833	0.018
1.595	-0.156	1.748	-0.079	1.212	0.133	1.605	-0.155	1.095	0.169	1.137	0.183
1.634	-0.117	1.158	0.169	1.367	-0.053	1.660	-0.114	1.404	-0.045	1.541	-0.187
1.126	0.194	1.436	-0.121	1.623	-0.118	1.357	-0.085	1.509	-0.199	1.645	-0.165
1.423	-0.162	1.650	-0.069	1.673	-0.124	1.472	-0.125	1.748	-0.056	1.758	-0.097
1.435	-0.023	1.164	0.174	0.907	0.085	1.552	-0.116	1.204	-0.134	1.040	0.138
1.599	-0.203	1.376	-0.049	1.265	0.007	1.663	-0.113	1.422	-0.163	1.388	-0.106
1.666	-0.116	1.455	-0.199	1.498	-0.189	1.758	-0.055	1.577	-0.118	1.537	-0.136
1.116	0.178	1.613	-0.122	1.599	-0.173	1.236	0.156	1.668	-0.092	1.608	-0.134
1.366	-0.067	0.869	0.020	1.688	-0.100	1.524	-0.119	0.922	0.073	1.720	-0.059
1.527	-0.112	0.986	0.063	1.733	-0.046	1.552	-0.116	1.052	0.087	1.742	-0.068
0.911	0.069	1.052	0.115	1.354	-0.089	0.924	0.066	1.126	0.141	1.365	-0.033
1.095	0.151	1.517	-0.146	1.379	-0.074	1.585	-0.124	1.603	-0.174	1.600	-0.126
1.707	-0.081	1.642	-0.114	1.169	0.200	1.742	-0.078	1.668	-0.100	1.568	-0.139
1.761	-0.084	1.699	-0.089	1.771	-0.031	1.384	-0.014	1.798	-0.050	1.872	-0.038
1.711	-0.090	0.951	0.054	1.067	0.116	1.796	-0.069	1.393	-0.025	1.221	0.098
0.855	0.060	1.578	-0.157	1.358	-0.045	0.941	0.080	1.668	-0.136	1.592	-0.128
1.072	0.174	1.711	-0.133	1.661	-0.083	1.107	0.178	1.816	-0.032	1.699	-0.074
1.436	-0.131	1.349	-0.012	1.019	0.086	1.581	-0.115	1.385	-0.095	1.355	-0.045
1.770	-0.050	1.416	-0.137	1.363	-0.044	1.893	-0.027	1.461	-0.117	1.373	-0.053
0.809	0.023	1.479	-0.125	1.382	-0.026	1.421	-0.019	1.590	-0.129	1.412	-0.080
1.763	-0.109	1.623	-0.150	1.664	-0.138	1.863	-0.044	1.385	-0.073	1.726	-0.109
1.070	0.119	1.606	-0.184	0.777	0.020	1.101	0.156	1.652	-0.127	1.138	0.137
1.776	-0.065	1.668	-0.159	1.215	0.086	0.736	0.020	1.709	-0.053	1.232	0.072
1.126	0.208	1.104	0.211								

TABLE E.27 (continued)

(Z/D) = 2.51		(λ = 1.327 cm)									
r' (cm)	V _r (cm/sec)	r' (cm)	V _r (cm/sec)	r' (cm)	V _r (cm/sec)	r' (cm)	V _r (cm/sec)	r' (cm)	V _r (cm/sec)	r' (cm)	V _r (cm/sec)
1.320	-0.177	1.016	0.038	1.022	-0.065	1.458	-0.172	1.126	0.068	1.136	0.134
1.475	-0.397	1.480	-0.320	1.594	-0.038	1.390	-0.014	1.623	-0.050	1.644	-0.113
1.454	-0.219	1.662	-0.079	1.025	-0.005	1.644	-0.132	1.683	-0.014	1.161	0.276
1.660	-0.055	1.692	0.030	1.544	-0.213	1.677	-0.087	1.017	0.031	1.552	-0.118
1.756	0.036	1.504	-0.088	1.612	-0.096	1.068	-0.047	1.568	-0.031	1.698	-0.039
1.197	0.099	1.578	-0.002								

TABLE E.28
RADIAL AND AXIAL VELOCITIES - DIGITIZER METHOD, Q=1.589 cm³/sec
0.20 cm I.D. CAPILLARY TUBE, LARGE RESERVOIR

(Z/D) = 30.67 (ϕ = 12.745 cm)									
r' (cm)	V _r (cm/sec)	V _z (cm/sec)	r' (cm)	V _r (cm/sec)	V _z (cm/sec)	r' (cm)	V _r (cm/sec)	V _z (cm/sec)	r' (cm)
12.940	0.562	2.827	14.111	-0.207	0.786	12.479	0.312	3.318	13.806
11.879	0.306	1.112	13.514	-0.271	1.931	11.670	0.217	1.287	12.964
10.316	0.153	0.216	12.030	0.344	1.646	9.813	0.098	0.119	11.617
10.761	0.185	0.478	10.737	0.218	0.530	14.650	-0.268	0.553	10.198
14.319	-0.120	0.708	14.137	-0.189	0.840	14.052	-0.203	0.955	13.345
13.764	-0.224	1.142	12.497	0.548	2.468	13.165	-0.278	2.839	10.332
12.763	0.235	3.895	14.754	-0.113	0.464	12.624	0.089	3.027	12.865
12.537	1.106	2.840	12.611	0.423	4.064	11.918	0.403	1.363	11.767
11.147	0.362	0.769	11.535	0.267	0.948	10.463	0.170	0.305	10.796
14.624	-0.202	1.152	10.318	0.114	0.313	13.739	-0.478	1.251	13.903
13.458	-0.585	1.782	13.620	-0.201	1.401	12.546	-0.292	3.551	13.627
12.274	0.204	2.603	13.197	-0.032	2.170	10.398	0.162	0.275	12.847
13.822	-0.335	1.299	12.556	0.044	1.767	12.671	0.919	5.288	11.591
11.754	0.293	1.163	10.910	0.337	0.562	9.712	0.082	0.115	10.005
(Z/D) = 15.34 (ϕ = 12.745 cm)									
r' (cm)	V _r (cm/sec)	V _z (cm/sec)	r' (cm)	V _r (cm/sec)	V _z (cm/sec)	r' (cm)	V _r (cm/sec)	V _z (cm/sec)	r' (cm)
13.471	-0.465	0.912	13.105	-0.154	5.760	13.277	-0.299	3.425	12.267
13.180	-0.243	3.836	12.889	-0.712	24.070	13.025	0.393	10.045	13.399
12.682	0.850	19.025	12.522	0.324	6.729	12.289	0.220	2.995	12.642
11.796	-0.235	0.563	12.079	-0.012	1.903	11.672	-0.028	0.702	13.570
12.971	-0.482	19.095	13.451	0.008	2.046	13.127	-0.477	5.538	13.024
13.009	0.364	11.003	12.625	1.712	15.191	12.708	1.768	24.915	12.217
12.257	0.203	2.673	12.059	-0.367	1.416	13.126	-0.405	4.474	11.669
12.850	0.362	14.177	13.147	-0.365	4.224	11.752	0.007	1.192	13.070
10.719	-0.196	0.114	12.277	0.086	3.276	13.443	0.005	1.192	11.975
12.690	0.498	17.161	13.147	-0.365	4.224	13.069	0.086	3.276	12.277
							V _r (cm/sec)	V _z (cm/sec)	
							0.148	2.032	
							0.053	3.096	
							0.640	10.068	
							-0.099	1.528	
							0.058	8.646	
							-0.189	1.810	
							-0.779	0.666	
							-0.030	6.547	
							-0.099	1.296	
							-0.030	6.547	

TABLE E.29

RADIAL AND AXIAL VELOCITIES - DIGITIZER METHOD, $Q=1.906 \text{ cm}^3/\text{sec}$
 0.20 cm I.D. CAPILLARY TUBE, LARGE RESERVOIR

$(Z/D) = 31.20$		$(\xi = 12.745 \text{ cm})$	
$r' \text{ (cm)}$	$V_r \text{ (cm/sec)}$	$V_z \text{ (cm/sec)}$	$r' \text{ (cm)}$
14.343	-0.407	0.719	13.511
13.640	-0.417	1.697	12.595
13.075	0.094	2.778	12.252
11.794	0.467	1.439	10.956
10.623	0.106	1.439	13.448
9.914	0.032	0.289	12.792
14.020	-0.057	0.870	11.697
12.781	0.547	6.064	14.261
12.562	0.702	4.039	12.991
12.265	0.446	2.254	12.543
11.459	0.678	1.175	12.044
13.792	-0.239	1.417	11.585
12.935	-0.083	4.552	13.548
12.389	0.378	3.710	12.963
11.840	0.456	1.969	12.330
11.189	0.180	0.876	12.054
9.922	0.092	0.228	10.862
13.190	0.353	3.354	13.643
12.537	0.298	5.487	12.252
12.292	1.359	3.593	11.367
11.907	0.435	1.470	13.357
12.532	0.486	5.706	12.906
12.141	0.668	2.135	12.367
10.493	0.137	0.338	11.137
14.510	-0.173	0.769	13.272
12.854	-0.241	1.455	11.893
13.332	-0.257	1.986	14.053
12.904	-0.265	6.376	12.805
11.501	0.440	1.186	12.504
			0.393
			5.098
			12.607
			13.261
			13.050
			14.020
			11.127
			12.047
			12.288
			12.668
			12.021
			10.197
			12.851
			9.818
			10.166
			11.615
			12.320
			12.444
			13.585
			12.820
			11.563
			12.329
			12.700
			13.579
			14.314
			9.502
			11.539
			12.071
			13.241
			13.870
			-0.516
			1.623
			13.080
			0.062
			2.670
			4.609
			3.391
			1.437
			5.208
			3.123
			0.615
			0.228
			1.068
			-0.876
			3.877
			-0.064
			5.971
			-0.252
			2.763
			0.217
			1.415
			0.369
			-0.396
			0.933
			-0.316
			2.108
			5.953
			0.418
			4.116
			0.939
			2.587
			0.945
			0.065
			0.277
			-0.295
			2.412
			0.333
			1.573
			-0.524
			1.410
			-0.312
			4.440
			0.049
			6.228
			12.784
			12.211
			1.321
			2.559
			0.157
			0.247
			-0.382
			4.509
			0.294
			0.719
			0.692
			1.992
			0.492
			5.848
			12.550
			11.978
			11.013
			13.059
			10.168
			12.211
			2.012
			2.177
			5.271
			2.084
			14.009
			12.972
			12.972
			11.896
			13.360
			10.096
			12.062
			12.234
			0.939
			4.116
			5.953
			2.108
			0.933
			1.415
			2.763
			5.971
			3.877
			0.615
			3.123
			5.208
			1.437
			3.391
			4.609
			2.670

TABLE E. 30
RADIAL AND AXIAL VELOCITIES - DIGITIZER METHOD, Q=2.383 cm³/sec
0.20 cm I.D. CAPILLARY TUBE, LARGE RESERVOIR

(Z/D) = 34.65				(ϕ = 12.745 cm)				
r' (cm)	V _r (cm/sec)	V _z (cm/sec)	r' (cm)	V _r (cm/sec)	V _z (cm/sec)	r' (cm)	V _r (cm/sec)	V _z (cm/sec)
14.535	-0.349	0.589	14.617	-0.108	0.495	13.266	-0.368	2.410
12.927	-0.271	6.397	13.261	-0.307	2.339	12.817	-0.339	6.396
12.728	-0.587	8.097	12.403	0.209	4.691	11.818	0.475	2.317
11.165	0.848	1.108	12.167	0.707	3.437	10.056	0.127	0.401
9.731	0.065	0.222	11.866	0.680	2.084	14.551	-0.378	0.951
14.373	-0.250	0.874	14.464	-0.148	0.714	13.218	-0.473	2.728
12.886	-0.213	7.217	13.629	-0.246	0.550	12.844	0.440	6.736
12.487	0.618	6.384	13.234	-0.285	3.231	12.348	0.492	4.638
12.239	0.434	2.893	13.020	-0.372	4.687	12.117	0.832	4.539
11.907	0.418	2.216	12.270	1.520	3.952	11.760	0.699	1.761
10.262	0.226	0.426	10.161	0.266	0.392	14.057	-0.332	1.094
13.831	-0.380	1.663	14.473	-0.140	0.850	13.538	-0.400	1.815
13.195	-0.147	3.092	13.179	-0.204	2.735	12.351	0.581	3.680
12.194	0.572	4.018	12.572	0.881	7.921	11.435	0.469	1.435
10.719	0.381	0.692	11.871	0.792	2.048	11.037	0.219	0.559
14.736	-0.081	0.507	11.429	0.454	1.446	13.895	-0.229	0.990
12.778	-0.211	6.577	11.088	0.462	1.097	12.198	1.015	3.692
11.553	0.597	1.652	13.109	-0.547	2.904	11.495	0.480	1.614
11.064	0.518	0.815	12.582	0.296	6.255	13.207	-0.604	3.684
13.102	-0.071	3.948	13.457	-0.594	1.976	12.934	-0.275	6.540
12.578	0.479	6.097	12.857	-0.737	5.993	12.320	0.216	4.484
11.797	0.551	2.096	12.458	0.133	6.117	11.442	0.538	1.366
9.429	0.117	0.230	11.185	0.238	1.163	14.487	-0.233	0.785
13.515	-0.225	1.643	13.674	-0.545	1.516	11.998	0.623	2.335
11.083	0.332	1.130	12.980	-0.116	4.551	12.868	0.088	7.794
12.320	0.867	4.788	12.352	1.132	5.935	12.023	0.662	2.737
11.740	0.607	2.185	11.229	0.452	1.488	11.169	0.314	1.021
13.061	-0.936	3.319	9.856	0.082	0.290	12.647	1.098	6.684
				</				

TABLE E.30 (continued)

(Z/D) = 34.65				(ϕ = 12.745 cm)			
r' (cm)	V _r (cm/sec)	V _z (cm/sec)	r' (cm)	V _r (cm/sec)	V _z (cm/sec)	r' (cm)	V _r (cm/sec)
12.138	0.437	3.771	13.425	-0.403	1.990	11.762	0.545
9.827	0.159	0.451	12.918	-0.097	3.698	9.518	0.141
11.633	0.602	1.492	12.098	0.465	2.859	11.695	0.468
(Z/D) = 17.33				(ϕ = 12.745 cm)			
r' (cm)	V _r (cm/sec)	V _z (cm/sec)	r' (cm)	V _r (cm/sec)	V _z (cm/sec)	r' (cm)	V _r (cm/sec)
13.017	-0.240	8.760	13.278	-0.565	3.078	12.342	-0.196
12.065	0.631	2.934	12.913	0.249	10.825	12.002	-0.216
11.379	0.009	0.943	11.825	-0.050	1.671	13.770	0.255
13.432	-0.412	2.430	13.987	0.504	0.778	13.253	-0.931
13.042	-0.197	14.725	13.248	-0.028	5.587	12.743	0.734
12.596	0.737	13.823	12.295	0.109	5.020	12.350	0.163
12.233	0.015	3.487	12.092	-0.050	2.204	11.792	-0.106
11.567	-0.174	0.228	13.556	-0.353	3.354	11.312	-0.353
10.928	-0.135	0.065	13.047	-0.144	14.762	10.441	-0.154
13.217	-0.600	6.989	12.572	1.482	13.239	13.088	-0.279
12.597	0.666	13.751	12.116	0.225	2.390	12.221	-0.244
11.623	-0.001	0.712	13.286	0.113	4.558	12.747	1.603
13.112	-0.331	9.918	12.399	0.410	4.815	12.983	0.415
12.509	1.307	9.250	11.778	-0.056	1.440	12.462	0.153
12.319	0.189	5.591	11.426	-0.171	0.716	11.996	-0.006
11.868	-0.360	1.467	13.034	-0.338	7.890	11.591	-0.138
11.414	-0.027	0.702	12.110	-0.028	3.041	13.767	0.080
13.560	-0.110	1.533	13.365	-0.066	4.196	12.022	0.019
11.673	-0.210	0.984	12.400	0.202	4.869	11.455	-0.071
12.612	0.828	17.847	11.831	0.055	1.674	12.328	0.954
12.105	-0.080	3.129	13.574	-0.442	1.555	11.661	-0.045
10.641	-0.274	0.109	12.835	0.216	32.595	13.117	-0.264
12.061	-0.097	2.275	12.400	0.120	4.984	12.157	-0.151
13.265	-0.202	3.837	11.780	-0.094	1.136	13.151	-0.356
13.056	-0.380	10.593	12.014	0.040	2.314	12.657	1.873
12.345	0.720	5.997	11.352	-0.235	0.590		
r' (cm)	V _r (cm/sec)	V _z (cm/sec)	r' (cm)	V _r (cm/sec)	V _z (cm/sec)	r' (cm)	V _r (cm/sec)
13.101	0.059	6.588	13.101	-0.196	3.078	12.342	-0.196
12.096	0.135	1.791	12.096	-0.216	10.825	12.002	-0.216
11.432	-0.013	1.269	11.432	0.255	1.671	13.770	0.255
13.365	-0.605	4.851	13.365	-0.931	0.778	13.253	-0.931
13.133	-0.277	35.669	13.133	0.734	5.587	12.743	0.734
12.190	0.657	4.274	12.190	0.163	5.020	12.350	0.163
11.726	-0.280	1.563	11.726	-0.106	2.204	11.792	-0.106
13.014	-0.104	0.632	13.014	-0.353	3.354	11.312	-0.353
12.242	0.090	0.079	12.242	-0.154	14.762	10.441	-0.154
3.528	0.213	9.742	3.528	-0.279	13.239	13.088	-0.279
2.596	-0.053	2.983	2.596	-0.244	2.390	12.221	-0.244
15.119	1.213	27.508	15.119	1.603	4.558	12.747	1.603
2.633	-0.003	17.410	2.633	0.415	4.815	12.983	0.415
0.989	-0.280	8.223	0.989	0.153	1.440	12.462	0.153
1.333	-0.034	1.512	1.333	-0.006	0.716	11.996	-0.006
10.460	-0.032	0.743	10.460	-0.138	7.890	11.591	-0.138
2.134	-0.038	0.785	2.134	0.080	3.041	13.767	0.080
10.892	-0.137	2.402	10.892	0.019	4.196	12.022	0.019
3.341	-0.126	0.736	3.341	-0.071	4.869	11.455	-0.071
0.652	0.083	6.286	0.652	0.954	1.674	12.328	0.954
27.244	-1.118	1.084	27.244	-0.045	1.555	11.661	-0.045
6.396	1.167	7.551	6.396	-0.264	32.595	13.117	-0.264
3.346	0.057	3.003	3.346	-0.151	4.984	12.157	-0.151
3.987	-0.172	7.019	3.987	-0.356	1.136	13.151	-0.356
1.262	-0.033	25.063	1.262	1.873	2.314	12.657	1.873

TABLE E.31
RADIAL AND AXIAL VELOCITIES - DIGITIZER METHOD, Q=2.701 cm³/sec
0.20 cm I.D. CAPILLARY TUBE, LARGE RESERVOIR

(Z/D) = 53.13 (ϕ = 12.745 cm)									
r' (cm)	V _r (cm/sec)	V _z (cm/sec)	r' (cm)	V _r (cm/sec)	V _z (cm/sec)	r' (cm)	V _r (cm/sec)	V _z (cm/sec)	r' (cm)
13.352	-0.123	0.778	13.334	-0.029	0.924	12.715	-0.040	1.040	12.956
12.529	-0.026	1.102	11.820	0.211	0.807	12.272	0.015	0.908	11.030
11.965	0.163	1.021	9.194	0.279	0.583	14.330	-0.251	0.585	9.346
14.821	-0.222	0.516	10.169	0.341	1.097	13.504	-0.133	0.681	14.165
12.802	0.085	0.964	13.935	-0.259	0.685	12.612	-0.120	1.046	13.781
12.197	0.230	0.905	13.458	-0.055	0.915	12.214	0.114	0.849	13.308
9.562	0.276	0.302	12.247	0.242	0.941	9.023	0.271	0.258	11.375
8.030	0.201	0.091	11.105	0.291	0.794	13.512	-0.143	0.734	12.311
8.833	0.193	0.238	14.169	-0.232	0.687	8.425	0.221	0.207	13.631
10.950	0.259	0.763	12.572	0.034	0.909	9.735	0.253	0.430	0.852
9.048	0.244	0.256	12.227	0.105	1.036	7.793	0.210	0.087	12.833
(Z/D) = 35.42 (ϕ = 12.745 cm)									
r' (cm)	V _r (cm/sec)	V _z (cm/sec)	r' (cm)	V _r (cm/sec)	V _z (cm/sec)	r' (cm)	V _r (cm/sec)	V _z (cm/sec)	r' (cm)
14.456	-0.341	2.710	14.455	-0.306	0.613	14.177	-0.237	1.306	13.362
14.101	-0.305	1.341	13.795	-0.115	3.697	13.486	-0.667	2.395	13.072
13.130	-0.665	4.958	13.013	-0.382	5.789	13.033	-0.088	4.019	12.835
12.974	-0.390	4.826	12.577	0.715	8.492	12.909	-0.298	5.932	12.464
12.523	0.349	8.414	12.226	0.764	5.295	12.069	0.738	3.624	11.989
11.993	0.736	2.805	11.634	0.664	1.978	11.355	0.541	1.302	11.559
11.144	0.494	1.639	11.246	0.412	1.418	10.752	0.121	0.788	11.054
10.363	0.313	0.879	10.358	0.457	1.055	14.456	-0.242	0.668	9.659
14.396	-0.152	0.991	9.574	0.114	0.291	13.727	-0.189	1.577	9.026
13.149	0.677	3.902	14.814	-0.396	0.743	13.023	0.110	5.663	14.550
12.956	0.142	4.738	13.521	-0.569	2.417	12.495	2.839	8.817	13.443

TABLE E.31 (continued)

(Z/D) = 35.42		(ϕ = 12.745 cm)						
r' (cm)	V _r (cm/sec)	V _z (cm/sec)	r' (cm)	V _r (cm/sec)	V _z (cm/sec)	r' (cm)	V _r (cm/sec)	V _z (cm/sec)
12.393	0.627	7.452	13.419	-0.528	3.755	12.270	1.005	5.159
11.985	1.007	3.131	12.861	0.363	7.485	11.875	0.691	2.515
11.552	0.427	1.331	12.301	0.578	4.005	11.520	0.507	1.957
11.387	0.622	1.569	12.174	0.769	3.335	11.311	0.713	1.377
11.300	0.511	1.352	11.697	0.518	1.669	10.926	0.410	1.082
10.477	0.182	0.843	14.704	-0.202	0.828	10.337	0.340	1.073
14.121	-0.038	1.351	13.696	-0.397	2.211	13.864	0.131	1.767
13.664	-0.461	2.224	12.381	0.279	6.629	13.501	-0.207	2.626
13.167	-0.710	5.026	14.314	-0.357	1.056	13.115	0.206	5.775
12.812	-0.046	9.503	13.493	0.458	2.400	12.394	0.826	5.480
12.517	0.154	6.236	13.011	-0.043	5.230	12.101	0.434	3.043
11.755	0.792	2.132	12.417	0.603	7.067	11.033	2.935	1.347
10.920	1.553	1.273	12.151	0.524	3.435	10.777	0.318	0.700
14.523	-0.163	0.929	11.755	0.905	2.166	14.288	-0.233	0.989
13.101	-0.750	3.536	10.194	0.193	0.562	12.929	-0.384	5.931
12.521	0.420	8.340	9.317	0.102	0.203	12.359	0.521	8.343
12.086	0.838	3.513	14.091	-0.367	1.250	11.825	0.534	2.401
11.570	0.284	1.752	13.096	-0.414	4.825	10.530	0.219	0.696
9.663	0.171	0.318	12.959	-1.707	6.024	12.917	-0.388	5.503
11.428	0.414	1.740	12.469	0.246	6.167	11.087	0.523	1.512
10.867	0.502	0.800	12.156	0.510	4.131	9.790	0.121	0.338
12.261	-0.199	1.328	11.367	0.458	1.789	12.695	-0.103	3.374
13.045	0.883	4.698	9.526	0.105	0.251	12.340	1.126	1.953
13.140	-0.681	6.027	12.779	-0.073	2.333			

TABLE E.31 (continued)

(2/D) = 17.71						(d = 12.745 cm)					
r' (cm)	V _r (cm/sec)	V _z (cm/sec)	r' (cm)	V _r (cm/sec)	V _z (cm/sec)	r' (cm)	V _r (cm/sec)	V _z (cm/sec)	r' (cm)	V _r (cm/sec)	V _z (cm/sec)
13.601	0.406	1.724	13.417	0.204	3.209	13.572	0.381	2.364	13.096	0.159	7.905
13.021	0.217	11.876	13.066	0.075	6.265	12.509	-0.039	9.716	12.408	1.101	9.109
12.071	0.111	2.354	12.169	0.017	2.705	11.948	0.027	2.777	10.659	-0.640	0.316
11.805	0.054	1.230	13.752	1.756	0.985	11.542	-0.092	0.619	13.189	0.543	3.862
12.495	0.315	4.815	12.437	1.007	10.035	12.465	0.308	9.156	12.383	0.571	7.992
12.293	-0.009	3.381	12.320	1.175	7.123	12.131	0.167	2.105	12.176	0.173	3.814
11.939	-0.098	1.954	12.051	-0.016	3.416	11.787	-0.015	0.960	11.905	0.139	2.353
10.538	-0.443	0.116	11.864	-0.070	0.567	13.399	-0.730	2.178	9.743	-0.646	0.013
13.467	-0.009	4.414	10.838	-0.584	0.391	13.168	-0.702	8.195	13.220	0.461	3.290
13.021	-0.678	20.157	13.007	-0.133	7.790	12.738	-0.430	26.539	12.923	-0.848	11.894
12.386	-0.056	4.732	12.332	0.392	8.234	12.343	0.445	5.714	12.237	0.108	6.082
12.051	0.086	2.887	13.475	-0.069	2.026	11.814	-0.074	1.421	13.073	-0.479	9.095
11.678	-0.245	1.058	12.913	0.122	20.184	10.302	-0.270	0.094	12.555	0.129	18.973
13.647	0.366	1.292	12.341	0.476	5.853	13.323	-0.345	3.548	11.806	-0.042	2.223
12.909	0.234	14.419	11.775	-0.580	1.172	12.968	-0.234	12.056	11.611	-0.189	1.097
12.854	-1.920	26.310	13.691	0.227	1.645	12.423	0.608	17.667	13.319	0.472	3.633
11.982	-0.068	2.400	13.274	-0.148	4.017	11.500	-0.220	0.539	13.188	0.166	5.594
12.372	0.013	7.902	12.963	-1.095	30.157	11.988	0.045	2.458	12.788	1.764	34.915
11.900	0.535	2.903	13.112	0.790	10.199	11.505	-0.261	0.667	12.726	-1.395	27.275
10.604	-0.832	0.298	12.513	0.263	11.851	13.301	0.264	4.208	13.046	0.627	6.463
12.683	1.189	31.963	12.378	0.304	7.021	12.789	-0.385	6.633	12.145	0.464	4.286
12.052	0.166	2.586	11.725	-0.123	1.135	11.643	-0.207	1.132			

TABLE E.32 (continued)

(Z/D) = 18.26		(ζ = 12.745 cm)									
r' (cm)	V _r (cm/sec)	V _z (cm/sec)	r' (cm)	V _r (cm/sec)	V _z (cm/sec)	r' (cm)	V _r (cm/sec)	V _z (cm/sec)	r' (cm)	V _r (cm/sec)	V _z (cm/sec)
13.510	-2.839	2.014	13.397	-0.115	2.274	13.455	-0.649	6.559	13.169	0.105	4.634
13.347	0.173	4.707	13.038	0.097	7.160	13.270	-0.485	4.287	12.916	-0.668	14.746
13.163	0.834	5.732	12.007	-0.151	3.281	13.016	-0.632	11.330	11.848	-0.209	2.501
12.378	-0.029	8.685	11.695	0.095	1.713	12.279	0.063	4.916	11.574	-0.122	1.259
11.799	0.037	1.515	11.118	-0.240	1.068	11.627	-0.165	0.705	13.725	0.051	1.746
11.559	0.068	1.195	13.474	0.459	2.118	13.821	0.234	1.432	13.425	-0.203	1.772
13.234	0.006	4.859	13.110	-0.355	6.607	12.241	0.352	6.028	12.551	0.186	18.908
11.643	0.093	1.587	11.226	-0.142	0.585	11.589	-0.167	1.329	10.857	-0.662	0.437
11.494	-0.093	1.005	14.033	0.328	1.257	13.308	-0.205	3.425	13.757	0.096	1.623
13.217	-0.057	7.472	11.832	0.205	1.893	12.948	-0.699	24.107	13.872	0.179	1.275
12.556	0.448	14.576	13.639	0.077	2.191	12.324	0.069	4.310	13.574	0.178	3.191
12.932	-0.157	16.935	12.399	0.336	6.952	12.346	0.158	7.443	11.985	-0.206	2.057
12.318	0.688	7.746	11.262	-0.315	0.327	12.053	-0.132	3.835	12.683	1.629	28.922
11.772	-0.107	1.687	12.908	-0.756	18.212	12.629	1.110	32.112	12.588	0.886	30.163
12.620	2.014	37.604	12.379	0.189	9.402						

TABLE E.33 (continued)

(Z/D) = 38.78		$(\phi = 12.745^\circ \text{ cm})$									
r' (cm)	V_r (cm/sec)	V_z (cm/sec)	r' (cm)	V_r (cm/sec)	V_z (cm/sec)	r' (cm)	V_r (cm/sec)	V_z (cm/sec)	r' (cm)	V_r (cm/sec)	V_z (cm/sec)
12.206	0.999	9.828	11.172	0.412	1.992	12.056	1.287	5.959	10.516	0.433	0.818
11.896	0.840	3.883	11.727	0.058	4.946	14.481	-0.027	1.013	11.657	0.729	3.375
13.630	-0.008	2.170	11.394	0.591	2.479	13.274	-0.454	3.774	11.246	0.557	1.748
12.507	0.380	9.844	10.447	0.349	0.856	12.339	0.812	8.532	14.091	-0.175	1.453
12.173	0.932	8.040	13.600	-0.368	2.068	11.935	1.028	4.378	13.057	-0.180	5.510
11.738	1.203	3.212	13.019	0.024	6.300	11.566	0.894	2.896	12.560	0.316	12.684
11.474	0.460	2.258	12.267	2.248	9.912	11.270	0.434	2.026	11.905	0.874	3.916
10.545	0.415	0.992	11.857	0.860	4.768	10.443	0.414	0.940	11.704	0.462	3.311
14.186	-0.333	0.825	11.497	0.524	2.583	13.676	-0.315	1.962	12.907	0.240	6.182
13.340	-0.264	3.157	12.826	-0.626	6.065	13.131	-0.252	4.476	12.618	0.133	9.014
13.007	-0.468	4.787	13.000	-0.493	5.322	12.782	0.340	10.587	12.656	0.520	8.190
12.023	0.762	5.262	13.040	-0.287	4.470	11.213	0.480	2.318	12.583	1.352	10.146
11.009	0.278	1.453	13.104	-0.051	5.837	10.109	0.204	0.661	12.640	-0.146	8.503
12.358	0.643	10.783									

(Z/D) = 19.39		$(\phi = 12.745^\circ \text{ cm})$									
r' (cm)	V_r (cm/sec)	V_z (cm/sec)	r' (cm)	V_r (cm/sec)	V_z (cm/sec)	r' (cm)	V_r (cm/sec)	V_z (cm/sec)	r' (cm)	V_r (cm/sec)	V_z (cm/sec)
12.976	-0.133	6.568	13.591	-0.131	3.270	13.232	-0.056	2.126	13.372	-0.506	3.366
13.525	-0.061	1.042	12.226	0.612	3.264	11.878	0.037	0.666	12.007	0.500	2.446
11.806	0.127	0.823	11.587	0.054	1.604	11.496	-0.001	0.617	11.256	-0.527	0.922
11.327	-0.148	0.955	13.657	-0.386	1.676	13.098	-0.537	7.452	13.056	-0.026	5.906
12.999	-1.492	10.589	12.872	-0.314	20.241	12.209	0.270	6.630	11.937	0.484	4.076
12.157	1.183	0.591	11.602	0.014	1.816	12.004	0.031	4.806	11.502	-0.041	1.066
11.931	0.559	3.259	11.275	-0.286	0.843	11.863	0.125	2.620	13.033	0.413	8.881
11.762	-0.240	2.161	12.072	0.105	5.452	11.612	0.209	1.545	11.964	0.423	3.147
11.378	-0.216	1.309	11.890	0.003	3.097	13.035	0.576	7.320	11.450	-0.738	1.076
12.329	1.274	12.401	13.809	0.204	1.681	12.082	0.402	5.284	13.210	-0.492	3.966
11.604	0.080	1.444	12.935	0.766	13.236	13.293	-1.065	3.009	12.282	0.870	11.424
13.218	-0.288	5.600	12.069	0.586	6.530	12.368	1.266	11.725	11.772	0.054	3.811

TABLE E. 34

RADIAL AND AXIAL VELOCITIES - DIGITIZER METHOD, Q=4.866 cm³/sec
0.20 cm I.D. CAPILLARY TUBE, LARGE RESERVOIR

(Z/D) = 59.18 (ξ = 12.745 cm)									
r' (cm)	V _r (cm/sec)	V _z (cm/sec)	r' (cm)	V _r (cm/sec)	V _z (cm/sec)	r' (cm)	V _r (cm/sec)	V _z (cm/sec)	r' (cm)
10.913	0.600	1.445	13.880	-0.344	1.891	12.194	0.298	2.040	13.021
11.790	0.352	1.799	12.358	-0.007	1.922	12.880	-0.332	2.159	12.126
13.047	-0.034	1.405	11.860	0.240	0.806	13.989	-0.419	1.302	11.707
14.236	-0.291	0.891	10.998	0.565	1.090	14.131	-0.362	0.996	10.810
13.549	-0.336	1.376	13.638	-0.108	1.491	13.227	-0.097	2.014	13.183
12.207	0.515	1.655	12.875	-0.133	2.148	11.905	0.448	2.098	13.599
11.214	0.309	1.275	13.028	-0.437	1.500	10.623	0.492	0.890	12.416
10.383	0.871	1.146	11.932	0.275	1.648	13.434	0.134	1.178	10.591
12.784	-0.083	1.634	12.431	0.129	1.704	12.287	0.580	2.010	11.611
12.212	0.236	2.234	13.979	-0.497	1.493	13.880	-0.353	1.304	13.421
13.821	-0.447	1.104	12.994	-0.401	1.622	13.366	-0.082	0.833	11.072
12.612	0.226	2.019	11.981	0.526	2.051	12.115	0.249	1.896	11.611

(Z/D) = 39.45 (ξ = 12.745 cm)									
r' (cm)	V _r (cm/sec)	V _z (cm/sec)	r' (cm)	V _r (cm/sec)	V _z (cm/sec)	r' (cm)	V _r (cm/sec)	V _z (cm/sec)	r' (cm)
14.135	-0.021	1.530	10.336	0.385	0.868	13.863	0.038	1.646	14.212
13.770	0.009	1.638	13.505	-0.254	3.354	13.713	0.099	1.890	13.329
13.639	-0.240	2.910	13.100	-0.701	5.492	13.262	-1.272	3.996	13.013
13.015	-1.455	4.860	12.292	0.626	9.916	13.030	-0.361	7.539	12.135
12.237	1.857	13.023	11.585	0.762	2.464	11.900	0.900	6.795	11.211
11.618	0.710	3.129	10.852	0.089	1.284	11.540	0.378	2.611	10.716
13.473	-0.809	4.346	13.141	-0.126	5.415	13.173	-0.088	3.948	13.049
12.775	-0.450	11.910	12.925	0.224	8.838	12.134	1.516	7.000	11.710
12.095	1.380	7.956	11.457	0.408	3.468	11.694	0.848	4.196	11.184
11.572	1.220	3.358	10.868	0.096	1.463	11.504	0.452	3.112	10.602
11.403	1.028	2.996	13.775	-0.146	2.041	10.872	0.270	1.292	12.951

TABLE E.34 (continued)

(Z/D) = 39.45				(ϕ = 12.745 cm)			
r' (cm)	V _r (cm/sec)	V _z (cm/sec)	r' (cm)	V _r (cm/sec)	V _z (cm/sec)	r' (cm)	V _r (cm/sec)
10.704	0.286	1.288	12.859	0.180	10.292	10.618	0.278
10.597	0.141	1.126	12.422	1.624	15.832	9.831	0.249
14.509	-0.050	0.923	11.828	0.536	4.540	13.732	0.131
13.305	-0.776	4.460	11.189	0.408	1.638	13.197	-0.280
13.056	-0.227	7.053	10.082	0.105	0.778	12.990	-0.280
12.916	-0.236	7.857	11.887	1.730	4.215	12.382	1.514
12.034	1.375	8.190	11.346	0.365	2.466	11.309	0.867
11.097	0.605	2.331	13.625	-0.296	2.444	13.380	-0.197
13.146	-0.879	6.510	12.900	-1.232	8.460	13.040	-0.396
12.581	0.768	15.261	12.193	1.692	10.601	12.612	1.899
12.449	1.504	13.173	11.246	0.620	2.427	12.233	1.206
12.264	1.254	10.168	14.149	0.060	1.070	12.042	0.915
11.956	0.330	5.814	13.295	-0.236	5.152	11.509	0.510
11.298	0.231	1.983	12.999	-0.427	6.604	10.464	0.140
13.641	-0.439	1.462	12.805	0.196	7.965	13.459	-0.286
12.970	-0.516	5.108	12.681	-0.181	14.978	12.849	-0.511
12.128	0.910	8.712	12.345	1.712	14.092	11.101	0.538
10.938	0.348	1.649	11.839	1.174	4.496	10.348	0.197
(Z/D) = 19.73				(ϕ = 12.745 cm)			
r' (cm)	V _r (cm/sec)	V _z (cm/sec)	r' (cm)	V _r (cm/sec)	V _z (cm/sec)	r' (cm)	V _r (cm/sec)
13.067	-0.103	10.282	13.560	0.106	2.708	12.999	0.120
12.323	1.452	13.008	12.987	-0.146	15.548	12.212	0.997
11.979	0.671	3.833	11.636	0.032	1.860	12.025	0.434
11.843	-0.111	3.057	11.290	-0.108	1.135	12.398	1.078
11.437	-0.157	1.525	12.964	-0.528	17.640	13.462	0.208
13.335	0.336	3.572	12.242	0.614	9.350	13.099	-0.112
12.946	-0.396	18.244	11.866	0.029	3.151	12.293	0.738
12.073	0.374	4.321	13.109	-0.343	8.103	11.664	0.474
r' (cm)	V _r (cm/sec)	V _z (cm/sec)	r' (cm)	V _r (cm/sec)	V _z (cm/sec)	r' (cm)	V _r (cm/sec)
10.704	-0.080	1.524	12.777	1.524	11.572	13.244	0.639
10.597	0.740	0.979	12.059	0.979	9.753	12.013	0.260
14.509	0.720	2.388	11.527	2.388	3.850	11.529	-0.160
13.305	0.426	4.831	10.777	4.831	14.897	13.331	0.120
13.056	1.008	5.275	11.860	5.275	1.644	12.818	0.754
12.916	0.463	12.535	11.455	12.535	9.108	12.023	0.292
12.034	-0.288	2.588	14.229	2.588	8.321	13.502	0.028
11.097	-0.010	3.060	13.487	3.060	2.652	11.751	-0.033
13.146	0.162	5.850	12.626	5.850			
12.581	0.640	14.694	11.445	14.694			
12.449	0.573	11.466	11.046	11.466			
12.264	-0.085	7.620	13.928	7.620			
11.956	-0.267	3.612	13.064	3.612			
11.298	-0.304	0.788	12.835	0.788			
13.641	0.360	3.392	12.762	3.392			
12.970	0.148	8.596	12.486	8.596			
12.128	0.376	1.514	10.983	1.514			
10.938	0.873	1.004	11.364	1.004			

TABLE E.35
RADIAL AND AXIAL VELOCITIES - DIGITIZER METHOD, Q=4.766 cm³/sec
0.30 cm I.D. CAPILLARY TUBE, LARGE RESERVOIR

(Z/D) = 21.90				(ϕ = 12.745 cm)			
r' (cm)	V _r (cm/sec)	V _z (cm/sec)	r' (cm)	V _r (cm/sec)	V _z (cm/sec)	r' (cm)	V _r (cm/sec)
14.102	-0.428	1.407	12.620	0.178	7.407	13.622	-0.190
13.011	0.236	6.631	11.175	0.314	1.474	12.827	0.251
12.274	0.433	5.551	12.622	0.951	6.977	12.475	0.455
11.897	0.364	2.755	12.015	0.604	3.342	12.682	0.498
9.434	0.042	0.166	11.069	0.470	1.084	14.629	-0.305
13.493	-0.490	3.594	13.361	-0.248	4.877	13.219	-0.495
12.922	-0.032	7.739	11.724	0.410	2.473	11.881	0.656
11.823	0.876	3.180	11.080	0.377	1.339	14.877	-0.262
13.436	-0.702	3.475	13.809	-0.230	1.835	13.064	-0.254
12.706	0.528	7.980	12.832	-0.160	8.187	12.492	0.637
12.056	0.799	3.986	11.144	0.608	1.201	11.258	0.523
10.254	0.162	0.448	13.589	-0.881	3.205	14.003	-0.281
11.738	0.591	2.384	11.839	0.258	2.074	11.566	0.495
11.298	0.720	1.308	10.787	0.280	0.769	13.902	-0.211
13.615	-0.573	2.991	13.077	-0.331	7.039	13.179	-0.147
13.070	-0.507	6.111	12.307	0.624	5.317	12.936	-0.164
12.524	0.437	6.867	11.341	0.283	1.267	11.954	0.392
14.179	-0.785	1.875	14.624	-0.252	0.988	13.494	-0.118
13.435	-0.918	4.633	12.856	-0.514	8.852	12.585	0.676
11.934	0.446	2.982	9.800	0.102	0.339	13.630	-0.580
13.288	-0.102	5.859	13.057	-0.364	6.032	12.938	-0.294
11.786	0.576	2.234	12.775	0.099	7.646	12.698	0.380
12.446	0.793	6.146	13.240	-0.529	6.300	11.815	0.505
11.153	0.429	1.319	12.796	0.262	7.682	10.947	0.432
9.968	0.153	0.888	13.318	-0.452	4.871	13.056	-0.126
12.941	0.083	8.983	12.818	-0.404	8.555	12.882	-0.331
12.190	0.439	3.132	11.781	0.531	2.588	11.961	0.580
11.778	0.565	2.516	14.643	-0.309	0.884	11.677	0.445

TABLE E.35 (continued)

(Z/D) = 21.90 (ϕ = 12.745 cm)									
r' (cm)	V _r (cm/sec)	V _z (cm/sec)	r' (cm)	V _r (cm/sec)	V _z (cm/sec)	r' (cm)	V _r (cm/sec)	V _z (cm/sec)	r' (cm)
9.375	0.355	0.138	13.493	-0.568	4.605	10.060	0.109	0.469	12.506
12.976	-0.317	7.543	12.417	0.582	4.301	12.733	0.348	7.975	12.247
10.878	0.341	0.993							
(Z/D) = 10.95 (ϕ = 12.745 cm)									
r' (cm)	V _r (cm/sec)	V _z (cm/sec)	r' (cm)	V _r (cm/sec)	V _z (cm/sec)	r' (cm)	V _r (cm/sec)	V _z (cm/sec)	r' (cm)
13.059	2.536	10.961	11.946	-0.061	2.027	12.784	0.962	37.429	11.633
11.729	-0.298	1.301	13.728	-0.080	2.628	13.240	-0.458	8.967	13.397
13.054	-0.960	22.179	13.239	-0.099	7.888	11.689	0.058	1.786	12.645
13.952	0.419	1.627	12.315	0.384	6.099	13.465	0.436	4.859	12.238
11.839	0.064	1.561	11.949	0.184	2.148	11.663	-0.156	1.123	11.309
10.844	-0.262	0.189	13.183	-0.007	9.769	13.728	0.045	2.763	12.527
13.274	-0.084	9.090	12.313	0.405	6.738	12.068	-0.048	2.892	12.077
13.888	0.451	1.946	13.828	-0.218	2.549	13.417	-0.487	5.323	11.586
13.010	0.032	32.085	12.326	0.061	5.525	12.193	-0.187	4.692	13.471
11.571	-0.179	1.123	12.509	0.739	13.174	13.187	-0.416	13.139	12.153
13.043	-0.339	15.396	11.736	-0.012	1.578	12.226	0.091	4.249	13.143
13.620	-0.081	2.816	12.905	0.539	31.449	13.365	0.219	4.741	12.946
12.349	0.610	7.269	12.589	0.407	28.030	11.192	-0.249	0.284	11.572
13.366	-0.300	5.552	12.827	-0.034	38.324	13.224	0.029	10.953	13.064
12.481	0.077	9.015	12.298	0.421	7.227	12.246	0.167	5.452	11.993
12.535	0.989	12.092	11.665	-0.052	1.708	11.420	-0.200	0.727	13.670
12.855	0.639	50.822	13.486	-0.379	4.837	13.480	0.294	5.608	13.403
13.206	-0.615	12.118	13.212	-0.725	9.824	12.555	0.893	15.320	12.357
12.250	-0.233	4.164	12.260	1.279	5.520	13.421	0.250	5.869	13.013
12.497	0.751	12.671	12.913	0.011	26.672	12.317	1.179	5.785	12.825
11.786	-0.208	1.553	12.773	2.464	35.773	12.696	0.839	30.412	12.537
12.922	3.336	38.176	12.861	2.199	37.617	12.735	3.330	30.027	

TABLE E.36 (continued)

(Z/D) = 11.56						(d = 12.745 cm)					
r' (cm)	V _r (cm/sec)	V _z (cm/sec)	r' (cm)	V _r (cm/sec)	V _z (cm/sec)	r' (cm)	V _r (cm/sec)	V _z (cm/sec)	r' (cm)	V _r (cm/sec)	V _z (cm/sec)
13.199	-1.202	18.802	11.921	0.173	2.993	13.134	1.664	27.911	11.666	0.207	1.341
13.406	1.848	6.686	11.389	-0.223	0.838	12.081	0.309	4.199	13.834	0.171	1.847
13.834	-0.147	3.039	13.275	-0.653	7.199	13.262	-0.552	12.121	12.593	1.041	22.343
12.416	-0.500	10.056	12.443	1.062	11.598	12.256	0.729	7.945	12.267	-0.185	5.931
12.024	-0.125	3.566	11.992	0.086	2.256	11.158	-0.227	0.511	12.401	1.168	10.778
13.270	1.408	9.128	11.967	-0.525	2.881	13.168	-0.418	20.691	11.792	0.180	2.408
12.448	0.273	11.729	11.879	0.355	2.827	11.977	0.144	2.746	13.034	-0.424	30.610
11.511	-0.385	1.136	12.481	1.024	17.011	11.385	-0.432	0.653	12.352	0.512	9.802
11.699	0.562	1.575	12.330	0.659	10.915						

TABLE E.37
RADIAL AND AXIAL VELOCITIES - DIGITIZER METHOD, Q=7.148 cm³/sec
0.30 cm I.D. CAPILLARY TUBE, LARGE RESERVOIR

(Z/D) = 23.12 (ϕ = 12.745 cm)									
r' (cm)	V _r (cm/sec)	V _z (cm/sec)	r' (cm)	V _r (cm/sec)	V _z (cm/sec)	r' (cm)	V _r (cm/sec)	V _z (cm/sec)	r' (cm)
11.905	1.403	5.631	13.461	-0.135	6.308	12.933	1.597	15.225	12.274
11.325	1.079	3.897	11.145	0.741	2.274	10.758	0.575	1.217	13.536
9.830	0.262	0.933	12.927	0.117	12.026	12.229	1.273	8.406	12.750
12.204	1.308	6.829	12.226	1.801	6.805	11.346	0.604	2.474	11.822
11.033	0.879	1.335	11.446	1.201	3.187	12.961	-0.526	12.348	8.898
13.519	-0.532	6.599	8.863	0.079	0.207	12.418	1.747	9.402	13.935
11.898	0.489	4.409	13.618	-0.605	4.117	10.852	0.425	1.110	11.173
10.661	0.344	1.146	14.149	0.179	2.597	13.277	-0.938	8.614	12.227
11.975	0.475	5.538	13.424	-0.937	5.744	11.246	0.181	2.260	12.421
9.225	0.062	0.299	13.108	-0.661	10.053	13.399	0.019	5.661	12.370
12.431	2.319	10.942	12.375	1.215	9.771	12.487	1.041	13.412	12.210
11.969	0.886	5.901	13.053	-1.571	9.651	13.043	-0.217	11.097	13.389
12.959	-0.386	11.411	13.095	0.036	7.621	11.694	0.843	4.344	12.411
(Z/D) = 11.92 (ϕ = 12.745 cm)									
r' (cm)	V _r (cm/sec)	V _z (cm/sec)	r' (cm)	V _r (cm/sec)	V _z (cm/sec)	r' (cm)	V _r (cm/sec)	V _z (cm/sec)	r' (cm)
12.241	0.053	5.638	12.214	0.139	6.016	10.967	-0.208	0.407	13.386
11.122	9.243	1.021	13.316	-0.256	9.386	11.080	-0.143	0.823	12.570
13.685	-0.132	3.566	13.238	-1.017	10.423	12.455	0.414	12.372	12.669
12.211	0.209	5.454	13.013	-0.297	33.086	12.154	0.539	5.124	12.688
12.855	1.060	40.341	12.664	2.716	33.701	12.135	0.082	5.112	12.103
11.251	-0.027	1.033	12.651	4.015	55.823	13.357	0.044	10.409	12.374
13.309	-0.561	13.060	12.809	0.963	56.740	12.212	0.538	5.237	12.371
11.276	-0.246	1.215	12.272	0.500	6.495	13.314	-0.001	12.473	12.209
12.411	1.742	11.241	11.359	0.126	1.262	12.222	1.284	5.481	11.872
12.412	0.967	14.007	12.876	1.079	66.834	12.309	0.935	7.994	
							V _r (cm/sec)	V _z (cm/sec)	
							-0.839	8.544	
							1.582	20.445	
							3.490	37.441	
							2.577	39.685	
							0.563	4.585	
							0.615	12.643	
							0.168	9.548	
							-0.062	6.198	
							-0.059	3.215	

TABLE E.38
RADIAL AND AXIAL VELOCITIES - DIGITIZER METHOD, Q=7.943 cm³/sec
0.30 cm I.D. CAPILLARY TUBE, LARGE RESERVOIR

(Z/D) = 24.08				(ϕ = 12.745 cm)			
r' (cm)	V _r (cm/sec)	V _z (cm/sec)	r' (cm)	V _r (cm/sec)	V _z (cm/sec)	r' (cm)	V _r (cm/sec)
14.123	-0.349	2.713	12.645	0.605	13.187	13.553	-0.091
12.443	0.898	9.276	12.408	0.553	11.117	13.296	-0.300
12.797	-0.090	17.741	12.638	0.380	13.672	12.591	1.525
12.368	2.744	13.895	13.347	-0.549	8.151	12.093	1.170
12.417	0.875	10.798	12.298	2.398	8.002	12.180	1.220
12.151	1.590	8.131	11.929	1.288	4.772	12.020	0.732
11.797	0.260	2.977	11.733	1.147	3.490	11.191	0.535
10.803	0.314	1.307	11.072	0.763	1.976	12.036	1.049
11.350	1.228	2.422	11.858	0.837	4.532	10.788	0.527
10.469	0.211	0.683	12.196	0.674	8.922	14.116	-0.379
12.347	0.952	12.357	11.667	0.940	4.088	12.004	1.063
11.809	0.754	5.323	11.147	0.728	1.789	13.085	-0.650
12.097	0.686	7.009	10.247	0.074	0.763	11.907	0.598
11.641	0.344	2.866	12.003	0.294	4.480	9.419	-0.462
12.798	-1.399	11.457	13.360	-0.679	8.171	12.374	0.929
12.208	0.967	10.999	11.408	0.966	2.792	11.941	2.000
11.393	0.400	2.783	11.579	0.682	2.894	9.811	0.122
9.947	-0.227	0.476	11.010	0.388	1.402	12.827	-0.259
11.680	0.622	4.152	12.401	1.927	10.997	11.651	1.045
10.250	-0.060	0.806	11.277	0.812	1.924		

r' (cm)	V _r (cm/sec)	V _z (cm/sec)	r' (cm)	V _r (cm/sec)	V _z (cm/sec)	r' (cm)	V _r (cm/sec)
12.540	-0.174	5.286	12.540	-0.174	15.454		
11.631	0.587	7.838	11.631	0.587	3.444		
12.162	2.005	13.102	12.162	2.005	6.528		
12.827	-0.328	6.779	12.827	-0.328	14.252		
12.141	0.777	7.443	12.141	0.777	7.650		
11.902	0.416	5.999	11.902	0.416	5.348		
11.476	0.240	2.197	11.476	0.240	2.806		
13.442	-0.479	5.405	13.442	-0.479	7.013		
10.946	0.065	1.444	10.946	0.065	1.505		
11.805	1.077	2.318	11.805	1.077	5.408		
11.309	0.607	6.761	11.309	0.607	2.217		
10.948	0.587	12.456	10.948	0.587	1.728		
12.178	1.035	5.128	12.178	1.035	9.500		
11.456	0.481	0.556	11.456	0.481	2.983		
12.944	-0.191	12.313	12.944	-0.191	16.678		
12.119	1.434	6.069	12.119	1.434	5.828		
11.486	0.568	0.717	11.486	0.568	2.534		
13.946	-0.683	14.384	13.946	-0.683	3.473		
11.829	0.894	3.151	11.829	0.894	5.440		

TABLE E.40

AXIAL AND RADIAL VELOCITIES - DIGITIZER METHOD, Q=9.531 cm³/sec
0.30 cm I.D. CAPILLARY TUBE, LARGE RESERVOIR

(Z/D) = 37.59 (ψ = 12.745 cm)

r' (cm)	V _r (cm/sec)	V _z (cm/sec)	r' (cm)	V _r (cm/sec)	V _z (cm/sec)	r' (cm)	V _r (cm/sec)	V _z (cm/sec)	r' (cm)	V _r (cm/sec)	V _z (cm/sec)
11.895	0.721	2.558	10.351	0.876	1.336	11.486	0.784	1.938	15.236	-0.559	1.077
11.116	0.625	1.859	12.655	-0.217	3.339	11.027	0.876	1.612	12.278	0.337	2.487
11.231	0.586	1.629	8.824	0.339	0.376	10.716	0.847	1.731	11.456	0.871	2.536
13.370	-0.545	2.617	14.296	-0.448	1.718	12.515	0.307	3.501	11.300	0.861	1.882
12.471	0.740	3.286	13.611	-0.216	2.381	12.069	0.561	3.320	13.130	-0.074	3.192
9.470	0.507	0.651	12.729	0.017	2.330	11.084	0.872	2.480	11.208	0.888	1.692
13.878	-0.362	1.870	9.786	0.734	0.637	12.293	0.753	2.680	11.900	0.810	2.790
11.831	0.442	2.564	11.590	0.874	2.274	14.006	-0.256	1.647	10.225	0.846	1.166
12.113	0.493	3.056	12.153	0.521	3.132	11.480	0.871	2.201	11.856	0.519	3.245
10.907	0.726	1.596	8.603	0.628	0.727	11.115	0.813	1.860	8.292	0.584	0.433

(Z/D) = 25.06 (ψ = 12.745 cm)

r' (cm)	V _r (cm/sec)	V _z (cm/sec)	r' (cm)	V _r (cm/sec)	V _z (cm/sec)	r' (cm)	V _r (cm/sec)	V _z (cm/sec)	r' (cm)	V _r (cm/sec)	V _z (cm/sec)
12.517	-0.251	15.360	14.956	-0.189	1.132	12.375	1.780	12.862	13.247	-0.040	12.747
11.922	1.497	7.669	12.182	3.759	7.723	11.382	0.476	2.756	11.750	0.186	3.875
11.286	0.315	2.770	10.997	0.470	1.834	11.209	0.522	2.363	10.947	0.417	1.795
10.806	0.359	1.814	12.262	0.756	9.937	10.347	0.372	1.025	12.060	1.920	7.523
9.526	0.089	0.449	11.928	0.745	5.992	9.062	0.091	0.299	11.286	0.611	2.720
12.191	0.580	7.601	10.106	0.188	0.709	11.676	0.704	3.622	12.597	1.683	18.713
11.335	0.277	1.960	12.540	1.645	17.472	9.571	0.168	0.462	12.119	0.720	10.011
8.981	0.121	0.191	12.029	0.477	5.346	13.352	-0.520	9.005	11.310	0.635	3.209
12.268	4.602	11.109	11.253	0.588	2.121	11.895	0.053	7.026	11.086	0.567	1.592

TABLE E.40 (continued)

(Z/D) = 25.06		(ξ = 12.745 cm)									
r' (cm)	V _r (cm/sec)	V _z (cm/sec)	r' (cm)	V _r (cm/sec)	V _z (cm/sec)	r' (cm)	V _r (cm/sec)	V _z (cm/sec)	r' (cm)	V _r (cm/sec)	V _z (cm/sec)
11.710	0.794	2.760	10.633	0.270	1.378	10.160	0.054	0.799	12.234	1.323	10.892
9.563	0.126	0.486	11.857	0.681	4.000	11.991	1.225	8.669	11.527	0.198	3.386
11.926	0.650	4.260	11.055	0.151	2.446	11.239	0.407	2.414	13.530	-0.749	6.483
10.820	0.543	1.196	12.311	1.661	11.983	10.696	0.308	1.341	12.002	0.656	5.800
14.572	-0.553	1.641	11.755	0.551	4.107	10.459	0.066	1.053	9.661	0.226	0.543
9.913	0.384	0.788	14.247	-0.464	2.862	11.727	0.418	3.653	12.117	1.872	9.139
13.390	-0.456	7.353	12.116	0.875	10.504	12.433	1.304	12.916	11.891	0.251	5.567
12.209	1.156	8.517	10.501	0.428	1.382	12.257	0.314	11.015	8.506	0.084	0.663
11.923	1.358	6.005	8.889	0.047	0.352	10.297	0.157	0.896	14.445	-0.356	1.963
8.963	0.050	0.238	13.416	-0.698	7.420	12.940	1.386	15.473	12.388	2.090	15.460
11.841	0.788	5.954	11.749	0.502	3.883	10.811	0.379	1.324	12.224	1.190	9.205
13.910	-0.710	3.317	13.053	1.631	15.071	13.081	-1.033	14.450	13.900	-0.652	3.682
12.990	0.143	16.661	12.403	3.100	13.811	12.011	0.955	6.342	12.561	1.201	18.110
13.753	-0.358	4.563	11.949	0.691	6.118	12.618	1.519	16.154	12.646	-0.425	16.319
12.440	1.107	12.332	12.349	1.823	11.704	13.357	-0.337	7.883			

(Z/D) = 12.53		(ξ = 12.745 cm)									
r' (cm)	V _r (cm/sec)	V _z (cm/sec)	r' (cm)	V _r (cm/sec)	V _z (cm/sec)	r' (cm)	V _r (cm/sec)	V _z (cm/sec)	r' (cm)	V _r (cm/sec)	V _z (cm/sec)
13.567	-0.478	8.178	12.605	0.970	17.796	12.609	2.267	33.729	11.217	-0.045	1.070
12.495	1.164	17.053	13.264	-0.566	17.381	12.188	0.537	8.845	11.308	-0.104	2.492
10.996	-0.255	0.838	14.073	0.484	2.116	12.551	1.987	31.306	12.263	0.646	8.657
12.102	0.742	6.179	11.904	0.375	5.067	11.501	-0.055	1.922	12.513	1.346	21.331
12.360	0.520	12.236	11.352	-0.281	1.403	11.055	-0.193	0.672	12.305	1.067	8.406
12.250	0.558	8.768	11.507	-0.121	1.913	13.207	-0.840	28.495	13.374	-0.002	9.768
13.122	-0.129	33.170	12.284	0.886	8.322	11.889	0.071	3.082	11.160	-0.152	0.973
11.269	-0.401	1.155	13.798	0.884	3.103	12.081	0.344	5.380	12.488	1.020	21.666
11.899	-0.057	3.106	12.122	0.462	7.113	11.540	-0.007	1.916	11.634	0.080	2.463

TABLE E.40 (continued)

(Z/D) = 12.53		(ϕ_c = 12.745 cm)									
r' (cm)	V_r (cm/sec)	V_z (cm/sec)	r' (cm)	V_r (cm/sec)	V_z (cm/sec)	r' (cm)	V_r (cm/sec)	V_z (cm/sec)	r' (cm)	V_r (cm/sec)	V_z (cm/sec)
13.252	-0.632	17.980	11.204	-0.213	1.366	12.133	1.093	6.637	13.520	0.213	5.341
10.521	-0.386	0.242	11.441	0.167	1.733	13.209	-0.510	18.810	13.011	-1.637	40.220
13.328	-0.177	12.206	12.834	-6.631	85.872	12.458	2.084	17.668	12.315	0.523	10.576
12.588	2.069	26.460	13.482	0.002	7.457	12.258	0.314	7.934	12.523	1.480	19.056
11.650	-0.022	2.461	12.395	2.206	15.574	11.172	-0.150	1.105	12.006	0.234	4.633
13.762	0.334	4.039	12.689	2.182	78.445	12.752	2.067	89.243	12.685	4.439	60.683
12.748	6.222	72.609	12.267	0.786	9.226						

TABLE E.41 (continued)

(Z/D) = 25.44		(ϕ = 12.745 cm)									
r' (cm)	V _r (cm/sec)	V _z (cm/sec)	r' (cm)	V _r (cm/sec)	V _z (cm/sec)	r' (cm)	V _r (cm/sec)	V _z (cm/sec)	r' (cm)	V _r (cm/sec)	V _z (cm/sec)
11.992	0.774	6.368	12.592	1.157	20.765	11.469	0.221	2.673	12.082	1.152	7.202
10.598	0.771	1.296	11.704	0.389	3.202	9.289	0.126	0.413	11.483	0.343	2.112
13.220	-0.603	10.110	8.624	0.034	0.157	13.510	-0.541	7.313	9.106	0.058	0.262
12.235	2.408	11.933	14.815	-0.140	1.368	12.132	0.866	9.452	11.989	1.076	7.201
11.836	0.831	4.643	11.862	0.970	4.156	11.824	0.919	5.960	11.572	0.544	2.605
11.735	0.531	4.423	11.516	0.698	3.623	11.534	0.291	3.990	11.076	0.339	2.225
11.358	0.349	3.040	10.695	0.230	1.583	10.022	0.206	1.020	9.952	0.125	0.974
9.872	0.196	0.700	13.122	-0.031	14.277	11.493	0.534	2.729	12.110	1.117	10.432
10.670	0.297	1.572	13.069	-0.029	13.572	10.152	0.156	0.990	12.729	0.154	18.075
13.718	-0.351	5.027	12.184	0.605	10.575	12.454	1.123	16.702	13.456	-0.094	7.836
12.243	1.221	10.130	13.359	-0.086	7.509	11.475	0.642	3.469	13.192	-0.758	9.888
8.680	0.159	0.389	12.613	1.081	19.186	11.600	0.788	2.995	12.599	1.067	19.512
13.578	-0.420	7.120	12.080	0.611	8.724	13.264	-0.276	9.899	12.015	0.685	7.219
12.121	1.014	9.929	13.861	-0.489	3.879	11.942	1.021	7.371	13.135	-0.321	12.184
13.321	-0.335	9.190	12.819	1.724	20.839	13.114	-0.101	12.190	12.695	0.265	21.344
11.758	1.099	5.580	12.296	1.383	14.189	12.110	0.866	8.755	11.843	1.041	5.579

(Z/D) = 12.72		(ϕ = 12.745 cm)									
r' (cm)	V _r (cm/sec)	V _z (cm/sec)	r' (cm)	V _r (cm/sec)	V _z (cm/sec)	r' (cm)	V _r (cm/sec)	V _z (cm/sec)	r' (cm)	V _r (cm/sec)	V _z (cm/sec)
12.414	1.579	13.116	14.086	0.563	3.681	12.200	0.817	9.565	13.243	-0.060	10.668
14.037	0.244	3.274	12.564	2.335	24.809	13.803	0.716	4.450	12.309	1.027	9.903
12.473	1.590	14.276	12.418	1.224	12.092	12.440	0.780	14.127	11.740	-0.354	2.696
12.354	0.924	12.944	11.485	-0.438	1.817	12.255	0.681	9.444	11.172	-0.088	1.350
12.149	0.167	5.301	12.504	1.779	24.686	12.272	1.116	9.458	12.195	0.933	8.925
12.184	0.456	5.948	11.978	0.779	4.827	11.900	0.242	11.123	11.245	-0.731	1.330
14.025	0.593	3.695	13.306	-0.220	10.260	12.311	0.711	11.123	12.797	2.662	41.039
12.236	0.411	6.997	12.178	0.254	6.805	12.441	1.216	11.123	11.855	397	3.749
13.782	0.065	3.404	12.639	3.082	50.251	12.506	3.001	11.123	12	1	60.984

TABLE E.41 (continued)

(Z/D) = 12.72		(ζ = 12.745 cm)									
r' (cm)	V_r (cm/sec)	V_z (cm/sec)	r' (cm)	V_r (cm/sec)	V_z (cm/sec)	r' (cm)	V_r (cm/sec)	V_z (cm/sec)	r' (cm)	V_r (cm/sec)	V_z (cm/sec)
12.223	1.168		12.265	0.236	9.356	11.895	0.310	3.982	12.512	2.852	38.500
13.666	0.583		13.161	-0.320	22.322	13.346	-0.724	12.719	12.277	1.026	9.385
13.125	-1.016		12.011	-0.470	4.779	12.488	-1.426	16.076	12.486	1.383	23.439
12.588	2.657		12.439	1.025	12.871	13.604	0.033	5.635	12.324	0.660	10.237
13.216	-1.506		13.174	-0.727	16.529	11.871	-0.068	4.734			

TABLE E.42

AXIAL AND RADIAL VELOCITIES - DIGITIZER METHOD, Q=11.120 cm³/sec
0.30 cm I.D. CAPILLARY TUBE, LARGE RESERVOIR

(Z/D) = 38.16

(ϕ = 12.745 cm)

r' (cm)	V _r (cm/sec)	V _z (cm/sec)	r' (cm)	V _r (cm/sec)	V _z (cm/sec)	r' (cm)	V _r (cm/sec)	V _z (cm/sec)	r' (cm)	V _r (cm/sec)	V _z (cm/sec)
13.638	-0.173	4.350	13.237	-0.361	22.852	13.790	-0.515	3.742	12.617	2.648	34.792
13.304	-0.764	16.636	12.386	1.956	16.922	13.243	1.306	20.285	11.731	0.162	2.834
12.261	0.375	8.992	12.766	4.223	73.497	12.237	0.459	10.462	12.299	1.135	11.028
12.752	0.867	84.389	12.021	1.027	5.690	11.935	0.750	5.081	12.758	4.394	71.741
12.328	1.163	14.293	12.141	0.432	7.467	12.052	1.022	6.124	12.611	2.311	39.432
12.329	0.943	10.581	12.642	4.079	73.630	12.274	1.404	9.278	11.427	0.095	1.975
12.013	0.838	6.296	13.261	-0.337	21.293	11.613	0.078	2.557	13.200	0.632	15.473
14.132	0.181	2.183	11.990	0.242	5.002	13.791	-0.086	3.717	11.911	0.035	3.157
13.471	-0.451	10.208	11.677	-0.157	2.213	12.337	0.451	14.362	11.519	-0.208	2.081
11.972	0.382	6.583	12.425	0.882	16.437	11.697	0.037	4.547	12.410	-0.051	23.554
13.943	0.118	4.135	12.241	0.736	11.213	10.878	-0.626	0.493	12.471	1.820	22.663
10.697	-0.331	0.434	11.968	1.111	5.438	13.287	-0.671	22.864	11.936	-0.076	2.891
12.487	0.927	15.353	12.568	1.763	25.778	12.306	0.622	9.146	12.225	0.314	7.634
10.659	-0.421	0.431	12.422	0.727	18.054	12.595	2.443	53.413	11.823	-0.271	3.600
12.006	-0.389	5.438									

(Z/D) = 25.44

(ϕ = 12.745 cm)

r' (cm)	V _r (cm/sec)	V _z (cm/sec)	r' (cm)	V _r (cm/sec)	V _z (cm/sec)	r' (cm)	V _r (cm/sec)	V _z (cm/sec)	r' (cm)	V _r (cm/sec)	V _z (cm/sec)
13.206	-0.892	9.773	12.903	0.679	18.387	13.130	0.757	9.928	12.632	1.529	20.172
12.551	-0.332	23.071	11.903	0.782	7.795	12.434	1.869	21.935	11.451	0.103	3.233
13.391	-0.697	8.527	11.103	0.605	2.343	12.676	-0.140	24.056	8.958	0.070	0.281
12.286	2.366	11.714	12.639	0.509	24.620	13.354	-0.710	9.889	11.818	0.065	4.660
12.681	0.416	20.694	10.350	0.282	1.218	12.328	-0.006	12.737	9.122	0.102	0.306
12.002	0.907	7.153	8.562	0.030	0.121	13.041	-1.478	15.744	13.477	-0.731	8.699

TABLE E.42 (continued)

(Z/D) = 25.44				(ϕ = 12.745)			
r' (cm)	V _r (cm/sec)	V _z (cm/sec)	r' (cm)	V _r (cm/sec)	V _z (cm/sec)	r' (cm)	V _r (cm/sec)
13.484	-0.435	6.248	11.710	0.795	4.263	12.635	2.110
11.898	1.505	7.065	12.397	0.908	15.048	11.634	1.366
12.545	-0.109	24.817	12.259	0.803	11.702	12.668	0.964
12.581	0.299	20.909	12.473	1.531	17.728	12.047	-0.298
12.014	1.036	8.082	12.287	1.122	13.662	12.328	1.163
12.052	1.022	6.124	11.667	-0.029	2.929	12.929	1.694
12.661	1.654	20.507	10.653	0.395	1.455	12.567	2.363
13.573	-0.763	8.960	13.757	-0.233	6.982	12.631	0.555
12.622	0.283	29.500	12.931	-0.939	26.727	12.539	0.967
12.212	0.233	9.060	8.606	0.020	0.177	12.042	1.637
11.487	0.807	4.717	13.814	0.178	4.287	11.338	0.480
10.124	0.268	1.060	12.063	0.893	8.438	12.826	0.949
12.366	2.669	18.963	12.481	4.320	18.824	12.577	1.594
11.802	1.127	5.626	11.958	1.323	6.647	11.484	0.812
11.311	1.739	3.199	11.492	0.269	3.351	10.128	0.267
14.102	-0.431	4.310	12.183	1.849	8.986	12.971	-0.053
12.727	2.024	24.059	10.466	0.313	1.060	12.682	0.631
14.310	-0.647	2.989	11.830	0.777	4.266	12.345	0.968
12.240	1.445	13.149	10.457	0.478	1.441	9.474	0.109
9.301	0.021	0.429	9.906	0.077	0.672		

(Z/D) = 12.72				(ϕ = 12.745)			
r' (cm)	V _r (cm/sec)	V _z (cm/sec)	r' (cm)	V _r (cm/sec)	V _z (cm/sec)	r' (cm)	V _r (cm/sec)
12.895	0.100	3.083	13.339	-0.753	3.138	12.739	0.622
8.313	0.359	0.310	11.737	1.154	2.395	7.826	0.304
13.572	0.297	2.562	10.596	0.841	1.354	12.982	-0.248
12.438	0.685	4.299	9.783	0.608	0.892	11.548	0.799

r' (cm)	V _r (cm/sec)	V _z (cm/sec)	r' (cm)	V _r (cm/sec)	V _z (cm/sec)	r' (cm)	V _r (cm/sec)

E.3 MATHEMATICAL SIMPLIFICATIONS

The use of Equation 3.47 and a tractable constitutive equation allows for the prediction of normal forces in the converging flow field. The magnitude and/or rate of growth of these normal forces have been suggested as an explanation for the onset of fracture. To predict the growth of the normal forces this analysis requires a prior knowledge of the magnitude of the velocity components which are then used to evaluate the components of the deformation rate tensor.

Assuming axial symmetry, the deformation rate tensor in a cylindrical coordinate system is given by

$$d_{<ij>} = \begin{bmatrix} v_{z,z} & \frac{1}{2}(v_{z,r} + v_{r,z}) & 0 \\ \frac{1}{2}(v_{z,r} + v_{r,z}) & v_{r,r} & 0 \\ 0 & 0 & \frac{v_r}{r} \end{bmatrix} \quad \text{E.1}$$

The magnitude of the shear component of the deformation rate tensor was obtained from plots of axial and radial velocities. Using the raw data tabulated in the preceding sections of this appendix, maximum values of $v_{z,r}$ and $v_{r,z}$ were estimated at several radial positions for the smallest and largest flow rates within region I and in reservoir S. The radial positions were arbitrarily chosen to 0.2D, 0.4D, 0.6D, 0.8D, and D where D is the internal diameter of the

capillary tube. The results are tabulated in Table E.43. The data show that the shear component of the deformation rate tensor can be evaluated as a first approximation by $V_{z,r}$ alone. The errors are less than 15%. Therefore, as a first approximation, the deformation rate tensor can be simplified as

$$d_{\langle ij \rangle} = \begin{bmatrix} V_{z,z} & \frac{1}{2}V_{z,r} & 0 \\ \frac{1}{2}V_{z,r} & V_{r,r} & 0 \\ 0 & 0 & \frac{V_r}{r} \end{bmatrix} \quad \text{E.2}$$

The mathematical analysis may be simplified further by comparison of the magnitudes of the radial velocity and axial velocity components. This was determined by estimating the maximum values of the ratio, $(V_r/V_z)_M$ at the same radial positions where the shear component was evaluated. These ratios are plotted in Figures E.1 to E.3. In addition to indicating that $(V_r/V_z)_M$ increases as we move away from the centerline, the data in Figures E.1 to E.3 also show that at the largest flow rate within region I the ratio $(V_r/V_z)_M$ is approximately equal to 0.10, even under worst condition, i.e., at a radial distance equal to one tube diameter. At radial positions greater than this, the ratio tends to be equal to zero. In reservoir L, region I extended to even higher flow

rates. Although not shown in Figures E.1 to E.3 the ratio, $(V_r/V_z)_M$, for these higher flow rates was in all cases less than 0.10. At the lowest flow rate where velocities were measured in reservoir S the radial velocity component is approximately equal to one half the magnitude of the axial velocity component. As an example, the data in Figure E.2 show that at a flow rate of $0.040 \text{ cm}^3/\text{sec}$ V_r approaches $0.60 V_z$ at r equal to $0.8D$. A photograph of this flow field is given in Figure 2.5. Within the vicinity of the centerline ($r < 0.2D$) the simplification $V_r < V_z$ holds to within 10% error.

In summary, for flow rates at the upper limit of region I, mathematical analyses can be simplified by assuming that

$$V_r < V_z \quad \text{E.3}$$

where $<$ implies an order of magnitude, and

$$V_{r,z} + V_{z,r} \approx V_{z,r} \quad \text{E.4}$$

At the lower limit of region I where velocities were measured

$$V_r \approx V_z \quad \text{E.5}$$

and

$$V_{r,z} + V_{z,r} \approx V_{z,r}$$

E.6

Only within the vicinity of the contraction ($r < 0.2D$) can we assume $V_r < V_z$.

TABLE E.43

SHEAR COMPONENT OF DEFORMATION RATE TENSOR

I.D. (cm)	Q (cm ³ / sec)	Shear Compon- ent (sec ⁻¹)	<u>RADIAL COORDINATE</u>				
			<u>.2D</u>	<u>.4D</u>	<u>.6D</u>	<u>.8D</u>	<u>D</u>
0.30	0.040	V _{r,z}	0.005	0.011	0.011	0.005	0.005
		V _{z,r}	0.800	0.292	0.208	0.017	-
	0.635	V _{r,z}	0.042	0.069	0.042	0.111	0.138
		V _{z,r}	-	4.200	3.300	2.500	-
0.20	0.040	V _{r,z}	0.060	0.105	0.105	0.075	0.180
		V _{z,r}	3.130	5.000	3.750	3.750	-
	0.318	V _{r,z}	0.088	0.163	0.150	0.066	0.012
		V _{z,r}	3.750	2.500	6.250	16.300	-
0.10	0.016	V _{r,z}	0.063	0.140	0.156	0.125	0.100
		V _{z,r}	0.500	1.000	1.250	1.250	-
	0.119	V _{r,z}	0.150	0.150	0.280	0.160	0.050
		V _{z,r}	-	0.750	1.250	1.500	-

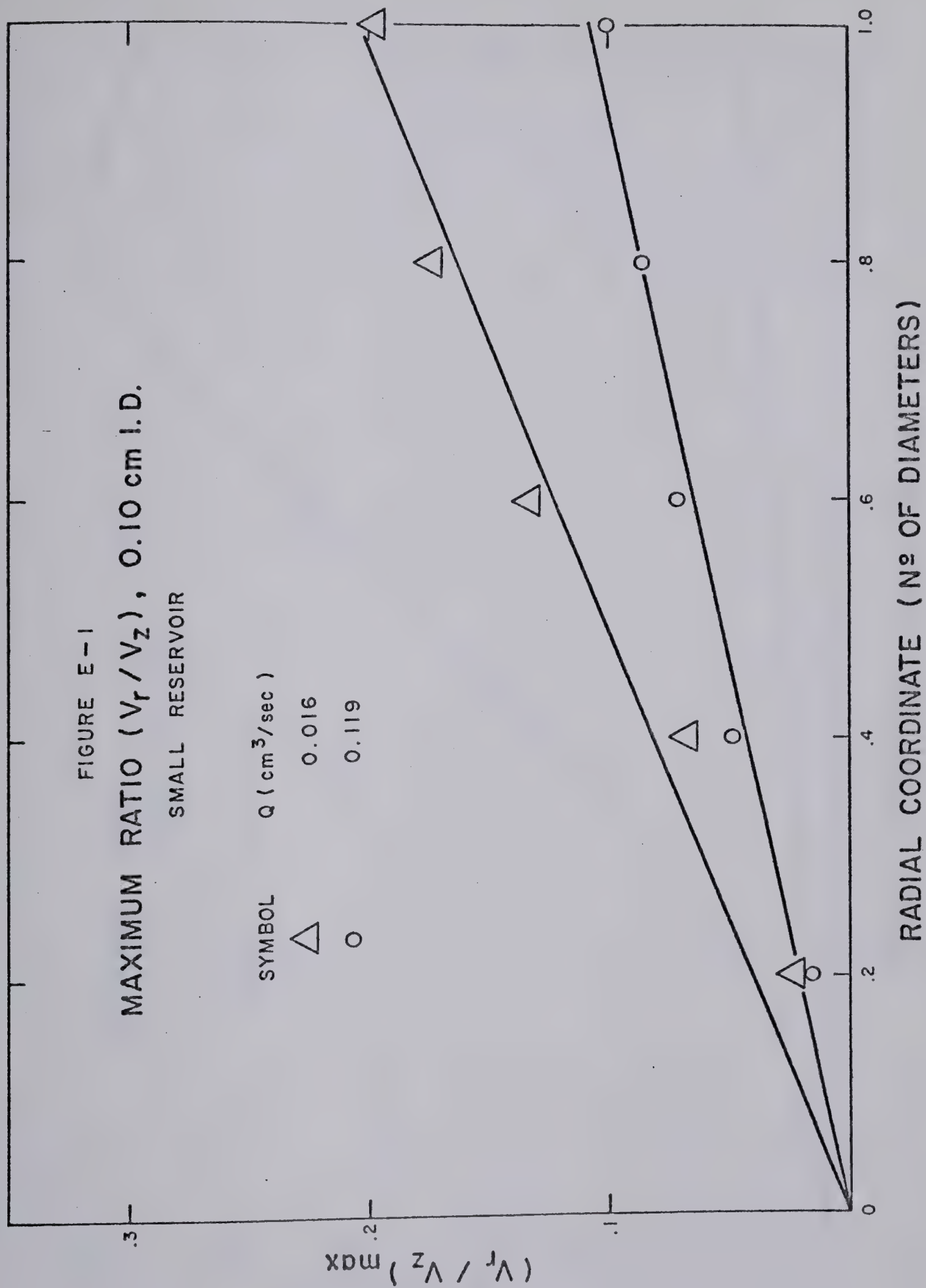
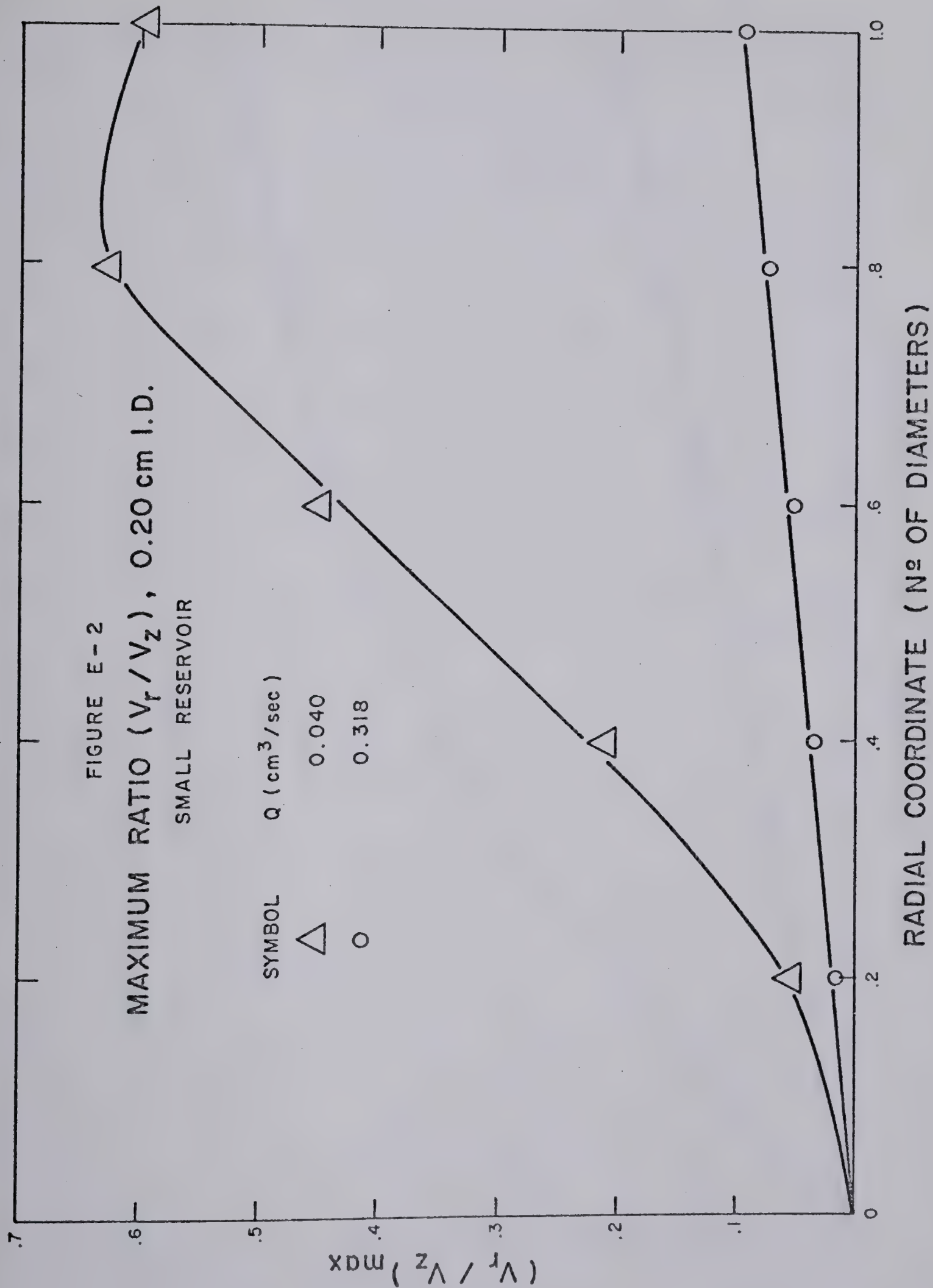
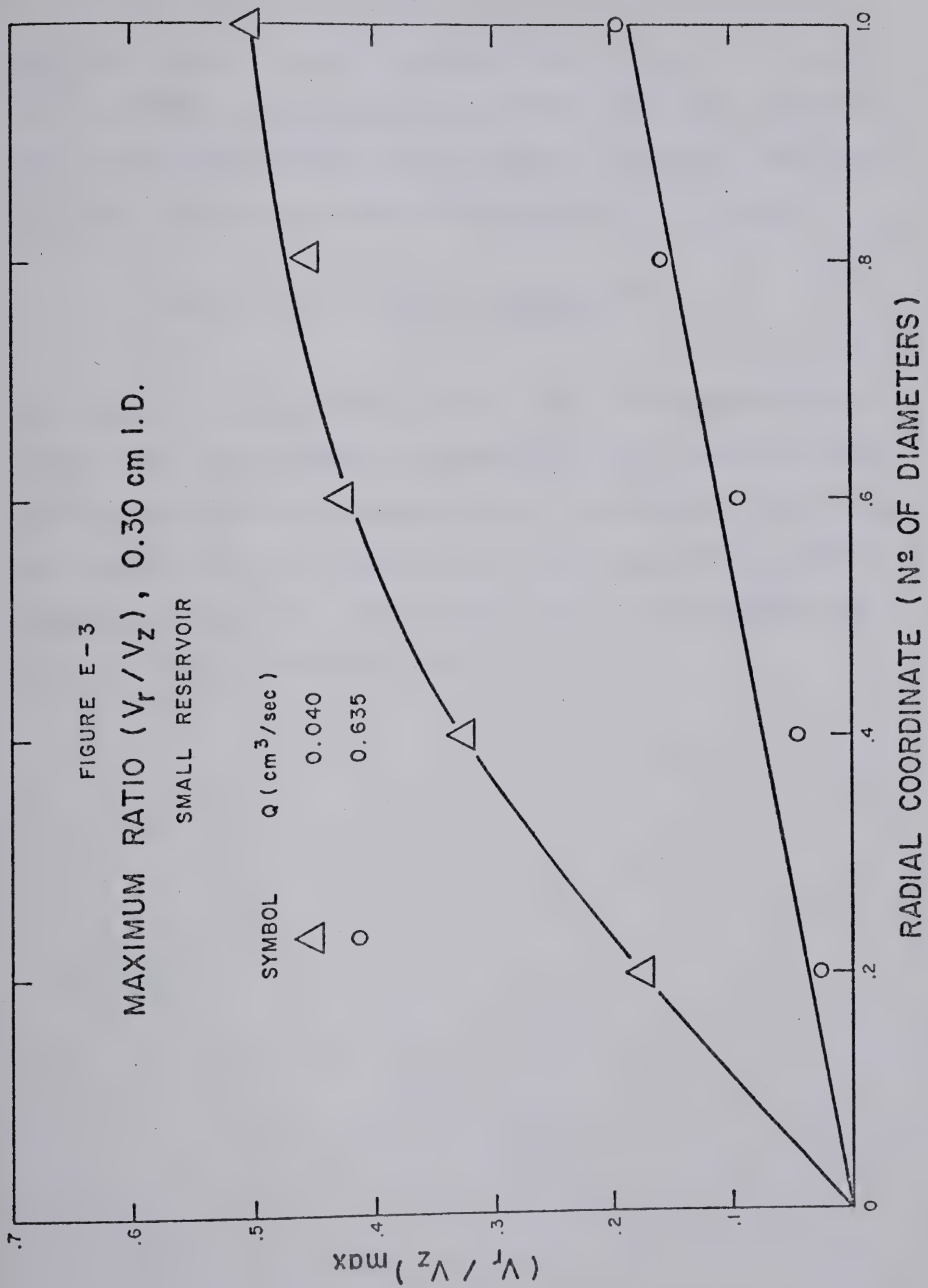


FIGURE E-2
 MAXIMUM RATIO (V_r/V_z), 0.20 cm I.D.
 SMALL RESERVOIR

SYMBOL	Q (cm ³ /sec)
\triangle	0.040
\circ	0.318





E.4 CENTERLINE AXIAL VELOCITIES

The centerline axial velocities for the three capillary tubes in each reservoir are plotted in Figures E.4 to E.10. As discussed in Chapter III the centerline axial velocities can be represented by Equation 3.20 with $c = 1.4$. On log-log coordinates Equation 3.20 yields

$$\log(V_z|_0) = \log V_0 - \frac{b}{2.303} \left(\frac{z}{D}\right)^{1.4} \quad \text{E.7}$$

Equation E.7 is plotted as solid lines in Figures E.4 to E.10. The least squares estimators of V_0 , the centerline axial velocity at the contraction, are given in Table E.44. The values of V_0 are used in the derivation of an empirical expression for local axial velocities the discussion of which is found in Chapter III.

TABLE E.44

CENTERLINE AXIAL VELOCITY AT CONTRACTION

RESERVOIR S

<u>I.D. (cm)</u>	<u>Q (cm³/sec)</u>	<u>V₀ (cm/sec)</u>
0.10 (L/D=55.08)	0.016	2.30
	0.040	5.80
	0.119	18.99
0.20 (L/D=54.96)	0.040	1.46
	0.159	7.50
	0.238	10.90
	0.318	14.00
0.30 (L/D=55.04)	0.040	0.70
	0.159	3.20
	0.318	5.97
	0.635	12.96

RESERVOIR L

0.20 (L/D=54.96)	0.159	5.40
	0.318	11.61
	0.794	27.82
	1.589	62.00
	1.906	75.00
	2.383	95.00
	2.701	115.00
	3.177	140.00
	3.812	165.00
0.30 (L/D=55.04)	4.866	220.00
	0.318	5.36
	0.635	12.21
	1.589	24.87
	4.866	90.80
	6.354	130.15
	7.148	170.77
	7.943	187.44
	9.531	239.00
	10.325	239.00
	11.120	267.00

FIGURE E-4
AXIAL CENTERLINE VELOCITY

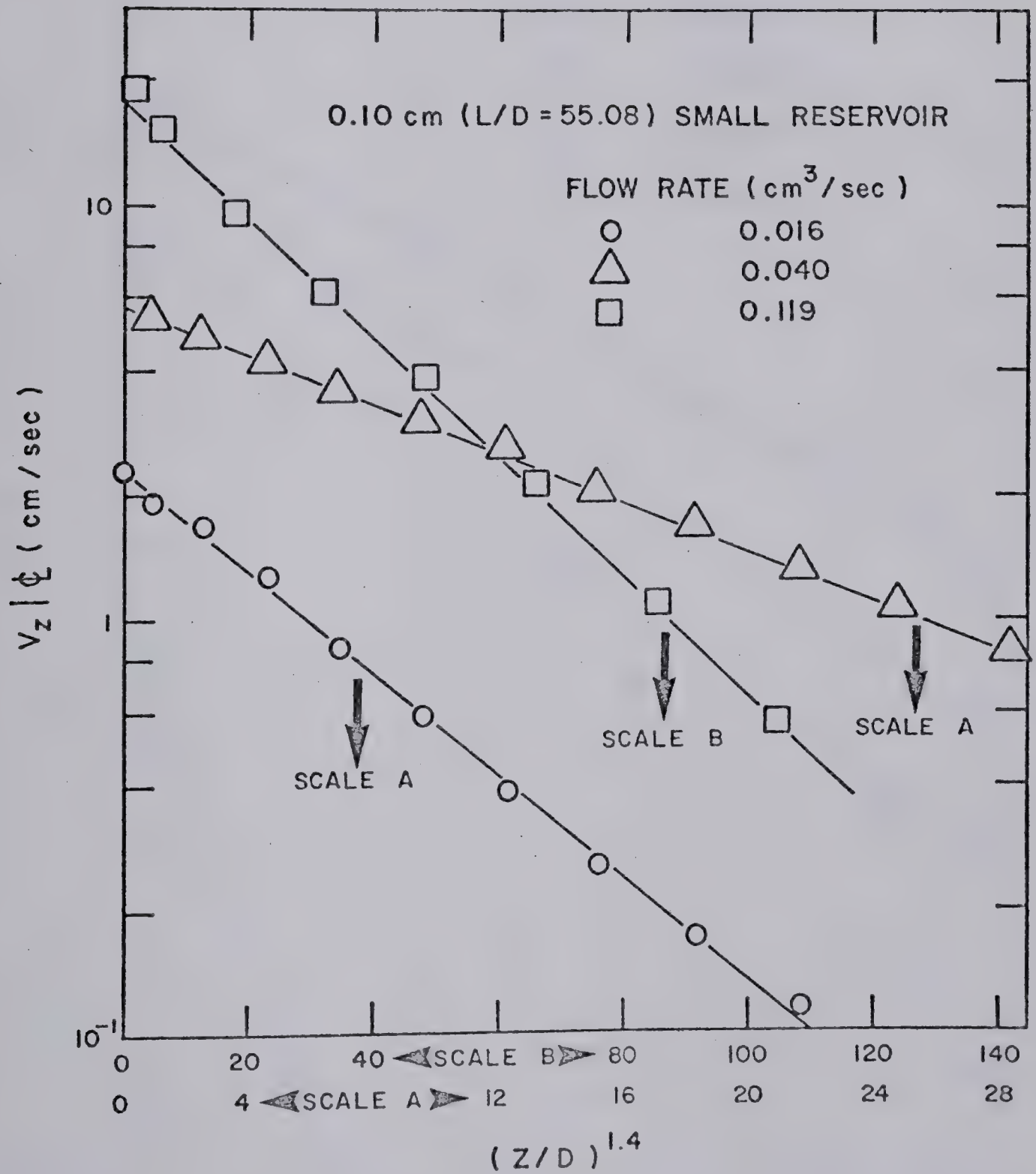


FIGURE E - 5
AXIAL CENTERLINE VELOCITY

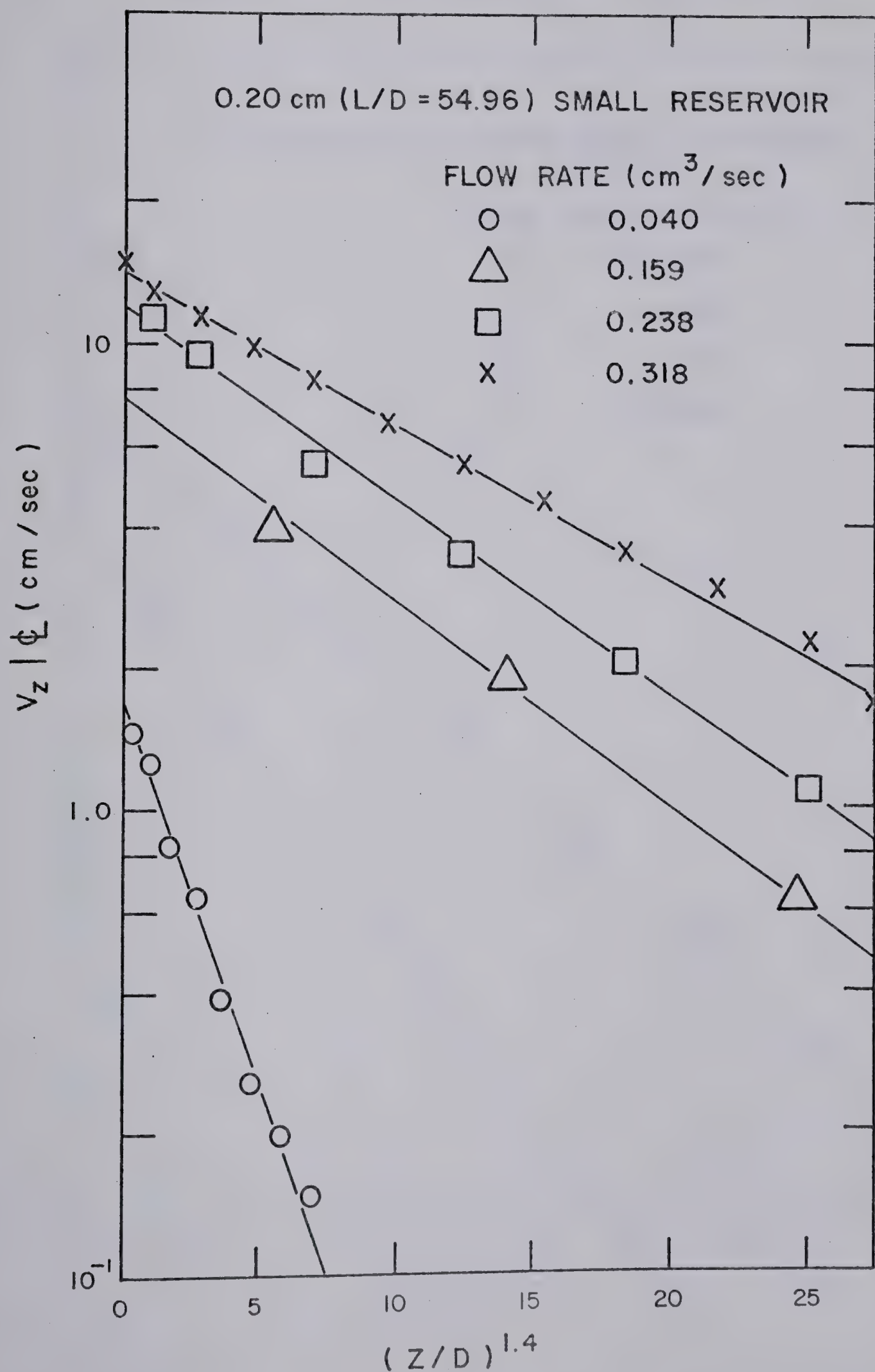


FIGURE E - 6
AXIAL CENTERLINE VELOCITY

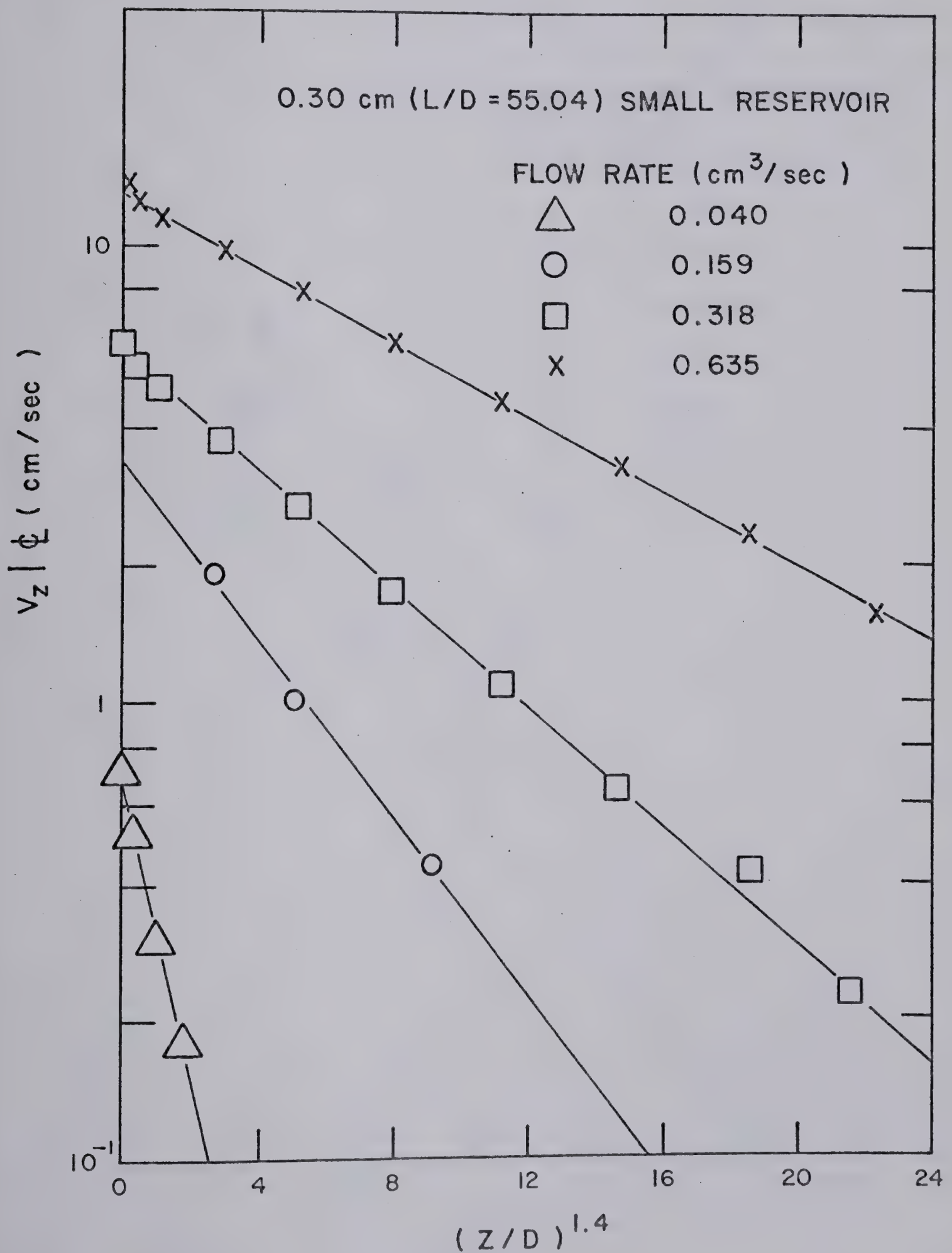


FIGURE E-7
AXIAL CENTERLINE VELOCITY

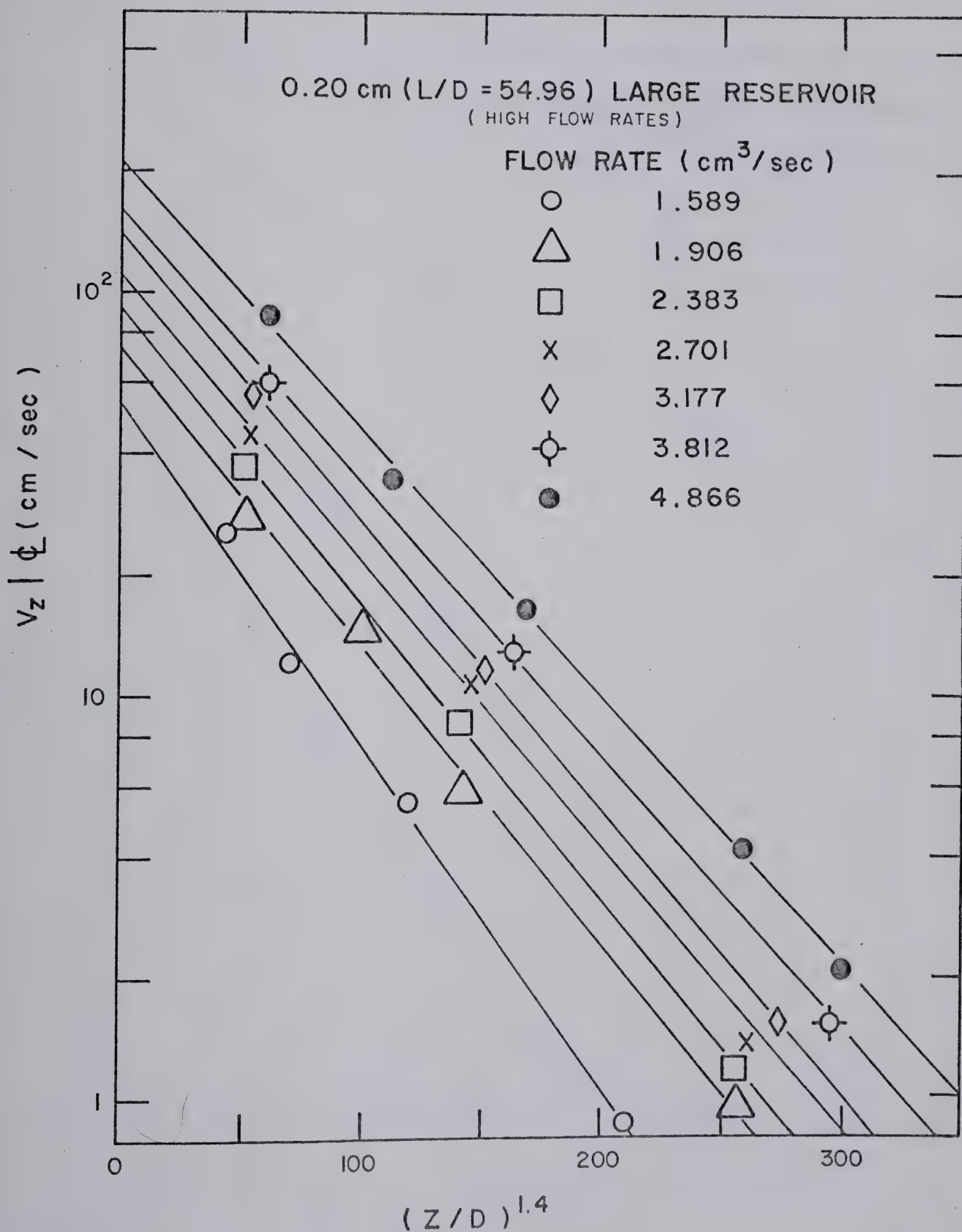


FIGURE E—8
AXIAL CENTERLINE VELOCITY

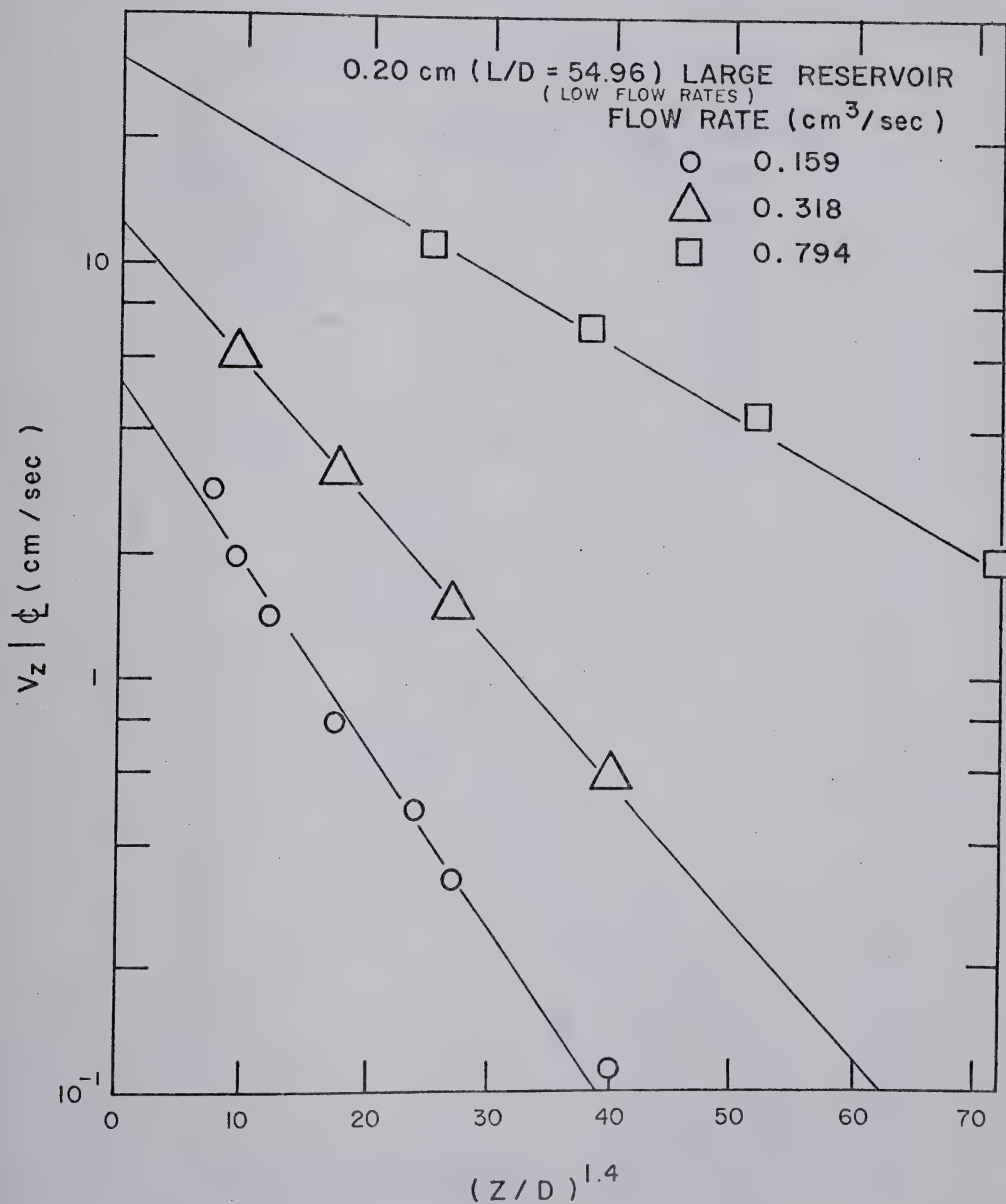


FIGURE E - 9
AXIAL CENTERLINE VELOCITY

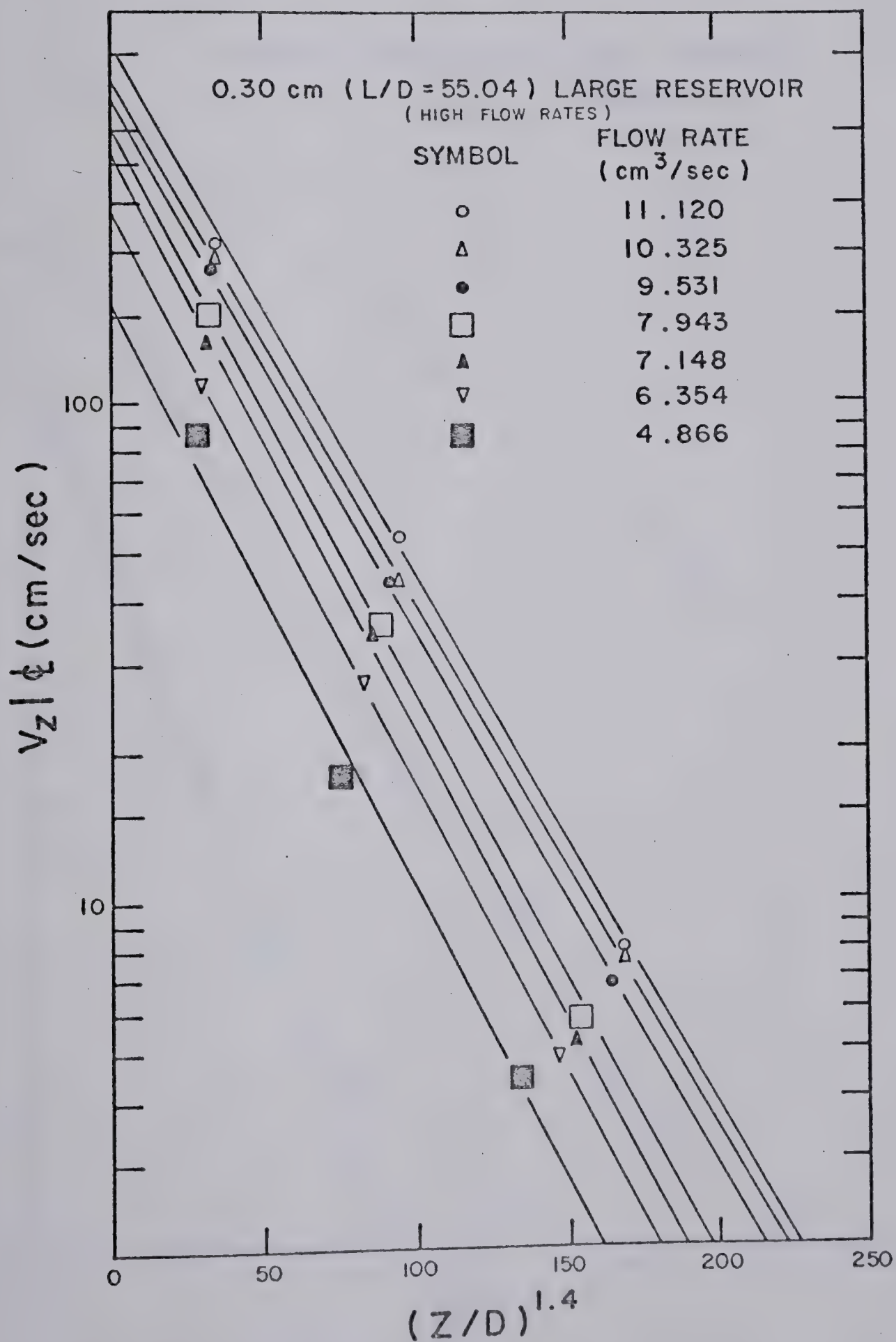
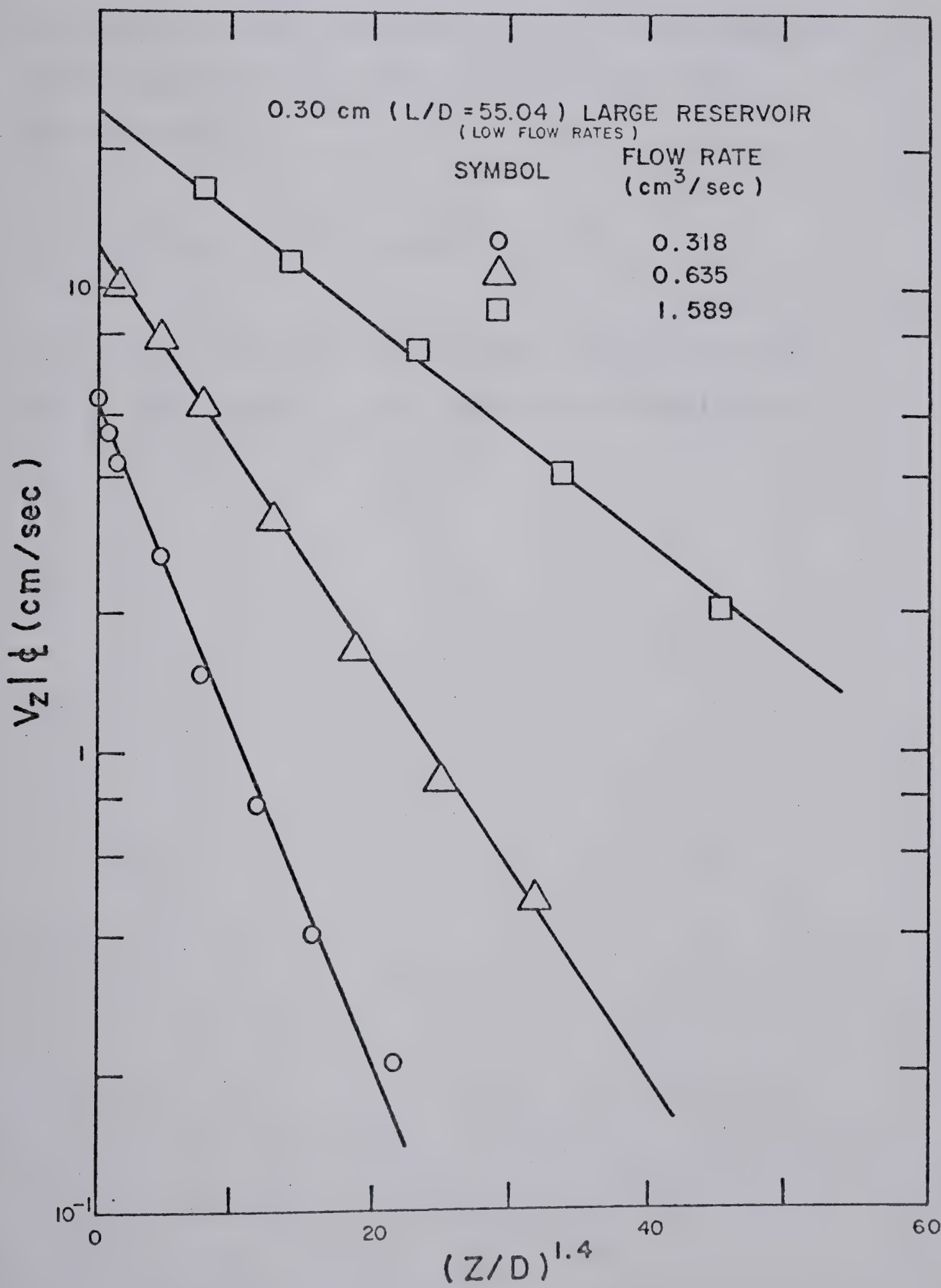


FIGURE E-10
AXIAL CENTERLINE VELOCITY



E.5 PARAMETER r_0

Parameter r_0 was defined in Chapter III as the radial distance where the axial velocity was equal to one half of the centerline axial velocity. Using this definition, the radial dependence of axial velocities was shown to be represented by

$$f(\eta) = \frac{V_z}{V_z} = (1 + 0.41 \eta^2)^{-2} \quad \text{E.8}$$

where η is a dimensionless radial coordinate equal to (r/r_0) . The values r_0 are tabulated in Table E.45.

TABLE E.45

VARIATION OF PARAMETER r_0 WITH RESERVOIR SIZE,
CAPILLARY TUBE I.D., FLOW RATE AND
DIMENSIONLESS AXIAL POSITION Z^{**}

Reservoir S

<u>I.D.</u> <u>(cm)</u>	<u>Flow Rate</u> <u>(cm³/sec)</u>	<u>Z^{**}</u>	<u>r₀</u> <u>(cm)</u>
0.10	.016	0.000	.037
		0.251	.043
		0.502	.053
		1.004	.084
		1.505	.141
		1.756	.202
		2.007	.220
	.040	0.158	.043
		0.316	.054
		0.474	.051
		0.632	.060
		0.949	.083
		1.265	.104
		1.581	.135
		1.897	.187
		2.214	.259
	.119	0.183	.043
		0.367	.047
		0.733	.064
		1.100	.077
		1.467	.113
		1.833	.185
		2.567	.360
0.20	.040	0.224	.082
		0.447	.092
		0.742	.120
		0.894	.133
		1.485	.190
		1.795	.249
	.159	0.736	.120
		1.472	.190
		2.207	.380

TABLE E.45 (continued)

Reservoir S

<u>I.D.</u> <u>(cm)</u>	<u>Flow Rate</u> <u>(cm³/sec)</u>	<u>z**</u>	<u>r₀</u> <u>(cm)</u>
0.20	.238	0.367	.087
		0.733	.110
		1.100	.144
		1.467	.185
		1.833	.293
	.318	0.000	.079
		0.159	.083
		0.317	.095
		0.635	.097
		0.952	.131
		1.428	.206
		1.745	.254
		1.903	.310
	.040	0.000	.098
		0.411	.129
		0.822	.197
		1.232	.218
		1.649	.290
0.30	.159	0.581	.165
		1.199	.235
		1.780	.370
	.318	0.000	.122
		0.145	.124
		0.291	.124
		0.583	.145
		0.875	.186
		1.457	.311
		1.749	.373
	.635	0.000	.114
		0.103	.114
		0.206	.119
		0.412	.134
		0.619	.145
		1.237	.260
		1.649	.388

TABLE E.45 (continued)

Reservoir L

<u>I.D.</u> <u>(cm)</u>	<u>Flow Rate</u> <u>(cm³/sec)</u>	<u>z**</u>	<u>r₀</u> <u>(cm)</u>
0.20	.159	1.106	.179
		1.738	.423
		2.366	.613
		3.163	.785
	.318	0.782	.134
		1.229	.211
		1.674	.408
		2.237	.761
	.794	0.990	.204
		1.345	.274
		1.696	.380
		2.118	.654
		2.469	1.071
	1.589	0.993	.200
		1.064	.215
		1.511	.295
		2.000	.480
		2.531	1.335
		2.980	1.575
	4.866	0.795	.165
		1.606	.400
		2.404	1.500
0.30	.318	0.000	.127
		0.414	.148
		0.822	.200
		1.236	.274
		1.647	.423
		2.058	.600
	.635	0.293	.135
		0.584	.145
		0.874	.204
		1.264	.290
		1.654	.444
		2.039	.719
		2.429	.846

TABLE E.45 (continued)

Reservoir L

<u>I.D.</u> <u>(cm)</u>	<u>Flow Rate</u> <u>(cm³/sec)</u>	<u>Z**</u>	<u>r₀</u> <u>(cm)</u>
0.30	1.589	0.553	.177
		0.860	.218
		1.228	.310
		1.597	.493
		1.962	.817
	4.866	0.816	.250
		1.631	.500
	11.120	0.627	.225
		1.254	.420
		1.881	1.500

. APPENDIX F

EDDY CENTERS AND CONE SEMI-ANGLES

F.1 EDDY CENTERS

This section contains the tabulated location of the centers of the eddies that surrounded the core of fluid in the inlet region. A summary of the tabulated data is given below.

EDDY CENTERS

<u>TABLE NO.</u>	<u>DIA. (cm)</u>	<u>RESERVOIR</u>	<u>L/D</u>
F.1	0.10	S	55.08
F.2	0.20	S	54.96
F.3	0.30	S	55.04
F.4	0.10	L	55.08
F.5	0.20	L	54.96
F.6	0.30	L	55.04

The location of the eddy centers was determined by four measurements, A, B, C, and D. Consider as a typical example the first entry in Table F.4. Since the magnification was 2.175 the actual distances A, B, C, and D are found by dividing by 2.175. This results in the location of the eddy centers as shown schematically in Figure F.1.A. However, for the data where the magnification was 24.437, e.g., the data in Table F.1 indicated by an asterisk, the actual distances A, B, C, and D are obtained by dividing by 24.437, with the distance D being measured from the opposite wall. Shown schematically in Figure F.1.B is the location of the eddy center for the first entry in Table F.1. The accuracy in the measurements was ± 0.32 cm at magnifications of 2.175, 9.063 or 24.437.

TABLE F.1

EDDY CENTER LOCATION

0.10 cm I.D. CAPILLARY, $L/D=55.08$, SMALL RESERVOIR

Magnification: 9.063

<u>Flow Rate</u> <u>(cc/sec)</u>	<u>A</u> <u>cm</u>	<u>B</u> <u>cm</u>	<u>C</u> <u>cm</u>	<u>D</u> <u>cm</u>
0.004*	7.620	7.303	23.495	23.813
0.012*	13.018	13.335	20.003	20.912
0.016*	15.558	15.240	19.050	19.845
0.024*	19.368	19.368	18.495	18.733
0.032*	22.543	22.860	18.098	18.258
0.040	10.160	10.160	6.350	17.780
0.079	13.970	14.288	6.510	17.305
0.119	16.510	16.510	6.668	17.463

* The magnification for these data was 24.437.

TABLE F.2

EDDY CENTER LOCATION

0.20 cm I.D. CAPILLARY, L/D=54.96, SMALL RESERVOIR

Magnification: 9.063

Flow Rate (cc/sec)	A <u>cm</u>	B <u>cm</u>	C <u>cm</u>	D <u>cm</u>
0.004*	3.175	3.175	-	25.083
0.012*	6.033	6.033	21.590	23.495
0.016*	7.620	8.890	18.098	21.273
0.024*	10.160	11.113	18.098	20.320
0.032*	11.905	12.700	17.780	19.050
0.040	6.033	6.033	6.668	17.620
0.059	7.460	7.460	6.350	17.620
0.079	8.890	8.573	6.190	17.780
0.103	10.317	10.638	6.190	17.780
0.159	12.065	11.748	6.190	17.780
0.318	14.288	14.605	6.590	17.940

* The magnification for these data was 24.437.

TABLE F.3

EDDY CENTER LOCATION

0.30 cm I.D. CAPILLARY, $L/D=55.04$, SMALL RESERVOIR

Magnification: 9.063

<u>Flow Rate</u> <u>(cc/sec)</u>	<u>A</u> <u>cm</u>	<u>B</u> <u>cm</u>	<u>C</u> <u>cm</u>	<u>D</u> <u>cm</u>
0.004*	1.588	1.588	24.295	24.448
0.012*	2.223	2.223	22.860	21.908
0.016*	3.810	3.810	20.955	20.701
0.024*	6.033	6.033	18.098	18.415
0.032*	7.938	7.938	17.145	17.145
0.040	3.970	3.970	6.350	17.940
0.079	5.398	5.398	6.033	18.098
0.119	6.668	6.668	5.875	18.098
0.159	7.938	7.938	6.350	18.258
0.238	9.365	9.365	6.350	18.415
0.318	10.795	10.795	6.350	18.258
0.394	11.590	11.590	6.350	18.098
0.477	12.383	12.383	6.350	18.258
0.635	13.653	13.653	5.875	18.098

* The magnification for these data was 24.437.

TABLE F.4

EDDY CENTER LOCATION

0.10 cm I.D. CAPILLARY, L/D=55.08, LARGE RESERVOIR

Magnification: 2.175

<u>Flow Rate</u> <u>(cc/sec)</u>	<u>A</u> <u>cm</u>	<u>B</u> <u>cm</u>	<u>C</u> <u>cm</u>	<u>D</u> <u>cm</u>
0.159	7.938	7.938	21.115	32.703
0.318	10.478	10.478	19.050	34.762
0.381	11.125	11.430	18.733	35.243
0.508	12.700	12.700	18.098	35.720
0.635*	13.970	13.495	17.305	35.878
0.794*	15.240	14.765	16.828	36.513
0.953*	16.353	15.240	16.510	36.673
1.120*	16.828	16.193	16.340	36.990
1.271*	17.145	16.670	16.510	36.990

* Measured only when the flow field was observed to be stable.

TABLE F.5

EDDY CENTER LOCATION

0.20 cm I.D. CAPILLARY, $L/D=54.96$, LARGE RESERVOIR

Magnification: 2.175

<u>Flow Rate</u> <u>(cc/sec)</u>	<u>A</u> <u>cm</u>	<u>B</u> <u>cm</u>	<u>C</u> <u>cm</u>	<u>D</u> <u>cm</u>
0.159	3.912	3.912	23.020	30.798
0.238	5.240	5.240	22.225	31.593
0.318	6.452	6.452	21.463	32.385
0.477	7.938	7.938	20.638	33.338
0.794	10.320	10.160	19.210	34.768
1.271	12.065	12.383	18.098	35.878
1.589	13.178	13.335	17.780	36.513
1.906*	13.970	12.860	17.297	36.673
2.383*	15.083	15.083	16.988	36.990
2.701*	15.718	15.400	16.828	36.830
3.177*	16.193	15.875	16.670	37.069
3.812*	16.993	16.828	16.353	37.313
4.766*	18.098	17.145	15.718	37.160

* Measured only when the flow field was observed to be stable.

TABLE F.6

EDDY CENTER LOCATION

0.30 cm I.D. CAPILLARY, $L/D=55.04$, LARGE RESERVOIR

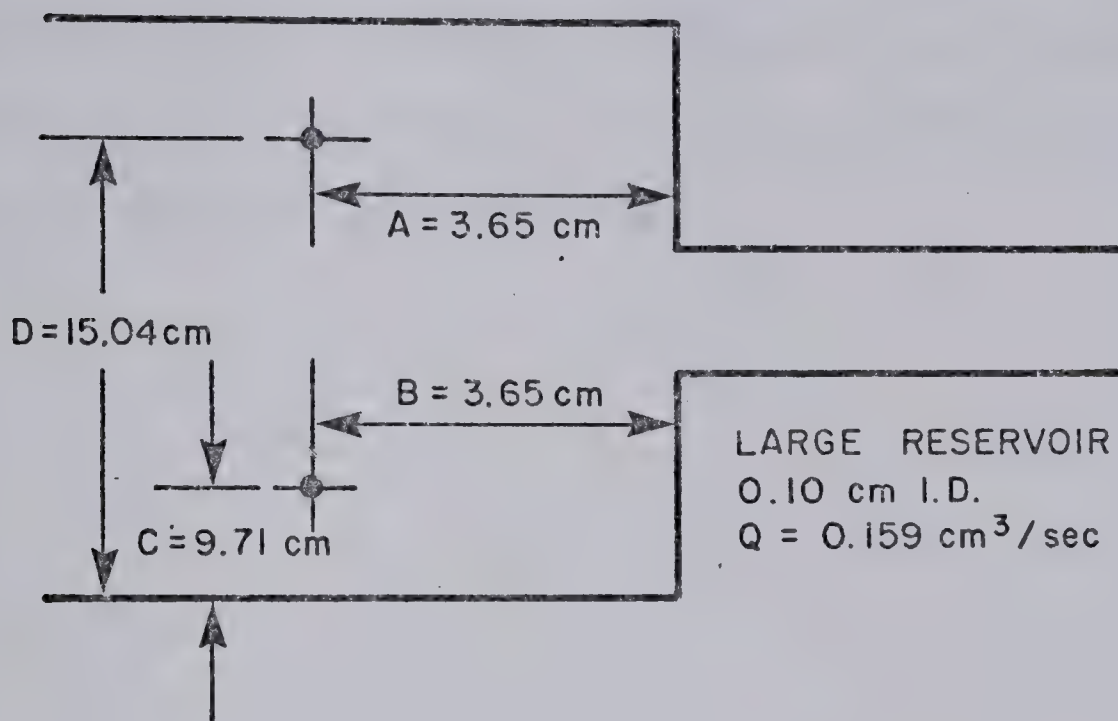
Magnification: 2.175

<u>Flow Rate</u> <u>(cc/sec)</u>	<u>A</u> <u>cm</u>	<u>B</u> <u>cm</u>	<u>C</u> <u>cm</u>	<u>D</u> <u>cm</u>
0.318	3.988	3.988	23.622	31.496
0.635	5.969	5.969	22.225	32.690
0.794	6.985	6.985	21.273	33.338
1.589	9.843	9.843	19.342	35.230
2.383	11.748	11.430	18.415	36.038
3.177	12.860	12.700	17.780	36.673
4.766	14.765	14.288	17.145	37.148
6.354*	15.558	17.623	16.828	37.226
7.148*	15.875	15.558	16.683	37.148
7.943*	16.193	15.718	16.683	37.465
8.737*	16.828	16.193	16.510	37.465
9.531*	17.145	16.353	16.353	37.625
10.325*	17.305	16.670	16.271	37.625
11.120*	17.145	16.670	16.510	36.990

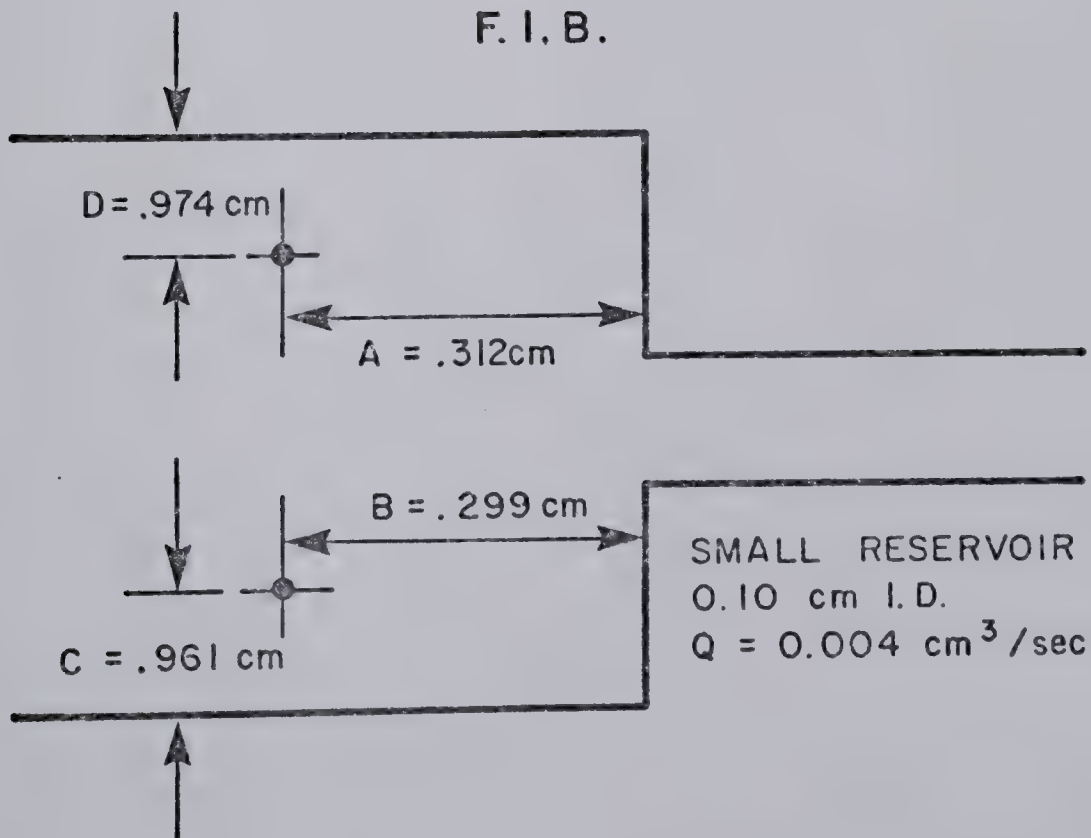
* Measured only when the flow field was observed to be stable.

FIGURE F-1
EDDY CENTER LOCATION

F. I. A.



F. I. B.



F.2 CONE SEMI-ANGLES

The cone semi-angle, measured in degrees, was defined in Chapter II, Section 2.3.4, as the angle tangent to the outermost streamline that entered into the capillary tube. The cone semi-angles in Tables F.7 and F.8 were measured at L/D ratios equal to 55.08, 54.96, and 55.04 for capillary tubes 1, 2, and 3 respectively.

TABLE F.7

CONE SEMI-ANGLES - SMALL RESERVOIR

<u>I.D.</u> <u>(cm)</u>	<u>Flow Rate</u> <u>(cm³/sec)</u>	<u>z/D</u>	<u>Cone Semi-</u> <u>angle</u> <u>(degrees)</u>
0.10	.016	0.00	3.5
		2.00	5.5
		4.00	8.0
		6.00	12.5
		8.00	22.5
		10.00	38.0
0.10	.040	0.00	2.0
		3.00	2.5
		6.00	2.8
		8.00	3.3
		11.00	6.7
		14.00	11.0
0.10	.119	0.00	1.0
		4.00	1.1
		8.00	1.5
		12.00	2.5
		16.00	3.3
		20.00	5.0
		24.00	8.0
		28.00	13.5
0.20	.040	0.00	8.0
		1.00	11.5
		2.00	16.0
		3.00	25.0
		4.00	32.0
0.20	.159	0.00	3.7
		1.57	4.5
		3.14	5.4
		4.72	7.6
		6.29	10.8
		7.86	17.8
		9.43	32.7

TABLE F.7 (continued)

<u>I.D.</u> <u>(cm)</u>	<u>Flow Rate</u> <u>(cm³/sec)</u>	<u>z/D</u>	<u>Cone Semi-</u> <u>angle</u> <u>(degrees)</u>
0.20	.238	0.00	2.7
		2.00	3.0
		4.00	4.1
		6.00	5.0
		8.00	10.0
		12.00	14.0
		16.00	15.0
0.20	.318	0.00	2.0
		3.00	3.0
		6.00	4.2
		8.00	7.0
		11.00	11.0
0.30	.040	0.00	18.0
		0.50	21.0
		1.00	28.0
		1.50	32.0
		2.00	39.0
		2.50	46.0
0.30	.159	0.00	6.5
		1.50	8.0
		2.09	9.7
		2.62	13.6
		3.14	18.8
		3.67	25.3
		4.19	33.1
0.30	.318	0.00	4.4
		1.00	4.7
		3.00	6.0
		4.00	9.5
		5.00	14.0
		6.00	19.0
		8.00	21.0
0.30	.635	0.00	3.2
		2.00	4.0
		4.00	5.0
		6.00	8.5
		8.00	11.0
		10.00	17.0
		11.00	21.0

TABLE F.8

CONE SEMI-ANGLES - LARGE RESERVOIR

<u>I.D.</u> <u>(cm)</u>	<u>Flow Rate</u> <u>(cm³/sec)</u>	<u>z/D</u>	<u>Cone Semi-</u> <u>angle</u> <u>(degrees)</u>
0.20	.159	0.00	3.5
		5.00	8.0
		10.00	14.5
		15.00	18.0
		20.00	21.0
		30.00	30.0
		40.00	40.0
0.20	.238	0.00	3.0
		4.54	5.5
		9.08	12.0
		13.62	13.0
		18.16	16.0
		22.70	17.0
0.20	.318	0.00	2.0
		3.01	3.0
		7.50	6.0
		10.50	8.5
		14.00	13.0
0.20	.794	0.00	1.0
		7.60	2.5
		10.00	4.0
		13.60	5.5
		20.00	11.0
		24.80	12.0
		30.00	13.5
		38.00	15.0
		40.00	16.5
		44.00	18.0
0.20	1.589	0.00	.65
		6.50	1.0
		10.00	1.35
		12.60	1.7
		18.80	2.5
		20.00	2.8
		25.00	4.0
		30.00	6.0
		31.50	6.5
		35.60	8.5
		40.00	12.0

TABLE F.8 (continued)

<u>I.D.</u> <u>(cm)</u>	<u>Flow Rate</u> <u>(cm³/sec)</u>	<u>z/D</u>	<u>Cone Semi-</u> <u>angle</u> <u>(degrees)</u>
0.30	.318	0.00	4.2
		1.40	4.5
		2.80	6.0
		4.20	9.0
		5.60	13.0
		6.00	16.0
		9.00	20.0
		11.00	22.0
0.30	.635	0.00	3.5
		3.00	5.2
		4.20	6.6
		5.00	7.5
		6.00	8.5
		8.00	15.0
		10.00	17.0
		12.00	19.0
0.30	.794	15.00	21.0
		0.00	2.5
		3.00	4.5
		6.00	9.0
		9.00	12.0
		12.00	15.0
		15.00	17.0
		18.00	20.0
0.30	1.589	21.00	24.0
		0.00	0.85
		2.24	1.0
		5.25	2.0
		9.18	4.0
		10.00	4.5
		13.20	6.0
		15.00	8.0
		17.10	8.5
		20.00	9.5
		21.10	9.0
		25.00	11.5
		30.00	15.0
		33.00	16.5
		40.00	20.0

TABLE F.8 (continued)

<u>I.D.</u> <u>(cm)</u>	<u>Flow Rate</u> <u>(cm³/sec)</u>	<u>z/D</u>	<u>Cone Semi-</u> <u>angle</u> <u>(degrees)</u>
0.30	3.177	0.00	0.8
		5.96	1.5
		9.95	4.0
		13.90	6.0
		17.90	10.5
		21.80	15.0
		25.80	18.0
		29.80	21.0
		33.80	26.0
		37.70	29.0
0.30	4.866	0.00	0.55
		3.00	1.0
		10.00	2.3
		20.00	7.0
		30.00	12.0
		40.00	19.0

APPENDIX G
ERROR ANALYSIS

The digitizer and direct methods used to measure velocity components were discussed in detail in Chapter II, Section 2.3. The sources of error in measuring axial and radial velocity components with these methods are:

- a. digitizer calibration,
- b. measuring the slope of the reservoir wall relative to the digitizer's X axis,
- c. measuring velocities over a band width rather than at a fixed upstream axial location,
- d. centering of the capillary tube, and
- e. depth of field of the camera.

Since the sources of error are assumed independent, the error in measuring velocity components is the sum of errors. Hence, for the digitizer method, the sources of error were "a" through "e" of the above whereas, for the direct method sources of error were "d" and "e".

G.1 DIGITIZER METHOD ERROR

The sources of error were calibration, slope of reservoir wall, measurement over a band width, centering of capillary tube, and depth of the camera field.

G.1.1 CALIBRATION

The full scale movement of the digitizer's cross hair for the X and Y axes were 33,000 counts and 32,000 counts respectively. The digitizer cross hair was moved 2.54 cm along the X and then along the Y axis in order to convert these readings into distances. Repeated measure-

ments, tabulated in Table G.1, resulted in a sample mean equal to 1414 counts and 1490 counts for the X and Y respectively. The standard deviation of the mean, arising from digitizer electronic error and error in positioning the cross hair, for the X and Y axes were 55.63 and 52.72 respectively. The calibration procedure was repeated at the upper and lower limits of the digitizer's X and Y axes in order to detect nonlinearity over the full range of the digitizer's X and Y axes. No nonlinearity was detected.

The relative errors in measuring axial and radial velocities can be evaluated by considering an example where the axial distance traversed by an aluminum dust particle was equal to 400 counts and another of 1000 counts. Expressed as percentages, the relative errors, within one standard deviation, for the axial velocity component are

$$\frac{55.63}{400} \times 100 \quad \text{or} \quad \frac{55.63}{1000} \times 100$$

or 18.9 percent and 5.6 percent. These errors are representative errors for axial velocities measured outside ($\eta > 1.5$) and within the WGS core respectively. In addition, blurry ends of the streaks resulted in a judgement error in positioning the cross hair. This error, determined by the time involved for the splitter to cut the beam of light, was less than 2 percent. Therefore, the sums of errors obtained by the propagation of error through addition, arising from digitizer electronic error, human factor, and the blurry ends of the streaks, were 20.9 percent and 7.6 percent out-

TABLE G.1

CALIBRATION OF DIGITIZER

X axis No. of counts measured over 2.54 cm	Y axis No. of counts measured over 2.54 cm
1402	1430
1416	1498
1366	1496
1418	1462
1440	1554
1418	1414
1388	1514
1410	1472
1408	1524
1428	1500
1388	1512
1408	1436
1464	1536
1402	1450
1454	1514
1390	1526
1364	1468
1470	1436
1416	1532
1426	1530
1390	1486
1423	1436
1419	1546
1410	1434
1412	1495
1415	1491
	1486
	1500
	1496

side and within the WGS core respectively.

The magnitude of the velocities were shown in the previous section of this appendix to be less than the axial velocities. The error was therefore larger than the error in measuring the axial velocity component. Qualitatively, this error was found to be, in the worst case, as large as 100 percent and under the best circumstances (largest number of counts) as small as 25 percent.

G.1.2 SLOPE OF THE RESERVOIR WALL

The axial and radial distances traversed by a single streak or by a number of streaks were measured relative to the wall of the reservoir. As shown in Figure 2.8 (page 66) the wall of the reservoir was not parallel to the X axis of the digitizer. It was therefore necessary to measure the slope of the wall of the reservoir relative to the digitizer's X axis, m_1 , to determine the axial distance, Δx , and radial distance, Δr , given by Equations G.1 and G.2.

$$\Delta x = \frac{(Y_4 - Y_3)m_1}{(m_1^2 + 1)^{\frac{1}{2}}} + \frac{(X_4 - X_3)}{(m_1^2 + 1)^{\frac{1}{2}}} \quad G.1$$

$$\Delta r = \frac{(Y_4 - Y_3)}{(m_1^2 + 1)^{\frac{1}{2}}} + \frac{(X_3 - X_4)m_1}{(m_1^2 + 1)^{\frac{1}{2}}} \quad G.2$$

Coordinates (X_3, Y_3) and (X_4, Y_4) were defined in Figure 2.7 (page 64). Due to mechanical error, error in positioning

the cross hair, and the resolution of the wall of the reservoir projected on to the digitizer screen, the error in measuring the slope m_1 was as large as 15 percent. The resulting error in measuring Δx or Δr was estimated by considering two streaks as typical examples; streak 1 was located near the outer edge of the WGS core and streak 2 was located near the centerline. The coordinates of these two streaks and the slope m_1 were

Streak 1

$$X_3 = 32.201 \text{ cm} \quad Y_3 = 45.889 \text{ cm}$$

$$X_4 = 33.427 \text{ cm} \quad Y_4 = 46.070 \text{ cm}$$

Streak 2

$$X_3 = 32.571 \text{ cm} \quad Y_3 = 48.822 \text{ cm}$$

$$X_4 = 33.006 \text{ cm} \quad Y_4 = 48.829 \text{ cm}$$

$$m_1 = 0.0279$$

By using the above data, Equation G.1, and an error of 15% in the value of m_1 , the error in measuring the axial distance Δx was found to be less than one tenth of one percent; hence, was considered to be negligible. A 15 percent error in m_1 resulted in a maximum 3.6 percent error in the evaluation of Δr , hence, a 3.6 percent error in the radial velocity component. The error in measuring Δr near the centerline was less than 1 percent.

G.1.3 UPSTREAM AXIAL LOCATION OF STREAKS

Streaks used in calculating velocities with the digitizer method were taken over a band width rather than at a fixed upstream axial location. This resulted in scatter in the measured velocities which depends upon the width of the band and the velocity gradient. The velocity gradient, in turn, is dependent upon both axial and radial positions. Taking these factors into account it was estimated that scatter in local axial and radial velocities ranged from 1 to 8 percent with the smallest scatter occurring along the centerline.

G.1.4 CENTERING OF CAPILLARY TUBE AND DEPTH OF FIELD OF CAMERA

Since the wall thickness of each length of capillary tube was not uniform it was necessary to center each capillary tube so that the center of the capillary tube and the center of the beam of light were in the same horizontal plane. The following procedure was used in centering the capillary tubes: With a level, the empty reservoir was adjusted so that it was in a horizontal plane. The capillary tube was then inserted into the holding device which was attached to the end plate. The light source was turned on and except for this source of light the room was in total darkness. The beam of light was clearly visible against the aluminum end wall of the reservoir and the side of the reservoir opposite the side where the adjustment slit was attached. By adjusting the level of the light source, a

plane passing through the center of the light beam was coincident with a plane passing through etched marks located on both sides of the reservoir. These etched marks represented a plane which was parallel to the viewing surface of the reservoir and passed through the center of the hole in the aluminum end plate. An eyepiece was focused on the area where the capillary tube was fitted flush with the aluminum end plate. The capillary tube was rotated by hand until the center of the beam of light and the center of the capillary tube was judged, by eye, to be in the same plane. A conservative estimate was that the capillary tube could be centered to within $1/5$ of the thickness of the beam of light.

Since the depth of field of the camera was always greater than the beam of light it was not possible to distinguish between aluminum dust particles that were at the top of the beam of light (nearest to the camera), at the bottom of the beam of light (farthest away from the camera), or at any intermediate plane lying within these limits. In fact, there was a distribution of positions which peaked at the center of the band. In the illustration below, the position $r + \frac{1}{2}sw$ and $r - \frac{1}{2}sw$, where sw is the slit width, represent the limits of the band at a radial position r .

_____	$r + \frac{1}{2} sw$	$\bar{V}_z + \Delta V_z$
_____	r	\bar{V}_z
_____	$r - \frac{1}{2} sw$	$\bar{V}_z - \Delta V_z$

If n streaks are observed within the band, roughly $n/2$ streaks would have velocity characteristic of position r while $n/4$ streaks would have velocities reflecting the top position $(r+\frac{1}{2}sw)$ and $n/4$ reflecting $(r-\frac{1}{2}sw)$. The variance, resulting from the velocity gradient, is

$$\begin{aligned}
 s^2 &= \frac{1}{n-1} \sum_{i=1}^n (\bar{V}_z - V_{z,i})^2 \\
 &= \frac{1}{n-1} \left[\sum_{i=1}^{n/2} (\bar{V}_z - \bar{V}_z)_i^2 + \sum_{i=n/2}^{3n/4} (\bar{V}_z - (\bar{V}_z + \Delta V_z))_i^2 \right. \\
 &\quad \left. + \sum_{i=3n/4}^n (\bar{V}_z + (\bar{V}_z - \Delta V_z))_i^2 \right] \\
 &\approx \frac{1}{2} (\Delta V_z)^2
 \end{aligned}
 \tag{G.3}$$

The error within one standard deviation is

$$\text{error} = V_z \pm 0.7 \Delta V_z
 \tag{G.4}$$

Taking these two sources of error into account, i.e., centering of the capillary tube and the depth of field of the camera, the error in measuring axial velocities at any radial position r was estimated from

$$\text{error} = V_z(r, z) \pm V_z(r \pm 0.55sw, z)
 \tag{G.5}$$

Equation G.5 implies that the larger the velocity gradient

the larger the error. The worst estimate of this error was obtained therefore by considering the velocity data measured in reservoir L for capillary tube 2 at a flow rate of $4.866 \text{ cm}^3/\text{sec}$ and at $Z/D = 19.73$. With the beam of light being 0.508 mm , the errors at several radial positions, i.e., $r = 0.0 \text{ cm}$, $r = 0.20 \text{ cm}$, $r = 0.40 \text{ cm}$, $r = 0.80 \text{ cm}$, $r = 1.2 \text{ cm}$, and $r = 1.6 \text{ cm}$, were 10%, 18%, 17%, 12%, 8%, and 6% respectively. Therefore, as radial distance increased the error passed through maximum; this is consistent with the velocity gradients passing through a maximum. The errors estimated at the same radial positions but at larger values of Z/D (farther upstream) were reduced substantially since the velocity gradients became smaller as Z/D increased. With capillary tube 3, the thickness of the beam of light was a smaller fraction of the diameter and the velocity gradients were not as large as those which occurred with capillary tube 2. Hence, the errors at the same flow rates and axial locations were less than those determined with capillary tube 2. In reservoir S, the maximum error at several radial and axial positions was determined with capillary tube 2 at a flow rate of $0.159 \text{ cm}^3/\text{sec}$. The magnitude of this error was comparable to the error determined in reservoir L.

In summary, the total error in measuring axial velocities is equal to the sum of the individual errors. Therefore, the error along the centerline was a maximum of 19 percent whereas, for radial locations other than along the center-

line, the error was a maximum of 47 percent. The velocities measured with the digitizer method and tabulated in Section E.2 of Appendix E were within the maximum 19 and 47 percents in reservoir L. In reservoir S, the velocities along the centerline and at radial locations other than along the centerline were within a maximum error of 15 and 25 percent respectively. The magnitude of the error in measuring the radial velocity component varied from 0.02 to 1.0 cm/sec.

G.2 DIRECT METHOD ERROR

The direct method was discussed in Chapter II, Section 2.3. Since axial velocities were measured as a continuous function of axial location along several streamlines, the main sources of error were due to (a) depth of field of camera, (b) centering of the capillary tube, and (c) the blurry ends of the streaks. The sum of these sources of error resulted in a maximum error of 12 percent along the centerline whereas, for values of r other than along the centerline but within the central core region, the maximum error was 20%.

G.3 PRESSURE TRANSDUCERS AND PRESSURE TAP ERROR

The calibration data for the four transducers are given in Appendix A, Section A.1. The resulting error was less than $1/2$ of one percent of the maximum tested pressure. No significant hysteresis was found over the full range for each diaphragm.

The presence of a pressure tap, as shown schematically

in Figure G.1, causes a deflection of the streamline into the pressure tap and an eddy or a system of eddies are set up in the pressure tap (155). The curvature of the streamline is such that the measured pressure are greater than the true values (pressures measured flush with the tube wall). The preceeding two factors combine to give a net pressure error. For a fixed flow rate, as the pressure tap size decreases ($d \rightarrow 0$) the net pressure error tends to zero (155). The pressure tap error for a finite hole size can be influenced by the hole diameter d , the fluid density ρ , the viscosity μ , and the local flow conditions at the surface. Within the boundary layer thickness the local axial velocity at a distance y away from the wall is given by

$$\frac{V_z}{\sqrt{\frac{\tau_w}{\rho}}} = f\left(\frac{y}{\nu} \sqrt{\frac{\tau_w}{\rho}}\right) \quad \text{G.6}$$

It is apparent that V_z , at a distance y , depends on τ_w , ρ , and μ . It is therefore the velocity gradient at the tube wall, described by the shear stress τ_w which defines the local flow conditions at the surface. Thus, the pressure error, ΔP_{er} , for a finite hole size can be written as

$$\Delta P_{er} = f(\tau_w, \rho, \mu, d) \quad \text{G.7}$$

or

$$\frac{\Delta P_{er}}{\tau_w} = f\left(\frac{d}{\nu} \sqrt{\frac{\tau_w}{\rho}}\right) \quad \text{G.8}$$

The dimensionless pressure error, $\Delta P_{er}/\tau_w$, was measured experimentally and plotted as a function of the Reynolds number (65, 155) based on the hole diameter (d) and frictional velocity ($\sqrt{\tau_w/\rho}$). By using these results the maximum pressure tap error was determined to be 13 dyn/cm^2 . This was considered to be negligible since the smallest measured total pressure loss, ΔP_t , was $3.089 \times 10^4 \text{ dyn/cm}^2$.

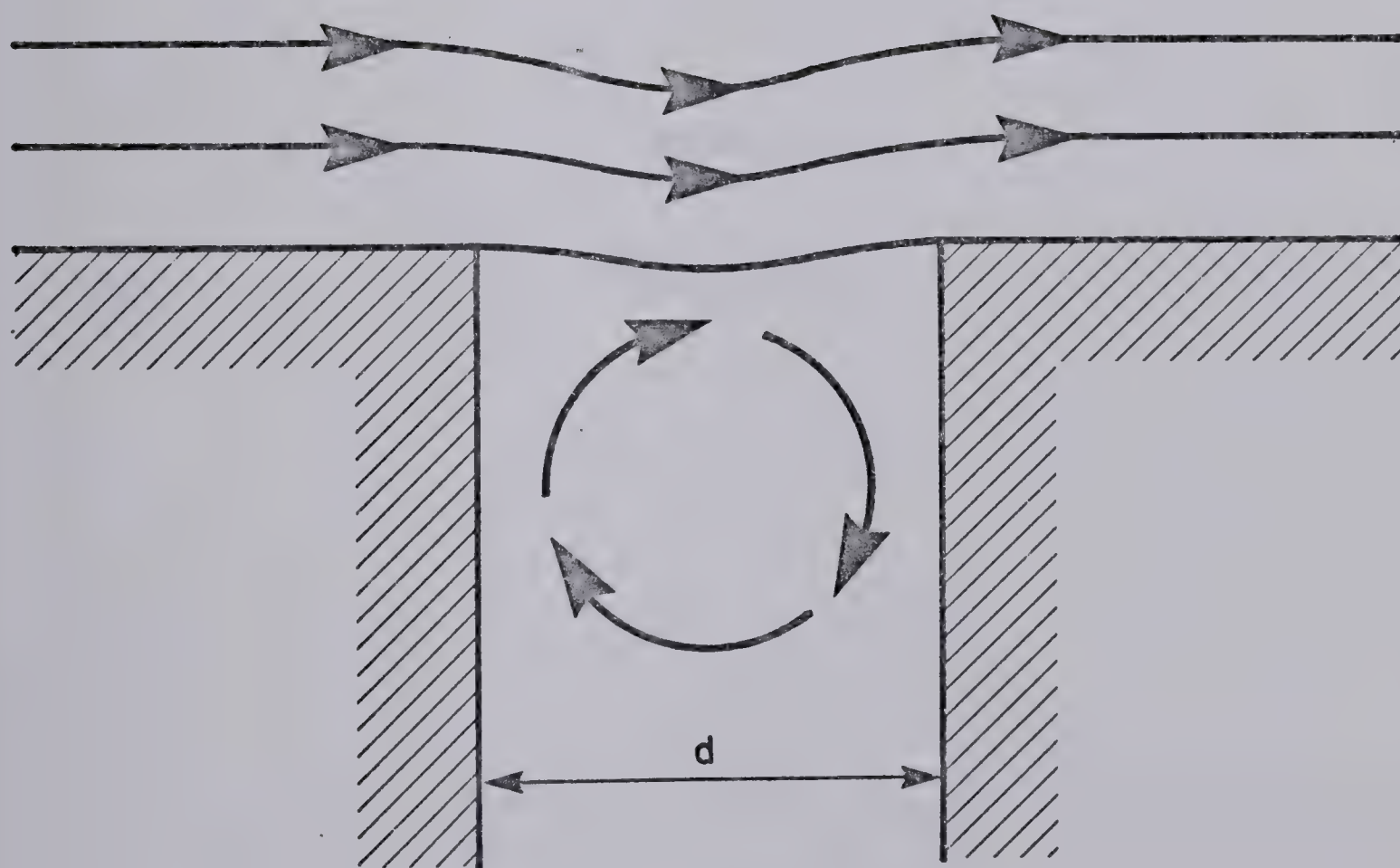
Tanner and Pipkin (163) concluded that the pressure tap error for viscoelastic solutions was proportional to the magnitude of the first normal stress difference. More recently, Novotny and Eckert (126) measured pressure tap errors for several concentrations (0.9%, 2.0% and 3.0%) of Polyox and found experimentally that the pressure tap error may be positive or negative. Based on these experimental data, the pressure tap errors are estimated to be as large as 40 percent of the magnitude of the first normal stress difference. The presence of a converging flow field within the reservoir augments the magnitude of the first normal stress difference from a value determined under SLSF conditions within the reservoir (90, 119). Therefore, evaluation of the first normal stress difference under SLSF yields a conservative estimate of this error. The apparent shear rate under SLSF in the reservoir, γ_R , in terms of the apparent shear rate in the capillary tube, is given by

$$\gamma_R = \gamma \left(\frac{D}{D_R} \right)^3$$

The maximum reservoir shear rate of 0.07 sec^{-1} occurred with capillary tube 1 at $Q=0.119 \text{ cm}^3/\text{sec}$ and from Figure D.6 (page 313) the normal stress was determined to be less than 10 dyn/cm^2 . The smallest measurement of ΔP_t , $2.2 \times 10^4 \text{ dyn/cm}^2$, was for run number 24, Table B.11 (page 268). Hence, the pressure tap error was estimated to be less than 0.05 percent. This was considered to be negligible.

FIGURE G-1

FLOW BEHAVIOUR AT PRESSURE TAP



APPENDIX H

NOMENCLATURE

a, a_1, a_2	parameters defined by Equation 3.14
A	cross sectional area of capillary tube
b	parameter defined by Equation 3.16
b_1	parameter defined by Equation 3.36
c	constant defined in Equation 3.20
C	concentration
C_1, C_2	constants in Equation 3.9
d	pressure tap diameter
D	I.D. of capillary tube
D_R	internal diameter of reservoir
EL	elasticity number, Equation 2.11
f	Fanning friction factor
$f(n')$	function defined by Equation 1.22
$f(\eta)$	dimensionless axial velocity defined by Equation 3.42
$f(\phi_0)$	function defined by Equation 3.10
G	elastic modulus, Equation 1.30
G_E	elastic modulus evaluated under extensional deformation
K	Couette correction factor
K'	Hagenbach correction factor
K_0	consistency index defined by Equation 1.15
K_1	proportionality constant defined by Equation 1.35
L	length of capillary tube
m	exponent in Equation 1.35
m_1	slope of reservoir wall relative to digitizer's X axis
M	number of streaks

MW	molecular weight
n	number of observations
n'	flow behavior index defined by Equation 1.14
N	number of slit and spokes on the chopping disc
N_{Re}	Reynolds number
N'_{Re}	generalized Reynolds number, defined by Equation 1.18
p	dimensionless parameter defined by Equation 3.9
P	pressure fluctuation
P_0	pressure measured in reservoir (Figure 1.1)
P_1	pressure measured at the contraction
P'_1	pressure defined in Figure 1.1
P^*_1	pressure defined in Figure 1.1
P_2	pressure measured in SLSF in capillary tube
\bar{P}	average pressure measured in reservoir, Equation 3.6
$(P_{11} - P_{22})_w$	primary normal stress in SLSF in capillary tube
P_{MAX}	maximum recorded pressure in reservoir
P_{MIN}	minimum recorded pressure in reservoir
P_u	pressure losses in upstream entry region, Equation 1.47
Q	volumetric flow rate
Q_c	volumetric flow rate evaluated at onset of instability
r	radial coordinate in a spherical or cylindrical coordinate system

r'	distance from reservoir wall to streak, Equation 2.4
r_0	radial location where axial velocity is equal to one half of centerline velocity
r_1	radial coordinate in spherical coordinate system where $\Gamma\theta_0$ is equal to unity
r_∞	radial location in spherical coordinate system where primary normal stress is equal to zero
R	capillary tube internal radius
R_0	universal gas constant
s	sample variance, Equation 3.3
sw	slit width
S	Hencky's strain measure, Equation 1.56
S_c	critical value of S given by Equation 3.51
S_R	recoverable shear strain
$(S_R)_M$	recoverable shear strain evaluated at fracture for polymer melts
$(S_R)_S$	recoverable shear strain evaluated at fracture for polymer solutions
t	time
t_∞	time for centerline velocity to attain 99% of fully developed centerline velocity under SLSF
$(t_\infty)_e$	experimental value of t_∞
T	absolute temperature
v	average velocity in capillary tube
v_1, v_2, v_3	velocity components in spherical coordin- ate system
$v_{1,1} _t$	stretch rate in spherical coordinates along the centerline measured upstream of the contraction

V_r	radial velocity, Equation 2.6
V_z	axial velocity in cylindrical coordinate system
$V_z _z$	axial velocity along the centerline
$V_{z,z} _z$	stretch rate in cylindrical coordinates along the centerline measured upstream of the contraction
V^*	dimensionless axial velocity, $V_z _z/V_0$
V_0	axial velocity along the centerline at the contraction
W	number of revolutions per minute
X/D	characteristic flow pattern length
X_1, X_2, X_3, X_4, X_5 X_6, X_7	coordinates defined in Figure 2.8
y	distance measured from capillary tube wall
Y_1, Y_2, Y_3, Y_4, Y_5 Y_6, Y_7	coordinates defined in Figure 2.8
z	axial distance upstream of contraction
z^*	dimensionless axial position variable, Equation 3.24
z^{**}	dimensionless axial position variable, Equation 3.39
z_0^{**}	dimensionless axial position variable where $\Gamma \theta_0 = 1.0$

Greek Symbols

α_1	proportionality constant defined by Equation 1.38
α_2	proportionality constant defined by Equation 1.34

β	contraction ratio, ratio of the area of the capillary tube to area of the reservoir
$\beta_1, \beta_2, \beta_3$	parameters defined in Equation 1.39
γ	apparent shear rate under SLSF in capillary tube
γ_R	apparent shear rate under SLSF in reservoir
$\dot{\gamma}_w$	shear rate at capillary tube wall under SLSF, Equation 1.16
Γ	stretch rate
Γ_c	stretch rate evaluated at onset of fracture
Γ_{\max}	maximum extensional stretch rate
ΔP	developed pressure loss over capillary tube length, L
ΔP_c	contraction loss
$(\Delta P_c)_{cr}$	contraction loss evaluated at onset of fracture
ΔP_d	pressure loss due to developed flow in capillary tube, Equation 1.26
ΔP_e	fraction of contraction loss due to elastic nature of fluid, Equation 1.25
ΔP_{er}	pressure tap error
ΔP_{exit}	exit pressure loss
ΔP_t	total pressure loss, Equation 1.24
ΔP_v	fraction of contraction loss due to viscous dissipation, Equation 1.27
Δr	radial distance defined by Equation 2.2
Δx	axial distance defined by Equation 2.1
ϵ_R	recoverable extensional strain
ϵ_t	end correction factor for viscoelastic fluids

ϵ_v	end correction factor for Newtonian fluids
η	dimensionless radial coordinate, r/r_0
θ	relaxation time
θ_0	zero shear relaxation time
μ	viscosity
μ_A	apparent viscosity
μ_E	elongational viscosity
μ_0	zero shear apparent viscosity
ρ	density
τ	extensional stress
$(\tau)_{cr}$	extensional stress evaluated at fracture
τ_w	shear stress at capillary tube wall under SLSF*
$(\tau_w)_c$	shear stress evaluated at onset of fracture
$(\tau_w)_M$	shear stress evaluated at fracture for polymer melts
$(\tau_w)_S$	shear stress evaluated at fracture for polymer solutions
ϕ_0	initial cone semi-angle
ϕ_R	cone semi-angles upstream of contraction
ϕ	dimensionless contraction loss (the sum of the viscous and inertial contributions)
ϕ_c	dimensionless contraction loss, viscous contribution
ϕ_H	dimensionless contraction loss, inertial contribution
ϕ_t	dimensionless contraction loss for viscoelastic fluid
χ	initial cone semi-angle measured in radians

B30192